A MULTIVARIATE ANALYSIS SEARCH FOR A SINGLE-TOP QUARK PRODUCED IN ASSOCIATION WITH MISSING ENERGY IN PROTON-PROTON COLLISIONS AT THE LARGE HADRON COLLIDER AT A CENTER-OF-MASS ENERGY OF $\sqrt{s} = 8$ TEV WITH THE ATLAS DETECTOR

By

Andrew McRae Chegwidden

A DISSERTATION

Submitted to
Michigan State University
in partial fulfillment of the requirements
for the degree of

Physics - Doctor of Philosophy

2017

ABSTRACT

A MULTIVARIATE ANALYSIS SEARCH FOR A SINGLE-TOP QUARK PRODUCED IN ASSOCIATION WITH MISSING ENERGY IN PROTON-PROTON COLLISIONS AT THE LARGE HADRON COLLIDER AT A CENTER-OF-MASS ENERGY OF $\sqrt{s} = 8$ TEV WITH THE ATLAS DETECTOR

By

Andrew McRae Chegwidden

This dissertation presents a search for single-top quarks produced in association with missing energy, denoted as monotop, using 20.3 fb^{-1} of proton-proton collision data at $\sqrt{s} = 8$ TeV recorded with the ATLAS detector. The search is conducted in two separate analyses consisting of a cut-based and a multivariate approach. As no deviation from the Standard Model prediction is observed, upper limits are set on the monotop production cross-section times branching ratio for resonant and non-resonant production of an invisible exotic state in association with a single-top quark. In the case of resonant production, for a spin-0 resonance with a mass of 500 GeV, an effective coupling strength above 0.13 is excluded at the 95% confidence level for an invisible spin-1/2 state with mass up to 100 GeV using the cut-based approach. In the case of non-resonant production, an effective coupling strength above 0.2 is excluded at the 95% confidence level for an invisible spin-1 state with mass up to 657 GeV and 799 GeV using the cut-based and multivariate approaches, respectively. In addition to setting observed limits at $\sqrt{s} = 8$ TeV, expected upper limits are set on the non-resonant production model for future levels of integrated luminosity expected to be recorded at $\sqrt{s} = 13$ TeV.

To my family...
...and to my wife

ACKNOWLEDGMENTS

No man is an island, entire of itself...

The people with whom I have chosen to surround myself have had a profound impact on my personal and professional life. The support, both emotional and technical, I have received has allowed this dissertation to come to fruition.

First, and foremost, I would like to thank my wife, Emily. You have been my rock and the source of infinite patience as I have meandered my way through this journey that is a doctoral dissertation. I am truly blessed that you are in my life and I am beyond excited to spend the rest of my life with you.

To my mother, father, and sister I would like to extend my love and to express the deep sense of happiness that I have knowing you are in my life.

I would like to acknowledge the support and guidance my advisor, University Distinguished Processor Chip Brock, has given me. You were the absolute best choice for an advisor and I would like to thank you from the bottom of my heart.

To my committee members I would like to express my gratitude for your time and effort and for reading this tome of a dissertation.

Thanks to Barbara Gonzalez for teaching me the steps necessary to complete an analysis and for showing me where the best tapas restaurant is in Geneva.

Thanks to all of the past and current graduate students with whom I shared many a late night in the office and commiserated over our coding-woes and lack of sleep.

I would also like to thank two women in particular, Brenda Wenzlick and Kim Crosslan, for helping me manage all the bureaucratic hurdles and for being my sounding board when I needed one.

TABLE OF CONTENTS

LIST OF TABLES

LIST OF FIGURES

Chapter 1

Introduction

Humans are curious creatures and it is a natural human endeavor to attempt to explain the observations we see in nature. This innate desire to understand the world around us has allowed humanity to advance beyond the stone-age, has put men on the moon, and has allowed us to build machines which can probe the very building blocks of space and time. It is this latter achievement which is the topic of this dissertation. The Large Hadron Collider, together with the ATLAS detector, has given particle physicists an invaluable tool in which to test the predictions made by the Standard Model of particle physics by colliding two beams of protons and recording the resultant collision events. It has also given the particle physics community the ability to test theories or conduct searches for particles which lie beyond the Standard Model.

This dissertation describes such a Beyond the Standard Model search for collision events with a single-top quark produced in association with missing energy, referred to hereafter as monotop events. This search uses the Large Hadron Collider data collected by the ATLAS experiment at a center-of-mass energy of 8 TeV and follows two different and distinct analysis approaches. The first is a cut-based approach where differences between signal and background topologies are exploited by placing cuts on two different kinematic variables. The results of this approach were published in [37] and represent the only published results of a search for monotop events using the ATLAS detector. An augmentation of this pub-

lished analysis is also presented where another topological cut was added onto the existing analysis to further improve the search. The second approach utilizes a multivariate analysis technique known as a Boosted Decision Tree to further improve the sensitivity of the search. Finally, this technique was also used to predict the sensitivity of this search for monotop events for the future of the experiment. To that end, this dissertation is organized into 15 chapters:

1. **Introduction**

2. **Standard Model** – This chapter describes the formalism of the Standard Model of particle physics. The particles, symmetries, and forces of the Standard Model are outlined.

3. **Beyond the Standard Model** – The limitations of the Standard Model are discussed along with the theory of monotop production.

4. **ATLAS and the LHC** – The designs of the Large Hadron Collider and the ATLAS detector are outlined. Individual sub-components of the detector are discussed in detail.

5. **Object Reconstruction** – A description of how the various physics objects are reconstructed from the raw electrical signals in the detector is presented in this chapter.

6. **Background and Signal Simulation** – This chapter describes the modeling of the signal and background processes used to compare data to background plus a potential monotop signal. The corrections which are applied to the simulations to improve the modeling are also presented.

7. **Object and Event Selection** – This chapter gives the criteria and methodologies used to select objects and events for the different analysis techniques.

8. **Systematic Uncertainties** – The sources of systematic uncertainties in the analysis are described in this chapter.

9. **Limit Setting Analysis** – This chapter describes the methodology used to evaluate the discovery limits for monotop events. A hybrid Frequentist-Bayesian procedure to calculate 95% confidence level limits on the cross-section times branching ratio for the various analysis techniques is explained.

10. **8 TeV Cut-Based Results** – The results of the published analysis along with the results of the augmentation of that analysis for the search of monotop events at 8 TeV are presented.

11. **Decision Trees** – This chapter is an overview of Decision Trees and outlines the optimization procedure of the Boosted Decision Tree's parameters.

12. **8 TeV BDT Results** – The results of the Boosted Decision Tree re-analysis of the 8 TeV data are presented in this chapter.

13. **Summary of 8 TeV Results** – This chapter serves as a summary for the different analysis techniques used for the search of monotop events at 8 TeV.

14. **Monotops at 13 TeV** – This chapter describes an analysis done using 13 TeV simulations to give predictions of future limits of monotop production.

15. **Conclusion**

Chapter 2

The Standard Model

The universe in which we live is comprised of fields. The theoretical framework which describes how these fields interact is known as Relativistic Quantum Field Theory (RQFT) and combines special relativity and quantum mechanics. Formulated in the 1960s and 1970s, the Standard Model (SM) is the application of RQFT to particle physics and describes all of the known particles and the mechanisms by which they interact with each other. While there are limitations to the SM, which will be discussed in a later chapter, the SM is considered to be one of the most successful theories in the whole of physics. That is to say it has both been able to explain almost all experimental results as well as to make successful predictions.

2.1 Standard Model particles

The SM can be broadly broken up into a theory of two different groups of particles: fermions and bosons. These two groups are distinct from each other by their value of the intrinsic quantum mechanical property spin. Fermions have half integer spin while bosons have integer spin. Fermions are also known as "matter particles" while spin-1 bosons are considered to be "force carriers" or "mediators." In all there are twelve particles of matter: six leptons and six quarks. The fermions are further grouped into three different generations organized

by their masses in Table 2.1.[1]

	Quarks			Leptons		
Gen.	Flavor	Charge	Mass [MeV]	Flavor	Charge	Mass [MeV]
I	u	2/3	$2.3^{+0.7}_{-0.5}$	e	-1	$0.510998928 \pm 0.000000011$
	d	-1/3	$4.8^{+0.5}_{-0.3}$	ν_e	0	$< 2 \times 10^{-6}$
II	c	2/3	$1.275 \pm 0.025 \times 10^3$	μ	-1	$105.6583715 \pm 0.0000035$
	s	-1/3	95 ± 5	ν_μ	0	$< 0.17 \times 10^{-6}$
III	t	2/3	$173.21 \pm 0.87 \times 10^3$	τ	-1	1776.86 ± 0.12
	b	-1/3	$4.18 \pm 0.03 \times 10^3$	ν_τ	0	$< 18.2 \times 10^{-6}$

Table 2.1: The electric charges and masses of the Standard Model fermions. For the quark charges the fractions are those of the fundamental electron charge. In this table and in the rest of this dissertation natural units are used such that $\hbar = c = 1$ [1].

The bosons are organized by the force they mediate and are shown in Table 2.2 along with their electric charges and masses.

Force	Boson	Charge	Mass [GeV]
Electromagnetic	γ	0	0
Weak	$W^\pm$	± 1	80.385 ± 0.015
Weak	Z	0	91.1876 ± 0.0023
Strong	g	0	0

Table 2.2: The electric charges and masses of the Standard Model gauge bosons [1].

2.2 Symmetries

The Standard Model is a locally invariant gauge theory which represents the fundamental particles as quantized fields. Locally invariant gauge theories have Lagrangians which are invariant with respect to local transformations of the fields. This is in contrast to global transformations which change the fields the same way at every point in space-time. Each gauge invariance leads to a conserved quantity and gauge bosons. These transformation

[1]Natural units will be used throughout this dissertation. For particle physics the natural units are such that $\hbar = c = 1$. As a result, mass and energy have the same units.

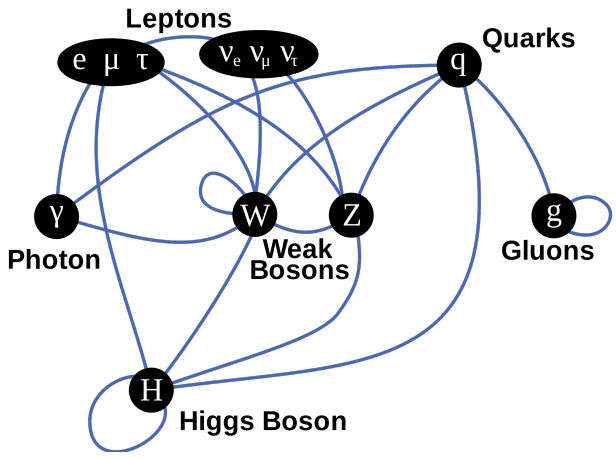

Figure 2.1: Summary of the SM particles and their interactions. The lines showing the various particle interactions are shown in blue.

invariances are described by symmetry groups. The SM is described by the combination of the three gauge symmetry groups,

$$\mathrm{SU}(3)_C \otimes \mathrm{SU}(2)_L \otimes \mathrm{U}(1)_Y \,. \tag{2.1}$$

The unbroken $\mathrm{SU}(3)_C$ group is the theory of the strong force known as quantum chromodynamics (QCD). The gauge bosons of this group are the eight massless gluons. The electromagnetic and weak interactions are unified in the unbroken gauge group of $\mathrm{SU}(2)_L \otimes \mathrm{U}(1)_Y$ whose four gauge bosons remain massless until the symmetry is broken. Once the symmetry of this combination is broken, the charged weak force ($W^{\pm}$) comes from the charged part of $\mathrm{SU}(2)_L$, while the neutral weak force (Z) comes from the linear combination of the neutral part of $\mathrm{SU}(2)_L$ and $\mathrm{U}(1)_Y$. The orthogonal combination of $\mathrm{SU}(2)_L$ and $\mathrm{U}(1)_Y$ becomes the $\mathrm{U}(1)_{\mathrm{em}}$ unbroken symmetry describing the electro-magnetic force. This is described in further detail in Section 2.3.4.1.

2.3 Standard Model Lagrangian

The Lagrangian governs the dynamics of the different fields and is defined as the difference of the kinetic and potential energies.

$$L = T - V \tag{2.2}$$

It should be noted that within the context of quantum field theory the Lagrangian *density*, $\mathcal{L}$, is used instead of the Lagrangian.[2] The relationship between the Lagrangian and its density is given by

$$L = \int \mathcal{L} \mathrm{d}^3 x. \tag{2.3}$$

The Standard Model Lagrangian can initially be split into two parts:

$$\mathcal{L}_{\mathrm{SM}} = \mathcal{L}_{\mathrm{fermion}} + \mathcal{L}_{\mathrm{gauge}}. \tag{2.4}$$

The $\mathcal{L}_{\mathrm{fermion}}$ term describes the kinetic energy of the fermions and their interactions with the gauge fields. The $\mathcal{L}_{\mathrm{gauge}}$ term describes kinetic and self-interaction terms of the gauge fields themselves. The parts of the Lagrangian associated with the Higgs boson and its interaction with the fermions, $\mathcal{L}_{\mathrm{Higgs}}$ and $\mathcal{L}_{\mathrm{Yukawa}}$ respectively, will be added later after spontaneous symmetry breaking as described in Section 2.3.4.

[2] Throughout the rest of this dissertation the term Lagrangian will be understood to mean the Lagrangian density.

2.3.1 Electromagnetic force and U(1)

The theory which describes the electromagnetic force is known as quantum electrodynamics (QED). To begin, consider the Lagrangian of a free fermion in the absence of any forces,

$$\mathcal{L} = \bar{\psi}\left(i\gamma^{\mu}\partial_{\mu} - m\right)\psi. \tag{2.5}$$

In Equation 2.5, ψ is the spinor field of the fermion of mass m and γ^{μ} are the Dirac matrices. The Lagrangian describing a gauge symmetry group must be invariant under local transformations with respect to some phase, θ. Unlike global transformations, which transform the fields the same way at every point in space-time, local transformations change the fields differently at different points in space-time. Take for example the fermion spinor field, ψ, such that a global phase transformation looks like

$$\psi \rightarrow \psi' = \exp^{-i\hat{Q}\theta}\,\psi. \tag{2.6}$$

A local phase transformation would then look like

$$\psi \rightarrow \psi' = \exp^{-i\hat{Q}\theta(x_{\mu})}\,\psi. \tag{2.7}$$

In this notation, $\hat{Q}$ is the charge operator and serves as the generator of the U(1) symmetry group and θ is an arbitrary function depending on space-time coordinates x_{μ}. The charge operator, $\hat{Q}$, is related to the fundamental electric charge by the eigenvalue equations

$$\hat{Q}\Psi = +e\Psi \qquad \text{and} \qquad \hat{Q}\overline{\Psi} = -e\overline{\Psi}. \tag{2.8}$$

The Lagrangian in Equation 2.5 is obviously invariant under a global U(1) transformation as described by Equation 2.6. This can be shown explicitly as

$$\begin{aligned}\mathcal{L}' &= \bar{\psi}' \left(i\gamma^\mu \partial_\mu - m\right) \psi' \\ &= \exp^{i\hat{Q}\theta}\, \bar{\psi} \left(i\gamma^\mu \partial_\mu - m\right) \exp^{-i\hat{Q}\theta}\, \psi \\ &= \bar{\psi} \left(i\gamma^\mu \partial_\mu - m\right) \psi \\ &= \mathcal{L}.\end{aligned} \tag{2.9}$$

The Lagrangian in Equation 2.5 is not invariant under a local U(1) transformation, as it stands. In order to make the Lagrangian invariant under a local U(1) gauge transformation, the partial derivative ∂_μ must be replaced with the gauge covariant derivative D_μ which is constructed by adding a spin-1 field $A_\mu(x)$ so that

$$D_\mu = \partial_\mu + ieA_\mu. \tag{2.10}$$

In order to remain invariant under local transformations the gauge field itself must also transform as

$$A_\mu \rightarrow A'_\mu = A_\mu + \partial_\mu \theta\big(x_\mu\big)\,, \tag{2.11}$$

which is the traditional gauge arbitrariness known from classical electrodynamics. The choice of transformation of the gauge field is arbitrary and this degree of freedom in determining the transformation allows constraints to be placed on the gauge field in a procedure known as gauge-fixing. Within QED the Lorentz covariant Lorentz gauge is often used such that

$$\partial^\mu A_\mu = 0. \tag{2.12}$$

After introducing this vector, it is treated as a physical quantum field requiring the addition of its kinetic energy in the Lagrangian. The field tensor is constructed such that,

$$F_{\mu\nu} = \partial_\mu A_\nu - \partial_\nu A_\mu, \tag{2.13}$$

which is invariant under the local transformation of Equation 2.11. The gauge invariant Lagrangian then becomes

$$\mathcal{L}_{\text{QED}} = \bar{\psi}\left(i\gamma^\mu D_\mu - m\right)\psi - \frac{1}{4}F_{\mu\nu}F^{\mu\nu}. \tag{2.14}$$

Expanding the covariant derivative gives a more easily understandable Lagrangian,

$$\mathcal{L}_{\text{QED}} = \bar{\psi}\left(i\gamma^\mu \partial_\mu - m\right)\psi - e\bar{\psi}\gamma^\mu\psi A_\mu - \frac{1}{4}F_{\mu\nu}F^{\mu\nu}. \tag{2.15}$$

The first term is simply the kinetic and mass energies of the initial free fermion. The second term is understood to be the interaction of the fermion's spinor field with the gauge field; the strength of which is given by the electric charge of the fermion, e. The final term describes the dynamics of the gauge field itself. By simply requiring that the Lagrangian be invariant with respect to local gauge transformations, a new massless field, A_μ, is introduced which is understood to be the photon. It should be noted that there is no term in the form of $A_\mu A^\mu$. Such a term would imply a photon mass but would also make the Lagrangian no longer invariant under local gauge transformations.

2.3.2 Weak force and SU(2) symmetry

The weak force is governed by the SU(2) gauge symmetry group. The Lagrangian of a free fermion can be written as

$$\mathcal{L} = \bar{\psi}\left(i\gamma^{\mu}\partial_{\mu} - m\right)\psi, \tag{2.16}$$

where $\psi = \begin{pmatrix} \psi_1 \\ \psi_2 \end{pmatrix}$ has two components. As was done with the formalism of QED, the Lagrangian of the weak force is required to be invariant under local gauge transformations in isospin space. In this symmetry group the fermion fields transform as,

$$\psi \rightarrow \psi' = \exp^{-ig\hat{T}^i\theta^i(x_\mu)}\,\psi, \tag{2.17}$$

where $\theta^i\big(x_\mu\big)$ is an arbitrary vector in isospin space, g is the coupling strength parameter, and $\hat{T}^i = \big(T^1, T^2, T^3\big)$ is the isospin operator whose components are the generators of the SU(2) symmetry transformations.

To remain gauge invariant three new gauge fields, W^i_μ, are introduced where

$$W^i_{\mu\nu} = \partial_\mu W^i_\nu - \partial_\nu W^i_\mu + g\epsilon^{ijk}W^j_\mu W^k_\nu. \tag{2.18}$$

The gauge covariant derivative, D_μ, is also introduced as

$$D_\mu = \partial_\mu + igT^iW^i_\mu, \tag{2.19}$$

and is usually written in terms of the Pauli matrices, σ^i, as

$$D_\mu = \partial_\mu + ig\frac{\sigma^i}{2}W^i_\mu, \tag{2.20}$$

where

$$T^i = \frac{\sigma^i}{2}. \tag{2.21}$$

The gauge invariant form of the W field part of the Lagrangian is chosen by introducing the term

$$\mathcal{L}_W = -\frac{1}{4} W^i_{\mu\nu} W^{i\mu\nu}. \tag{2.22}$$

The weak force Lagrangian then becomes

$$\begin{aligned} \mathcal{L}_{\text{weak}} &= \bar{\psi}\left(i\gamma^\mu D_\mu - m\right)\psi - \frac{1}{4} W^i_{\mu\nu} W^{i\mu\nu} \\ &= \bar{\psi}\left(i\gamma^\mu \partial_\mu - m\right)\psi - g\bar{\psi}\gamma^\mu \frac{\sigma^i}{2} W^i_\mu \psi - \frac{1}{4} W^i_{\mu\nu} W^{i\mu\nu}. \end{aligned} \tag{2.23}$$

Much like the Lagrangian of the U(1) symmetry group, three distinct terms can be seen. The first term gives the kinetic and mass energy terms of the fermion. The second term gives the interaction energy of the fermion with the three gauge boson fields, W^i, with strength g. The third term describes the dynamics of the gauge boson fields. The SU(2) group is not sufficient to predict the bosons' masses. More precisely, local gauge invariance with respect to SU(2) requires the bosons to have zero mass. It is known from experiment, however, that the gauge bosons do indeed have mass and so the Lagrangian of Equation 2.23 cannot correspond to reality. These bosons obtain their masses through a process called spontaneous symmetry breaking (SSB) which will be discussed Section 2.3.4.

2.3.3 Unbroken SU(2) ⊗ U(1)

The electromagnetic and weak forces unified when the symmetry $\mathrm{SU}(2)_L \otimes \mathrm{U}(1)_Y$ is conserved. The generators of this unified group are the weak hypercharge, Y, and the weak

isospin, T. Within the electroweak model the gauge fields are modeled as an isotriplet, W^i_μ with coupling g, in the $\mathrm{SU}(2)_L$ group and as an isosinglet, B_μ with coupling g', in the $\mathrm{U}(1)_Y$ group. The electroweak Lagrangian is then

$$\mathcal{L}_{\mathrm{EW}} = -\frac{1}{4}W^i_{\mu\nu}W^{i\mu\nu} - \frac{1}{4}B_{\mu\nu}B^{\mu\nu} + \bar{\psi}i\gamma^\mu D_\mu\psi, \tag{2.24}$$

where $B_{\mu\nu} = \partial_\mu B_\nu - \partial_\nu B_\mu$ and the covariant derivative is written as

$$D_\mu = \partial_\mu + i\left(g\frac{\sigma^i}{2}W^i_\mu + g'\frac{Y}{2}B_\mu\right). \tag{2.25}$$

The massless fermion fields in this theory can be broken up into their left- and right-handed chiral components,

$$\psi = \psi_{\mathrm{L}} + \psi_{\mathrm{R}}. \tag{2.26}$$

The left-handed components of the fermion fields are given as doublets in isospin space for the leptons and quarks respectively as

$$\psi^i_{\mathrm{L}} = \begin{pmatrix} \nu^i_{\mathrm{L}} \\ \ell^i_{\mathrm{L}} \end{pmatrix} \qquad \text{and} \qquad \psi^i_{\mathrm{L}} = \begin{pmatrix} u^i_{\mathrm{L}} \\ d^i_{\mathrm{L}} \end{pmatrix}. \tag{2.27}$$

The right-handed components of the fermion fields are singlets in isospin space

$$\Psi^i_{\mathrm{R}} = \ell^i_{\mathrm{R}} \qquad \text{and} \qquad \Psi^i_{\mathrm{R}} = d^i_{\mathrm{R}}; u^i_{\mathrm{R}} \tag{2.28}$$

where $i = 1, 2, 3$ and corresponds to the three generations of fermions. It should be noted that right-handed neutrinos are not allowed within the SM and that right-handed leptons

do not participate in the weak interaction.

	Generation			Quantum Numbers		
	I	II	III	T_3	Y/2	Q
Quarks	$\begin{pmatrix} u \\ d \end{pmatrix}_L$	$\begin{pmatrix} c \\ s \end{pmatrix}_L$	$\begin{pmatrix} t \\ b \end{pmatrix}_L$	$1/2$ $-1/2$	$1/6$	$2/3$ $-1/3$
	u_R	s_R	t_R	0	$2/3$	$2/3$
	d_R	c_R	b_R	0	$-1/3$	$-1/3$
Leptons	$\begin{pmatrix} \nu_e \\ e \end{pmatrix}_L$	$\begin{pmatrix} \nu_\mu \\ \mu \end{pmatrix}_L$	$\begin{pmatrix} \nu_\tau \\ \tau \end{pmatrix}_L$	$1/2$ $-1/2$	$-1/2$ $-1/2$	0 -1
	e_R	μ_R	τ_R	0	-1	-1

Table 2.3: The SM fermion fields and their quantum numbers [1].

2.3.4 Spontaneous symmetry breaking

Up until now there has been no mechanism to explain either the fermion or the gauge boson masses. Mass terms for the gauge bosons and fermions could have arbitrarily been introduced, but doing so would leave the theory non-renormalizable and not locally gauge invariant. This is because fermion masses couple left- and right-handed components, which transform differently under $\mathrm{SU(2)_L}$, while gauge boson masses explicitly break the gauge symmetry, as mentioned earlier. Introducing the $\mathcal{L}_{\mathrm{Higgs}}$ and $\mathcal{L}_{\mathrm{Yukawa}}$ terms together with the breaking of their symmetries endows the bosons and fermions with their masses, respectively, in such a way as to maintain the gauge symmetry and keep the theory renormalizable. This process is known formally as spontaneous symmetry breaking or colloquially as the Higgs mechanism.

2.3.4.1 Higgs mechanism

The additional Lagrangian term, $\mathcal{L}_{\text{Higgs}}$, has the form

$$\mathcal{L}_{\text{Higgs}} = (D^{\mu}\Phi)^{\dagger} D_{\mu}\Phi - V(\Phi)\,. \tag{2.29}$$

This mechanism introduces a weak isospin doublet of the Higgs field,

$$\Phi = \begin{pmatrix} \phi^{+} \\ \phi^{0} \end{pmatrix}, \tag{2.30}$$

where ϕ^{+} is an electrically charged field and ϕ^{0} is electrically neutral. The potential energy of the Higgs field is

$$V(\Phi) = \mu^{2}\Phi^{\dagger}\Phi + \lambda\left(\Phi^{\dagger}\Phi\right)^{2}. \tag{2.31}$$

Consider two cases, one where $\mu^{2} > 0$ and one where $\mu^{2} < 0$. In the first case, where $\mu^{2} > 0$, the potential has a unique minimum at $\Phi = 0$ which corresponds to a vacuum state of

$$\langle\Phi\rangle_{0} = \begin{pmatrix} 0 \\ 0 \end{pmatrix}. \tag{2.32}$$

This type of potential and zero energy ground state would correspond to an unbroken symmetry with a ground state that is symmetric under the U(1) and SU(2) phase rotations. The case where $\mu^{2} < 0$ leads to a potential without a unique minimum and is that of a spontaneously broken symmetry. The ground state of Φ in this case can be found by looking

for the minimum of $V(\Phi)$ and is found at

$$|\Phi| = v = \sqrt{-\frac{\mu^2}{\lambda}}, \tag{2.33}$$

where v is the vacuum expectation value (vev). The corresponding vacuum state would be

$$\langle\Phi\rangle_0 = \begin{pmatrix} 0 \\ \frac{v}{\sqrt{2}} \end{pmatrix}. \tag{2.34}$$

The choice of only allowing the neutral field to be non-zero is a consequence of the gauge choice. Any choice of vacuum related by a gauge transformation on Φ is degenerate. In the Higgs mechanism the degrees of freedom corresponding to fluctuations in these directions can be absorbed (i.e. "eaten") by the gauge bosons. The potential takes the form shown in Figure 2.2.

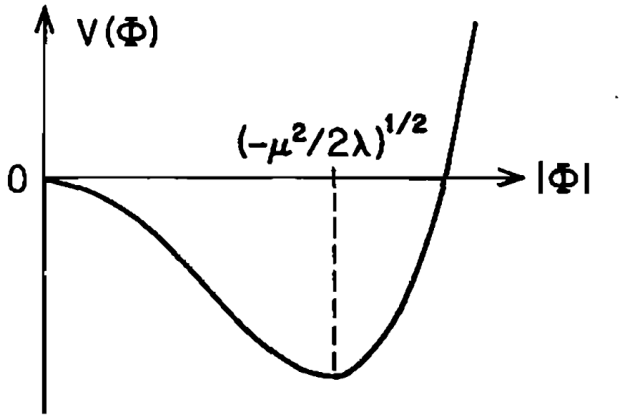

Figure 2.2: The Higgs potential and its non-zero vacuum expectation value [19].

Perturbation theory generally requires that the vev of a field to be equal to zero. Without

loss of generality the Higgs field can be expanded around the non-zero vev,

$$\Phi(x) = \frac{1}{\sqrt{2}} \begin{pmatrix} 0 \\ \\ h(x) + v \end{pmatrix}, \tag{2.35}$$

where the real field, $h(x)$, has a zero vev. Together with the definitions of the Higgs field in Equation 2.35 and the covariant derivative in Equation 2.25, the kinetic term in Equation 2.29 takes the form

$$\begin{aligned}
(D^\mu \Phi)^\dagger D_\mu \Phi &= \left| \left(\partial_\mu + ig \frac{\sigma^i}{2} W_\mu^i + ig' \frac{Y}{2} B_\mu \right) \frac{1}{\sqrt{2}} \begin{pmatrix} 0 \\ \\ v \end{pmatrix} \right|^2 \\
&= \frac{v^2}{8} \left| \left(g\sigma^i W_\mu^i + g' Y B_\mu \right) \begin{pmatrix} 0 \\ \\ 1 \end{pmatrix} \right|^2 \\
&= \frac{v^2}{8} \left| \begin{pmatrix} gW_\mu^1 - igW_\mu^2 \\ \\ gW_\mu^3 + g'YB_\mu \end{pmatrix} \right|^2 \\
&= \frac{v^2}{8} \left[g^2 \left| W_\mu^1 - iW_\mu \right|^2 + \left(gW_\mu^3 - g'YB_\mu \right)^2 \right],
\end{aligned} \tag{2.36}$$

where terms with $h(x)$ have been ignored. The physical states for the charged gauge bosons that are observed can be defined as

$$W_\mu^\pm = \frac{1}{\sqrt{2}} \left(W_\mu^1 \mp iW_\mu^2 \right). \tag{2.37}$$

The g^2 term in Equation 2.36 gives the charged gauge boson mass as

$$M_W = \frac{1}{2} vg. \tag{2.38}$$

In order to unify the electromagnetic interaction with the weak interaction, the electromagnetic term ieA_μ in Equation 2.10 must be contained within the neutral term $i\left(g\frac{\sigma^3}{2}W_\mu^3 + g'\frac{Y}{2}B_\mu\right)$ in Equation 2.25. Therefore mixing of the W_μ^3 and B_μ terms must be a linear combination of the photon field, A_μ, and another neutral field, Z_μ,

$$\begin{pmatrix} Z_\mu \\ A_\mu \end{pmatrix} = \begin{pmatrix} \cos(\theta_w) & -\sin(\theta_w) \\ \sin(\theta_w) & \cos(\theta_w) \end{pmatrix} \begin{pmatrix} W_\mu^3 \\ B_\mu \end{pmatrix}. \tag{2.39}$$

The neutral gauge bosons can then be written as

$$A_\mu = \sin(\theta_w)\, W_\mu^3 + \cos(\theta_w)\, B_\mu \tag{2.40a}$$

$$Z_\mu = \cos(\theta_w)\, W_\mu^3 - \sin(\theta_w)\, B_\mu, \tag{2.40b}$$

where θ_w is the weak mixing angle (also called the Weinberg angle) and is defined by the ratio of the electroweak coupling constants as

$$\tan(\theta_w) = \frac{g'}{g}. \tag{2.41}$$

Equations 2.40a and 2.40b can be inverted so that

$$W_\mu^3 = \cos(\theta_w)\, Z_\mu + \sin(\theta_w)\, A_\mu \qquad \text{and} \tag{2.42a}$$

$$B_\mu = \cos(\theta_w)\, A_\mu - \sin(\theta_w)\, Z_\mu. \tag{2.42b}$$

The neutral term in Equation 2.25 can then be written in terms of the neutral gauge bosons,

A_μ and Z_μ as

$$\begin{aligned} i\left(g\frac{\sigma^3}{2}W_\mu^3 + g'\frac{Y}{2}B_\mu\right) =& iA_\mu\left[g\sin(\theta_w)\,\frac{\sigma^3}{2} + g'\frac{Y}{2}\cos(\theta_w)\right] + \\ & iZ_\mu\left[g\cos(\theta_w)\,\frac{\sigma^3}{2} - g'\frac{Y}{2}\sin(\theta_w)\right]. \end{aligned} \tag{2.43}$$

Relating the first term in Equation 2.43 to the neutral term in QED, ieA_μ the values of the couplings g and g' appear as

$$g = \frac{e}{\sin(\theta_w)} \qquad \text{and} \tag{2.44a}$$

$$g' = \frac{e}{\cos(\theta_w)}, \tag{2.44b}$$

as do the relationship between charge, isospin, and hypercharge

$$Q = T^3 + \frac{Y}{2}. \tag{2.45}$$

The couplings g and g' are related to the electromagnetic coupling, e, and the neutral weak coupling, g_Z, by

$$g_Z = \frac{g'}{\sin(\theta_w)} = \frac{g}{\cos(\theta_w)} = \frac{e}{\cos(\theta_w)\sin(\theta_w)}. \tag{2.46}$$

The mass terms for the neutral gauge bosons are then

$$M_Z = \frac{1}{2}vg_Z \qquad \text{and} \tag{2.47a}$$

$$M_A = 0. \tag{2.47b}$$

The fact that the photon remains massless is indicative of the fact that the $\mathrm{U(1)_{em}}$ symmetry

is unbroken by the Higgs vacuum.

2.3.4.2 Yukawa coupling and fermion masses

The interaction between the leptons and the Higgs field, Φ, gives the leptons their masses. This is accomplished by including a $\mathcal{L}_{\text{Yukawa}}$ in the electroweak Lagrangian.

$$\mathcal{L}_{\text{Yukawa}} = -g_\ell \left[\bar{\Psi}_L \Phi \Psi_R + \bar{\Psi}_R \Phi^\dagger \Psi_L \right] \tag{2.48}$$

Breaking the symmetry again with the non-zero vev of the Higgs field in Equation 2.35 the Lagrangian becomes

$$\mathcal{L}_{\text{Yukawa},\ell} = -\frac{g_\ell v}{\sqrt{2}} \ell_R \ell_L - \frac{g_\ell}{\sqrt{2}} \ell_L h \ell_R. \tag{2.49}$$

The leptons now have both a coupling to the Higgs field (second term) as well as a mass (first term) given by

$$m_\ell = g_\ell \frac{v}{\sqrt{2}}. \tag{2.50}$$

However, the couplings, g_ℓ, remain free parameters of the theory so that the masses are not predicted and must be experimentally determined. In a similar manner, the quarks obtain their masses from the spontaneous symmetry breaking via their coupling with the Higgs field.

2.3.5 Strong force and SU(3)

Quantum chromodynamics is the theory which describes the strong force interaction between the quarks and gluons. It is constructed from the SU(3) unbroken symmetry group in an analogous way as the weak force was constructed with the SU(2) group. In the unbroken

$SU(3)_C$ group the conserved quantity is the color charge and the gauge bosons (the gluons) are massless. $SU(3)_C$ never undergoes spontaneous symmetry breaking and thus remains a conserved symmetry with massless gauge bosons. QCD is also a non-abelian gauge theory such that the generators of the group do not commute with each other but instead adhere to the Lie algebraic relationship

$$\left[T^a, T^b\right] = if^{abc}T^c, \tag{2.51}$$

where T^a are the eight generators of the group and f^{abc} are the structure constants of SU(3). The full QCD Lagrangian is written as

$$\mathcal{L}_{\text{QCD}} = \sum_{a=1}^{8} -\frac{1}{4}F_a^{\mu\nu}F_{a\mu\nu} + \sum_{\alpha=1}^{6}\sum_{j,k=1}^{3} \overline{q}_{\alpha j}\left(i\gamma_\mu D^\mu_{jk} - m_j\delta_{jk}\right)q_{\alpha k}, \tag{2.52}$$

where the summations are over the eight generators of the group (a), the six quark flavors (α), and the three color indices (j, k). $F_a^{\mu\nu}$ is the gluon field tensor given by

$$F_a^{\mu\nu} = \partial^\mu G_a^\nu - \partial^\nu G_a^\mu - g_s f_{abc} G_b^\mu G_c^\nu, \tag{2.53}$$

where G_a^μ are the gauge fields (which are understood to be the gluons) and g_s is the strong force coupling. The covariant derivative, D^μ_{jk}, in the Lagrangian is given by

$$D^\mu_{jk} = \delta_{jk}\partial^\mu + ig_s\left(T^a\right)_{jk} G_a^\mu. \tag{2.54}$$

The QCD Lagrangian is easier understood if it is broken down into three parts: a kinetic

piece, a quark-gluon interaction piece, and two gluon self-interaction pieces.

$$\mathcal{L}_{\text{kinetic}} = -\frac{1}{4}\sum_{a=1}^{8}\left(\partial_\mu G_\nu^a - \partial_\nu G_\mu^a\right)^2 + \sum_{j,k=1}^{3}\overline{q}_{\alpha j}\left(i\gamma^\mu\partial_\mu - m_j\right)\delta_{jk} \tag{2.55a}$$

$$\mathcal{L}_{\text{qqg}} = -g_s\sum_{j,k=1}^{3}\sum_{\alpha=1}^{6}\overline{q}_{\alpha j}\gamma_\mu\left(T_a\right)_{jk}q_k G_a^\mu \tag{2.55b}$$

$$\mathcal{L}_{\text{ggg}} = \frac{g_s}{2}\sum_{a,b,c=1}^{8} f_{abc}\left(\partial_\mu G_\nu^a - \partial_\nu G_\mu^a\right)\left(G_b^\mu G_c^\nu\right) \tag{2.55c}$$

$$\mathcal{L}_{\text{gggg}} = -i\frac{g_s^2}{4}\sum_{a,b,c,d,e=1}^{8} f_{abc}f_{ade}G_{b\mu}G_{c\nu}G_d^\mu G_e^\nu \tag{2.55d}$$

2.3.6 Color confinement and hadronization

Color confinement is an important aspect of QCD which is not readily apparent when looking at the Lagrangian. Color confinement requires that particles carrying the color charge do not exist in isolation. Instead, quarks and gluons exist as hadrons; either in two- or three-quark states bound together by gluons. Color confinement is the reason why bare quarks and gluons cannot be observed directly. Any bare quark originating from a scattering process combines with other color-carrying particles created spontaneously in the vacuum to form colorless hadrons in a process called hadronization. The top quark, due to its heavy mass, is special. It is the only quark which decays before it has a chance to hadronize. As will be shown Section 2.3.7, it decays almost exclusively into a b quark and W boson. It is this special property of the top quark which gives physicists the unique opportunity to study a bare quark.

2.3.7 Cabibbo-Kobayashi-Maskawa matrix

The Cabibbo-Kobayashi-Maskawa (CKM) Matrix is a unitary matrix which relates the quark mass eigenstates to the weak force eigenstates. The matrix describes the probability that one quark flavor will transition to another in weak interactions involving the $W^{\pm}$ boson.

$$\begin{pmatrix} d' \\ s' \\ b' \end{pmatrix} = \begin{pmatrix} V_{11} & V_{12} & V_{13} \\ V_{21} & V_{22} & V_{23} \\ V_{31} & V_{32} & V_{33} \end{pmatrix} \begin{pmatrix} d \\ s \\ b \end{pmatrix} \tag{2.56}$$

In this notation, the subscripts denote quark generation such that the elements describe the flavor change of a down-type quark of a given generation to an up-type quark in another (or same) generation. The choice to write the matrix in the down-type representation is arbitrary, as it can also be written so that it describes transitions from up-type quarks to down-type quarks. There are four degrees of freedom in this matrix: three angles and one CP violating phase, δ. CP stands for charge-parity and describes the idea that the laws of physics should be the same if particles are replaced with anti-particles (Charge Symmetry) while at the same time inverting the spatial coordinates (Parity Symmetry). While the strong and electromagnetic forces seem to be CP conserving processes, the weak interaction is slightly CP violating. The angles are denoted as θ_{12}, θ_{23}, and θ_{13} and correspond to rotations in $i-j$ flavor-space. Mixing between the i^{th} generation and the j^{th} generation is

zero when $\theta_{ij} = 0$. The matrix can be written in terms of these angles and phase as

$$V_{\text{CKM}} = \begin{pmatrix} c_{12}c_{13} & s_{12}c_{13} & s_{13}\exp^{-i\delta} \\ -s_{12}c_{23} - c_{12}s_{23}s_{13}\exp^{i\delta} & c_{12}c_{23} - s_{12}s_{23}s_{13}\exp^{i\delta} & s_{23}c_{13} \\ s_{12}s_{23} - c_{12}c_{23}s_{13}\exp^{i\delta} & -c_{12}s_{23} - s_{12}c_{23}s_{13}\exp^{i\delta} & c_{23}c_{13} \end{pmatrix}, \quad (2.57)$$

where $c_{ij} \equiv \cos(\theta_{ij})$ and $s_{ij} \equiv \sin(\theta_{ij})$. The current values of the matrix elements are determined by experiment [1]. They are given as

$$|V_{\text{CKM}}| = \begin{pmatrix} 0.97425 \pm 0.00022 & 0.2253 \pm 0.0008 & 0.00413 \pm 0.00049 \\ 0.225 \pm 0.008 & 0.986 \pm 0.016 & 0.0411 \pm 0.0013 \\ 0.0084 \pm 0.0006 & 0.0400 \pm 0.0027 & 1.021 \pm 0.032 \end{pmatrix}. \quad (2.58)$$

Important to the analysis in this dissertation are the elements involving the top quark, $\left|V_{t\{b,s,d\}}\right|$. The transition probability of a top quark changing flavor to a d or s quark is quite small as evident by the small values of the off-diagonal matrix elements V_{td} and V_{ts} (V_{31} and V_{32}). It is therefore assumed that all top quarks decay into a W boson and a b quark in the remainder of this dissertation.

2.4 Summary

The predictions made by the Standard Model have been verified by numerous experiments. The discovery of the Higgs Boson in 2012 was the final particle predicted by the SM to be observed by experiment and was heralded as a crowning achievement of the theory. Numerous other predictions made by the SM, such as the anomalous magnetic dipole of the electron, have agreed with experimental observations to astonishingly accurate precision. As accurate

as the theory is as a model of reality, it is still an incomplete theory. Some of the limitations of the SM will be explained in the following chapter.

Chapter 3

Beyond the Standard Model

The Standard Model of particle physics is an astonishingly accurate theory. However, particle physicists have known for some time that the theoretical framework which they use to explain the way all the known particles in our universe interact is flawed, or at the very least, incomplete. Limitations of the SM are well-known and many theories have been developed in attempts to address them. Usually these theories, colloquially known as Beyond the Standard Model (BSM) theories, involve some sort of simple extension. In these types of theories new particles or couplings are introduced to explain phenomena or observations that the SM is incapable of explaining.

The inability to incorporate the gravitational force into the formulation of the SM is one such limitation of the theory. If the gravitational force were to be incorporated into the SM then it would need a spin-2 force carrier to mediate it, the graviton. If the graviton does indeed exist then a potential quantum theory of gravity could be included in the SM.

The SM provides no explanation as to what may happen at energies approaching that of the grand unification theory (GUT) scale. This is the hypothetical scale at which the coupling constants of the electromagnetic, weak, and strong forces might become equal in strength and and such grand unification theories postulate that the symmetry groups of the SM originate from a higher symmetry that is unbroken at that scale. While this is the realm of theoretical physics as the energies in question are beyond what experiments are currently able to probe,

it is nonetheless a limitation of the SM.

The SM also leaves physicists with many other unanswered questions. Why are the physical masses we observe for particles so sensitive to the parameters of the model (fine tuning problem)? How can relatively light mass scales like M_W, M_Z, or M_H arise naturally in the SM where the GUT scale is so much larger (hierarchy problem)? Why is the SM not a "natural" theory in that the parameters of the theory span many orders of magnitude ("un"-naturalness problem)? All of these questions are related to one another and are not answered by the SM.

Perhaps one of the most glaring limitations of the SM is its inability to describe nearly 95% of the mass-energy content in the observable universe, the so-called "dark sector." Astronomical observations of galaxies and supernovae have shown that the amount of mass-energy which is able to be described by the SM is only roughly 5% of the total mass-energy in the universe. This means the most successful theory in the history of physics is only able to describe and make predictions concerning a small portion of the universe. The dark sector is postulated to be comprised of both dark matter and dark energy. There are many theories describing what dark matter could be and numerous experiments are actively looking for evidence of its existence. Dark matter does not have a clearly stated definition and can be loosely defined as matter which is massive and has, at most, a very weak coupling to the SM particles. Experiments such as the Large Underground Xenon dark matter experiment (LUX) [38] attempt to directly detect an interaction of a dark matter particle with its active medium while collider experiments attempt to detect the inference of dark matter particles as missing energy in a collision. While neither experimental approach has yet to succeed in detecting any evidence of dark matter, it is generally accepted that it does exist. The theory described in this chapter could, in some interpretations, be considered a theory of

dark matter and evidence of its existence could begin to shed light on the dark sector.

3.1 Extensions of the Standard Model

Developing BSM theories can generally follow one of two routes. The first route is a top-down approach where a theory is proposed such that the SM is extended to address an unsolved issue. Such a theory can then make predictions through the use of perturbation theory or by exploiting its symmetries by introducing new un-fixed parameters which determine an expected signature at collider experiments. Many BSM theories follow this approach where they seek to explain what the SM cannot by introducing new symmetries and their corresponding particle states. The canonical example of such a theory is the Minimal Supersymmetric Standard Model (MSSM). The MSSM theory predicts that every SM particle has a supersymmetric partner and, in some interpretations of this theory, those supersymmetric partners might be considered as dark matter candidates. Theories of this nature are accompanied by limitations, however. Many times top-down theories have numerous free parameters which must be determined by experiment. In the case of MSSM there are numerous free parameters and benchmark choices of these parameters must be made to simplify the experimental tests of the theory. Even then, a specific signature is not indicative of a specific choice of model parameters.

The second route is a bottom-up approach. In this route, a desired experimental signature is chosen and a "model" is built up which can give rise to such a signature. The search in this dissertation follows such an approach.

3.2 Monotop production in hadron collisions

Several models predict the production of events with large missing energy due to hypothetical particles escaping detection associated with a single reconstructed object. In most analyses the single reconstructed object is a photon [39, 40], a jet [41, 42], or a W or Z boson [43, 44]. Such analyses are called mono-X searches. A cartoon drawing of such a mono-X process is shown in Figure 3.1.

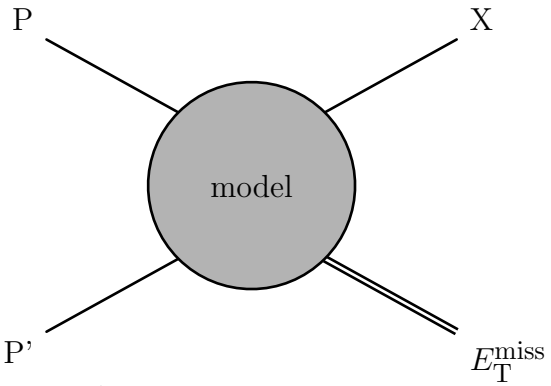

Figure 3.1: A cartoon drawing showing a mono-X type process. Two incoming particles interact to produce a single reconstructed object, X, and missing transverse energy, $E_{\mathrm{T}}^{\mathrm{miss}}$.

The search for singly produced top quarks in association with large missing energy follows the spirit of these searches. "Monotop" events have the benefit of a cleaner experimental signature than generic mono-jet models. In monotop events the flavor of the quark final state is fixed which limits the possibilities of partons in the initial state.

3.3 Monotop production in the Standard Model

The SM does not allow for a tree-level production of monotop events without the presence of additional quarks in the final state as such a process would violate baryon number

conservation.[1] Baryon number, defined as

$$B = \frac{1}{3}\left(n_q - \bar{n}_q\right), \tag{3.1}$$

is a conserved quantum number in the SM. It is possible, however, to produce a SM monotop event through a loop-induced associate production of a single-top quark in association with a Z boson decaying into a $\nu\bar{\nu}$ pair as is shown in Figure 3.2.

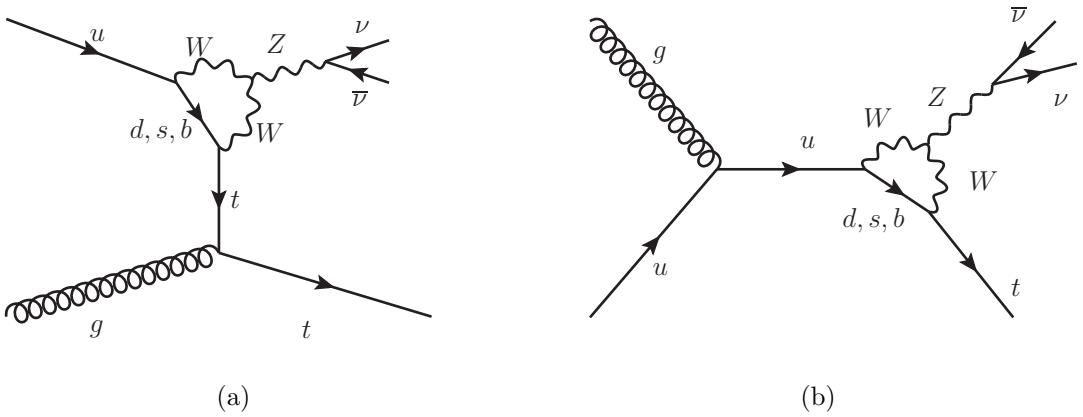

(a) (b)

Figure 3.2: Feynman diagrams of (a) t-channel and (b) s-channel loop-induced associate production of a single-top quark and a Z boson decaying into a $\nu\overline{\nu}$ pair in the SM.

However, such events are suppressed by the Glashow-Ilipoulos-Maianai (GIM) mechanism and two factors of off-diagonal CKM matrix elements [45]. The GIM mechanism is responsible for suppressing flavor-changing neutral current (FCNC) interactions such as neutral kaon decay, shown in Figure 3.3.

[1] "Tree-level" refers to Feynman diagrams which do not contain any closed loops.

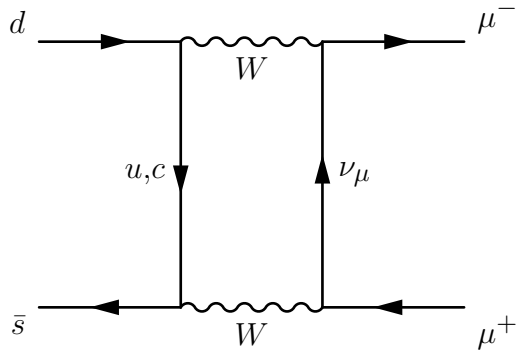

Figure 3.3: The decay process $K^0 \to \mu^+\mu^-$. The contribution to the amplitude of the diagram with the u quark is almost exactly cancelled by the contribution of the diagram with the c quark by a factor of $(m_c^2 - m_u^2)/m_W^2$. This mechanism typically suppresses FCNC interactions needed for SM monotop production. Any evidence of monotop events at tree-level would then be a clear sign of physics beyond the SM.

3.4 Monotop production in BSM theories

Monotop production in BSM theories generally falls into one of two classes. In the first class, a bosonic resonance is produced by two down-type anti-quarks and decays into a top quark and a neutral exotic fermion which violates baryon number conservation. In some SU(5) models, the resonance is a leptoquark which decays into a top and an anti-neutrino $\left(\bar{d}\bar{d} \to V \to t\bar{\nu}\right)$ [46]. In certain SUSY models baryon number and lepton number are no longer conserved. Such models have couplings which violate the conserved quantity

$$R = (-1)^{3B+L+2S}, \tag{3.2}$$

where B is baryon number, L is lepton number, and S is spin. In such R-parity violating models the resonance is a top squark decaying into a top quark and a missing neutralino $\left(\bar{d}\bar{d} \to \tilde{t}_i \to t\tilde{\chi}_0^1\right)$ [47].

In a second class of theories, such events are produced through a non-resonant process where a single-top quark is produced in association with a neutral boson that has flavor-changing couplings to the top and light quarks [48]. In R-parity conserving SUSY models, this would

occur with a cascade production of a neutralino pair $\left(ug \to \tilde{u}_i\tilde{\chi}_0^1 \to t\tilde{\chi}_0^1\tilde{\chi}_0^1\right)$ giving rise to missing energy and a single-top quark [49]. In other models, the neutral boson, produced through a *u*-*t* or *c*-*t* coupling, decays into neutral stable particles [50, 51, 52, 53].

3.5 Monotop models

Four different production modes, two resonant and two non-resonant, which would give rise to monotop signatures are investigated in this dissertation.

- **S1** – a spin-0 color triplet +2/3 boson resonance produced by the annihilation of two down-type anti-quarks, and decaying into a top quark and a spin 1/2 neutral fermion;
- **S2** – a spin-1 color triplet +2/3 boson resonance produced by the annihilation of two down-type anti-quarks, and decaying into a top quark and a spin 1/2 neutral fermion;
- **S3** – a spin-0 color singlet neutral boson produced by non-resonant quark-gluon fusion in association with a top quark; and
- **S4** – a spin-1 color singlet neutral boson produced by non-resonant quark-gluon fusion in association with a top quark.

The names of these models follow the convention used in [54].[2] Models S1 and S2 are resonant production modes involving baryon number violating processes while the S3 and S4 models are non-resonant processes involving FCNCs.

[2] In [55], the S1, S2, S3, and S4 scenarios are named SII.s, SII.v, SI.s, and SI.v respectively.

3.5.1 Resonant production mode

The baryon-violating S1 and S2 models can be constructed through the Lagrangians shown in Equations 3.3 and 3.4,

$$\mathcal{L}_{S1} = \epsilon^{ijk}\epsilon^{\alpha\beta\gamma}\varphi_\alpha \bar{d}^{i,c}_\beta \left[(a^q_{SR})_{ij} + (b^q_{SR})_{ij}\gamma_5\right] d^j_\gamma + \varphi_\alpha \bar{u}^{\alpha,k}\left[(a^{1/2}_{SR})_k + (b^{1/2}_{SR})_k\gamma_5\right]\chi + h.c., \tag{3.3}$$

$$\mathcal{L}_{S2} = \epsilon^{ijk}\epsilon^{\alpha\beta\gamma}X_{\mu,\alpha}\bar{d}^{i,c}_\beta \left[(a^q_{VR})_{ij} + (b^q_{VR})_{ij}\gamma_5\right]\gamma^\mu d^j_\gamma + X_{\mu,\alpha}\bar{u}^{\alpha,k}\left[(a^{1/2}_{VR})_k + (b^{1/2}_{VR})_k\gamma_5\right]\gamma^\mu\chi' + h.c.\ . \tag{3.4}$$

The tree-level Feynman diagrams for these resonant monotop Lagrangians are shown in Figure 3.4.

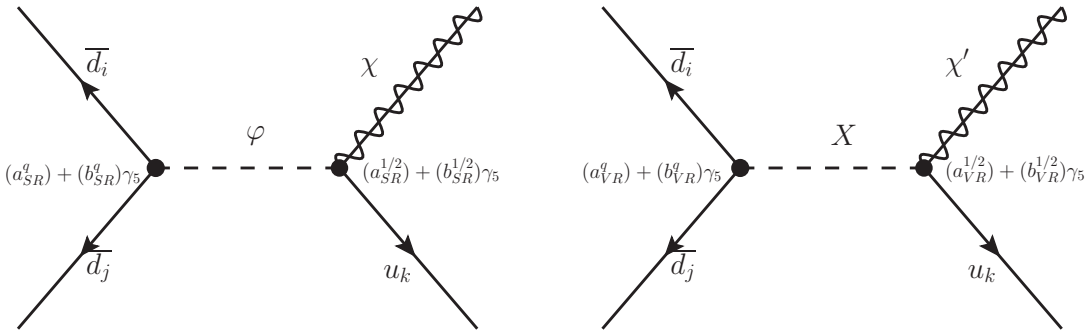

Figure 3.4: Feynman diagrams of tree-level order processes leading to monotop events for the (a) S1 and (b) S2 models. The black-dot vertices indicate exotic couplings, whose structures are given with the notations used in Equations 3.3 and 3.4, with implicit generation indices.

In Equations 3.3 and 3.4 exotic couplings and fields are introduced. The indices $\{\alpha, \beta, \gamma\}$ run over the color charge, while the indices $\{i, j, k\}$ run over generations. The BSM fields φ and X represent the spin-0 and spin-1 boson resonances in the S1 and S2 models respectively. The BSM fields χ and χ' represent spin-1/2 fermions from the decay of the φ and X resonances.

The general couplings are matrices whose elements span over the three generations of matter. The ones labeled a are scalar or vector couplings and the ones labeled b are pseudo-scalar or pseudo-vector couplings. These are denoted by the subscript SR and VR respectively. $\epsilon^{\alpha\beta\gamma}$ (ϵ^{ijk}) is the fully anti-symmetric tensor and has color (generation) indices. The couplings $(a^q)_{ij}$ and $(b^q)_{ij}$ describe the interaction of two down-type anti-quarks of generations i and j to the colored resonance: φ for the S1 model and X for the S2 model. The fully anti-symmetric tensor, ϵ^{ijk}, necessarily requires that the scalar and pseudo-vector couplings vanish for identical generations of initial partons. In order to produce the monotop topology the up-type quark produced with the neutral fermions χ and χ' would be the third generation top quark, so that $k = 3$. For this reason we see that $\left(a_{SR}^{1/2}\right)_k = \left(b_{SR}^{1/2}\right)_k = 0$ for the S1 model and $\left(a_{VR}^{1/2}\right)_k = \left(b_{VR}^{1/2}\right)_k = 0$ for the S2 model if $k = 1$ or $k = 2$.

3.5.2 Non-resonant production mode

The S3 and S4 models of monotop production involve FCNC processes. While such processes are not strictly forbidden in the SM, they are highly suppressed by the GIM mechanism and evidence of such processes would point to physics beyond the SM. The Lagrangians describing these two models are shown in Equations 3.5 and 3.6,

$$\mathcal{L}_{S3} = \phi \bar{u}^i \left[\left(a_{FC}^0\right)_{ij} + \left(b_{FC}^0\right)_{ij} \gamma_5 \right] u^j + h.c., \tag{3.5}$$

$$\mathcal{L}_{S4} = V_\mu \bar{u}^i \left[\left(a_{FC}^1\right)_{ij} + \left(b_{FC}^1\right)_{ij} \gamma_5 \right] \gamma^\mu u^j + h.c.\ . \tag{3.6}$$

The tree-level Feynman diagrams for these non-resonant monotop Lagrangians are shown in Figure 3.5.

In Equations 3.5 and 3.6 exotic couplings and fields are again introduced. The fields ϕ and V

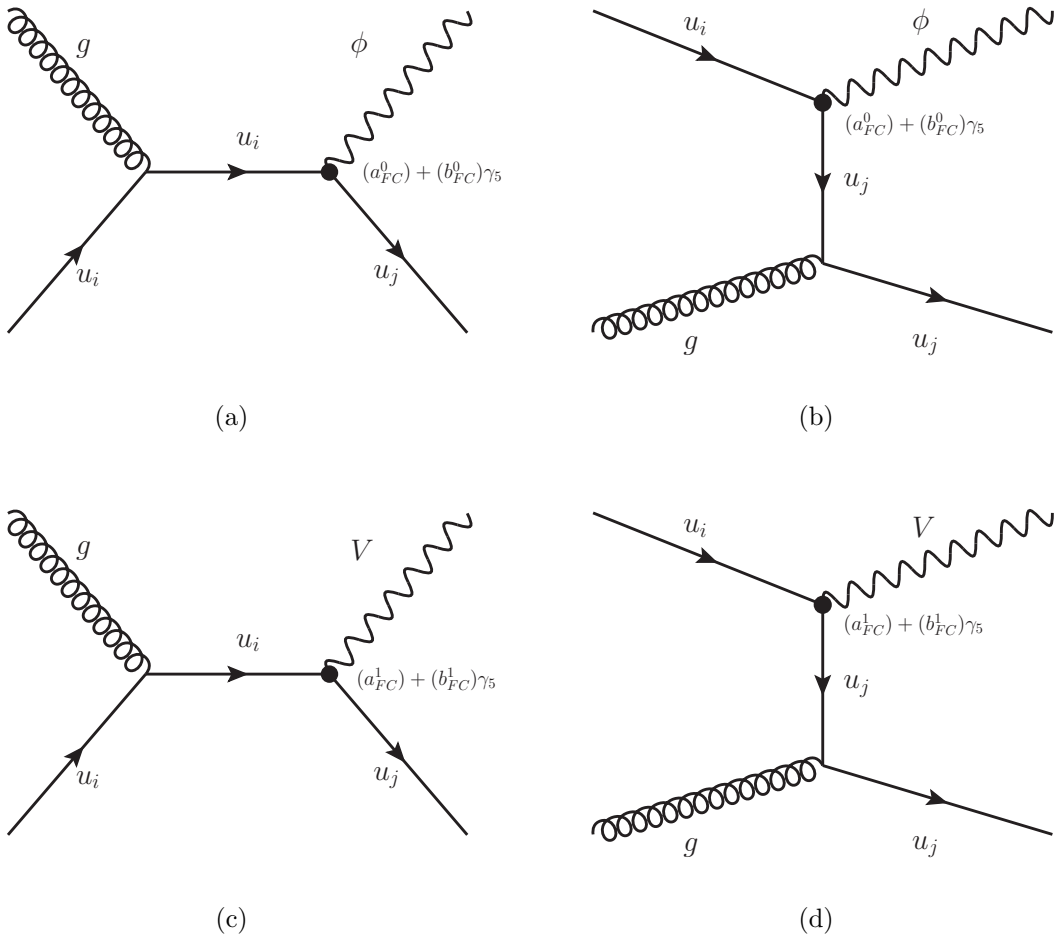

Figure 3.5: Feynman diagram of tree-level order processes leading to monotop events for the (a) s- and (b) t-channel in the S3 model, and (c) s- and (d) t-channel in the S4 model. The black-dot vertices indicate exotic couplings, whose structures are given with the notations used in Equations 3.3 through 3.6, with implicit generation indices.

represent the spin-0 and spin-1 neutral bosons of the S3 and S4 models respectively.[3] Non-zero couplings $\left(a^0_{FC}\right)_{ij}$, $\left(b^0_{FC}\right)_{ij}$, $\left(a^1_{FC}\right)_{ij}$, and $\left(b^1_{FC}\right)_{ij}$ would allow the FCNC interaction between two up-type quarks of generations i and j and the neutral bosons. Like was done in the S1 and S2 models, the couplings are taken to be zero when both the generation indices do not correspond to the top quark, i.e when $i \neq 3$ and $j \neq 3$.

[3]Notice that ϕ in Equation 3.5 is a different field than φ in Equation 3.3.

3.5.3 Model refinement

The models can be further refined by strictly enforcing gauge invariance to the SM symmetry group $\mathrm{SU}(3)_C \otimes \mathrm{SU}(2)_L \otimes \mathrm{U}(1)_Y$. This implies that each introduced field must be a member of the $\mathrm{SU}(2)_L \otimes \mathrm{U}(1)_Y$ electroweak gauge group such that exotic particles must be $\mathrm{SU}(2)_L$ singlets, doublets, or triplets. In the case where the exotic particles are doublets or triplets, additional particles would need to be introduced in the models with non-zero electric charge. Several strong constraints on the parameters of this extended model would also be needed in order to describe monotop events. The structure of the couplings are also constrained by the spin of the exotic boson. The couplings involving a spin-0 boson connect two fermions of opposite chiralities, left or right, while the couplings of a spin-1 boson connect fermions of the same chirality [48]. Taking these considerations into account there are only two remaining models that are considered

- **$\mathbf{S1_R}$** – resonant production of a +2/3 charged spin-0 boson decaying into a right-handed top quark and a neutral spin-1/2 fermion and
- **$\mathbf{S4_R}$** – non-resonant production of a neutral spin-1 boson in association with a right-handed top quark.

The reduced Lagrangians are then

$$\mathcal{L}_{\mathrm{S1_R}} = \epsilon^{ijk}\epsilon^{\alpha\beta\gamma}\varphi_\alpha \bar{d}^{i,c}_{\beta,R}\left(a^{q}_{\mathrm{S1_R}}\right)_{ij} d^{j}_{\gamma,R} + \varphi \bar{u}^{k}_{R}\left(a^{1/2}_{\mathrm{S1_R}}\right)_{k}\chi + h.c. \tag{3.7}$$

$$\mathcal{L}_{\mathrm{S4_R}} = \left(a_{\mathrm{S4_R}}\right)_{ij} V_\mu \bar{u}^{i}_{R}\gamma^\mu u^{j}_{R} + h.c., \tag{3.8}$$

where

$$\left(a^q_{\mathrm{S1_R}}\right)_{ij} = 2\left(a^q_{\mathrm{SR}}\right)_{ij} = 2\left(b^q_{\mathrm{SR}}\right)_{ij} \tag{3.9}$$

$$\left(a^{1/2}_{\mathrm{S1_R}}\right)_k = 2(a^{1/2}_{\mathrm{SR}})_k = 2(b^{1/2}_{\mathrm{SR}})_k \tag{3.10}$$

$$\left(a_{\mathrm{S4_R}}\right)_{ij} = 2\left(a^1_{\mathrm{FC}}\right)_{ij} = 2\left(b^1_{\mathrm{FC}}\right)_{ij}. \tag{3.11}$$

For the $\mathrm{S1_R}$ model, the anti-symmetric tensor, ϵ^{ijk}, requires that the resonance only be produced by two down-type quarks of different generations. Further constraints on the coupling of the resonance to the two initial state partons arise from $K^0 - \overline{K^0}$ mixing. A representative Feynman diagram for $K^0 - \overline{K^0}$ mixing is shown in Figure 3.6.

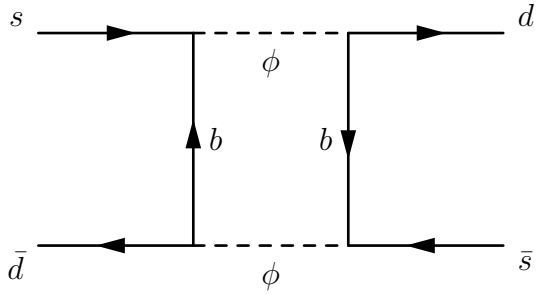

Figure 3.6: Representative Feynman diagram for $K^0 - \overline{K^0}$ mixing.

It is shown in [20] that the $K^0_L - K^0_S$ mass difference, Δ_{m_K}, arising from new physics and SM contributions places limits on the coupling parameters of the resonance to the two initial state partons. Specifically, it is shown that the coupling strength of the resonance to a first and third or a second and third generation initial state is limited if it is assumed that the sum of the SM and BSM contributions to Δ_{m_K} do not exceed the experimental value by more than 1σ. Figure 3.7 shows the allowed coupling values of the resonance to third generation quarks in the initial state for masses of the resonance less than 2 TeV with this constraint in mind [20].

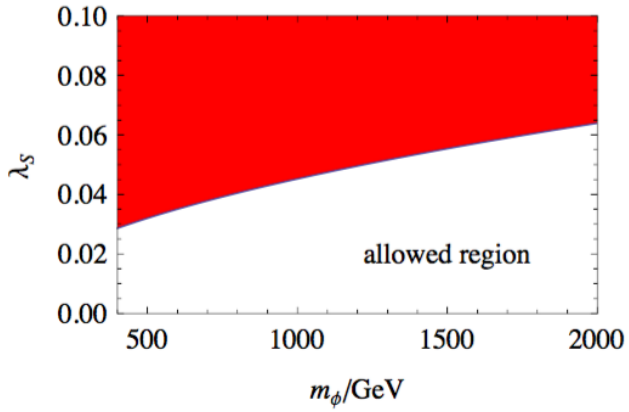

Figure 3.7: The allowed values of the coupling parameter involving a third generation initial state parton to the resonance, λ_S, as a function of the resonance mass, m_ϕ. This notation corresponds to $\lambda_S = (a^q_{\mathrm{S1_R}})_{13} = (a^q_{\mathrm{S1_R}})_{23}$. It should also be noted that m_ϕ in the figure is the mass of the scalar resonance and corresponds to m_φ in the $\mathrm{S1_R}$ model [20].

Furthermore the parton distribution functions involving third generation quarks are small compared with those of the first two generations. For these reasons it is assumed that

$$\left(a^q_{\mathrm{S1_R}}\right)_{i3} = \left(a^q_{\mathrm{S1_R}}\right)_{3j} = 0. \tag{3.12}$$

To simplify the model further it is assumed that the non-zero exotic couplings of both models are equal. All couplings are then labeled as

$$a_{\mathrm{R}} \equiv \left(a^q_{\mathrm{S1_R}}\right)_{12} = \left(a^q_{\mathrm{S1_R}}\right)_{21} = \left(a^{1/2}_{\mathrm{S1_R}}\right)_3 = \left(a_{\mathrm{S4_R}}\right)_{13} = \left(a_{\mathrm{S4_R}}\right)_{31}. \tag{3.13}$$

The final Lagrangians of the two models are then

$$\mathcal{L}_{\mathrm{S1_R}} = \epsilon^{ijk}\epsilon^{\alpha\beta\gamma}\varphi_\alpha \bar{d}^{i,c}_{\beta,R} a_{\mathrm{R}} d^j_{\gamma,R} + \varphi \bar{t}_R a_{\mathrm{R}} \chi + h.c. \tag{3.14}$$

$$\mathcal{L}_{\mathrm{S4_R}} = a_{\mathrm{R}} V_\mu \bar{u}_R \gamma^\mu t_R + h.c.\ . \tag{3.15}$$

The corresponding Feynman diagrams are shown in Figure 3.8.

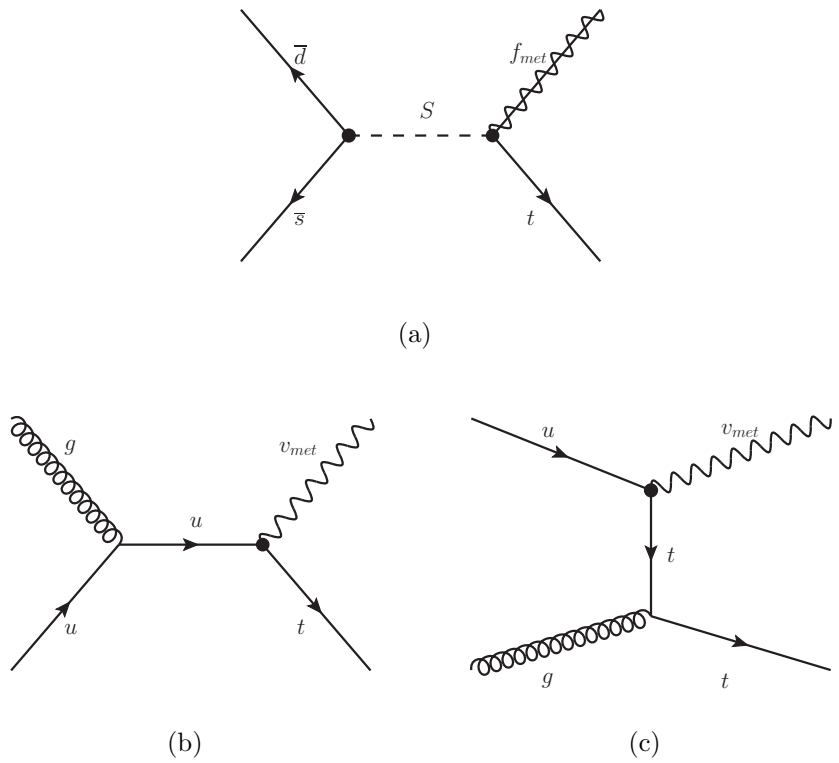

Figure 3.8: Feynman diagrams of tree-level order processes leading to monotop events: (a) production of a colored scalar resonance S decaying into a top quark and a spin-1/2 fermion, f_{met}, in the S1_{R} model, (b) s- and (c) t-channel non-resonant production of a top quark in association with a spin-1 boson, v_{met}, in the S4_{R} model. The black-dot vertices indicate the exotic coupling a_{R}.

The scalar resonance is named S and the neutral spin-1/2 fermion is named f_{met} in the S1_{R} model and the neutral spin-1 boson is named v_{met} in the S4_{R} model. The quantum numbers of the exotic particles are summarized in Table 3.1.

3.5.4 Invisible particle decay modes

The values of the model parameters which must be chosen are the mass of the scalar resonance, $m(S)$, the masses of the final state exotic particles, $m(f_{\text{met}})$ and $m(v_{\text{met}})$, and the value of the exotic coupling, a_{R}. The choices of these parameters are motivated by both

Model	Particle	Spin	Electric charge	Anti-particle	Hypercharge	Color multiplicity
$S1_R$	S	0	+2/3	$\overline{S}$	+2/3	triplet
	f_{met}	1/2	0	f_{met}	0	singlet
$S4_R$	v_{met}	1	0	v_{met}	0	singlet

Table 3.1: Names and quantum numbers of the exotic particles in the $S1_R$ and $S4_R$ models.

physics as well as experimental considerations. The f_{met} and v_{met} particles are assumed to result in missing transverse energy as their experimental signature and it is important to understand their possible decay modes.

3.5.4.1 f_{met} decay

The f_{met} particle can decay into a top quark and the scalar resonance, S, as shown in Figure 3.9. If the mass of the resonance, $m(S)$, is greater than the sum of the masses of the top quark and the f_{met} particle, then this decay mode would be extremely off-shell. This has the effect of making the decay width of the f_{met} particle small compared to its mass. The ATLAS detector has dimensions on the order of a few meters for the Inner Detector, calorimeters, and muon spectrometer. For $m(S) = 500$ GeV and a coupling value of $a_R = 0.2$ the decay length of the f_{met} particle is longer than these dimensions if $m(f_{met}) < 80$ GeV [20]. This is shown in Figure 3.10. Furthermore, searches using the ATLAS detector have shown that the efficiency of detecting displaced vertices further than 0.35 m from the interaction point is nearly zero [56]. It is therefore assumed that for $m(f_{met}) < 100$ GeV any decay would occur outside the detector and/or would not be fully reconstructed and thus would register as missing transverse energy in the detector.

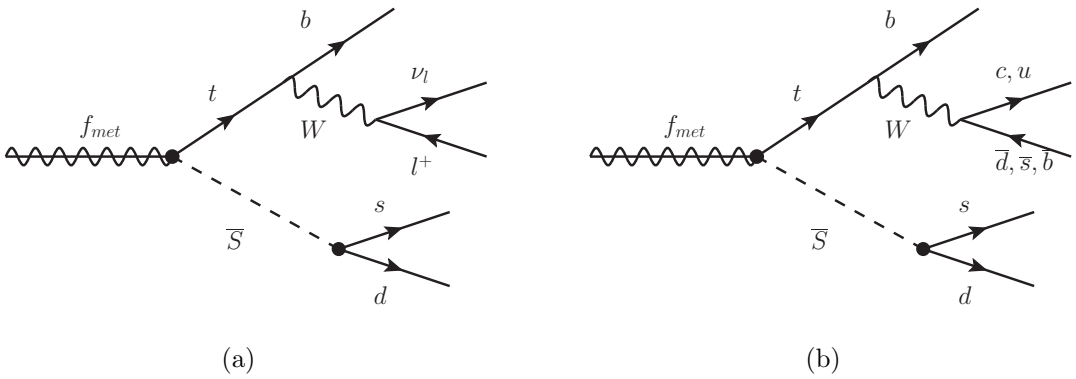

Figure 3.9: Feynman diagrams of the 2-body decay of the spin-1/2 invisible fermion f_{met} in the S1_R model in the (a) semi-leptonic and (b) fully-hadronic channels.

3.5.4.2 v_{met} decay

Depending on its mass, the v_{met} particle can have multiple decay modes inside the detector which depend on the relative masses of the top quark and the mass of the v_{met} particle. If $m(v_{\text{met}}) > m(t)$ then the v_{met} particle can decay into a $\overline{u}$-t pair via a tree-level process or into a q-q' pair through a loop process if $m(v_{\text{met}}) < m(t)$. These decay modes are shown in Figure 3.11.

Another possibility is that the v_{met} particle decays into a set of stable invisible particles, $v_{\text{met}} \rightarrow \chi\chi$, making it part of a "dark sector" not described by the S4_R Lagrangian in Equation 3.15. This decay mode is preferred as it retains the monotop topology. In order to retain the monotop topology the decay modes shown in Figure 3.11 must be constrained by limiting the parameters of the non-resonant Lagrangian described in Equation 3.15. These constraints on the parameters of the Lagrangian have an interplay with bounds originating from the relic density of dark matter in the universe. If χ is a stable particle and the only mediator of interactions between the SM and the dark section is v_{met}, then the annihilation process $\chi\chi \rightarrow v_{\text{met}} \rightarrow t\bar{u}$ and $\bar{t}u$ solely determines the relic abundance of χ.[4] In the case

[4]The dark matter relic abundance can be calculated through analytic solutions of the Boltzmann equation

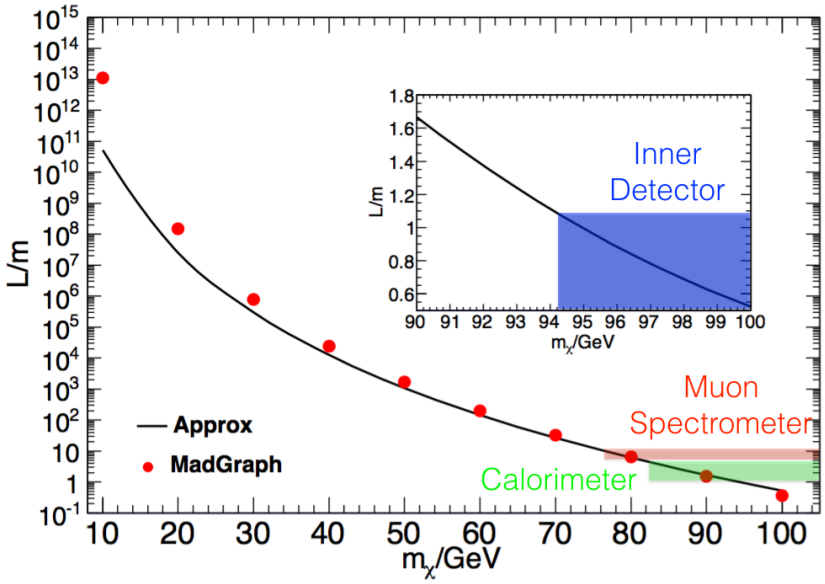

Figure 3.10: The decay length of the f_{met} particle as a function of its mass. The lengths shown are for a coupling value of $a_{\text{R}} = 0.2$ and a mass of the scalar resonance of $m(S) = 500$ GeV. Also shown are the radial dimensions of various detector subsystems [20].

where the mass of the v_{met} particle is less than the top quark mass, the annihilation process is kinematically forbidden so that the annihilation of dark matter particles can only proceed through three or four-body final states via a virtual top quark. The cross-sections of these processes are suppressed by the loop factors such that the annihilation process is too slow and χ would overpopulate the universe. If the mass of the v_{met} particle is larger than the top quark mass then two-body final states are allowed. However, the observed relic abundance requires that the couplings be fairly large in this case, which would again cause χ to overpopulate the universe in the light mass region. It is therefore required that a_{R} be small enough so as not to cause an overpopulation of χ when compared to the observed relic abundance. Values of a_{R} smaller than 0.5 are reasonable. It should be noted that the smaller a_{R} becomes, the more difficult it is to detect the monotop signal.

as was done in [48].

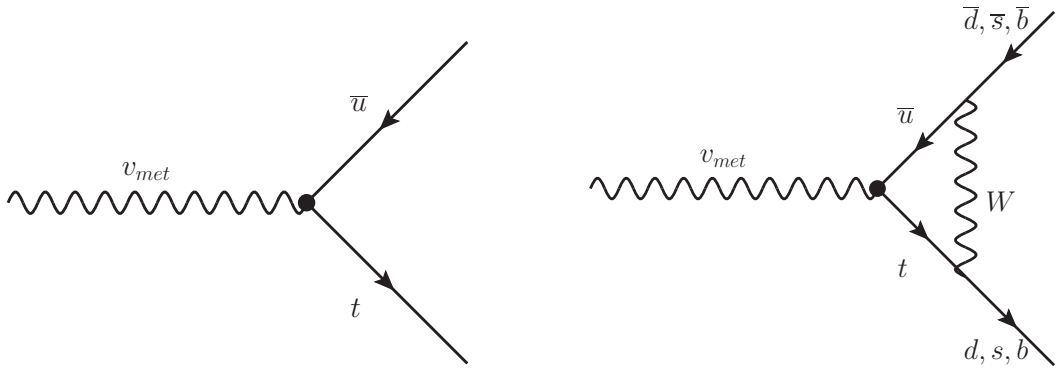

(a) (b)

Figure 3.11: Feynman diagrams of the di-quark decay of the spin-1 invisible boson, v_{met}, in the S4_{R} model via (a) a tree and (b) a loop process.

3.5.5 Choice of model parameters

The model parameters are chosen such that the production cross-sections are large enough to be reasonably sensitive at the LHC luminosity and energy. Production cross-sections for the S1_{R} and S4_{R} models were calculated using the matrix-element generator MADGRAPH5 at a center of mass energy of $\sqrt{s} = 8$ TeV [57]. The cross-sections times branching ratio (BR) as well as the width of the resonance of the S1_{R} model for a resonance mass of $m(S) = 500$ GeV and a coupling value of $a_{\text{R}} = 0.2$ are shown in Table 3.2. As the table shows, the cross-sections vary only slightly. This is a result of the similar kinematics of the model for the chosen mass range of the f_{met} particle.

The cross-sections times branching ratio for the S4_{R} model with a coupling value of $a_{\text{R}} = 0.2$ are shown in Table 3.3. The cross-section diverges as the mass of the v_{met} particle tends to 0 GeV. However, when the mass is exactly zero the cross-section has a finite value. Feynman diagrams for the production of monotop events with semi-leptonic and fully-hadronic decays of the top quark are shown in Figures 3.12 and 3.13 respectively.

$m(f_{\mathrm{met}})$ [GeV]	$\sigma \times \mathrm{BR}(\mathrm{t} \to \ell\nu\mathrm{b})$ [pb]	$\sigma \times \mathrm{BR}(\mathrm{t} \to \mathrm{q\bar{q}b})$ [pb]	$\Gamma(S)$ [GeV]
0	1.107	2.214	3.492
20	1.102	2.205	3.491
40	1.089	2.180	3.487
60	1.068	2.137	3.481
80	1.039	2.078	3.472
100	1.001	2.003	3.461

Table 3.2: Theoretical predictions for the product of the production cross-section and the branching ratio of a top quark decay into a semi-leptonic or fully-hadronic final state, in the $\mathrm{S1_R}$ model. Values are given for a resonance mass of $m(S) = 500$ GeV and for a coupling of $a_{\mathrm{R}} = 0.2$, as a function of the mass of the neutral fermion $m(f_{\mathrm{met}})$. The total widths $\Gamma(S)$ of the resonance are also shown.

$m(v_{\mathrm{met}})$ [GeV]	$\sigma \times \mathrm{BR}(\mathrm{t} \to \ell\nu\mathrm{b})$ [pb]	$\sigma \times \mathrm{BR}(\mathrm{t} \to \mathrm{q\bar{q}b})$ [pb]
0	96.03	192.4
25	359.0	717.9
50	113.4	226.9
75	59.86	119.5
100	37.45	74.82
125	25.35	50.68
150	18.00	35.96
200	9.662	19.28
250	5.506	11.02
300	3.328	6.656
400	1.372	2.738
500	0.6345	1.270
600	0.3192	0.6354
700	0.1698	0.3383
800	0.09417	0.1883
900	0.05472	0.1091
1000	0.03259	0.06479

Table 3.3: Theoretical predictions for the product of the production cross-section and the branching ratio of a top quark decay into a semi-leptonic or fully-hadronic final state, in the $\mathrm{S4_R}$ model. Values are given for a coupling of $a_{\mathrm{R}} = 0.2$, as a function of the mass of the invisible spin-1 state $m(v_{\mathrm{met}})$.

3.6 Summary

The analysis in this dissertation focuses on the search for leptonically decaying monotop events using the two benchmark models, $\mathrm{S1_R}$ and $\mathrm{S4_R}$, described in the previous sections.

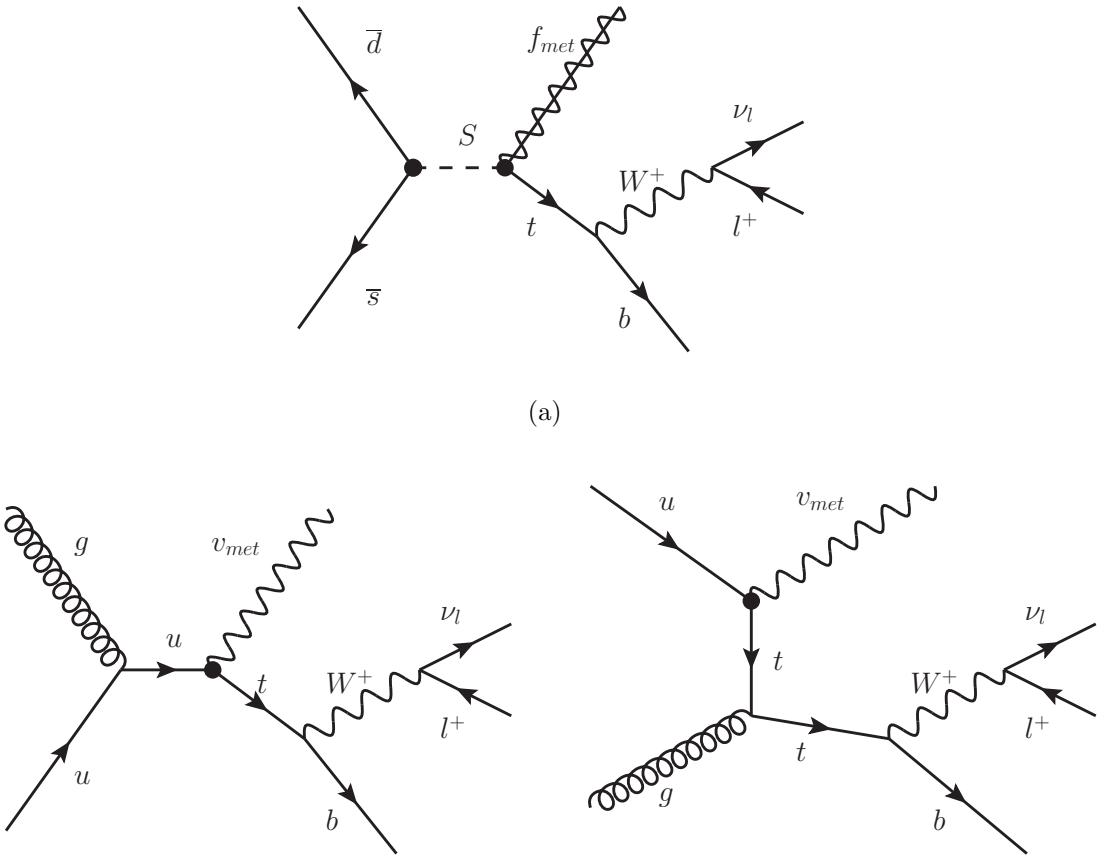

Figure 3.12: Feynman diagrams of tree-level order processes leading to monotop events with a semi-leptonic topology for (a) production of a colored scalar resonance S decaying into a top quark and a spin-1/2 fermion f_{met} in the S1_{R} model, (b) s-, and (c) t-channel non-resonant production of a top quark in association with a spin-1 boson v_{met} in the S4_{R} model.

In both models the coupling value, a_{R} is fixed at 0.2 and the other free parameter, the mass of either the f_{met} or v_{met} particle, is allowed to vary. In the S1_{R} model the mass of the scalar resonance, S, is fixed at 500 GeV. While the analysis techniques used to perform a search for both resonant and non-resonant monotop production are similar, they are performed independently. Later chapters will describe the different search techniques used and the further constraints that are placed on the models' parameters.

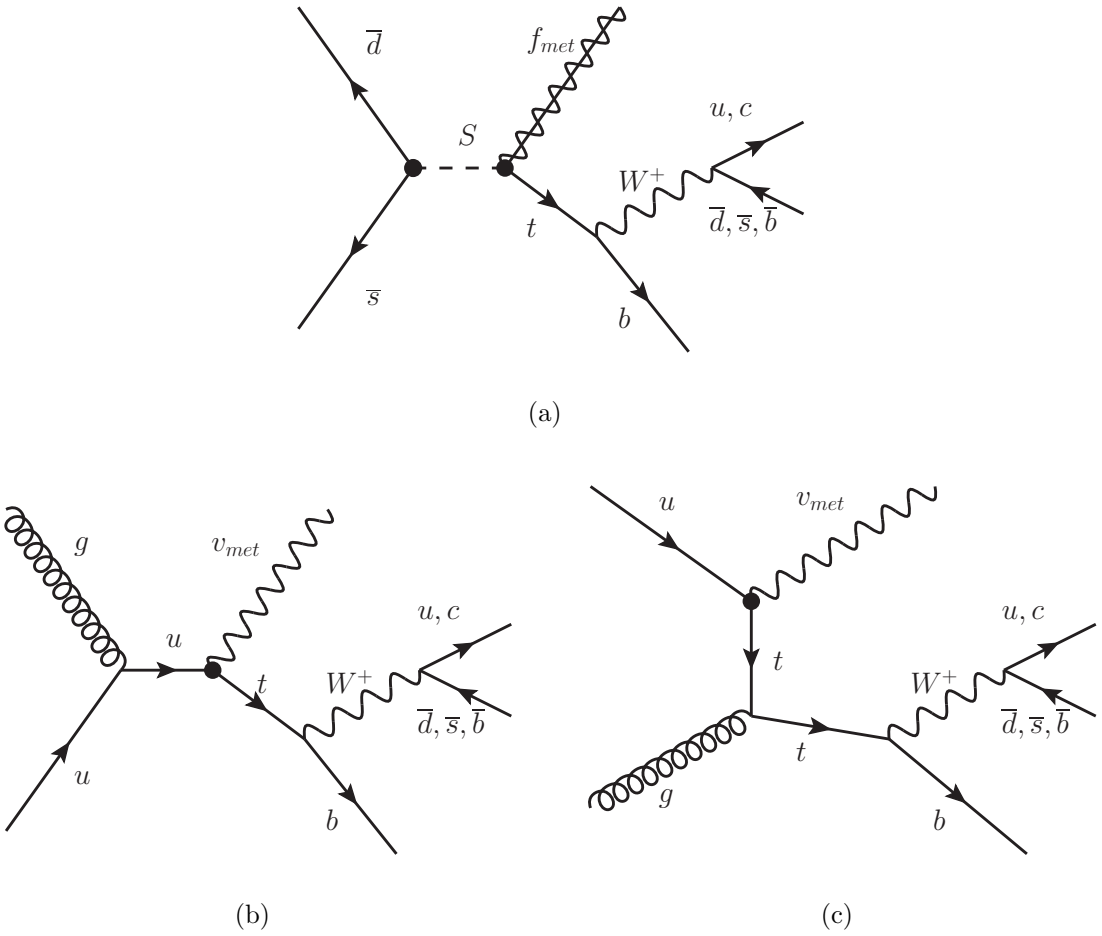

Figure 3.13: Feynman diagrams of tree-level order processes leading to monotop events with a fully-hadronic topology for (a) production of a colored scalar resonance S decaying into a top quark and a spin-1/2 fermion $f_{\rm met}$ in the $\rm S1_R$ model, (b) s-, and (c) t-channel non-resonant production of a top quark in association with a spin-1 boson $v_{\rm met}$ in the $\rm S4_R$ model.

Chapter 4

ATLAS and the LHC

The Large Hadron Collider (LHC), on the border between France and Switzerland in the CERN complex, is the largest and most energetic particle collider in the world. It was designed to circulate two beams of protons, each of 7 TeV of kinetic energy, in opposite directions and have them collide at four interaction points along its 27 km long ring. Four large particle detectors sit at these interaction points: ALICE [58], LHCb [59], CMS [60] and ATLAS [23]. The locations of these detectors along the LHC ring are shown in Figure 4.1. This chapter will discuss the design layout of the LHC accelerator complex and the design specifications of the ATLAS detector.

4.1 Large Hadron Collider

The Large Hadron Collider is the last stage of the CERN accelerator chain. In order to reach their final LHC energy, the protons are sent through a series of accelerators which progressively increase their energy before they are finally injected into the LHC main ring.

4.1.1 Accelerator complex

The protons which eventually collide at collision points along the LHC main ring originate from a very unassuming looking bottle of hydrogen gas. The hydrogen gas is fed into a cath-

ode chamber in the "duoplasmatron" where electrons are used to dissociate the H_2 molecules into their constituent protons as well as strip the molecules of their electrons. The resulting protons are then accelerated to an energy of 90 keV. Once leaving the duoplasmatron the protons are sent through a 1 m long radio-frequency (RF) quadrupole where they are focused, separated into bunches, and accelerated to 750 keV. From there the protons are injected into the linear accelerator 2 (LINAC2) [61]. Inside the LINAC2 an alternating electric field accelerates the protons to 50 MeV. The LINAC2 uses a series of drift tubes to shield the protons from the electric field when the field points in the direction that would otherwise decelerate them. The LINAC2 also incorporates quadrupole magnets which confine the protons to a tight beam.

The protons then pass through a series of three synchrotron accelerators. The first of these accelerators is the Proton Synchrotron Booster (PSB) [62]. The beam coming from the LINAC2 is split into four parts and each part is injected into one of the four superimposed rings in the PSB. The 50 m diameter rings use sixteen synchrotron magnets to bend and focus the beams. A radio-frequency cavity in each ring accelerates the protons to 1.4 GeV after which the beams are recombined. From the PSB the beam is sent to the Proton Synchrotron (PS) [63] where it is split into a train of 72 bunches and accelerated to 25 GeV before being injected into the Super Proton Synchrotron (SPS) [64]. The SPS has a radius of 1100 m and accelerates the beam to 450 GeV. The beam is further split into bunch trains consisting of up to 4×72 bunches before they are finally injected into the LHC. A sequence of 12 injection cycles from the SPS into the LHC gives the LHC its nominal 2,808 bunch configuration.

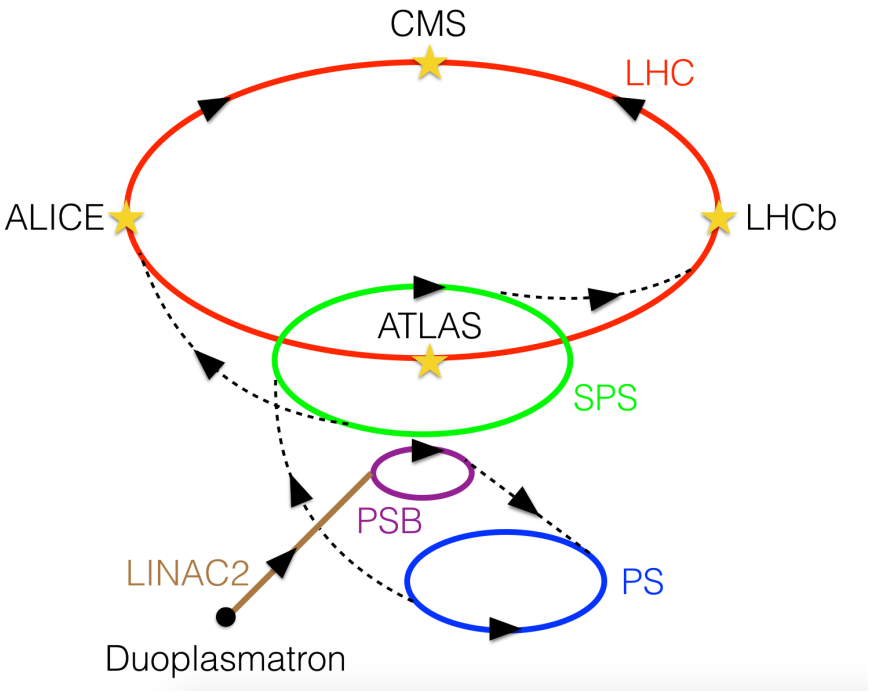

Figure 4.1: A cartoon drawing showing the LHC accelerator chain. Protons are produced in the duoplasmatron and are then accelerated through a series of linear and synchrotron accelerators before being injected into the LHC. Also shown are the four large experiments along the LHC ring.

4.1.2 LHC design

The LHC was designed to circulate two proton beams along its 27 km ring and collide them at a center of mass energy of $\sqrt{s} = 14$ TeV. Eight superconducting radio-frequency cavities along each beam accelerate the beams to their final energies while at the same time keeping the protons grouped in their bunches. An electric field is generated inside each of the cavities with a radio-frequency of 400 MHz. During the acceleration phase the protons feel a small force in the direction of motion. As the protons circumnavigate the ring they receive more and more energy from the RF cavities and need to be kept in a circular path as they accelerate. This is accomplished through the use of 1,232 dipole magnets each of which has a maximum field strength of 8.4 T and operates at 1.9 K requiring 100 tons of liquid helium connected through a distribution system.

The energy loss due to synchrotron radiation emitted during the bending of the electrically charged protons is regained in the superconducting RF cavities. The electric fields in the cavities are generated in such a way that the protons in each bunch arrange themselves into RF "buckets." Inside these buckets the protons in the center of the buckets are given an optimal amount of energy while protons on the edges of the buckets are either given more or less energy as necessary to bring them into the center. In this way the 2,808 bunches are kept longitudinally focused. This concept is shown in Figure 4.2. 392 quadrupole and higher order multi-pole magnets are used for focusing the beams in the transverse directions.

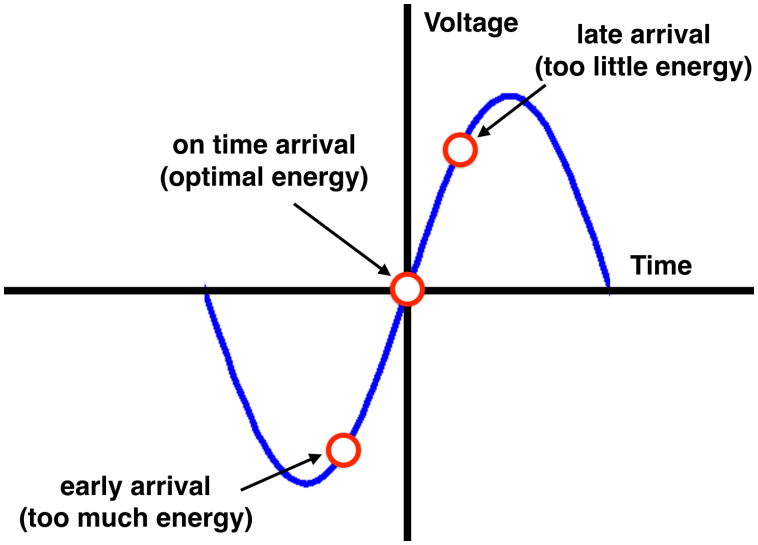

Figure 4.2: A cartoon drawing showing synchrotron motion in an RF bucket. Protons which arrive too early (too much energy) are given a slight de-acceleration by a negative voltage. Protons which arrive too late (too little energy) are given a slight acceleration by a positive voltage. This oscillation keeps the protons in their correct bunches.

The design and technologies of the LHC allow for collision rates at energies never before seen in accelerator physics. Each of the 2,808 bunches contains approximately 100 billion protons. With a design bunch spacing of 25 ns, only one out of ten RF buckets is filled with protons and each bunch is separated from the adjacent by 7.5 m which corresponds to a bunch crossing rate of 40 MHz. As the beams collide at the interaction points the probability of

an interaction taking place between two protons is quantified by the cross-section, σ. A calculation of the total hadronic cross-section for proton-proton collisions at the LHC is not currently possible from first principles. The distances involved in the collision process, while small, are still too large to allow for a perturbative QCD calculation. The measured value at a center-of-mass energy of $\sqrt{s} = 7$ TeV is approximately 100 mb as seen in Figure 4.3 [21].

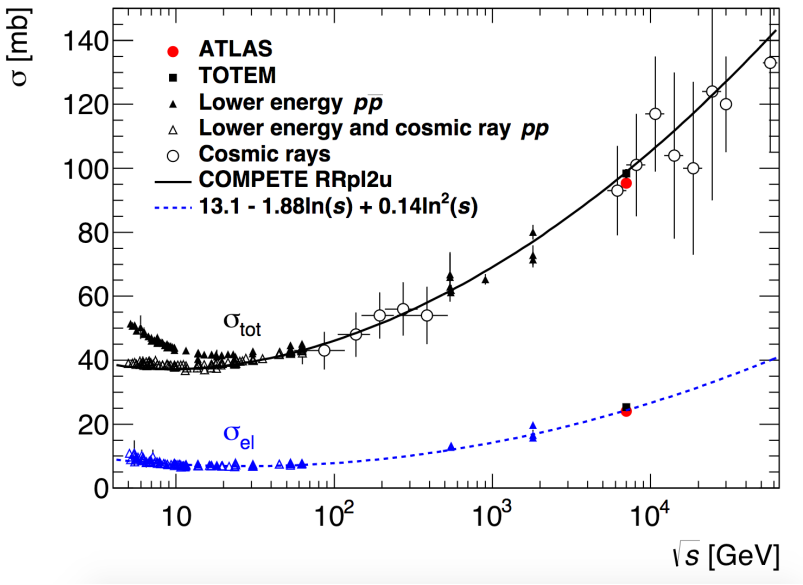

Figure 4.3: The measurements of the total and elastic cross-sections of proton-proton collisions at $\sqrt{s} = 7$ TeV [21].

Instantaneous luminosity, L, is a measure of the number of protons passing through a given area in a given amount of time.[1] At the design luminosity of $L = 10^{34}$ cm^{-2}s^{-1} this corresponds to a total interaction rate of 1 GHz. As collisions occur in the beam, the luminosity decreases over time and as a result the beams are periodically dumped and a new injection sequence is initiated to bring the luminosity back up to its maximum value. As luminosity is a function of time, the integrated luminosity is a measure of the total number of protons

[1] From this point forward the term luminosity will be understood to mean instantaneous luminosity.

passing through a certain area in some period of time.

$$L_{\text{int}} = \int L(t)\ dt \tag{4.1}$$

The total number of proton-proton collisions in a period of time is then given by the product of the integrated luminosity and the total interaction cross-section. Typically, however, the total integrated luminosity is quoted as the amount of data taken. In 2012 the total integrated luminosity delivered by the LHC at $\sqrt{s} = 8$ TeV was 22.8 fb^{-1}. Of this amount, 20.3 fb^{-1} is used as collision data in this dissertation. Figure 4.4 shows the total integrated luminosity during the period known as Run1, in which data were recorded from 2010-2012 at both 7 and 8 TeV beam energies.

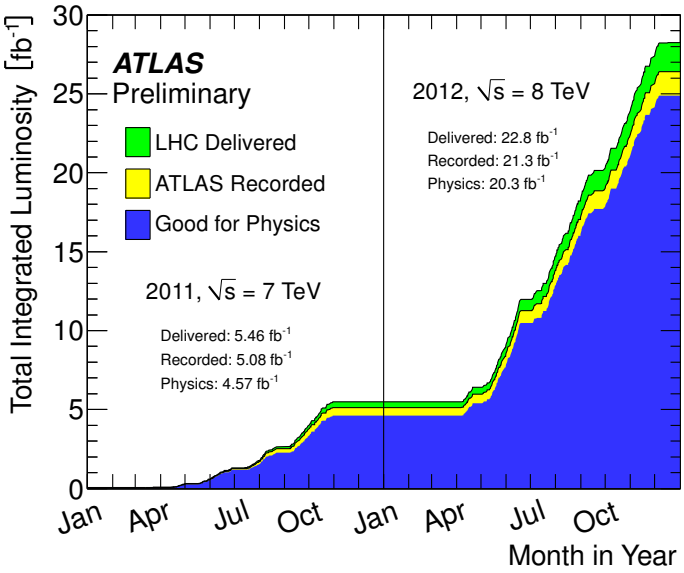

Figure 4.4: The total integrated luminosity delivered by the LHC, recorded by the ATLAS detector, and deemed good for physics analyses during Run1.

High luminosity is a design feature of the LHC and it allows for tremendous amounts of data to be recorded and increases the number of rare (low cross-section events). The mean number of inelastic collisions between protons per bunch crossing, $\langle\mu\rangle$, increases with luminosity.

Figure 4.5 shows the average number of inelastic collisions per bunch crossing for Run1.

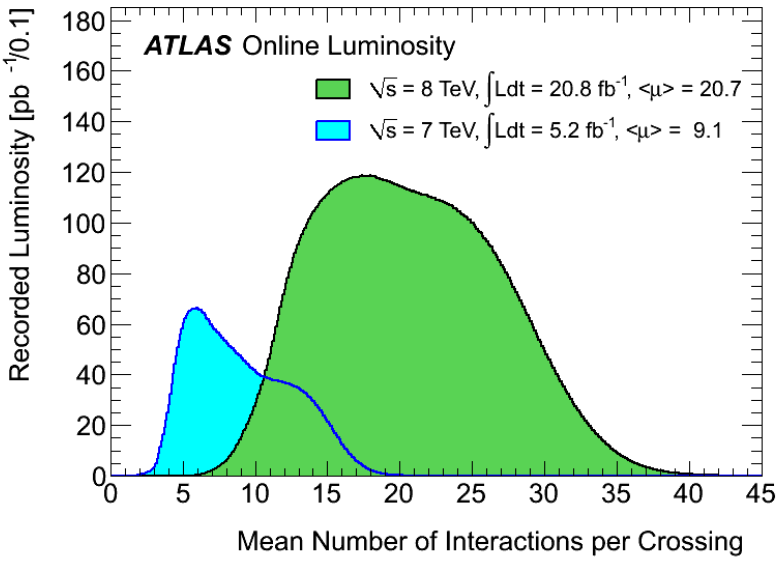

Figure 4.5: The luminosity-weighted distribution of the mean number of interactions per bunch crossing during Run1. The mean number of interactions corresponds to the mean of the poisson distribution on the number of interactions per crossing calculated for each bunch. In this calculation the σ_{inel} is taken to be 71.5 mb for $\sqrt{s} = 7$ TeV and 73.0 mb for $\sqrt{s} = 8$ TeV [22].

The multiple interactions per bunch crossing, generically referred to as pileup, can present a challenge to the detectors along the beam. There are two sources of pileup. First, the presence of multiple interactions within the same bunch crossing produces additional signals in the detectors which can be difficult to resolve from each other. This is known as in-time pileup. In addition, there is a finite signal integration time for various parts of the detectors such that interactions from a previous bunch crossing can affect the signal readout of interactions in future bunch crossings. This is known as out-of-time pileup. Given a particular luminosity, there is a trade-off between in-time and out-of-time pileup. The effect of pileup must be understood in any analysis.

4.2 The ATLAS detector

The ATLAS (A Toroidal LHC ApparatuS) detector is the largest multi-purpose particle detector ever constructed.[2] It stands 25 meters tall, measures 44 meters from end to end, weighs approximately 7,000 tons, and sits 92 meters underground at one of the LHC's collision points. Its size belies the precision of the instrumentation of which it is comprised. The function of the detector is to measure and record the energies and trajectories of various particles emanating from the hard scatter event at the interaction point. As a multi-purpose detector it is able to collect data for a wide range of physics analyses and a wide variety of event topologies. It was designed with these general requirements in mind:

- Fast and radiation-hard electronic components are needed to handle the high particle flux seen in the detector. The detector should be fast enough to distinguish particles in one scattering event from another.

- The detector should be nearly hermetic, covering as much volume as possible. Limiting the amount of service equipment and supporting structures was key to keeping near full angular coverage.

- Good charged particle momentum resolution while minimizing material in the inner tracker is paramount. Many processes involve subsequent decays of long-lived particles at secondary vertices. The ability to match tracks to associated vertices is essential.

- The design of the calorimeter system should give excellent energy measurements of electromagnetic and hadronic particles. This is crucial for accurate missing energy calculations that are implicit in many interesting processes.

[2] ATLAS is arguably the most tortured and contrived acronym in all of physics.

- Good muon identification and momentum resolution over a wide range of momenta as well as efficient charge identification of highly energetic muons are critical.
- A robust trigger system capable of determining which events should be recorded is necessary. Given the high luminosity of the LHC beam, it is important to be able to quickly and accurately tell the difference between background processes and physics processes of interest.

These requirements drove the design of the five main subsystems of the detector described below.

- A magnet system consisting of solenoid and three toroid magnets supply the necessary magnetic fields to separate the trajectories of charged particles.
- An inner detector provides track information as well as vertex reconstruction for charged particles.
- A calorimeter system measures the energies of the hadrons, electrons, and photons.
- A muon spectrometer measures muon positions and momenta.
- A trigger and data acquisition system reads and and records event information from the electronic read-outs of the detector subsystems.

4.2.1 Detector geometry

The ATLAS detector uses a right-handed coordinate system whose origin is the interaction point (IP) which nominally lies at the center of the detector. The positive x-axis points towards the center of the LHC ring, the positive y-axis points upwards, and the z-axis points

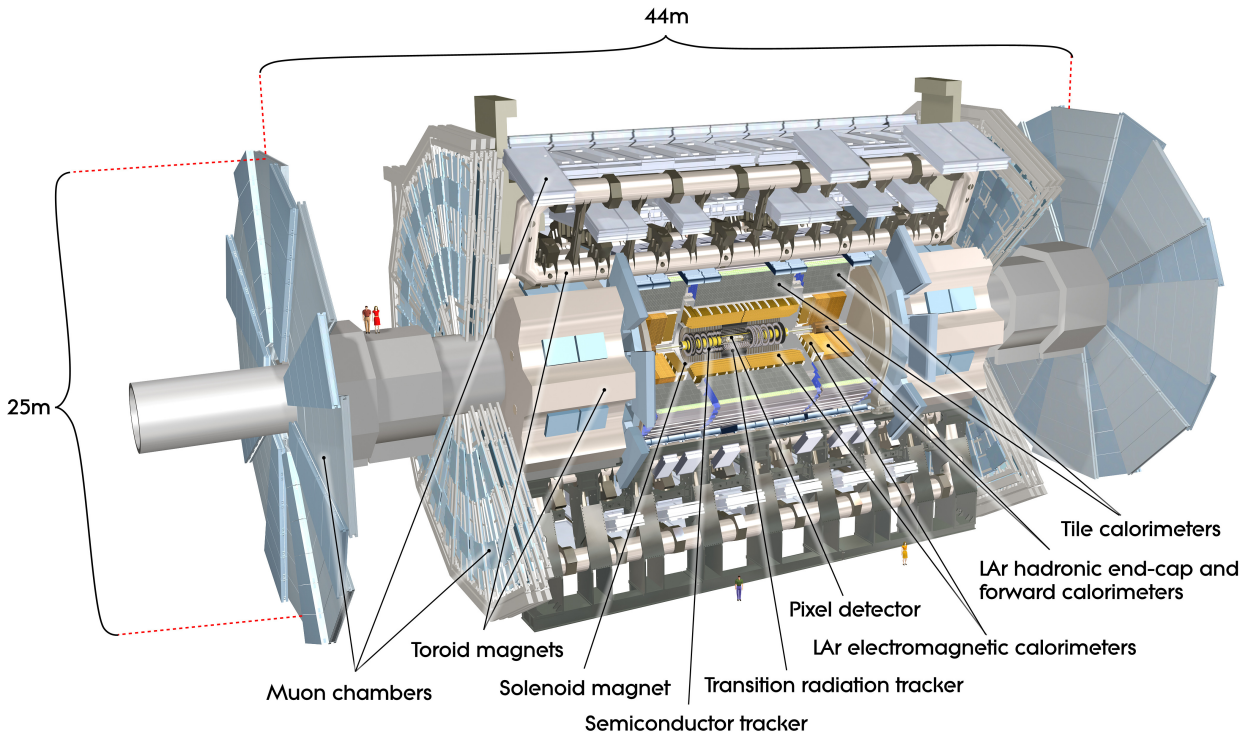

Figure 4.6: A schematic representation of the ATLAS detector showing the size of the detector and the relative positions of its subsystems [23].

along the beam axis. Two angles are defined in this choice of a coordinate system. The azimuthal angle, ϕ, is defined from the positive x-axis and wraps around the beam axis towards the positive y-axis. The polar angle, θ, is the angle subtended from the positive z-axis. Typically the polar angle is given in terms pseudorapidity. The rapidity, y, of an object is defined as

$$y \equiv \frac{1}{2} \ln \left[\frac{E + p_z}{E - p_z} \right]. \tag{4.2}$$

In the case of relativistic particles, the mass of the particles can be neglected ($|\vec{p}| \approx E$) and the rapidity can be written in terms of the pseudorapidity as

$$y \approx \eta = \frac{1}{2} \ln \left[\frac{|\vec{p}| + p_z}{|\vec{p}| - p_z} \right] = -\ln \left[\tan \left(\frac{\theta}{2} \right) \right]. \tag{4.3}$$

Small values of η correspond to trajectories more parallel to the transverse plane, while large values of η correspond to more forward (i.e. along the beam-axis) trajectories. Figure 4.7 shows a graph of η as a function of θ.

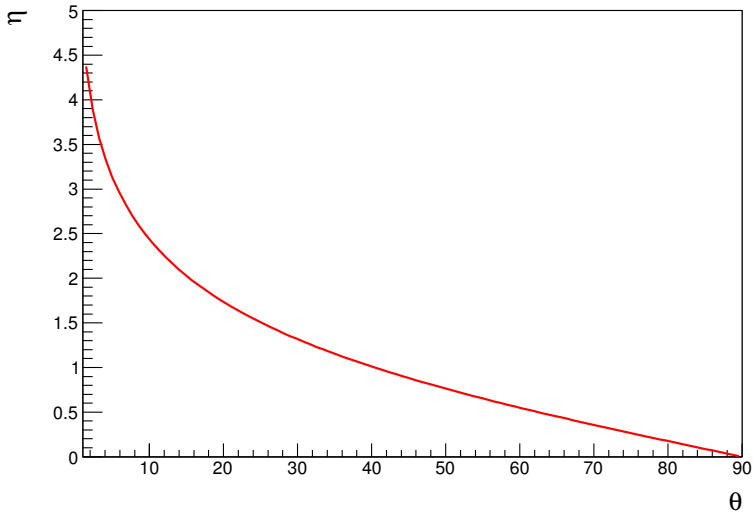

Figure 4.7: The value of the pseudorapidity, η, as a function of the polar angle, θ. Particles which are closer to the beam line and thus have high η values are said to be "forward."

The difference between two pseudorapidity measurements is a Lorentz invariant quantity.[3] The $\Delta\eta$ of two particles is independent of any boost in the beam line direction. This is beneficial for hadron collider experiments because the longitudinal momentum of the partons in the hard scatter event can carry different momentum fractions of their proton.

The $x-y$ plane is referred to as the transverse plane. As the total transverse energy of the beam is known *a priori*, most measurable quantities are defined in the transverse plane. The transverse momentum p_{T}, transverse energy E_{T}, and missing transverse energy $E_{\mathrm{T}}^{\mathrm{miss}}$ are all defined in the transverse plane. The measure of how far apart two objects are in $\eta-\phi$

[3]Technically rapidity, not pseudorapidity, is the Lorentz invariant quantity. However, at the collision energies of the LHC the two quantities are almost identical and it is assumed that pseudorapidity is also a Lorentz invariant quantity.

space is the quantity ΔR and is given by

$$\Delta \mathrm{R} = \sqrt{(\Delta\eta)^2 + (\Delta\phi)^2}. \tag{4.4}$$

4.2.2 Magnet system

As electrically charged particles move through a magnetic field the Lorentz force they experience alters their trajectories. The direction and degree by which the trajectories of the particles are bent is a function of both the sign of their electric charge as well as their momenta. Particles with higher momenta have a larger radius of curvature, r, than particles with lower momenta. It is this relationship that aids the ATLAS detector in both particle identification and momentum determination.

The ATLAS magnetic system consists of one inner solenoid aligned on the beam axis which provides a 2 T axial magnetic field for the Inner Detector, and three outer air-core toroids which provide a 0.5 T magnetic field to bend muon trajectories. The geometry of these magnets is shown in Figure 4.8.

A barrel toroid provides a 0.5 T magnetic field for the central region, and two end-cap toroids provide 1 T magnetic fields for the end-cap regions of the muon spectrometer [65, 23]. A high magnetic field without an iron core greatly benefits the ATLAS detector since iron would introduce massive amounts of passive material (material not dedicated to particle measurements) and would degrade the intrinsic resolution of the muon spectrometer. The choice to have three toroidal magnets instead of one was based on both cost and the need to be able to access the inner parts of the detector. This choice does affect the field strength in what is known as the transition-region between the barrel and end-cap toroids in the region

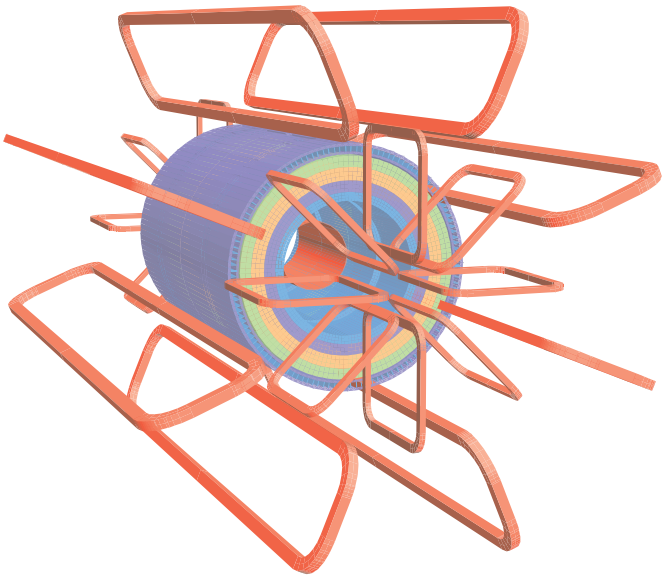

Figure 4.8: The ATLAS detector magnetic geometry. Visible are the barrel and end-cap toroids. The solenoid lies inside the calorimeter volume [23].

$1.4 \lesssim |\eta| \lesssim 1.6$ as shown in Figure 4.9.

4.2.3 Inner detector

The purpose of the ATLAS Inner Detector (ID) is to provide momentum and particle track measurements for charged particles emanating from the primary vertex (PV) at the hard scatter event and any secondary vertices from subsequent decays of particles. Three independent sub-detectors work in parallel to aid in particle identification and vertex reconstruction of charged particles. These sub-detectors are arranged in a cylindrical envelope at increasing radii from the beam line. The inner most elements of the ID are the Pixel detector and the Semiconductor Tracker (SCT). The outer layer of the ID consists of the Transition Radiation Tracker (TRT). These components of the ID are discussed in Sections 4.2.3.1 - 4.2.3.3. The ID covers a pseudorapidity range of $|\eta| < 2.5$ and extends 1150 mm from the beam line. The radial positions of the ID sub-detectors are shown in Figure 4.10.

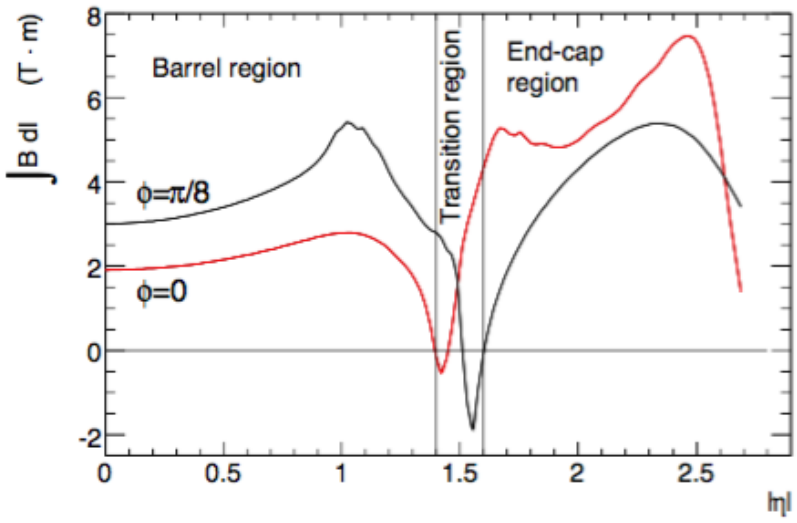

Figure 4.9: The ATLAS muon spectrometer integrated magnetic field strength as a function of $|\eta|$ [12].

4.2.3.1 Pixel detector

The Pixel detector is the closest sub-detector to the interaction point and consists of 1,744 silicon pixel sensors giving a total of 80 million read-out channels [24]. The nominal pixel size is 50 μm in the ϕ direction and 400 μm in the z direction. The original design consisted of three barrel layers at R = 50.5, 88.5, and 122.5 mm respectively. In 2014 a fourth layer called the Insertable B-Layer (IBL) was installed at radius of 33.4 mm from the beam pipe with 50 μm $\times$ 250 μm pixels [66]. The original three layers were designed for a peak luminosity of 10^{34} cm^{-2}s^{-1}. As the luminosity is expected to increase with LHC upgrades, this fourth layer was inserted to help preserve tracking performance and vertex reconstruction efficiency.[4] Additionally, there are three end-cap disks at z = 495, 580, and 650 mm. These 92 million silicon pixels function as ionization detectors. Ionizing radiation in the form of charged particles create electron/hole pairs in the silicon. These charge carriers are subject to an applied electric field which creates an induced current. This current is then amplified

[4]This upgrade to the pixel detector was installed after the end of Run1 and so was not present for the data included in this dissertation.

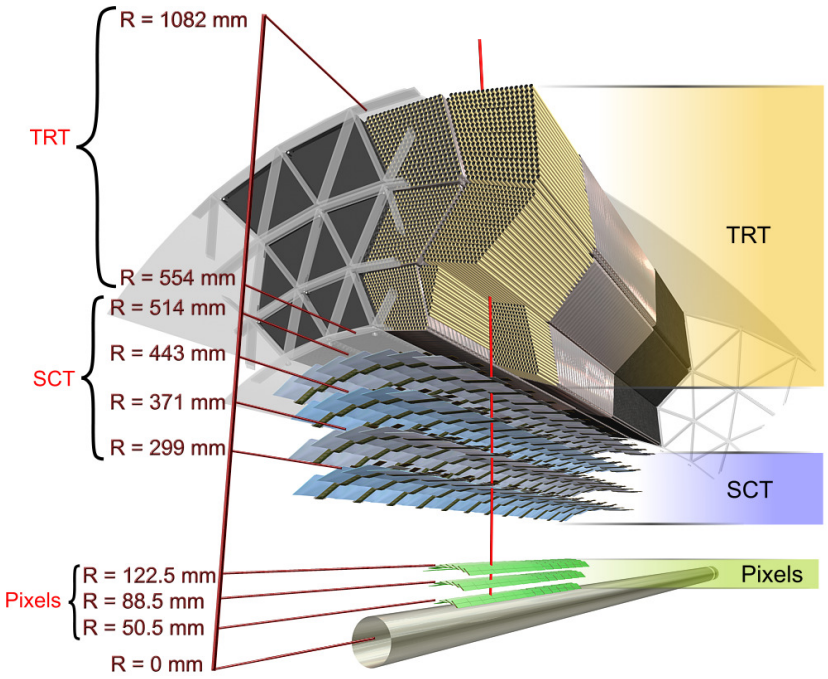

Figure 4.10: A schematic showing the radial positions of the ID components. Not shown are the end-cap regions of the detector sub-components.

and read out as a hit in an individual pixel. Three hits are possible for each track in the pseudorapidity range of $|\eta| < 2.5$. It has a position resolution of 10 μm in the $r - \phi$ plane and 115 μm along the z-axis. Figure 4.11 shows a schematic view of the Pixel detector in its original three-layer configuration.

4.2.3.2 Semiconductor tracker

The Semiconductor Tracker lies just outside of Pixel detector. Like the Pixel detector, the SCT uses silicon as its detection medium and covers the range $|\eta| < 2.5$. However, instead of pixels the SCT uses silicon strips arranged in four stereo layers. Each layer is composed two silicon strips which are angled with respect to each other by 40 mrad to allow for a 3D measurement. The SCT provides eight hits for each charged particle track and has a position resolution of 17 μm in the $r - \phi$ plane and 580 μm along the z-axis [67, 68].

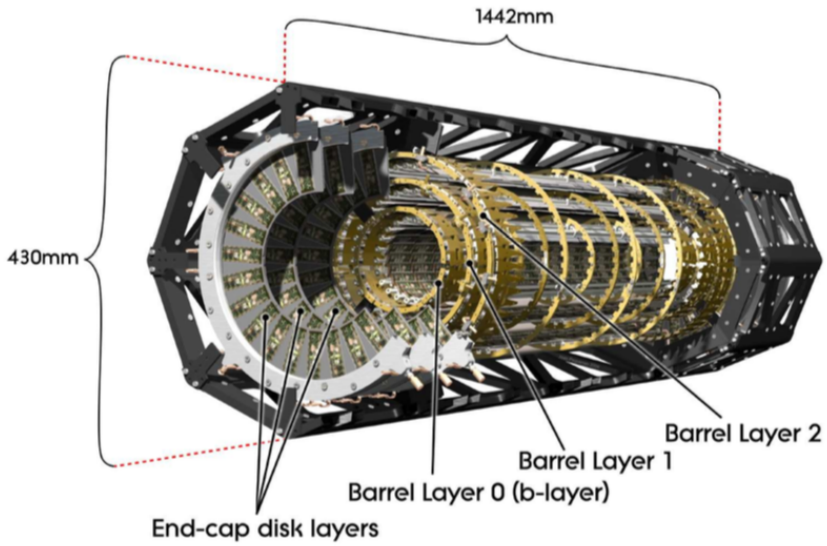

Figure 4.11: A schematic showing the original three layers of the Pixel detector. Not shown is the Insertable B-Layer installed in 2014 [24].

4.2.3.3 Transition radiation tracker

The Transition Radiation Tracker is the last sub-detector of the ID and is the most radially outward of the three. It has three major modular components: the barrel and two end-caps [69, 70]. It is a drift tube system covering $|\eta| < 2$ and consists of 4 mm diameter straw tubes kept at a high potential filled with a $Xe/CO_2/O_2$ mixture and an electrically grounded 30 μm tungsten wire in the center of each tube. As charged particles pass through the gaseous mixture they produce ionizing radiation. These charge carriers travel down the tungsten wire and are read out by the TRT electronics as a signal current. The 300,000 straw tubes typically provide around 35 hits per track and a position resolution of ~ 170 μm in the $r - \phi$ plane. As the straws are aligned parallel to the beam line, the TRT does not provide a position measurement in the z-axis direction.

In addition to the tracking measurements, the TRT is able to aid in charged particle identification. In between the drift tubes are radiator foils consisting of various materials of differing dielectric constants. In this way the TRT can make use of transition radiation (TR). When a

relativistic charged particle traverses a boundary of two different dielectric constants (ϵ_1,ϵ_2) a soft X-ray photon is emitted. These photons ionize the xenon gas inside the straw tubes with a much higher energy deposition than a charged particle typically does. Whether or not a charged particle emits TR is dependent on its Lorentz factor, γ. Consider a charged pion and an electron. The pion, being almost 300 times more massive than the electron, would have a smaller γ than an electron with the same momentum. In the ATLAS detector, typically only electrons have a high enough γ to generate TR. For a given momentum one would expect more of these high-threshold TR hits from an electron than from a pion. In this way, the TRT is able to distinguish between electrons and pions over a momentum range between 1 and 150 GeV [25]. A cross-sectional schematic of a charged particle track traversing through the TRT drift tubes is shown in Figure 4.12.

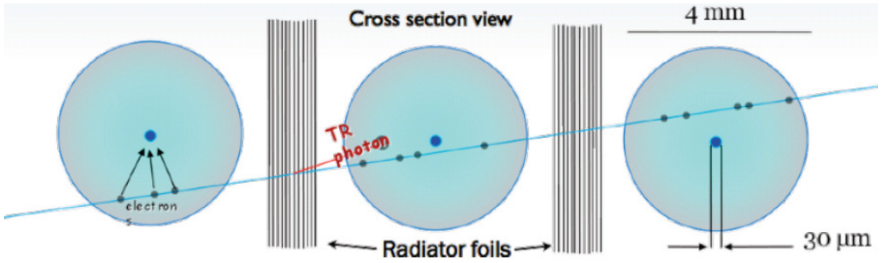

Figure 4.12: A cross-sectional schematic of a charged particle track moving through the TRT drift tubes showing how ionization clusters are generated either by the charged particle itself or by induced transition radiation photons [25].

4.2.4 Calorimeters

The purpose of the ATLAS calorimeter system is to measure the energies and positions of both hadrons and electromagnetic particles. The ATLAS detector uses sampling calorimeters consisting of alternating layers of a passive material in which the particles interact to form electromagnetic or hadronic showers and an active material in which the shower particles

interact through ionization or scintillation processes to generate a signal. The materials used and the geometry in which they are arranged can have a dramatic impact on the effectiveness of a calorimeter's design. An ideal calorimeter would be infinitely deep so that no energy escapes undetected and it would not include any extraneous matter such as cabling or mechanical support structures which would alter the measurements and create cracks in the calorimeter's coverage. Any real calorimeter, however, is limited by both budgetary constraints as well as the need for support structures and other passive material needed to support and read out the detector. Minimizing this service equipment is a both major design challenge and is crucial in building an efficient detector. The ATLAS detector consists of electromagnetic and hadronic calorimeters and are shown in Figure 4.13.

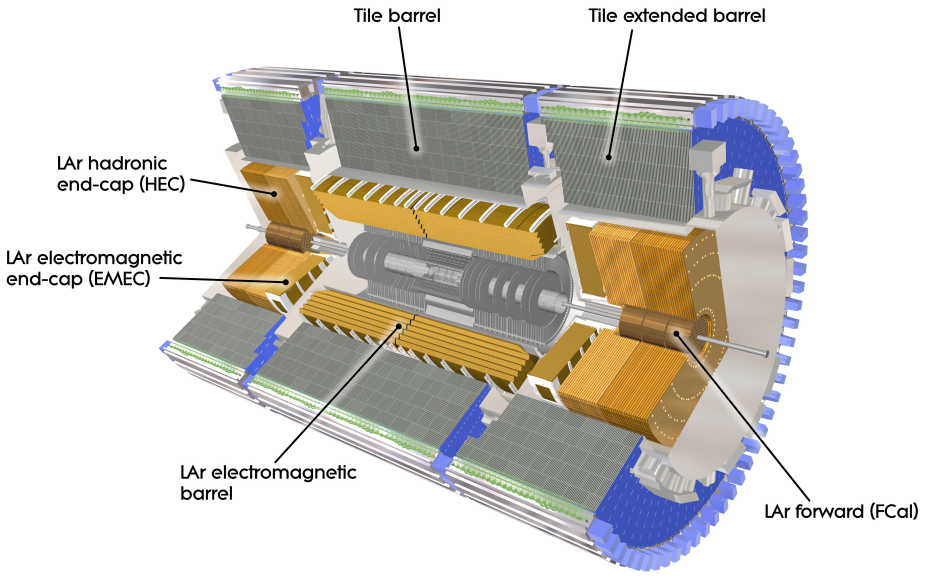

Figure 4.13: A schematic drawing of the ATLAS calorimeter systems [25].

4.2.4.1 Electromagnetic showers

High energy electromagnetic particles primarily interact with matter via two processes: bremsstrahlung in the case of charged particles and pair production in the case of photons. A diagram showing these processes is shown in Figure 4.14. An incident photon interacts with the absorbing material and produces an electron-positron pair. The electrons and positrons then emit bremsstrahlung photons by interacting with the electrons or atomic nuclei of the absorbing material. The shower continues to grow in this way until the photons fall below the pair production threshold energy (approximately the rest mass energy of the electron-positron pair) and the electrons fall below the critical energy, E_C, of the material which is defined as the energy where energy loss due to bremsstrahlung and ionization are equal. Materials with a higher atomic number have a lower critical energy. Once the particles fall below E_c, ionization becomes dominant and the shower begins to die out as the particles ionize the active material and lose energy. This ionization radiation in the active medium is read out as a signal at the calorimeter's electrodes.

The profiles of the resultant electromagnetic showers are described by two parameters: the radiation length, X_0, and the Molière radius, R_M. The radiation length is defined as the mean distance a particle must traverse through a medium such that its energy is reduced by a factor of $1/e$ and describes the longitudinal movement of a particle through a medium. For most absorbing materials this value is on the order of 1 cm. The Molière radius describes the transverse development of the shower and is the radius which contains 90% of the shower's energy. Its value is proportional to the radiation length and inversely proportional to the critical energy,

$$R_M \propto \frac{X_0}{E_c}. \tag{4.5}$$

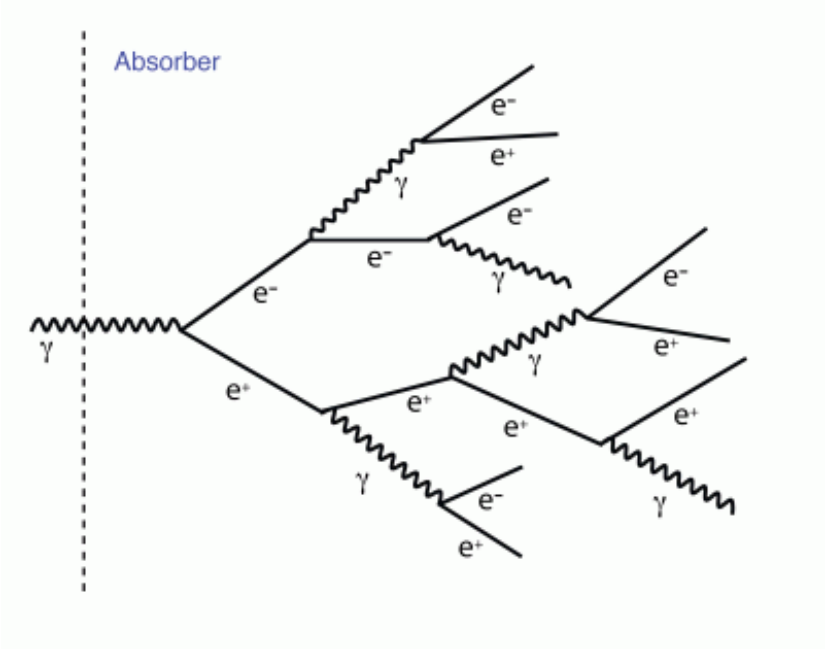

Figure 4.14: A diagram showing an example of an electromagnetic shower. A cascade of photons and electron-positron pairs propagate through the calorimeter depositing their energy in the active medium.

Care must be taken when deciding the choice of materials in a calorimeter. Nominally, calorimeters are designed to reduce the transverse dispersion of an electromagnetic shower in order to have better spatial resolution, while at the same time considering other factors such as cost and radiation tolerance.

4.2.4.2 Hadronic showers

Hadronic showers are much more complex than electromagnetic showers. They are characterized by a material's nuclear interaction length, λ_{int}, which is defined as the mean free path of a hadron before it interacts with atomic nuclei. Nuclear interaction lengths are typically much larger than EM radiation lengths. As a result hadronic calorimeters need to be both denser and deeper than EM calorimeters. Hadronic showers cascade through materials by way of secondary hadron production, nuclear de-excitation, and pion and muon decay

processes. An incident hadron traverses through the absorbing material until it interacts via the strong force with a nucleus in the absorbing material to produce a number of secondary hadrons, most notably pions and nucleons. This process continues until the energy of the hadrons falls below the pion production energy threshold. The neutral pions themselves decay into a pair of photons which produces two electromagnetic showers which often are close together and result in one measured shower. In this way, hadronic showers have a large fraction of their energy dissipated in the form of electromagnetic showers. Contributions from neutrons and photons from nuclear interactions can be substantial in a hadronic shower. However, only a fraction of this energy is recorded in the calorimeter. A hadronic shower's energy can be roughly divided into four parts:

- **Detectable electromagnetic component** – typically from $\pi_0 \to \gamma\gamma$ decay processes,
- **Detectable non-electromagnetic component** – ionization energy from charged hadrons such as protons, charged pions, etc,
- **Undetectable component** – inelastic nuclear collisions, and
- **Missing energy** – any energy carried off by non-interacting neutrinos in the decay processes.

Thus, considerable effort needs to be placed in modeling how hadronic showers propagate through a calorimeter in order to fully reconstruct an incident hadron's energy. A diagram showing an example of a hadronic shower with these four parts labeled is shown in Figure 4.15.

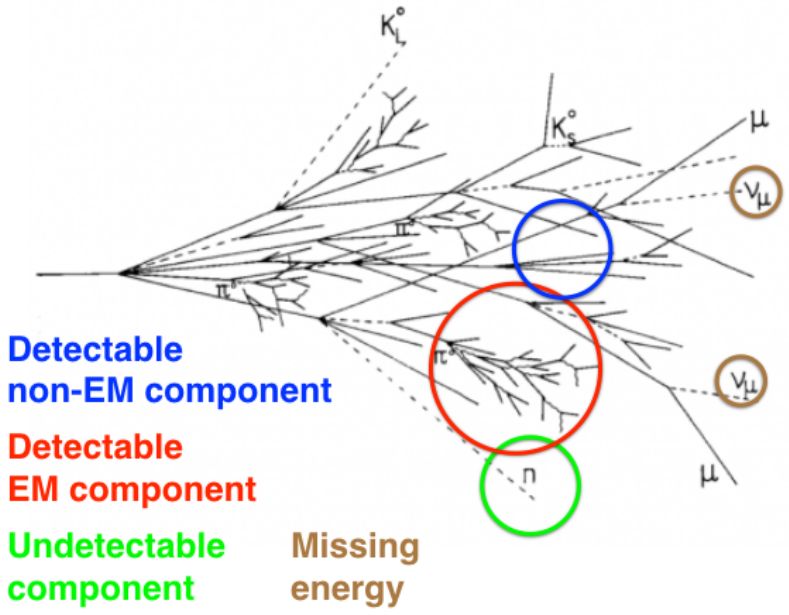

Figure 4.15: A diagram showing an example of a hadronic shower. An incident hadron collides with an atomic nucleus and starts a cascade of hadronic and electromagnetic energy.

4.2.4.3 Electromagnetic calorimeter

The electromagnetic calorimeter (ECal) consists of a barrel region and two end-cap regions (EMEC). The barrel region has two identical half-barrels separated by a 4 mm gap at $z = 0$. The two end-cap regions are each divided into an inner and outer wheel. Both the barrel and the end-cap calorimeters use liquid argon (LAr) as their active medium and lead for their absorbing material. Liquid argon was chosen for its linear response behavior and its intrinsic radiation-hardness. The alternating layers of active and absorbing materials are arranged in an accordion style geometry (see Figure 4.16) which provides high spatial resolution, good uniformity in the azimuthal direction, and fast signal readout. In the barrel region the accordion folds are angled so that the width of the LAr gap remains constant and the measurements are independent of ϕ. The barrel region is made up of three longitudinal sampling layers with varying granularities in η and ϕ. The first layer, which has the highest

η granularity of the three layers, is used for γ/π^0 separation where the η measurement is important. The second layer is where the majority of the energy is deposited and has moderate granularity in η and ϕ. The third layer is only used for the highest energy particles. As the showers are widely dispersed at this depth in the calorimeter, the cell sizes can be increased without loss of resolution. In the end-cap region, where the geometry is more difficult, the LAr gap could not be kept constant by simply varying the accordion wave height and folding angle. As such, a two coaxial wheel configuration is used where the calorimeter response is kept uniform by varying the applied voltage to the electrodes as a function of η.

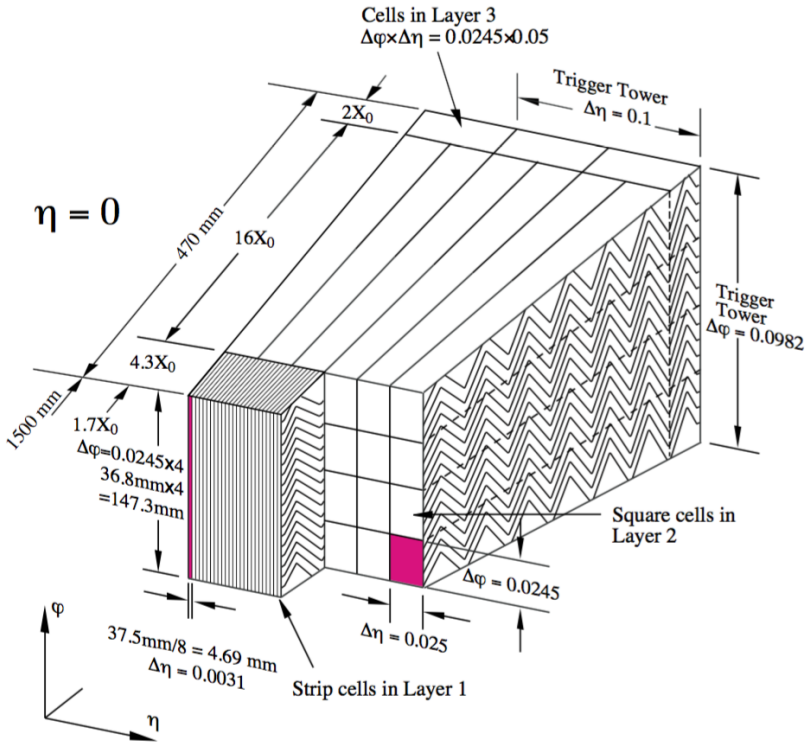

Figure 4.16: A sketch of the accordion structure of the barrel region of the ECal. The granularity of the cells in $\eta - \phi$ space are shown. Also shown is the depth of each layer given in terms of radiation length, X_0 [23].

In addition, both the barrel and the end-cap regions have a presampler to account for energy lost in the ID, solenoid, and other matter before the calorimeter. The main parameters of

the EM accordion calorimeter and presampler are shown in Table 4.1. The region between the barrel and the end-cap, $1.37 < |\eta| < 1.52$, is known as the "crack" region. Service equipment for the cryostat and ID introduces extra material which makes it difficult to fully reconstruct objects whose tracks lie in this region. Most ATLAS analyses, including the one in this dissertation, do not include electrons from this region.

Electromagnetic Calorimeter		
Accordion Calorimeter	**Barrel**	**End-cap**
Absorbing Material	lead	lead
Sampling Material	LAr	LAr
Coverage	$\|\eta\| < 1.475$	$1.375 < \|\eta\| < 3.2$
Segmentation	3 layers	2-3 layers
Cell granularity		
$(\Delta\eta \times \Delta\phi)$		
Layer1	0.003×0.1	0.003×0.1
Layer2	0.025×0.025	0.025×0.025
Layer3	0.050×0.025	0.050×0.025
Thickness $[X_0]$		
Layer1	4.3	4.4
Layer2	16	
Layer3	2	
# of channels	102,400	62,208 per end-cap
Presampler	**Barrel**	**End-cap**
Absorbing Material	lead	lead
Sampling Material	LAr	LAr
Coverage	$\|\eta\| < 1.475$	$1.375 < \|\eta\| < 3.2$
Segmentation	1 layer	1 layer
Cell granularity		
$(\Delta\eta \times \Delta\phi)$	0.025×0.1	0.1×0.1
Thickness $[X_0]$	0.08	0.03
# of channels	7,808	768 per end-cap

Table 4.1: Shown are some of the main design specifications of the ATLAS electromagnetic calorimeter system [2, 3, 4].

4.2.4.4 Hadronic and forward calorimeters

The hadronic calorimeter system consists of a large scintillating tile hadronic barrel calorimeter (TILECAL) [5], two liquid argon end-cap calorimeters (HEC) [6], and a liquid argon forward calorimeter (FCal) [7]. They are used to measure the energy of hadronic showers in an event.

4.2.4.4.1 Hadronic tile calorimeter The TILECAL is subdivided into a long barrel region 5.8 m in length and two extended barrels 2.6 m in length each. A 600 mm gap between the barrel region and the extended barrel regions allows for service cables to read the Inner Detector as well as to provide space for the liquid argon cables. It is a sampling calorimeter which uses steel as its absorbing material and scintillator as its active material and covers the region $|\eta| < 1.7$ with inner and outer radii of 2.28 m and 4.25 m. Each of the barrel subassemblies consist of 64 wedge-shaped modules, each subtending 5.625 degrees in azimuth. Radially, these modules are segmented into three layers which have a thickness of 1.5, 4.1, and 1.8 λ_{int} in the barrel region and 1.5, 2.6, and 3.3 λ_{int} in the extended barrel regions. The modules consist of alternating layers of steel and scintillating material. The hadronic shower particles interact with the scintillating material to produce photons. These photons are collected by wavelength shifting fibers, detected by photomultiplier tubes (PMTs), and read out as an electronic signal. A schematic drawing of one of the modules is shown in Figure 4.17(a) and some of the main design specifications are shown in Table 4.2.

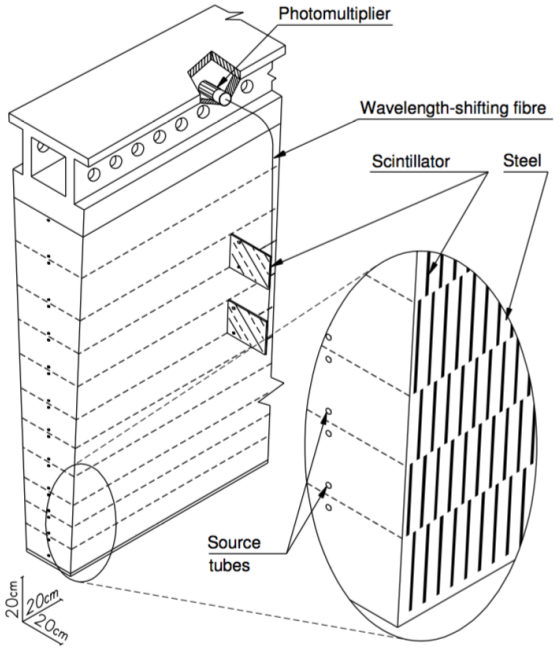

(a)

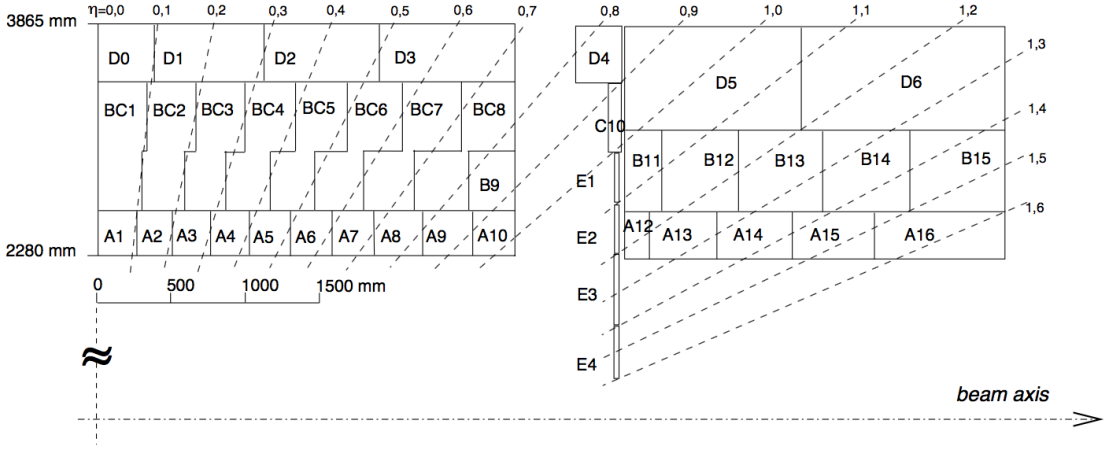

(b)

Figure 4.17: (a) A schematic sketch showing the optical readout of a TILECAL module. Wavelength shifting fibers collect the photons produced in the scintillating material which are then read out by the photomultiplier tubes (b) A schematic showing the segmentation in depth and in η of the TILECAL modules in the barrel (left) and extended barrel (right). The three sampling layers, A, BC, and D, can be seen in the drawing. [5].

Hadronic Tile Calorimeter		
	Long Barrel	**Extended Barrel**
Absorbing Material	steel	steel
Sampling Material	scintillator	scintillator
Coverage	$\|\eta\| < 1.0$	$0.8 < \|\eta\| < 1.7$
Cell granularity ($\Delta\eta \times \Delta\phi$)		
Layer 1	0.1×0.1	0.1×0.1
Layer 2	0.1×0.1	0.1×0.1
Layer 3	0.2×0.1	0.2×0.1
Thickness [λ_{int}]		
Layer 1	1.5	1.5
Layer 2	4.1	2.6
Layer 3	1.8	3.3
# of channels	5,760	1,792 per extended barrel

Table 4.2: Some of the main design specifications of the ATLAS hadronic tile calorimeter [5].

4.2.4.4.2 Hadronic end-cap calorimeter The end-caps of the hadronic calorimeter use copper as their absorber and LAr as their sampling medium. The HEC consists of two wheels in each end-cap, HEC1 (front) and HEC2 (rear), and covers a range of $1.5 < |\eta| < 3.2$ with an outer radius of 2 m. The design of the HEC is similar to that of the barrel region. Each of the four wheels consists of 32 individual wedge-shaped modules. The modules in the front wheels are made of 24 copper plates, each 25 mm thick. The rear wheels are made of 16 copper plates with a thickness of 50 mm. This results in a more coarse sampling fraction in the rear wheels (4.4% for HEC1 as compared to 2.2% for HEC2). Figure 4.18 shows an $R-z$ schematic view of the HEC modules. Table 4.3 shows some of the main design specifications of the ATLAS hadronic end-cap calorimeter.

4.2.4.4.3 Forward calorimeter The FCal covers a range of $3.1 < |\eta| < 4.9$ and provides detector acceptance for forward jets. Being so close to the beam pipe the FCal is exposed

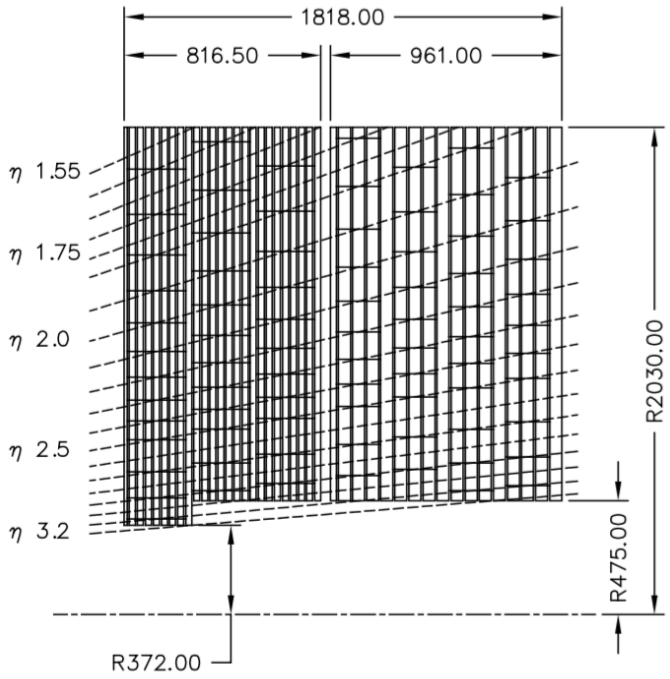

Figure 4.18: A schematic sketch showing an $R-z$ view of the hadronic end-cap calorimeter. The dimensions shown are in mm [6].

to very high particle flux. It was designed to be as dense as possible in order to handle this flux and to limit radiation exposure to the muon system behind it. Each FCal is split into an electromagnetic module (FCal1) and two hadronic modules (FCal2 and FCal3). Their placement is shown in Figure 4.19(a). FCal1 uses copper as its absorbing material while FCal2 and FCal3 use tungsten. Tungsten has a shorter λ_{int} than copper and was chosen to provide better containment and to limit lateral dispersion of the hadronic showers. To further reduce hadronic radiation seen in the muon spectrometer, a copper alloy shielding plug is inserted behind FCal3. The modules use copper plates with holes drilled through them and in which electrodes are inserted. The electrodes consist of a co-axial copper or tungsten rod wound with radiation-hard plastic fiber with a LAr gap in-between. This design is shown in Figure 4.19(b) for FCal1, but the design is similar for FCal2 and FCal3. Table 4.4 shows some of the main design specifications of the ATLAS forward calorimeter.

Hadronic End-Cap Calorimeter	
Absorbing Material	copper
Sampling Material	LAr
Coverage	$1.5 < \|\eta\| < 3.2$
Longitudinal segmentation	4 layers
Cell granularity	
$(\Delta\eta \times \Delta\phi)$	
$1.5 < \|\eta\| < 2.5$	0.1×0.1
$2.5 < \|\eta\| < 3.2$	0.2×0.2
Thickness $[X_0]$	≈ 103
Thickness $[\lambda_{\text{int}}]$	≈ 12
# of channels	3,072 per end-cap

Table 4.3: Some of the main design specifications of the ATLAS hadronic end-cap calorimeter [6].

Forward Calorimeter			
	FCAL1	**FCAL2**	**FCAL3**
Function	Electromagnetic	Hadronic	Hadronic
Absorbing Material	copper	tungsten	tungsten
LAr gap [μm]	269	376	508
Coverage	$3.1 < \|\eta\| < 4.9$	$3.1 < \|\eta\| < 4.9$	$3.1 < \|\eta\| < 4.9$
Cell granularity			
$(\Delta\eta \times \Delta\phi)$	0.1×0.1	0.2×0.2	0.2×0.2
Thickness $[X_0]$	27.6	91.3	89.2
Thickness $[\lambda_{\text{int}}]$	2.66	3.68	3.60
# of channels	1,008	500	254

Table 4.4: Some of the main design specifications of the ATLAS forward calorimeter [7].

4.2.4.5 Calorimeter energy resolution

The energy resolution of a sampling calorimeter takes the form

$$\frac{\sigma(E)}{E} = \frac{a}{\sqrt{E}} \oplus \frac{b}{E} \oplus c, \tag{4.6}$$

where the first term is called the sampling or stochastic term, the second term is called the noise term, and the third term is called the constant term. The $\oplus$ symbol indicates that a quadratic sum should be taken of the three terms. The stochastic term includes

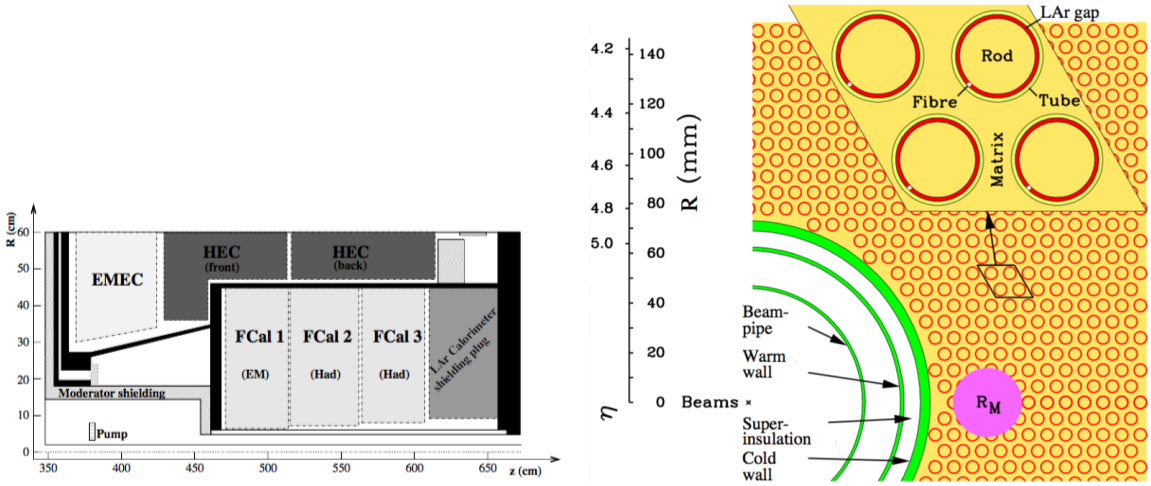

(a) (b)

Figure 4.19: (a) A schematic drawing showing the position of the FCal modules in relation to the electromagnetic and hadronic end-cap calorimeters. (b) The design structure of FCal1 with its matrix of copper plates and tubes with the LAr gap for the electrodes. The Molière radius, R_M, is also shown [23].

the shower's intrinsic quantum fluctuations as a result of the choice of absorber and active material as well as the thickness and number of sampling layers. In sampling calorimeters the amount of energy deposited in the active layer fluctuates on an event by event basis because the active layers are interwoven with the absorbing layers. The noise contribution to the energy resolution is due to electronic noise of the calorimeter's electronic readout components. Typically scintillator-based sampling, as in the TILECAL, has lower noise levels than charge based readouts, as in the ECal. The constant term includes contributions to the energy resolution which do not depend on the energy of the particle. The geometry and non-uniformities in the calorimeter are encapsulated in the constant term. From low to high energy of the incident particles the noise, stochastic, and constant terms dominate. The electromagnetic calorimeter was designed to have the following energy resolution,

$$\frac{\sigma_{\mathrm{EM}}(E)}{E} = \frac{10\%}{\sqrt{E}} \oplus 0.7\%, \tag{4.7}$$

and the hadronic calorimeter was designed such that

$$\frac{\sigma_{\text{had}}(E)}{E} = \frac{50\%}{\sqrt{E}} \oplus 3\% \quad \text{for } |\eta| < 3.2 \tag{4.8a}$$

$$\frac{\sigma_{\text{had}}(E)}{E} = \frac{100\%}{\sqrt{E}} \oplus 10\% \quad \text{for } 3.1 < |\eta| < 4.9. \tag{4.8b}$$

Prior to installation, the EM and hadronic calorimeter components were subjected to electron and pion test beams in order to determine their energy resolutions. Table 4.5 shows the results for individual calorimeter components after the effects due to electronic noise were filtered out. When combined, the results perform as well if not better than the design specifications listed in Equations 4.7 and 4.8.

Energy Resolution Fit Parameters			
Calorimeter	**Beam Type**	**Stochastic Term**	**Constant Term**
EM Barrel	electron	$(10.1 \pm 0.1)\%$	$(0.17 \pm 0.04)\%$
EM End-cap	electron	$10\% - 12.5\%$	0.6%
HEC	pion	$(70.6 \pm 1.5)\%$	$(5.8 \pm 0.2)\%$
TILECAL	pion	$(56.4 \pm 0.4)\%$	$(5.5 \pm 0.1)\%$
FCAL (EM)	electron	(28.5 ± 1.0)	(3.5 ± 0.1)
FCAL (Had)	pion	$(94.2 \pm 1.6)\%$	$(7.5 \pm 0.4)\%$

Table 4.5: The fit parameters for various ATLAS calorimeter sub systems using test beams [8, 9, 10, 11, 12].

4.2.5 Muon spectrometer

Muons are much more massive than electrons, have a longer decay time than hadrons, and escape the inner detectors and calorimeters with minimal energy loss. The muon spectrometer (MS), is the outermost portion of the ATLAS detector and is used to measure momenta and trajectories and to trigger the presence of muons [71]. It has detection stations comprised

of four main sub-components. Two of the components, the Monitored Drift Tube (MDT) chambers and the Cathode Strip Chambers (CSC), are used for high precision tracking and momenta measurements. The other two, the Resistive Plate Chambers (RPC) and Thin Gap Chambers (TGC), are used as inputs to the trigger system. The main parameters of the muon spectrometer are shown in Table 4.6. Figure 4.20 shows the locations of the muon spectrometer subsystems within the detector.

Muon Spectrometer					
			Resolution		
Component	**Function**	**Coverage**	$\boldsymbol{z, R}$	$\boldsymbol{\phi}$	**time**
MDT	tracking	$\lvert\eta\rvert < 2.7$	35 μm (z)	–	–
CSC	tracking	$2.0 < \lvert\eta\rvert < 2.7$	40 μm (R)	5 mm	7 ns
RPC	trigger	$\lvert\eta\rvert < 1.05$	10 mm (z)	10 mm	1.5 ns
TCG	trigger	$1.05 < \lvert\eta\rvert < 2.7$	2-6 mm (R)	3-7 mm	4ns

Table 4.6: The function, coverage, and resolution of the four muon spectrometer subsystems.

4.2.5.1 Precision tracking chambers

The main performance goal of the precision tracking chambers is a 10% momentum resolution for 1 TeV muon tracks. Tracks this energetic correspond to a sagitta of 500 μm and so a spatial resolution of 50 μm is required. The sagitta is a geometric term and is defined as the distance of the center of an arc to its base (see Figure 4.21).

Equation 4.9 shows how the sagitta measurement is related to the magnetic field, B, and the transverse momentum, p_{T}, of the muon. The trajectories of lower p_{T} muons are bent further than those of higher p_{T} muons. As such, the sagitta measurement is much greater for less energetic muons. As the momentum of the muons increases, the curvature of their tracks begins to approach a straight line. This makes a momentum measurement increasingly

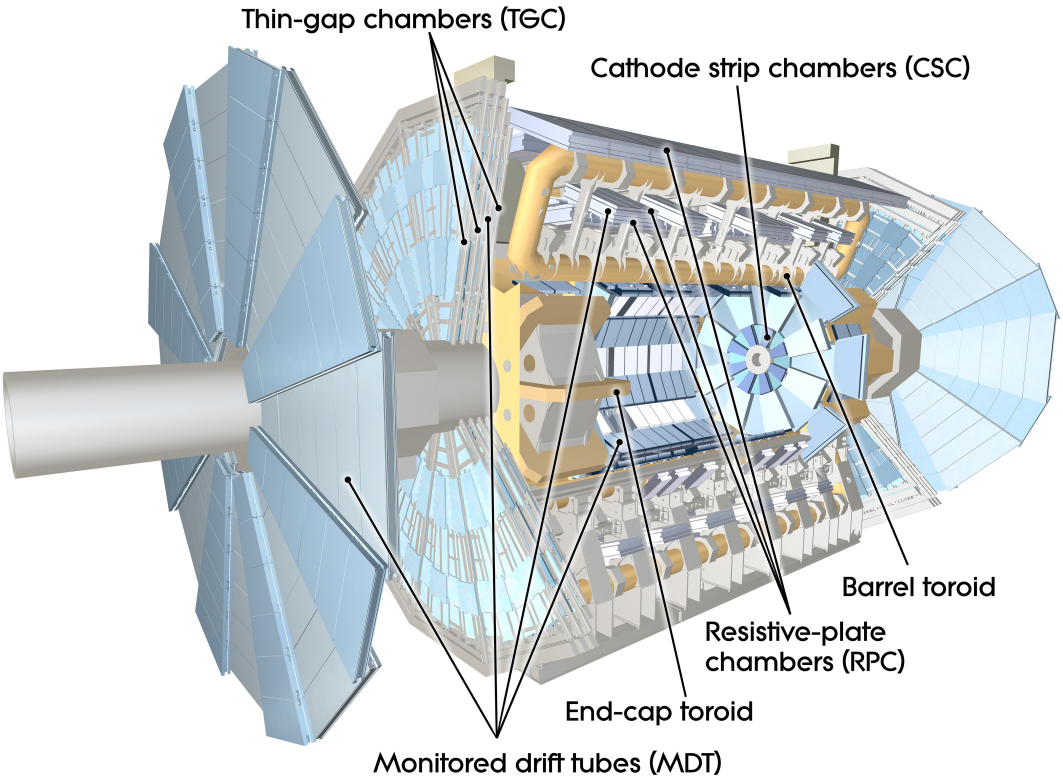

Figure 4.20: A drawing showing the locations of the muon spectrometer components in the ATLAS detector.

difficult as there is a finite resolution in the detector instrumentation.

$$s \propto \frac{B}{p_{\mathrm{T}}} \tag{4.9}$$

The measurement of the muon tracks is made in the $R - z$ projection, in the direction parallel to the magnetic field's bending direction. The MDT chambers, covering the region

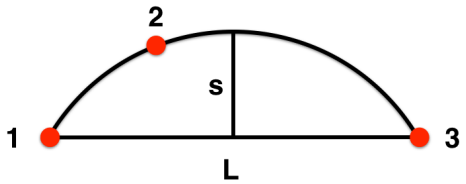

Figure 4.21: The sagitta, s, of a three point measurement.

$|\eta| < 2.7$, measure the z component while the CSCs measure the R component in the $2.0 < |\eta| < 2.7$ region. The precision detectors are located in three widely-separated stations at increasing distances from the interaction point. Most high p_{T} muons traverse all three stations. However, there are regions where these stations overlap and other regions where support structures or service equipment exist. The number of stations traversed by muons as a function of $|\eta|$ and ϕ is shown in Figure 4.22.

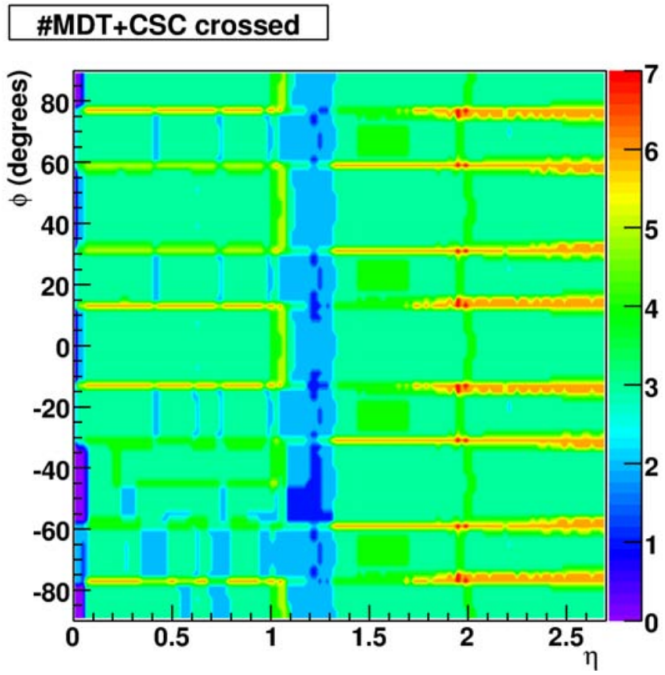

Figure 4.22: The number of muon stations traversed by muons passing through the precision tracking chambers as a function of $|\eta|$ and ϕ. The region $1.1 < |\eta| < 1.3$ contains support structures and cables which limit the number of stations a passing muon typically crosses [12].

4.2.5.1.1 Monitored drift tube chambers The MDT chambers consist of three to eight layers of 30 mm diameter aluminum drift tubes. The tubes act as cathodes and are filled with an argon carbon dioxide mixture. Muons ionize the gas mixture as they pass through and the electrons resulting from this ionization are collected at 50 μm tungsten wires kept at a 3.27 kV potential serving as anodes. A cross-section of an MDT tube is

shown in Figure 4.23.

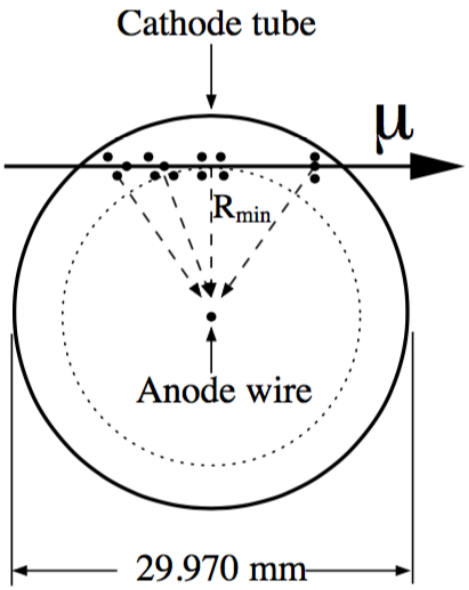

Figure 4.23: A cross-sectional view of an MDT.

4.2.5.1.2 Cathode-strip chambers MDT chambers are unable to handle the high particle flux in the forward region of the detector ($|\eta| > 2$). In this region cathode strip chambers are used instead. The CSC system consists of two end-caps with sixteen chambers in each end-cap (eight big and eight small). The CSCs are multi-wire proportional chambers (MWPCs) whose wires are oriented in the radial direction. The cathodes are segmented in each chamber. One has strips perpendicular to the wire which provides the precision measurement. The other has strips parallel to the wire providing the transverse coordinate. Figure 4.24 shows the layout of a CSC end-cap with its eight small and eight large chambers.

4.2.5.2 Trigger chambers

This section will discuss the muon trigger chambers. A trigger is a predetermined selection criterion used to select events of an interesting nature and the ATLAS trigger system will

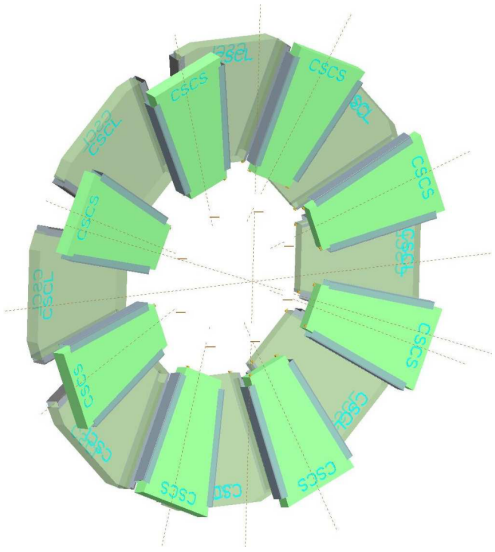

Figure 4.24: The layout of a CSC end-cap with its eight small and eight large chambers. The placement of this end-cap in the detector can be seen in Figure 4.20.

be explained in Section 4.2.6. The high precision muon measurements made in the MDTs or CSCs have maximal drift times of 500 and 30 ns respectively which are longer than the 25 ns bunch spacing of the LHC beam and are too slow to serve as a trigger. The trigger chambers for the ATLAS muon spectrometer consist of two types of detectors, Resistive Plate Chambers (RPCs) [72] in the barrel region and Thin Gap Chambers (TGCs) [73] in the end-cap regions. These detector technologies are not meant to provide precision measurements, but rather are designed to provide fast electronic signal readout of the presence of muon tracks to the Level-1 Muon Trigger electronics. The main design properties of these trigger chambers are good time resolution for accurate bunch-crossing identifications, adequate spatial resolution to approximately discriminate muon momenta, and second-coordinate measurements in the non-bending direction with a resolution on the order of 10 mm. In order to allow for a wide range of triggers, the chambers must provide acceptance out to $|\eta| < 2.4$ and over the full ϕ range.

4.2.5.2.1 Resistive plate chambers The Resistive Plate Chambers cover the barrel region in the pseudorapidity range of $|\eta| < 1.05$ and are arranged in three concentric cylindrical layers. Each RPC consists of two parallel plates with a 2 mm gap of tetrafluoroethane ($C_2H_2F_4$) gas between them. Muons ionize the gas between the plates which is read as an electronic signal. Because they are a wireless strip detector, the RPCs have a time resolution of 1.5 ns.

4.2.5.2.2 Thin gap chambers Thin Gap Chambers provide the muon trigger in the end-cap region covering a pseudorapidity range of $1.05 < |\eta| < 2.4$. TCGs have a structure similar to that of MWPCs. The TCGs have a finer segmentation than the RPCs at the cost of a slightly higher time resolution of 4 ns.

4.2.6 Trigger and data acquisition

ATLAS is both incapable of and not interested in recording every single event.[5] The vast majority of collisions of the protons do not involve enough energy to produce the sort of interesting physics processes for which the detector was intended to study. The inelastic cross-section of the LHC, $\mathcal{O}(10^{11}$ pb), far exceeds that of the more rare and interesting physics processes. Figure 4.25 shows how the cross-sections of various interesting SM processes compare against the total inelastic cross-section.

The goal of the trigger and data acquisition (TDAQ) system is to filter the overwhelming number of uninteresting "background" events in search of rare processes. The TDAQ system uses a three-tiered approach to reduce the input 40 MHz bunch crossing rate to a final

[5] In the context of the TDAQ system, an "event" refers to the record of all the detector information in a single bunch crossing. This is in contrast to its use later in this dissertation where an "event" refers to a single interaction between incident particles, of which there may be many in a single bunch crossing.

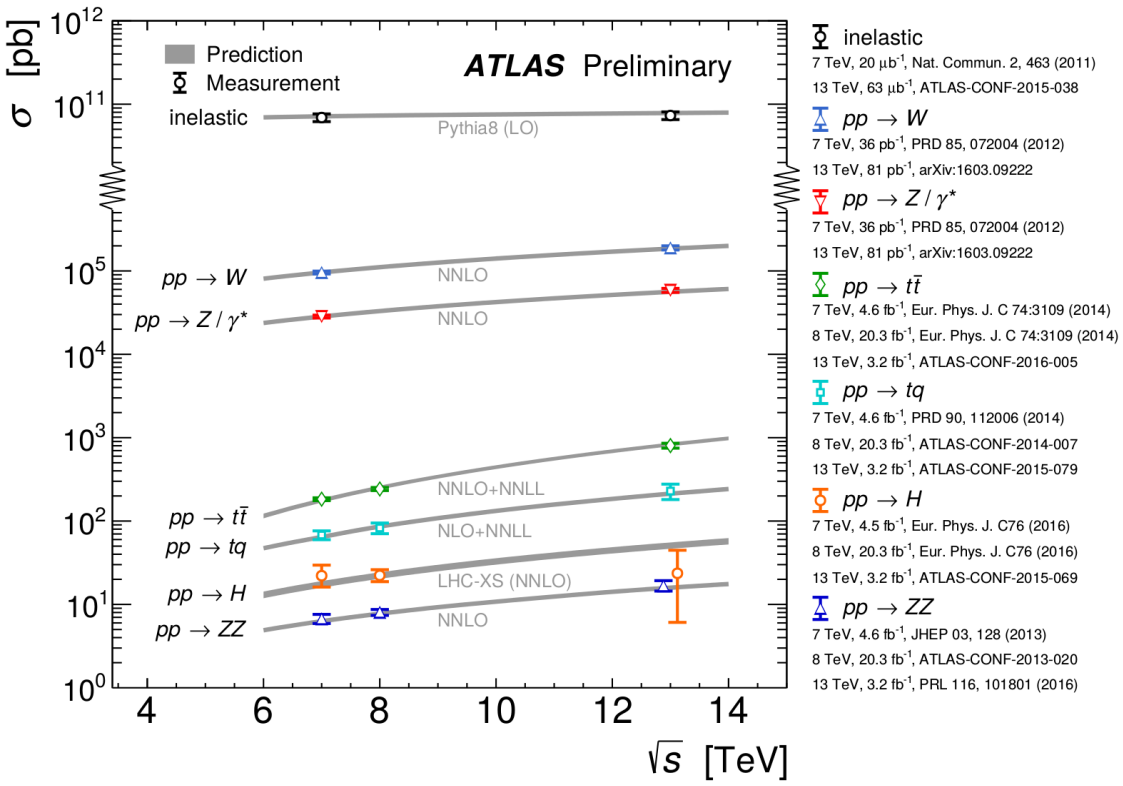

Figure 4.25: A summary of the various SM cross-section calculations and measurements by ATLAS as a function of center-of-mass energy [26].

output rate on the order of a few hundred Hz. Initially, the Level-1 (L1) trigger uses a reduced detector granularity to form an initial decision on what might be an interesting event. Regions of interest (RoIs) are formed in the L1 trigger which are then sent to the Level-2 (L2) trigger. The L2 trigger uses the full detector granularity to further decide whether or not to retain the event. If the event is retained then its information is sent to the event filter (EF) for final processing and recording.

For a general purpose detector like ATLAS these rare processes cover a wide range of physics with a wide range of event topologies. In order to identify interesting event topologies, the TDAQ system uses pre-defined trigger menus at each level of decision-making. These trigger menus consist of lists of selection criteria known as triggers. The progressive reduction in rate allows the use of more complex triggers making use of more detector information at

each level. Figure 4.26 shows an overview of the TDAQ system. Subsequent sections will explain the individual components seen in the figure.

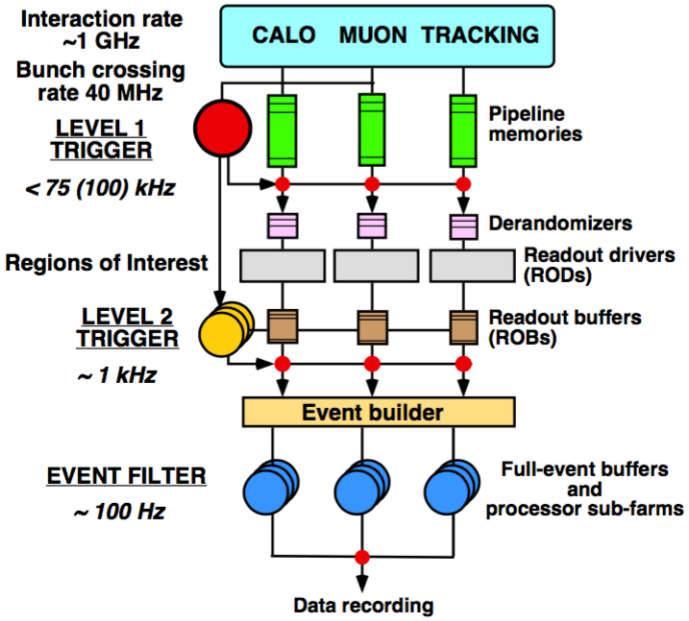

Figure 4.26: A block diagram of the ATLAS TDAQ system. The real-time path is in black, while the readout data paths are in grey [27].

4.2.6.1 Level-1 trigger

The first stage in the ATLAS TDAQ system is the L1 trigger. It is the job of the L1 trigger to reduce the initial input rate of 40 MHz down to 75 kHz. The L1 trigger is a hardware-based, pipelined system in which a Central Trigger Processor (CTP) is fed detector information from the L1 calorimeter trigger system (L1Calo) [28] and the L1 muon trigger system (L1Muon) [27] in order to make a decision as to whether or not to send event information to the next level in the trigger chain.

The L1 trigger has to deliver a decision for every bunch crossing. The latency (time taken to form and execute a trigger decision) of the L1 trigger is much longer than the designed bunch spacing of 25 ns. The L1 trigger was designed to have a latency of less than 2.5 μs.

During the latency period information from all detector channels ($\mathcal{O}(10^8)$ channels) must be retained in pipeline memories until a decision is made. The size of the detector itself also presents a challenge. A muon traveling to the furthest TGC could experience a time-of-flight of ~ 0.75 μs. In addition, signals might take as long as 0.4 μs to travel along the 80 m cables to and from the trigger hardware which is located in a separate room off the detector called USA15.

Once a decision is made by the L1 trigger, a Level-1 Accept (L1A) signal is sent which tells the detector front-end readout systems whether or not to read out the event information in the pipeline memories. Events which are selected to be kept by the L1 trigger are read out from the front-end electronics by readout drivers (RODs). The RODs are detector specific readout buffers (ROBs) and are stored there until the L2 trigger decision is made.

4.2.6.1.1 L1Calo The L1Calo trigger is located off the detector in USA15 and consists of three main subsystems: the PreProcessor (PP), the Cluster Processor (CP), and the Jet/Energy-sum Processor (JEP). The PP consists of 124 PreProcessor Modules (PPMs) housed in eight crates. Four crates process trigger-tower signals from the EM calorimeter while the other four process the signals from the hadronic calorimeter. These trigger-towers are analog sums in regions of granularity in $\Delta\eta \times \Delta\phi$ of 0.1×0.1 for the central regions and 0.4×0.4 in the forward regions of the calorimeters. The analog pulses are quite broad and the PP uses a digital filtering technique to associate them to a specific bunch crossing. The PP also serves to help suppress signal noise and to turn off problematic channels before sending the digital signals to the two algorithmic processors, the Cluster Processor (CP) and the Jet/Energy-sum Processor (JEP).

The CP is housed in four crates. Each crate contains 14 Cluster Processor Modules (CPMs)

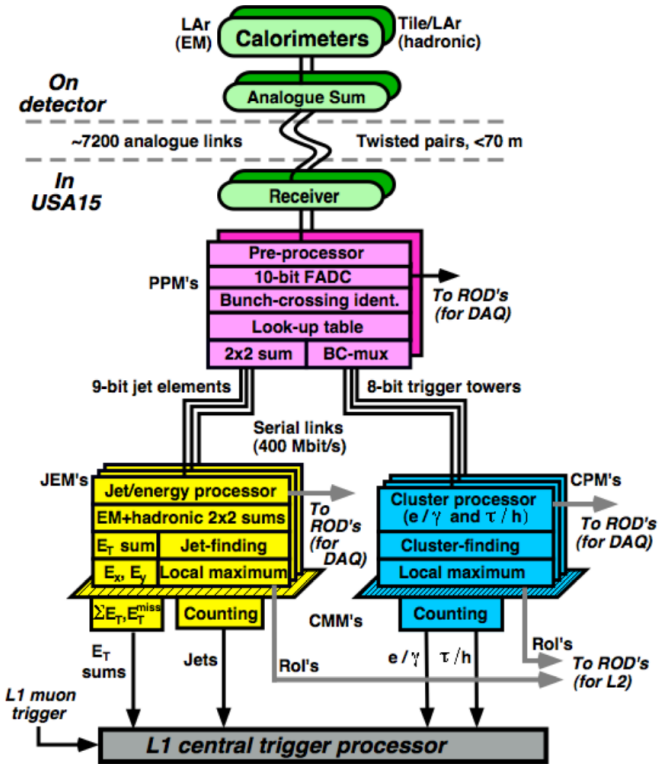

Figure 4.27: A block diagram of the ATLAS L1Calo trigger system. Analog signals from the calorimeters are digitized by the PreProcessor and are sent to the Jet/Energy-sum Processor and the Cluster Processor. Modules in each of those systems look for high p_{T} jets and electromagnetic objects [28].

and is responsible for one calorimeter quadrant (see Figure 4.28). The CP identifies and counts candidate electrons, photons, and taus which have a p_{T} higher than that programmed in the trigger menu by looking for isolated energy clusters in the EM calorimeters. In the case of electrons or photons the CPMs ensure that there is no energy deposited directly behind the cluster in the hadronic calorimeters. In the case of hadronically decay taus, energy clusters are allowed to penetrate into the hadronic calorimeters.

The JEP is a two-crate system, with each crate containing 16 Jet/Energy Modules (JEMs). Each calorimeter quadrant is covered by eight JEMs. Each JEM is responsible for identifying and counting hadronic energy clusters as well as serving as the first stage in the calculation of $E_{\mathrm{T}}^{\mathrm{miss}}$ and total E_{T}.

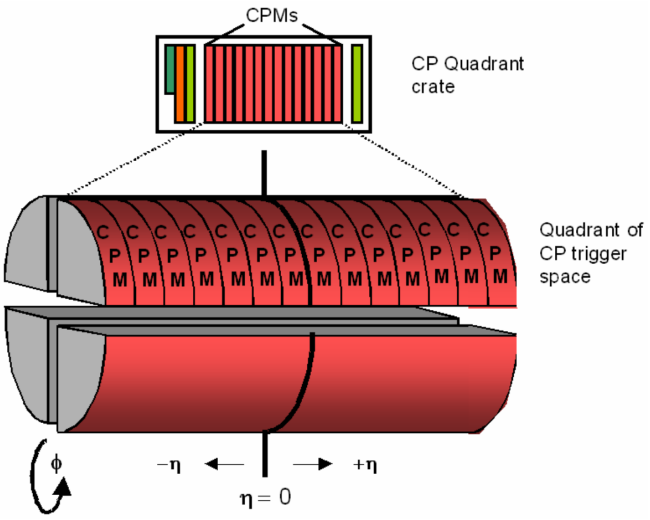

Figure 4.28: The layout of one crate of Cluster Processor Modules. Each crate is responsible for one quadrant in ϕ of the EM calorimeter. The layout of the Jet/Energy-sum Processor is similar, but with eight Jet Energy Modules per quadrant [28].

The CP and JEP systems send their counting results as well as position information to the Common Merger Modules (CMMs). The CMMs merge the results by counting the total number of electron, photon, tau, and jet hits, and by summing the total E_{T}, E_{x}, and E_{y} sent by the JEMs. The the position information of the RoIs identified in the CPMs and JEMs are sent to the RODs so that the L2 trigger system will have access to the detector information identified as being of interest.[6]

4.2.6.1.2 L1Muon The L1Muon trigger system is based on three trigger stations. The barrel region ($|\eta| < 1.05$) is covered by three stations of Resistive Plate Chambers while the end-cap region (($|\eta| > 1.05$) consists of three Thin Gap Chamber stations (see Figure 4.30). Each of these stations has two detector planes each of which are read out in two orthogonal projections, η (bending plane) and ϕ (non-bending plane). The basic principle of the

[6]The Common Merger eXtended (CMX) modules replaced the CMMs after the long shut-down period following Run1. These modules were built and tested by Michigan State University and are described in Appendix J.

L1Muon trigger algorithm is to require a coincidence of hits in the different chambers within some "road." The width of the road is related to the p_{T} threshold which is to be applied. Once muon candidates have been identified, they are passed to the Muon-to-CTP Interface (MUCTPI) which is responsible for collecting all the muon candidates and counting them appropriately. There are areas with station overlap and it is the job of the MUCTPI to ensure that muon candidates identified by more than one station are not doubly counted. It is also the job of the MUCPTI to pass all the information from the L1Muon trigger on to the CTP.

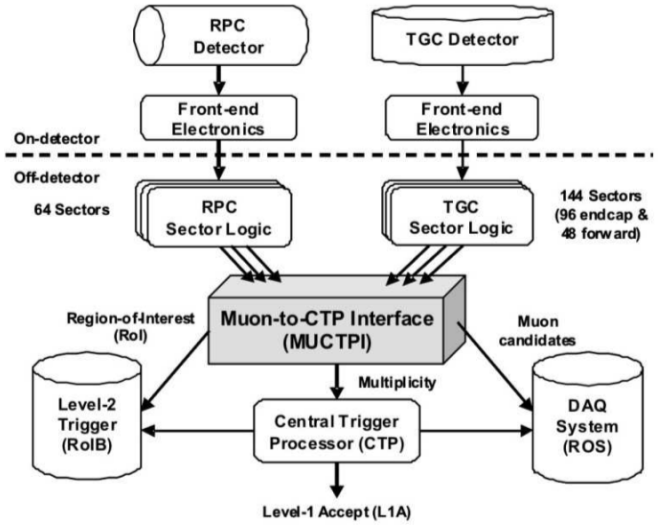

Figure 4.29: An overview of the ATLAS L1Muon trigger system [29].

4.2.6.2 High level trigger

The High Level Trigger (HLT) consists of the L2 trigger system as well as the event filter (EF). The purpose of the high level trigger is to reduce the L1 accept rate of ~ 75 kHz down to ~ 200 Hz. In practice the output rate of the HLT is not limited by the speed at which data can be written, but rather by offline computing resources and disk storage space available. Unlike the Level-1 trigger which uses specialized hardware for its logic decisions, the HLT

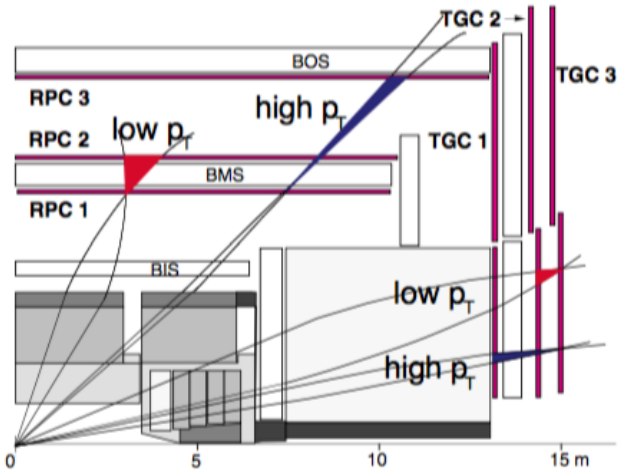

Figure 4.30: A longitudinal view of the barrel and end-cap L1Muon trigger systems. Three stations of Resistive Plate Chambers and three of Thin Gap Chambers define the barrel and end-cap systems respectively [27].

is software-based. Upon receiving a L1Accept signal, data from the front-end buffers on the detector elements are sent to the Read-out System (ROS) through Read-out Drivers (RODs). The ROS is responsible for receiving the data from the detector elements and storing them for as long as it takes the HLT to make a decision on the event. The HLT looks at the RoIs identified by the Level-1 trigger system. These RoIs correspond to regions in the detector where the Level-1 trigger has identified interesting activity. In this way the HLT only needs to analyze data provided by the ROS in a small area of the detector as opposed to having to analyze detector information over the full solid angle. Limiting the amount of area the HLT needs to analyze allows the HLT to process the full detector granularity within the RoI. This is unlike the Level-1 system which looks at a more course granularity in order to make a fast decision. A final output rate of $\sim$ 200 Hz corresponds to around 300 MB/s written to offline storage farms.

Chapter 5

Object Reconstruction

Until events are reconstructed they merely exist as electronic signals retrieved from the detector and terms like electron, muon, missing transverse energy, or jet have no meaning. This chapter describes the reconstruction algorithms and techniques used to take the raw signals from individual sub-components of the detector – either the actual detector in the case of data or the simulated detector in the case of Monte Carlo – and turn them into the physics objects for use in an analysis.[1] Within these algorithms are various quality control criteria which dictate how and when objects are reconstructed.

5.1 Tracks

When charged particles traverse through the Inner Detector they create electron/hole pairs in the silicon pixels of the pixel detector and silicon strips of the SCT or ionizing radiation in the TRT. These charge carriers are read out by the different components of the ID and interpreted as "hits" in the detector representing points in space. The ID can provide up to 3, 4, and 36 hits per charged particle track in the pixel detector, the SCT, and the TRT respectively. These measurements allow for an efficient reconstruction of tracks. Track reconstruction in ATLAS follows a two-pronged approach. First an "inside-out" strategy defines track

[1] Monte Carlo refers to computer simulations of physics processes and will be described in greater detail in Chapter 6.

candidates based on hits in the pixel and SCT detectors which are then extended to attempt to fit hits in the TRT [30]. This strategy is augmented by an "outside-in" strategy where hits in the TRT are backtracked to the two inner silicon detectors.

5.1.1 Inside-out strategy

Initially, track seeds are formed from a combination of the measurements in the pixel and SCT detectors and a three-dimensional representation of these hits is created to form "silicon spacepoints." In the pixel detector a spacepoint is the center of a cluster of pixels. In the SCT it is formed by finding the intersection of the strips on the front and back sides of a module. At this stage the tracks are built by using a window search given through the seed direction. Hits that fall within the window are collected and potential tracks are formed using a simplified Kalman filtering. The Kalman filtering algorithm uses repeated measurements over time, including uncertainties, to give better estimates of variables than a single measurement can provide. To save CPU time this filtering process uses material maps instead of the full ATLAS geometry to correct track predictions for scattering against passive medium and energy losses [74]. The Kalman filtering algorithm uses parameters related to the effects of charged particles interactions with detector materials as well as five "perigee parameters" describing the track's point of closest approach to the z-axis. These perigee parameters are described below and are shown in Figure 5.1.

- $\boldsymbol{\frac{q}{p}}$ – the charge of a particle divided by its momentum
- $\boldsymbol{\phi_0}$ – the angle with the x-axis in the $x-y$ plane at the perigee point
- $\boldsymbol{\theta_0}$ – the angle with the beam line in the $r-z$ plane at the perigee point

- $\boldsymbol{z_0}$ – the longitudinal impact parameter; the z coordinate of the track at the perigee point

- $\boldsymbol{d_0}$ – the signed transverse impact parameter; the closest distance to the beam line in the transverse plane

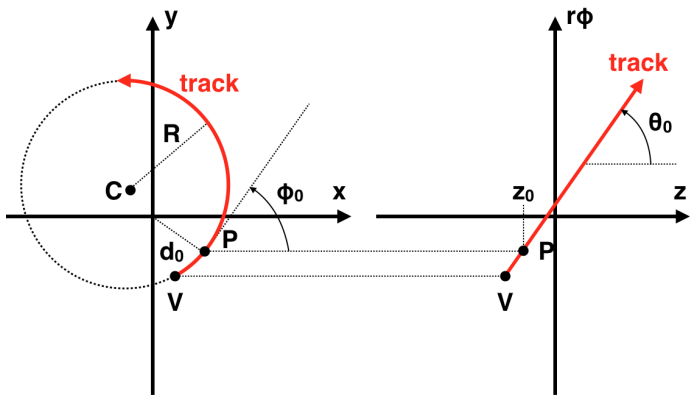

Figure 5.1: The track parameters for a charged particle track in the Inner Detector. The point V indicates the vertex of the track and the point P is the point of closest approach (perigee). The transverse impact parameter, d_0, and the azimuthal angle are shown in the bending plane ($x-y$ plane). The longitudinal impact parameter, z_0, and the polar angle are shown in the non-bending plane ($r\phi - z$ plane).

The Kalman filtering algorithm is an iterative process of determining the optimal track parameters from one measurement to the next. At each measurement surface the track parameters are re-evaluated and extrapolated to the next measurement surface. The aim of the algorithm is to determine the precise values of the track parameters at both the perigee point and at the outermost endpoint of the track.

Once track candidates have been fitted, it is possible that many fake tracks or overlapping track segments with shared hits will result. These ambiguities are resolved by assigning a score to the tracks in which fully reconstructed tracks receive higher scores than smaller track segments. Which detectors contribute measurements to the tracks is also a factor in determining a track's score. Precision measurements in the pixel detector add more to

the score than either the SCT or TRT measurements as the pixel detector has the highest resolution of the three ID components. Figure 5.2 shows an example of the ambiguity inherent in the track candidates.

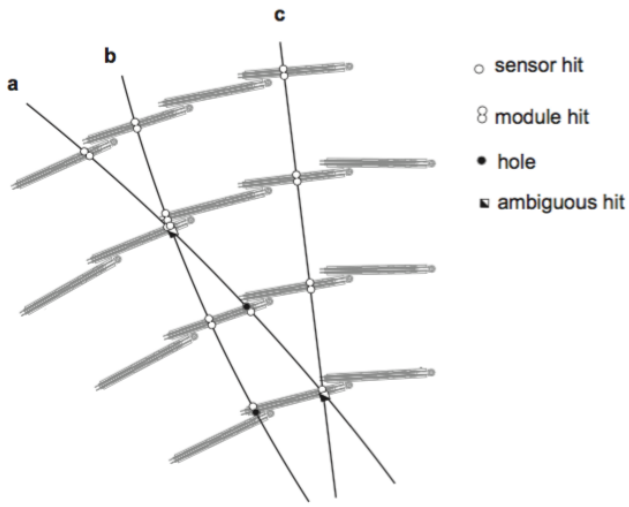

Figure 5.2: A drawing showing the track ambiguity solving process. Tracks **a**, **b**, and **c** in the SCT barrel are shown and share several hits. A module hit representing measurements on both sides of the SCT silicon strips receives a higher score than a single sensor hit without an associated backside hit [30].

Tracks candidates that are found through the Kalman algorithm and which survive the ambiguity solving process are used as inputs to find compatible sets of TRT measurements. An extension of the Kalman filtering algorithm together with the same ambiguity solving process determines which tracks from the pixel and SRT detectors get matched to hits in the TRT [75]. Successfully matched tracks are used in the reconstruction of objects such as jets, electrons, and muons.

5.1.2 Outside-in strategy

Not all tracks can be found with the inside-out strategy. Tracks originating from secondary vertices further inside the Inner Detector volume (e.g. K_s decays or b-quark hadronization)

may not have sufficient silicon hits to score high enough to survive the ambiguity-resolving process. The outside-in strategy follows a similar procedure for determining track candidates, but begins with hits in the TRT and attempts to match tracks to the pixel or SRT measurements. This backtracking serves to augment the inside-out approach and hits that have already been assigned tracks using the inside-out procedure are not used.

5.2 Electrons

Electrons are reconstructed by identifying energy deposition in the electromagnetic calorimeter and, in the case of central electrons ($|\eta| < 2.5$), associating those energy clusters with reconstructed tracks from the ID. Once reconstructed, these electron candidates need to be identified as being final state electrons from interesting physics properties, misidentified hadronic jets faking electrons, or electrons from pion decays in the showering process. Clustering algorithms together with other selection criteria help to distinguish these signal electrons from those in background or secondary processes.

5.2.1 Sliding-window clustering algorithm

The longitudinal and lateral dispersion of electromagnetic showers typically cause incident electrons to deposit their energy in multiple calorimeter cells. Clustering algorithms are used to group these cells and to identify energy clusters of potential electron candidates and the sliding-window clustering algorithm is used here [14, 76]. The first step is to build towers where the energy deposited in all longitudinal layers of the electromagnetic calorimeter is summed in a grid of $N_\eta^{\text{grid}} \times N_\phi^{\text{grid}}$ calorimeter cells of size $\Delta\eta \times \Delta\phi$. The next step is seed-finding where a window of $N_\eta^{\text{window}} \times N_\phi^{\text{window}}$ is moved across the tower grid. If the

sum of the transverse energy of the towers contained in the window is a local maximum above some threshold energy, E_T^{thresh}, then a precluster is formed. The position of the precluster is computed as the energy-weighted center (in η and ϕ) of all cells within a window of $N_\eta^{\text{pos}} \times N_\phi^{\text{pos}}$ around the tower at the center of the sliding window. Using a smaller window for the position calculation makes the computation less sensitive to noise. If any two preclusters have positions within a $N_\eta^{\text{dupl}} \times N_\phi^{\text{dupl}}$ window of each other, the precluster with the largest transverse energy is kept while the other is removed. This step continues until the whole tower grid has been evaluated. The values of the parameters used in the sliding-window algorithm are shown in Table 5.1.

Sliding-Window Clustering Algorithm Parameters	
Parameter	**Value**
$N_\eta^{\text{grid}} \times N_\phi^{\text{grid}}$	200×256
$\Delta\eta \times \Delta\phi$	0.025×0.025
$N_\eta^{\text{window}} \times N_\phi^{\text{window}}$	3×5
E_T^{thresh}	2.5 GeV
$N_\eta^{\text{pos}} \times N_\phi^{\text{pos}}$	3×3
$N_\eta^{\text{dupl}} \times N_\phi^{\text{dupl}}$	2×2

Table 5.1: Parameter values for the sliding-window clustering algorithm [13].

5.2.2 Track association

Tracks are extrapolated from the last measurement in the ID to the middle layer of the EM calorimeter. The η and ϕ coordinates of these extrapolations are then compared to the coordinates of the seed clusters calculated in the sliding-window clustering algorithm. A

track is considered to be associated to an energy cluster if the difference in η between the track impact point in the electromagnetic calorimeter and the cluster barycenter is less than 0.05. Electron energy losses due to bremsstrahlung in the azimuthal direction are accounted for by allowing for a $|\Delta\phi| < 0.1$ in the direction the track is bent. If more than one track is associated with the same energy cluster, tracks with hits in the pixel detector or SCT are given priority and the one with the smaller ΔR is chosen. Once a track has been associated with an energy cluster, the cluster is then rebuilt to include a window of 3×7 (5×5) longitudinal towers of cells in the barrel (endcaps) of the EM calorimeter. The final energy of the cluster is then determined by summing four different energy contributions [12]:

- the estimated energy deposited in material in front of the EM calorimeter,
- the measured energy deposit in the cluster,
- the estimated lateral (within the EM calorimeter) leakage, and
- the estimated longitudinal (beyond the EM calorimeter) leakage.

5.2.3 Electron identification

Reconstructed electron candidates can be isolated signal electrons from interesting event topologies or they can be from jets misidentified as electrons, electrons from photon conversions, or electrons from neutral pion decays. Jets tend to have a wider lateral dispersion in their shower shapes in addition to more tracks. Pions typically decay after the first layer of the ID. In order to identify these signal electrons from background electrons a series of discriminating variables such as those describing the shapes of the electromagnetic showers, properties of the tracks in the ID, and the matching between tracks and energy clusters are used. A list of these variables is shown in Table 5.2.

Electron Discrimination Variables		
Type	**Description**	**Name**
Hadronic leakage	Ratio of E_{T} in the first layer of the hadronic calorimeter to the E_{T} of the EM cluster for $\lvert\eta\rvert < 0.8$ and $\lvert\eta\rvert > 1.37$	R_{Had1}
	Ratio of E_{T} in hadronic calorimeter to the E_{T} of the EM cluster for $0.8 < \lvert\eta\rvert < 1.37$	R_{Had}
Third layer of EM calorimeter	Ratio of the energy in the third later to the total layer	f_3
Middle layer of EM calorimeter	Lateral shower width, $\sqrt{\frac{\Sigma E_i \eta_i^2}{\Sigma E_i} - \left(\frac{\Sigma E_i \eta_i}{\Sigma E_i}\right)^2}$, where E_i is the energy and η_i is the pseudorapidity of cell i and the sum is calculated within a window of 3×5 cells	$W_{\eta 2}$
	Ratio of the energy in 3×7 cells over the energy in 7×7 cells centered at the cluster position	R_η
Strip layer of EM calorimeter	Shower width, $\sqrt{\left(\Sigma E_i \left(i - i_{\mathrm{max}}\right)^2\right)\left(\Sigma E_i\right)}$, where i runs over all strips in a window of $\Delta\eta \times \Delta\phi \approx 0.0625 \times 0.2$, corresponding typically to 20 strips in η, and i_{max} is the index of the highest-energy strip	W_{stot}
	Ratio of the energy difference between the largest and second largest energy deposits in the cluster over the sum of these energies	E_{ratio}
Track quality	Number of hits in the B-layer (discriminates against photon conversions)	n_{Blayer}
	Number of hits in the pixel detector	n_{pixel}
	Number of total hits in the pixel and SCT detectors	n_{Si}
	Transverse impact parameter	d_0
TRT	Total number of hits in the TRT	n_{TRT}
	Ratio of the number of high-threshold hits to the total number of hits in the TRT	F_{HT}
Track-cluster matching	$\Delta\eta$ between the cluster position in the strip layer and the extrapolated track	$\Delta\eta_1$
	$\Delta\phi$ between the cluster position in the middle layer and the extrapolated track	$\Delta\phi_2$
	Ratio of the cluster energy to the track momentum	E/p
Conversions	Veto electron candidates matched to reconstructed photon conversions	isConv

Table 5.2: The definitions of electron discrimination variables [13].

Three different selection menus, based on different cuts on these variables, are used to define three types of electrons: loose, medium, and tight. The procedure for determining these classes includes binning the electron candidates in both E_{T} and η. Binning in E_{T} is necessary because shower shapes as well as track properties depend greatly on the energy of the electron. For example, electrons with higher E_{T} have narrower shower shapes. Binning in η is necessary in order to account for the varying amounts of passive material the electron must traverse in different parts of the detector which can affect the shower shapes. From loose to medium to tight, the cuts are chosen in such a way as to provide increasing background rejection at the cost of some identification efficiency. Additional variables are added as well as tightening cuts on existing variables when moving from the loose to the tight selection menus. Table 5.3 shows the variables used by the different menus.

Electron Identification Menus			
Variable	**Loose**	**Medium**	**Tight**
$R_{\mathrm{Had(1)}}$	✓	✓	✓
f_3		✓	✓
$W_{\eta 2}$	✓	✓	✓
R_{η}	✓	✓	✓
W_{stot}	✓	✓	✓
E_{ratio}	✓	✓	✓
n_{Blayer}		✓	✓
n_{pixel}	✓	✓	✓
n_{Si}	✓	✓	✓
d_0		✓	✓
n_{TRT}		✓	✓
F_{HT}		✓	✓
$\Delta\eta_1$	✓	✓	✓
$\Delta\phi_2$			✓
E/p			✓
!isConv			✓

Table 5.3: The electron identification menus [13].

5.2.4 Electron isolation

In order to further reject hadronic jets posing as electrons, isolation criteria which impose restrictions on either the information in the calorimeter or in the associated track are used [77]. For calorimeter isolation the variable $E_{\mathrm{T}}^{\mathrm{cone}\Delta\mathrm{R}}$ is used which is defined as the sum of the transverse energy deposited in the calorimeter cells in a cone of ΔR around the electron (see Figure 5.3). A 5×7 window surrounding the barycenter of the electron is subtracted from this sum. This window is sufficient to collect 95% of the electron's energy. In the case of track isolation the variable $p_{\mathrm{T}}^{\mathrm{cone}\Delta\mathrm{R}}$ is used which is defined as the sum of the transverse momentum of tracks with $p_{\mathrm{T}} > 1$ GeV in a cone of ΔR around the electron (excluding the track of the electron itself). Only tracks coming from the primary vertex and having at least four hits in the pixel and silicon strip detectors are included in the sum.

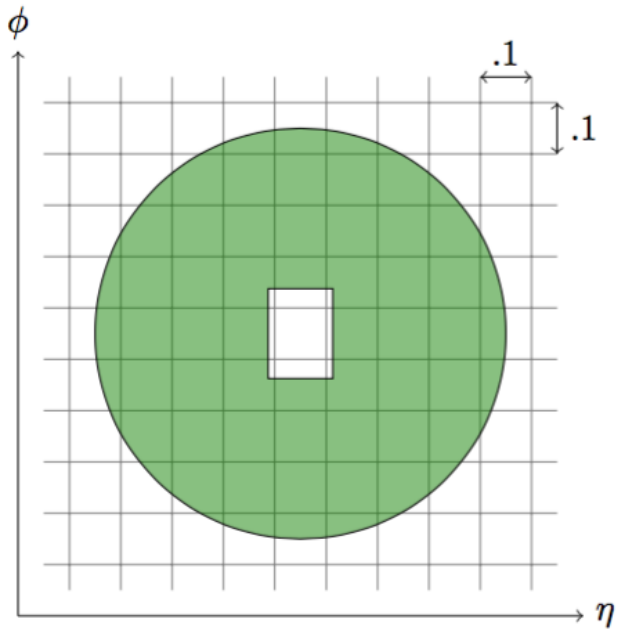

Figure 5.3: The $E_{\mathrm{T}}^{\mathrm{cone}\Delta\mathrm{R}}$ variable is calculated using the energy deposited in calorimeter cells in a cone of ΔR around the electron and ignoring the 5×7 window of cells around the center of the cone. A cone size of ΔR=0.40 is shown here.

5.3 Muons

Muons are identified and reconstructed with information from the muon spectrometer, the Inner Detector, and the calorimeter systems [78, 36]. Depending on the criteria used, muons can be classified into four different types:

- **Stand-Alone (SA) muons** – An SA muon trajectory is only reconstructed in the MS and must traverse at least two layers of MS chambers to provide a track measurement. SA muons are typically used to extend acceptance in the range of $2.5 < |\eta| < 2.7$, not covered by the ID.

- **Segment-tagged (ST) muons** – An ID track is classified as an ST muon if, after being extrapolated to the MS, it is associated with at least one local track segment in either the MDT or CSC chambers. ST muons are also used to increase detector acceptance in the case where the muon only crosses one layer of MS chambers.

- **Calorimeter-tagged (CaloTag) muons** – A track in the ID is identified as a CaloTag muon if it is associated with an energy deposition in the calorimeter compatible with a minimum ionizing particle. A CaloTag muon has the lowest purity but it recovers acceptance in regions of the MS with limited instrumentation.

- **Combined (CB) muons** – A CB muon is one with a track reconstruction independently performed in both the ID and the MS and combined to form the final muon track. This is the main type of reconstructed muon and has the highest purity of all the muon types. This analysis uses CB muons exclusively.

5.3.1 CB muon reconstruction

Combined muons are reconstructed by pairing MS tracks with ID tracks. The tracks from the MS are extrapolated back to the interaction point taking into account the bending of the tracks as well as energy losses in the calorimeter. Inner Detector tracks within a cone around the extrapolated MS tracks are paired. This "outside-in" approach limits the combinatorics as there are typically more tracks in the ID than in the MS. Inner Detector tracks must meet the following quality requirements:

- They must contain at least one hit in the pixel detector.
- They must have at least five SCT hits.
- There can be at most two active pixel or SCT sensors traversed by the track without hits.
- There must be at least nine hits in the TRT if the track falls between $0.1 < |\eta| < 1.9$.

While the ID has excellent muon p_{T} resolution at low values of p_{T}, its resolution begins to degrade at higher values. Conversely, the muon spectrometer does not perform as well at low values of muon p_{T} at it does at higher values. By combining the tracks of the two detectors the resolution of the combined track performs well across the entire p_{T} spectrum. This is shown in Figure 5.4.

5.3.2 Muon isolation

Isolation criteria are applied to reconstructed muon candidates in order to reduce the possibility that a reconstructed muon is produced from a hadron decay. Hadrons can decay leptonically and result in a muon inside a jet which can then be seen in the MS. Two types

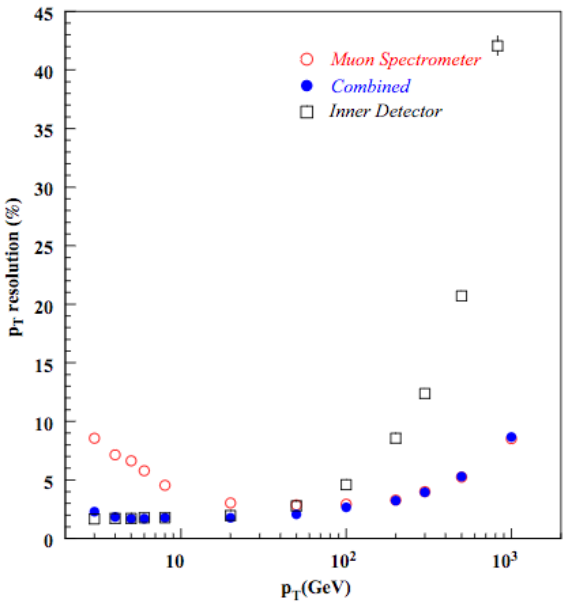

Figure 5.4: The p_{T} resolution of muon tracks using just the Inner Detector (black squares), just the muon spectrometer (red circles), and using the combined muon track reconstruction method (blue circles) [31].

of variables are used to assess muon isolation: the track-based isolation variable, ${p_{\mathrm{T}}}^{\mathrm{varcone}\Delta\mathrm{R}}$ and the colorimeter-based isolation variable, ${E_{\mathrm{T}}}^{\mathrm{topocone}\Delta\mathrm{R}}$. The track-based variable is defined as the sum of the transverse momenta of all the tracks within a cone of ΔR around the muon, excluding the muon track itself. Tracks included in the summation are further required to have $p_{\mathrm{T}} > 1$ GeV, $|\eta| < 2.5$, have a longitudinal impact parameter with respect to the primary vertex less than 3mm, and at least 7 silicon hits in the ID. The calorimeter-based variable is defined as the sum of the energies of topological clusters in a cone of radius ΔR around the muon, excluding the energy deposited the muon itself.

5.4 Jets

Many physics objects lead to final states consisting of quarks or gluons. As colored partons, they cannot exist as final state objects and instead hadronize to form hadrons inside the

detector and subsequently deposit their energy in the hadronic calorimeter. The collimated sprays of hadronized and fragmented particles are called jets. Jets serve as the link between what is seen in the detector and the underlying physics at the partonic level and can provide kinematic information of the originating partons. Jet finding algorithms map the momenta of the final state particles seen in the calorimeter and tracker into the momenta of a certain number of jets. There are likely many jets in a given event and it is necessary to be able to tell which energy deposits correspond to which jets.

There are two main types of jet finding algorithms: cone and clustering. Cone algorithms take a top-down approach where the most energetic particle in the event serves as the seed. The momenta of the surrounding particles within a cone of radius R are summed and a jet is defined. The seed and the summed particles are removed from the event and the process iterates until no particles remain. Clustering algorithms, on the other hand, take a bottom-up approach. Cones are formed by merging particles which have the smallest difference in transverse momentum based on a distance measure and iterating until a jet of some pre-defined radius is formed. This process is continued until all particles are clustered into jets. Jets in this analysis are reconstructed wth a type of clustering algorithm called the anti-k_t clustering algorithm [14].

5.4.1 Anti-k_{t} algorithm

The anti-k_t algorithm is based on distance measures. The distance, d_{ij}, between particles i and j is defined as

$$d_{ij} = \min\left(k_{\mathrm{t}i}^{2p}, k_{\mathrm{t}j}^{2p}\right)\frac{\Delta_{ij}^2}{R}, \tag{5.1}$$

where $k_{\mathrm{t}i}$ is the transverse momentum of the i^{th} particle, Δ_{ij} is the spatial separation

between the i^{th} and j^{th} particles in $\eta - \phi$ space, and R is the pre-defined jet radius. The distance between any particle, i, and the beam is defined as

$$d_{i\text{B}} = k_{\text{t}i}^{2p}. \tag{5.2}$$

All distances of d_{ij} and $d_{i\text{B}}$ are computed to identify the smallest. If the smallest is a d_{ij} measurement, then the momenta of the two particles, i and j, are summed into a new particle. Distances are then recomputed again (with the previous sum acting as a new particle) and the next smallest distance is determined. If the smallest distance is $d_{i\text{B}}$ then particle i is removed and it is called a jet. This process is iterated until all particles are clustered into jets. The parameter R scales the distance d_{ij} with respect to $d_{i\text{B}}$ so that any pair of final jets are at least separated by R. The parameter p dictates the relative power of energy vs. geometric scales. In the case of the anti-k_t algorithm $p = -1$. Jets in this analysis use topological calorimeter clusters and a cone radius of $R = 0.4$.

5.4.2 Topological clustering algorithm

The topological clustering algorithm is used to identify energy clusters in the hadronic and electromagnetic calorimeters which are used as inputs to the anti-k_t jet finding algorithm [14]. The algorithm groups neighboring cells that have significant energy relative to the expected noise level. Unlike the sliding-window algorithm which uses a grid of cell towers covering the three longitudinal layers of the electromagnetic calorimeter, the topological clustering algorithm uses individual cells to build three-dimensional clusters. As a result the topological clusters can be variable in size as opposed to the fixed window size of the sliding-window algorithm. The algorithm consists of two steps. The first step is to identify seeds and to

build the clusters. Seeds are identified as cells with a signal-to-noise ratio higher than some threshold value, t_{seed}. The noise value used in the ratio is a quadratic sum of the both the electronic noise and the noise due to pileup (see Section 4.1.2).

$$\sigma_{\text{noise}} = \sqrt{\left(\sigma_{\text{noise}}^{\text{electronic}}\right)^2 + \left(\sigma_{\text{noise}}^{\text{pile-up}}\right)^2} \tag{5.3}$$

The noise due to pileup for a given cell is evaluated from Monte Carlo simulation and is a function of the number of collisions per bunch crossing, $\langle\mu\rangle$, and a given bunch spacing, Δt. Figure 5.5 shows the total per-cell noise in various parts of the calorimeters as a funciton of η when no beam is present and with a simulated pileup of $\langle\mu\rangle = 30$ and a bunch spacing of 50 ns.

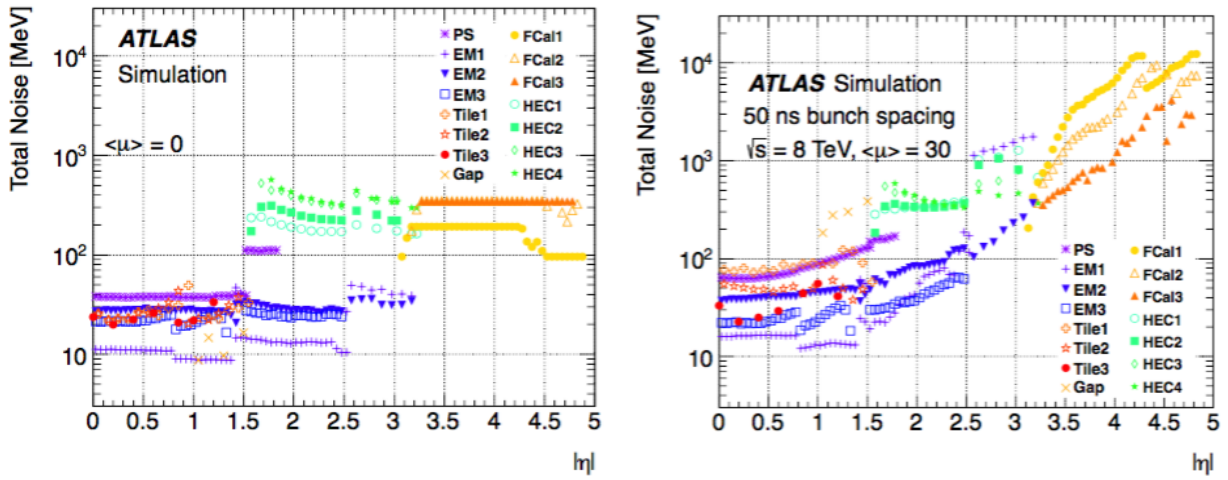

(a) (b)

Figure 5.5: (a) The per-cell electronic noise when no beam is present ($\langle\mu\rangle = 0$) (b) The total noise per-cell at $\langle\mu\rangle = 30$ and 50 ns bunch spacing [32].

These seed cells form a list which is ordered in descending value of signal-to-noise ratio. Neighboring cells are then added to the seed cell if they themselves are not a seed and if their signal-to-noise ratio is above the neighbor threshold, t_{neighbor}. The seeds can then

grow into proto-clusters and can be merged together if they both share a neighboring cell. Once the clusters have been formed, cells on their outer perimeter with a signal-to-noise ratio higher than t_{cell} are added and the cluster is finalized. If the total energy of the cluster is less than some value, E_T^{cut}, the cluster is dropped from consideration.

Cluster splitting is the second part of the topological clustering algorithm. There can be many overlapping showers, especially in the forward region or in high pileup conditions, and as such the clusters can grow to be quite large. In an ideal situation the clusters would be isolated but this is atypical. Local maxima within the clusters can be identified which are then used to create smaller clusters from the original. The parameters for the topological clustering algorithms are shown in Table 5.4.

Topological Clustering Algorithm Parameters	
Parameter	**Value**
t_{seed}	4
t_{neighbor}	2
t_{cell}	0
$\left\|E_T^{\text{cut}}\right\|$	0 GeV

Table 5.4: Parameter values for the topological clustering algorithm used in jet building [14].

5.4.3 Jet vertex fraction

The number of reconstructed jets increases with increased pileup. Jets tend to deposit their energy across a wide area of the detector and as the number of pileup jets increases these energy depositions begin to overlap each other and the quality of the reconstructed jet kinematics decreases. Suppression of these pileup jets is mitigated by a cut on the jet vertex

fraction variable (JVF) which is a measure of the fraction of jet energy associated with a particular primary vertex. The principle of the jet vertex fraction is shown in Figure 5.6 and is defined as the summed track p_{T} for all tracks matched to a given jet and associated with a particular primary vertex, PV_0, divided by the summed p_{T} of all tracks matched to the jet, independent of any primary vertex,

$$\mathrm{JVF}(\mathrm{jet}, \mathrm{PV}_0) = \frac{\sum_k p_{\mathrm{T}}\left(\mathrm{track}_k^{\mathrm{jet}}, \mathrm{PV}_0\right)}{\sum_n \sum_l p_{\mathrm{T}}\left(\mathrm{track}_l^{\mathrm{jet}}, \mathrm{PV}_n\right)}. \tag{5.4}$$

The value of JVF runs between 0 and 1. A jet is more likely to have originated from the primary vertex in question if it has a JVF closer to 1.

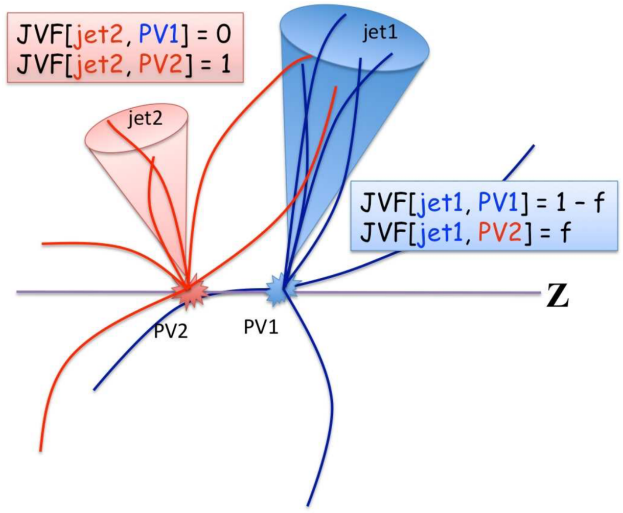

Figure 5.6: A carton drawing showing the JVF principle [33].

5.4.4 Overlap removal

The reconstruction algorithms for leptons and jets are performed independently of each other and, as such, it is possible for a single set of tracks and energy deposits to be reconstructed as both a lepton and a jet. This overlap between jets and leptons creates an ambiguity since

the lepton could, in actuality, have originated from the jet. In such an event, a jet found within a cone of $\Delta R = 0.2$ around an electron is removed and the corresponding electron is reconstructed with the additional energy deposits of the removed-jet. If any remaining jets with $p_T > 25$ GeV are found close to an electron within a cone of $\Delta R = 0.4$, then the electron is removed from the event record and its energy is added to the jet. This is because the electron efficiency corrections are only valid for a $\Delta R > 0.4$. If a reconstructed jet with $p_T > 25$ GeV and a jet vertex fraction greater than 0.5 overlaps a muon within a cone of $\Delta R = 0.4$, the muon is removed.

5.4.5 *b*-tagging

As a top quark decays almost exclusively into a bottom quark and a W boson, distinguishing jets containing b-hadrons from jets containing other lighter quarks is crucial. Jets containing b-hadrons (called b-tagged or b-quark jets) are characterized by a displaced vertex and a large transverse impact parameter, d_0. The bottom quark's relatively large mass and long lifetime (as compared to an up or down quark) allows it to travel a few millimeters at the LHC before decaying into a lighter hadron via the weak interaction.

Distinguishing jets containing b-hadrons from those containing other flavor hadrons is accomplished by b-tagging algorithms, of which there are many types. The most widely used ones are IP3D, SV1, JetFitterCombNN, and MV1 [79, 80]. In order for an algorithm to be effective, both the efficiency of identifying a jet originating from a b-quark should be high and the probability of mistakenly tagging a jet originating from a light-flavor parton as a b-jet must be low.

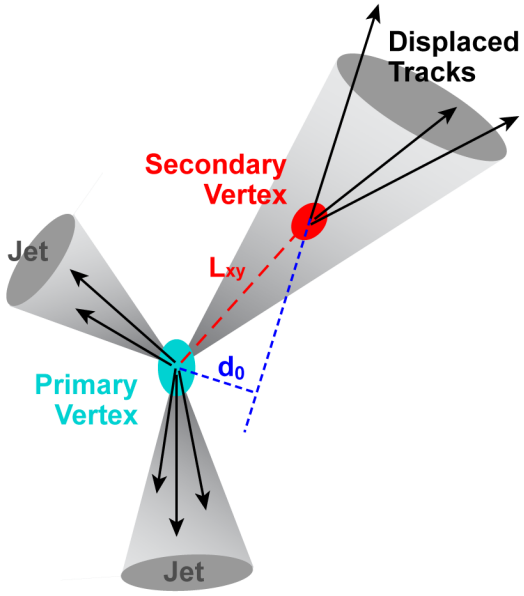

Figure 5.7: An illustration showing the secondary vertex and large transverse impact parameter of a jet containing a b-hadron [34].

5.4.5.1 Impact parameter based algorithms

IP3D is a transverse impact parameter-based algorithm making use of both the transverse and longitudinal impact parameters. It uses a log-likelihood ratio method in which for each track the impact parameters are compared to two-dimensional probability functions from simulation for both the b- and light-flavor jet hypotheses.

5.4.5.2 Vertex based algorithms

SV1 is a secondary vertex-based algorithm which attempts to reconstruct an inclusive displaced secondary vertex within the jet. The algorithm looks at all tracks which are significantly displaced from the primary vertex and are associated to the jet. Vertex candidates are formed for track pairs with a vertex fit of $\chi^2 < 4.5$. Vertices which are likely to be compatible with relatively long-lived particles such as from K_s or Λ decays are rejected. All remaining tracks are combined into a single inclusive vertex where an iterative process removes the

track yielding the largest contribution to χ^2 of the vertex fit until this contribution passes a pre-defined threshold.

5.4.5.3 Decay chain based algorithms

The JetFitterCombNN algorithm makes use of the topology of weak b- and c-hadron decays inside the jet. The algorithm uses a Kalman filter to find a common line between the primary vertex and the b- and c-vertices. The discrimination among b-, c-, and light jets is based on a likelihood calculation using similar variables as in the SV1 tagging algorithm.

5.4.5.4 Combined algorithms

The MV1 b-tagger is a neural network-based algorithm that uses the output weights from the IP3D, SV1 and JetFitterCombNN algorithms as inputs. This combination of vertex- and impact parameter-based algorithms makes use of the strengths of each. The high purity (low mistag rate) of vertex-based algorithms and the high b-tagging efficiency of impact parameter-based algorithms are combined to form a better performing algorithm. Figure 5.8 shows how the MV1 tagging algorithm compares against other algorithms in both efficiency and light-flavor-jet rejection.

The MV1c tagging algorithm is a variant of the MV1 algorithm and provides increased c-jet rejection. The 57% efficiency working point of the MV1c tagging algorithm is used in this analysis for b-tagging and tags jets at 97% purity with a c-jet rejection factor of 13.28. As c-jets are more kinematically similar to b-jets than are light-quark jets, an improved c-jet rejection factor is useful.

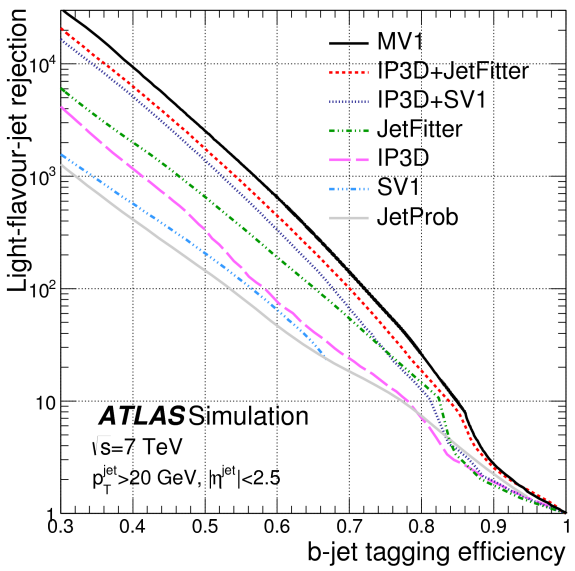

Figure 5.8: Light-flavor-jet rejection versus b-jet efficiency for various tagging algorithms using simulated $t\bar{t}$ events [35].

5.5 Missing transverse energy

On an event by event basis, partons within a proton carry an unknown fraction of the proton's energy. It is therefore impossible to know for certain the energy at which the partons collide. However, the beams collide in such a way that the total momentum in the transverse plane is zero. As such, the total vector sum of the collision products' momenta must also sum to zero in the transverse plane. Any non-zero sum is labeled $E_{\mathrm{T}}^{\mathrm{miss}}$ and is indicative of neutrinos, long-lived or stable non-interacting particles which escape detection, or miss-measurement. $E_{\mathrm{T}}^{\mathrm{miss}}$ is calculated as the negative vector sum of the energy of all particles detected in an event. In addition, energy deposits not associated with reconstructed objects, so-called "soft terms," are included in the vector sum.

5.6 Triggers

As described in Section 4.2.6 the ATLAS trigger system consists of three levels. Monotop events in the electron channel are triggered by requiring at L1 a transverse energy deposit, E_{T}, above 18 GeV. At the HLT, the full granularity of the calorimeter as well as tracking information are available and the reconstructed calorimeter cluster is matched to a track. The HLT trigger electron object is then required to be isolated and have $E_{\mathrm{T}} > 24$ GeV (trigger designation: EF_e24vhi_medium1). The electron channel is also triggered on events with an E_{T} threshold of 30 GeV at L1 and 60 GeV at the HLT but without an isolation requirement (trigger designation: EF_e60_medium1). The full trigger chain for the electron channel is then the logical OR between EF_e24vhi_medium1 and EF_e60_medium1.

Muon channel events are triggered at L1 if a muon track has $p_{\mathrm{T}} > 15$ GeV. These tracks are matched to an EF muon track have $p_{\mathrm{T}} > 24$ GeV and satisfying isolation criteria (trigger designation: EF_mu24i_tight) or having $p_{\mathrm{T}} > 36$ GeV without any isolation cuts (trigger designation: EF_mu36_tight). As with the electron channel, the full trigger chain for the muon channel is the logical OR between EF_mu24i_tight and EF_mu36_tight. The trigger efficiencies for the electron and muon channels are shown in Figure 5.9. Electron and muon triggers are fully efficient above 30 GeV at the EF stage.

5.7 Summary

The purpose of these reconstruction algorithms was to clearly define what constitutes a lepton, jet, and missing energy in an event and for these definitions to be common to signal, background, and data samples. With a common reconstruction of these physics objects in place, the signal and SM backgrounds can be simulated and the data can be reconstructed.

Chapter 6 will describe how such simulations are performed and Chapter 7 will describe how events are selected to be included in the analysis based on various kinematic and topological information.

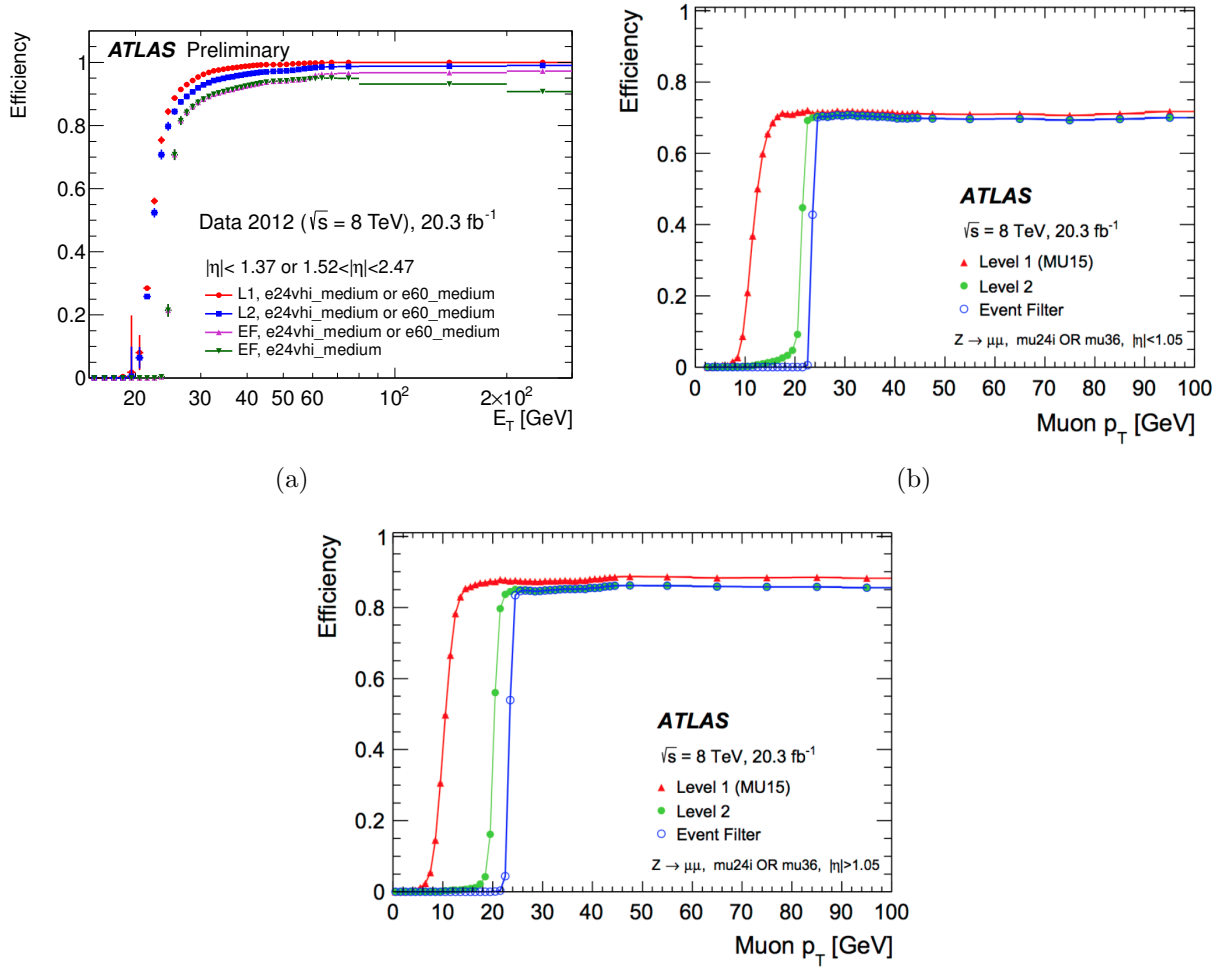

(a) (b)

(c)

Figure 5.9: (a) Trigger efficiencies of the e24vhi_medium1 OR e60_medium1 triggers for electrons. (b) Trigger efficiencies of the mu24i OR mu36 triggers for the three trigger levels the barrel region. (c) Trigger Efficiencies of the mu24i OR mu36 triggers for the three trigger levels in the endcap region.

Chapter 6

Background and Signal Simulation

The topology of a monotop event can be mimicked by numerous different processes. Broadly, these background processes can be grouped into two different groups: reducible and irreducible. Reducible backgrounds are processes whose final states do not exactly mirror that of the signal, but, for reasons related to the reconstruction of their final states, can masquerade as signal events. Irreducible backgrounds are processes whose final state particles exactly match those of signal events. The backgrounds included in this analysis were top-pair production ($t\bar{t}$), single-top production (ST), W/Z+jets production, diboson production, and QCD multijet production. This chapter describes the modeling of the signal as well as the background processes. For references to branching ratios in this chapter as well as later in this dissertation the following values are used:

$$\mathrm{BR}\left(t \to Wb\right) = 1 \tag{6.1a}$$

$$\mathrm{BR}\left(W \to \ell\nu\right) = 0.324 \tag{6.1b}$$

$$\mathrm{BR}\left(W \to q\bar{q}\right) = 0.676 \tag{6.1c}$$

$$\mathrm{BR}\left(Z \to \ell^{+}\ell^{-}\right) = 0.104 \tag{6.1d}$$

6.1 Event generation

Simulating different physics processes involves either generating events with computer simulations known as Monte Carlo (MC) or with data-driven methods. All of the backgrounds in this analysis were modeled with MC except for the multijets contribution which was estimated using a data-driven method. The MC method makes use of various simulations known as event generators. These event generators use random number sampling to expand the quantum field theory equations at the level of partons for a specified Feynman diagram and to perform the integration over the allowed phase space. Due to theoretical or numerical challenges, this expansion is usually done at leading order (LO) or next-to-leading order (NLO). In the case where a simulation was created at LO, an overall normalization k-factor was applied which adequately takes into account the predicted effects of higher order corrections to the cross-section.

6.1.1 Parton Distribution Functions

The colliding protons of the LHC beams are comprised of constituent partons (quarks, antiquarks, and gluons) and it is these partons that interact with each other in a collision event. When generating collision events, event generators must be given the momentum of the colliding partons as an input. While the total energy of the protons is known, the momentum fraction each parton carries within a proton is not known *a priori* and must be modeled using theoretical predictions which are fit to data. Parton Distribution Functions (PDFs) model the fraction of the proton's momentum each constituent parton is likely to carry and are parameterizations which come from fits to the world's data. In this way they are not known from first principles but instead are experimentally derived. Numerous PDF

sets are available and the choice of which one to use is largely based on the type of process being simulated. The order at which a process is generated, LO or NLO, determines the order of the PDF set that should be used. In this analysis three different PDF sets were used: CT10 [81], CTEQ6L1 [82], and MSTW2008LO [83].

6.1.2 Event generators

A wide variety of event generators exist. Some serve as multi-purpose generators able to both generate the hard scatter process as well as subsequent parton showering and hadronization. Others are tailored for a more specific purpose and are only at the parton level. Below is a list of generators used in this analysis with a description of each:

- **MadGraph** – A multi-leg, LO generator used to generate amplitudes and events for the monotop signal [57].
- **Powheg** – An NLO generator used for the generation of $t\bar{t}$ and Wt- and s-channel single-top events [84].
- **Pythia** – A multi-purpose, LO generator used in this analysis to simulate hadronization, parton fragmentation/showering, and initial and final state radiation [85, 86].
- **Herwig** – A multi-purpose, LO generator used in this analysis to simulate diboson events. It is also used to model hadronization, parton fragmentation/showering, and initial and final state radiation for other processes [87].
- **Alpgen** – A multi-leg LO, generator capable of generating multiple particle final states used in this analysis for the generation of W/Z+jets events [88].

- **AcerMC** – A LO generator dedicated to generating backgrounds for top quark physics. It is used in this analysis to generate t-channel single-top events [89].

6.1.3 Detector simulation

After a process has been generated, the effects of the detector need to be simulated as well. When final state particles traverse the detector, they interact with the material and magnetic fields inside it and these effects are modeled in great detail using detector simulations. The vast majority of the computing time used to generate events is spent simulating how particles interact with the active and passive components of the detector and how the detector itself responds to these particles. The two simulations used in this analysis were GEANT4 [90] and ATLFASTII [91]. GEANT4 is the standard detector simulation used in ATLAS analyses and is the more accurate of the two. This simulation very precisely models the geometry, material composition, and the magnetic fields of the detector and accounts for the various effects the detector has on the final state particles. In addition, GEANT4 models the electronic read outs of the various detector sub-components in order to simulate how energy depositions in the active detector elements are transformed into the digital outputs of the electronics. Simulating an individual event with GEANT4 requires anywhere from 5-20 minutes of computing time. The complicated detector geometry and the accuracy to which GEANT4 describes the detector make the necessary computing time prohibitive for many scenarios. Hence another package is used to simulate events with a faster, parameterized detector simulation in order to achieve additional statistics.

Most common physics processes like $t\bar{t}$, single-top, and W/Z+jets are utilized by numerous different analyses within ATLAS and so considerable world-wide resources have been deployed to create large samples of common reactions and store their outputs in many in-

termediate locations. For such processes GEANT4 was used to generate events. For other processes, like monotop events which have extremely small cross-sections, the ATLFASTII detector simulation was used in order to generate the required amount of statistics including multiple samples with different parameterizations needed to complete a full analysis.

Almost 90% of the time used to simulate events with GEANT4 is spent modeling the calorimeter and its response. ATLFASTII uses the same simulation for the Inner Detector and muon system as GEANT4, but uses the FastCaloSim package which reduces the time spent modeling the calorimeter by an order of magnitude [92]. The FastCaloSim package uses a parameterized simulation of the hadronic showers' longitudinal and lateral energy profiles as opposed to fully simulating them and is able to reduce the time spent simulating these showers by an order of magnitude. The end result with either simulation is an MC-produced sample that is equivalent in format to the data that are recorded.

6.2 Signal simulation

The signal samples were generated with the matrix element (ME) leading-order multi-leg generator MadGraph5 and were showered/hadronized with Pythia8. The input PDF used in the generation of the monotop signal was MSTW2008 [83]. For the $S1_R$ model, samples were created with the mass of the f_{met} particle varying from 0 to 100 GeV in steps of 20 GeV and the mass of the S resonance was fixed at 500 GeV. For the $S4_R$ model, samples were created with the mass of the v_{met} particle varying from 0 to 150 GeV in steps of 25 GeV, to 300 GeV in steps of 50 GeV, and then to 1000 GeV in steps of 100 GeV. All exotic couplings values were fixed at $a_R = 0.2$. While samples for both the fully-hadronic and semi-leptonic decay of the top quark were produced, this analysis only considered the semi-

leptonic decay channel. The cross-section times branching ratios for each of the different mass hypothesis are shown in Table 6.1. All the signal samples are passed though the detector simulation package ATLFASTII. In order to verify the effect of the use of the fast simulation on the signal modeling, two signal samples for each model (one for the lowest mass and one for the highest mass) were also simulated with the GEANT4 full-simulation package. The agreement between the ATLFASTII and GEANT4 simulations are within 1σ and are shown in Figures 6.1 and 6.2. More distributions showing the agreement between signal samples produced with either ATLFASTII or GEANT4 for other kinematic variables are shown in Appendix A.

6.3 Background simulation

MC simulation samples were used to model the kinematic distributions of most of the SM background processes. How the different background samples were generated as well as how they can mimic the monotop final state topology is described in this section.

6.3.1 Single-top

The LO Feynman diagrams for the various single-top production channels at the LHC are shown in Figure 6.3. The s- and Wt-channels were produced at NLO using the POWHEG event generator with the CT10 PDF set. The t-channel process was generated using the LO ACERMC v3.8 generator with the CTEQ6L1 PDF set. PYTHIA v6.426 is used for parton showering and hadronization for each channel.

The s-channel process can lead to a monotop final state topology if one of the two b-quarks (either from the virtual W decay or from the decay of the top quark) escapes detector

Model	**Mass [GeV]**	$\boldsymbol{\sigma \times}$ **BR** $\mathbf{(t \to \ell\nu b)}$ **[pb]**
$S1_R$	0	1.11
	20	1.10
	40	1.09
	60	1.07
	80	1.04
	100	1.00
$S4_R$	0	96.03
	25	359.00
	50	113.40
	75	59.86
	100	37.45
	125	25.35
	150	18.00
	200	9.66
	250	5.51
	300	3.33
	400	2.75
	500	1.27
	600	0.64
	700	0.34
	800	0.19
	900	0.11
	1000	0.07

Table 6.1: The cross-section times branching ratios for all the different signal samples used in this analysis. The second column indicates the f_{met} (v_{met}) mass in the case of the $S1_R$ ($S4_R$) model. The BR for $t \to \ell\nu b$ is 0.324.

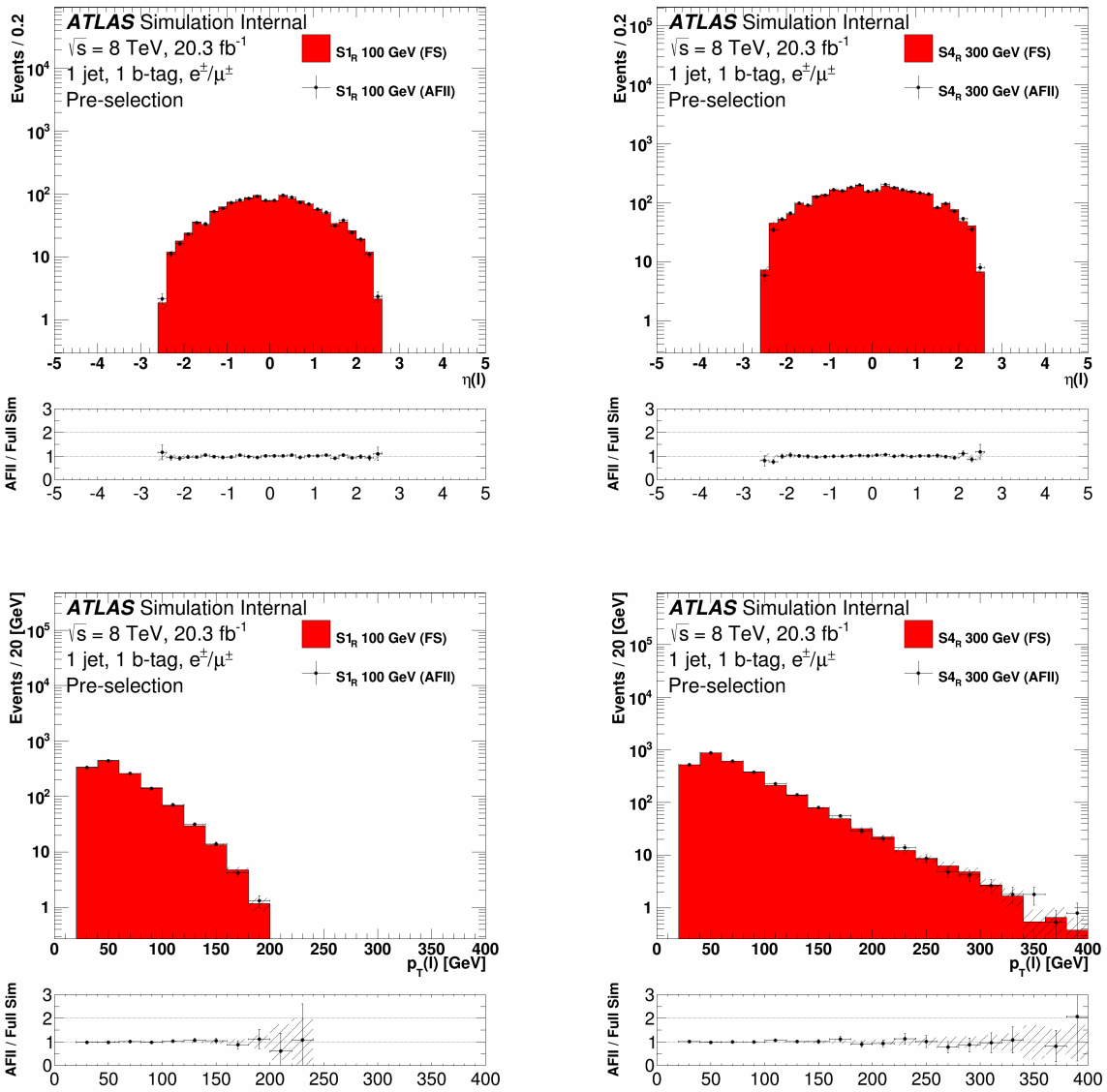

Figure 6.1: Comparison of ATLFASTII vs. GEANT4 samples for the $\eta(\ell)$ (top) and $p_{\mathrm{T}}(\ell)$ (bottom) distributions for the $\mathrm{S1_R}$ model with an f_{met} mass of 100 GeV (left) and for the $\mathrm{S4_R}$ model with a v_{met} mass of 300 GeV (right). Plots are shown in the combined electron and muon channel. Uncertainties are statistical uncertainties only.

acceptance. In the t-channel process, the monotop signal can be mimicked if the light quark jet produced in association with the top quark is not reconstructed. Dilepton decays of Wt events can also lead to a monotop topology if one of the two leptons is not reconstructed. The cross-section times branching ratios as well as the k-factors for the three single-top

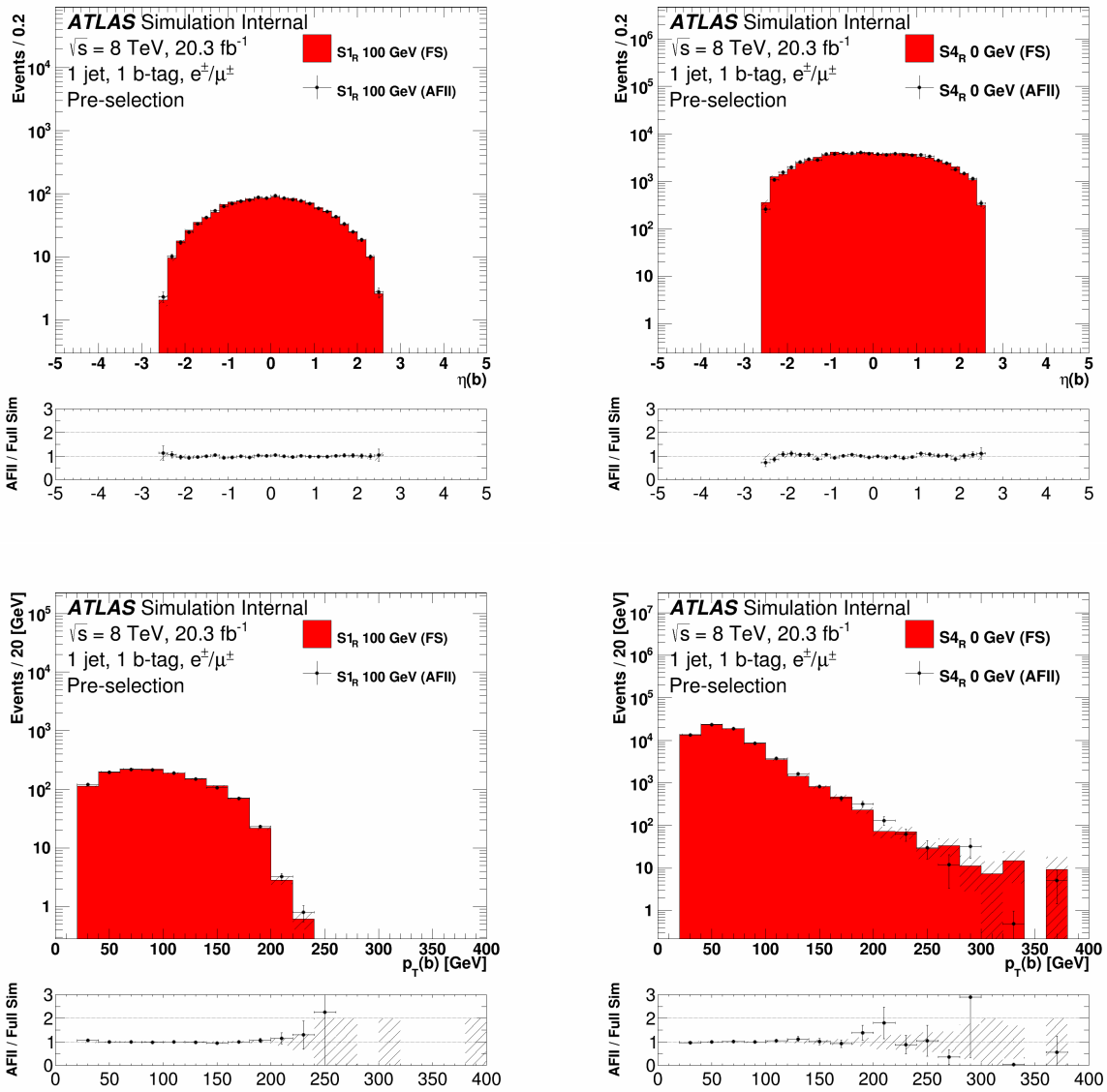

Figure 6.2: Comparison of ATLFASTII vs. GEANT4 samples for the $\eta(b)$ (top) and $p_{\mathrm{T}}(b)$ (bottom) distributions for the $\mathrm{S1_R}$ model with an f_{met} mass of 100 GeV (left) and for the $\mathrm{S4_R}$ model with a v_{met} mass of 300 GeV (right). Plots are shown in the combined electron and muon channel. Uncertainties are statistical uncertainties only.

channels are shown in Table 6.2.

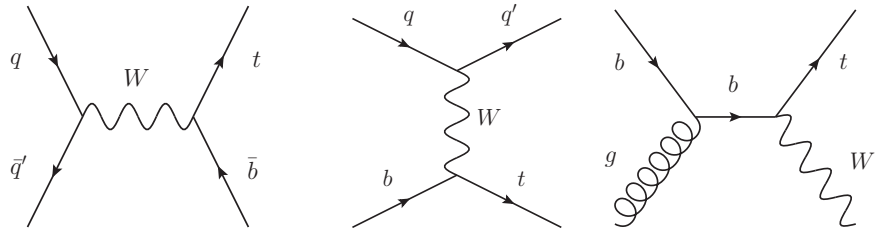

(a) (b) (c)

Figure 6.3: Single-top event production Feynman diagrams in the (a) s-, (b) t-, and (c) Wt-channels.

Sample	$\boldsymbol{\sigma} \times$ **BR [pb]**	$\boldsymbol{k}$**-factor**
ST s-channel (ℓ+jets)	1.6424	1.1067
ST t-channel (ℓ+jets)	25.748	1.1043
ST Wt-channel	20.461	1.0933

Table 6.2: The cross-sections and k-factors for all the nominal single-top quark MC samples used in this analysis [15, 16, 17]. The cross-section column includes the branching ratios but not k-factor corrections. ℓ indicates e, μ, or τ. The ℓ+jets parenthetical indicates that only events in which the top quark decays leptonically were generated.

6.3.2 $t\bar{t}$

The LO Feynman diagrams for $t\bar{t}$ production at the LHC are shown in Figure 6.4. The sample was produced at NLO using the POWHEG event generator with the CT10 PDF set. Parton showering as well as hadronization and radiative effects were added using PYTHIA v6.426. Both top quarks decay into a W and a b-quark and the W from each top quark can decay either leptonically into a lepton-neutrino pair or hadronically into a pair of jets.[1] A $t\bar{t}$ event can mimic a monotop event in multiple ways. If both W bosons decay leptonically then the signal can be mimicked if one of the b-quarks and one of the leptons are both not reconstructed. If one W decays leptonically while the other decays hadronically then the

[1]The $t\bar{t}$ sample used in this analysis was generated such that events were required to have at least one leptontically decaying W. The "no full-had" parenthetical in Table 6.3 explicitly states the fact that no fully-hadronic $t\bar{t}$ decays were generated.

event can mimic the signal if one b-quark and both light quark jets from the W decay are both not fully reconstructed. The cross-section times branching ratio as well as the k-factor for the $t\bar{t}$ process are shown in Table 6.3.

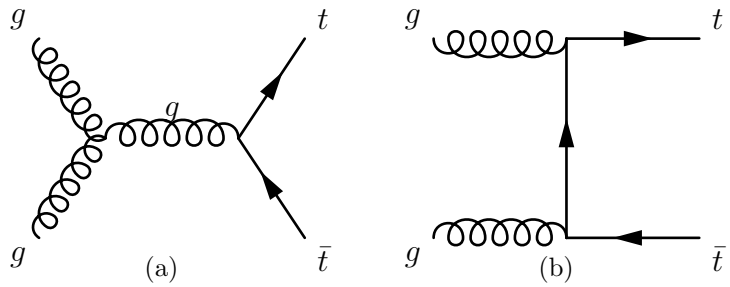

Figure 6.4: The tree-level Feynman diagrams for $t\bar{t}$ production at the LHC in the (a) s- and (b) t-channels.

Sample	$\boldsymbol{\sigma} \times$ **BR [pb]**	$\boldsymbol{k}$**-factor**
$t\bar{t}$ (no full-had.)	114.51	1.1992

Table 6.3: The cross-section and k-factor of the nominal $t\bar{t}$ MC sample used in this analysis [18]. The cross-section column does not include the k-factor correction. The "no full-had" parenthetical is shorthand for "no fully hadronic final states" and indicates that only events in which at least one top quark decays leptonically were generated.

6.3.3 W boson plus jets

Another important background to the monotop signal is the production of a W boson in association with jets. If one of the jets comes from a heavy flavor quark then the event can have the same final state topology as a monotop event. In addition, possible misidentification of a light quark jet as a b-quark jet, can contribute to background contamination in the signal topology. The background contributions from W plus jets production were simulated using the LO multileg Alpgen v2.14 ME generator coupled with the CTEQ6L1 PDF set. These samples were combined with Pythia v6.42 for the parton shower and the underlying event.

The samples were generated with up to five additional partons. Additional W boson samples with associated heavy-quark production ($Wb\bar{b}$, $Wc\bar{c}$ and Wc) were also produced. Consider and event with a W, c-quark, and u-quark in the final state. This type of event may be generated in both the $Wc + 1$ parton sample as well as the $W + 2$ partons sample. When combining multiple ALPGEN samples, it was necessary to veto certain classes of events in each sample to avoid this double counting. The heavy flavor overlap removal (HFOR) procedure was applied to such samples [93]. The procedure is outlined below, where Np is the number of additional partons generated in the event:

- $\boldsymbol{W}$**+Np** – Remove all events with heavy flavor jets. Remove all events in which heavy flavor quark pairs are not matched to one reconstructed jet.
- $\boldsymbol{Wc}$**+Np** – Remove all events in which the heavy flavor quark pairs are not matched to one reconstructed jet.
- $\boldsymbol{Wc\bar{c}}$**+Np** – Remove all events in which $b\bar{b}$ pairs are not matched to one reconstructed jet. Remove all events in which $c\bar{c}$ pairs are matched to one reconstructed jet.
- $\boldsymbol{Wb\bar{b}}$**+Np** – Remove all events in which $b\bar{b}$ pairs are matched to one reconstructed jet.

6.3.4 Diboson

The Feynman diagrams for the diboson processes at the LHC are shown in Figure 6.5. The samples were produced with HERWIG v6.52 with the CTEQ6L1 PDF set and required that at least one of the bosons decays leptonically. They represent one of the smallest backgrounds to the monotop signal but were added for completeness. The cross-section times branching ratios as well as the k-factors for the three diboson channels are shown in Table 6.5.

Sample	$\sigma \times$ BR [pb]	k-factor
$Z \rightarrow ee$ + 0 partons	718.97	1.18
$Z \rightarrow ee$ + 1 parton	175.70	1.18
$Z \rightarrow ee$ + 2 partons	58.875	1.18
$Z \rightarrow ee$ + 3 partons	15.636	1.18
$Z \rightarrow ee$ + 4 partons	4.0116	1.18
$Z \rightarrow ee$ + 5 partons	1.2592	1.18
$Z \rightarrow \mu\mu$ + 0 partons	719.16	1.18
$Z \rightarrow \mu\mu$ + 1 parton	175.74	1.18
$Z \rightarrow \mu\mu$ + 2 partons	58.882	1.18
$Z \rightarrow \mu\mu$ + 3 partons	15.673	1.18
$Z \rightarrow \mu\mu$ + 4 partons	4.0057	1.18
$Z \rightarrow \mu\mu$ + 5 partons	1.2544	1.18
$W \rightarrow e\nu$ + 0 partons	8127.3	1.1330
$W \rightarrow e\nu$ + 1 parton	1792.7	1.1330
$W \rightarrow e\nu$ + 2 partons	542.18	1.1330
$W \rightarrow e\nu$ + 3 partons	147.65	1.1330
$W \rightarrow e\nu$ + 4 partons	37.736	1.1330
$W \rightarrow e\nu$ + 5 partons	11.962	1.1330
$W \rightarrow \mu\nu$ + 0 partons	8127.3	1.1330
$W \rightarrow \mu\nu$ + 1 parton	1792.7	1.1330
$W \rightarrow \mu\nu$ + 2 partons	542.18	1.1330
$W \rightarrow \mu\nu$ + 3 partons	147.65	1.1330
$W \rightarrow \mu\nu$ + 4 partons	37.736	1.1330
$W \rightarrow \mu\nu$ + 5 partons	11.962	1.1330
$W \rightarrow l\nu + b\bar{b}$ + 0 partons	55.66	1.133
$W \rightarrow l\nu + b\bar{b}$ + 1 parton	45.25	1.133
$W \rightarrow l\nu + b\bar{b}$ + 2 partons	23.16	1.133
$W \rightarrow l\nu + b\bar{b}$ + 3 partons	11.20	1.133
$W \rightarrow l\nu + c\bar{c}$ + 0 partons	150.2	1.133
$W \rightarrow l\nu + c\bar{c}$ + 1 parton	132.7	1.133
$W \rightarrow l\nu + c\bar{c}$ + 2 partons	71.84	1.133
$W \rightarrow l\nu + c\bar{c}$ + 3 partons	30.26	1.133
$W \rightarrow l\nu + c$ + 0 partons	808.0	1.52
$W \rightarrow l\nu + c$ + 1 parton	267.7	1.52
$W \rightarrow l\nu + c$ + 2 partons	69.89	1.52
$W \rightarrow l\nu + c$ + 3 partons	20.56	1.52
$W \rightarrow l\nu + c$ + 4 partons	4.308	1.52

Table 6.4: All the W/Z+jets MC samples used in this analysis. The cross-section column does not include the k-factor corrections. l indicates e, μ or τ.

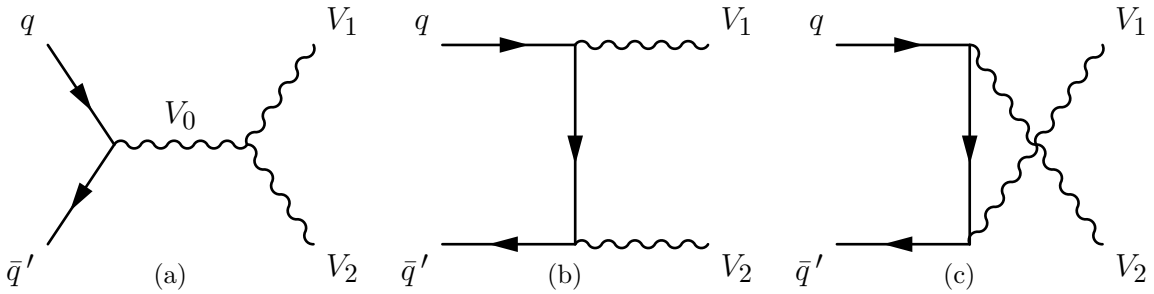

Figure 6.5: The tree-level Feynman diagrams for diboson production in hadron colliders through the (a) s-, (b) t-, (c) and u-channel production modes. In the SM, W^+W^- and $W^\pm Z$ can be produced in all modes while ZZ can only be produced in the t- and u-channels. $V_i = W$, Z, or γ.

Sample	$\boldsymbol{\sigma} \times$ **BR [pb]**	***k*-factor**
WW	12.416	1.6833
ZZ	0.99081	1.5496
WZ	3.6706	1.9011

Table 6.5: The cross-sections and k-factors for all the diboson MC samples used in this analysis. The cross-section column does not include the k-factor corrections.

6.3.5 QCD multijets modeling

The QCD multijet background is modeled using the data-driven matrix method [94]. Differences in the identification between "real" prompt leptons and "fake" leptons were exploited to give an estimation for the multijet contribution to the background. Real leptons arise from W or Z decays while fake leptons arise from misidentified hadrons, photon conversions, or from leptons produced from heavy flavor decays inside jets. It is these fake leptons that were modeled in the multijet estimation.

6.3.5.1 Matrix method

In the matrix method, data events were processed into "tight" and "loose" samples. In the tight sample the tight lepton reconstruction was applied. In the loose sample there was no isolation requirement for either electrons or muons and the electron identification criteria was

relaxed from the tight criteria to the less restrictive loose criteria (see Table 5.3). The two samples only differ in the criteria for lepton reconstruction as all other kinematic selections were identical. A lepton which passed the tight criteria also passed the loose criteria and all the events in the tight sample were also present in the the loose sample. The number of events in the tight and loose samples, N_{tight} and N_{loose}, can be broken down into contributions from real and fake leptons

$$N^{\text{loose}} = N^{\text{loose}}_{\text{real}} + N^{\text{loose}}_{\text{fake}}, \tag{6.2a}$$

$$N^{\text{tight}} = N^{\text{tight}}_{\text{real}} + N^{\text{tight}}_{\text{fake}}. \tag{6.2b}$$

Equation 6.2b can be written in terms of the real and fake efficiencies, ϵ_{real} and ϵ_{fake},

$$N^{\text{tight}} = \epsilon_{\text{real}} N^{\text{loose}}_{\text{real}} + \epsilon_{\text{fake}} N^{\text{loose}}_{\text{fake}}. \tag{6.3}$$

These efficiencies are the fractions of loose real and fake leptons that also satisfy the tight lepton identification criteria and are given by

$$\epsilon_{\text{real}} = \frac{N^{\text{tight}}_{\text{real}}}{N^{\text{loose}}_{\text{real}}} \qquad \text{and} \qquad \epsilon_{\text{fake}} = \frac{N^{\text{tight}}_{\text{fake}}}{N^{\text{loose}}_{\text{fake}}}. \tag{6.4}$$

If the efficiencies are known and N^{tight} and N^{loose} are counted then Equations 6.2a and 6.3 can be solved for $N^{\text{tight}}_{\text{fake}}$ as

$$N^{\text{tight}}_{\text{fake}} = \frac{\epsilon_{\text{fake}}}{\epsilon_{\text{real}} - \epsilon_{\text{fake}}} \left(\epsilon_{\text{real}} N^{\text{loose}} - N^{\text{tight}} \right). \tag{6.5}$$

The real and fake efficiencies were calculated by the ATLAS top-fakes working group us-

ing control samples enriched in real and fake leptons respectively using the tag-and-probe method [95].

6.3.5.2 Electron channel

For electrons, ϵ_{real} was calculated utilizing the tag-and-probe method on $Z \to e^+e^-$ events. In this method, one electron passing the tight electron identification criteria serves as the tag and one electron passing the loose identification criteria serves as the probe. The probe is considered unbiased due to the less stringent requirements placed upon it. The fraction of events where the probe electron also passes the tight criteria gives a good estimation of ϵ_{real}. The fake electron efficiencies, ϵ_{fake}, were calculated in a similar manner by counting events in an e+jets sample enriched in fake electrons by requiring low $m_{\text{T}}(\ell, E_{\text{T}}^{\text{miss}}) + E_{\text{T}}^{\text{miss}}$.

6.3.5.3 Muon channel

For muons, the real efficiencies were measured in a μ+jets data sample with very large $m_{\text{T}}(\ell, E_{\text{T}}^{\text{miss}})$, while the fake rates were measured by counting events in a μ+jets data sample where the reconstructed muons have a transverse impact parameter significance $d_0/\sqrt{\sigma(d_0)}$ greater than 5. A large muon impact parameter is indicative of heavy flavor quark decays which produce fake muons. To calculate the contribution of the multijets background in the analyzed data sets, each event passing the "loose" selection detailed above is re-weighted, with a weight w_{tight} if the selected lepton satisfies the "tight" requirement and w_{loose} if it satisfies only the "loose" requirement. The event weights w_{tight} and w_{loose} were calculated from ϵ_{real} and ϵ_{fake} as described below.

6.3.5.4 Event re-weighting

Generally speaking, both ϵ_{real} and ϵ_{fake} depend strongly on the η and p_{T} of the lepton. As such, the shape of the relevant kinematic distributions need to be modeled as well as the raw number of events. Equation 6.5 can be generalized to apply a weight, w_i, to each data event, i, passing the loose or tight selection,

$$w_i = \frac{\epsilon_{\text{fake}}}{\epsilon_{\text{real}} - \epsilon_{\text{fake}}} \left(\epsilon_{\text{real}} - \delta_i\right), \tag{6.6}$$

where the Kronecker delta is equal to 1 if the i^{th} event passes the tight selection and 0 otherwise. The weights were built in such a way that the sum of the weights equals the number of tight events containing a fake lepton,

$$\sum_i w_i = N_{\text{fake}}^{\text{tight}}. \tag{6.7}$$

6.4 Corrections to simulated samples

Both GEANT4 or ATLFASTII do an excellent job of recreating how events would appear in the actual detector. However, the detector simulation is not perfect and while the MC simulated samples are a close representation of data, corrections need to be applied to enhance the agreement.

6.4.1 Efficiency corrections

In order to report reliable physics results, the simulated samples were corrected to reproduce the efficiencies seen in data. The ratio between the efficiency in data and the efficiency in

simulation defines a scale factor (SF). Scale factors for various efficiencies are multiplicative, were applied to simulation results, and were generally close to one.

6.4.1.1 Electrons

The scale factors of selected electrons are given by

$$\mathrm{SF} = \left(\frac{\epsilon_{\mathrm{data}}}{\epsilon_{\mathrm{MC}}}\right)_{\mathrm{reco}} \left(\frac{\epsilon_{\mathrm{data}}}{\epsilon_{\mathrm{MC}}}\right)_{\mathrm{ID}} \left(\frac{\epsilon_{\mathrm{data}}}{\epsilon_{\mathrm{MC}}}\right)_{\mathrm{isolation}} \left(\frac{\epsilon_{\mathrm{data}}}{\epsilon_{\mathrm{MC}}}\right)_{\mathrm{trigger}}, \tag{6.8}$$

which is a product of the scale factors due to electron reconstruction, identification, isolation, and trigger efficiencies as a function of η and E_{T}. In order to calculate the efficiencies in data it is necessary to have an unbiased sample of events containing real leptons. As was done in the multijet estimation, the tag-and-probe method was used on an unbiased sample containing $Z \to e^+e^-$.[2] Oppositely charged electrons whose invariant mass is within 10 GeV of the Z boson mass were chosen. One electron which passes very stringent identification and reconstruction criteria serves as the tag while the other electron satisfying much less restrictive criteria serves as the probe. The fraction of events in which the probe passes additional reconstruction or identification criteria serves as the efficiency in data. The same procedure was done on simulated $Z \to e^+e^-$ events to determine the reconstruction and identification efficiencies in MC. The combined efficiencies for electron reconstruction and identification along with the associated scale factors are shown in Figure 6.6. The electron isolation and trigger scale factors were also applied to the simulated samples and all have values very close to one.

[2]Unbiased in this case means a sample with a minimal number of kinematic cuts.

6.4.1.2 Muons

The scale factors applied to selected muons are determined by the same equation used for electrons, Equation 6.8, but were calculated using $Z \to \mu^+\mu^-$ events. Events were chosen such that the di-muon invariant mass was within 10 GeV of the Z boson mass. One of the muons is required to be a CB muon and serves as the tag. The other muon is an "MS" track muon and serves as the probe. An attempt is made to match the probe muon to the reconstructed muons in the event. A match is deemed successful when the muon and the probe have the same electric charge and are within a cone of $\Delta\mathrm{R} = 0.05$ of each other. The fraction of matches seen in data divided by the fraction of matches seen in simulated samples serves as the muon scale factor. These efficiencies and scale factors are dependent on the p_T and η of the muon and are shown in Figure 6.7 for the CB muon type used in this dissertation. The muon isolation and trigger scale factors were also applied to the simulated samples and all have values very close to one.

6.4.1.3 Jets

Efficiency corrections related to the cut on the Jet Vertex Fraction were applied to simulated jets as a function of jet p_T and $\langle\mu\rangle$. These scale factors were determined by analyzing $Z \to \ell^+\ell^-+$ jets events in both simulation and data and calculating the efficiency of the cut on each. The efficiencies and scale factors are shown in Figure 6.8.

6.4.2 Pileup and luminosity corrections

To properly include the effect of multiple proton-proton collisions per bunch crossing (pile-up) in the signal and background simulations, the events were re-weighted using the average

number of inelastic interactions per collision in order to reproduce the data conditions (see Figure 4.5). In addition, both the signal and background samples were re-weighted to match the total integrated luminosity seen in the Run1 data set, 20.3 fb^{-1}. An additional scale factor was also applied to get the correct correlation between the mean number of interactions and the number of reconstructed primary vertices.

6.4.3 Simulation agreement with data

The agreement between the background simulation and data are shown in Figure 6.9 for η and p_{T} distributions of the lepton and b-jet to be within 1σ. More distributions for other variables are shown in Appendix B and show similar agreement between simulation and data.

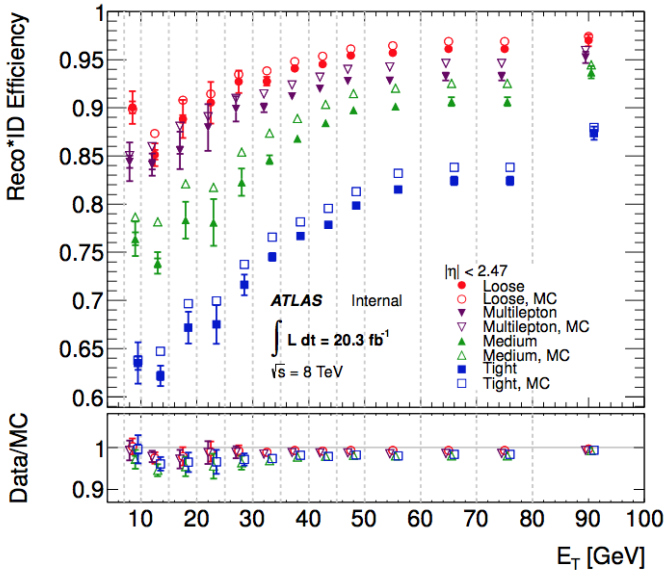

(a)

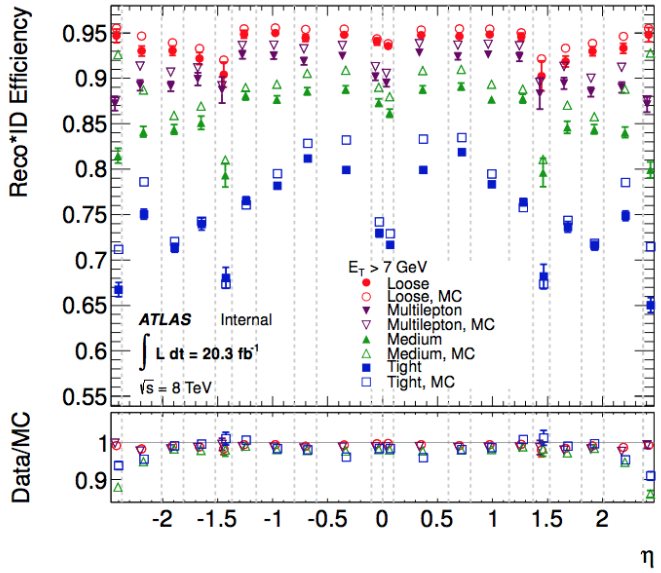

(b)

Figure 6.6: Measured electron reconstruction times identification efficiencies as a function of (a) E_{T} and (b) η for the various electron types. This analysis uses the tight electron identification which are shown in blue. The uncertainties are statistical (inner error bars) and statistical+systematic (outer error bars). The dashed lines indicate the bins in which the efficiencies are calculated. The bottom plot serves as the combined scale factors [13].

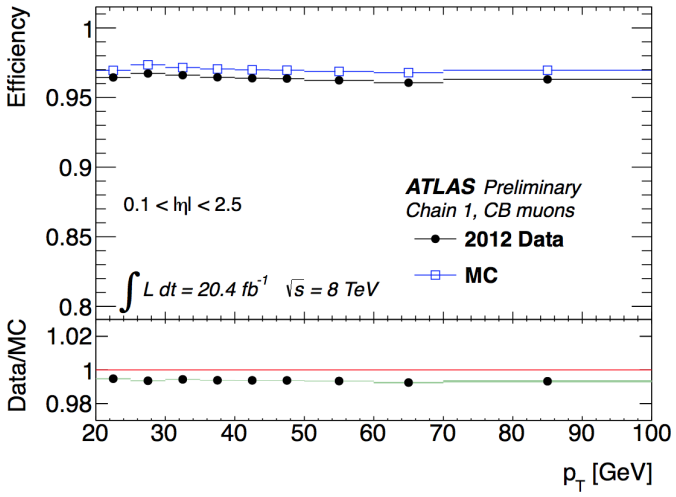

(a)

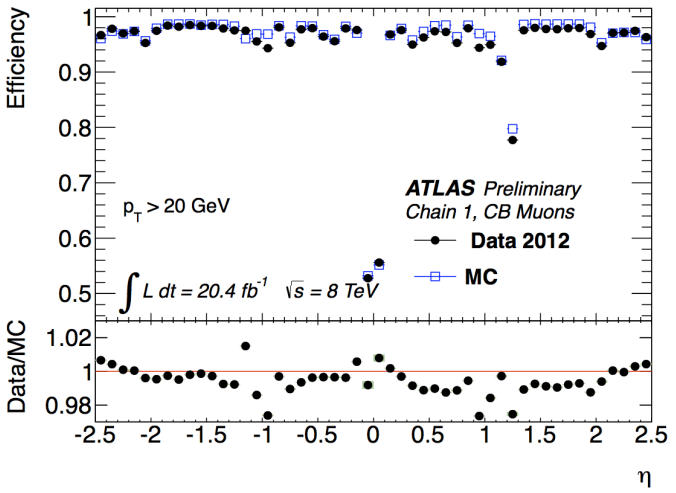

(b)

Figure 6.7: Measured muon reconstruction times identification efficiencies as a function of (a) p_{T} and (b) η for the CB muons used in this dissertation. The bottom plot serves as the combined scale factors [36].

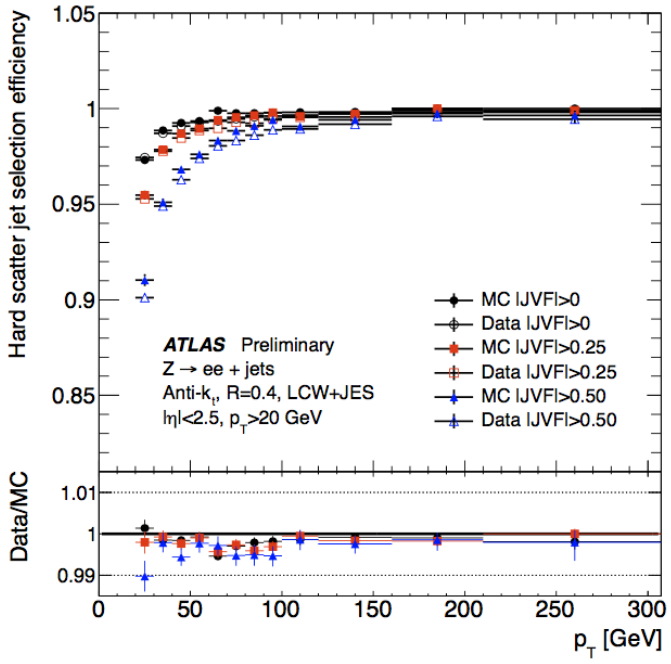

(a)

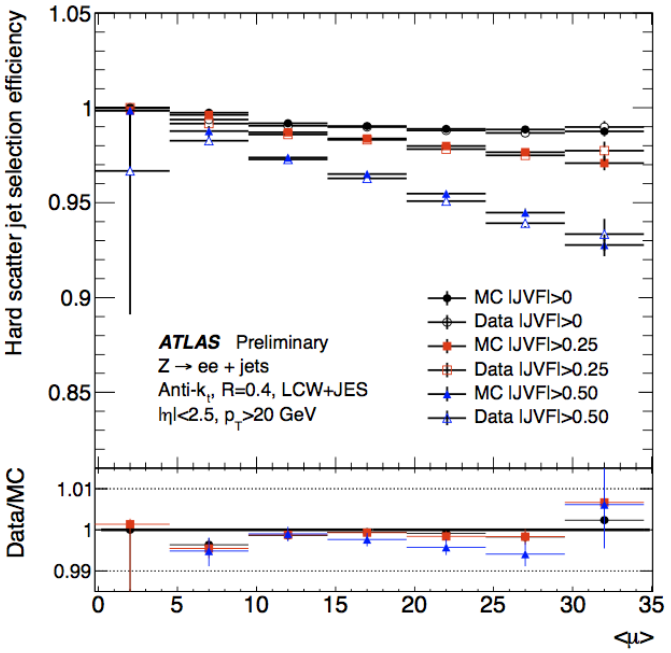

(b)

Figure 6.8: Measured jet selection efficiencies as a function of (a) p_{T} and (b) $\langle\mu\rangle$ for different JVF operating points. This analysis uses the 0.50 operating point. The bottom inlet serves as the scale factors [33].

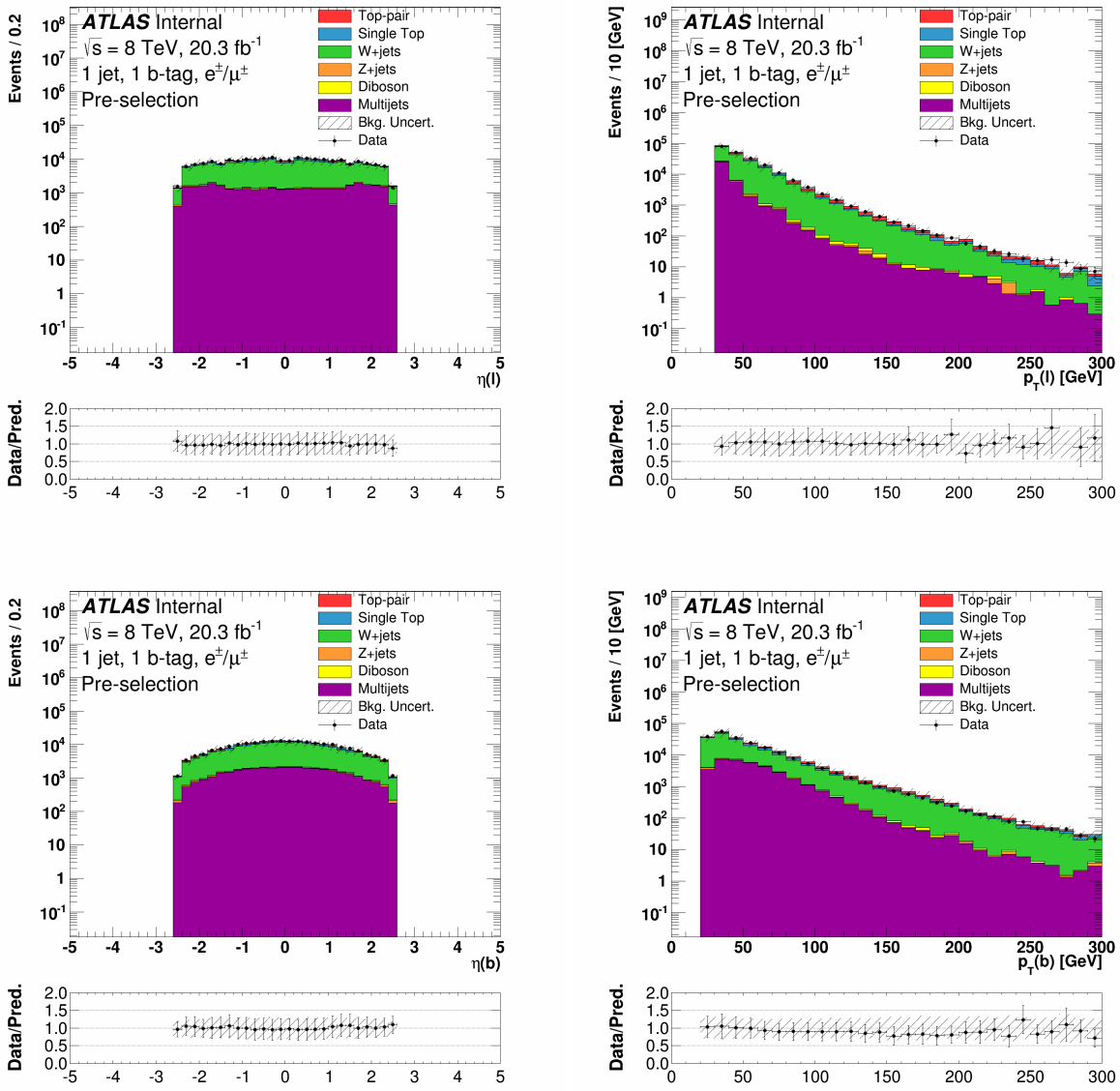

Figure 6.9: Distributions of η (left) and p_{T} (right) for the lepton (top) and b-jet (bottom) in the combined electron/muon channel in the pre-selection region. The uncertainty band on the expected background corresponds to the errors due to the statistical uncertainties added in quadrature with the cross-section and normalization uncertainties.

Chapter 7

Object and Event Selection

This analysis uses LHC $\sqrt{s} = 8$ TeV collision data measured by the ATLAS detector during Run1 in 2012 which recorded 21.3 fb^{-1} of integrated luminosity. Of this total, only collisions occurring while the LHC beam was stable and in which the detector was functioning properly are used and corresponds to 20.3 fb^{-1} of useable data collected by the ATLAS detector during Run1. Two different approaches were used to discern signal events from background events in this dissertation. A cut-based approach using two kinematic variables was first used. This was the methodology used in the first published paper for a monotop search using ATLAS data [37]. The second approach uses a Multivariate Analysis (MVA) technique called a Boosted Decision Tree (BDT) as described in Chapter 11 and was completed subsequent to the cut-based analysis. The goal of the BDT was to improve upon the published results of the cut-based analysis. Both approaches use the same samples with the same definitions for physics objects, but with different selection cuts applied.

7.1 Object definitions

This section describes the set of criteria applied to each physics object. The same object definitions are applied to both background and signal samples as well as to the data.

7.1.1 Electrons

Reconstructed electrons in this analysis are required to meet the following criteria:

- Electrons must pass the tight identification criteria.
- Electrons must have a longitudinal impact parameter, z_0 from the primary vertex less than 2 mm.
- Electrons must pass calorimeter-based isolation cuts for a cone size of $\Delta R = 0.2$ and track-based isolation cuts with a cone size of $\Delta R = 0.3$.
- Electrons which are within $\Delta R = 0.4$ of a jet with $p_T > 25$ GeV are not considered.
- Only electrons with $p_T > 30$ GeV are considered.
- Electrons are required to have $|\eta| < 2.47$. Electrons falling into the calorimeter barrel-endcap transition region (crack region) corresponding to $1.37 < |\eta| < 1.52$ are excluded.

7.1.2 Muons

Reconstructed muons in this analysis are required to meet the following criteria:

- Muons must pass the tight identification criteria for CB muons.
- Muons must have a longitudinal impact parameter, z_0, from the primary vertex less than 2 mm.
- Muons must pass track-based isolation cuts for a cone size of $\Delta R = 0.3$.
- Muons must not be within a cone of $\Delta R = 0.4$ around a jet with $p_T > 25$ GeV and a jet vertex fraction greater than 0.5.

- Only muons with $p_{\mathrm{T}} > 30$ GeV are considered.
- Muons are required to have $|\eta| < 2.5$.

7.1.3 Jets

Jets in this analysis must meet the following criteria

- Jets must have $p_{\mathrm{T}} > 25$ GeV.
- Only central jets are allowed with $|\eta| < 2.5$.
- Jets with $p_{\mathrm{T}} < 50$ GeV are required to have a jet vertex fraction greater than 0.5.
- Jets overlapping with an electron within a cone of $\Delta\mathrm{R} = 0.2$ are not considered.
- Jets tagged as b-jets must meet all previous jet object criteria.
- Only jets which have an MV1c discriminant value > 0.3511 are considered to be b-jets. This corresponds to the 57% efficiency working point.

7.2 Event pre-selection

Most events in the collected data have final states which do not match the monotop signal topology. The purpose of event selection cuts was to increase the ability to discern signal events from background events by picking those events which most closely match that of the signal topology. Monotop events in this analysis have a final state consisting of one lepton, one b-tagged jet, and missing transverse energy. As such the following event level cuts were applied to both the simulated samples as well as to data.

- Events must have exactly one lepton.
- Events must have exactly one jet which is required to be tagged as a b-jet.
- Events must have $E_{\mathrm{T}}^{\mathrm{miss}} > 35$ GeV.

In order to reduce the amount of multijet background present, a triangular cut of $E_{\mathrm{T}}^{\mathrm{miss}} + m_{\mathrm{T}}(\ell, E_{\mathrm{T}}^{\mathrm{miss}}) > 60$ GeV was used. Multijets, more so than any other background, are characterized by events with low $E_{\mathrm{T}}^{\mathrm{miss}}$ and low $m_{\mathrm{T}}(\ell, E_{\mathrm{T}}^{\mathrm{miss}})$ as is shown in Figure 7.1. This cut was nearly 100% efficient when applied to signal and data. Table 7.1 defines the event yields in what is known as the pre-selection region after having applied this triangular cut. The dominant backgrounds in this region are W+jets and multijets. While not kinematically similar to the monotop signal, their high cross-sections and significant fluctuations are the reasons those two backgrounds dominate in this region.

Pre-Selection Region		
Background	**Events**	**[%] of Tot.**
$t\bar{t}$	10629.8 ± 56.0	5.0
Single-top s-chan	762.6 ± 6.1	0.4
Single-top t-chan	12687.0 ± 40.8	6.0
Single-top Wt-chan	2312.6 ± 40.9	1.1
W+heavy flavor	119079.9 ± 453.1	56.1
W+light jets	28558.3 ± 430.3	13.4
Z+light jets	1547.3 ± 62.7	0.7
Diboson	1320.0 ± 18.8	0.6
Multijet	35443.5 ± 202.5	16.7
Total Background	212340.9 ± 665.0	
Data	211338	

Table 7.1: Number of expected background events and the number of observed events in the pre-selection region. The quoted errors include statistical uncertainties only.

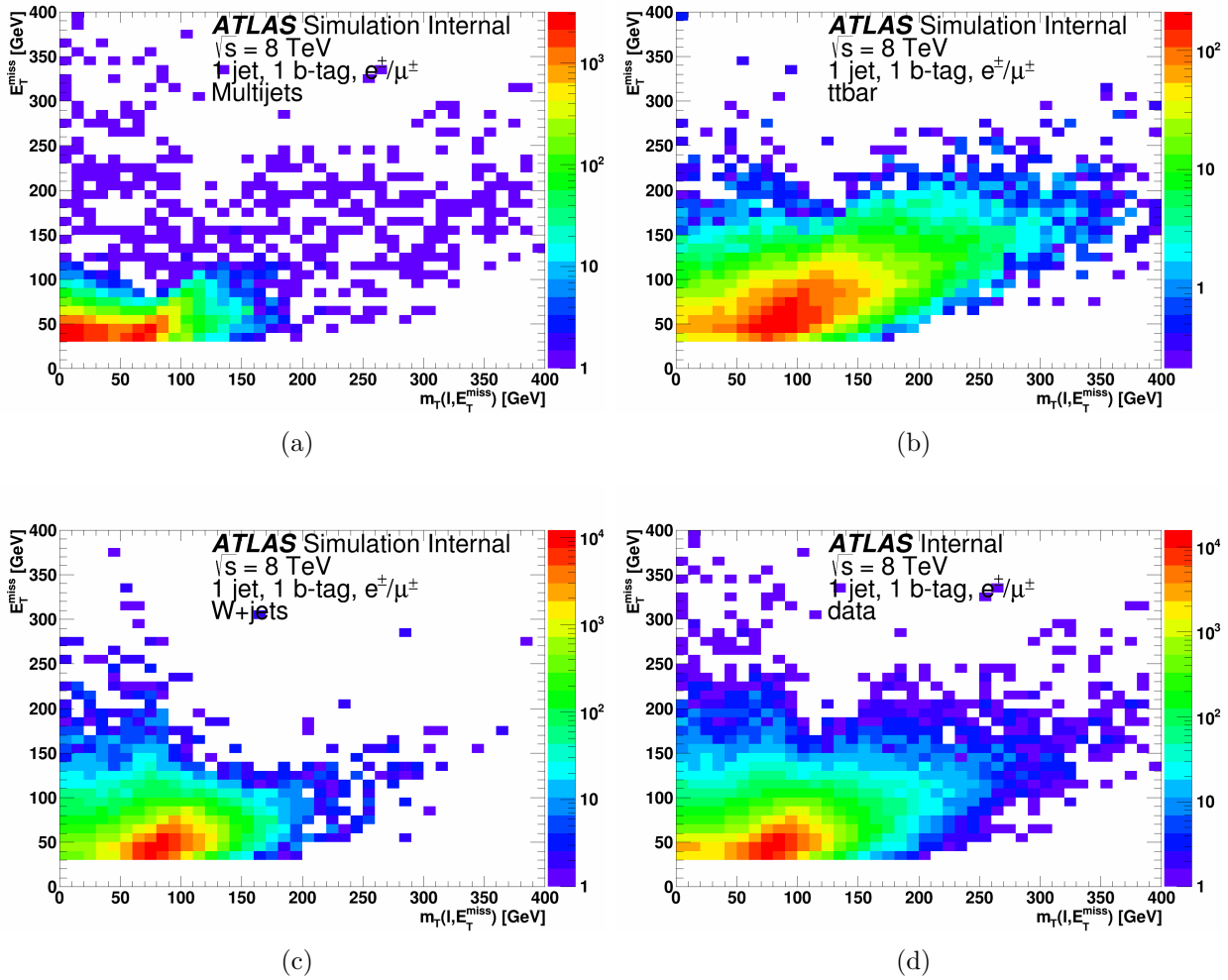

(a) (b) (c) (d)

Figure 7.1: Two-dimensional plots of $E_{\mathrm{T}}^{\mathrm{miss}}$ vs $m_{\mathrm{T}}(\ell, E_{\mathrm{T}}^{\mathrm{miss}})$ for (a) multijets, (b) $t\bar{t}$, (c) W+jets, and (d) data.

7.3 Background validation

Control regions (CR) are regions of phase space where the background is dominant and signal contamination is kept to a minimum and were defined in order to validate the background modeling. In these control regions the data/background prediction is close to unity if the backgrounds are modeled appropriately. In order to define these control regions cuts on two kinematic variables, $m_{\mathrm{T}}(\ell, E_{\mathrm{T}}^{\mathrm{miss}})$ and $\Delta\phi(\ell, b)$, were used.

Pre-Selection Region		
Signal	**Events**	$\frac{S}{\sqrt{S+B}}$
$S1_R$ 0 [GeV]	1445.3 ± 11.1	3.3
$S1_R$ 20 [GeV]	1438.9 ± 11.0	3.1
$S1_R$ 40 [GeV]	1435.7 ± 11.0	3.1
$S1_R$ 60 [GeV]	1406.0 ± 10.7	3.0
$S1_R$ 80 [GeV]	1346.7 ± 10.4	2.9
$S1_R$ 100 [GeV]	1293.9 ± 10.0	2.8
$S4_R$ 0 [GeV]	71515.9 ± 734.1	134.2
$S4_R$ 25 [GeV]	303719.8 ± 3184.4	422.8
$S4_R$ 50 [GeV]	95680.7 ± 919.0	172.4
$S4_R$ 75 [GeV]	52058.9 ± 492.8	101.2
$S4_R$ 100 [GeV]	32332.0 ± 306.8	65.4
$S4_R$ 125 [GeV]	22421.0 ± 210.2	46.3
$S4_R$ 150 [GeV]	15733.7 ± 148.5	32.9
$S4_R$ 200 [GeV]	8638.6 ± 80.5	18.4
$S4_R$ 250 [GeV]	4887.1 ± 45.6	10.5
$S4_R$ 300 [GeV]	2974.0 ± 27.7	6.4
$S4_R$ 400 [GeV]	1205.1 ± 11.3	2.6
$S4_R$ 500 [GeV]	540.2 ± 5.1	1.1
$S4_R$ 600 [GeV]	266.6 ± 2.6	0.6
$S4_R$ 700 [GeV]	136.0 ± 1.3	0.3
$S4_R$ 800 [GeV]	75.1 ± 0.7	0.2
$S4_R$ 900 [GeV]	42.1 ± 0.4	0.09
$S4_R$ 1000 [GeV]	24.9 ± 0.2	0.05

Table 7.2: Number of expected signal events in the pre-selection region. The quoted errors include statistical uncertainties only. The third column shows the significance of the signal where S and B are the number of signal and background events respectively.

7.3.1 Transverse mass

The $m_{\mathrm{T}}(\ell, E_{\mathrm{T}}^{\mathrm{miss}})$ variable is the transverse mass between the lepton and the $E_{\mathrm{T}}^{\mathrm{miss}}$ and in most SM processes is calculated with the lepton and neutrino from a W decay. Consider the equation for the transverse mass between two objects,

$$m_{\mathrm{T}}(A, B) = \sqrt{2p_{\mathrm{T}}(A)\ p_{\mathrm{T}}(B)\,[1 - \cos(\Delta\phi(A, B))]}. \tag{7.1}$$

Equation 7.1 has a cutoff at the invariant mass of the $A - B$ pair. For events in which $m_{\mathrm{T}}(\ell, E_{\mathrm{T}}^{\mathrm{miss}})$ is calculated with the decay products of a W boson, the $m_{\mathrm{T}}(\ell, E_{\mathrm{T}}^{\mathrm{miss}})$ is kinematically limited to be less than 80 GeV. In cases where events contain multiple neutrinos or events with an off-shell W, the transverse mass between the lepton and $E_{\mathrm{T}}^{\mathrm{miss}}$ may be larger than the W mass. The calculation of $m_{\mathrm{T}}(\ell, E_{\mathrm{T}}^{\mathrm{miss}})$ for the monotop signal involves the lepton from the W decay together with the vector sum of the associated neutrino and either the f_{met} or v_{met} particle. The f_{met} and v_{met} particles, which escape detection, have the effect of increasing the value of $m_{\mathrm{T}}(\ell, E_{\mathrm{T}}^{\mathrm{miss}})$ beyond what is normally seen in the SM backgrounds. Figure 7.2 shows the distribution of $m_{\mathrm{T}}(\ell, E_{\mathrm{T}}^{\mathrm{miss}})$ for the backgrounds, signal, as well as for data. There is a clear peak at the W mass for the SM backgrounds with a sharply falling distribution beyond. The distributions for the signal, however, do not fall off as sharply as the backgrounds. This is especially clear in Figure 7.2(b) where the processes are normalized to unity in order to better see their shapes.

7.3.2 Phi separation

The angular separation between the lepton and b-jet is smaller when they originate from the decay of the same top quark than in the case of processes without top quarks such as W/Z+jets or multijet backgrounds. The monotop signal, having its lepton and b-jet originating from the top quark decay, is characterized by smaller angular separations of the lepton and b-jet pair. This is shown in Figure 7.3. Again, the differences in the shapes become more pronounced when looking a plot normalized to unity as in Figure 7.3(b).

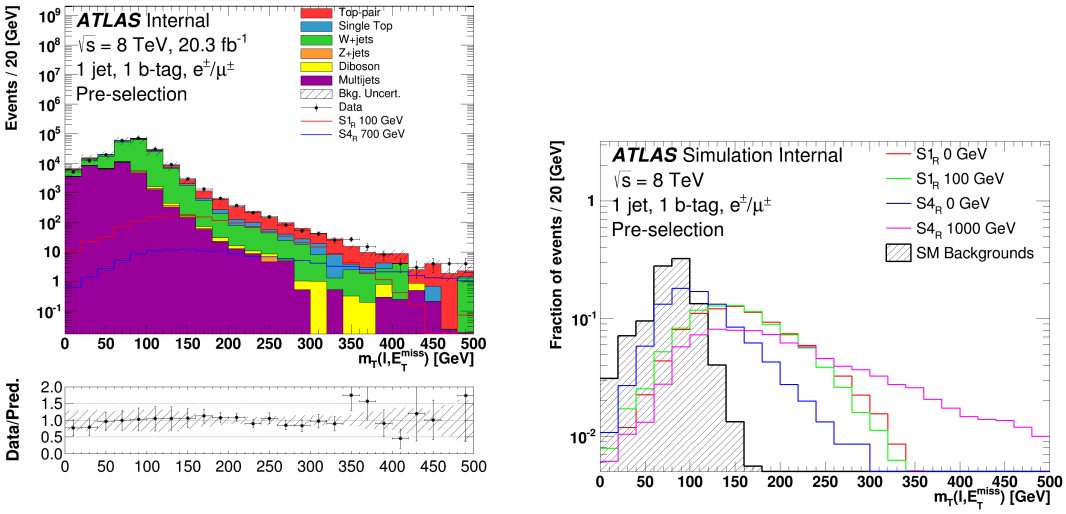

(a) (b)

Figure 7.2: (a) The distribution of $m_{\mathrm{T}}(\ell, E_{\mathrm{T}}^{\mathrm{miss}})$ in the pre-selection region. The background uncertainty corresponds to the statistical uncertainty added in quadrature with the cross-section uncertainties of the backgrounds. (b) The distribution of $m_{\mathrm{T}}(\ell, E_{\mathrm{T}}^{\mathrm{miss}})$ in the pre-selection region normalized to unity for the backgrounds and various signal models.

7.4 Control regions

In order to validate the background modeling in various areas of phase space, three orthogonal control regions were defined based on cuts on $m_{\mathrm{T}}(\ell, E_{\mathrm{T}}^{\mathrm{miss}})$ and $\Delta\phi(\ell, b)$. Three CRs (CR1, CR2, and CR3) were chosen in order to validate the background modeling in three distinct regions phase space populated by different backgrounds. References to these control regions by name will be made in later chapters. Figure 7.4 shows two-dimensional plots of $m_{\mathrm{T}}(\ell, E_{\mathrm{T}}^{\mathrm{miss}})$ and $\Delta\phi(\ell, b)$ for the multijet and W+jets backgrounds as well as the 100 and 700 GeV mass points for the $\mathrm{S1_R}$ and $\mathrm{S4_R}$ signal models respectively. As it can be seen, the two dominant backgrounds are concentrated in regions of low $m_{\mathrm{T}}(\ell, E_{\mathrm{T}}^{\mathrm{miss}})$ and higher values of $|\Delta\phi(\ell, b)|$. The CR1 control region, where events are required to satisfy 60 GeV $< m_{\mathrm{T}}(\ell, E_{\mathrm{T}}^{\mathrm{miss}}) <$ 120 GeV, allows for the validation of the W+jets and multijet models. The CR2 control region, where events are required to satisfy 120 GeV $< m_{\mathrm{T}}(\ell, E_{\mathrm{T}}^{\mathrm{miss}}) <$ 150 GeV

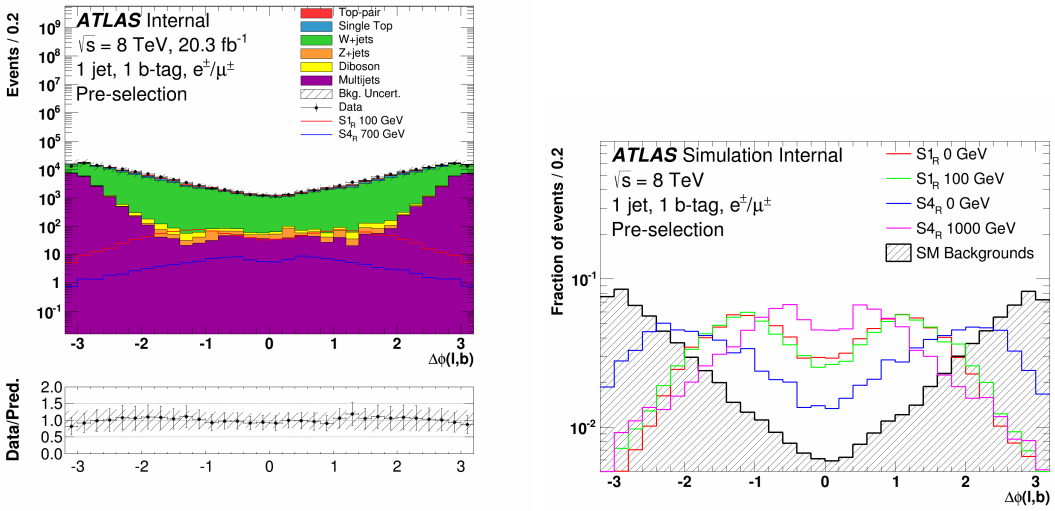

(a) (b)

Figure 7.3: (a) The distribution of $\Delta\phi(\ell, b)$ in the pre-selection region. The background uncertainty corresponds to the statistical uncertainty added in quadrature with the cross-section uncertainties of the backgrounds. (b) The distribution of $\Delta\phi(\ell, b)$ in the pre-selection region normalized to unity.

and $|\Delta\phi(\ell, b)| < 1.8$, allows for validation of the background modeling in a kinematic region closer to the signal region (SR). The CR3 control region, where events are required to have two b-tagged jets and which satisfy $m_{\mathrm{T}}(\ell, E_{\mathrm{T}}^{\mathrm{miss}}) > 150$ GeV and $|\Delta\phi(\ell, b)| < 1.8$, are selected in order to validate the modeling of the $t\bar{t}$ background. The control regions are summarized below and in Figure 7.5.

- **CR1** – 60 GeV $< m_{\mathrm{T}}(\ell, E_{\mathrm{T}}^{\mathrm{miss}}) <$ 120 GeV; this region is enriched in W+jets and multijets background events.

- **CR2** – 120 GeV $< m_{\mathrm{T}}(\ell, E_{\mathrm{T}}^{\mathrm{miss}}) <$ 150 GeV and $|\Delta\phi(\ell, b)| < 1.8$; this region is closer to the signal region kinematics.

- **CR3** – $m_{\mathrm{T}}(\ell, E_{\mathrm{T}}^{\mathrm{miss}}) > 150$ GeV, $|\Delta\phi(\ell, b)| < 1.8$ and 2 b-tagged jets; this region is enriched in $t\bar{t}$ events.

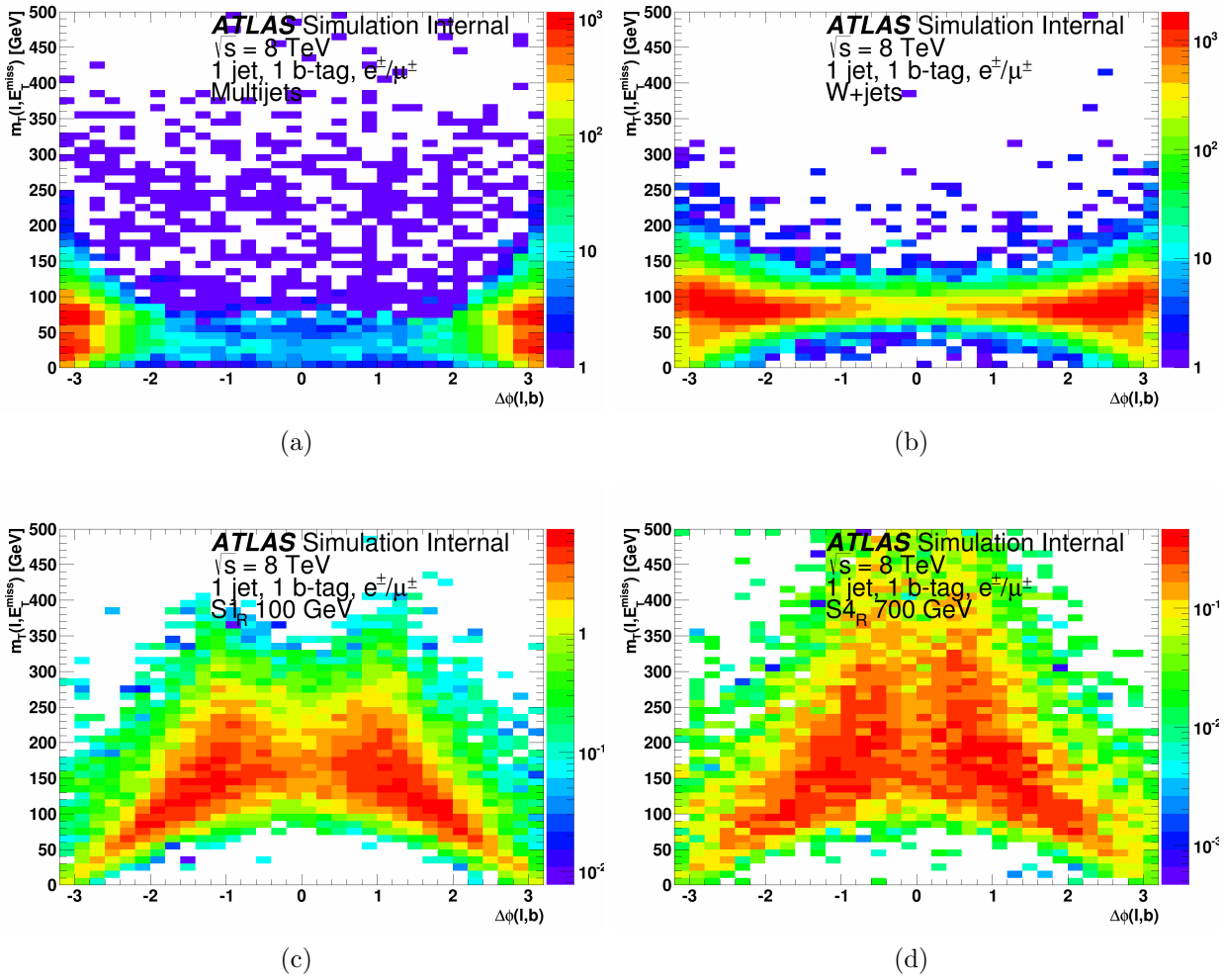

Figure 7.4: Two-dimensional plots of $\Delta\phi(\ell, b)$ vs $m_{\mathrm{T}}(\ell, E_{\mathrm{T}}^{\mathrm{miss}})$ for (a) multijets, (b) W+jets, (c) the 100 GeV $\mathrm{S1_R}$ signal model, and (d) the 700 GeV $\mathrm{S4_R}$ signal model.

7.4.1 Event yields

The expected number of background events and the number of observed events in the combined electron/muon channel are shown in Tables 7.3, 7.4, and 7.5 for CR1, CR2, and CR3 respectively. Processes were normalized to their cross-sections and to the total integrated luminosity seen in data during Run1, 20.3 fb^{-1}. In CR1 W+jets and multijets dominate while in CR2 and in CR3, $t\bar{t}$ dominates.

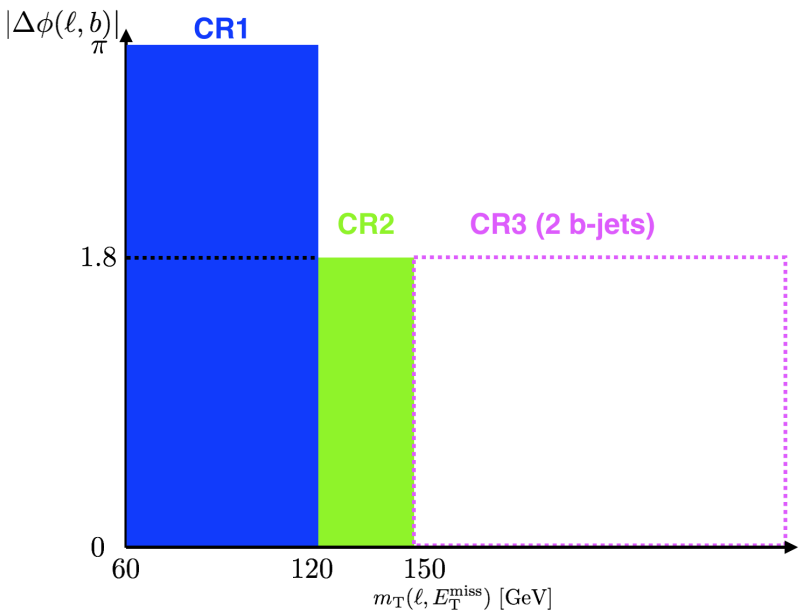

Figure 7.5: A sketch depicting the control regions defined in this analysis in $m_{\mathrm{T}}(\ell, E_{\mathrm{T}}^{\mathrm{miss}})$ – $|\Delta\phi(\ell, b)|$ space.

7.4.2 Kinematic distributions

Kinematic distributions in the three control regions are shown Figures 7.6 and 7.7 for $m_{\mathrm{T}}(\ell, E_{\mathrm{T}}^{\mathrm{miss}})$ and $\Delta\phi(\ell, b)$ respectively. Taking into account the uncertainties shown in these plots, the discrepancies do not exceed one standard deviation in most cases and it can be concluded that the backgrounds were properly modeled. More control region plots are shown in Appendix B which show similar agreement between the predicted values and data.

7.5 Cut-based signal region

This section describes the procedure used to optimize the event selection using a cut-based analysis.

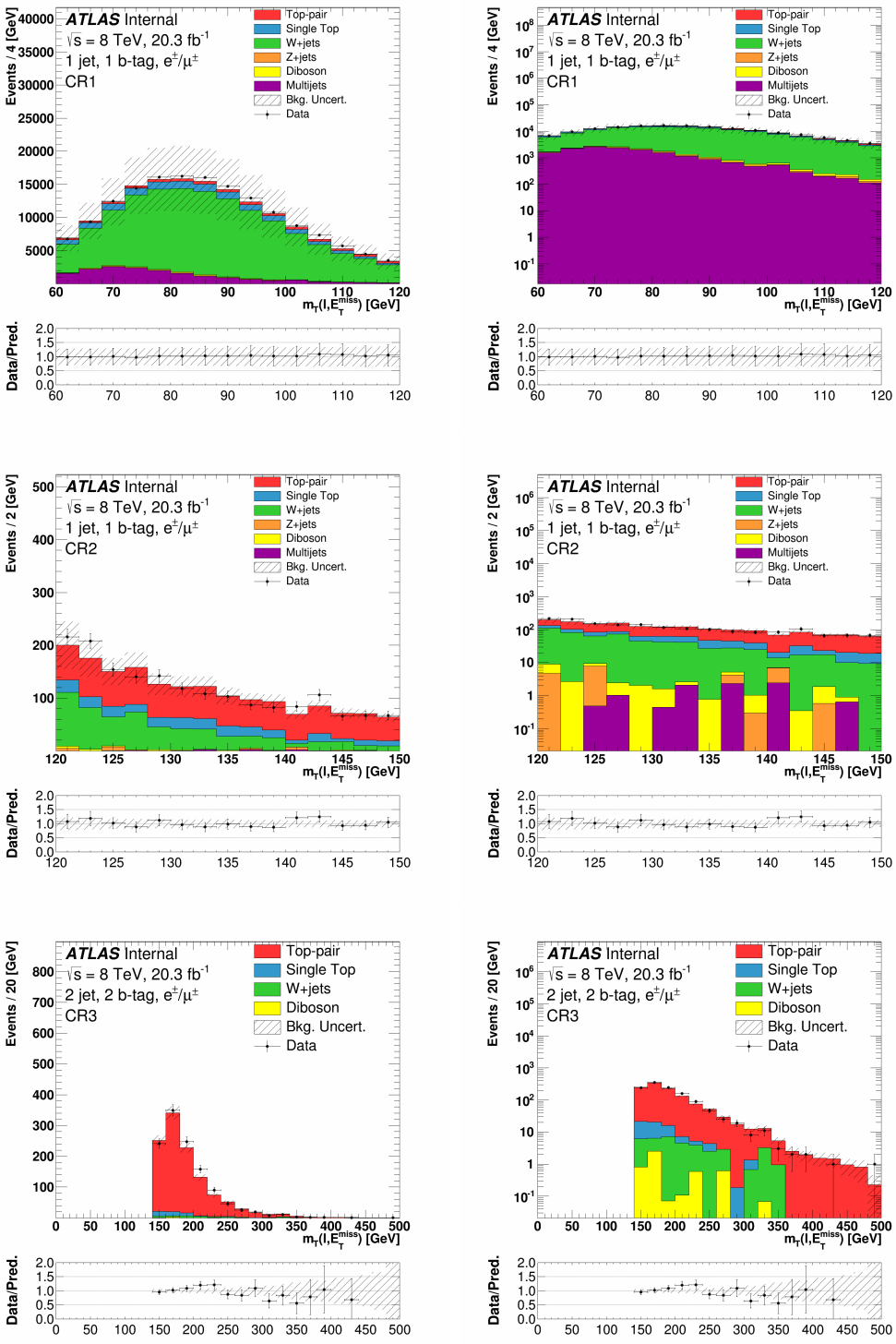

Figure 7.6: Distributions of $m_{\mathrm{T}}(\ell, E_{\mathrm{T}}^{\mathrm{miss}})$ in CR1 (top), CR2 (middle), and CR3 (bottom) in the combined electron/muon channel, in linear (left) and log (right) scale. The uncertainty band on the expected background corresponds to the errors due to the statistical uncertainties added in quadrature with the cross-section and normalization uncertainties.

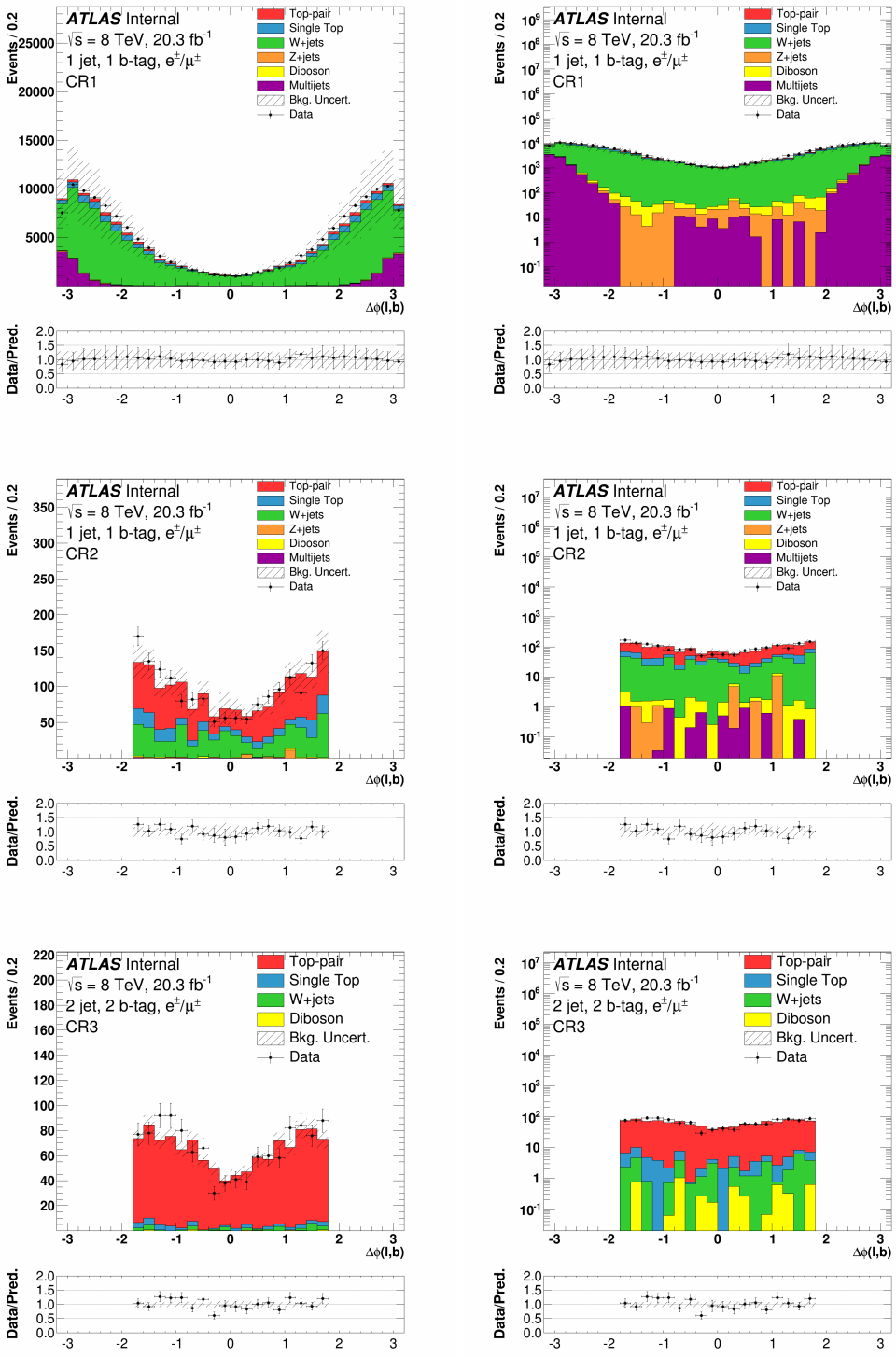

Figure 7.7: Distributions of $\Delta\phi(\ell, b)$ in CR1 (top), CR2 (middle), and CR3 (bottom) in the combined electron/muon channel, in linear (left) and log (right) scale. The uncertainty band on the expected background corresponds to the errors due to the statistical uncertainties added in quadrature with the cross-section and normalization uncertainties.

CR1		
Background	**Events**	**[%] of Tot.**
$t\bar{t}$	5135.0 ± 39.0	3.3
Single-top s-chan	560.8 ± 5.3	0.4
Single-top t-chan	9639.1 ± 35.6	6.2
Single-top Wt-chan	1156.6 ± 28.9	0.7
W+heavy flavor	95650.2 ± 406.4	61.2
W+light jets	25392.1 ± 419.7	16.3
Z+light jets	1044.3 ± 53.1	0.7
Diboson	968.9 ± 16.2	0.6
Multijet	16657.7 ± 173.3	10.7
Total Background	156204.8 ± 614.9	
Data	159627	

Table 7.3: Number of expected background events and the number of observed events in CR1. This region is enriched with W+jets and multijet events. The quoted errors include statistical uncertainties only.

7.5.1 Signal region optimization

In order to improve the sensitivity of the search analysis, an optimization of the event selection was performed in the signal region defined by $m_{\mathrm{T}}(\ell, E_{\mathrm{T}}^{\mathrm{miss}}) > 150$ GeV in addition to the pre-selection cuts applied in Section 7.2. The discriminating power of the variables $m_{\mathrm{T}}(\ell, E_{\mathrm{T}}^{\mathrm{miss}})$ and $\Delta\phi(\ell, b)$ was exploited. The expected excluded signal strength, as is outlined in Chapter 9, was calculated for various cuts on $m_{\mathrm{T}}(\ell, E_{\mathrm{T}}^{\mathrm{miss}})$ and $\Delta\phi(\ell, b)$. All systematic uncertainties detailed in Chapter 8 were included in the calculations. The value of the cuts on $m_{\mathrm{T}}(\ell, E_{\mathrm{T}}^{\mathrm{miss}})$ range from a lower threshold of 150 to 300 GeV in steps of 10 GeV and the value of the cuts on $|\Delta\phi(\ell, b)|$ range from an upper threshold of 3.0 to 1.0 in steps of 0.2. The optimization procedure was performed using one mass hypothesis $m(f_{\mathrm{met}}) = 100$ GeV for the $\mathrm{S1_R}$ model, for which the kinematic distributions have small variations across the mass range included in this analysis. In the case of the $\mathrm{S4_R}$ model, three mass hypotheses were studied: $m(v_{\mathrm{met}}) = 0$, 100, and 300 GeV. The results of the optimization procedure

CR2		
Background	**Events**	**[%] of Tot.**
$t\bar{t}$	864.2 ± 16.0	50.8
Single-top s-chan	3.6 ± 0.4	0.2
Single-top t-chan	56.6 ± 2.7	3.3
Single-top Wt-chan	175.4 ± 11.3	10.3
W+heavy flavor	415.4 ± 26.0	24.4
W+light jets	146.5 ± 32.4	8.6
Z+light jets	19.5 ± 9.6	1.1
Diboson	18.1 ± 2.2	1.1
Multijet	0.8 ± 5.3	0.0
Total Background	1700.2 ± 47.4	
Data	1748	

Table 7.4: Number of expected background events and the number of observed events in CR2. This region has kinematics closer to that of the signal region. The quoted errors include statistical uncertainties only.

CR3		
Background	**Events**	**[%] of Tot.**
$t\bar{t}$	1085.4 ± 18.4	92.8
Single-top s-chan	0.6 ± 0.2	0.1
Single-top t-chan	2.5 ± 0.6	0.2
Single-top Wt-chan	42.2 ± 5.8	3.6
W+heavy flavor	23.4 ± 6.3	2.0
W+light jets	10.3 ± 3.8	0.9
Z+light jets	0.0 ± 3.1	0.0
Diboson	4.8 ± 1.3	0.4
Multijet	0.0 ± 8.6	0.0
Total Background	1169.2 ± 22.6	
Data	1203	

Table 7.5: Number of expected background events and the number of observed events in CR3. This region is enriched in $t\bar{t}$ events. The quoted errors include statistical uncertainties only.

are shown in Figures 7.8 and 7.9.

For the resonant $S1_R$ model, a local minimum of the expected limit was found at a selection of $m_T(\ell, E_T^{miss}) > 210$ GeV and $|\Delta\phi(\ell, b)| < 1.2$. For the non-resonant $S4_R$ model a local

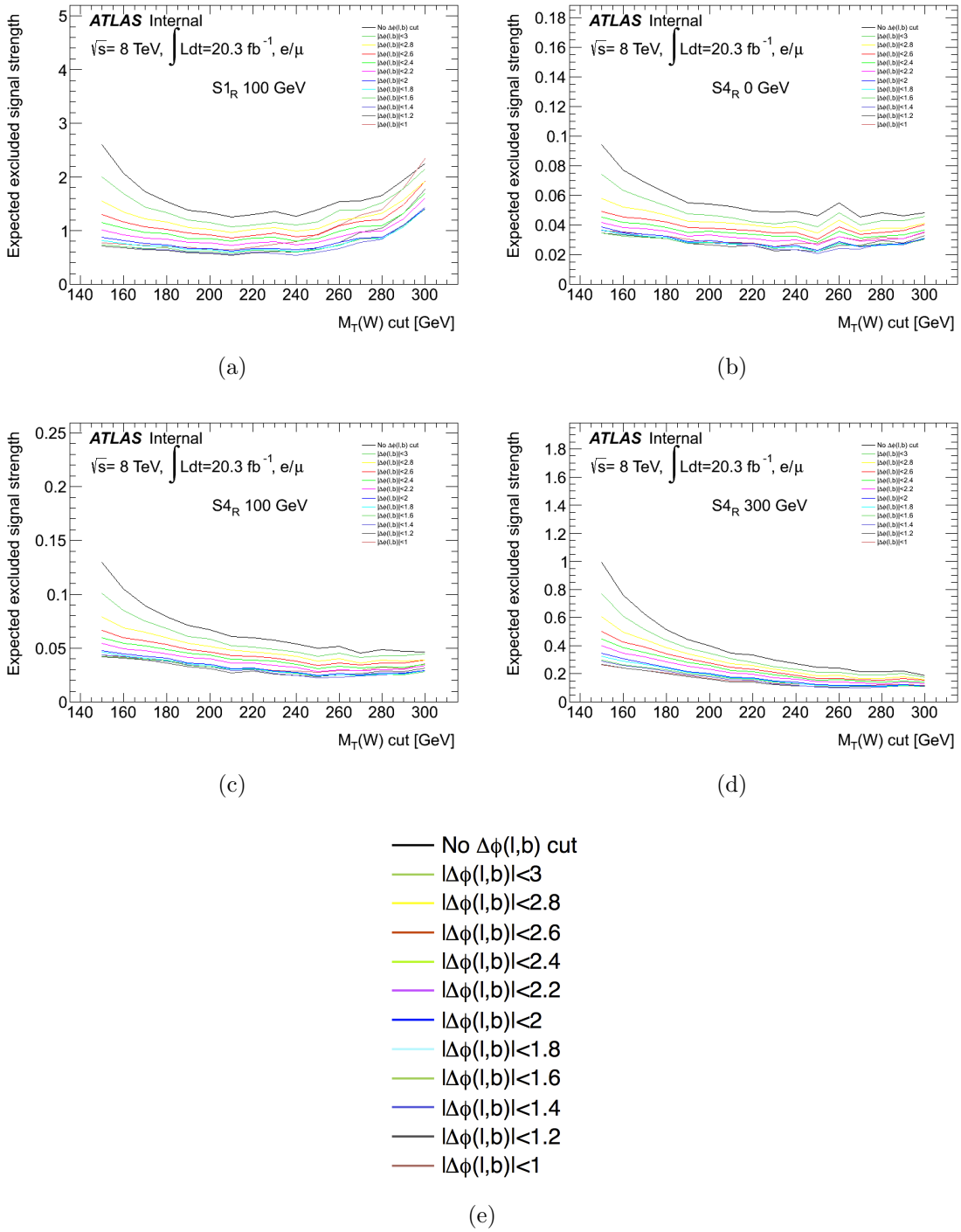

Figure 7.8: Expected excluded signal strength as a function of the value of the lower $m_{\mathrm{T}}(\ell, E_{\mathrm{T}}^{\mathrm{miss}})$ threshold. The different lines indicate the different values of the threshold on $|\Delta\phi(\ell, b)|$. Plots are shown for the optimization of (a) the resonant $\mathrm{S1_R}$ model with $m(f_{\mathrm{met}}) = 100$ GeV and the non-resonant $\mathrm{S4_R}$ model with (b) $m(v_{\mathrm{met}}) = 0$ GeV, (c) $m(v_{\mathrm{met}}) = 100$ GeV, and (d) $m(v_{\mathrm{met}}) = 300$ GeV. (e) The legend which appears in each of the plots in this figure. In these figures the axis label, $\mathrm{M_T(W)}$, corresponds the $m_{\mathrm{T}}(\ell, E_{\mathrm{T}}^{\mathrm{miss}})$ variable described in the text.

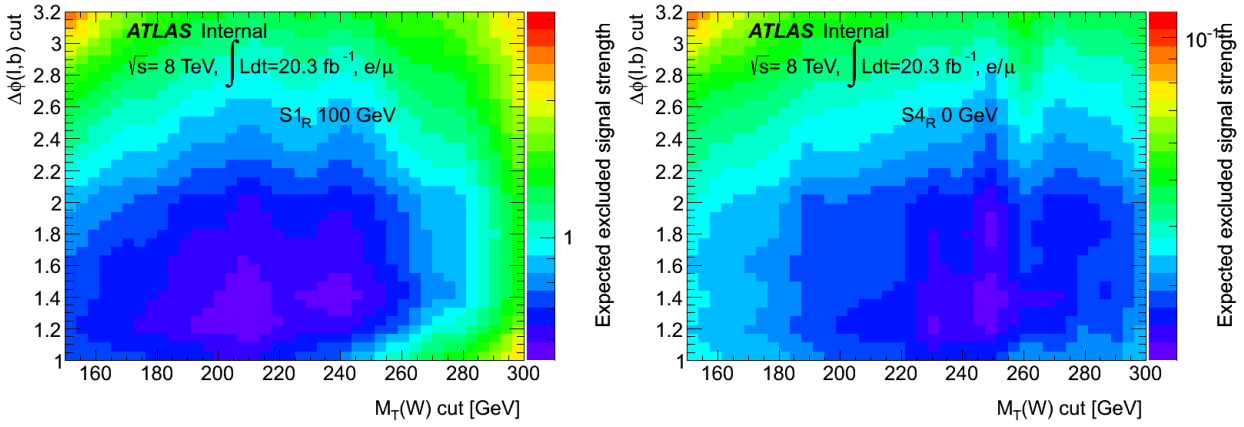

(a)

(b)

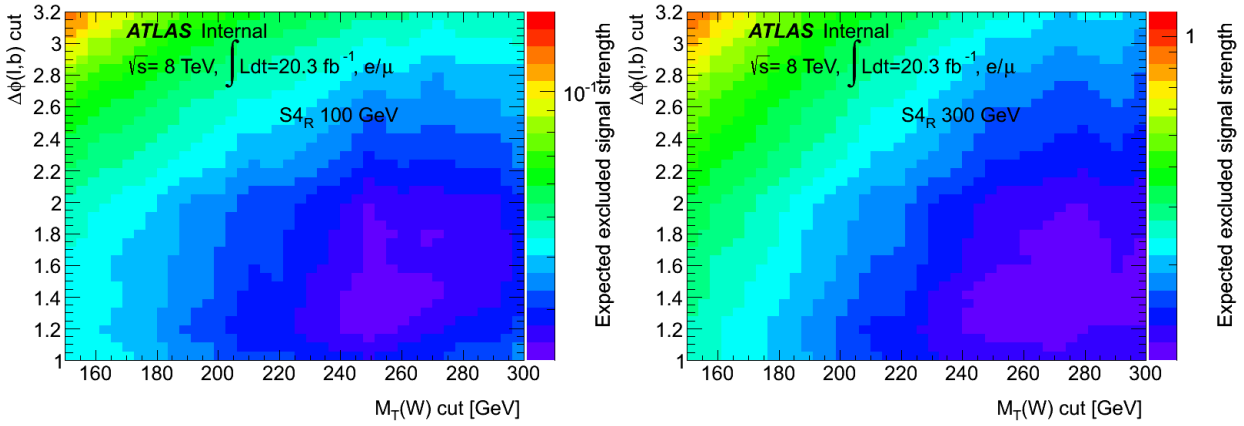

(c)

(d)

Figure 7.9: Expected excluded signal strength as a function of the value of the lower $m_{\mathrm{T}}(\ell, E_{\mathrm{T}}^{\mathrm{miss}})$ threshold and of the higher $|\Delta\phi(\ell, b)|$ threshold. Plots are shown for the optimization of (a) the resonant $\mathrm{S1_R}$ model with $m(f_{\mathrm{met}}) = 100$ GeV and the non-resonant $\mathrm{S4_R}$ model with (b) $m(v_{\mathrm{met}}) = 0$ GeV, (c) $m(v_{\mathrm{met}}) = 100$ GeV, and (d) $m(v_{\mathrm{met}}) = 300$ GeV. In these figures the axis label, $\mathrm{M_T(W)}$, corresponds the $m_{\mathrm{T}}(\ell, E_{\mathrm{T}}^{\mathrm{miss}})$ variable described in the text.

minimum for all three mass hypotheses was found at a selection of $m_{\mathrm{T}}(\ell, E_{\mathrm{T}}^{\mathrm{miss}}) > 250$ GeV and $|\Delta\phi(\ell, b)| < 1.4$. Two optimized search regions are then defined:

- **SR1** – This is the optimized signal region for the resonant $\mathrm{S1_R}$ model. A selection of $m_{\mathrm{T}}(\ell, E_{\mathrm{T}}^{\mathrm{miss}}) > 210$ GeV and $|\Delta\phi(\ell, b)| < 1.2$ is applied to the signal, background, and data samples.

- **SR2** – This is the optimized signal region for the non-resonant $\mathrm{S4_R}$ model. A selection of $m_{\mathrm{T}}(\ell, E_{\mathrm{T}}^{\mathrm{miss}}) > 250$ GeV and $|\Delta\phi(\ell, b)| < 1.4$ is applied to the signal, background, and data samples.

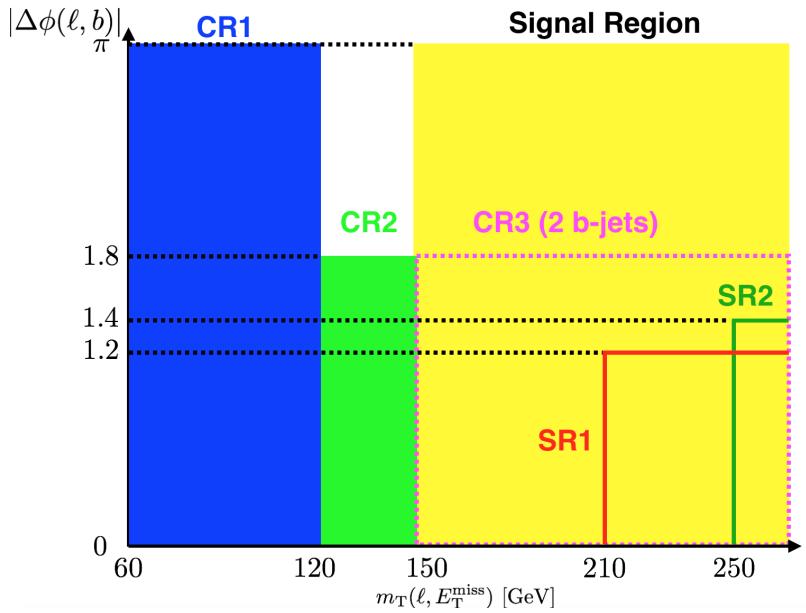

Figure 7.10: A sketch depicting the various control and signal regions defined in this analysis in the $m_{\mathrm{T}}(\ell, E_{\mathrm{T}}^{\mathrm{miss}}) - |\Delta\phi(\ell, b)|$ space. SR1 is the optimized signal region for the resonant $\mathrm{S1_R}$ model and SR2 is the optimized signal region for the non-resonant $\mathrm{S4_R}$ model.

7.5.2 Event yields

The expected number of events for the various backgrounds and signal samples are shown in Tables 7.6 and 7.7 for the SR1 and SR2 optimized signal regions respectively.

SR1		
Sample	**Electron**	**Muon**
$S1_R$ 0 [GeV]	$120.7 \pm 3.2\ ^{+6.9}_{-7.1}$	$132.7 \pm 3.4\ ^{+8.9}_{-9.5}$
$S1_R$ 20 [GeV]	$121.8 \pm 3.2\ ^{+7.1}_{-7.5}$	$132.2 \pm 3.4\ ^{+8.3}_{-7.0}$
$S1_R$ 40 [GeV]	$117.7 \pm 3.1\ ^{+6.6}_{-6.7}$	$127.4 \pm 3.3\ ^{+7.4}_{-7.4}$
$S1_R$ 60 [GeV]	$114.3 \pm 3.0\ ^{+6.4}_{-7.1}$	$115.9 \pm 3.1\ ^{+8.5}_{-6.2}$
$S1_R$ 80 [GeV]	$105.5 \pm 2.9\ ^{+6.1}_{-6.4}$	$113.8 \pm 3.0\ ^{+5.9}_{-5.6}$
$S1_R$ 100 [GeV]	$92.5 \pm 2.6\ ^{+5.2}_{-5.7}$	$93.3 \pm 2.7\ ^{+6.6}_{-5.3}$
$t\bar{t}$	$83.7 \pm 4.8\ ^{+16.9}_{-15.6}$	$105.3 \pm 5.7\ ^{+24.0}_{-24.0}$
Single-top s-channel	$0.00 \pm 0.04 \pm 0.00$	$0.00 \pm 0.04 \pm 0.00$
Single-top t-channel	$0.00 \pm 0.07 \pm 0.00$	$0.00 \pm 0.07 \pm 0.00$
Single-top Wt-channel	$9.6 \pm 2.7\ ^{+6.3}_{-5.9}$	$9.5 \pm 2.4\ ^{+9.7}_{-9.4}$
W+light jets	$0.2 \pm 0.2 \pm 0.2$	$2.0 \pm 1.6\ ^{+3.0}_{-2.8}$
W+heavy flavor	$10.5 \pm 3.9\ ^{+6.9}_{-5.7}$	$16.7 \pm 4.9\ ^{+9.0}_{-9.1}$
Diboson	$0.3 \pm 0.2\ ^{+0.1}_{-0.3}$	$1.0 \pm 0.5\ ^{+0.6}_{-0.6}$
Z+jets	$0.00 \pm 3.11 \pm 0.00$	$0.00 \pm 3.1 \pm 0.00$
Multijet	$0.00 \pm 0.5 \pm 0.00$	$0.4 \pm 1.1\ ^{+0.5}_{-0.5}$
Total Background	$104.4 \pm 7.5\ ^{+19.3}_{-17.7}$	$134.92 \pm 8.12\ ^{+29.06}_{-27.87}$
Data	103	135

Table 7.6: Number of expected background and $S1_R$ signal events in the SR1 signal region, for the electron and muon channels separately. The absolute statistical and systematic uncertainties are shown.

7.5.3 Kinematic distributions

Kinematic distributions in the two optimized selection regions are shown Figures 7.11, 7.12 for $m_{\mathrm{T}}(\ell, E_{\mathrm{T}}^{\mathrm{miss}})$ and $\Delta\phi(\ell, b)$ respectively. More signal region plots are shown in Appendix C.

7.6 BDT signal region

This section describes the procedure used to optimize the event selection for use in an MVA search technique. As will be shown in Chapter 10, the $S1_R$ resonant model was excluded across the entirety of the mass range of the f_{met} particle and for this reason the MVA

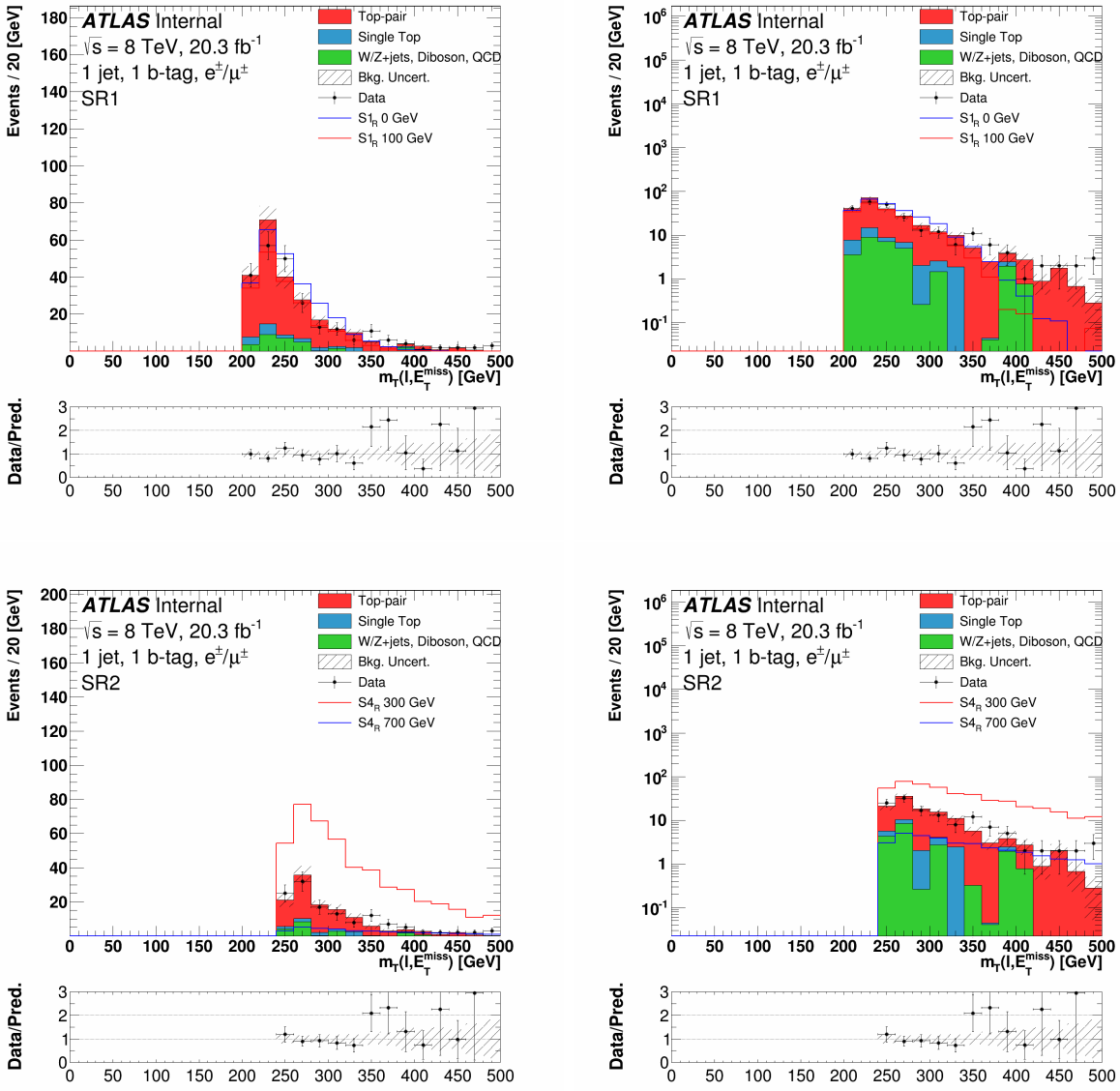

Figure 7.11: Distributions of $m_{\mathrm{T}}(\ell, E_{\mathrm{T}}^{\mathrm{miss}})$ in the optimized SR1 signal region (top), and the optimized SR2 signal region (bottom) in the combined electron/muon channel, in linear (left) and log (right) scale. The uncertainty band on the expected background corresponds to the errors due to the statistical uncertainties added in quadrature with the cross-section and normalization uncertainties.

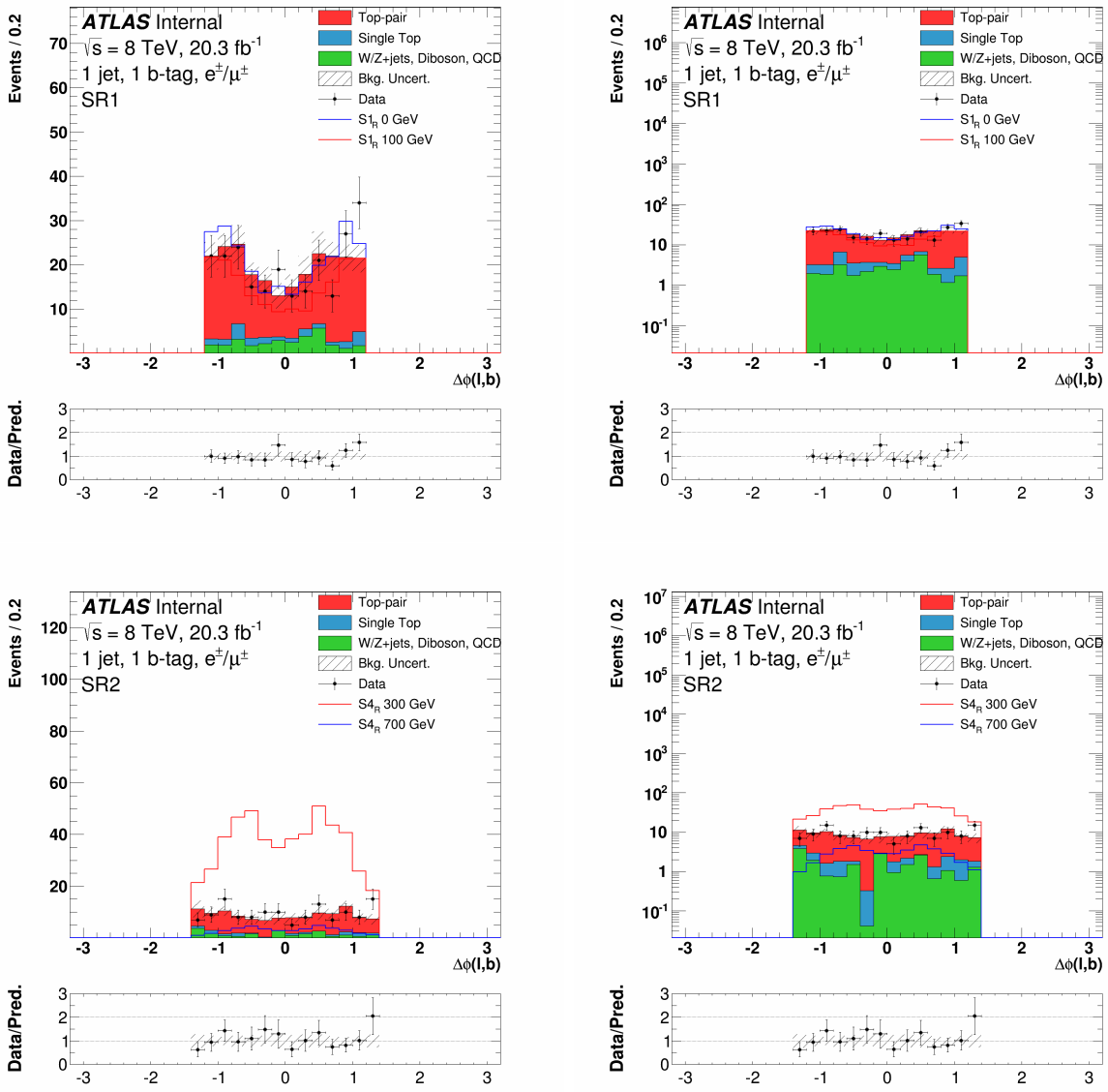

Figure 7.12: Distributions of $\Delta\phi(\ell, b)$ in the optimized SR1 signal region (top), and the optimized SR2 signal region (bottom) in the combined electron/muon channel, in linear (left) and log (right) scale. The uncertainty band on the expected background corresponds to the errors due to the statistical uncertainties added in quadrature with the cross-section and normalization uncertainties.

SR2		
Sample	**Electron**	**Muon**
$S4_R$ 0 [GeV]	$1105.6 \pm 87.7\ ^{+83.4}_{-89.1}$	$1322.3 \pm 100.4\ ^{+146.5}_{-108.2}$
$S4_R$ 25 [GeV]	$5644.9 \pm 420.1\ ^{+438.3}_{-512.7}$	$7588.1 \pm 499.7\ ^{+474.6}_{-568.6}$
$S4_R$ 50 [GeV]	$2121.8 \pm 133.3\ ^{+171.9}_{-151.4}$	$2477.1 \pm 149.1\ ^{+189.4}_{-221.3}$
$S4_R$ 75 [GeV]	$1427.5 \pm 79.8\ ^{+98.6}_{-130.1}$	$1570.7 \pm 85.6\ ^{+137.4}_{-99.0}$
$S4_R$ 100 [GeV]	$1146.2 \pm 56.3\ ^{+78.6}_{-106.1}$	$1230.1 \pm 59.5\ ^{+118.0}_{-80.1}$
$S4_R$ 125 [GeV]	$861.6 \pm 39.9\ ^{+60.2}_{-70.8}$	$1021.2 \pm 45.0\ ^{+93.2}_{-88.2}$
$S4_R$ 150 [GeV]	$741.7 \pm 31.5\ ^{+51.1}_{-58.9}$	$785.4 \pm 33.0\ ^{+60.7}_{-53.0}$
$S4_R$ 200 [GeV]	$531.7 \pm 19.6\ ^{+35.3}_{-36.6}$	$598.4 \pm 21.1\ ^{+42.0}_{-36.8}$
$S4_R$ 250 [GeV]	$360.1 \pm 12.1\ ^{+22.6}_{-27.2}$	$392.4 \pm 12.9\ ^{+34.2}_{-28.7}$
$S4_R$ 300 [GeV]	$239.1 \pm 7.7\ ^{+15.6}_{-16.7}$	$273.7 \pm 8.4\ ^{+23.2}_{-22.7}$
$S4_R$ 400 [GeV]	$123.2 \pm 3.5\ ^{+8.2}_{-8.9}$	$138.5 \pm 3.8\ ^{+10.8}_{-11.1}$
$S4_R$ 500 [GeV]	$63.4 \pm 1.7\ ^{+4.2}_{-4.9}$	$70.7 \pm 1.9\ ^{+5.4}_{-5.1}$
$S4_R$ 600 [GeV]	$33.6 \pm 0.9\ ^{+2.3}_{-2.2}$	$38.6 \pm 1.0\ ^{+3.3}_{-3.1}$
$S4_R$ 700 [GeV]	$19.1 \pm 0.5\ ^{+1.5}_{-1.6}$	$21.3 \pm 0.5\ ^{+1.9}_{-1.5}$
$S4_R$ 800 [GeV]	$10.6 \pm 0.3\ ^{+0.8}_{-0.9}$	$12.6 \pm 0.3\ ^{+1.0}_{-1.1}$
$S4_R$ 900 [GeV]	$6.2 \pm 0.2\ ^{+0.4}_{-0.5}$	$7.6 \pm 0.2\ ^{+0.6}_{-0.7}$
$S4_R$ 1000 [GeV]	$3.9 \pm 0.1\ ^{+0.3}_{-0.3}$	$4.4 \pm 0.1\ ^{+0.4}_{-0.3}$
$t\bar{t}$	$42.2 \pm 3.4\ ^{+10.1}_{-9.3}$	$51.5 \pm 3.9\ ^{+12.1}_{-12.6}$
Single-top s-channel	$0.00 \pm 0.04 \pm 0.00$	$0.00 \pm 0.04 \pm 0.00$
Single-top t-channel	$0.00 \pm 0.07 \pm 0.00$	$0.00 \pm 0.07 \pm 0.00$
Single-top Wt	$5.7 \pm 1.9\ ^{+3.9}_{-3.6}$	$4.0 \pm 1.6\ ^{+5.8}_{-5.7}$
W+light jets	$0.8 \pm 0.8\ ^{+0.8}_{-0.8}$	$2.7 \pm 2.7\ ^{+3.5}_{-2.2}$
W+heavy flavor	$5.3 \pm 2.3\ ^{+3.4}_{-3.1}$	$10.6 \pm 3.3\ ^{+7.5}_{-6.7}$
Diboson	$0.3 \pm 0.2\ ^{+0.3}_{-0.4}$	$0.7 \pm 0.5\ ^{+0.2}_{-0.2}$
Z+jets	$0.00 \pm 3.11 \pm 0.00$	$0.00 \pm 3.11 \pm 0.00$
Multijet	$0.00 \pm 0.95 \pm 0.00$	$0.8 \pm 1.1\ ^{+1.1}_{-1.1}$
Total Background	$54.3 \pm 5.6\ ^{+11.4}_{-10.5}$	$70.4 \pm 6.9\ ^{+15.7}_{-15.6}$
Data	56	77

Table 7.7: Number of expected background and $S4_R$ signal events in the SR2 signal region, for the electron and muon channels separately. The absolute statistical and systematic uncertainties are shown.

approach focuses solely on the non-resonant $S4_R$ model. Topological and kinematic cuts described in subsequent sections are applied to the same pre-selection region as the cut-based analysis in order to define a BDT selection region. The aim of the BDT selection

region is to select events which are topologically similar to monotop events but not cut so harshly as to leave the BDT with too few events on which to train.

7.6.1 Charge asymmetry

The LHC is a proton-proton collider where the protons are made up of three valence quarks (uud) together with a gluon field. Other quark flavors like c-, b-, and s-quarks, known as sea quarks, can come into existence within the proton as excitations of the vacuum. As such, how various processes are affected by charge conjugation can be understood by looking at the Feynman diagrams describing their production modes.

7.6.1.1 Backgrounds

Top-pair production at the LHC primarily proceeds through gluon-gluon fusion as seen in Figure 6.4. This is a charge symmetric process where charge conjugation does not alter the final state. Similarly, the single-top Wt-channel process is also charge symmetric. Its main production mode at the LHC is through a b-quark and a gluon interaction. As b-quarks in the proton only arise as b-$\bar{b}$ pairs spontaneously emerging from the vacuum, the process is symmetric under charge conjugation. The single-top s- and t-channels, however, are charge asymmetric. The s-channel process involves a q-$\bar{q}'$ weak interaction as is shown in Figure 6.3(a). If the process proceeds through a u-$\bar{d}$ interaction, the final state will have a positively charged lepton and if the process proceeds through a $\bar{u}$-d interaction, the final state will have a negatively charged lepton. The 2:1 ratio of up to down quarks in the proton, then, is responsible for the charge asymmetry seen in the s-channel process. The single-top t-channel interaction proceeds through a q-b interaction. In order to have a positively charged lepton in the final state a u-$\bar{b}$ interaction is needed. A d-b interaction yields a negatively

charged lepton. So like the s-channel process, the t-channel process is charge asymmetric as a result of the ratio of up to down quarks in the proton. For W+jets events a positively charged lepton can be produced from initial states such as $u\bar{d}$ or $c\bar{s}$ while a negatively charged lepton can be produced with $\bar{u}d$ or $\bar{c}s$ in the initial state. The charge asymmetry estimated using 7 TeV data was found to be roughly 0.54 (0.57) and 0.55 (0.58) for W+heavy heavy (W+light jets) in the electron and muon channels respectively [96]. This is similar to the 0.52 (0.56) and 0.53 (0.60) seen in the 8 TeV samples.

7.6.1.2 Signal

The non-resonant $S4_R$ model can only proceed through the interaction of an up-type quark with a gluon. For a top-quark to be in the final state the initial parton must be a u- or $\bar{u}$-quark. For the final state to contain a positively charged lepton, a u-quark needs to be in the initial state as a $\bar{u}$-quark yields a negatively charged lepton. As it is much more likely that a u-quark rather than a $\bar{u}$-quark is present in the proton, the overall process is highly charge asymmetric. As the mass of the v_{met} particle is increased, the initial state partons must carry a higher fraction of the proton's momentum. As a consequence, it becomes increasingly less likely that a $\bar{u}$-quark in the proton will have the necessary energy to produce these higher mass particles and the asymmetry of the model increases as $m(v_{\text{met}})$ increases. This can be seen directly in Table 7.8 where the lepton charge cut efficiency increases as $m(v_{\text{met}})$ is increased.

7.6.1.3 Effects on event yields and kinematics

The event yields for both background and signal samples after requiring a positively charged lepton in the final state are shown in Tables 7.9 and 7.10 respectively. Comparing the columns

Lepton Charge Cut Efficiency			
Sample	**Efficiency**		
	Electron	**Muon**	**Combined**
$S4_R$ 0 [GeV]	0.81	0.81	0.81
$S4_R$ 25 [GeV]	0.84	0.86	0.85
$S4_R$ 50 [GeV]	0.85	0.85	0.85
$S4_R$ 75 [GeV]	0.84	0.85	0.85
$S4_R$ 100 [GeV]	0.86	0.86	0.86
$S4_R$ 125 [GeV]	0.86	0.87	0.86
$S4_R$ 150 [GeV]	0.86	0.87	0.86
$S4_R$ 200 [GeV]	0.87	0.88	0.88
$S4_R$ 250 [GeV]	0.88	0.89	0.89
$S4_R$ 300 [GeV]	0.89	0.90	0.89
$S4_R$ 400 [GeV]	0.90	0.90	0.90
$S4_R$ 500 [GeV]	0.91	0.93	0.92
$S4_R$ 600 [GeV]	0.92	0.92	0.92
$S4_R$ 700 [GeV]	0.92	0.94	0.93
$S4_R$ 800 [GeV]	0.93	0.94	0.94
$S4_R$ 900 [GeV]	0.94	0.94	0.94
$S4_R$ 1000 [GeV]	0.94	0.95	0.94
$t\bar{t}$	0.50	0.49	0.50
Single-top s-chan	0.64	0.64	0.64
Single-top t-chan	0.65	0.66	0.66
Single-top Wt-chan	0.50	0.50	0.50
W+light jets	0.56	0.60	0.58
W+heavy flavor	0.52	0.53	0.53
Diboson	0.58	0.58	0.58
Z+jets	0.55	0.51	0.52
Multijet	0.50	0.50	0.50
Total Background	0.52	0.53	0.53
Data	0.54	0.54	0.54

Table 7.8: The efficiency of selecting only positively charged leptons for the various background and signal models. Values are shown in the electron, muon, and combined electron and muon channels.

showing the cross-section significance (CSS), $S/\sqrt{S+B}$, in Tables 7.2 and 7.10 it can be seen that selecting only positively charged leptons increases the signal to background ratio. Figure 7.13 shows the distribution of $p_{\mathrm{T}}(\ell)$ for the SM backgrounds before and after the lepton electric charge cut is applied. The bottom inlet in this figure shows that the efficiency

of the lepton electric charge cut is consistent with the 0.53 lepton charge cut efficiency in Table 7.8 across the entire distribution. Additional distributions of other kinematic variables are presented in Appendix D and show a similar behavior of the efficiency.

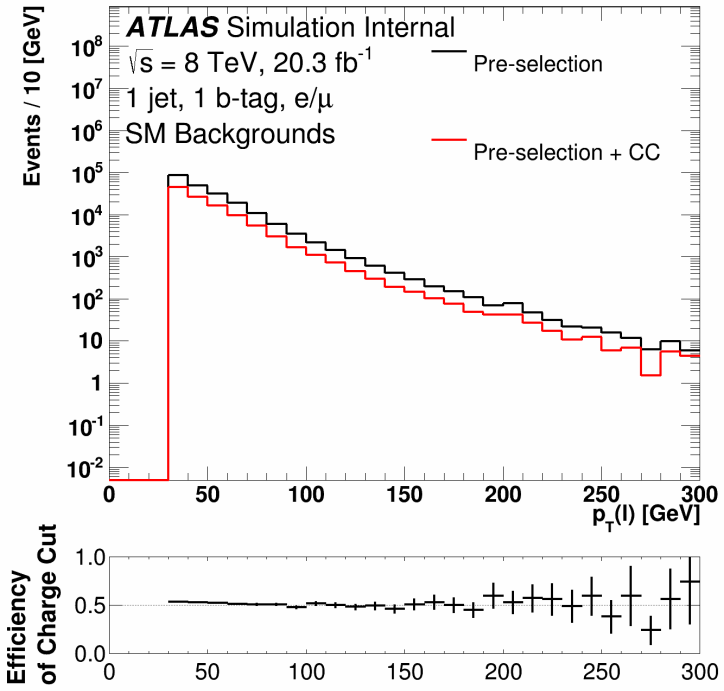

Figure 7.13: Distributions of $p_{\mathrm{T}}(\ell)$ in the combined electron and muon channel in the pre-selection region with and without a cut on the electric charge of the lepton. The black curve shows the distribution in the pre-selection region and the red curve shows the distribution in the pre-selection region when the additional cut on the electric charge of the lepton is applied. The inlet in the bottom of the figure shows the efficiency of the charge cut on a bin-by-bin basis. The error bars in the inlet only include statistical uncertainties.

7.6.2 Kinematic cuts

To further refine the selection for the BDT selection region, cuts on two kinematic variables were used, $p_{\mathrm{T}}(\ell^{+})$ and $E_{\mathrm{T}}^{\mathrm{miss}}$. These variables were chosen over the more complicated $m_{\mathrm{T}}(\ell, E_{\mathrm{T}}^{\mathrm{miss}})$ and $\Delta\phi(\ell, b)$ variables because they are subject to less mismodeling. Cuts were

Pre-Selection + Lepton Charge Cut		
Background	**Events**	**[%] of Tot.**
$t\bar{t}$	5275.4 ± 39.5	4.7
Single-top s-chan	488.4 ± 4.9	0.4
Single-top t-chan	8365.5 ± 33.1	7.5
Single-top Wt-chan	1164.0 ± 28.9	1.0
W+heavy flavor	60298.9 ± 321.4	54.1
W+light jets	16617.9 ± 326.1	14.9
Z+light jets	810.7 ± 46.6	0.7
Diboson	765.8 ± 14.2	0.7
Multijet	17706.8 ± 107.6	15.9
Total Background	111493.3 ± 476.5	
Data	114092	

Table 7.9: The expected number of background events and the observed data events in the pre-selection region with the additional lepton charge cut applied in the combined electron and muon channel is shown. The quoted errors include statistical uncertainties only.

chosen to maximize the CSS, while at the same time retaining enough events on which to train the BDT.

7.6.2.1 Transverse momentum of the lepton

A plot of the CSS calculated with various backgrounds and the 700 GeV $S4_R$ signal sample is shown in Figure 7.14(a) to show how the individual backgrounds respond to a $p_T(\ell^+)$ cut. The x-axis indicates the cut on the kinematic variable such that only events with a $p_T(\ell^+) > X$ are included in the calculation. The plot shows the five dominant backgrounds in the Pre-Selection+Lepton Charge Cut region. Each curve shows the CSS as if it were the only background to the signal. For completeness the black curve showing the calculation with the full slate of background samples is included as well. As can be seen in the figure, the CSS begins to level out, or begins to decrease in the case of the $t\bar{t}$ and single-top t-channel samples, at 100 GeV. Figure 7.14(b) shows the CSS for four different mass samples when the entire

Pre-Selection + Lepton Charge Cut		
Signal	**Events**	$\frac{S}{\sqrt{S+B}}$
$S4_R$ 0 [GeV]	57748.5 ± 658.8	140.4
$S4_R$ 25 [GeV]	257422.8 ± 2933.6	423.8
$S4_R$ 50 [GeV]	81492.8 ± 848.1	185.5
$S4_R$ 75 [GeV]	44124.3 ± 453.7	111.9
$S4_R$ 100 [GeV]	27801.9 ± 284.7	74.5
$S4_R$ 125 [GeV]	19327.3 ± 195.2	53.4
$S4_R$ 150 [GeV]	13592.2 ± 137.9	38.4
$S4_R$ 200 [GeV]	7581.2 ± 75.4	22.0
$S4_R$ 250 [GeV]	4328.8 ± 42.9	12.7
$S4_R$ 300 [GeV]	2657.2 ± 26.1	7.9
$S4_R$ 400 [GeV]	1089.0 ± 10.7	3.2
$S4_R$ 500 [GeV]	497.2 ± 4.9	1.5
$S4_R$ 600 [GeV]	246.0 ± 2.5	0.7
$S4_R$ 700 [GeV]	126.6 ± 1.3	0.4
$S4_R$ 800 [GeV]	70.5 ± 0.7	0.2
$S4_R$ 900 [GeV]	39.6 ± 0.4	0.1
$S4_R$ 1000 [GeV]	23.5 ± 0.2	0.07

Table 7.10: The expected number of signal events in the pre-selection region with the additional lepton charge cut applied in the combined electron and muon channel is shown. The quoted errors include statistical uncertainties only

background estimation was included in the calculation. As the mass of the v_{met} particle is increased the p_{T} of the lepton increases. This is evident by looking at the increasing CSS of the 700 and 1000 GeV samples in the figure. While placing a $p_{\text{T}}(\ell^+) > 100$ GeV cut decreases the CSS for the lower mass samples, it increases that of the higher mass ones.

7.6.2.2 Missing transverse energy

Plots similar to the ones in Figure 7.14 but showing the effect of a $E_{\text{T}}^{\text{miss}}$ cut after having applied a $p_{\text{T}}(\ell^+) > 100$ GeV cut are shown in Figure 7.15. A modest cut of $E_{\text{T}}^{\text{miss}} > 100$ GeV increases the CSS but retains enough events to allow the BDT to exploit further correlations between variables.

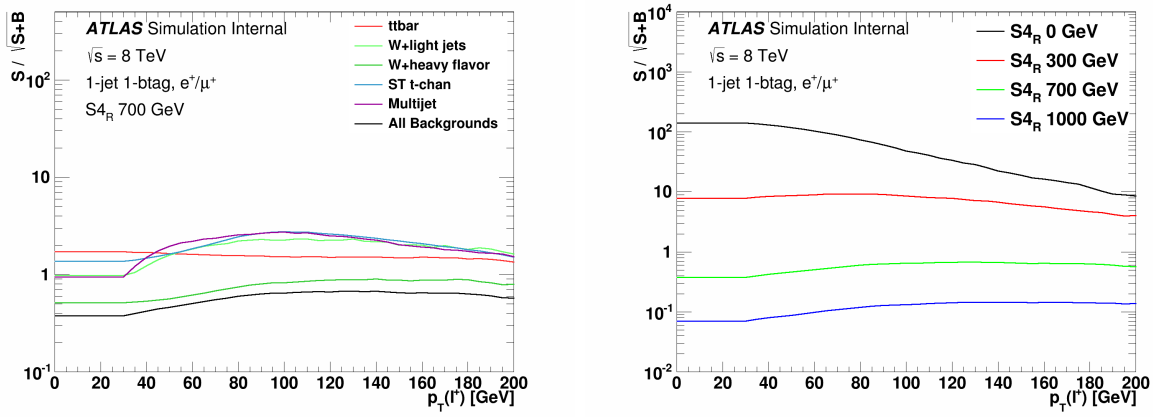

(a) (b)

Figure 7.14: (a) The CSS calculated with the 700 GeV $S4_R$ signal sample as a function of a cut on $p_T(\ell^+)$. The individual curves indicate what backgrounds were included in the calculation. The black curve corresponds to the case where all backgrounds are included. (b) The CSS as a function of a cut on $p_T(\ell^+)$ for various values of the v_{met} particle's mass. Each curve is calculated with all backgrounds included.

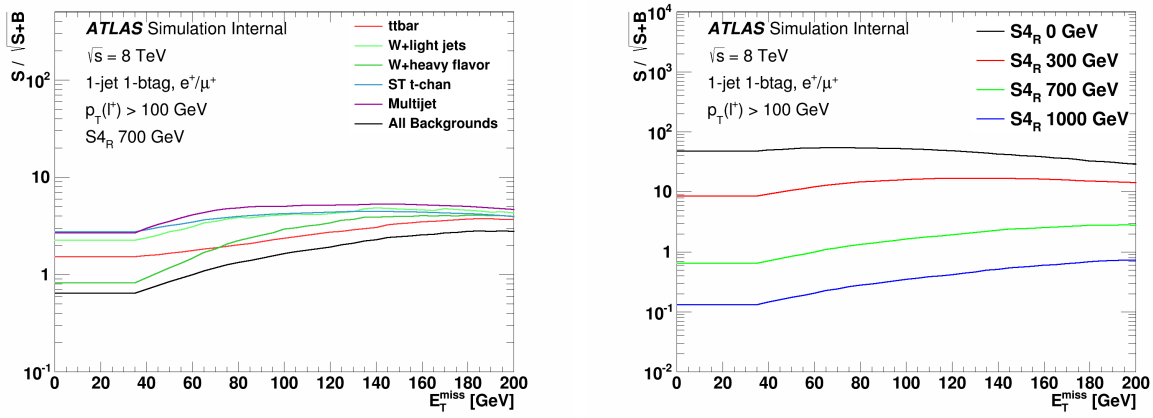

(a) (b)

Figure 7.15: (a) The CSS calculated with the 700 GeV $S4_R$ signal sample as a function of a cut on E_T^{miss} with an implicit cut of $p_T(\ell^+) > 100$ GeV applied. The individual curves indicate what backgrounds were included in the calculation. The black curve corresponds to the case where all backgrounds are included. (b) The CSS as a function of a cut on E_T^{miss} with an implicit cut of $p_T(\ell^+) > 100$ GeV applied. The different curves correspond to various values of the v_{met} particle's mass. Each curve is calculated with all backgrounds included.

Figure 7.16 shows the same CSS calculations after having applied the $p_{\mathrm{T}}(\ell^{+}) > 100$ GeV and $E_{\mathrm{T}}^{\mathrm{miss}} > 100$ GeV cuts. Figure 7.16(a) shows that any harsher cut on $p_{\mathrm{T}}(\ell^{+})$ only serves to lower the CSS while Figure 7.16(b) shows that increasing the $E_{\mathrm{T}}^{\mathrm{miss}}$ cut only slightly increases the CSS.

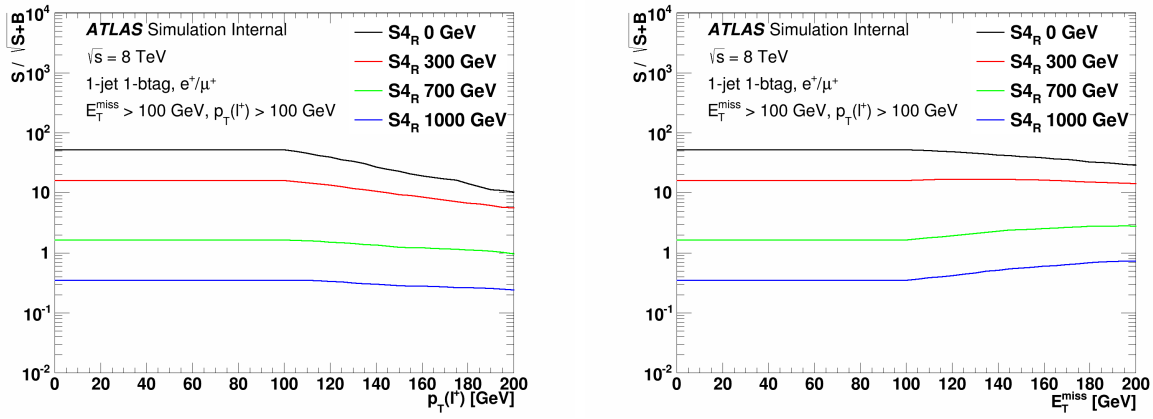

(a) (b)

Figure 7.16: (a) The CSS as a function of a cut on $p_{\mathrm{T}}(\ell^{+})$ with an implicit cut of $p_{\mathrm{T}}(\ell^{+}) > 100$ GeV and $E_{\mathrm{T}}^{\mathrm{miss}} > 100$ GeV for various values of the v_{met} particle's mass. (b) The CSS as a function of a cut on $E_{\mathrm{T}}^{\mathrm{miss}}$ with an implicit cut of $p_{\mathrm{T}}(\ell^{+}) > 100$ GeV and $E_{\mathrm{T}}^{\mathrm{miss}} > 100$ GeV for various values of the v_{met} particle's mass.

7.6.3 Event yields

The event yields for the various signal models as well as the SM backgrounds for the BDT selection region are shown in Table 7.11. As the table shows, $t\bar{t}$ and W+jets dominate the backgrounds in this region with small but non-negligible contributions coming from the single-top t- and Wt-channels.

BDT Selection		
Sample	**Electron**	**Muon**
$S4_R$ 0 [GeV]	$1511.3 \pm 104.4\ ^{+123.2}_{-143.7}$	$1599.0 \pm 110.0\ ^{+221.8}_{-180.9}$
$S4_R$ 25 [GeV]	$6849.0 \pm 469.4\ ^{+704.5}_{-703.5}$	$8654.5 \pm 540.1\ ^{+876.9}_{-734.4}$
$S4_R$ 50 [GeV]	$2700.1 \pm 153.1\ ^{+262.6}_{-254.4}$	$2991.7 \pm 165.0\ ^{+295.0}_{-230.7}$
$S4_R$ 75 [GeV]	$1717.4 \pm 87.8\ ^{+131.9}_{-166.9}$	$1866.8 \pm 94.6\ ^{+183.7}_{-153.3}$
$S4_R$ 100 [GeV]	$1344.8 \pm 62.1\ ^{+109.5}_{-133.0}$	$1407.1 \pm 64.7\ ^{+115.5}_{-130.0}$
$S4_R$ 125 [GeV]	$968.6 \pm 42.9\ ^{+72.8}_{-77.1}$	$1178.4 \pm 48.7\ ^{+100.9}_{-103.8}$
$S4_R$ 150 [GeV]	$824.5 \pm 33.8\ ^{+61.6}_{-66.1}$	$832.0 \pm 34.2\ ^{+67.8}_{-60.5}$
$S4_R$ 200 [GeV]	$533.8 \pm 19.8\ ^{+43.5}_{-41.3}$	$606.3 \pm 21.3\ ^{+47.5}_{-44.4}$
$S4_R$ 250 [GeV]	$364.0 \pm 12.3\ ^{+29.0}_{-30.0}$	$379.2 \pm 12.9\ ^{+36.5}_{-26.3}$
$S4_R$ 300 [GeV]	$244.0 \pm 7.8\ ^{+18.2}_{-20.1}$	$251.4 \pm 8.1\ ^{+23.5}_{-24.0}$
$S4_R$ 400 [GeV]	$115.8 \pm 3.4\ ^{+8.5}_{-9.8}$	$124.5 \pm 3.7\ ^{+10.1}_{-10.9}$
$S4_R$ 500 [GeV]	$59.6 \pm 1.7\ ^{+4.4}_{-5.1}$	$63.5 \pm 1.8\ ^{+5.5}_{-4.6}$
$S4_R$ 600 [GeV]	$31.8 \pm 0.9\ ^{+2.5}_{-2.3}$	$33.9 \pm 0.9\ ^{+3.0}_{-3.0}$
$S4_R$ 700 [GeV]	$17.3 \pm 0.5\ ^{+1.5}_{-1.5}$	$18.6 \pm 0.5\ ^{+1.7}_{-1.6}$
$S4_R$ 800 [GeV]	$9.6 \pm 0.3\ ^{+0.7}_{-0.8}$	$11.1 \pm 0.3\ ^{+0.9}_{-0.9}$
$S4_R$ 900 [GeV]	$5.7 \pm 0.2\ ^{+0.4}_{-0.4}$	$6.5 \pm 0.2\ ^{+0.6}_{-0.5}$
$S4_R$ 1000 [GeV]	$3.5 \pm 0.1\ ^{+0.3}_{-0.3}$	$3.9 \pm 0.1\ ^{+0.4}_{-0.3}$
$t\bar{t}$	$95.7 \pm 5.3\ ^{+28.8}_{-27.4}$	$99.8 \pm 5.4\ ^{+24.4}_{-22.9}$
Single-top s-channel	$1.2 \pm 0.2\ ^{+0.5}_{-0.5}$	$1.1 \pm 0.2\ ^{+0.2}_{-0.2}$
Single-top t-channel	$19.3 \pm 1.4\ ^{+4.5}_{-4.4}$	$17.3 \pm 1.4\ ^{+4.4}_{-4.4}$
Single-top Wt-channel	$22.1 \pm 3.8\ ^{+10.8}_{-11.3}$	$20.2 \pm 3.6\ ^{+11.9}_{-11.8}$
W+light jets	$26.1 \pm 7.2\ ^{+14.6}_{-14.8}$	$14.5 \pm 5.0\ ^{+10.9}_{-9.4}$
W+heavy flavor	$52.3 \pm 8.6\ ^{+30.4}_{-29.6}$	$60.0 \pm 8.9\ ^{+38.8}_{-38.5}$
Diboson	$1.5 \pm 0.5\ ^{+0.8}_{-0.4}$	$2.7 \pm 0.8\ ^{+1.0}_{-0.8}$
Multijet	$8.1 \pm 2.6\ ^{+9.7}_{-9.7}$	$0.0 \pm 0.4 \pm 0.0$
Total Background	$226.2 \pm 13.7\ ^{+46.9}_{-45.7}$	$215.6 \pm 12.7\ ^{+48.8}_{-47.5}$
Data	216	258

Table 7.11: Number of expected background and $S4_R$ signal events in the BDT selection region, for the electron and muon channels separately. The absolute statistical and systematic uncertainties are shown.

7.6.4 Kinematic distributions

Kinematic distributions for $m_T(\ell^+, E_T^{miss})$ and $\Delta R(\ell^+, b)$ are shown in Figure 7.17 for the BDT selection region. More BDT selection region plots are shown in Appendix C. The

bi-modal nature of the the plots showing the $m_{\mathrm{T}}(\ell^+, E_{\mathrm{T}}^{\mathrm{miss}})$ is an interesting consequence of the chosen cuts. The peak at $m_{\mathrm{T}}(\ell^+, E_{\mathrm{T}}^{\mathrm{miss}})$ values below the W mass of 100 GeV is enriched in single-top and W+jets events. These types of events, which have a lepton and a single neutrino from the W decay have a maximum value of $m_{\mathrm{T}}(\ell^+, E_{\mathrm{T}}^{\mathrm{miss}})$ at the W mass (see Section 7.3.1). The second peak around 225 GeV is enriched in $t\bar{t}$ events. In these types of events both top quarks can decay leptonically and the vector sum of the two neutrinos allows for the $m_{\mathrm{T}}(\ell^+, E_{\mathrm{T}}^{\mathrm{miss}})$ to reach values beyond the W mass.

7.7 Summary

The SR1 and SR2 signal regions define the event selections for the cut-based approach to the search for monotop events and the BDT selection region defines the event selection used for the BDT analysis. Chapter 11 will describe the process of training a BDT and later chapters will describe how the two different analysis strategies were implemented and the methodologies used to place limits on monotop production for the different models.

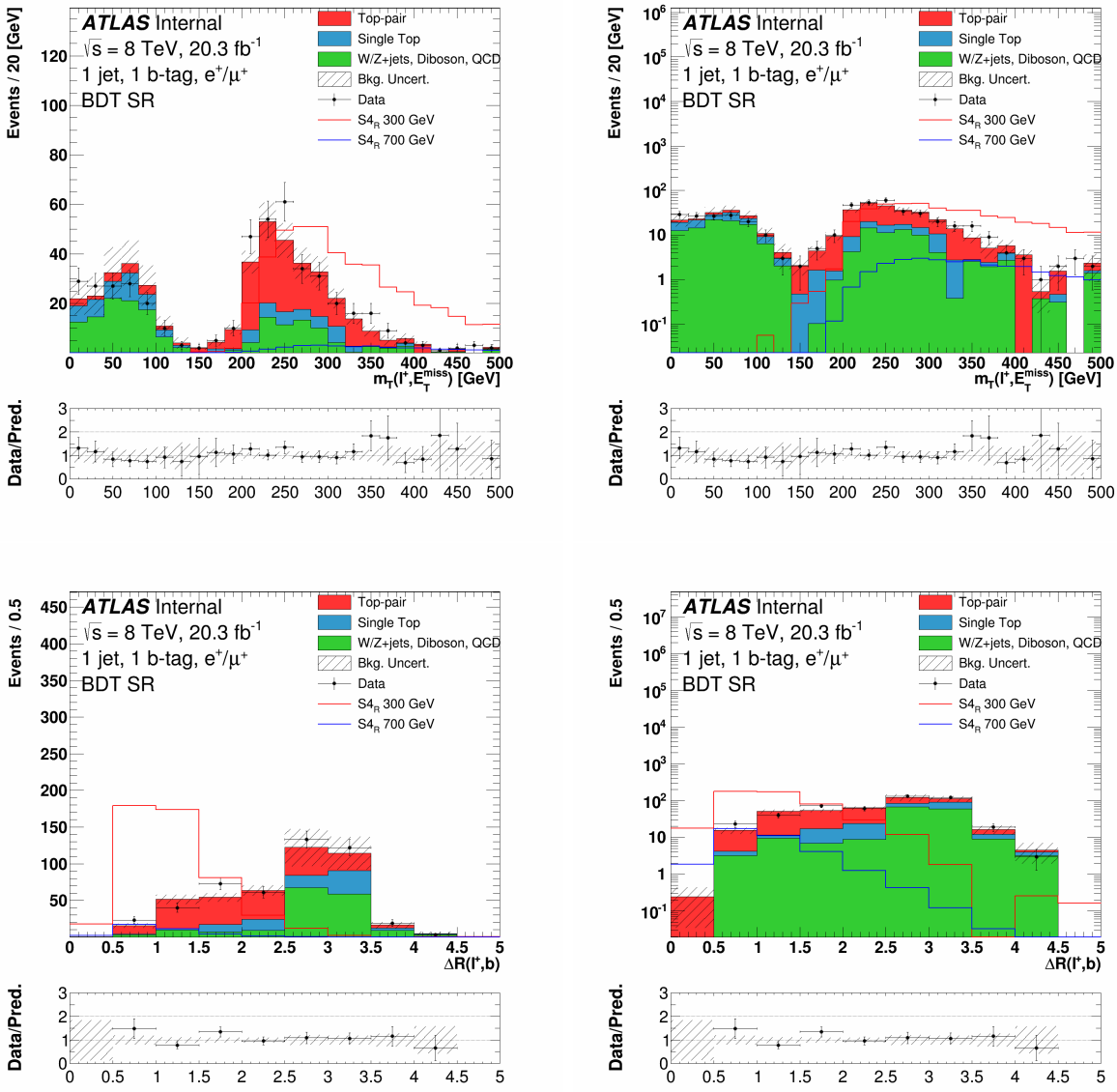

Figure 7.17: Distributions of $m_{\mathrm{T}}(\ell^{+}, E_{\mathrm{T}}^{\mathrm{miss}})$ (top) and $\Delta\mathrm{R}(\ell^{+}, b)$ (bottom) in the optimized BDT selection region in the combined electron/muon channel, in linear (left) and log (right) scale. The uncertainty band on the expected background corresponds to the errors due to the statistical uncertainties added in quadrature with the cross-section and normalization uncertainties.

Chapter 8

Systematic Uncertainties

As with any calculation or measurement, uncertainties need to be quantified. Uncertainties can be broadly categorized into those which affect the overall normalization of the signal and background simulations and those affecting the shapes of the kinematic distributions. This chapter describes the sources of systematic uncertainties used in this dissertation, how they are calculated, and their overall effects on simulated signal and background samples.

8.1 Normalization uncertainties

These are the uncertainties which affect the overall normalization of the samples:

- **Integrated luminosity** – The uncertainty on the total integrated luminosity calculation is 1.9% and is determined in [22]. This normalization uncertainty affects both signal and background measurements.

- **Cross-sections** – Monte Carlo simulations for both signal and background are normalized to their respective cross-sections. The uncertainties on the theoretical cross-section calculations for the top quark samples are functions of the scale PDF+α_S uncertainties added in quadrature and use a top quark mass of 172.5 GeV. They are +5.3/-5.7% for $t\bar{t}$, ±6.8% for the Wt-channel, ±3.9% for the s-channel, and +3.9/-2.2% for the t-channel. For the diboson and W+light jets samples the Berends-Giele scaling is used to

calculate the cross-section uncertainty [97]. In this method the inclusive cross-section uncertainty is 4% for diboson and 5% for W+light jets and an additional 24% is added in quadrature for each selected jet. For a 1-jet selection the Berends-Giele scaling corresponds to a 24.3% uncertainty on the diboson cross-section and a 24.5% uncertainty on the W+light jets cross-section. For W+heavy flavor jets the uncertainty is 50%.

- **Multijet normalization** – The multijets background is estimated from data by utilizing the matrix method as described in Section 6.3.5.1. The associated systematic uncertainties are estimated by propagating the uncertainties on the real and fake efficiencies to the event weights. Six independent sources of systematic uncertainties have been considered, three for each of the two lepton flavors, and take into account the contamination of real leptons in the control regions for fake leptons as well as the uncertainties arising from using alternate methods for the efficiency calculations. For electrons, the sources of systematic uncertainties are:

  ♢ Monte Carlo estimation of real electrons in the fake electron control region (electron fake MC): The total MC-estimated yield for the contamination of real electrons in the control region used to estimate the fake efficiencies was shifted up and down by 10%.

  ♢ Estimation of fake electron efficiencies using an alternate method (electron fake alternate): The fake efficiencies were measured in a different control region defined by a different set of cuts on $E_{\mathrm{T}}^{\mathrm{miss}}$ and $m_{\mathrm{T}}(\ell, E_{\mathrm{T}}^{\mathrm{miss}})$.

  ♢ Estimation of real electron efficiencies using an alternate method (electron real alternate): The real efficiencies were measured with an alternative sample consisting of e+jets with high $E_{\mathrm{T}}^{\mathrm{miss}}$.

For muons, the sources of systematic uncertainties are:

- ♢ Monte Carlo estimation of real muons in the fake muon control region (muon fake MC): The total MC-estimated yield for the contamination of real muons in the control region used to estimate the fake efficiencies is shifted up and down by 10%.
- ♢ Estimation of fake muon efficiencies using an alternate method (muon fake alternate): The fake efficiencies were measured in a different control region of a μ+jets sample with low $m_{\mathrm{T}}(\ell, E_{\mathrm{T}}^{\mathrm{miss}})$ and low $m_{\mathrm{T}}(\ell, E_{\mathrm{T}}^{\mathrm{miss}}) + E_{\mathrm{T}}^{\mathrm{miss}}$.
- ♢ Estimation of real muon efficiencies using an alternate method (muon real alternate): The real efficiencies were measured with an alternative sample consisting of high $m_{\mathrm{T}}(\ell, E_{\mathrm{T}}^{\mathrm{miss}})$ events.

- **Statistical uncertainties** – The uncertainty due to the limited size of the MC samples is included. These uncertainties are calculated by adding the individual event weights in quadrature within each bin and for each source. For processes with non-zero expected events this effect can be as large as 100%. For processes with 0 expected events, a 68% CL upper limit is computed (see Section 9.7.2).

8.2 Shape uncertainties

In the following sections the shape uncertainties are described for various objects in the analysis.

8.2.1 Electrons

The uncertainties for electrons are described below:

- **Electron trigger, reconstruction, identification, and isolation efficiencies** – The uncertainties in the electron efficiency measurements were determined by varying the electron selections used in each efficiency calculation. These uncertainties were evaluated by the ATLAS e/γ combined performance group [13].

- **Electron energy scale and resolution** – The impact of the uncertainties in electron energy scale and of the electron energy resolution are evaluated by scaling or smearing the transverse momentum of the electron by $\pm 1\sigma$ and re-applying the object and event selections to the simulation samples. Also included in the uncertainty measurements are the statistical uncertainties in the samples used in the calculations.

8.2.2 Muons

The uncertainties for muons are described below:

- **Muon trigger, reconstruction, identification, and isolation efficiencies** – The uncertainties in the muon efficiency measurements were determined by varying the muon selections entering into each calculation and by modifying the background estimation method. These uncertainties were evaluated by the ATLAS muon combined performance group [36].

- **Muon momentum scale and resolution** – The impact of the uncertainties in muon momentum scale and of the muon momentum resolution are evaluated by scaling or smearing the transverse momentum of the muon by $\pm 1\sigma$ and re-applying the object

and event selections to the simulation samples. Also included in the uncertainty measurements are the statistical uncertainties in the samples used in the calculations.

8.2.3 Jets

The uncertainties for jets are described below:

- **Jet reconstruction efficiency** – The uncertainty on the jet reconstruction efficiency is evaluated by randomly dropping jets from fully simulated MC events and determining the induced production rate variations.

- **Jet energy scale** – The jet energy scale uncertainty is a measure of how well-understood the calorimeter's response is to a particle of known energy, depends on the transverse momentum and pseudorapidity of the reconstructed jets, and includes the uncertainty on the b-tagged jet energy scale. This uncertainty is evaluated by re-scaling the energy of each simulated jet by $\pm 1\sigma$ and then re-applying the object and event selections.

- **Jet energy resolution** – The jet energy resolution uncertainty is a measure of how precisely the energy of a jet can be measured and is extracted by smearing the energy of the jets by $\pm 1\sigma$ and then re-applying object and event selection to the simulation samples.

- **Jet vertex fraction efficiency** – The uncertainty associated with the efficiency of the cut on the jet vertex fraction is estimated by smearing the associated weights by $\pm 1\sigma$.

- ***b*-tagging** – The uncertainties associated with the efficiency scale factors for b-quark, c-quark, and light quark jet-tagging are evaluated by shifting each scale factor associated with each efficiency by $\pm 1\sigma$ and re-applying object and event selections. This yields three uncertainties: b-tagging uncertainty, c-tagging uncertainty, and mis-tagging uncertainty.

8.2.4 Missing transverse energy

The uncertainties associated with the $E_{\mathrm{T}}^{\mathrm{miss}}$ calculation are described below:

- **Effects of lepton and jet objects** – The lepton and jet energy scale and resolution uncertainties are propagated to the $E_{\mathrm{T}}^{\mathrm{miss}}$ calculation through a re-calculation of the $E_{\mathrm{T}}^{\mathrm{miss}}$ using the smeared or scaled values of the leptons and jets. The impact of the lepton and jets measurements on the $E_{\mathrm{T}}^{\mathrm{miss}}$ calculation are then evaluated by re-applying event selections after their scale and resolutions are varied by $\pm 1\sigma$.

- **Soft cell scale and resolution** – The effects of the energy scale and resolution uncertainties on the soft jet terms entering into the $E_{\mathrm{T}}^{\mathrm{miss}}$ calculation are estimated by varying the scales and resolutions by $\pm 1\sigma$ and then re-applying object and event selections to the simulated samples.

8.2.5 Generator uncertainties

The uncertainties in the simulations associated with the choice of event modeling and parton showering generators are described below:

- ***$t\bar{t}$* generator** – The dependence of the predicted $t\bar{t}$ yield on the MC event generator is estimated by comparing the nominal Powheg+Pythia sample to three alternative

samples; one generated with POWHEG+HERWIG, one with MC@NLO+HERWIG, and one with ALPGEN+HERWIG. For each alternative sample the differences in acceptance with the nominal sample is taken as the up and down variation of the yields. The largest relative difference arising from the comparison of the nominal POWHEG+PYTHIA with the ALPGEN+HERWIG sample is taken as the up and down uncertainty.

- ***s*-, *Wt*-, and *t*-channel generators** – The uncertainties on the choice of MC generators used to generate single-top s- and Wt-channel events are estimated by comparing the differences in acceptance between the nominal POWHEG+PYTHIA and alternative MC@NLO+HERWIG samples. The modeling uncertainties associated with the single-top t-channel generator is estimated by comparing the difference in acceptance between the nominal ACERMC+PYTHIA sample and an alternative aMC@NLO+HERWIG sample. For each process, the difference in acceptance between the nominal and alternate sample is taken as the $\pm 1\sigma$ generator uncertainty.

- ***Wt*-channel NLO calculation scheme** – For the Wt-channel the systematic uncertainty associated with the choice of NLO calculation schemes, namely the so-called diagram-removal (DR) and diagram-subtraction (DS) schemes, is calculated. At NLO, real and virtual corrections to the LO Wt-channel diagrams also contribute to $t\bar{t}$ production. Thus at NLO the cross-section of the Wt-channel is contaminated by diagrams giving a $t\bar{t}$ final state. In the DR scheme, diagrams common to Wt and $t\bar{t}$ are removed from the NLO calculation; namely those with two on-shell top quarks. This scheme removes the interference between the Wt and $t\bar{t}$ diagrams but is not gauge invariant. In the DS scheme the effect of these diagrams are calculated but are parameterized and subtracted in the NLO calculation. The degree to which these two schemes differ

in the generation of Wt-channel events is a measure of the uncertainty of Wt-channel production.

- **Initial and final state radiation** – The dependence on the ISR/FSR model for the $t\bar{t}$ sample is determined from a set of dedicated AcerMC+Pythia samples generated by varying the Pythia ISR and FSR parameters. For each process, two MC samples were created with enhanced and diminished showering. The difference in acceptance between the two samples was halved, symmetrized, and taken as the $\pm 1\sigma$ uncertainty.

8.3 Total relative uncertainties

The relative uncertainties for each of the systematics are detailed in Tables 8.1, 8.2, 8.3, for the SR1, SR2, and BDT selection regions respectively. The relative uncertainties are listed for the total background and for a representative mass point for the signal and are listed separately for the electron and muon channels. Detailed tables for individual backgrounds and signal mass points are listed in Appendix F.

Table 8.4 lists the three largest systematic uncertainties in each of the selection regions for signal and background listed separately for the electron and muon channels. The backgrounds are dominated by cross-section, $t\bar{t}$ modelling, and jet energy scale uncertainties while the signal is dominated by b-tagging, jet energy scale/resolution, and lepton energy/momentum scale uncertainties.

SR1 Selection Region				
	Backgrounds		**S1$_R$ 100 GeV**	
	Electron	**Muon**	**Electron**	**Muon**
Luminosity	± 1.9	± 1.9	± 1.9	± 1.9
Cross-section	**+10.0/–10.4**	**+11.3/–11.7**	-	-
Generator			-	-
$t\bar{t}$	**± 9.5**	**± 14.4**	-	-
$t\bar{t}$ ISR/FSR	± 6.9	± 4.3	-	-
Wt-chan	± 5.1	± 2.0	-	-
Wt-chan NLO calc	± 0.9	± 6.5	-	-
Matrix Method				
Fake alternate	-	± 0.3	-	-
Fake MC	-	-	-	-
Real alternate	-	± 0.3	-	-
Jets				
Energy resolution	± 3.8	± 4.0	± 1.4	**± 2.5**
Energy scale	**+10.1/–4.9**	**+9.7/–4.4**	+0.8/–1.5	+0.9/–1.7
Reconstruction	-	± 0.6	-	± 0.9
Vertex fraction	+1.6/–4.4	+2.5/–4.9	**+0.8/–2.4**	**+4.6/–2.2**
b-tag	± 4.6	± 4.4	**± 3.4**	**± 3.5**
$c\tau$-tag	± 0.8	± 0.9	-	-
mis-tag	± 0.9	± 0.8	-	-
$\boldsymbol{E}_{\mathbf{T}}^{\mathbf{miss}}$				
Resolution	± 2.0	–1.8/+1.3	+0.0/–0.6	+0.5/–0.2
Scale	+0.9/+1.1	–0.3/–0.6	–0.7/+0.2	+0.5/+0.2
Leptons				
Identification	-	+0.2/–1.4	-	± 0.6
Energy/Momentum resolution	+4.5/+0.5	–0.4/–1.9	–1.1/–0.6	+0.2/+0.3
Energy/Momentum scale	+3.7/–2.1	–0.5/–2.2	**+1.9/–2.2**	+0.7/+0.1
Reconstruction	± 0.5	± 0.4	± 0.4	± 0.4
Isolation	± 2.6	± 0.5	± 2.6	±5
Trigger	± 0.6	+1.8/-0.0	± 0.6	+1.8/–0.0
Total	+18.5/-16.9	+20.4/-20.4	+5.6/–6.2	+7.0/–5.6

Table 8.1: Relative systematic uncertainties in % for the total expected background yield and the S1$_R$ 100 GeV signal sample in the SR1 selection region. Dashed entries indicate that the systematic either does not apply or is less than 0.05%. The three largest uncertainties both for background and signal in each channel are in bold face.

SR2 Selection Region				
	Backgrounds		**S4$_{\mathrm{R}}$ 700 GeV**	
	Electron	**Muon**	**Electron**	**Muon**
Luminosity	± 1.9	± 1.9	± 1.9	± 1.9
Cross-section	**+10.2/–10.5**	**+13.0/–13.3**	-	-
Generator				
$t\bar{t}$	± 5.8	**± 11.2**	-	-
$t\bar{t}$ ISR/FSR	**± 11.8**	± 7.6	-	-
Wt-chan	± 4.9	± 5.5	-	-
Wt-chan NLO calc	± 3.8	± 5.8	-	-
Jets				
Energy resolution	± 6.5	± 6.2	**± 3.8**	± 2.1
Energy scale	**+11.1/–7.8**	+3.9/–8.1	**+4.1/–3.5**	**+5.0/–4.0**
Reconstruction	-	± 4.5	-	± 0.3
Vertex fraction	+3.0/–3.6	**+6.3/–8.0**	+1.4/–2.9	**+4.7/–2.6**
b-tag	± 4.8	± 4.5	**± 4.3**	**± 4.4**
$c\tau$-tag	± 0.7	± 0.7	-	-
mis-tag	± 0.5	± 1.4	-	± 0.1
$\boldsymbol{E}_{\mathbf{T}}^{\mathbf{miss}}$				
Resolution	+3.8/+0.8	–2.3/+1.1	+0.4/–0.1	± 0.3
Scale	–4.0/+0.5	–5.0/–2.7	+0.0/+0.2	± 0.2
Leptons				
Identification	-	–3.8/–4.5	-	+0.3/–0.1
Energy/Momentum resolution	–0.3/–1.0	–4.0/–0.3	+0.2/–0.6	± 0.1
Energy/Momentum scale	+7.6/–4.4	–4.6/–0.3	+1.1/–1.6	+0.5/–0.3
Reconstruction	± 0.5	± 0.4	± 0.4	± 0.4
Isolation	± 2.7	± 0.5	± 2.7	± 0.5
Trigger	± 0.7	+1.8/-0.0	± 0.6	+1.9/-0.0
Total	+21.1/-19.3	+22.4/-22.1	+8.0/–8.2	+8.8/–7.1

Table 8.2: Relative systematic uncertainties in % for the total expected background yield and the S4$_{\mathrm{R}}$ 700 GeV signal sample in the SR2 selection region. Dashed entries indicate that the systematic either does not apply or is less than 0.05%. The three largest uncertainties both for background and signal in each channel are in bold face.

BDT Selection Region				
	Backgrounds		**$S4_R$ 700 GeV**	
	Electron	**Muon**	**Electron**	**Muon**
Luminosity	± 1.9	± 1.9	± 1.9	± 1.9
Cross-section	**± 17.8**	**± 19.3**	-	-
Generator				
$t\bar{t}$	**± 9.5**	± 8.5	-	-
$t\bar{t}$ ISR/FSR	± 4.3	± 3.2	-	-
s-chan	± 0.2	-	-	-
t-chan	± 1.8	± 1.7	-	-
Wt-chan	± 4.4	± 4.9	-	-
Wt-chan NLO calc	± 1.3	± 1.2	-	-
Matrix Method				
Fake alternate	± 2.6	-	-	-
Fake MC	± 0.6	-	-	-
Real alternate	± 3.4	-	-	-
Jets				
Energy resolution	± 6.1	± 8.3	**± 3.9**	± 3.1
Energy scale	+4.2/–4.8	**+8.8/+3.1**	**+4.2/–3.3**	**+5.1/–5.0**
Reconstruction	-	± 3.4	-	± 0.6
Vertex fraction	± 2.6	+8.0/–1.2	+1.3/–2.9	**+3.7/–2.8**
b-tag	± 4.0	± 4.0	**± 4.6**	**± 4.7**
$c\tau$-tag	± 3.1	± 3.3	± 0.1	± 0.1
mis-tag	± 5.9	± 2.3	-	± 0.3
$\boldsymbol{E}_{\mathbf{T}}^{\mathbf{miss}}$				
Resolution	**+6.8/+4.8**	**+7.4/+10.1**	+0.1/–0.0	–0.8/–0.3
Scale	+2.3/–2.1	+2.9/+1.2	± 0.2	–0.0/–0.6
Leptons				
Identification	-	+4.0/–0.8	-	–0.2/–0.7
Energy/Momentum resolution	–1.8/–0.8	+3.1/–1.0	+0.4/–0.0	± 0.1
Energy/Momentum scale	+2.5/–5.6	+5.5/+2.3	+1.9/–1.7	–0.7/+0.1
Reconstruction	± 0.5	± 0.4	± 0.5	± 0.4
Isolation	± 2.5	± 0.5	± 2.7	± 0.5
Trigger	± 0.6	+1.8/-0.0	± 0.6	+1.9/–0.0
Total	+20.7/–20.2	+22.6/–22.0	+8.4/–8.4	+9.0/–8.4

Table 8.3: Relative systematic uncertainties in % for the total expected background yield and the $S4_R$ 700 GeV signal sample in the BDT selection region. Dashed entries indicate that the systematic either does not apply or is less than 0.05%. The three largest uncertainties both for background and signal in each channel are in bold face.

	SR1		SR2		BDT	
	Electron	**Muon**	**Electron**	**Muon**	**Electron**	**Muon**
Background	xsec	$t\bar{t}$ gen	$t\bar{t}$ ISR/FSR	xsec	xsec	xsec
	JES	xsec	JES	$t\bar{t}$ gen	$t\bar{t}$ gen	JES
	$t\bar{t}$ gen	JES	xsec	JVF	$E_{\mathrm{T}}^{\mathrm{miss}}$ res	$E_{\mathrm{T}}^{\mathrm{miss}}$ res
Signal	b-tag	b-tag	b-tag	JES	b-tag	JES
	JVF	JVF	JES	JVF	JES	b-tag
	ees	mums	JER	b-tag	JER	JVF

Table 8.4: The three largest systematic uncertainties in each of the signal regions for signal and background listed separately for the electron and muon channel. In this notation xsec is the cross-section uncertainty, JES is the jet energy scale uncertainty, JER is the jet energy resolution, JVF is the jet vertex fraction uncertainty, b-tag is the b-tagging uncertainty, $t\bar{t}$ gen is the $t\bar{t}$ generator uncertainty, $t\bar{t}$ ISR/FSR is the uncertainty on intial and final state radiation for the $t\bar{t}$ background, $E_{\mathrm{T}}^{\mathrm{miss}}$ res is the missing transverse energy resolution uncertainty, ees is the electron energy scale uncertainty, and mums is the muon momentum scale uncertainty.

Chapter 9

Limit Setting Analysis

This chapter describes the methodology used to evaluate the discovery limits in comparison to background for monotop events with large $E_{\mathrm{T}}^{\mathrm{miss}}$. The analysis uses a combination of both the electron and muon channels with all uncertainties included to calculate exclusion limits on the production cross-section times branching ratio for the various mass hypotheses in the monotop signal models. Both the published, cut-based results and the BDT re-analysis use the techniques described in this chapter.

9.1 Hypothesis testing

Hypothesis testing is performed using a hybrid Frequentist-Bayesian approach based on the CL_s procedure described in Section 9.4 and implemented in the Optimized Tool for Hybrid Limits Computation package (OpTHyLiC) [98, 99]. The test statistic, q, is the log-likelihood ratio (LLR). The Neyman-Pearson lemma states that when performing a hypothesis test between two simple hypotheses, the likelihood-ratio test is the most powerful. It is, however, more convenient to use its logarithm because the products in the likelihood become summations and the exponentials are converted into simple factors. Parameters which maximize the likelihood also maximize the log-likelihood. The LLR of the two hypotheses in this analysis

is given by

$$q = \text{LLR} = -2\ln\left(\frac{\mathcal{L}(\text{data}|H_1)}{\mathcal{L}(\text{data}|H_0)}\right). \tag{9.1}$$

H_1 corresponds to the test hypothesis which admits the presence of the monotop signal in addition to the SM backgrounds and H_0 is the null hypothesis which only admits the SM backgrounds. The expected number of events is

$$N^{\text{exp}}(\mu, \vec{\theta}) = \mu s(\vec{\theta}) + b(\vec{\theta}). \tag{9.2}$$

In Equation 9.2, s and b are the expected number of signal and background events and μ is the signal strength used to test the sensitivity of the search. Both the signal and background yields are functions of nuisance parameters, $\vec{\theta}$, which parameterize the effects of the statistical and systematic uncertainties. The null hypothesis corresponds to $\mu = 0$ resulting in $N^{\text{exp}} = b(\vec{\theta})$ while the test hypothesis corresponds to $N^{\text{exp}} = \mu s(\vec{\theta}) + b(\vec{\theta})$ where μ is allowed to vary. The full likelihood, including all nuisance parameters, is given by

$$\mathcal{L}(\mu, \vec{\eta}) = \prod_{c,l}\left[\frac{(\mu s_{cl} + b_{cl})^{N_{cl}}}{N_{cl}!}e^{-(\mu s_{cl}+b_{cl})}\right] f(s'_{cl}; s^{\text{nom}}_{cl}, \sigma_{cl}) \prod_i f(b'_{cil}; b^{\text{nom}}_{cil}, \sigma_{cil}) \prod_j \mathcal{G}(\eta_j). \tag{9.3}$$

In Equation 9.3 the following definitions are used:

- **Indices** – The index c runs over the number of channels. In this analysis there are two channels, one each for electrons and muons. The index i runs over the number of backgrounds. All of the SM backgrounds described in Chapter 6 are included. The index l runs over the number of bins in the discriminating distribution. In the case a BDT discriminant is used (as is described in Chapter 11), l runs over all 5 bins. In the case of the cut-based analysis there was only one bin. The index j runs over the different

nuisance parameters which correspond to the different systematic uncertainties listed in Chapter 8.

- **Yields** – The event yield actually observed in data in channel c and bin l is N_{cl}^{obs}. The nominal yields for the signal (for channel c and bin l) and background (for process i, channel c, and bin l) are s_{cl}^{nom} and b_{cil}^{nom} respectively. The variations of these nominal yields under the effect of systematic uncertainties are s_{cl} and b_{cl} for signal and background respectively. The event yield in channel c and bin l when varied by systematic uncertainties is $N_{cl} = \mu s_{cl} + \sum_i b_{cl}$.

- **Signal strength** – The signal strength, μ, is defined as the actual signal rate divided by the signal cross-section times branching ratio.

- **Nuisance parameters** – The set of nuisance parameters, $\vec{\theta}$, can be divided into two subsets. Those in the first subset, $\{s'_{cl}, b'_{cil}\}$, account for the statistical uncertainties due to the finite size of the samples used to estimate the signal and background yields and are constrained by the functions $f(s'_{cl}; s_{cl}^{\text{nom}}, \sigma_{cl})$ and $f(b'_{cil}; b_{cil}^{\text{nom}}, \sigma_{cil})$. The "prime" in this notation merely serves to show the distinction between the nuisance parameters associated with the statistical uncertainties of the signal and backgrounds and the actual yields themselves. Those in the second subset, $\{\eta_j\}$, account for the systematic uncertainties and are constrained by the Gaussian function, $\mathcal{G}(\eta_j)$.

- **Statistical uncertainties** – The absolute statistical uncertainty for the signal process in channel c and bin l is σ_{cl}. The absolute statistical uncertainty for background process i in channel c and bin l is σ_{cil}.

9.2 Treatment of statistical uncertainties

The nuisance parameters s'_{cl} and b'_{cil} account for the statistical uncertainties in the nominal signal and background samples and are constrained by a probability density function (PDF). The PDF used in this analysis is the normal distribution which has the form

$$f_{\text{norm}}(y; y^{\text{nom}}, \sigma) = \frac{1}{\sigma\sqrt{2\pi}} \exp\left(-\frac{(y - y^{\text{nom}})^2}{2\sigma^2}\right). \tag{9.4}$$

In Equation 9.4, y is the nuisance parameter (s'_{cl} or b'_{cil}), y^{nom} is the unvaried yield (s^{nom}_{cl} or b^{nom}_{cil}), and σ is the statistical uncertainty which is the square root of the sum of the squared weights in the l^{th} bin of either the signal sample or the i^{th} background sample (σ_{cl} or σ_{cil}).

9.3 Treatment of systematic uncertainties

The systematic uncertainties on the nominal yields are taken into account by including the subset of nuisance parameters, $\{\eta_j\}$, all of which are assumed to be 100% uncorrelated. The total number of nuisance parameters is equal to the total number of systematic uncertainties, including all channels, backgrounds, and signals. The term constraining the nuisance parameters in the likelihood function, Equation 9.3, can be factorized into the product of individual constraint terms. The nuisance parameter for each systematic uncertainty is constrained by a standard normal PDF, $\mathcal{G}$, of the form

$$\mathcal{G}(\eta_j) = \frac{1}{\sqrt{2\pi}} \exp^{-\frac{\eta_j^2}{2}}. \tag{9.5}$$

The effect of the systematic uncertainties on the background and signal yields is described

by the relations of the form

$$y = y^{\text{nom}} \times k^{\text{syst}}(\{\eta_j\}), \tag{9.6}$$

where k^{syst} is the function describing the variation of the yield. These functions are related to the yields and nuisance parameters by

$$s_{cl} = s_{cl}^{\text{nom}} \times k_{cl}^{\text{syst}}(\{\eta_j\}) \tag{9.7a}$$

$$b_{cl} = \sum_i b_{cil} = \sum_i b_{cil}^{\text{nom}} \times k_{cil}^{\text{syst}}(\{\eta_j\}) \tag{9.7b}$$

An additive method is used to combine the effect of multiple nuisance parameters such that

$$k^{\text{syst}}(\{\eta_j\}) - 1 = \sum_j \left[h_j^{\text{syst}}(\eta_j) - 1 \right]. \tag{9.8}$$

For each systematic uncertainty, j, the corresponding nuisance parameter, η_j is chosen such that $\eta_j = 0$ corresponds to no variation, $\eta_j = +1$ corresponds to a $+1\sigma$ variation, and $\eta_j = -1$ corresponds to a -1σ variation. The values of h^{syst} for $\eta_j = 0$, $+1$, and -1 are shown below

$$h^{\text{syst}}(\eta_j = 0) = 1 \tag{9.9a}$$

$$h^{\text{syst}}(\eta_j = +1) = h_j^{\uparrow} + 1 \tag{9.9b}$$

$$h^{\text{syst}}(\eta_j = -1) = h_j^{\downarrow} + 1. \tag{9.9c}$$

The terms $h_j^{\uparrow}$ and $h_j^{\downarrow}$ are the relative variations of the yield when systematic j is varied by $+1\sigma$ and -1σ respectively. The functions $h^{\text{syst}}(\eta_j)$ need to be continuous and able to interpolate for $\eta_j \in [-1, +1]$ and extrapolate for $\eta_j > +1$ and $\eta_j < -1$ such that

Equations 9.9 are satisfied. There are various choices for the function $h_j^{\text{syst}}(\eta_j)$ and the same interpolation and extrapolation scheme used in the McLimit software package is used in this analysis [100]. The McLimit interpolation is defined as

$$h^{\text{syst}}(\eta_j) = \begin{cases} 1 + B & \text{if } B \geq 0 \quad (9.10a) \\ e^B & \text{if } B < 0 \quad (9.10b) \end{cases}$$

where

$$B = \begin{cases} \eta_j h_j^{\uparrow} (1 - R) + RQ & \text{if } \eta_j > 0 \quad (9.11a) \\ -\eta_j h_j^{\downarrow} (1 - R) + RQ & \text{if } \eta_j < 0 \quad (9.11b) \end{cases}$$

and

$$Q = \eta_j \frac{h_j^{\uparrow} - h_j^{\downarrow}}{2} + \eta_j^2 \frac{h_j^{\uparrow} + h_j^{\downarrow}}{2} \qquad \text{and} \qquad R = \frac{1}{1 + 3\left|\eta_j\right|}. \quad (9.12)$$

9.4 Determination of observed upper limits

The observed upper limit on the signal strength, μ_{up}, is determined from the CL_s method using the test statistic q_μ such that

$$q_\mu = -2 \ln \frac{\mathcal{L}(\mu)}{\mathcal{L}(\mu = 0)}. \quad (9.13)$$

The test statistic is computed using the nominal likelihood

$$\mathcal{L}(\mu) = \mathcal{L}(\mu, \{s'_{cl}\} = \{s_{cl}^{\text{nom}}\}, \{b'_{cil}\} = \{b_{cil}^{\text{nom}}\}, \{\eta_j\}), \quad (9.14)$$

and by using the log-likelihood, reduces to the form

$$q_\mu = \sum_{c,l} q_\mu^{cl}. \tag{9.15}$$

For channel c and bin l the test statistic is given by

$$q_\mu^{cl} = 2\left[\mu s_{cl}^{\text{nom}} - N_{cl}\ln\left(\frac{\mu s_{cl}^{\text{nom}} + b_{cl}^{\text{nom}}}{b_{cl}^{\text{nom}}}\right)\right]. \tag{9.16}$$

The distributions of q_μ under the signal plus background and background-only hypotheses are determined by generating numerous pseudo-experiments from the marginal likelihood where the effects of the nuisance parameters are integrated away

$$\mathcal{L}_{\text{marg}}(\mu) = \int \mathcal{L}(\mu, \{s'_{cl}, b'_{cil}, \eta_j\}) \prod_j \mathrm{d}\eta_j \prod_{c,l} \mathrm{d}s'_{cl} \prod_i \mathrm{d}b'_{cil}. \tag{9.17}$$

This is done by generating nuisance parameter values from their constraint PDFs and then generating values of N_{cl} using those nuisance parameter values. The observed value of the test statistic, q_μ^{obs} is given by

$$q_\mu^{\text{obs}} = q_\mu(\{N_{cl}\} = \{N_{cl}^{\text{obs}}\}). \tag{9.18}$$

The p-value of the signal plus background hypothesis is defined as the probability, $\mathcal{P}$, to find a value of q_μ greater than or equal to q_μ^{obs} such that

$$p_{s+b} = \mathcal{P}\Big(q_\mu \geq q_\mu^{\text{obs}} | \mu s + b\Big) \tag{9.19}$$

Similarly, the p-value of the background-only hypothesis is the probability of finding a value of q_μ less than or equal to q_μ^{obs} such that

$$p_b = \mathcal{P}\Big(q_\mu \leq q_\mu^{\text{obs}} | b\Big) \,. \tag{9.20}$$

The CL_s is computed according to

$$\text{CL}_s(\mu) = \frac{p_{s+b}}{1 - p_b} \leq \alpha, \tag{9.21}$$

where α corresponds to a stated confidence level (CL). The upper limit is found by searching for a value of μ such that Equation 9.21 is equal to 0.05 which corresponds to a $1 - \alpha = 95\%$ CL. Signal cross-sections times branching ratios corresponding to signal strengths, μ, for which $\text{CL}_s < 0.05$ are considered excluded at the 95% CL. If the experimental sensitivity to a given value of μ is very low, then as the numerator in Equation 9.21 decreases so does the denominator and the equation cannot be satisfied. In this way the exclusion of parameters of the model in cases of low sensitivity is suppressed. A diagram representing the different values in Equation 9.21 is shown in Figure 9.1.

9.5 Determination of expected upper limits

The expected limits on the signal strength under the background-only hypothesis are also calculated. Five different values are calculated in this analysis: the median, $\pm 1\sigma$, and $\pm 2\sigma$ quantiles which are defined using the standard normal distribution. The quantiles, Z, and their corresponding probabilities, p, are related by the cumulative distribution function of

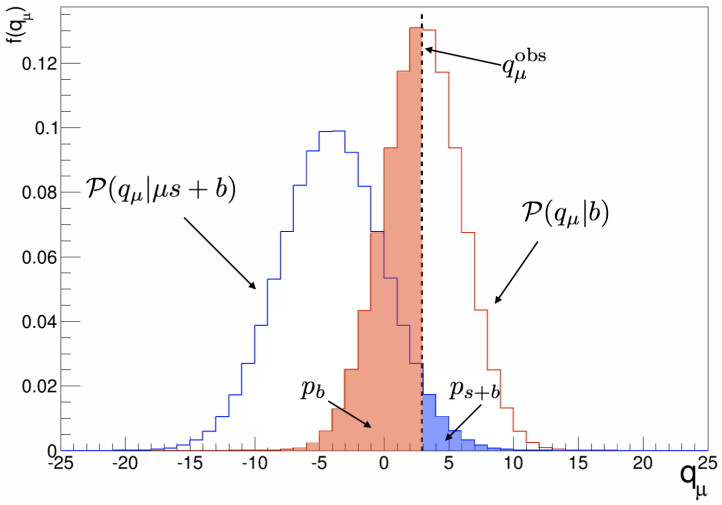

Figure 9.1: A representative plot showing the probability distribution functions of the test statistic, q_μ, under the background-only hypothesis (red) and the signal plus background hypothesis (blue). The blue and red shaded regions correspond to Equations 9.19 and 9.20 respectively. The value of μ is chosen such that Equation 9.21 is satisfied. The values in this plot are meant to illustrate the CL_s procedure and are not indicative of real values.

the standard normal distributions, Φ, as

$$Z = \Phi^{-1}(p). \tag{9.22}$$

The values of these quantiles are shown in Table 9.1.

Z	-2	-1	median	+1	+2
p	0.0228	0.1587	0.5	0.8413	0.9772

Table 9.1: The probability values for the median, $\pm1\sigma$, and $\pm2\sigma$ quantiles of the standard normal distribution.

The expected limits are calculated in the same way as the observed limits were in Section 9.4, replacing q_μ^{obs} with q_μ^{exp}. The value of q_μ^{exp} is chosen from the distribution of q_μ under the background-only hypothesis (red curve in Figure 9.1) which corresponds to the quantiles in Table 9.1 of that distribution. The upper limits on the signal strength for each quantile are then found by searching for values of μ such that Equation 9.21 is equal to 0.05.

9.6 Limit setting

The upper limits on the observed signal strength and on the expected signal strength are calculated independently for each signal sample corresponding to the different mass hypotheses in each model.

9.7 Assumptions

Two assumptions were made concerning systematic uncertainties which have variations of the nominal yields larger than 100% and processes which have zero expected events.

9.7.1 Systematic uncertainties larger than 100%

In some regions of selected phase space the expected number of events for various background processes can be quite small. Variations of these yields when subjected to systematic uncertainties can then be larger than 100%. Such large variations can be induced by large statistical fluctuations which are already taken into account by the limit setting procedure. These large variations can cause instabilities in the limit setting procedure if not handled correctly. In such cases the variations are taken to be exactly 100%.

Region	**Channel**	**Process**	**Systematic**	**Nom. Yield ± stat**	**Var. Yield ± stat**	**Relative Variation**
SR1	electron	Diboson	$E_{\mathrm{T}}^{\mathrm{miss}}$ res.	0.3±0.2	0.7±0.5	133%
SR1	muon	W+light	$E_{\mathrm{T}}^{\mathrm{miss}}$ res.	2.0±1.6	4.3±2.8	114%
SR2	muon	W+light	JVF	2.7±2.7	5.7±4.1	113%

Table 9.2: List of cases where a systematic causes a relative shift greater than 100%. The expected number of events for the nominal and under the effect of the systematic are given together with their statistical uncertainties.

9.7.2 Processes with zero expected events

The limit setting procedure uses a 68% upper CL in order to take into account fluctuations according to Poisson statistics. For MC generated background processes this upper limit is given by the formula for a Poisson distribution with zero expected events at a given CL as

$$b = -\ln(1 - \mathrm{CL})\,. \tag{9.23}$$

For a 68% CL this corresponds to $b = 1.14$ [101]. This upper limit, N_{UL}, is then scaled to the integrated luminosity with

$$N_{\mathrm{UL}} = b\frac{L\sigma}{N_{\mathrm{MC}}}, \tag{9.24}$$

where σ is the theoretical cross-section of the process and N_{MC} is the number of un-weighted simulated events prior to any selection. When a process is estimated with several MC samples, as is the case with W/Z+jets, the highest possible upper limit used. This procedure has been used for other analyses using ATLAS data with very small expected event yields [102]. The values of N_{UL} are shown in Appendix E.

For background samples not generated from MC, such as the multijet background, another approach is utilized to correctly handle zero event yields. In the multijet estimation the events yields are the sum of the negative and positive weights determined by the matrix method. In regions of phase space with relatively few un-weighted events, situations can arise where the sum of the positive weights are not large enough to compensate for the sum of the negative weights. This leads to the unphysical negative event yields. In such cases it is assumed that the event yield is exactly zero. Instances of this nature only occur in a very small number of bins in the tails of the distributions where the yield is expected to be

close to zero. The validity of this assessment can be checked in the control plots in CR3 shown in Appendix B. In this region, where the kinematics are closer to that of the signal region, there are no multijet events and no discrepancy between the prediction and data. A good estimate for the upper statistical limit for the multijet background with zero expected events is the absolute value of the sum of the weights since it gives the weighted events yield that would be needed to pass the selection in order to give exactly zero expected events.

9.8 Summary

The limit setting procedure outlined above was performed in the electron, muon, and combined electron/muon channels for both the $S1_R$ and $S4_R$ monotop models using all systematic uncertainties described in Chapter 8. The results of the procedure using the cut-based and BDT analysis approaches are shown in Chapters 10 and 12 respectively with a summary of the 8 TeV results presented in Chapter 13.

Chapter 10

8 TeV Cut-Based Results

The limit setting procedure outlined in Chapter 9 was performed for each of the individual mass hypotheses in the $S1_R$ and $S4_R$ models. The cut-based analysis, using the Signal Region 1 and Signal Region 2 selection regions defined in Chapter 7 for the $S1_R$ and $S4_R$ models respectively and with a coupling value of $a_R = 0.2$, was published in 2014. Those results, along with an augmentation of the cut-based analysis where an additional cut on the electric charge of the lepton was applied to the events in the SR2 selection region are presented in this chapter. This additional selection requirement was not part of the original analysis and was applied in an effort to improve upon the published results.

10.1 Limit plot explanation

Expected and observed 95% CL limits were calculated for the electron, muon, and combined electron/muon channels and plots of the expected and observed 95% CL limits on the cross-section times branching ratio for both the $S1_R$ and $S4_R$ models will be shown and described below. As the production cross-sections are proportional to the square of the coupling parameter, a_R, expected and observed 95% CL limits on the coupling parameter as a function of the mass of either the f_{met} or v_{met} particles are presented as well.

Examples of these plots using a generic toy model are shown in Figure 10.1. In these types of plots the solid (dashed) black lines indicate the observed (expected) 95% CL limits

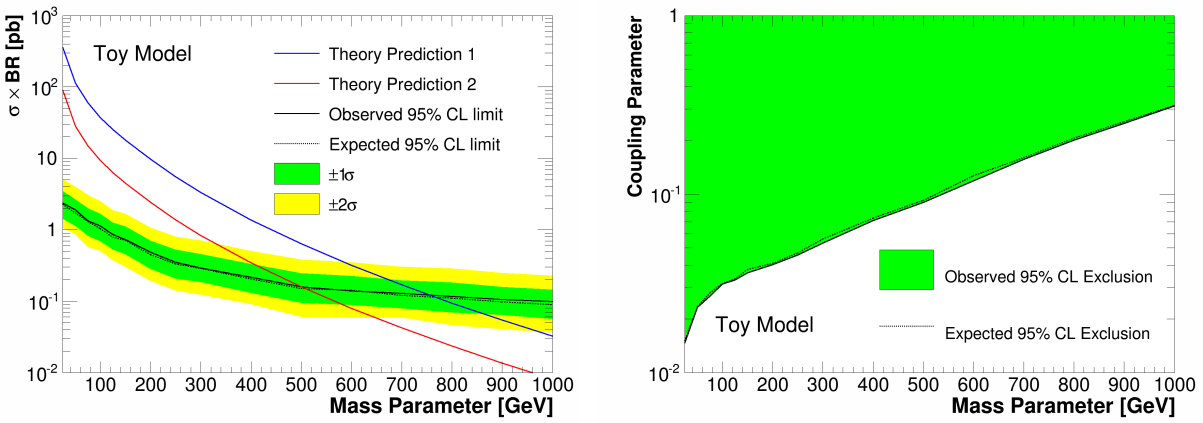

Figure 10.1: Example plots using a toy model showing the expected and observed 95% CL limits on cross-section times branching ratio (left) and coupling parameter (right) as a function of a generic mass parameter.

as calculated in Section 9.4 (9.5). For the plots depicting limits on the cross-section times branching ratio, the colored solid lines indicate the theoretical predictions for different values of a_{R}. The green and yellow bands in these plots are the $\pm 1\sigma$ and $\pm 2\sigma$ bands on the expected limits without signal respectively. Values of the mass of either the f_{met} or v_{met} particle for which the observed (expected) limits fall below that of the theoretical predictions are said to be excluded at the 95% CL. For the plots of the 95% CL limits on a_{R}, the observed and expected limits are shown. The green area represents the region of a_{R} parameter space which is excluded at the 95% CL.

A monotop signal present in the data would manifest itself as an excess in the observed 95% CL limit curve over the expected limits in the plots showing the limits on cross-section times branching ratio. This excess would be present at the corresponding mass of the f_{met} or v_{met} particle which constituted the signal and would rise significantly above the expected limits. The degree to which this excess would rise above the expected limits would indicate either evidence or discovery of the signal. Claiming evidence of a signal requires an excess of 3σ

while claiming discovery requires a 5σ excess.[1]

10.2 Published cut-based results

This section re-states the results from the published, cut-based analysis for the resonant $S1_R$ and non-resonant $S4_R$ models [37]. The results of the limit setting procedure for the $S1_R$ model are shown in Figures 10.2 and 10.3 with the corresponding values listed in Table 10.1. As Figure 10.2 shows, the entirety of the mass range can be excluded for a coupling value of $a_R = 0.2$. The flat nature of the plots in Figures 10.2 and 10.3 is due to the similarities in kinematic distributions across the whole mass range of the f_{met} particle studied. The results for the $S4_R$ model are shown in Figures 10.4 and 10.5 with the corresponding values listed in Table 10.2.

Cut-Based $S1_R$ Limits					
	Theory, LO	**Expected 95% CL**		**Observed 95% CL**	
$m(f_{\text{met}})$ **[GeV]**	$(a_R = 0.2)$ **[pb]**	$\sigma\times$ **BR [pb]**	a_R	$\sigma\times$ **BR [pb]**	a_R
0	1.11	0.40	0.121	0.34	0.111
20	1.10	0.38	0.117	0.32	0.108
40	1.09	0.40	0.121	0.34	0.112
60	1.07	0.41	0.124	0.44	0.114
80	1.04	0.42	0.127	0.36	0.117
100	1.00	0.58	0.139	0.41	0.128

Table 10.1: Expected and observed 95% CL limits on the production cross-section times branching ratio and coupling parameter as a function of the mass of the f_{met} particle for the $S1_R$ model with a resonance with a mass of 500 GeV in the combined electron/muon channel for the cut-based analysis. The LO theoretical predictions and limits on $\sigma \times$ BR are shown for a coupling value of $a_R = 0.2$.

[1] The 3σ and 5σ criteria are subjective but generally accepted as the appropriate thresholds for "evidence" and "discovery" of a signal at collider experiments.

Cut-Based $S4_R$ Limits					
	Theory, LO	**Expected 95% CL**		**Observed 95% CL**	
$m(v_{\text{met}})$ [GeV]	($a_R = 0.2$) [pb]	$\sigma\times$ BR [pb]	a_R	$\sigma\times$ BR [pb]	a_R
0	96.0	2.14	0.030	2.19	0.030
25	359.0	1.56	0.013	1.55	0.013
50	113.4	1.39	0.022	1.41	0.022
75	59.9	1.13	0.027	1.12	0.027
100	37.5	0.90	0.031	0.89	0.031
125	25.7	0.76	0.035	0.75	0.034
150	18.0	0.65	0.038	0.65	0.038
200	9.66	0.47	0.044	0.46	0.044
250	5.51	0.40	0.055	0.40	0.054
300	3.33	0.37	0.067	0.37	0.066
400	1.37	0.29	0.093	0.30	0.093
500	0.63	0.26	0.130	0.27	0.129
600	0.32	0.24	0.173	0.24	0.174
700	0.17	0.23	0.233	0.24	0.234
800	0.09	0.23	0.314	0.23	0.314
900	0.06	0.22	0.404	0.22	0.405
1000	0.03	0.21	0.510	0.21	0.507

Table 10.2: Expected and observed 95% CL limits on the production cross-section times branching ratio and coupling parameter as a function of the mass of the v_{met} particle for the $S4_R$ model in the combined electron/muon channel for the cut-based analysis. The LO theoretical predictions and limits on $\sigma \times$ BR are shown for a coupling value of $a_R = 0.2$.

10.3 Cut-based results with lepton charge selection

The results of the limit setting procedure for the $S4_R$ model utilizing the cut-based analysis with the additional cut on the electric charge of the lepton are shown in Figures 10.6 and 10.7 with the corresponding values listed in Table 10.3.

10.4 Summary

The published, cut-based analysis was able to exclude the $S1_R$ model for the entirety of the mass range of the f_{met} particle and the $S4_R$ model for masses of the v_{met} particle up to 657 GeV for a coupling value of $a_R = 0.2$. The addition of a lepton electric charge cut was

Cut-Based + Lepton Charge Cut $S4_R$ Limits					
	Theory, LO	**Expected 95% CL**		**Observed 95% CL**	
$m(v_{\text{met}})$ [GeV]	($a_R = 0.2$) [pb]	$\sigma\times$ BR [pb]	a_R	$\sigma\times$ BR [pb]	a_R
0	96.0	1.52	0.025	1.41	0.024
25	359.0	1.14	0.011	1.07	0.011
50	113.4	0.96	0.018	0.90	0.018
75	59.9	0.79	0.023	0.72	0.022
100	37.5	0.63	0.026	0.58	0.025
125	25.7	0.56	0.030	0.53	0.029
150	18.0	0.45	0.032	0.42	0.031
200	9.66	0.32	0.037	0.30	0.035
250	5.51	0.28	0.045	0.25	0.043
300	3.33	0.25	0.055	0.23	0.043
400	1.37	0.21	0.078	0.19	0.074
500	0.63	0.18	0.107	0.17	0.103
600	0.32	0.17	0.145	0.16	0.140
700	0.17	0.16	0.194	0.14	0.184
800	0.09	0.16	0.257	0.14	0.247
900	0.06	0.15	0.332	0.14	0.318
1000	0.03	0.14	0.413	0.13	0.413

Table 10.3: Expected and observed 95% CL limits on the production cross-section times branching ratio and coupling parameter as a function of the mass of the v_{met} particle for the $S4_R$ model in the combined electron/muon channel for the cut-based analysis with an additional cut on the electric charge of the lepton. The LO theoretical predictions and limits on $\sigma \times$ BR are shown for a coupling value of $a_R = 0.2$.

able to improve the limits on the $S4_R$ model to exclude masses of the v_{met} particle up to 734 GeV. The following two chapters will outline the analysis technique used to improve upon these results even further through the use of a Multivariate Analysis technique called a Boosted Decision Tree.

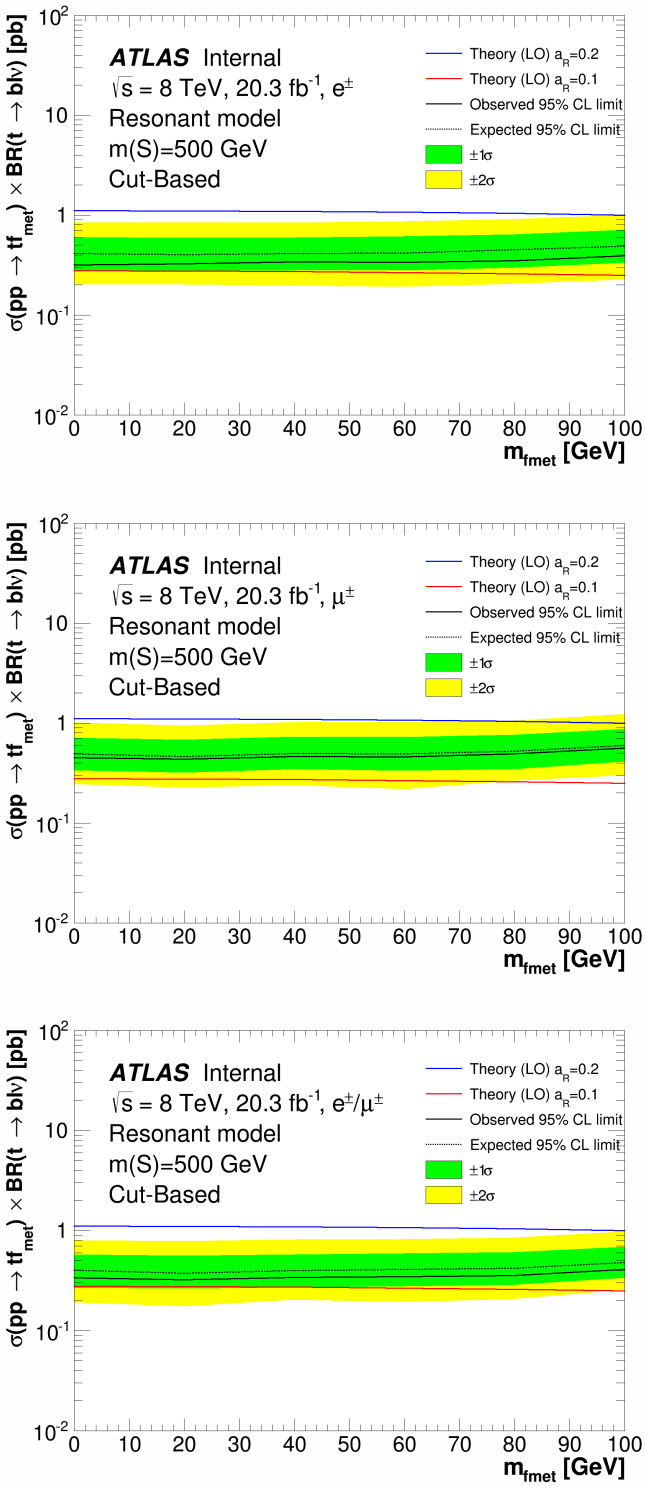

Figure 10.2: Expected and observed 95% CL limits on the cross-section times branching ratio for the $S1_R$ model with a resonance mass of 500 GeV in the electron (top), muon (middle), and combined electron/muon channel (bottom) for the cut-based analysis. The predicted LO cross-section times branching ratio values are shown for different values of a_R.

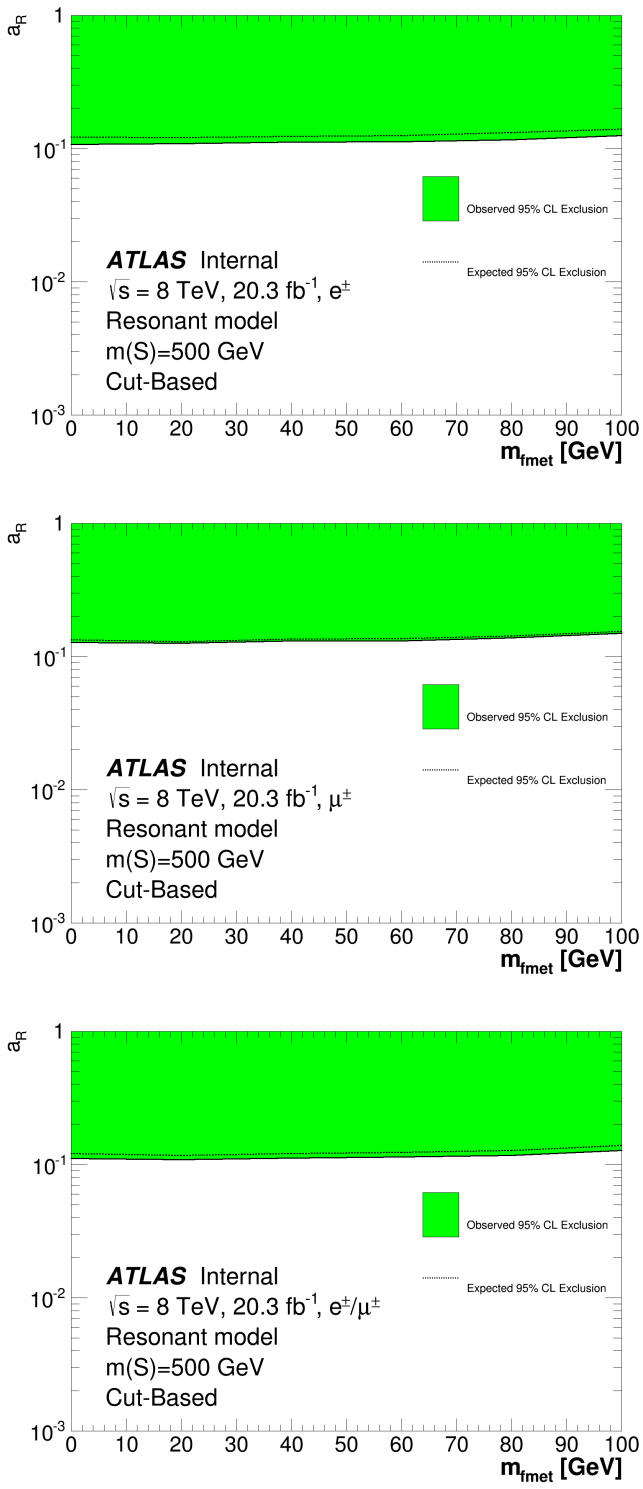

Figure 10.3: Expected and observed 95% CL limits on the coupling parameter, a_{R}, for the $\mathrm{S1_R}$ model with a resonance mass of 500 GeV in the electron (top), muon (middle), and combined electron/muon channel (bottom) for the cut-based analysis.

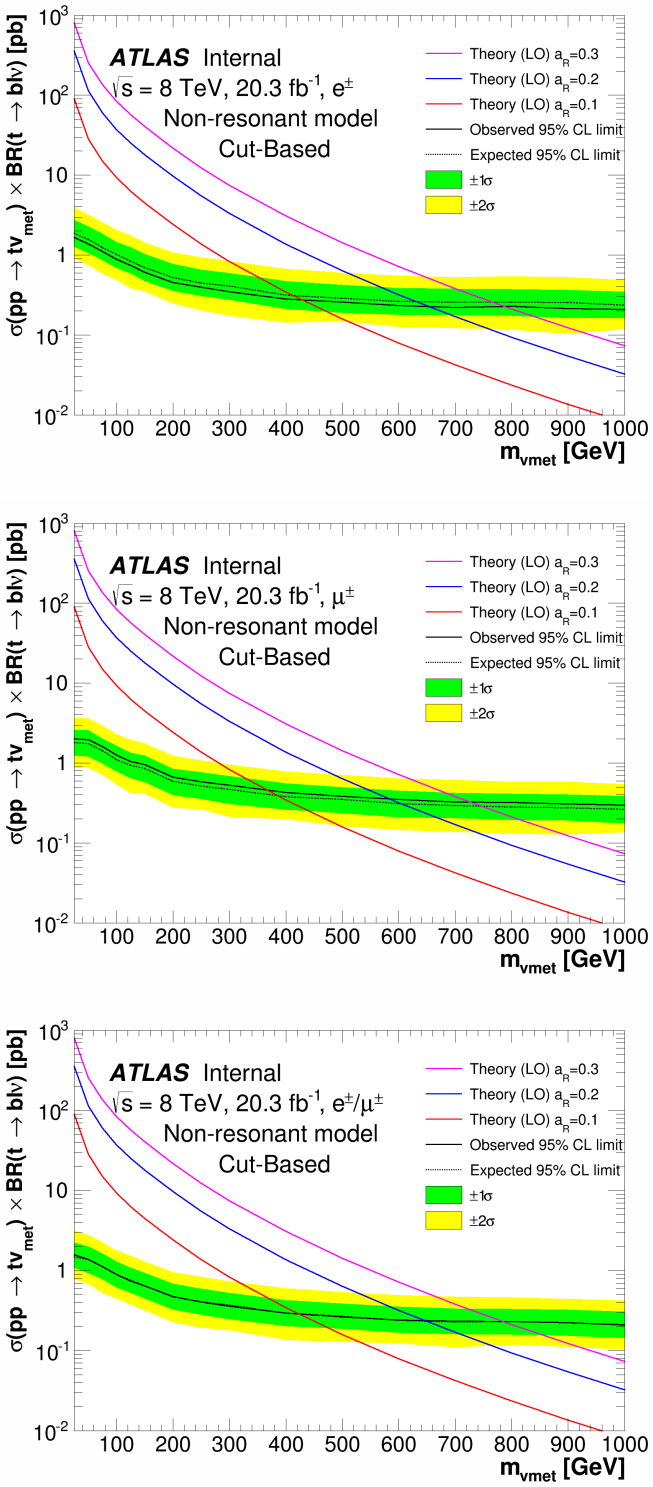

Figure 10.4: Expected and observed 95% CL limits on the cross-section times branching ratio for the $S4_R$ model in the electron (top), muon (middle), and combined electron/muon channel (bottom) for the cut-based analysis. The predicted LO cross-section times branching ratio values are shown for different values of a_R.

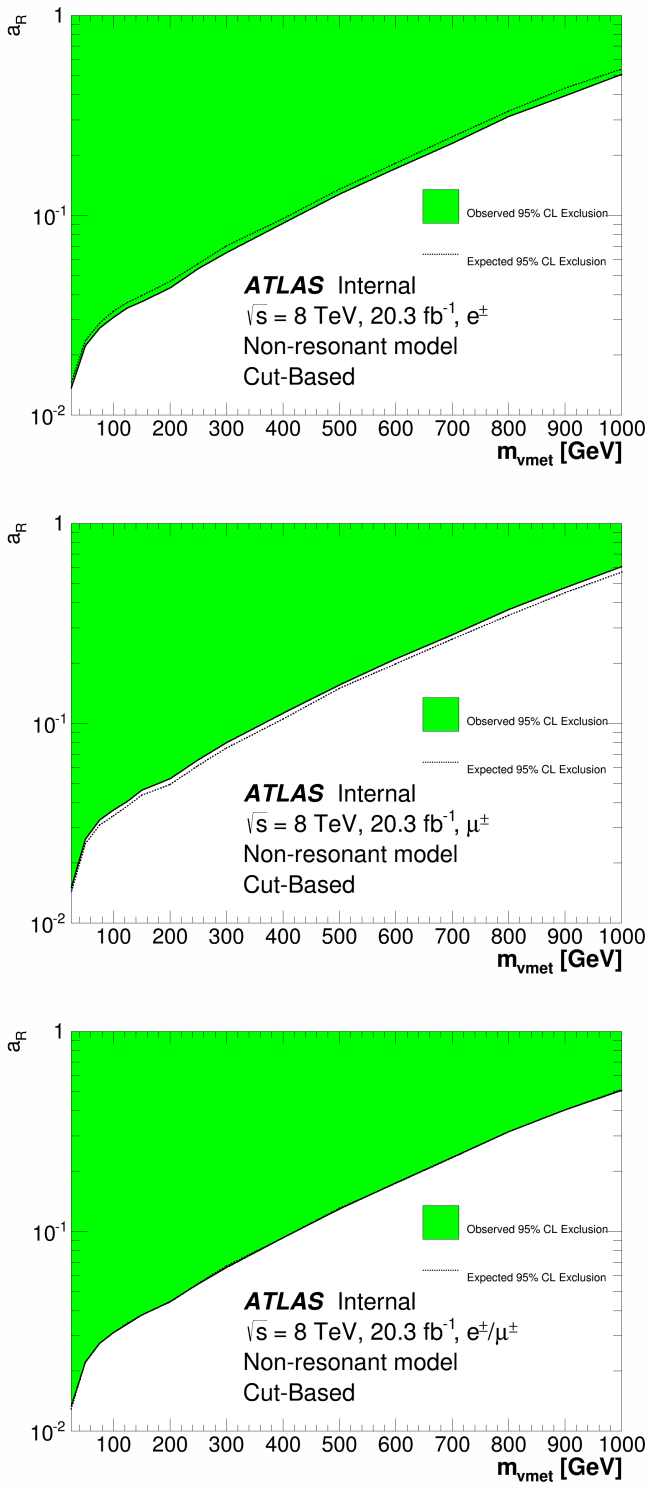

Figure 10.5: Expected and observed 95% CL limits on the coupling parameter, a_{R}, for the $\mathrm{S4_R}$ model in the electron (top), muon (middle), and combined electron/muon channel (bottom) for the cut-based analysis.

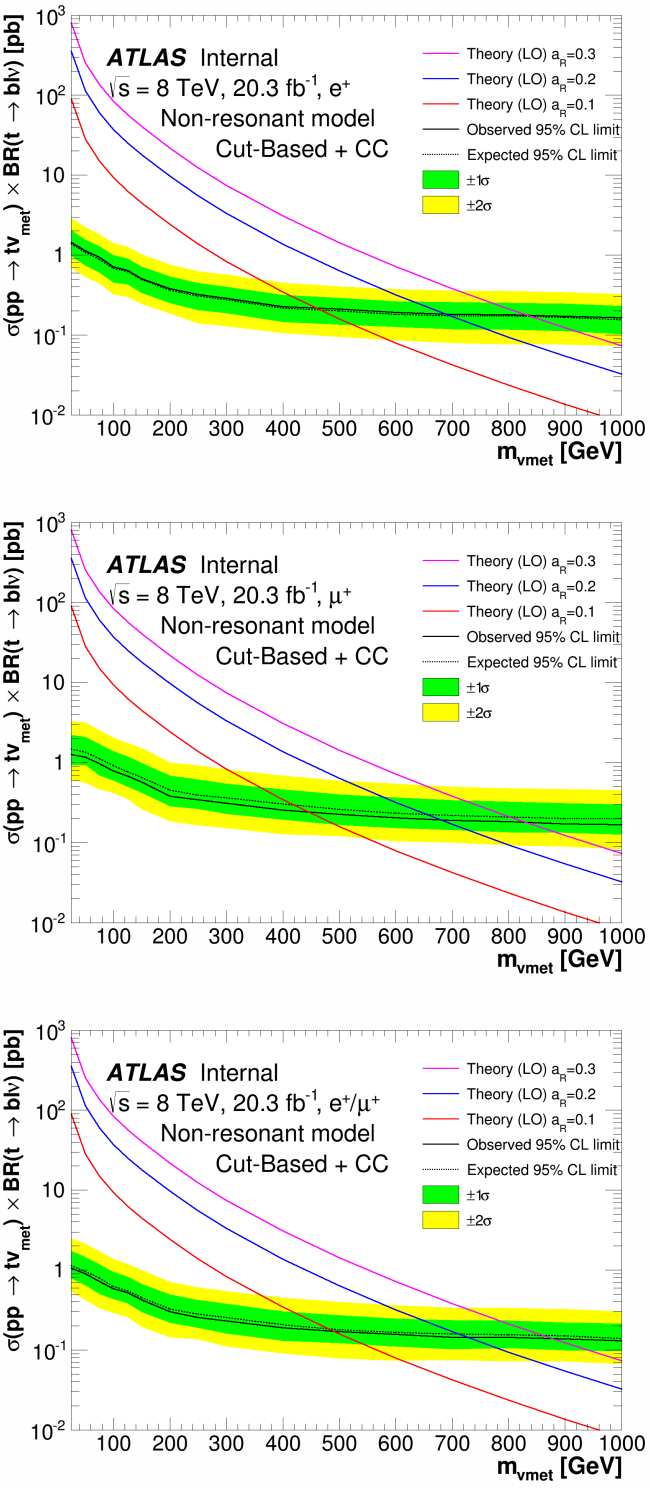

Figure 10.6: Expected and observed 95% CL limits on the cross-section times branching ratio for the $S4_R$ model in the electron (top), muon (middle), and combined electron/muon channel (bottom) for the cut-based analysis with an additional cut on the electric charge of the lepton. The predicted LO cross-section times branching ratio values are shown for different values of a_R.

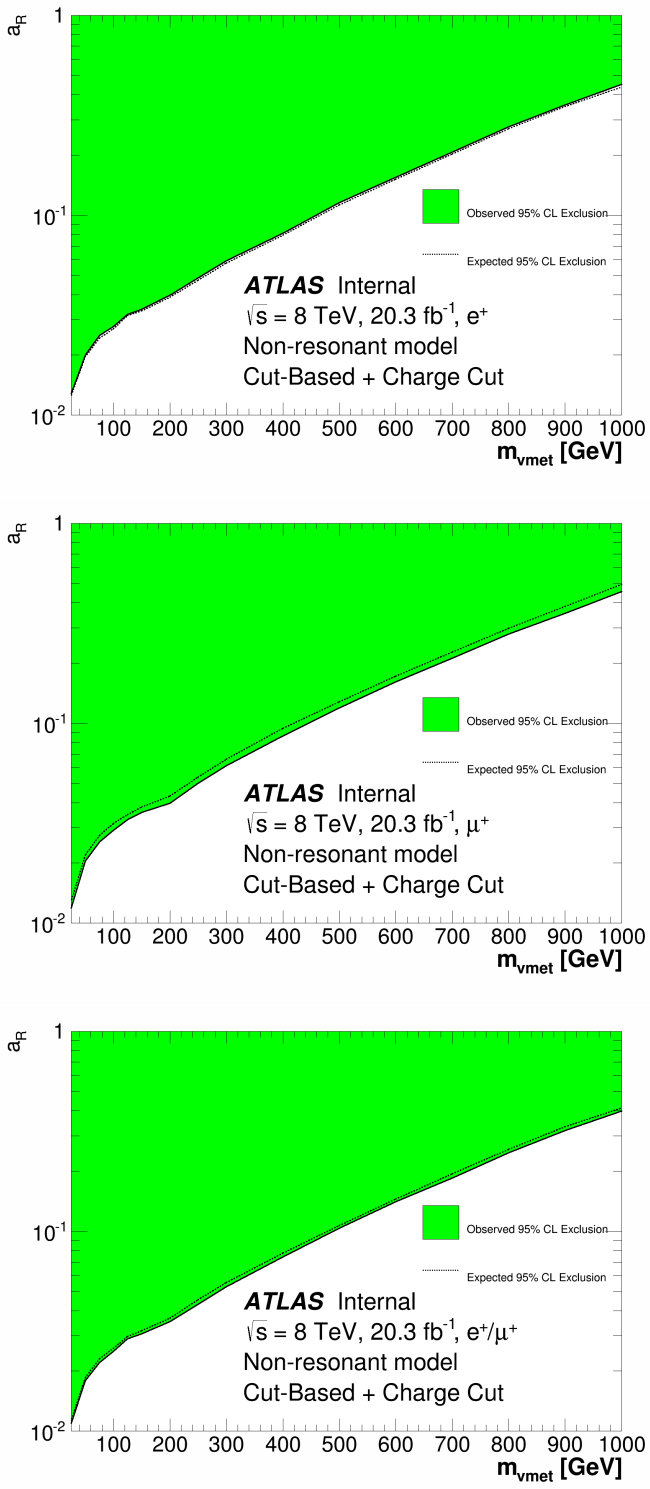

Figure 10.7: Expected and observed 95% CL limits on the coupling parameter, a_{R}, for the $\mathrm{S4_R}$ model in the electron (top), muon (middle), and combined electron/muon channel (bottom) for cut-based analysis with an additional cut on the electric charge of the lepton.

Chapter 11

Decision Trees

This dissertation describes both a published cut-based analysis and an improved re-analysis utilizing a Boosted Decision Tree multivariate technique. This chapter introduces the Decision Tree (DT) techniques and outlines the optimization procedure used in the search for monotop events using a BDT.

11.1 Multivariate analysis techniques

Multivariate analysis techniques have been utilized extensively in analyses over the past couple of decades. The power of an MVA lies in its ability to recognize correlations among kinematic variables that are often too difficult to see by eye or are difficult to exploit by simple cut-based analyses. These correlations can be combined into one discriminating variable, the MVA discriminant. A simple cut-based analysis typically uses two or three variables to discriminate between background and signal events while an MVA can use dozens.

Specific MVA techniques attempt to solve one of two types of problems: regression and classification. MVAs designed to solve regression problems attempt to predict the future value of a specific variable given an input data set. Those designed to solve classification problems attempt to group data into classes. The search for monotop events falls into this latter category of problems where the goal is to classify events as being either signal (monotop) or background (single-top, $t\bar{t}$, dibosons, W+jets, and multijets). There are many types of

MVA techniques that can be used to solve this problem: neural networks, Fisher discriminants, and Boosted Decision Trees (BDTs) are among the techniques used in particle physics. There is no easy answer to the question of which type of MVA should be used in an analysis. Generally speaking, BDTs are a good choice if an analysis has multiple discriminating variables which exhibit non-linear correlations. This analysis uses a BDT and makes use of a multivariate analysis program called the Toolkit for Multivariate Analysis (TMVA) [103] integrated into the ROOT framework. ROOT is an object-oriented framework developed by CERN and designed for particle physics data analyses [104]. TMVA encompasses a multitude of different MVA methods. It is very well-documented and can be used directly "out of the box" but is also highly configurable.

11.2 Decision Tree overview

In particle physics a Decision Tree is used as a tool to classify data events as either being "signal-like" or "background-like" based on simple kinematic cuts. Before the logic of a DT is applied to data, it must first be built, or "trained", using simulated data in which the classes (signal or background) are known *a priori*. Monte Carlo samples of simulated signal and background are used to train a DT to find the appropriate kinematic cuts such that the output of the DT is able to correctly classify the events according to their class. Once a DT has been properly trained, the logic encoded in its output is then applied to real data in which the classes of the events are not known in an attempt to discern signal from background.

The basic idea of a DT can be illustrated by considering a simplified example involving a set of events described by only two variables, X and Y, and in which the classes are

already known. By plotting these events against those variables, as is shown in Figure 11.1, a Decision Tree can be built to find cuts on variables X and Y such that the entire set can be classified into signal and background regions solely defined by those cuts.

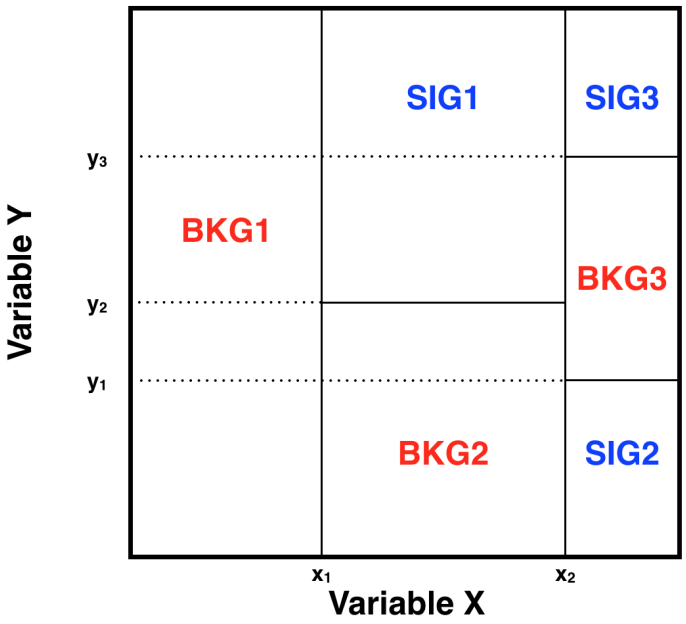

Figure 11.1: A cartoon drawing showing a set of signal and background regions defined by variables X and Y.

This is essentially the classification problem. The Decision Tree first looks at the entirety of the set and makes a decision at this first node (Node 1) as to how to best split the sample according to a cut on either variable X or Y. In this example the DT first notices that if the set is split into two daughter nodes, one with events satisfying $X < x_1$ and one with events satisfying $X > x_1$, a region can be classified that consists entirely of background events (BKG1). This is shown in Figure 11.2. As no further discrimination is needed for events with $X < x_1$, this first daughter node becomes what is called a leaf.[1]

For events with $X > x_1$ further splitting is needed to fully classify the set. At this point the Decision Tree notices that at Node 2 another cut on X can further divide the set into events

[1] A leaf is simply a node for which no further classification is required or some threshold criterion has been met. Leaves are assigned the class to which the majority of their events belong.

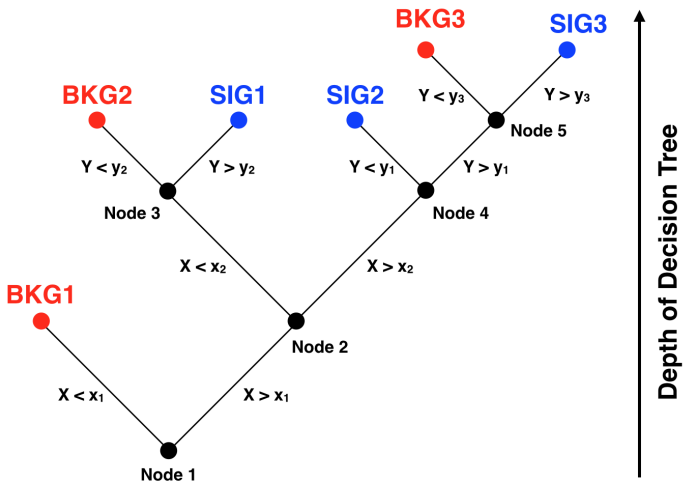

Figure 11.2: The basic structure of a Decision Tree which classifies events into signal and background regions.

with $X < x_2$ (Node 3) and $X > x_2$ (Node 4). At Node 3 the DT finds that a cut on the Y variable can further classify the set into a region entirely composed of signal events (SIG1) and a region entirely composed of background events (BKG2). Again, as these two regions are now fully classified these nodes become leaves. This process of splitting the set into nodes by applying cuts on the input variables in order to classify events as signal or background is continued until the set is fully classified. The output of the DT can then be used to classify events in a separate set of data in which the class is not known by simply applying the algorithm to those events until they are classified as either signal or background. While this process can easily be done by eye in this simplified case, in higher dimensional problems (more variables) or cases involving overlapping regions of signal and background, a Decision Tree can be a powerful tool to solve the classification problem. The process described above is a simple binary Decision Tree in which the entire set can be classified into regions which contain exclusively background or signal events. In most applications, including the case of the search for monotop events, the events are much more difficult to classify.

11.3 Training algorithm

Decision Trees follow a basic training algorithm in order to classify events at each node. The basic input to a DT is list of samples known to be either background or signal, each of which are described by a list of variables, $\vec{x}$. Each event in theses samples has an associated weight, w, which corresponds to the cross-section of the process. A basic overview of the training algorithm steps is listed below with a more in-depth explanation of each level to be explained in later sections.

1. Normalize the signal and background samples such that the sum of the weights of each sample are equal and satisfy

$$\sum_{j=0} w_j = \sum_{k=0} w_k = 1, \tag{11.1}$$

   where j and k run over the number of (unweighted) events and w_j and w_k are the weights of each signal and background event in the samples respectively.

2. Begin the DT by selecting all of the events in the training sample, $s + b$, and call these events the initial node.

3. For each variable in $\vec{x}$ find the cut on that variable which provides the best signal to background separation based on some pre-defined metric. This metric could be the Cross Entropy, Gini, or Misclassification Error indices described in Section 11.3.2.

4. Choose the variable and associated cut which gives the best separation.

5. Split the initial node into two daughter nodes based on this variable's cut. One node will contain a sub-set of the original number of events which passes the cut and one

will contain events which do not.

6. In each of these two daughter nodes look at the complete set of variables again and find the variable and associated cut which best discriminates between signal and background events in each node.

7. Apply steps 3 through 6 on all subsequent nodes until all nodes become leaves. The criterion for when a node becomes a leaf is a pre-defined parameter. Leaves which contain more signal (background) events than background (signal) events are classified as signal (background) leaves.

The final event output of an individual Decision Tree, $D_n(\vec{x}_i)$, called the discriminant, is a value that is either $+1$ or -1 corresponding to whether an event is classified as signal or background respectively. Here n is the index for the tree number. In the case of a single tree $n = 1$. In the case where many trees are built, which will be explained in detail in later sections, n runs from 1 to the total number of trees.

11.3.1 Event weight normalization

The first step in the training algorithm is to normalize the sum of the signal and background weights to the same value which is set to one by convention, although any value is sufficient without loss of generality. The reason the samples are normalized in this fashion is to maximize the sensitivity to signal and background characteristics. Consider the case of an extremely rare signal against a large background. If the samples were not so normalized, then the classifier would see very few signal events against a large number of background events and it would surmise that really any cut would separate signal from background as

the purity of any leaf would already be close to zero or one.[2]

11.3.2 Node splitting

The splitting of a Decision Tree's node is the most important part of the training algorithm and encompasses steps 3 through 6 listed above. It is here where the DT decides on which variable to cut and what the value of that cut should be. To this end, each node is assessed a purity value, p. Purity is defined as

$$p = \frac{\sum\limits_{j} w_j s_j}{\sum\limits_{j} w_j s_j + \sum\limits_{k} w_k b_k} = \frac{s}{s+b}. \tag{11.2}$$

As the signal and background samples were normalized in the first step of the training algorithm, the first node is always fully mixed with a purity at the maximum value of 0.5. Various separation indices can be chosen and the three most common choices are the Cross Entropy, Gini, and Misclassification Error. Each index is a function of purity and are defined as

$$\text{Cross Entropy Index} = -p\ln(p) - (1-p)\ln(1-p) \tag{11.3a}$$

$$\text{Gini Index} = 2p(1-p) \tag{11.3b}$$

$$\text{Misclassification Index} = 1 - \max(p, 1-p) \tag{11.3c}$$

As can been seen in Figure 11.3, each index has a maximum value when the node is full-mixed, i.e. when the purity is at its maximum value, $p = 0.5$. The DT attempts to find the

[2] In the view of a classifier, the ability to identify background is equally as important as the ability to identify signal.

best variable and optimal cut on that variable which maximizes the *difference* between the value of the index before the split and the value after the split. The node before the split, node 0, contains some number of events, N_0. After the split there are two nodes, node 1 and node 2, containing N_1 and N_2 events respectively where $N_0 = N_1 + N_2$. The change in the value of the index is given by

$$\Delta\text{Index} = \text{Index}_0 - \left[\left(\frac{N_1}{N_0}\right)\text{Index}_1 + \left(\frac{N_2}{N_0}\right)\text{Index}_2\right]. \tag{11.4}$$

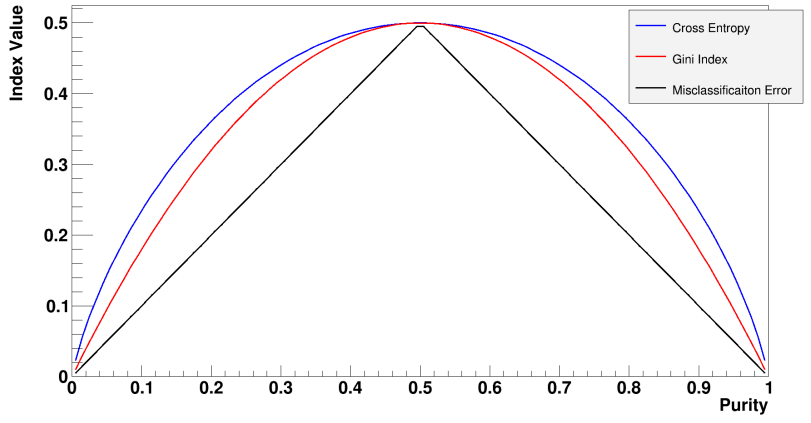

Figure 11.3: Various separation indices which can be used in the node splitting step of the training algorithm. All indices have a maximum value when the node is fully-mixed between background and signal events, $p = 0.5$. As a cut that selects signal is just as useful as one that selects background, all the indices are symmetric around the fully-mixed case.

11.4 Limitations of decision trees

While a simple binary Decision Tree is easy to understand it does have inherent limitations and potential pitfalls. Statistical fluctuations in the training sample may cause an instability in a DT's classifier response. Consider a node in which two variables show similar separation power. A fluctuation in the training sample may cause the training algorithm to spuriously

select a split leading to a non-optimal result. The whole structure of the tree is altered beyond this node since the effect of this fluctuation is propagated to subsequent nodes. One technique in which to lessen the impact of this limitation is called "boosting."

11.5 Boosting

The training algorithm described in Section 11.3 builds one Decision Tree. The real power of Decision Trees lies in the ability to train many trees which, when taken together, perform better as a classifier than any single individual tree. Consider three uncorrelated Decision Trees, each of which has been trained such that it correctly classifies events as signal or background 70% of the time. Taken as an ensemble, events are classified based on a majority vote and the performance is always better than any of the original trees by themselves. Equation 11.5 shows this principle.

$$\% \text{ events classified correctly} = 0.7^3 + 3\left(0.7^2 \times 0.3^1\right) = 0.78 \tag{11.5}$$

The first term is the probability that all three DTs classify an event correctly. The second term is the probability that two DTs classify the event correctly and one does not. The factor of 3 in front of the second term takes into account that there are three ways for two classifiers to be correct and one to be incorrect. In this example, the ensemble of the three DTs correctly classifies events 78% of the time even while the individual classifiers only correctly classify events 70% of the time.

Boosting turns a collection of individually trained trees into an ensemble. The basic concept is that events which are incorrectly classified by one tree are weighted more heavily (boosted)

in the training of the subsequent tree. The final discriminant value for event i, $D(\vec{x}_i)$, after training multiple trees is then a weighted average of the discriminant values of the individual trees, $D_n(\vec{x}_i)$. There are numerous boosting algorithms available and this analysis uses the Adaptive Boost (AdaBoost) algorithm [105]. This algorithm is the most widely used choice and is rather straightforward. The AdaBoost algorithm steps are listed below.

1. Train the n^{th} Decision Tree.

2. Calculate the misclassification rate of the n^{th} tree, ϵ_n, described as the fraction of events classified incorrectly into signal or background leaves. This rate is defined as

$$\epsilon_n = \frac{\sum_{i=1}^{N_{\text{events}}} w_i^n \times (\text{isMisclassified})_i^n}{\sum_{i=1}^{N_{\text{events}}} w_i^n}, \tag{11.6}$$

   where isMisclassified is a Boolean expression that has a value of 1 if the event was classified incorrectly and 0 if it was classified correctly.

3. Calculate the boost weight, α_n. This quantity is defined as

$$\alpha_n = \beta \ln\left(\frac{1-\epsilon_n}{\epsilon_n}\right), \tag{11.7}$$

   where β is known as the AdaBoost parameter.

4. Modify the weight of each misclassified event in the training sample so that the i^{th} event weight in the $(n+1)^{\text{th}}$ tree becomes

$$w_i^{n+1} \rightarrow w_i^n \times e^{\alpha_n \times \text{isMisclassified}}. \tag{11.8}$$

5. Re-normalize the training sample with these new weights and iterate steps 1 through 4 until N trees are trained so that the result of the process is the final discriminant value given by

$$D(\vec{x}_i) = \frac{\sum_{n=1}^{N} \alpha_n D_n(\vec{x}_i)}{\sum_{n=1}^{N} \alpha_n}. \tag{11.9}$$

The discriminant output of any one individual tree, $D_n(\vec{x}_i)$, is either $+1$ or -1 depending on whether an event was classified as signal or background. The boosting algorithm turns the discriminant output of a single DT into a more performant discriminant variable, $D(\vec{x}_i)$, with values between -1 and $+1$.[3] A consequence of the boosting algorithm is that trees built later in the chain focus more and more on fewer and fewer misclassified events and by construction perform progressively worse and worse by tending towards 50% (towards random guessing). However, the relative weights of these trees' terms in Equation 11.9 are small when compared to earlier trees so they count less. The final discriminant value given by Equation 11.9 can be thought of as an expansion around the very first tree in which later trees have smaller boosting weights, α_n, and thus are seen as small corrections to the overall discriminant value. This behavior can be seen in Figure 11.4.

11.6 Understanding the discriminant output

In order to better understand how the value of the BDT discriminant is calculated, consider the simple case of a BDT with two trees, $n = 1$ and $n = 2$, each attempting to classify the same 100 events (50 background and 50 signal events) and using the same two discriminating variables, x and y. Figure 11.5 shows the output of each individual tree.

[3] The more trees which are trained the more continuous-looking the discriminant variable becomes.

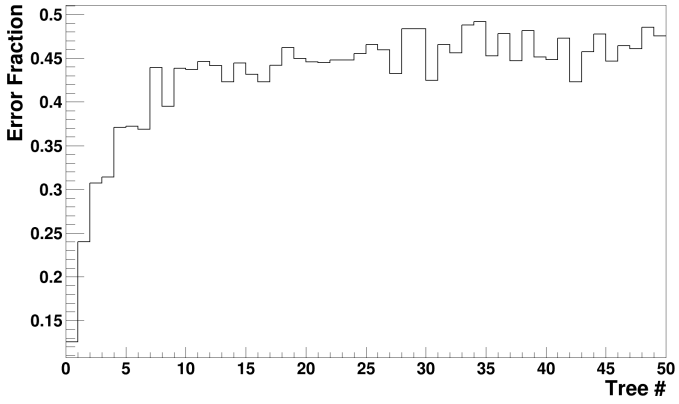

(a)

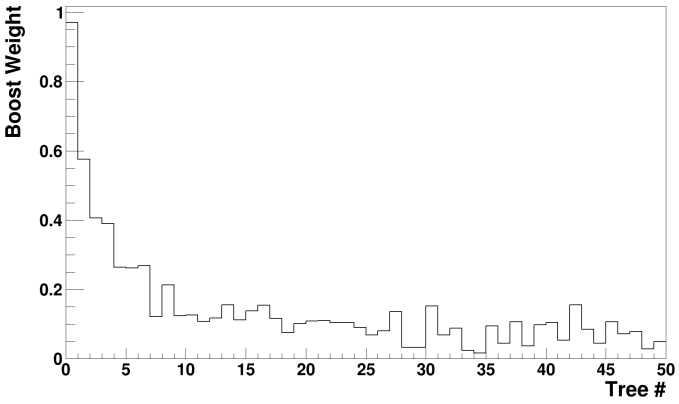

(b)

Figure 11.4: (a) The error fraction, ϵ_n, as a function of the tree number trained. Later trees do no better than random guessing. (b) The boosting weight, α_n, as a function of the tree number trained. Later trees provide progressively smaller corrections to the discriminant output as a whole.

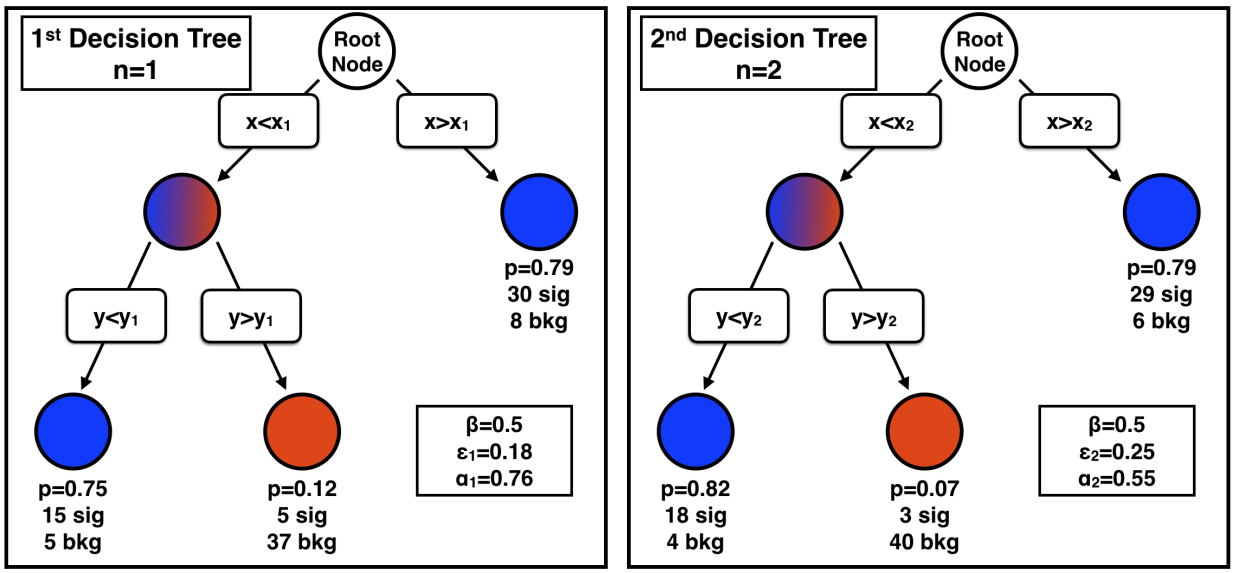

Figure 11.5: The output of the two individual Decision Trees used in a BDT is shown. On the left is shown the output of the first tree with its corresponding boost weight, α_1. On the right is shown the output of the second tree with its corresponding boost weight, α_2. Here the subscripts refer to the tree number. In this example $x_1 \neq x_2$ and $y_1 \neq y_2$.

The first tree finds three leaves by identifying cuts on x and y and the misclassification rate is 0.18 as given by Equation 11.6, where the weights, w_i^1, for the first tree are all equal to 1. Equation 11.7 gives the corresponding boost weight for the first tree, α_1, as 0.76 when given $\beta = 0.5$. If this were the only tree to be trained then the final discriminant output for event i would depend on the values of x and y of that event. If event i had $x_i > x_1$ then Equation 11.9 would yield a discriminant value of

$$D(x_i, y_i) = \frac{\alpha_1 D_1(x_i, y_i)}{\alpha_1} = \frac{0.76 \times 1}{0.76} = +1. \tag{11.10}$$

The discriminant value of any event is then just $+1$ or -1 when only using one tree and is solely determined by which type of leaf in which it terminates. Training another tree adds more complexity to the calculation of the discriminant value. According to the 4^{th} step in the AdaBoost algorithm, before the second tree is trained, any event which was misclassified

in the first tree has its weight multiplied by a factor of $e^{\alpha_1} = 2.14$ so that the second tree sees it as being more important than the correctly classified events. This has the effect of potentially altering the cut values the second tree might find. This is shown in the right hand plot of Figure 11.5 where the second tree found different values of cuts on x and y than were found in the first tree. Using the equations referenced for the first tree, the misclassification weight and the corresponding boost weight for the second tree can then be calculated.[4]

The final discriminant value is then determined on an event-by-event basis by applying the kinematic logic in each individual tree to a terminal leaf (signal or background) and using Equation 11.9 to calculate the final value of the discriminant. For example, consider event i whose variables put it in a signal leaf in the first and second tree. The final discriminant value would then be

$$D(x_i, y_i) = \frac{\alpha_1 D_1(x_i, y_i) + \alpha_2 D_2(x_i, y_i)}{\alpha_1 + \alpha_2} = \frac{(0.76 \times 1) + (0.55 \times 1)}{0.76 + 0.55} = 1. \tag{11.11}$$

If, however, the event ended up in a signal leaf in the first tree but a background leaf in the second tree then the final discriminant value would be

$$D(x_i, y_i) = \frac{(0.76 \times 1) + (0.55 \times -1)}{0.76 + 0.55} = 0.16 \tag{11.12}$$

Determining an event's discriminant value for a BDT trained with numerous trees is a matter of determining what kind of leaf in which the event terminated in each of the trees and then performing the summations in Equation 11.9. It should be noted that while the discriminant value for a BDT trained with numerous trees does become more and more continuous, it is

[4]The event re-weighting step is not shown but is implicit in the calculation of the misclassification rate and boost weight.

still bounded by $-1 < D < +1$. If an event falls into a signal (background) leaf in every single tree then it will have a value of $+1$ (-1). If the BDT is trained and boosted properly, then each subsequent tree has a lower boost weight and thus contributes less to the sum.

11.7 BDT optimization for monotop events

How the different parameters of a Boosted Decision Tree are adjusted can have a profound impact on the performance of the final discriminant output. Each analysis can have a different parameter optimization based on the sample size and kinematics of the signal and background samples used. The following is a list of parameters which have been optimized for the search for monotop events:

- **Input sample splitting** – In a BDT analysis, the background and signal samples are each divided into testing and training subsets. The training subset is the collection of events on which the BDT will train its algorithm. The testing subset contains the remaining events on which the BDT will then test the trained results. In this analysis the signal and background samples are split in half (by number of unweighted events in each sample). A diagram showing this idea is shown in Figure 11.6.

- **Event weight normalization** – Events are normalized in the training sample so that the sum of weights in the signal and background samples are equal. This is described in detail in Section 11.3.1.

- **Boosting algorithm** – The boosting algorithm used in this analysis is the Adaptive Boost algorithm described in Section 11.5.

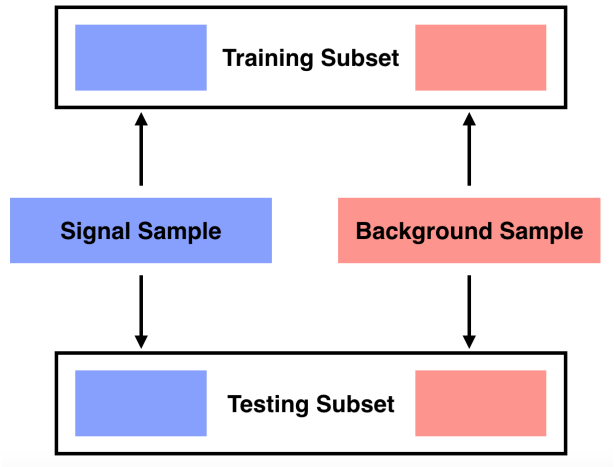

Figure 11.6: A cartoon drawing showing how the background and signal samples are split into testing and training samples.

- **Adaptive Boost parameter, β** – This is the value by which the boost is multiplied in the Adaptive Boost algorithm. Its value was set at 0.5.

- **Minimum node size** – This parameter controls the minimum number events necessary to be present in a node for the node splitting portion of the training algorithm to continue. Nodes that have fewer than this number automatically become leaves and are classified by their purity (signal if $p > 0.5$ and background if $p < 0.5$). In this analysis, this value was set to 5% of the training sample size.

- **Maximum depth of trees** – This parameter controls the maximum number of nodes along the longest path from the root node to the farthest leaf node. In this analysis, this value was set to 4.

- **Separation index** – This is the metric by which a decision is made on which variable to cut and at what value at each of the nodes and is described in Section 11.3.2. The Gini Index is used in this analysis.

- **Number of trees to train** – This parameter, also called the number of boosting

cycles, is the number of trees in the BDT forrest. This value was set to 50.

- **Number of grid points for variable cuts** – This parameter defines the number of grid points in each input variable range used in finding the optimal cut in the node splitting step of the training algorithm. In this analysis, this value was set to 200.

- **List of input variables** – While this is not a tuned parameter of the BDT algorithm, it is an important input in the training of a BDT. Details on what variables were chosen and why are described in Section 11.7.8.

In order to assess the impact these various parameters have on the final BDT discriminant output, a figure of merit, the cross-section significance (CSS), was used to determine the optimal parameter values:

$$\text{CSS} = \frac{\sum_i w_i s_i}{\sqrt{\sum_i w_i s_i + \sum_k w_k b_k}} = \frac{s}{\sqrt{s+b}}. \tag{11.13}$$

In Equation 11.13 the original values of the weights of the signal and background samples, w_i and w_k, are used and not the re-normalized ones in the training algorithm. Ideally a multidimensional scan spanning the entirety of the parameter space would be used when optimizing the parameters. However, this would be computing intensive and would be difficult to assess by the simple CSS metric. Parameters were optimized by varying an individual parameter across some scanning region while keeping the remaining parameters fixed at their default values. Once the optimal parameter values were chosen, this process was repeated again with the new optimal parameter values serving the place as the default values of the unvaried parameters.

11.7.1 Overtraining

"Overtraining" of a BDT can occur when it learns the unique statistical fluctuations in the training sample which can cause the output to perform differently on samples without such fluctuations. This can occur when the BDT has too many degrees of freedom relative to the size of the training samples. All the BDT parameters play a role in determining how much overtraining is present in a given configuration. However, the number of trees and the maximum allowed depth of those trees have the greatest impact on how much overtraining a particular configuration has. In principle an individual tree could have a very large depth such that each leaf contains only signal or only background. In such a case perfect discrimination would be achieved and the CSS would be at a true maximum. However, such a tree would be highly overtrained in that it would have learned the exact statistical fluctuations in the training sample.

Figure 11.7 shows a cartoon example of how an undertrained, overtrained, and properly trained discriminant would behave when plotted against two generic variables, X and Y. In this figure the black lines are representative depictions of how each BDT would delineate between signal and background. In the case of overtraining, shown in Figure 11.7(b), the BDT follows every fluctuation in the separation between signal and background.

The metric used to test whether or not a particular BDT configuration is overtrained is the Kolmogorov-Smirnov (K-S) test which computes the probability that two samples originated from the same distribution. A separate K-S statistic is generated for the signal and background samples for each BDT configuration. If the BDT is not overtrained then it will not have learned the unique statistical fluctuations of the training samples and will perform similarly when applied to the testing and training samples. A BDT is considered to be

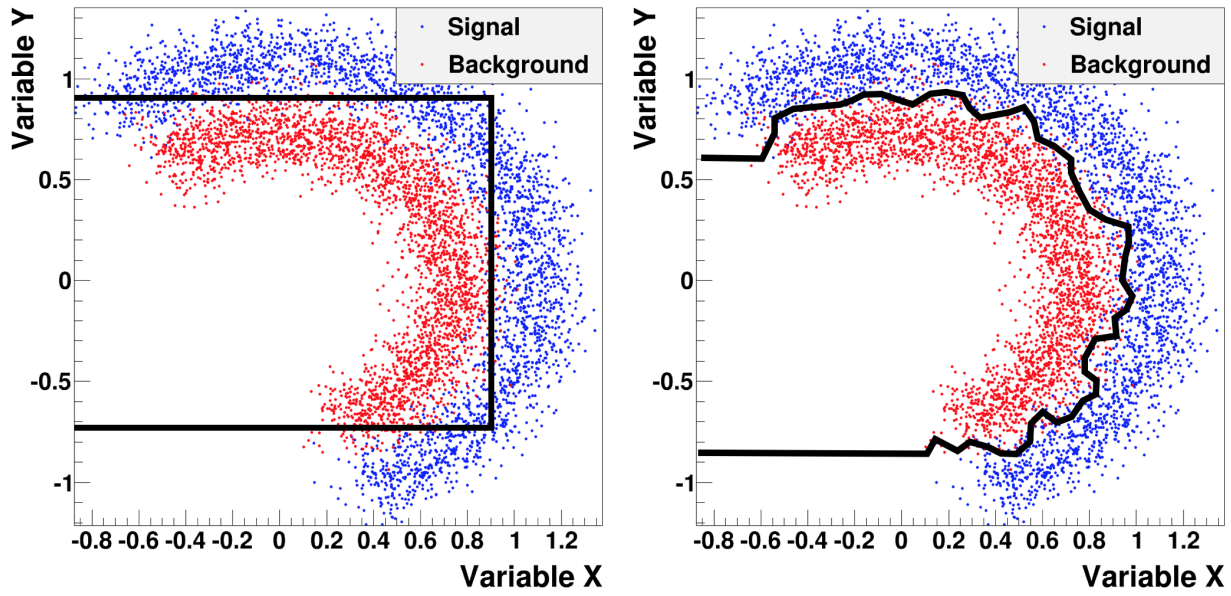

(a)

(b)

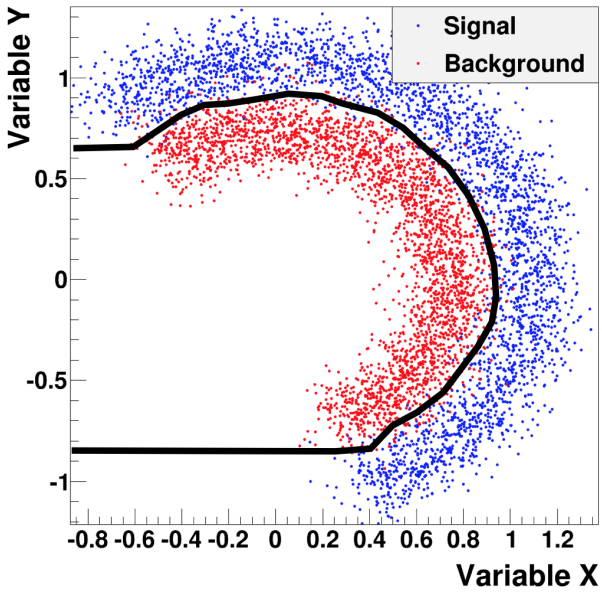

(c)

Figure 11.7: (a) This is an example of clear undertraining of the sample. The correlations between variables and the separation between signal and background can easily be seen but is not being exploited by the discriminant. The BDT in this situation likely does not contain enough trees or does not go to sufficient depth. (b) This is an example of clear overtraining of the sample. The BDT has learned the unique statistical fluctuations in the sample. It is likely that the BDT in this example contains far too many trees of too great of depth for the given statistics of the training sample. (c) This is a properly trained BDT. The discriminant has found the correlations between the variables and does a good job at separating signal from background without learning the unique statistical fluctuations of the samples.

overtrained when its K-S test result is less than 0.5 for either the signal or the background. As the variables in the training and testing samples do in fact originate from the same distribution, a K-S value less than 0.5 would indicate that more likely than not the BDT has been overtrained.

11.7.2 Number of trees

The number of trees (also known as boosting cycles) which are trained in a BDT has a large impact on the BDT's final discriminant output. Training too few trees can leave the BDT incapable of fully exploiting the correlations between variables and limit the amount of separation between signal and background. If too many trees are trained then the BDT begins to focus on only a select few events and the whole BDT starts to learn the statistical fluctuations of the training sample. This was shown in Figure 11.4(b) where the boost weight, α, became smaller and smaller and eventually leveled out. As more and more trees are trained the hard to classify events get more and more attention. This has the effect of causing the tree to focus on only those previously misclassified events. As such, the other events play an insignificant role in the node splitting process and the tree as a whole has a misclassification rate near 50% (no better than random guessing). Training any more trees than this may increase the overall performance of the BDT slightly, but it begins to have a larger and larger impact on the amount of overtraining present. In this analysis the number of trees to be trained was scanned from 1 to 250 in steps of 1. Figure 11.8 shows a plot of the CSS as a function of the number of trees trained. The CSS grows rapidly with the first few trees trained and then begins to level out at 50 trees. The optimal value was chosen to be 50 trees as this gave a reasonably good CSS with limited overtraining.

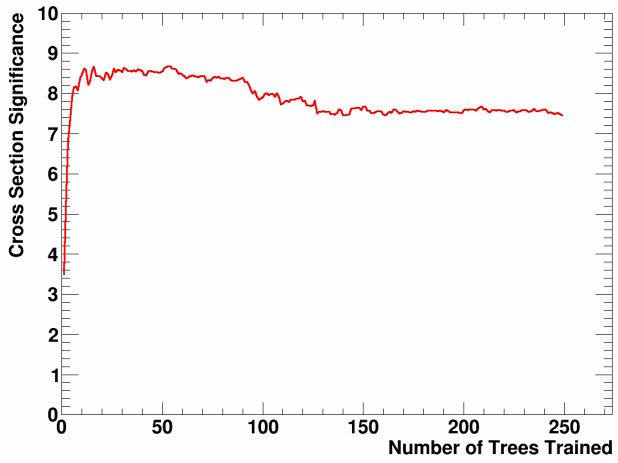

Figure 11.8: A plot of the CSS as a function of the number of trees trained in the BDT.

11.7.3 Separation index

No discernible difference in performance was found among the three separation indices from Equations 11.3b, 11.3a, and 11.3c and so the Gini Index was chosen.

11.7.4 Minimum node size

Deciding when a decision node becomes a leaf is an important part of the node splitting portion of the training algorithm. As one follows the logic line down the DT there are manifestly fewer and fewer events in each node. A DT could continue to split its nodes until the purity of each node reaches 0 or 1 depending on whether or not it is made of entirely background or signal events respectively. Such a tree would be highly overtrained and some threshold criterion is required in order to prevent this from happening. While specifying the maximum tree depth can help reduce overtraining, it does not address the problem of nodes which are not at the maximum depth but may have a small number of events on which to calculate the separation index. Splitting such nodes, ones higher up in the tree than the maximum depth but with few events, tends to lead to overtraining. A way around this is to

set a threshold for the minimum number of events in a node to continue. If the node event count is below this threshold, then it is automatically classified as a signal or background leaf depending on its purity. A scan of the minimum node size parameter was conducted to optimize this trade-off between performance and overtraining. Values for the minimum node size between 1-20% of the training sample were scanned in steps of 1%. A plot showing the CSS as a function of the minimum node size is shown in Figure 11.9. There is a general downward trend of the CSS as the minimum node size is increased and the jagged nature of the plot is a result of the limited statistics of the training sample. An optimal value of 5% was chosen at it gave the best performing BDT with limited overtraining.

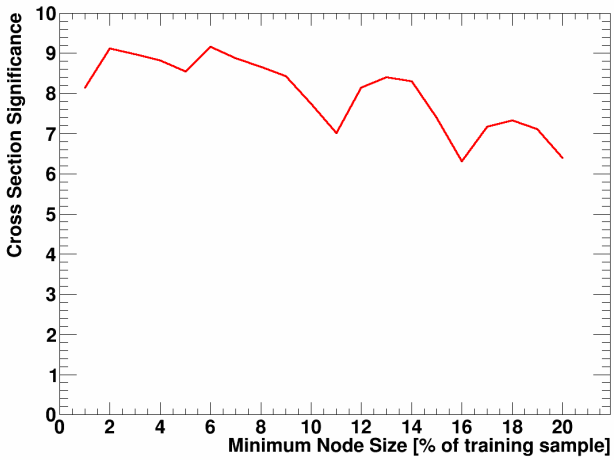

Figure 11.9: A plot of the CSS as a function of minimum node size. The value of 5% provides both a high CSS as well as not being subject to overtraining. The jagged nature of the plot is a result of the limited statistics in the training sample.

11.7.5 Depth of trees

The maximum tree depth is the parameter which controls how large the tree is allowed to grow, i.e. how many nodes it can have. The maximum number of nodes is given by

$$\text{Maximum \# of Nodes} = 2^{\text{Maximum Depth}} - 1. \tag{11.14}$$

A tree could have fewer than the maximum number of nodes if certain nodes have fewer than the minimum number of events necessary to continue the training algorithm (see Section 11.7.4). At the maximum depth, all nodes automatically become leaves and are classified by their purity. Limiting the depth to which a tree can grow is one method that can help reduce the amount of overtraining in a BDT. The maximum tree depth parameter was scanned from 2 to 7 and a plot of the CSS as a function of the maximum depth can be seen in Figure 11.10. A maximum depth of 4 was chosen as it lead to the highest performing BDT.

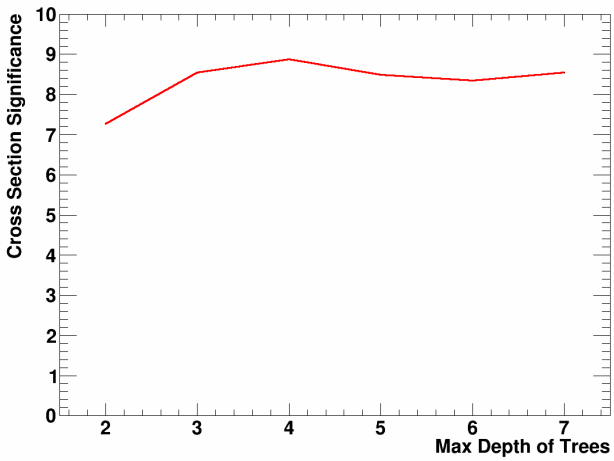

Figure 11.10: A plot of the CSS as a function maximum tree depth allowed. A maximum tree depth of 3 was chosen as it provides both a high CSS as well as not being subject to overtraining.

11.7.6 AdaBoost parameter

The effect of the boosting parameter of the AdaBoost algorithm, β, can be seen in Equation 11.7. The boosting weight, α_n, is a measure of how fast the algorithm learns from one tree to the next. If α_n is high, then the algorithm places greater importance on correctly classifying previously incorrectly classified events. The lower the value of β, the lower the value of α_n becomes. As an overall scaling factor of the boosting weight, β is a way to control how fast the algorithm learns from its previous mistakes. Learning at a slower rate allows for more boosting cycles and can help limit overtraining. The value of β was scanned between 0.05 and 2.0 in steps of 0.05. The plot of the CSS as a function of β can be seen in Figure 11.11. A value of 0.5 was chosen for β.

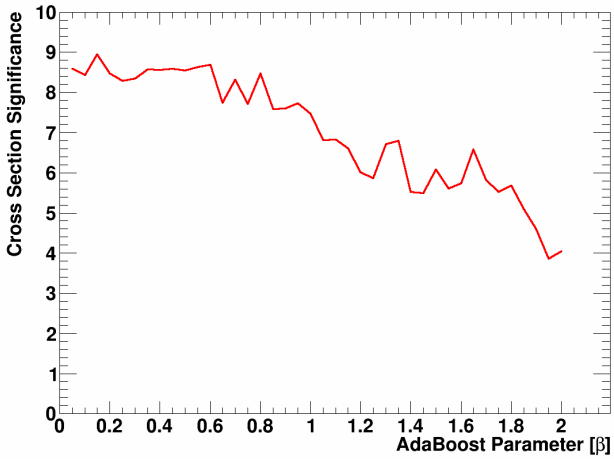

Figure 11.11: A plot of the CSS as a function of the boosting parameter, β. The value of $\beta = 0.5$ provides both a high CSS as well as not being subject to overtraining.

11.7.7 Number of gridpoints for variable cuts

In the node splitting step of the training algorithm the BDT attempts to find the variable and associated cut which gives the largest increase in the separation index between the parent

node and its two daughter nodes. In order to do this, the BDT must be told what size steps in which to scan over the variables' distributions. Choosing too coarse of a granularity and the ability to see differences between signal and background shapes becomes difficult. There is, however, no drawback to making the granularity as fine as the user would like other than an increase in computing time. The number of grid points chosen for this analysis was taken to be 200, which is the maximum that the TMVA program allows.

11.7.8 Input variable selection

One of the first steps in developing a well-performing DT is to determine what discriminating variables to use. Variables should be chosen with a high discriminating power in order to fully exploit the differences between signal and background events but the addition of well-modeled variables with less does not degrade the performance of the BDT. The training algorithm does not know it is a poorly performing variable until it attempts to calculate the change in the separation index but the inclusion of poorly performing variables does no damage. It simply slows down the training algorithm and increases the computational load. There are several metrics which can be used to determine whether or not a variable does well in separating signal from background. The method chosen in this analysis was to map the signal efficiency, ϵ_{sig}, to the background rejection, $(1 - \epsilon_{\text{bkg}})$, for a series of cuts on a particular variable and to take the area of the shape between the resultant curve and the line $\epsilon_{\text{sig}} = (1 - \epsilon_{\text{bkg}})$. The maximum area this shape can encompass is 0.5 and corresponds to the case of 100% signal efficiency and 100% background rejection across the the entire cut range.

As can be seen in Figures 11.12(b) and 11.12(d) the variables $\Delta\text{R}(\ell, b)$ and $E_{\text{T}}^{\text{miss}}$ do well to discriminate the background processes from the 700 GeV signal sample. These types of plots

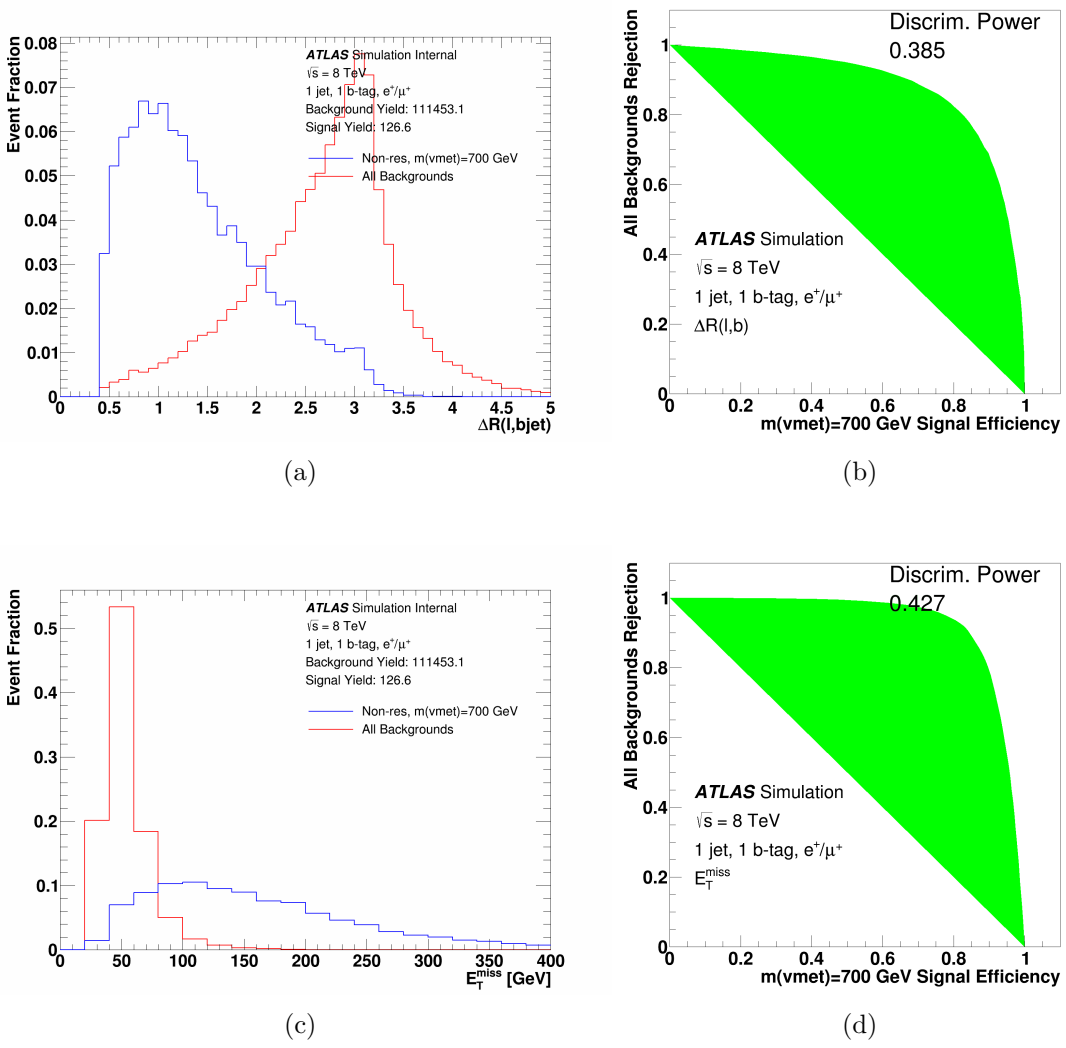

Figure 11.12: On the left are shown distributions normalized to unity of (a) $\Delta\mathrm{R}(\ell, b)$ and (c) $E_{\mathrm{T}}^{\mathrm{miss}}$ for the background processes and the 700 GeV non-resonant signal sample. On the right are shown plots of the signal efficiency and background rejection mapping for the background processes and the 700 GeV non-resonant signal sample as a function of successive cuts on (b) $\Delta\mathrm{R}(\ell, b)$ and (d) $E_{\mathrm{T}}^{\mathrm{miss}}$.

are generated by calculating the signal efficiency and background rejection for different cut values of the discriminating variable (ΔR(ℓ, b) and $m_{\mathrm{T}}(\ell, E_{\mathrm{T}}^{\mathrm{miss}})$ in the case of Figure 11.12). A plot showing the discriminating power of all the different variables used in the analysis at each the 17 mass point signal samples is shown in Figure 11.13. There is a clear trend that the angular variables as well as $m_{\mathrm{T}}(\ell, E_{\mathrm{T}}^{\mathrm{miss}})$ and $E_{\mathrm{T}}^{\mathrm{miss}}$ provide higher discriminating power as the mass v_{met} particle is increased. Additional plots showing the discriminating power of the input variables for individual background processes are shown in Appendix G.

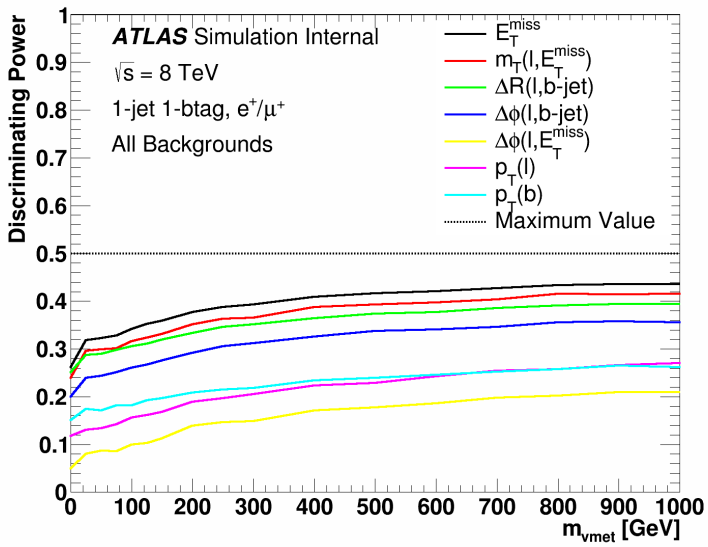

Figure 11.13: The discriminating power of the input variables of the BDT as a function of the mass of the v_{met} particle.

The final list of variables used as inputs in the BDT training is shown below.

- $\boldsymbol{E_{\mathrm{T}}^{\mathrm{miss}}}$ – The total amount of missing transverse energy in the event.
- $\boldsymbol{m_{\mathrm{T}}(\ell, E_{\mathrm{T}}^{\mathrm{miss}})}$ – The transverse mass of the lepton and the missing transverse energy which is given by

$$m_{\mathrm{T}}(\ell, E_{\mathrm{T}}^{\mathrm{miss}}) = \sqrt{2p_{\mathrm{T}}(\ell)E_{\mathrm{T}}^{\mathrm{miss}}\left[1 - \cos\Big(\Delta\phi(\ell, E_{\mathrm{T}}^{\mathrm{miss}})\Big)\right]}. \tag{11.15}$$

- $\boldsymbol{\Delta R(\ell, b)}$ – The separation in $\eta - \phi$ space of the lepton and b-jet.
- $\boldsymbol{\Delta\phi(\ell, b)}$ – The azimuthal separation of the lepton and b-jet.
- $\boldsymbol{\Delta\phi(\ell, E_T^{miss})}$ – The azimuthal separation of the lepton and the missing transverse energy vector.
- $\boldsymbol{p_T(\ell)}$ – The transverse momentum of the lepton.
- $\boldsymbol{p_T(b)}$ – The transverse momentum of the b-jet.

11.7.9 Choice of signal sample

The 700 GeV monotop signal sample is used to train the BDT in this analysis and was motivated by the current mass exclusion limit of 657 GeV with an effective coupling strength of 0.2 [37]. Training and optimizing 17 different BDTs on the 17 different mass point signal samples would have been cumbersome and redundant and generating BDTs on the samples whose masses had already been excluded was unnecessary. As such, the signal sample corresponding to the mass of the v_{met} particle closest to the current mass exclusion limit was chosen.

11.8 Discriminant output

The summary of optimized BDT parameters is presented in Table 11.1 and the final BDT output discriminant variable is shown in Figure 11.14. Signal events (shown in blue) have values which are closer to +1 while background events (shown in red) have values which are closer to −1. The background events with values close to −1 are easily separated from the signal events. Background events which have values greater than zero tend to be the events

which are harder to separate from signal events. Those backgrounds with similar final state topologies as the signal will tend to look more signal-like.

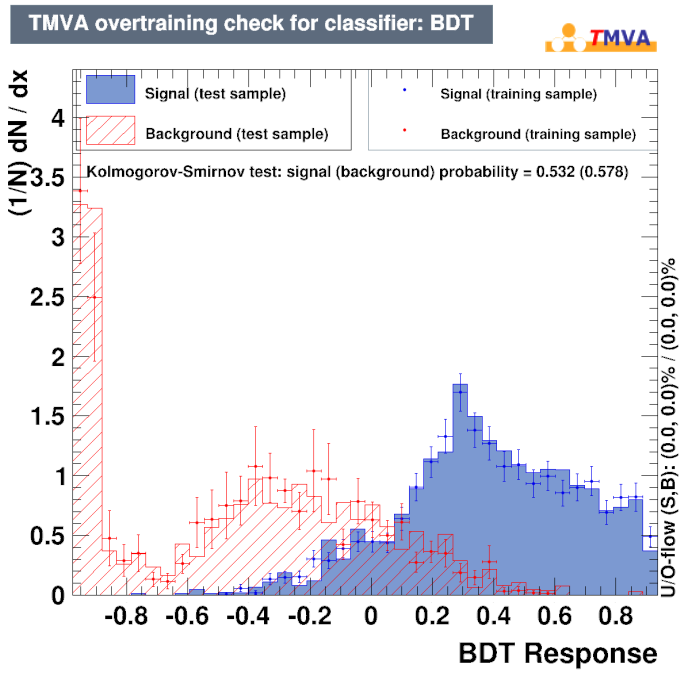

Figure 11.14: A plot of the BDT discriminant output with the optimized parameters shown in Table 11.1. The plot shows the value of the BDT response variable for the testing samples (solid and hashed filled plots) as well as for the training samples (point entries) for both signal (blue) and for background (red). The vertical error bars show the statistical uncertainties in the training samples.

Figure 11.15 shows the shape of the BDT discriminant for various backgrounds and the 700 GeV signal sample. As is shown in the figure, the backgrounds are peaked closer to a value of -1 while the signal peaks more towards $+1$. The red curve represents the $t\bar{t}$ background and is the most prominent background in the last bin (the most signal-like bin). This can be attributed to dilepton $t\bar{t}$ events where two neutrinos are present which increases the $E_{\mathrm{T}}^{\mathrm{miss}}$ of the event and makes it look more like the signal. The solid (dashed) blue line represents the single-top t-channel (Wt-channel) process. The t-channel process only has one neutrino in the event from the decay of the W and so the $E_{\mathrm{T}}^{\mathrm{miss}}$ is kinematically constrained to values below the W mass. Consequently, the discriminant value for the t-channel process

does not extend far into the signal-like region of the distribution where one would expect high $E_{\mathrm{T}}^{\mathrm{miss}}$. The Wt-channel, however, can have two neutrinos in an event which allows the $E_{\mathrm{T}}^{\mathrm{miss}}$ to reach higher values and thus be more difficult to separate from the signal. The $W+$ jets processes are represented by the green curve. Their extremely large cross-sections as compared to the other backgrounds allow for more events to populate the tails of their distributions. It is these events that end up in the signal-like region of the discriminant distribution.

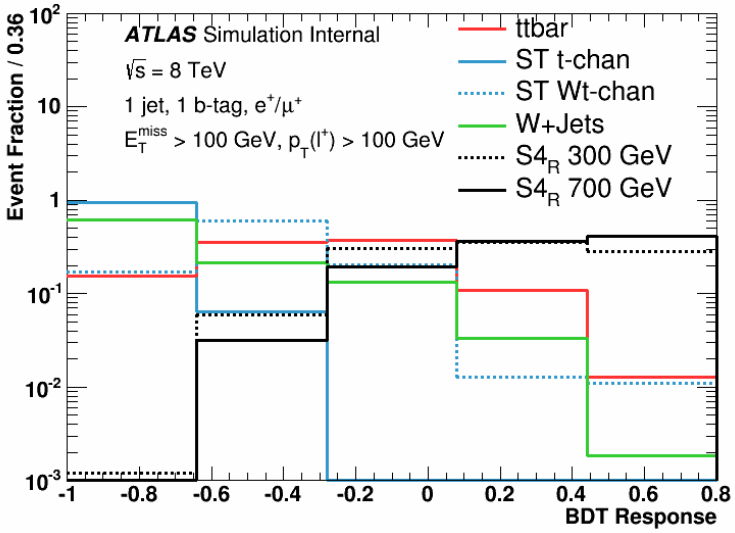

Figure 11.15: A plot of the BDT discriminant output normalized to unity for various individual backgrounds and the 300 and 700 GeV signal sample.

Optimized BDT Parameters	
Parameter	**Value**
Number of trees	50
Separation Index	Gini
Minimum leaf size	5%
Maximum depth	4
AdaBoost parameter	0.5
Number of gridpoints for cut	200

Table 11.1: A summary of the BDT parameters used in this analysis.

11.9 Summary

After properly training and optimizing a BDT for the search of non-resonant monotop events, the logic encoded in the BDT was applied to data as well as to the monotop signal and the expected SM backgrounds. This can be seen in Figure 11.16.

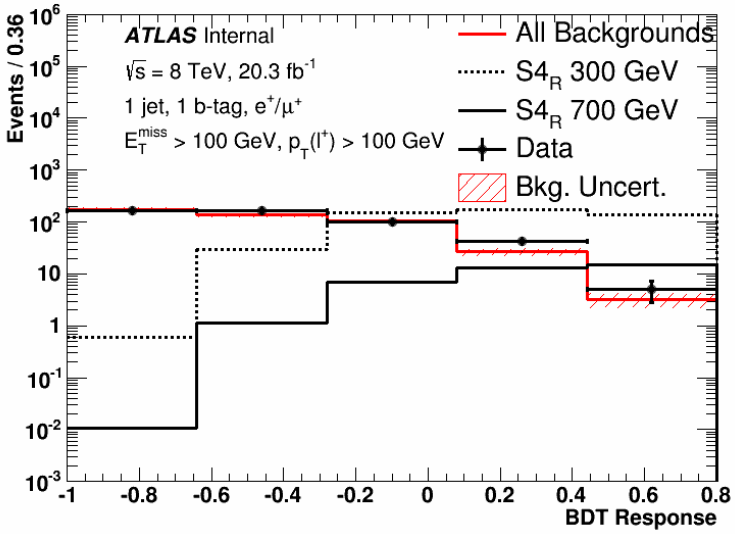

Figure 11.16: A plot of the BDT discriminant output for the SM backgrounds, the 300 and 700 GeV signal samples, and data. The uncertainties include statistical uncertainties only.

The BDT distribution of data events closely matches that of the background in the first three bins of Figure 11.16. This shows that the backgrounds were modeled appropriately as it is expected that little separation should be seen in these bins. In the last two bins, the "signal-like bins," the data begins to separate from the expected background showing signs that some other process might be contributing to the data. In order to ascertain whether this slight excess in data can be attributed to the monotop signal or simply a statistical fluctuation, an analysis utilizing all systematic and statistical uncertainties outlined in Chapter 8 was performed. The methodology detailed in Chapter 9 was applied to the distributions to perform such an analysis, the results of which are shown in Chapter 12.

Chapter 12

8 TeV BDT Results

The results of the BDT re-analysis are presented in this chapter. The same limit setting procedure used in the cut-based analysis was used to calculate 95% CL limits on the production cross-section times branching ratio and coupling parameter.

12.1 BDT re-analysis results

The results of the limit setting procedure for the $S4_R$ model utilizing the BDT re-analysis as described in Chapter 11 are shown in Figures 12.1 and 12.2 with the corresponding values listed in Table 12.1.

12.2 Summary

Through the use of a BDT, masses of the v_{met} particle were able to be excluded up to 799 GeV for the $S4_R$ model. This represents a 22% improvement in the mass exclusion of the $S4_R$ model over the original analysis completed in 2014 and is the strongest limit placed on the production of a single-top quark in association with a BSM neutral particle for the 8 TeV running of the LHC. The following chapter will summarize the 8 TeV results for all of the different analysis strategies.

BDT $S4_R$ Limits					
	Theory, LO	**Expected 95% CL**		**Observed 95% CL**	
$m(v_{\text{met}})$ **[GeV]**	$(a_R = 0.2)$ **[pb]**	$\sigma\times$ **BR [pb]**	a_R	$\sigma\times$ **BR [pb]**	a_R
0	96.0	2.72	0.034	2.25	0.031
25	359.0	2.26	0.016	1.91	0.015
50	113.4	1.72	0.025	1.53	0.023
75	59.9	1.30	0.029	1.08	0.027
100	37.5	1.03	0.033	0.92	0.031
125	25.7	0.79	0.035	0.69	0.033
150	18.0	0.71	0.040	0.59	0.036
200	9.66	0.45	0.043	0.39	0.040
250	5.51	0.33	0.049	0.28	0.045
300	3.33	0.29	0.059	0.24	0.053
400	1.37	0.21	0.077	0.17	0.071
500	0.63	0.15	0.907	0.13	0.090
600	0.32	0.14	0.134	0.11	0.118
700	0.17	0.12	0.169	0.10	0.157
800	0.09	0.11	0.217	0.09	0.200
900	0.06	0.10	0.268	0.09	0.249
1000	0.03	0.09	0.331	0.08	0.312

Table 12.1: Expected and observed 95% CL limits on the production cross-section times branching ratio and coupling parameter as a function of the mass of the v_{met} particle for the $S4_R$ model in the combined electron/muon channel for the BDT analysis. The LO theoretical predictions and limits on $\sigma \times$ BR are shown for a coupling value of $a_R = 0.2$.

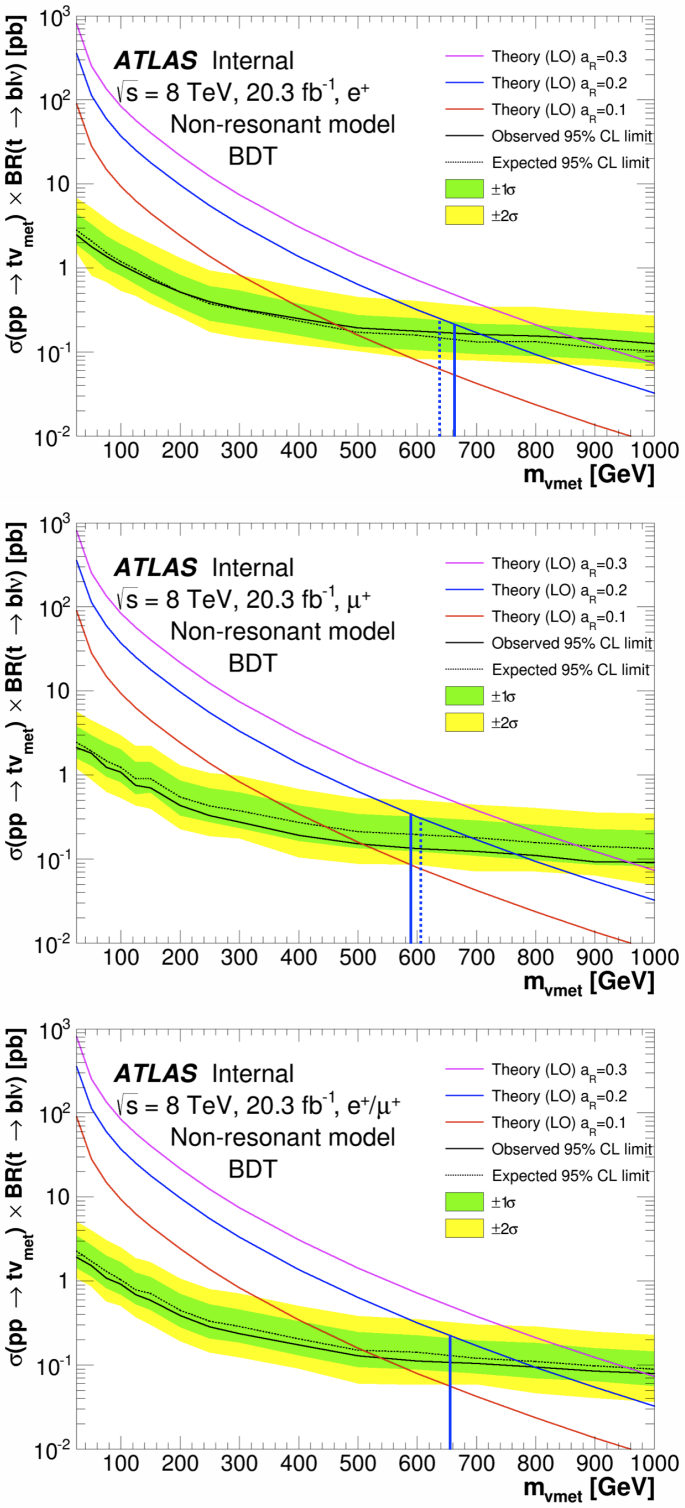

Figure 12.1: Expected and observed 95% CL limits on the cross-section times branching ratio for the $S4_R$ model in the electron (top), muon (middle), and combined electron/muon channel (bottom) for the BDT analysis. The predicted LO cross-section times branching ratio values are shown for different values of a_R. The solid (dashed) vertical blue line indicates the observed (expected) 95% CL mass exclusion limit from the published cut-based analysis for a coupling value of $a_R = 0.2$.

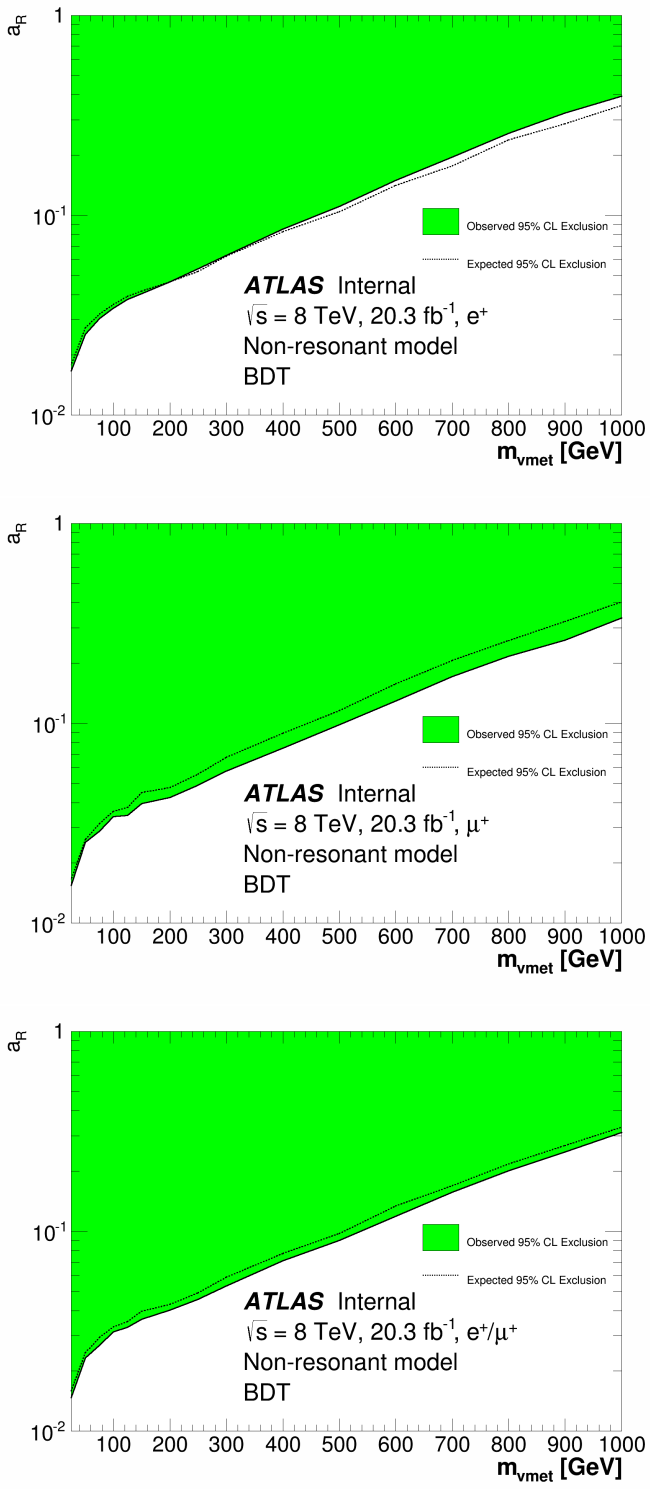

Figure 12.2: Expected and observed 95% CL limits on the coupling parameter, a_{R}, for the $\mathrm{S4_R}$ model in the electron (top), muon (middle), and combined electron/muon channel (bottom) for the BDT analysis.

Chapter 13

Summary of 8 TeV Results

This chapter summarizes all of the results of the different analyses conducted at 8 TeV in this dissertation:

- **Cut-based** – This was the first analysis conducted at the LHC in the search for monotop events and was published in 2014. This analysis was able to exclude the $S1_R$ model across the entirety of the mass range of the f_{met} particle for coupling strength greater than 0.13 and the $S4_R$ model for masses of the v_{met} particle up to 657 GeV for a coupling strength equal to 0.2.

- **Cut-based with lepton charge cut selection** – This was an augmentation of the original cut-based analysis with the additional selection on the electric charge of the lepton and was able to improve the $S4_R$ result to 734 GeV.

- **BDT re-analysis** – This analysis used a Boosted Decision Tree and was able to further improve the mass exclusion limit on the $S4_R$ model to 799 GeV.

These results are summarized in Table 13.1. Figure 13.1 shows the 95% CL on cross-section times branching ratio and coupling parameter, a_R, for the cut-based plus charge cut and BDT analyses as compared to the baseline cut-based analysis for the $S4_R$ model. As the figure shows, the additional cut on the charge of lepton improves the sensitivity of the cut-based analysis fairly equally across the entirety of the mass range. As the BDT was optimized

with the 700 GeV signal sample, the fact that it performs worse than the cut-based approach in the low mass region is to be expected. The BDT, however, out-performs the cut-based analysis (both with and without a lepton charge cut) in the ostensibly more-interesting high mass region where the cut-based approach was unable to set limits.

Analysis Channel	**Expected 95% CL $v_{\mathbf{met}}$ mass limit [GeV]**			**Observed 95% CL $v_{\mathbf{met}}$ mass limit [GeV]**		
	Cut-Based		BDT	Cut-Based		BDT
	published result	+ lepton charge cut		published result	+ lepton charge cut	
Electron	639	698	749	662	691	711
Muon	606	664	692	589	685	774
Combined	657	714	775	657	734	799

Table 13.1: Expected and observed 95% CL limits on the mass of the v_{met} particle for the $\mathrm{S4_R}$ model in the electron, muon, and combined electron/muon channels. Mass exclusions for the cut-based analysis, the cut-based analysis with an additional cut on the electric charge of the lepton, and for the BDT analysis are shown. Results are shown for the case where $a_{\mathrm{R}} = 0.2$.

These results represent the definitive conclusions regarding the likelihood of a single-top quark produced with a missing BSM neutral particle using the Run1 dataset of the LHC. These results were augmented by further refinements of the published values through the introduction of an electric charge selection of the lepton and the Boosted Decision Tree re-analysis of the data. The next logical step in the evolution of the search for monotop events is then to analyze data created at a higher center-of-mass energy and with considerably more total integrated luminosity. Chapter 14 will show the first-look at monotop production at 13 TeV and will make predictions for the sensitivity of this analysis at values of total integrated luminosity expected in the future.

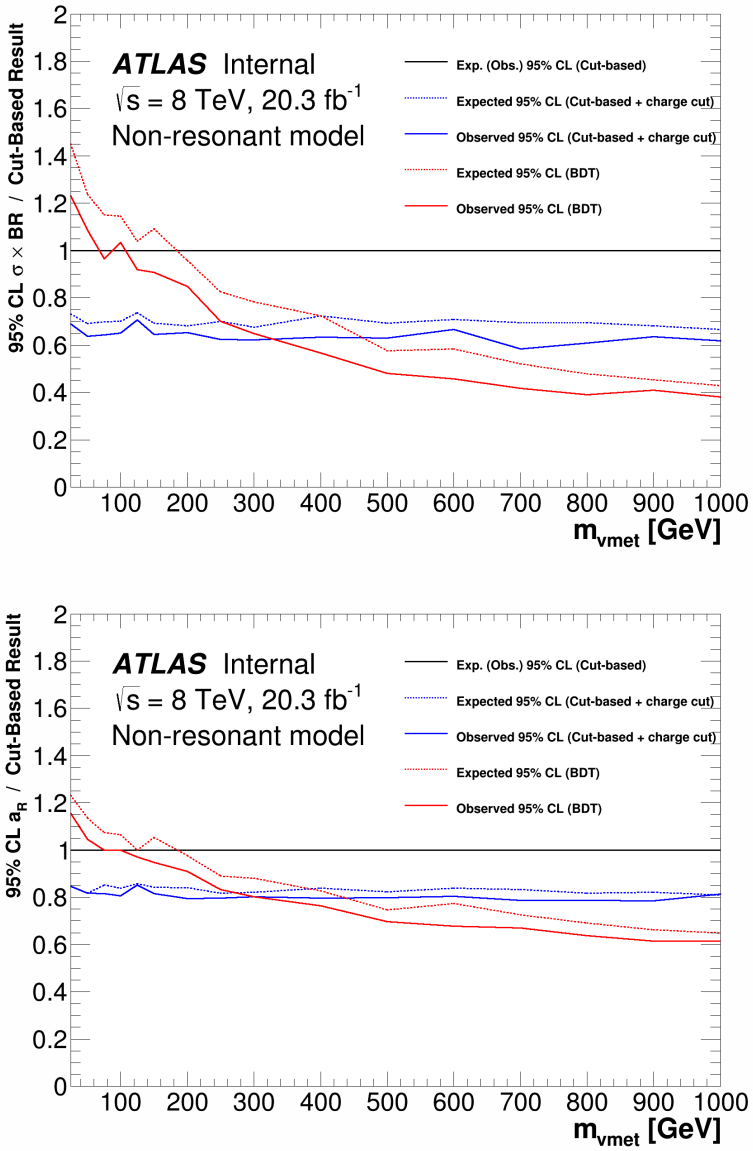

Figure 13.1: A comparison of the different 95% CL limits on cross-section times branching ratio (top) and coupling parameter (bottom) in the combined electron/muon channel. The curves show the expected and observed limits for the cut-based analysis with an additional cut on the electric charge of the lepton (blue) and the BDT analysis (red) as compared to the published cut-based analysis results (black).

Chapter 14

Monotop at 13 TeV

The limits presented in this dissertation using collision data collected at $\sqrt{s} = 8$ TeV represent the most sensitive limits set on the production of monotop events at a collider to date. The natural extension of this analysis is to utilize data collected at the current LHC center-of-mass energy of 13 TeV to either trigger a discovery or to further push the limits to higher masses of the v_{met} particle. This chapter describes an analysis done using simulated signal and background samples generated at a center-of-mass energy of 13 TeV to elucidate what future analyses could expect as the amount of total integrated luminosity increases during Run2 and beyond. This analysis at 13 TeV follows the same methodologies used in the 8 TeV BDT re-analysis to optimize both event selection and BDT parameterization.

14.1 Signal simulation

Monotop signal samples for the $S4_R$ model were generated at 13 TeV with MadGraph and showered/hadronized with Pythia8 for masses of the v_{met} particle ranging from 0 to 2.5 TeV and a coupling value of $a_R = 0.2$, the cross-sections of which are shown in Table 14.1.

14.2 Background simulation

The following 13 TeV MC background simulations were used in this analysis:

Model	Mass [GeV]	$\sigma \times$ BR ($t \to \ell\nu b$) [pb]
$S4_R$	0	197.58
	25	777.29
	50	245.13
	75	130.60
	100	82.93
	150	41.32
	200	23.41
	250	14.19
	300	9.08
	500	2.15
	750	0.55
	1000	0.18
	1250	0.069
	1500	0.030
	1750	0.014
	2000	0.0067
	2250	0.0034
	2500	0.0018

Table 14.1: The cross-section times branching ratios for the monotop signal samples produced at 13 TeV for a coupling value of $a_R = 0.2$. The second column indicates the mass of the v_{met} particle.

- $t\bar{t}$ – Generated with POWHEG and showered with PYTHIA6.
- **Single-top** – All single-top processes (s-, t-, and Wt-channels) were generated with POWHEG and showered with PYTHIA6.
- W/Z**+jets** – Generated and showered with SHERPA v2.2.
- **Dibosons** – Generated and showered with SHERPA v2.1.

No multijet estimate was available at the time of this analysis. However, as will be discussed in later sections, this lack of a multijet estimate was expected to be insignificant in the region of phase space which the analysis used to perform the BDT analysis.

14.3 Event pre-selection

Events were initially pre-selected to include exactly 1 b-tagged jet, 1 lepton, and $E_{\mathrm{T}}^{\mathrm{miss}} > 35$ GeV. The $p_{\mathrm{T}}(\ell)$ and $E_{\mathrm{T}}^{\mathrm{miss}}$ distributions for the pre-selection region are shown in Figure 14.1. Multijet events are characterized by low values of $E_{\mathrm{T}}^{\mathrm{miss}}$ and the lack of a multijet estimate shows up as an excess in data in regions with $E_{\mathrm{T}}^{\mathrm{miss}} < 75$ GeV. Similarly, the $p_{\mathrm{T}}(\ell)$ spectrum shows an excess in the data which can also attributed to a lack of a multijet estimate. For comparison, the distributions in the same pre-selection region of $p_{\mathrm{T}}(\ell)$ and $E_{\mathrm{T}}^{\mathrm{miss}}$ without multijet events are shown for the 8 TeV samples in Figure 14.2. Similar Data/MC discrepancies are seen in the 8 TeV distributions as the 13 TeV distributions when multijet events are excluded.

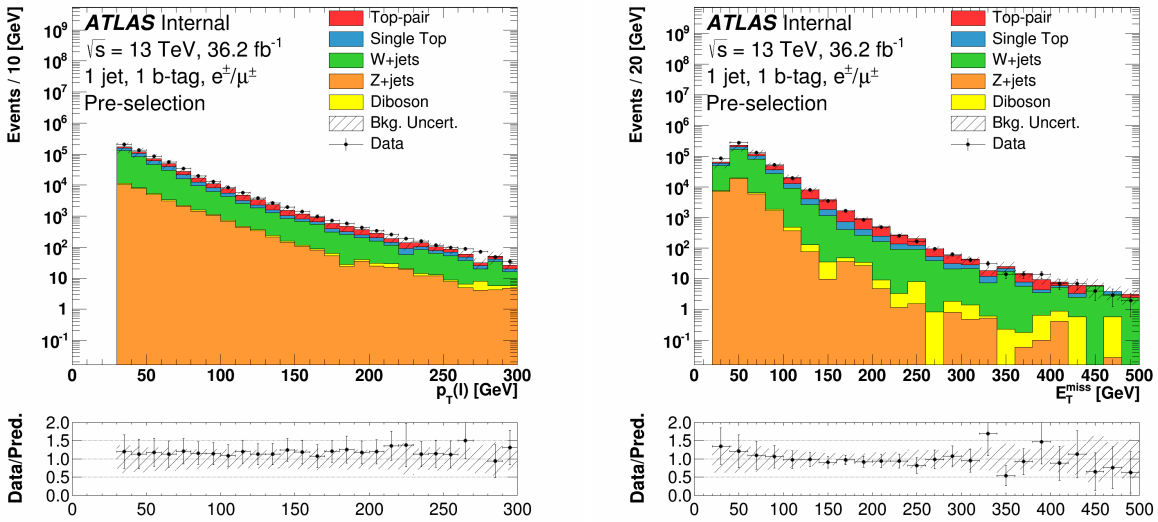

Figure 14.1: The distributions of $p_{\mathrm{T}}(\ell)$ (left) and $E_{\mathrm{T}}^{\mathrm{miss}}$ (right) in the pre-selection region. The uncertainty band on the expected background corresponds to the errors due to the statistical uncertainties added in quadrature with the cross-section and normalization uncertainties.

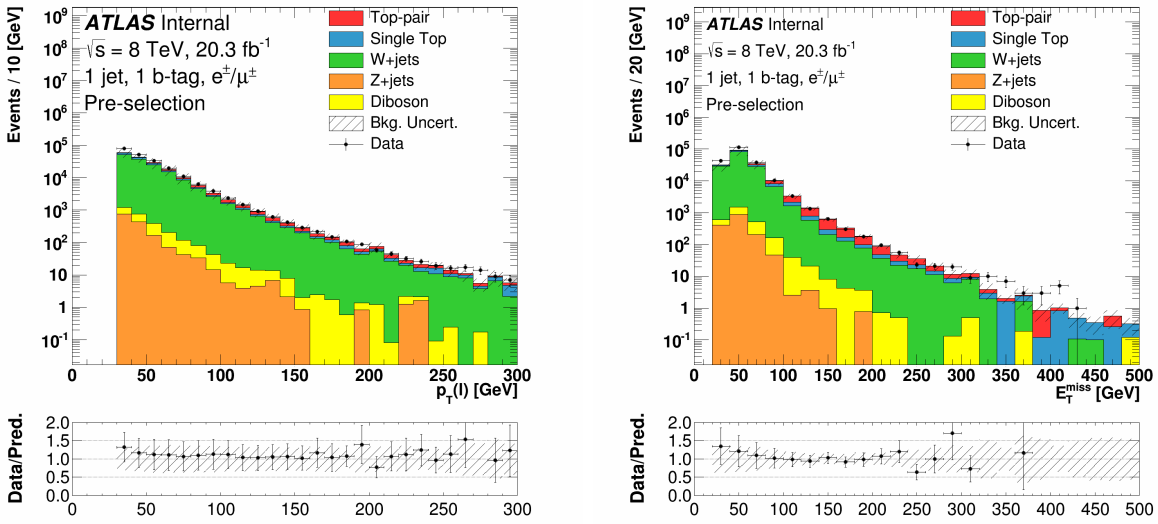

Figure 14.2: The distributions of $p_{\mathrm{T}}(\ell)$ (left) and $E_{\mathrm{T}}^{\mathrm{miss}}$ (right) in the pre-selection region for the 8 TeV samples with multijet events not included. Similar disagreement between data and MC can be seen here as in Figure 14.1.

14.4 BDT signal region

In order to optimize the event selection for use in a BDT analysis $p_{\mathrm{T}}(\ell)$ and $E_{\mathrm{T}}^{\mathrm{miss}}$ were used to select events which were topologically and kinematically similar to monotop events. In addition to these two variables, events were selected which had a positively charged lepton in the final state. Figure 14.3 shows the cross-section significance as a function of cuts on $p_{\mathrm{T}}(\ell^{+})$ and $E_{\mathrm{T}}^{\mathrm{miss}}$. As the figure shows, a cut requiring $p_{\mathrm{T}}(\ell^{+}) > 100$ GeV and $E_{\mathrm{T}}^{\mathrm{miss}} > 175$ GeV serves to increase the CSS of the selected events. Cutting any harsher on either $p_{\mathrm{T}}(\ell^{+})$ or $E_{\mathrm{T}}^{\mathrm{miss}}$ does not raise the CSS significantly and can be seen directly in Figure 14.4 where those two cuts have already been made. The BDT signal region is then defined as having

- exactly one b-tagged jet,
- exactly one positively charged lepton with $p_{\mathrm{T}} > 100$ GeV, and
- $E_{\mathrm{T}}^{\mathrm{miss}} > 175$ GeV.

In the 8 TeV analysis the multijet contributed only 2% to the event yield in the BDT selection region. In the 13 TeV analysis the contribution of multijet events in the BDT selection region was expected to be at the 2% level or lower as the $E_{\mathrm{T}}^{\mathrm{miss}}$ cut of 175 GeV would likely have removed all but a few multijet events. As such, the lack of a multijet estimate is not a significant effect.

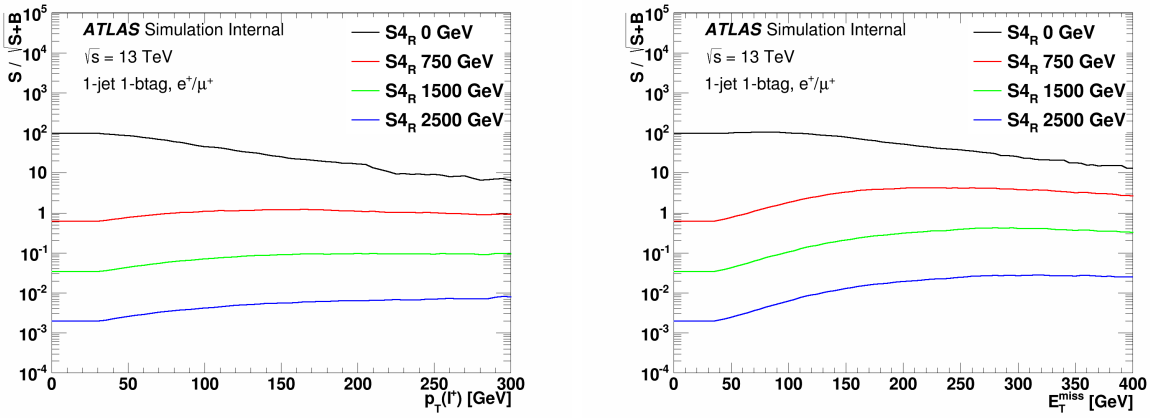

Figure 14.3: The CSS as a function of a cut on $p_{\mathrm{T}}(\ell^{+})$ (left) and $E_{\mathrm{T}}^{\mathrm{miss}}$ (right) for various values of the v_{met} particle's mass.

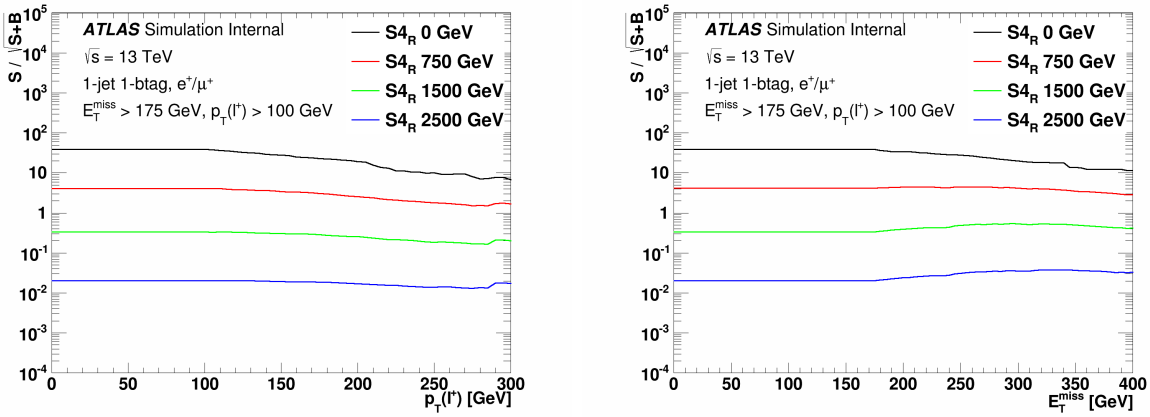

(a) (b)

Figure 14.4: The CSS calculated with for various mass points of the v_{met} particle in the $\mathrm{S4_R}$ as a function of a cut on (a) $p_{\mathrm{T}}(\ell^{+})$ and (b) $E_{\mathrm{T}}^{\mathrm{miss}}$ with explicit cuts of $E_{\mathrm{T}}^{\mathrm{miss}} > 175$ GeV and $p_{\mathrm{T}}(\ell^{+}) > 100$ GeV applied.

14.5 BDT optimization

The same procedure for the optimization of the BDT parameters at 8 TeV was utilized for the 13 TeV analysis. The BDT parameters were optimized with the 750 GeV signal sample along with the available background estimates. The cross-sectional significance was used as the defining metric in determining the optimal values when scanning over the different BDT parameters. The results of the scans are shown in Figure 14.5 and summarized in Table 14.2.

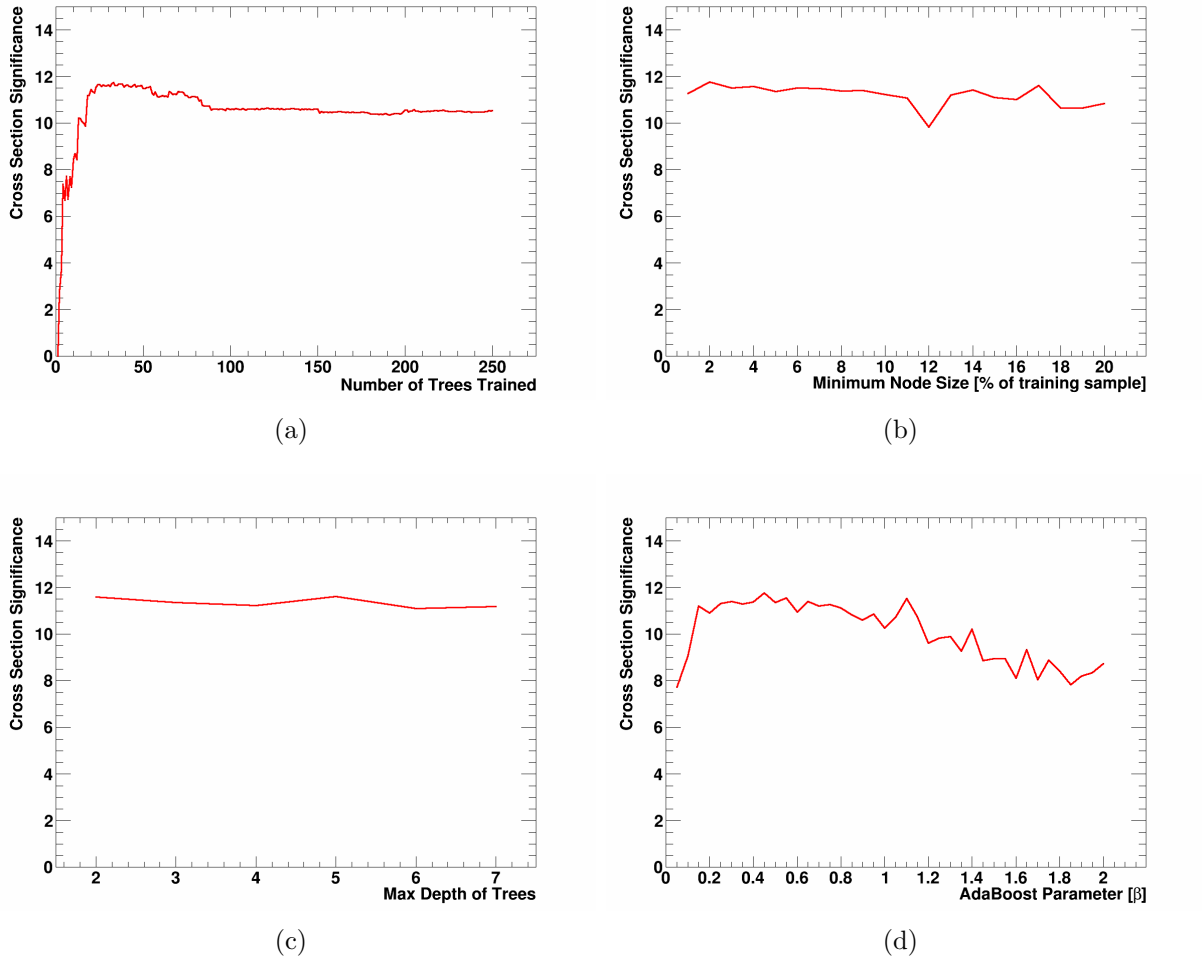

Figure 14.5: A plot of the CSS as a function of the (a) number of trees trained in the BDT, (b) the minimum node size, (c) the maximum tree depth allowed, and (d) the boosting parameter, β.

Optimized BDT Parameters	
Parameter	**Value**
Number of trees	48
Separation Index	Gini
Minimum leaf size	5%
Maximum depth	3
AdaBoost parameter	0.6
Number of gridpoints for cut	200

Table 14.2: A summary of the BDT parameters used in the 13 TeV analysis.

14.6 Discriminant shape

The resultant BDT discriminate shape is shown in Figure 14.6.

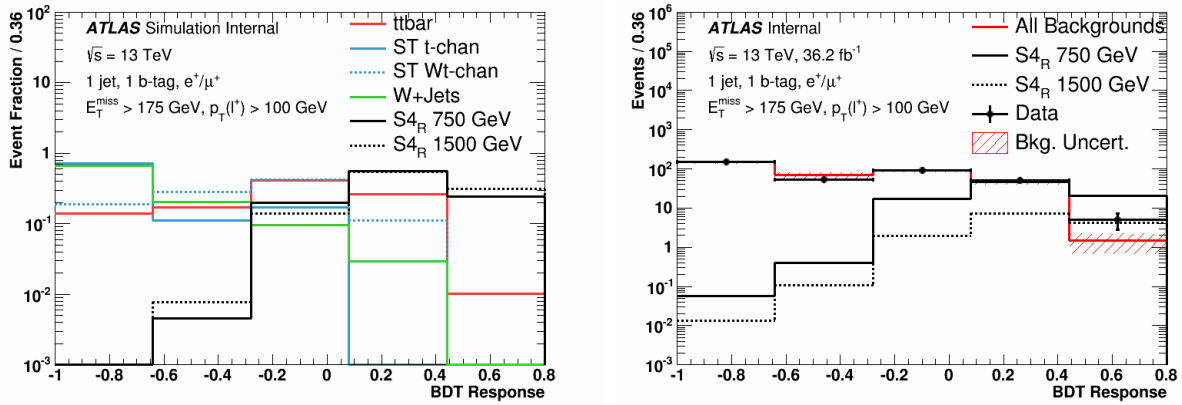

(a) (b)

Figure 14.6: (a) A plot of the BDT discriminant variable normalized to unity for various individual backgrounds and the 750 and 1500 GeV signal samples. (b) A plot of BDT discriminant output for the SM backgrounds, the 750 and 1500 GeV signal samples, and 36.2 fb^{-1} of data collected during Run2 of the LHC at 13 TeV. The uncertainties are statistical uncertainties only.

14.7 Systematic uncertainties

Unlike the analyses done at 8 TeV, the full slate of systematic uncertainties was not used in the 13 TeV analysis. Instead, a parameterization was used in which the effect of systematic

uncertainties was estimated and applied as a normalization uncertainty to the backgrounds and signal samples independently. For this parameterization Table 8.3 was used. In the 8 TeV BDT re-analysis of the data the total relative systematic uncertainties of the background and signal samples were roughly 20% and 10% respectively. The events selected in the 8 TeV BDT re-analysis occupy a similar region of phase-space as the 13 TeV BDT analysis and so the relative systematic uncertainties calculated at 8 TeV were applied to the 13 TeV event selection. This parameterization was not ideal and likely an over-estimate of the true uncertainties, but it served as a baseline estimate.

14.8 Statistical uncertainties

Consider a MC sample generated with N events, which models a process with a cross-section of σ, and scaled to a luminosity $\mathcal{L}$. Each event in such a sample would have an event weight, w, given by

$$w = \frac{\sigma\mathcal{L}}{N}. \tag{14.1}$$

The statistical uncertainty after selecting events with efficiency ϵ is then the sum in quadrature of the squared weights of the selected events,

$$\begin{aligned} \sigma_{\text{stat}} &= \sqrt{\sum_{1}^{N\epsilon} w^2} \\ &= \sigma\mathcal{L}\sqrt{\frac{\epsilon}{N}}. \end{aligned} \tag{14.2}$$

The relative statistical uncertainty is then the statistical uncertainty divided by the number

of selected events,

$$\frac{\sigma_{\text{stat}}}{N\epsilon} = \frac{\sigma\mathcal{L}}{N^{3/2}\sqrt{\epsilon}}. \tag{14.3}$$

Equation 14.3 shows that MC samples describing processes with large cross-sections require a large number of generated events so that statistical uncertainties do not overwhelm the search. Likewise, when trying to give predictions of a search at higher luminosities it is necessary to use samples with an increasing number of generated events. Figure 14.7 shows the relative statistical uncertainty of the $t\bar{t}$ sample as a function of total integrated luminosity for various samples sizes and selection efficiencies. As the luminosity is increased the relative statistical uncertainty grows and at 313 fb^{-1} becomes unity for a sample produced with one million events with a 2% selection efficiency (dashed red curve in Figure 14.7).

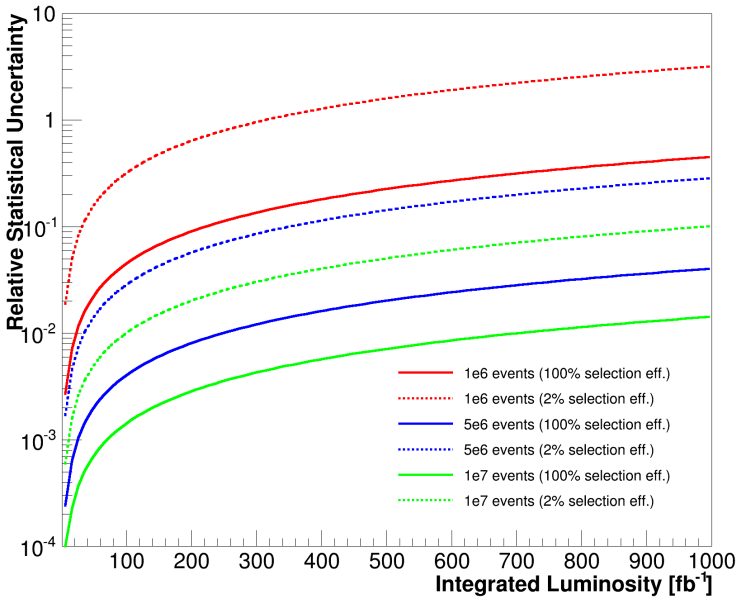

Figure 14.7: The relative statistical uncertainty of a sample with $\sigma = 451.7$ pb generated with various numbers of events and selection efficiencies as a function of total integrated luminosity.

If an analysis has a 5% relative statistical uncertainty at luminosity $\mathcal{L}_0$, then in order to

maintain that same level of relative statistical uncertainty at $10\mathcal{L}_0$ the same analysis would require samples which had $10^{2/3} = 4.6$ times as many events. This is not feasible given the current computational limitations of event generation. In Run1 of the LHC, ATLAS did not experience multiple orders of magnitude increase in integrated luminosity. At the end of Run2, however, it is expected that the experiment will collect 150 fb^{-1} of data and later runs will likely reach thousands of inverse femtobarns of data. The current level of MC-generated statistics will not sufficiently describe the data set expected beyond Run2. In order to give predictions at these levels of total integrated luminosity while working with the current MC samples generated at fixed numbers of events, three different methods were used:

- **No statistical uncertainties** – The effects of the statistical uncertainties were turned off in the limit setting procedure which treats MC samples as if they have an infinite number of generated events. This method gives the maximum expected limit one would expect and is treated here as the "best-case" scenario.

- **"Standard" method** – The current MC statistics were used in the limit setting procedure at each value of luminosity. The statistical uncertainties were calculated with Equation 14.2 and grow linearly with luminosity. This method is an under-estimation of the power of the analysis as the effects of the limited sample sizes drastically reduce the sensitivity of the search at high levels of integrated luminosity.

- **"Idiogram" method** – In this method the effect of increasing the statistics of the MC samples is mimicked. A Gaussian probability distribution function is generated on an event-by-event basis with the value of the BDT discriminant as the mean and a standard deviation of 1/4 the bin-width. For each event, a discriminant value is randomly generated from the Gaussian x number of times and events are then re-

weighted by $\frac{1}{x}$, effectively reducing the statistical uncertainties by a factor of $\sqrt{x}$. In this way the overall number of events is increased and the subsequent statistical uncertainties decrease in a consistent way. This method gives an estimation of the expected limits by parameterizing the factor by which the sample sizes are increased. In this analysis a factor of 10 was chosen.

14.8.1 Validating the idiogram method

In order to validate the idiogram method two tests were conducted:

- **Test 1** – The idiogram method was performed on 10% of MC events but sampling 10 times from the distribution function each event. This resultant expected limits were compared to the "standard" method, the results of which are shown in Figure 14.8(a). It was expected that increasing the statistics with the idiogram method by a factor of 10 while only using 10% of the total number of events available (green curve) should give similar results as the standard method (blue curve). The agreement between the two methods in figure shows that this test was validated.

- **Test 2** – The resolution of the BDT discriminant variable was examined by changing the value of the standard deviation of the distribution function from which the added events were sampled and comparing the resultant expected limits. The results are shown in Figure 14.8(b). Values of the standard deviation smaller than 1/4 of the bin width converge to give similar results.

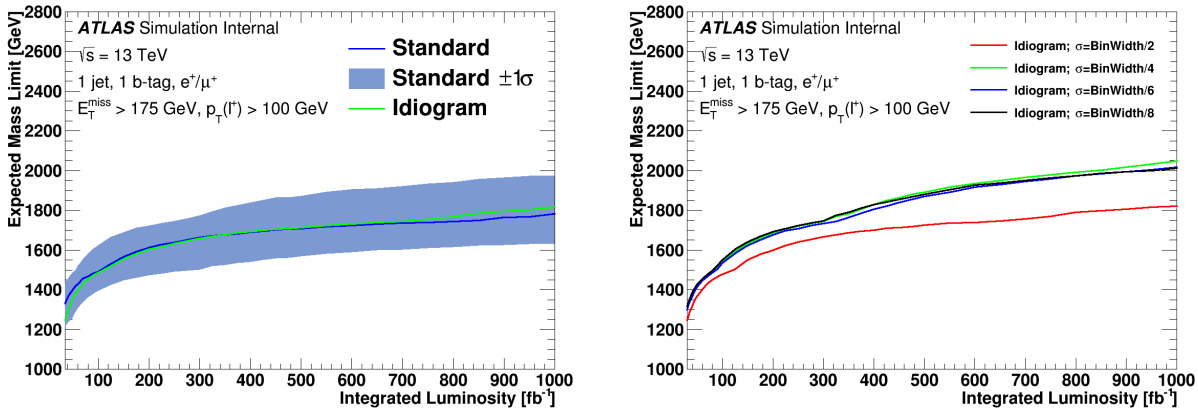

(a) (b)

Figure 14.8: (a) Expected limits as a function of total integrated luminosity for the standard application of statistical uncertainties (dark blue line) and the idiogram method with a 10x factor and only using 10% of the samples' events (green line). The $\pm 1\sigma$ band for the standard case is shown in light blue. The standard application and the idiogram method show good agreement and validates the first test. (b) Expected limits as a function of total integrated luminosity for the idiogram method for various choice of the standard deviation of the Gaussian distribution function. While using $\sigma = \text{BinWidth}/2$ proved to be too large for the choice for the standard deviation, the other values converged to give the same results.

14.9 Results

The limit setting procedure outlined in Chapter 9 was performed for each of the individual mass hypotheses in the $S4_R$ model. As a first extrapolation, the entirety of Run2 was used, which is expected to reach 150 fb^{-1} by the end of 2018. The 95% CL limits on the cross-section times branching ratio at this amount of data is shown in Figure 14.9, suggesting that the expected mass-exclusion limit could reach 1500 GeV, almost doubling the limit set at 8 TeV.

Expected 95% CL limits were also calculated for the cross-section times branching ratio for values of total integrated luminosity up to 1000 fb^{-1}, which includes the early running of the High-Luminosity LHC period of the mid 2020s, and are shown in Figure 14.10.[1] Limits

[1]The High-Luminosity LHC project is designed to increase the instantaneous luminosity of the LHC beams to 5-7 times their nominal values and is planned to be installed during Long Shutdown 3 (LS3) from

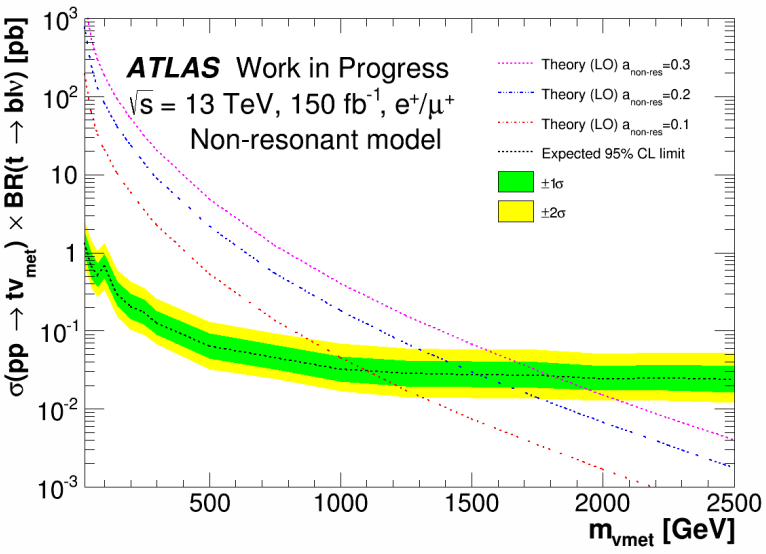

Figure 14.9: Expected 13 TeV limits on the monotop production cross-section times branching ratio at 150 fb^{-1}.

were calculated for the following cases:

- **No uncertainties** – The effects of both statistical and systematic uncertainties were turned off in the limit setting procedure (black curve).
- **"Standard" uncertainties** – Expected limits were calculated with statistical uncertainties only, systematic uncertainties only, and with both statistical and systematic uncertainties (blue, red, and magenta curves respectively).
- **"Idiogram" method** – The idiogram method was used with and without the effects of systematic uncertainties (dashed green and solid green curves respectively).

The degree to which the Stat+Sys (magenta) and Stat-only (blue) curves overlap shows that this analysis is statistically limited at high levels of integrated luminosity. This is also evident by the fact that the Sys-only (red) curve gives more sensitive limits than the Stat-only (blue)

2024 to mid 2026.

curve. Increasing the the number of statistics by a factor of 10 with the idiogram method improves the sensitivity of the search as expected.

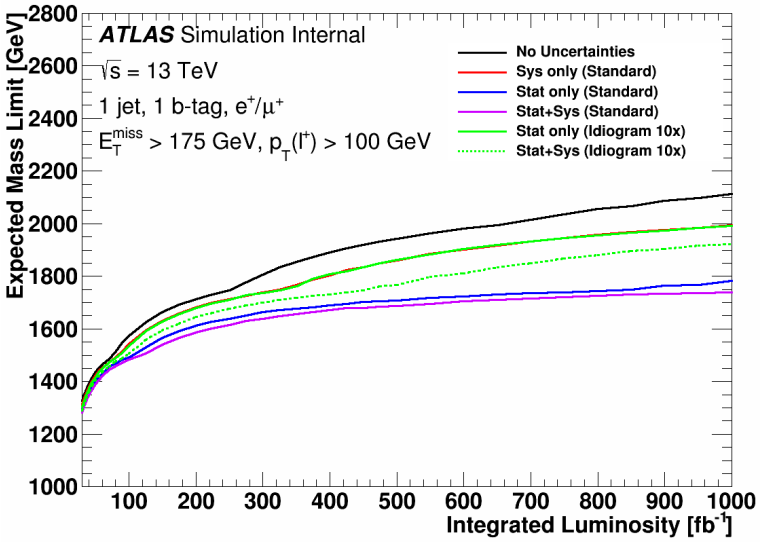

Figure 14.10: Expected 13 TeV limits as a function of total integrated luminosity.

Collecting more data allows the collaboration to better understand the detector's response and improves the modeling of the backgrounds. As such, it is expected that as more data is collected the relative systematic uncertainties in an analysis will decrease. Figure 14.11 shows the expected 95% CL limits with the relative systematic uncertainties of the samples scaled as a function of integrated luminosity. For this figure the relative systematic uncertainties (20% for background samples and 10% for signal samples) are scaled by the factor $\sqrt{\mathcal{L}_0/\mathcal{L}}$ where $\mathcal{L}_0 = 30$ fb^{-1}. In this way the effects of the systematic uncertainties decrease as more data is collected and the expected limits quickly approach the "stat-only" limits.

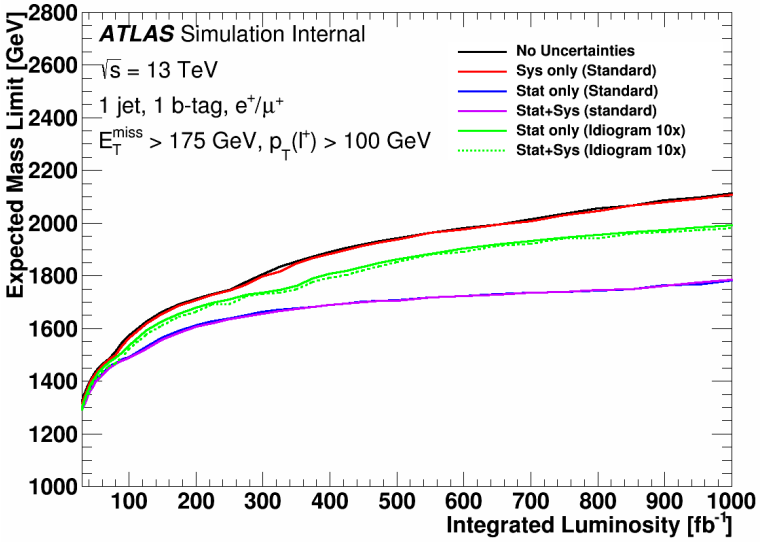

Figure 14.11: Expected 13 TeV limits as a function of total integrated luminosity with the relative systematic uncertainty scaled as $\sqrt{\mathcal{L}_0/\mathcal{L}}$ where $\mathcal{L}_0 = 30$ fb^{-1}

14.10 Conclusions

Table 14.3 shows the mass-exclusion limits for 150, 300, and 1000 fb^{-1} of expected data for the various methods used in this analysis. The limits on the production of monotop events are expected to further increase with increased data collected at 13 TeV. While future analyses will need to be updated at higher luminosities to optimize event selection and BDT parameterization, the expected limits generated with this analysis show that stronger limits will likely be placed on the production of monotop events in the future. It is also concluded that the amount of MC generated will need to increase in the future or risk being dominated by MC statistical uncertainties.

Expected 95% CL Mass-Exclusion Limits [GeV]							
$\int \mathcal{L}\,dt$ [fb^{-1}]	No Uncert.	Standard Method			Idiogram Method		
		Stat Only	Stat & Sys	Stat & Scaled-Sys	Stat Only	Stat & Sys	Stat & Scaled-Sys
150	1663	1567	1540	1558	1627	1593	1620
300	1806	1663	1639	1657	1737	1700	1734
1000	2114	1782	1740	1781	1991	1922	1989

Table 14.3: Expected mass-exclusion limits of the v_{met} particle for the various methods in this analysis. Values are shown for three different future values of total integrated luminosity: 150, 300, and 1000 fb^{-1}

Chapter 15

Conclusion

A search for single-top quarks produced in association with missing energy in proton-proton collisions at the Large Hadron Collider with a center-of-mass energy of $\sqrt{s} = 8$ TeV was presented in this dissertation. Both cut-based and multivariate analyses were performed in order to provide both expected and observed 95% CL limits on the monotop production cross-section times branching ratio.

The cut-based approach, which was the first monotop analysis using the ATLAS detector, was able to exclude the resonant $S1_R$ monotop model across the entirety of the mass range of the f_{met} particle for values of the coupling parameter greater than 0.13 and a resonance mass of 500 GeV as well as the non-resonant $S4_R$ model for masses of the v_{met} particle up to 657 GeV with a coupling value of 0.2. An augmentation of this analysis making use of a topological cut on the electric charge of the final state lepton improved the sensitivity of the search excluding masses of the v_{met} particle up to 734 GeV.

A re-analysis of the data making use of a Boosted Decision Tree multivariate analysis technique extended the mass-exclusion limits of the non-resonant model to 799 GeV. This limit represents the strongest limit a collider experiment has set to date on the production of monotop events.

The monotop topology remains a potential probe into physics Beyond the Standard Model. Predictions for the future of the monotop analysis at a center-of-mass energy of $\sqrt{s} = 13$ TeV

were also presented. Expected 95% CL limits on the production cross-section times branching ratio for the non-resonant model as a function of integrated luminosity show that the current level of MC production is not sufficient to describe the amount of data expected beyond Run2 of the LHC.

It is the opinion of the author of this dissertation that the ATLAS collaboration should continue with the monotop measurement in Run2. The monotop model still has many areas of parameter space which have yet to be excluded and these areas will be reachable with the increased center-of-mass beam energies and integrated luminosity expected in Run2 and beyond. The resources required to make this measurement are minimal in both person-power and MC event generation and are certainly worth the potential discovery of a signal.

APPENDICES

Appendix A

Comparison of the ATLFASTII and GEANT4 signal modeling

This appendix presents distributions comparing signal samples simulated with the fast simulation (ATLFASTII) and the full simulation (GEANT4). Distributions in the pre-selection region are shown for the $S1_R$ model for the mass of the f_{met} particle equal to 0 and 100 GeV and for the $S4_R$ model for the mass of the v_{met} particle equal to 0 and 1000 GeV in the combined electron and muon channel. In all plots the ATLFASTII simulation is labeled as AFII in the legend while the GEANT4 simulation is labeled as FS.
The two different simulations are consistent with each other when their statistical uncertainties are taken into account. While the tails of some of the distributions do show some degree of inconsistency, these inconsistencies can be attributed to a lack of statistics in those regions of phase-space. It can be concluded that the fast simulation for signal event generation sufficiently modeled the detector.

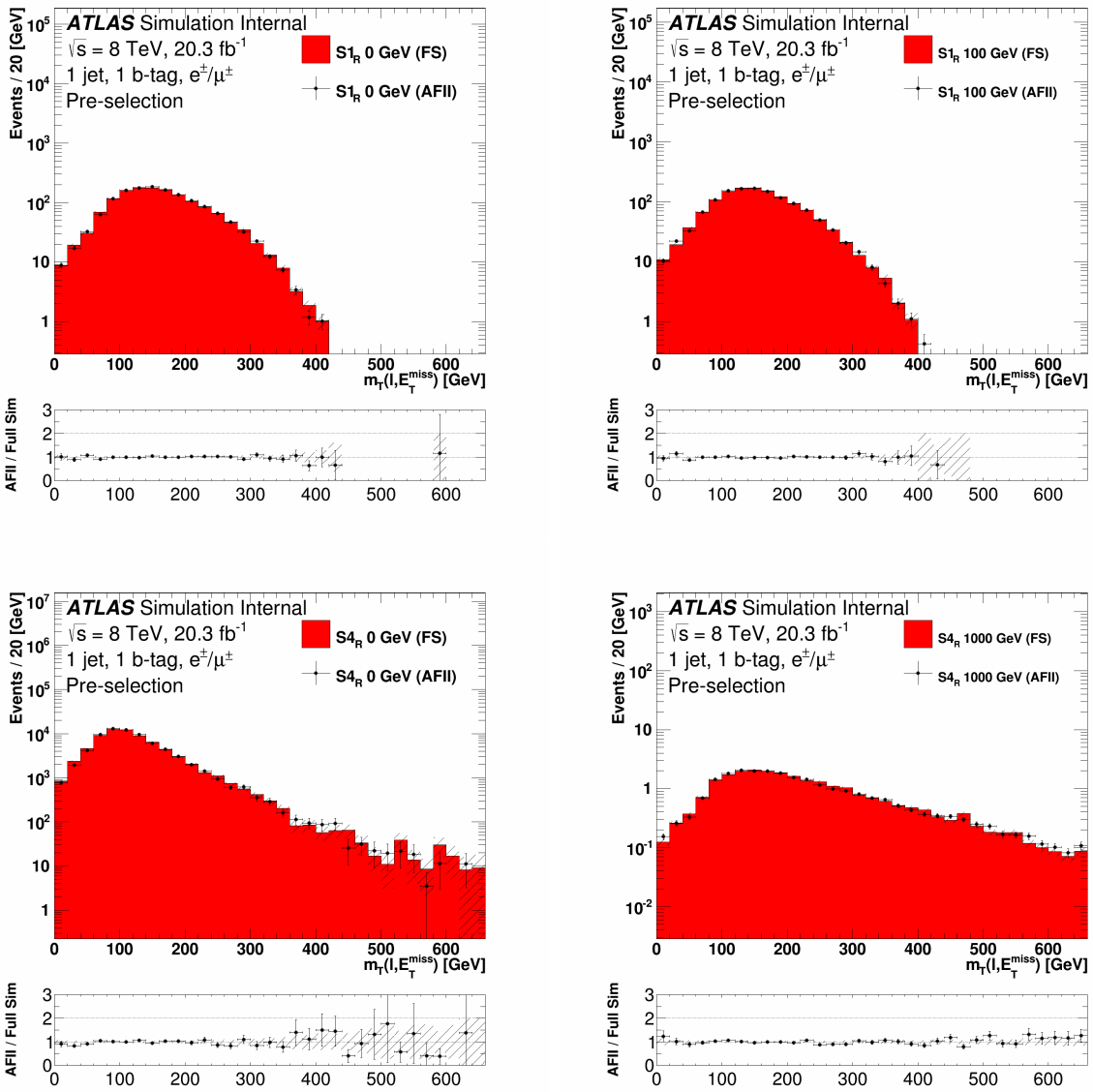

Figure A.1: Comparison of ATLFASTII and GEANT4 samples for the $m_{\mathrm{T}}(\ell, E_{\mathrm{T}}^{\mathrm{miss}})$ shape for the $\mathrm{S1_R}$ model with an f_{met} mass of 0 and 100 GeV and for $\mathrm{S4_R}$ model with a v_{met} mass of 0 and 1000 GeV in the pre-selection region. Plots are shown in the combined electron and muon channel. Uncertainties are statistical uncertainties only.

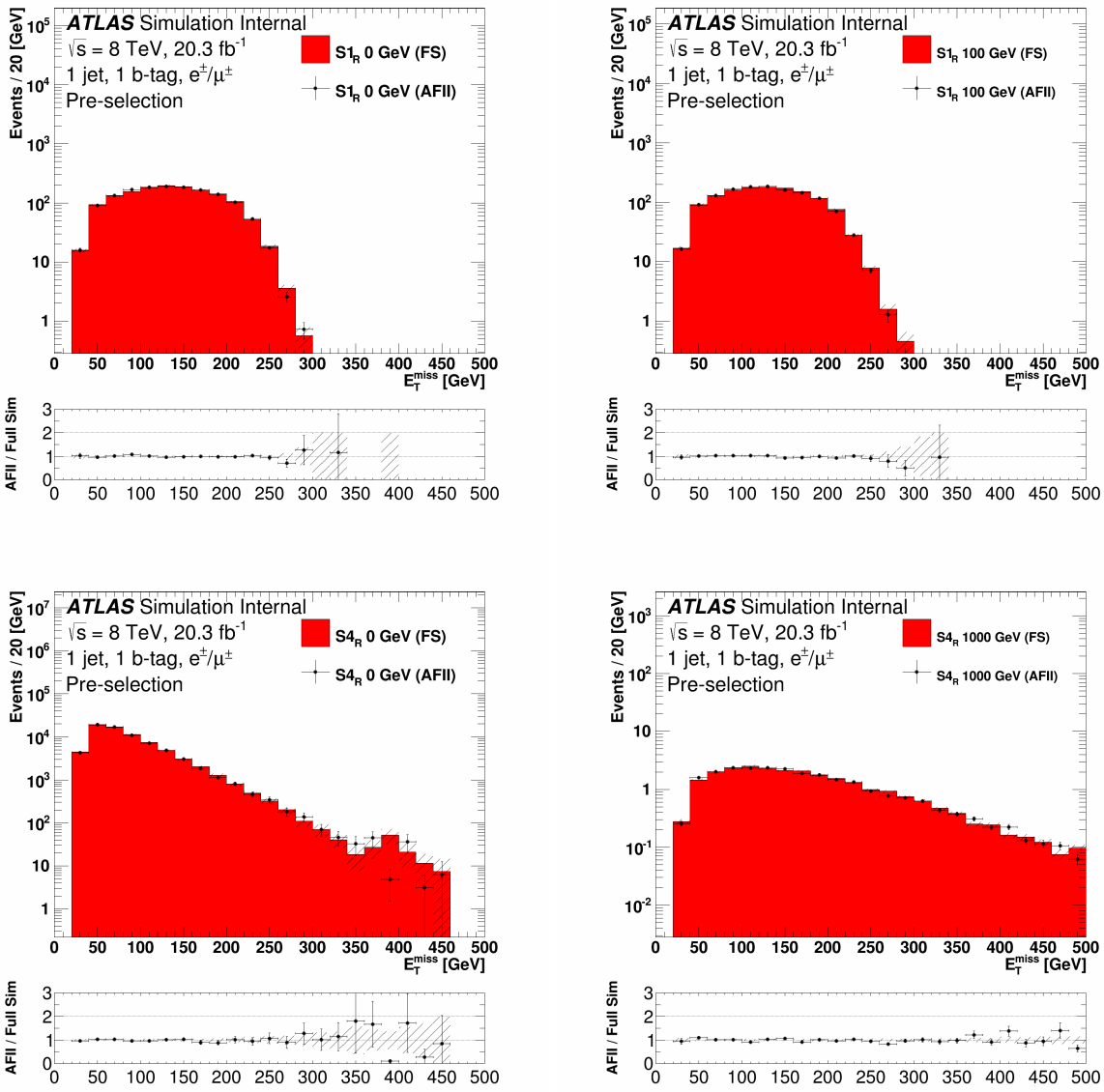

Figure A.2: Comparison of ATLFASTII and GEANT4 samples for the $E_{\mathrm{T}}^{\mathrm{miss}}$ shape for the $\mathrm{S1_R}$ model with an f_{met} mass of 0 and 100 GeV and for $\mathrm{S4_R}$ model with a v_{met} mass of 0 and 1000 GeV in the pre-selection region. Plots are shown in the combined electron and muon channel. Uncertainties are statistical uncertainties only.

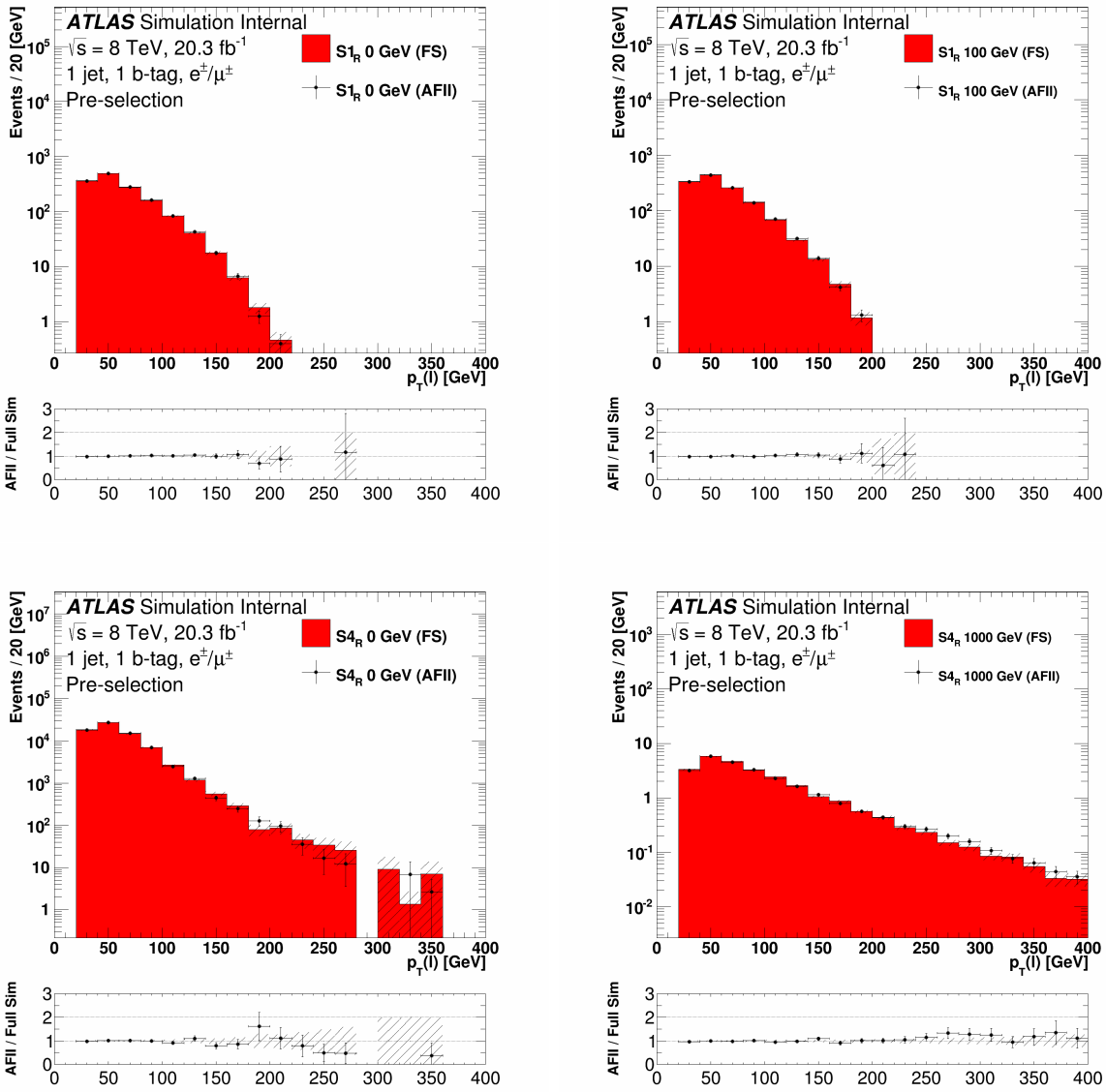

Figure A.3: Comparison of ATLFASTII and GEANT4 samples for the $p_{\mathrm{T}}(\ell)$ shape for the $\mathrm{S1_R}$ model with an f_{met} mass of 0 and 100 GeV and for $\mathrm{S4_R}$ model with a v_{met} mass of 0 and 1000 GeV in the pre-selection region. Plots are shown in the combined electron and muon channel. Uncertainties are statistical uncertainties only.

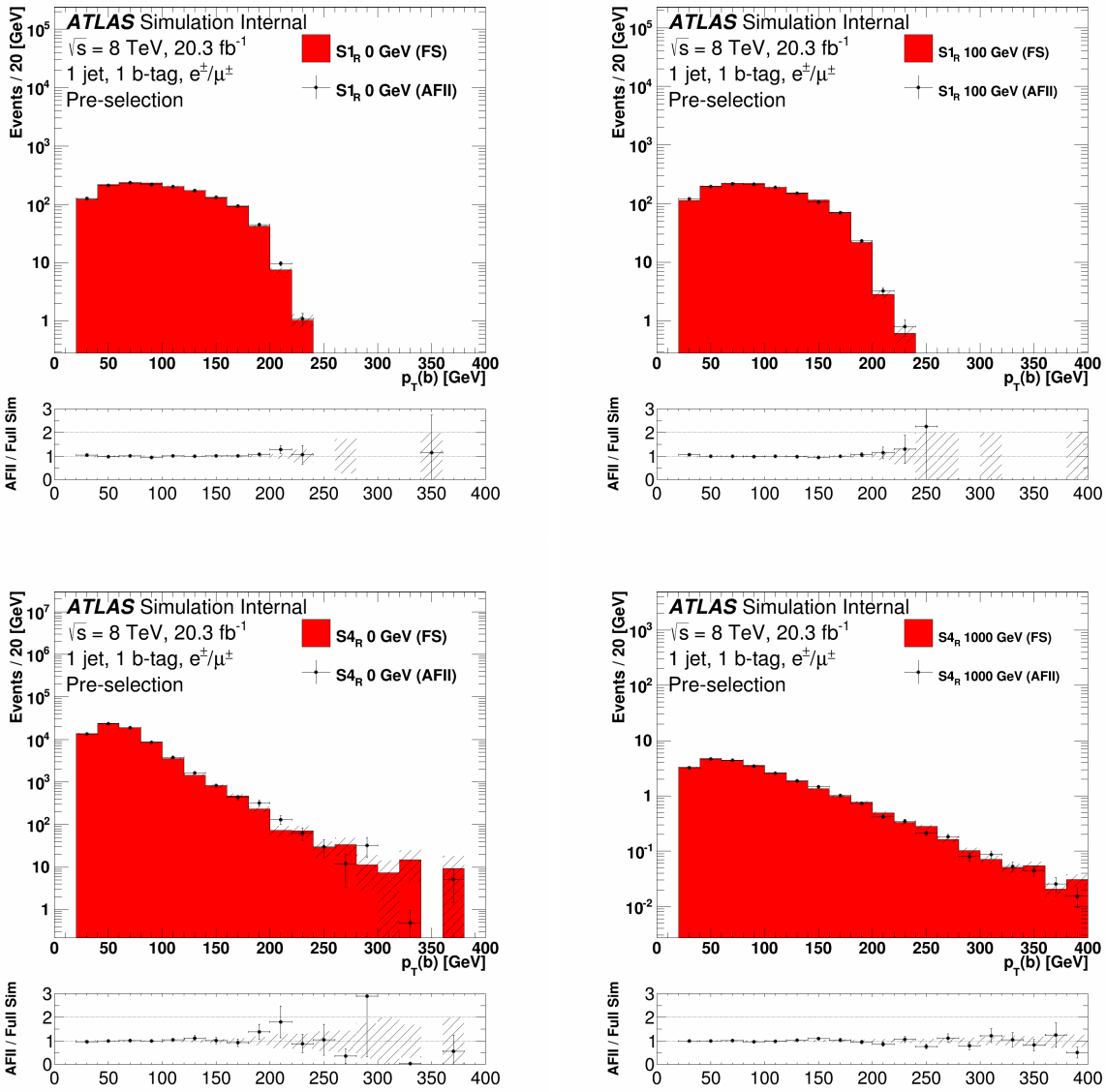

Figure A.4: Comparison of ATLFASTII and GEANT4 samples for the $p_{\mathrm{T}}(b)$ shape for the $\mathrm{S1_R}$ model with an f_{met} mass of 0 and 100 GeV and for $\mathrm{S4_R}$ model with a v_{met} mass of 0 and 1000 GeV in the pre-selection region. Plots are shown in the combined electron and muon channel. Uncertainties are statistical uncertainties only.

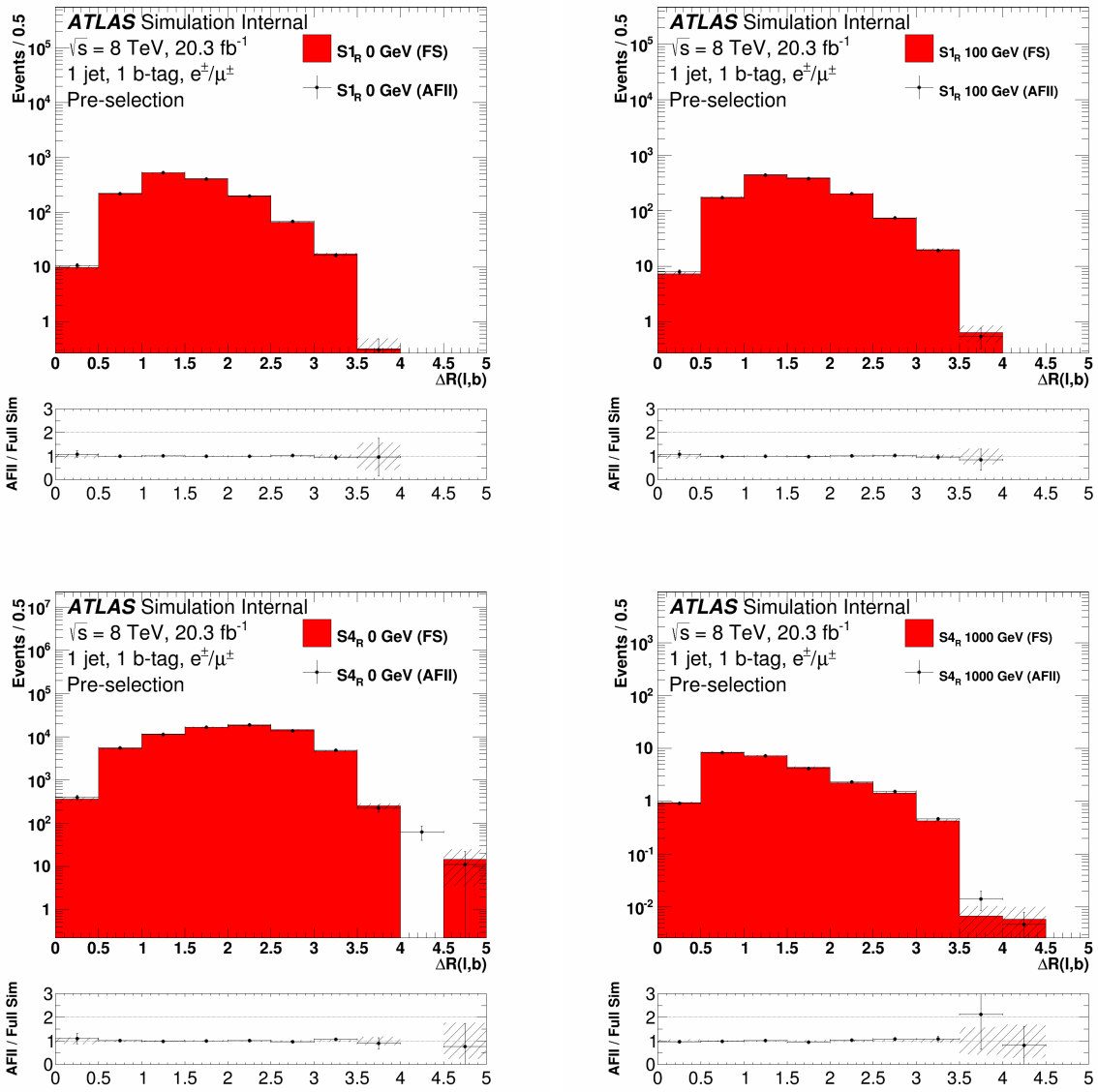

Figure A.5: Comparison of ATLFASTII and GEANT4 samples for the $\Delta R(\ell, b)$ shape for the $S1_R$ model with an f_{met} mass of 0 and 100 GeV and for $S4_R$ model with a v_{met} mass of 0 and 1000 GeV in the pre-selection region. Plots are shown in the combined electron and muon channel. Uncertainties are statistical uncertainties only.

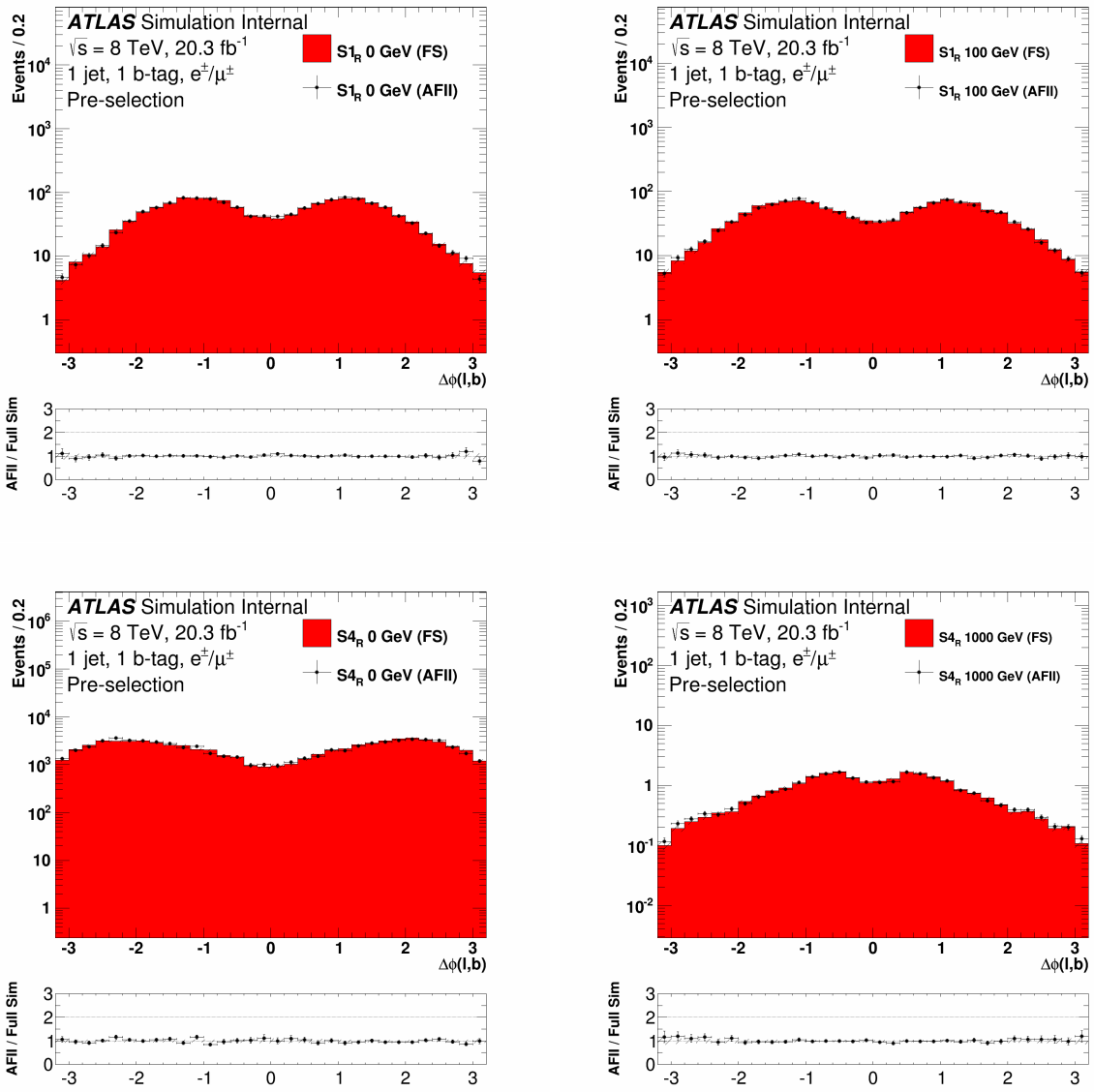

Figure A.6: Comparison of ATLFASTII and GEANT4 samples for the $\Delta\phi(\ell, b)$ shape for the $S1_R$ model with an f_{met} mass of 0 and 100 GeV and for $S4_R$ model with a v_{met} mass of 0 and 1000 GeV in the pre-selection region. Plots are shown in the combined electron and muon channel. Uncertainties are statistical uncertainties only.

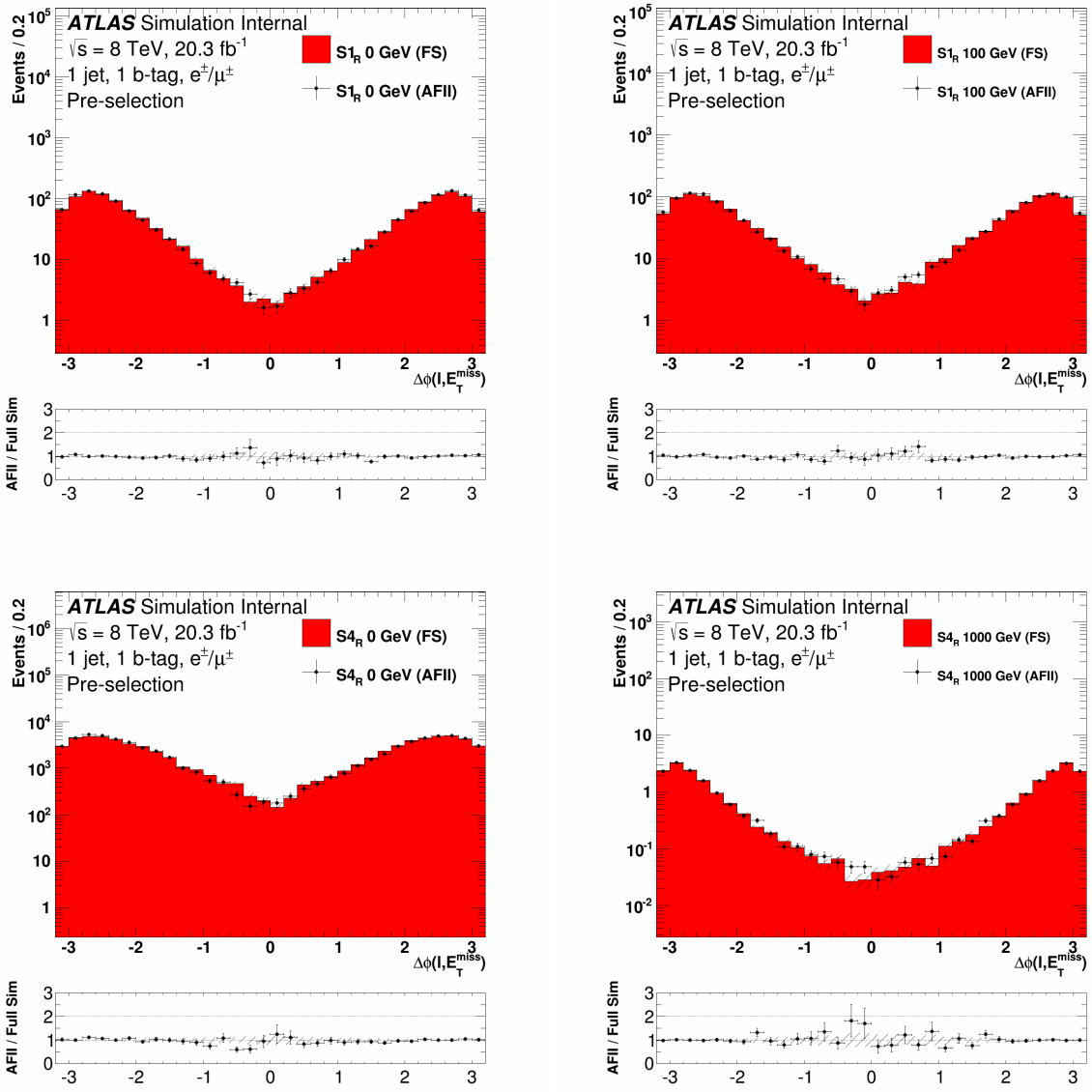

Figure A.7: Comparison of ATLFASTII and GEANT4 samples for the $\Delta\phi(\ell, E_{\mathrm{T}}^{\mathrm{miss}})$ shape for the $\mathrm{S1_R}$ model with an f_{met} mass of 0 and 100 GeV and for $\mathrm{S4_R}$ model with a v_{met} mass of 0 and 1000 GeV in the pre-selection region. Plots are shown in the combined electron and muon channel. Uncertainties are statistical uncertainties only.

Appendix B

8 TeV control region plots

This appendix presents plots comparing the SM predictions to the data observations in the various control regions. Distributions of the $m_{\mathrm{T}}(\ell, E_{\mathrm{T}}^{\mathrm{miss}})$, $E_{\mathrm{T}}^{\mathrm{miss}}$, $p_{\mathrm{T}}(\ell)$, $p_{\mathrm{T}}(b)$, $\Delta\mathrm{R}(\ell, b)$, $\Delta\phi(\ell, b)$, and $\Delta\phi(\ell, E_{\mathrm{T}}^{\mathrm{miss}})$ are shown in the pre-selection region (Section B), in CR1 (Section B), in CR2 (Section B), and in CR3 (Section B).

Pre-selection region

This section presents distributions of variables for simulated background and data events in the pre-selection region defined in Section 7.2. Shapes for the $S1_R$ model with an invisible particle mass of 100 GeV and the $S4_R$ model with an invisible particle mass of 700 GeV are also over-layed. Figures B.1 and B.2 show the transverse mass between the lepton and missing transverse energy, $m_T(\ell, E_T^{miss})$. Figures B.3 and B.4 show the missing transverse energy, E_T^{miss}. Figures B.5 and B.6 show the transverse momentum of the lepton, $p_T(\ell)$. Figures B.7 and B.8 show the transverse momentum of the b-jet, $p_T(b)$. Figures B.9 and B.10 show the spatial separation in $\eta-\phi$ space between the lepton and b-jet, $\Delta R(\ell, b)$. Figures B.11 and B.12 show the angular separation in ϕ between the lepton and b-jet, $\Delta\phi(\ell, b)$. Figures B.13 and B.14 show the angular separation in ϕ between the lepton and the missing transverse energy, $\Delta\phi(\ell, E_T^{miss})$.

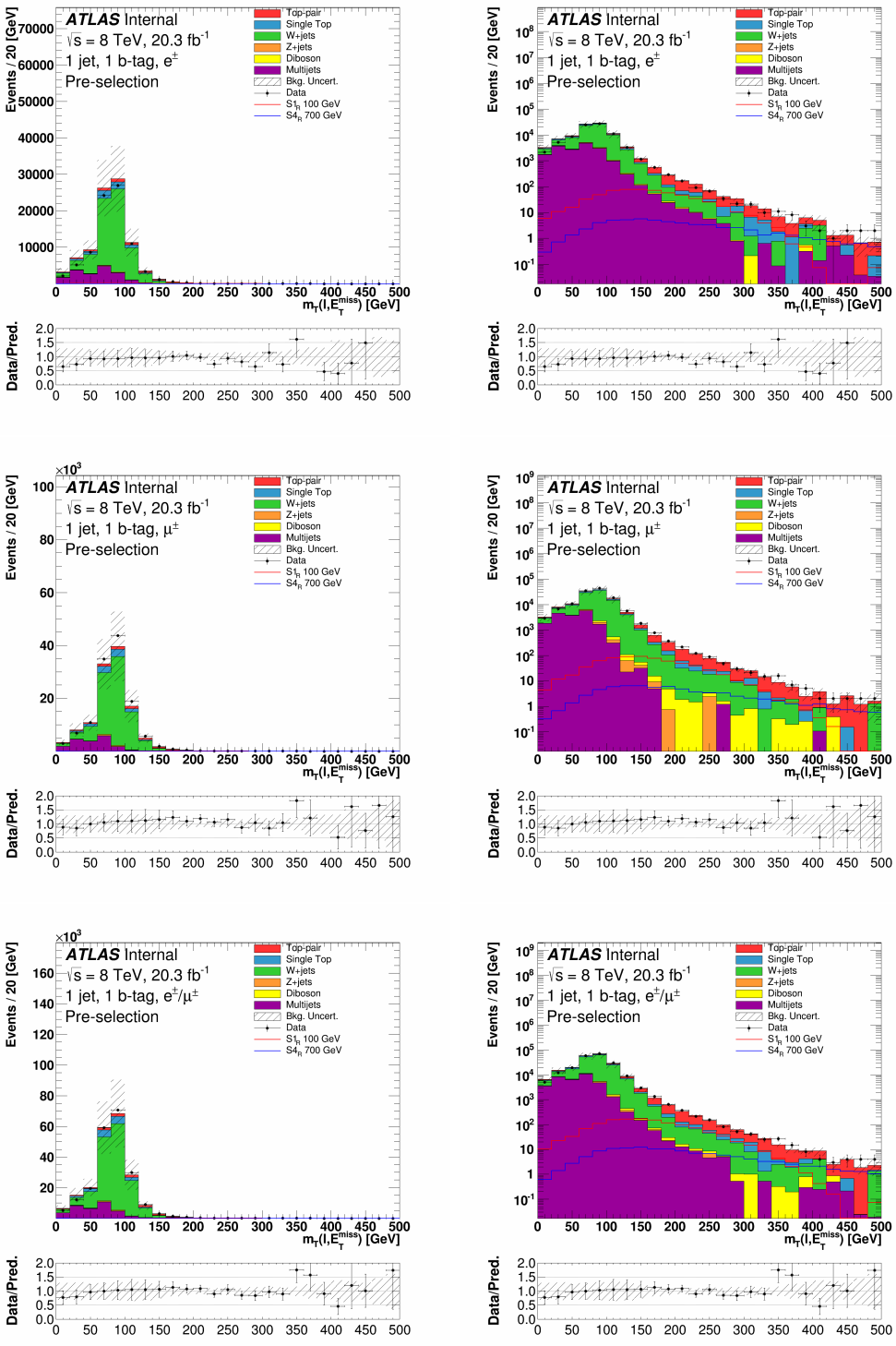

Figure B.1: Distributions of $m_{\mathrm{T}}(\ell, E_{\mathrm{T}}^{\mathrm{miss}})$ for the electron (top), the muon (middle), and the combined (bottom) channels in the pre-selection region, in linear (left) and log (right) scale. The uncertainty band on the expected background corresponds to the errors due to the statistical uncertainties added in quadrature with the cross-section and normalization uncertainties.

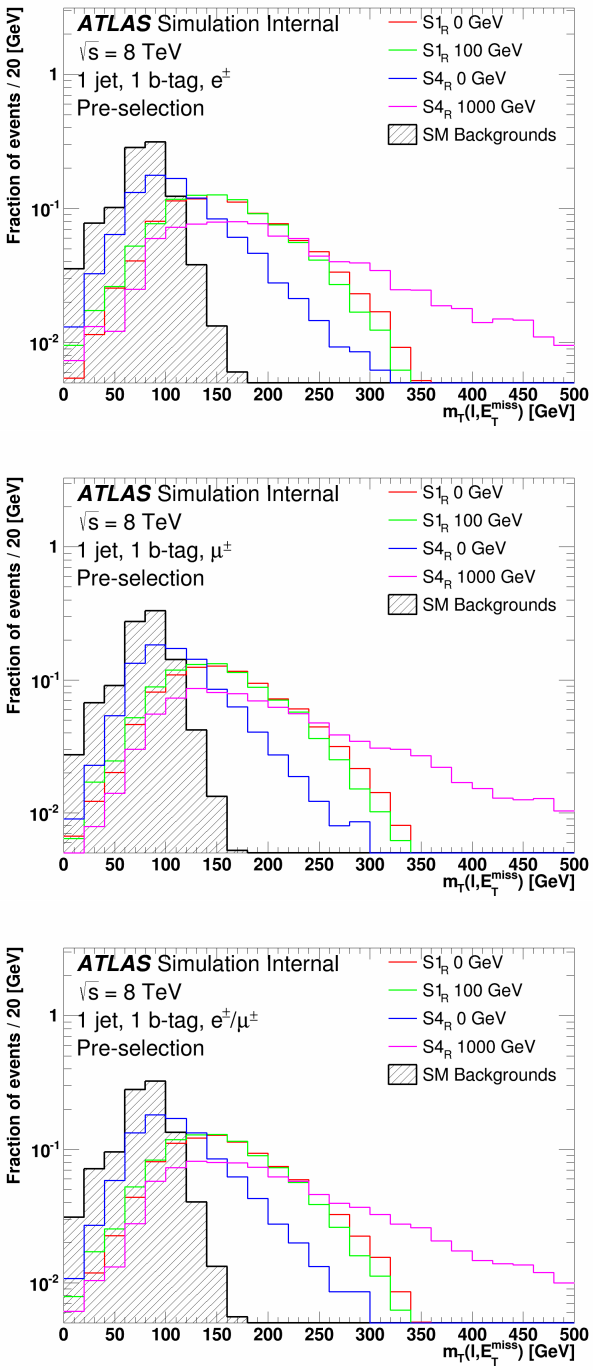

Figure B.2: Distributions of $m_{\mathrm{T}}(\ell, E_{\mathrm{T}}^{\mathrm{miss}})$ normalized to unity for the electron (top), the muon (middle), and the combined (bottom) channels in the pre-selection region for the highest and lowest mass hypotheses of both the $\mathrm{S1_R}$ and $\mathrm{S4_R}$ models. The SM background is also shown.

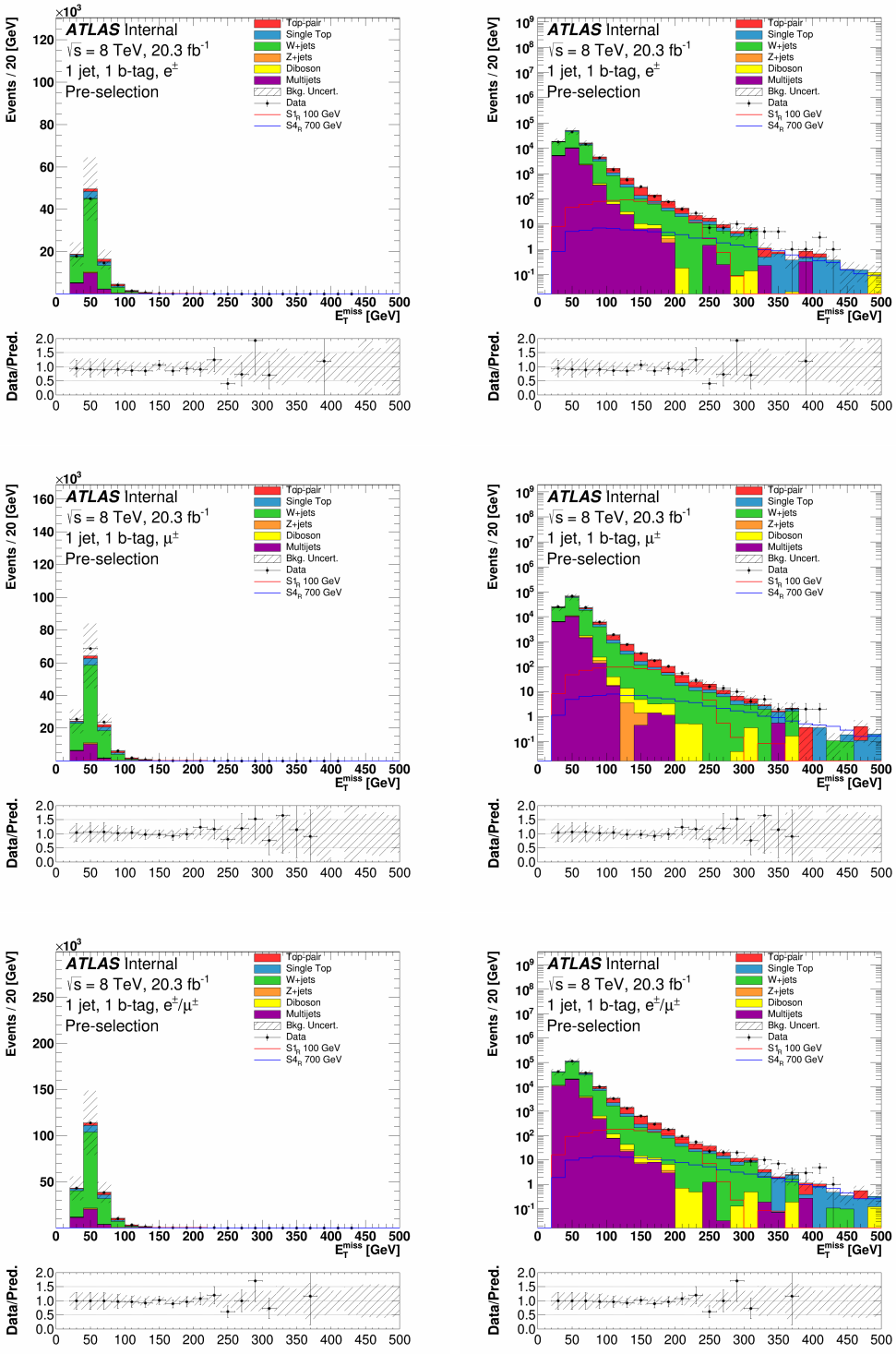

Figure B.3: Distributions of $E_{\mathrm{T}}^{\mathrm{miss}}$ for the electron (top), the muon (middle), and the combined (bottom) channels in the pre-selection region, in linear (left) and log (right) scale. The uncertainty band on the expected background corresponds to the errors due to the statistical uncertainties added in quadrature with the cross-section and normalization uncertainties.

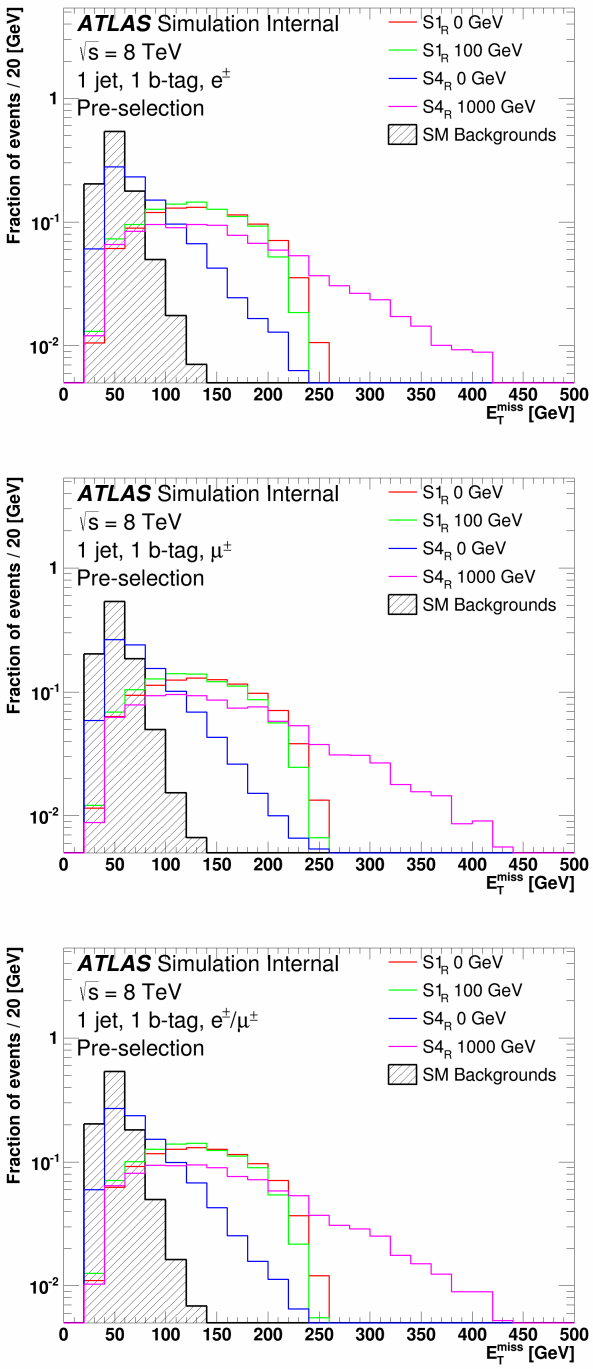

Figure B.4: Distributions of $E_{\mathrm{T}}^{\mathrm{miss}}$ normalized to unity for the electron (top), the muon (middle), and the combined (bottom) channels in the pre-selection region for the highest and lowest mass hypotheses of both the $\mathrm{S1_R}$ and $\mathrm{S4_R}$ models. The SM background is also shown.

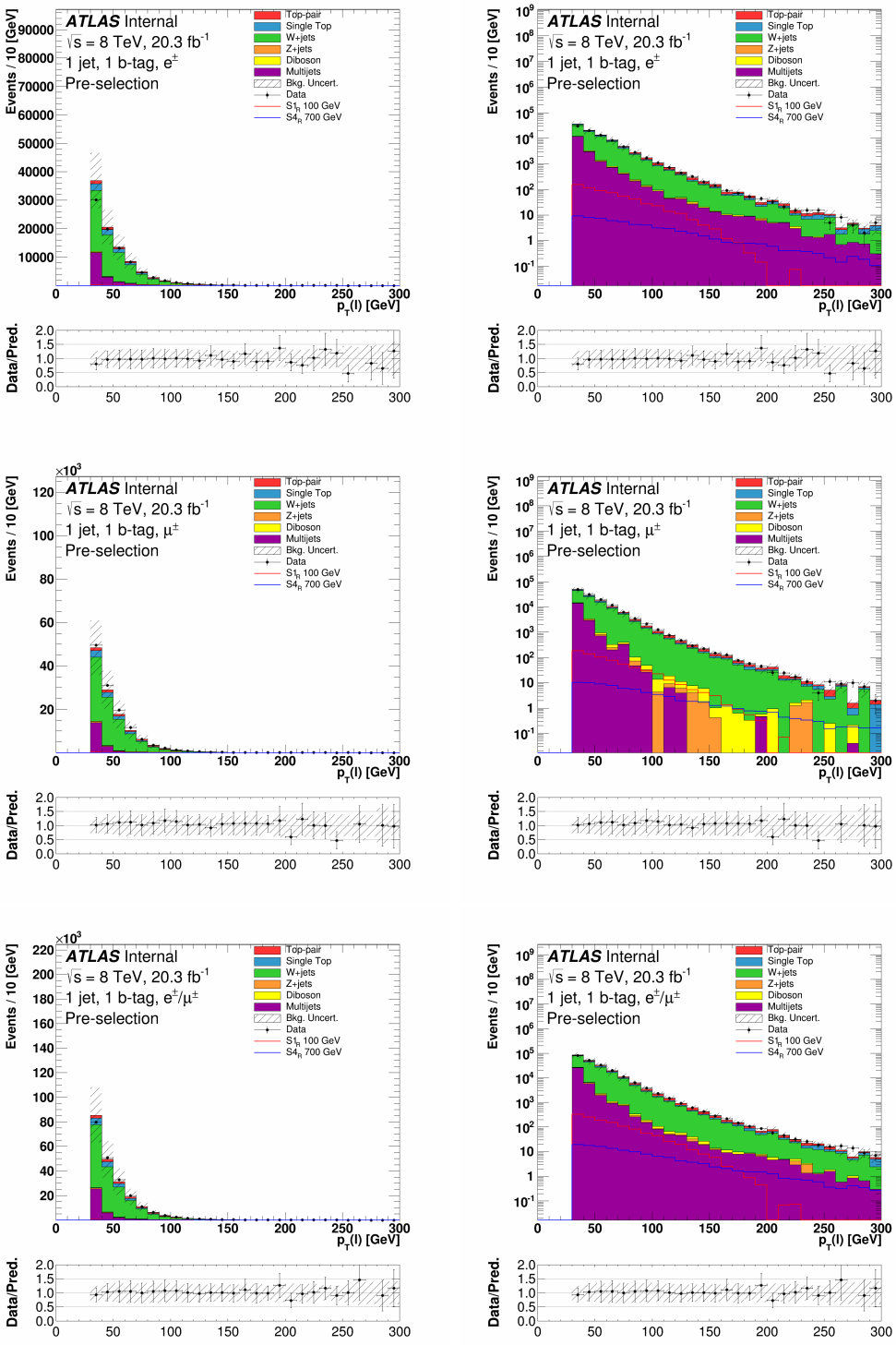

Figure B.5: Distributions of $p_{\mathrm{T}}(\ell)$ for the electron (top), the muon (middle), and the combined (bottom) channels in the pre-selection region, in linear (left) and log (right) scale. The uncertainty band on the expected background corresponds to the errors due to the statistical uncertainties added in quadrature with the cross-section and normalization uncertainties.

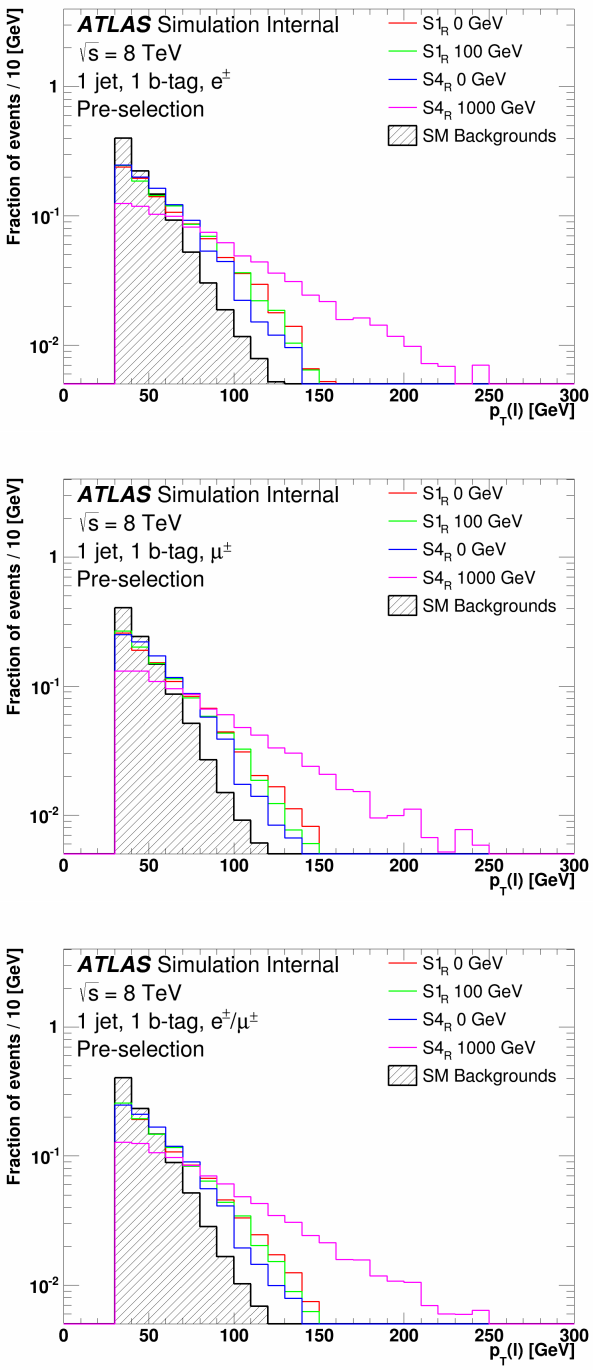

Figure B.6: Distributions of $p_{\mathrm{T}}(\ell)$ normalized to unity for the electron (top), the muon (middle), and the combined (bottom) channels in the pre-selection region for the highest and lowest mass hypotheses of both the $\mathrm{S1_R}$ and $\mathrm{S4_R}$ models. The SM background is also shown.

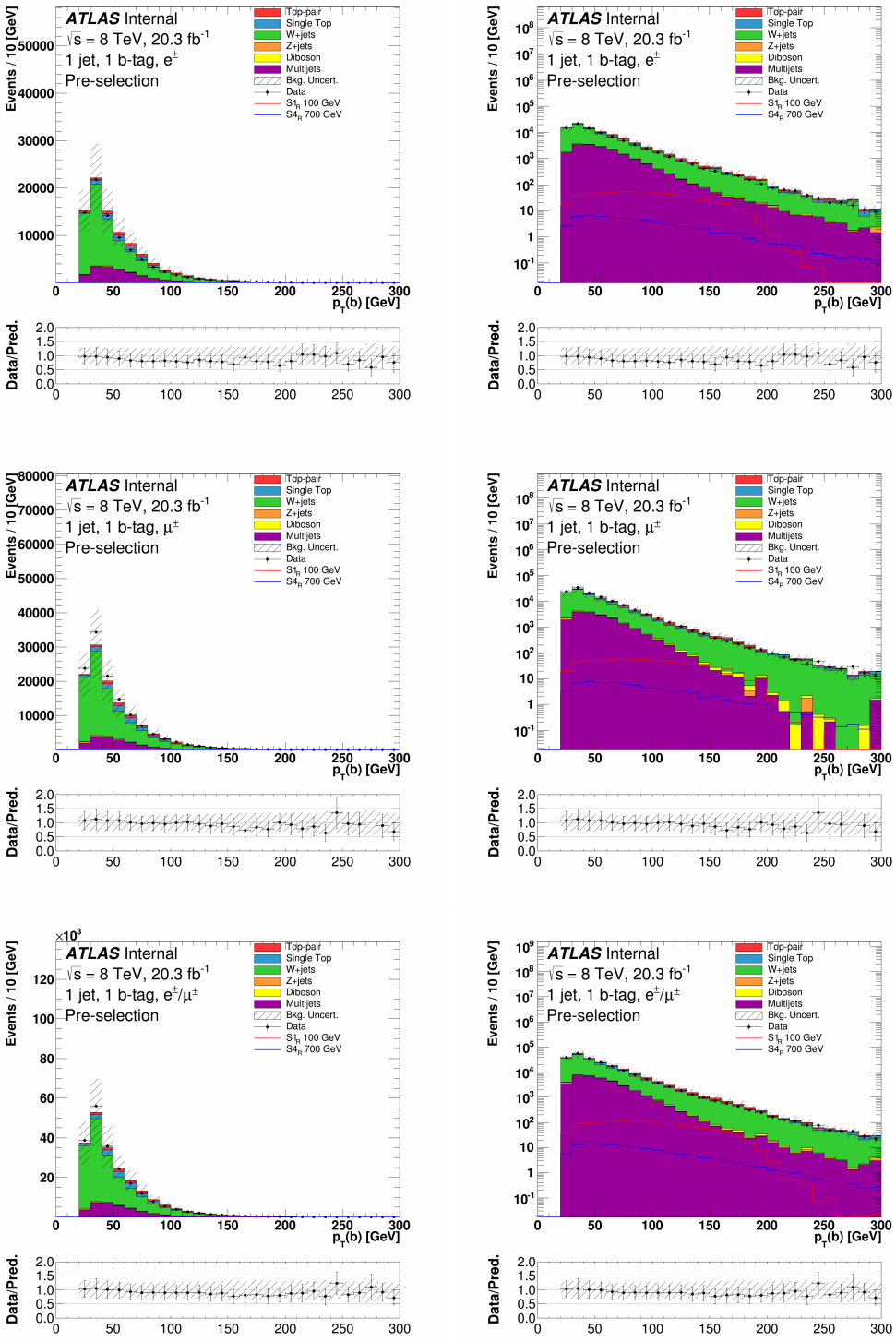

Figure B.7: Distributions of $p_{\mathrm{T}}(b)$ for the electron (top), the muon (middle), and the combined (bottom) channels in the pre-selection region, in linear (left) and log (right) scale. The uncertainty band on the expected background corresponds to the errors due to the statistical uncertainties added in quadrature with the cross-section and normalization uncertainties.

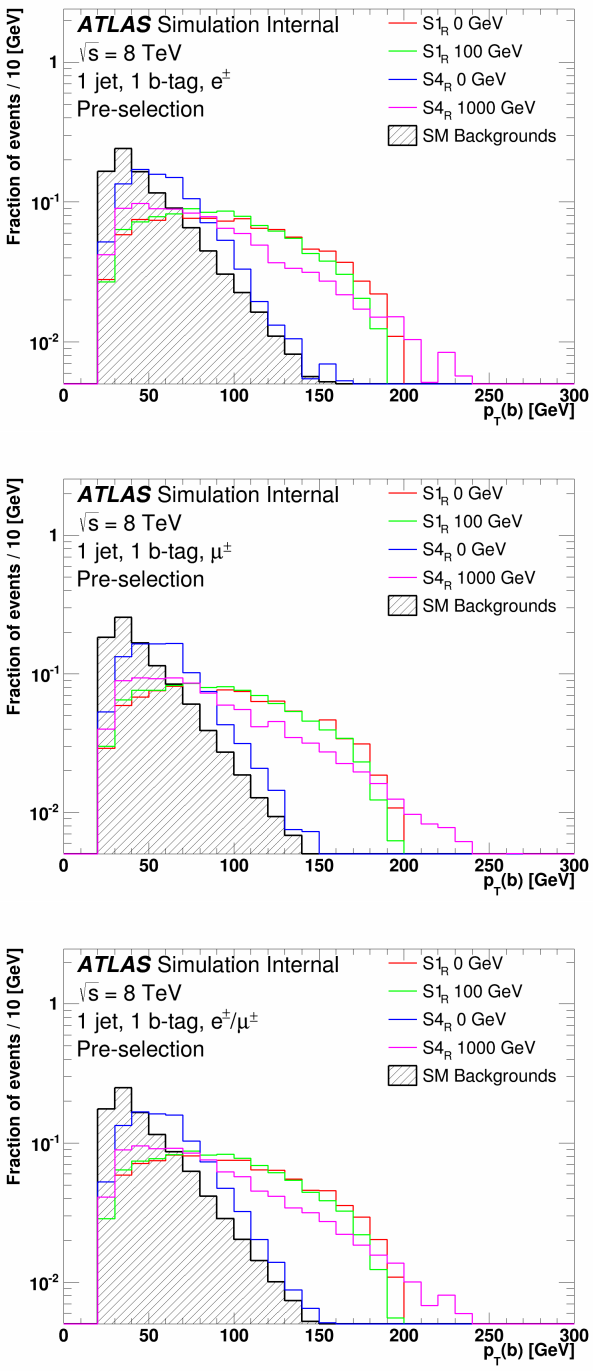

Figure B.8: Distributions of $p_{\mathrm{T}}(b)$ normalized to unity for the electron (top), the muon (middle), and the combined (bottom) channels in the pre-selection region for the highest and lowest mass hypotheses of both the $\mathrm{S1_R}$ and $\mathrm{S4_R}$ models. The SM background is also shown.

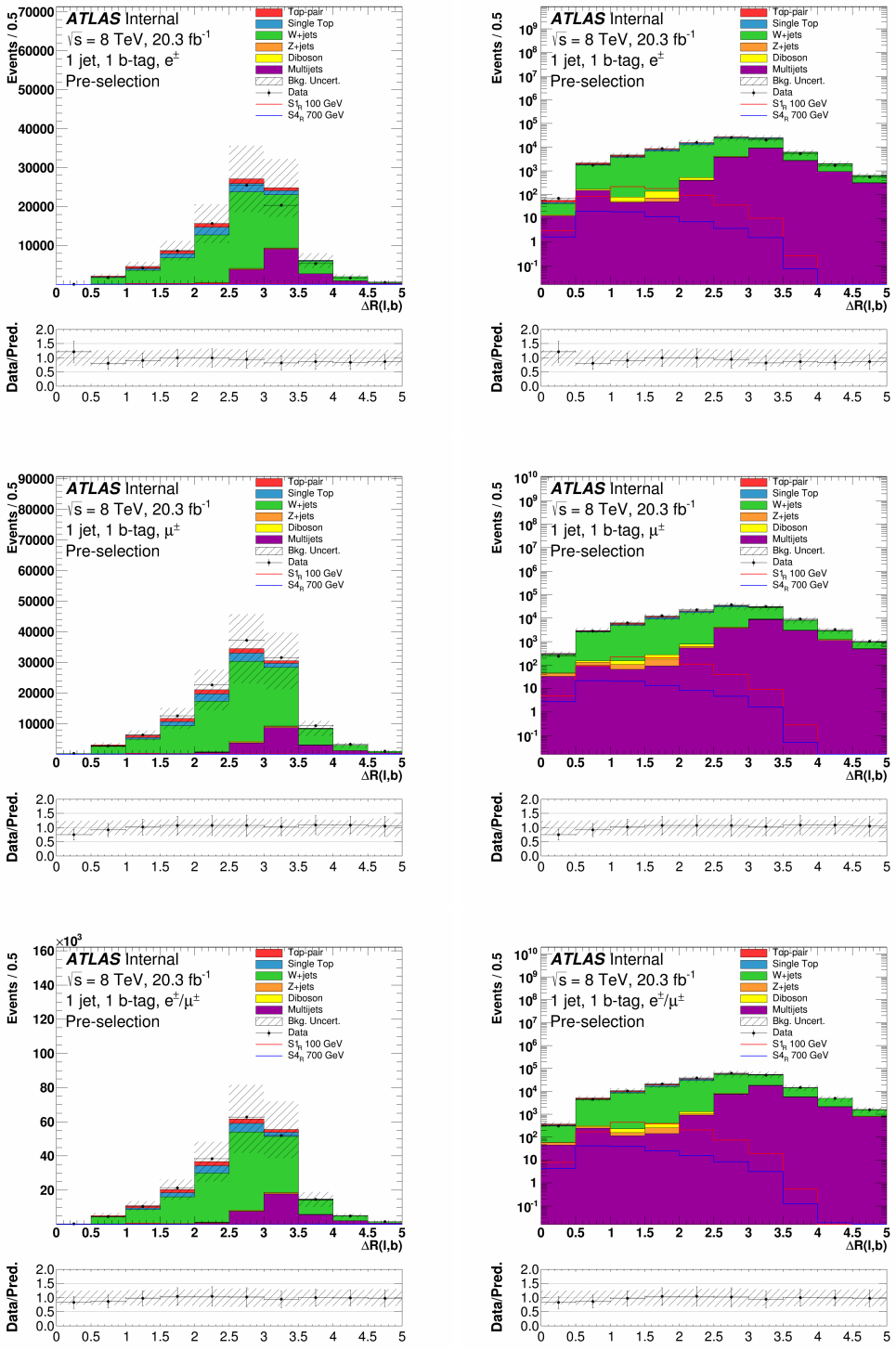

Figure B.9: Distributions of $\Delta\mathrm{R}(\ell, b)$ for the electron (top), the muon (middle), and the combined (bottom) channels in the pre-selection region, in linear (left) and log (right) scale. The uncertainty band on the expected background corresponds to the errors due to the statistical uncertainties added in quadrature with the cross-section and normalization uncertainties.

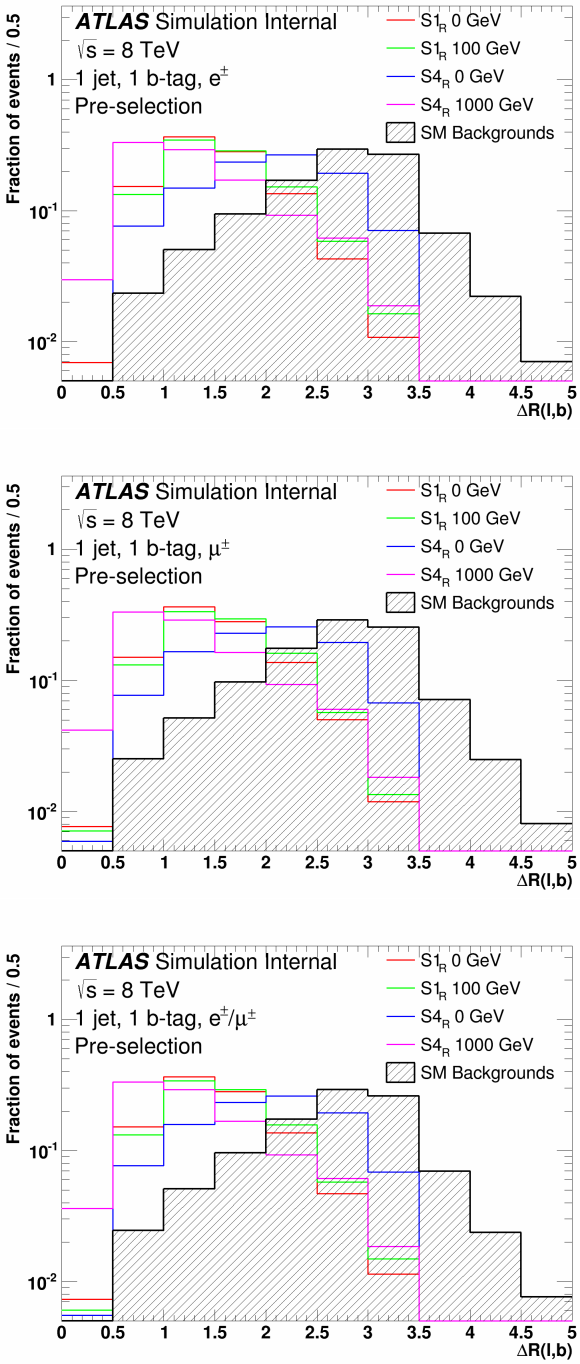

Figure B.10: Distributions of $\Delta\mathrm{R}(\ell, b)$ normalized to unity for the electron (top), the muon (middle), and the combined (bottom) channels in the pre-selection region for the highest and lowest mass hypotheses of both the $\mathrm{S1_R}$ and $\mathrm{S4_R}$ models. The SM background is also shown.

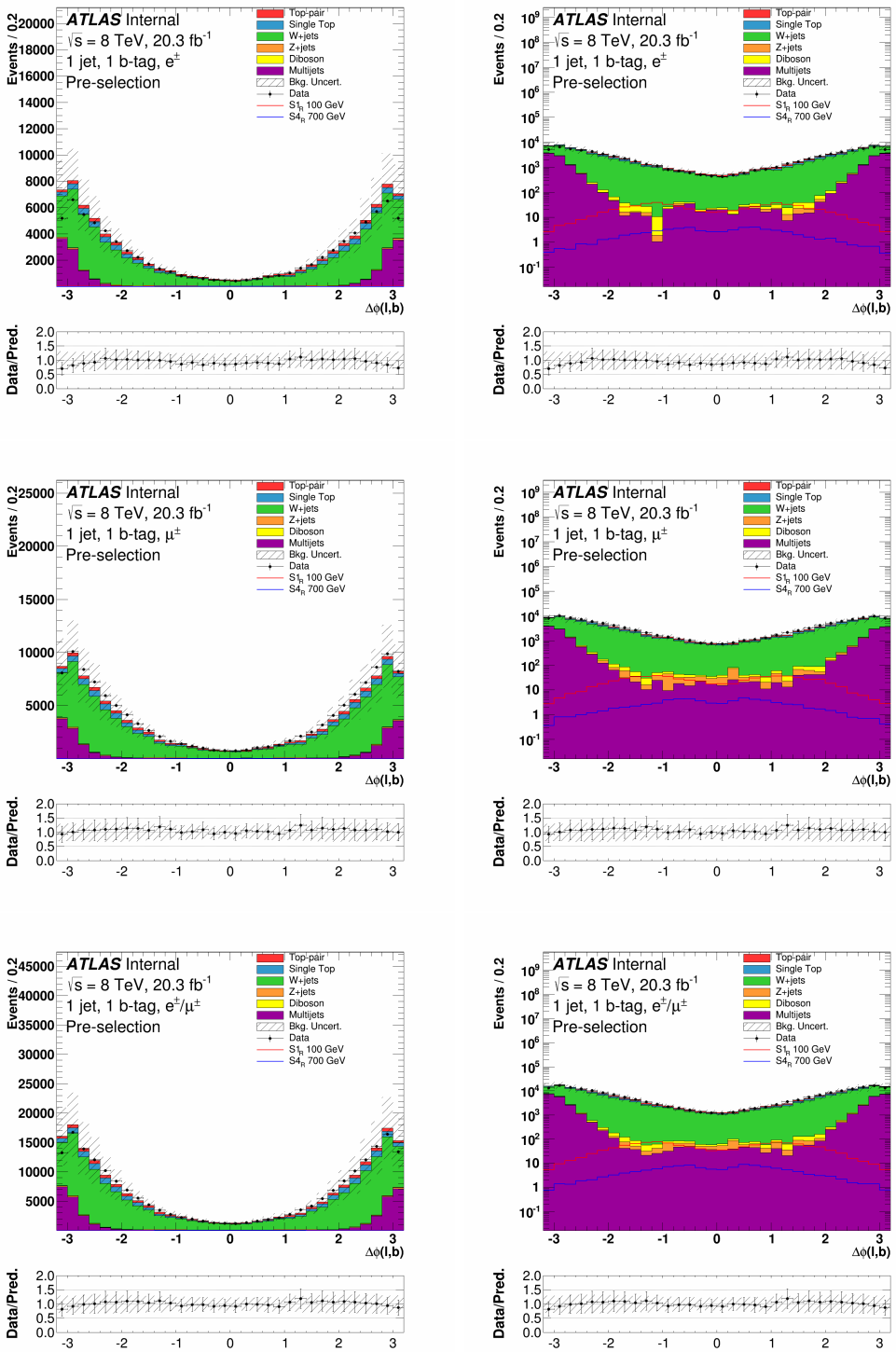

Figure B.11: Distributions of $\Delta\phi(\ell, b)$ for the electron (top), the muon (middle), and the combined (bottom) channels in the pre-selection region, in linear (left) and log (right) scale. The uncertainty band on the expected background corresponds to the errors due to the statistical uncertainties added in quadrature with the cross-section and normalization uncertainties.

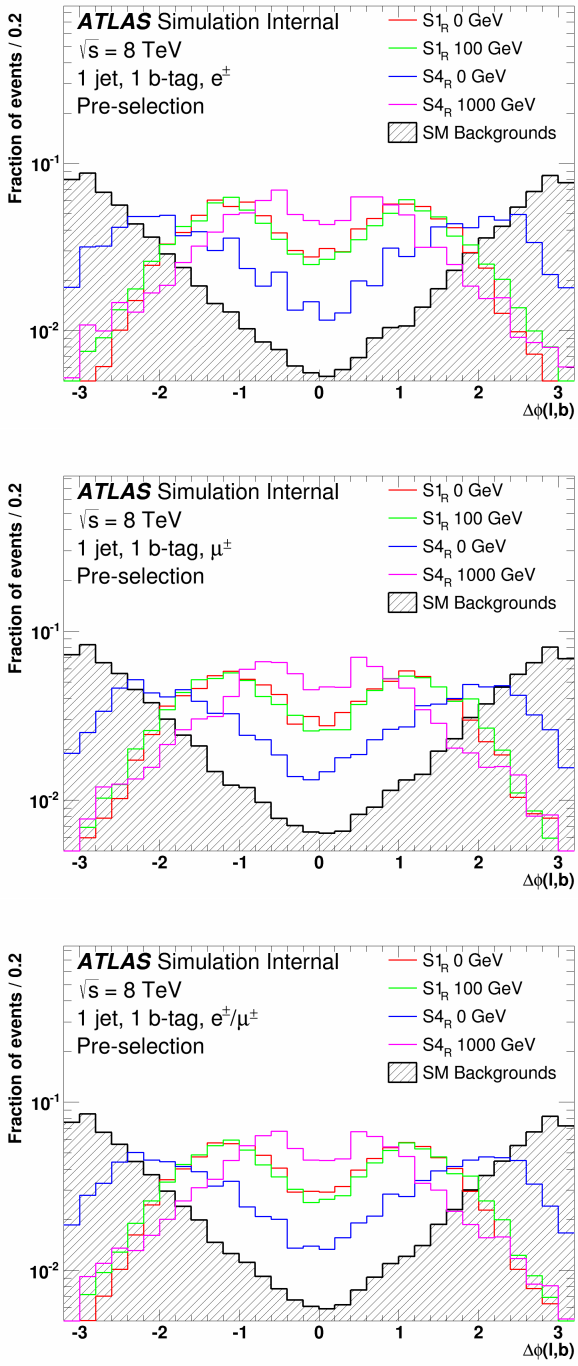

Figure B.12: Distributions of $\Delta\phi(\ell, b)$ normalized to unity for the electron (top), the muon (middle), and the combined (bottom) channels in the pre-selection region for the highest and lowest mass hypotheses of both the $S1_R$ and $S4_R$ models. The SM background is also shown.

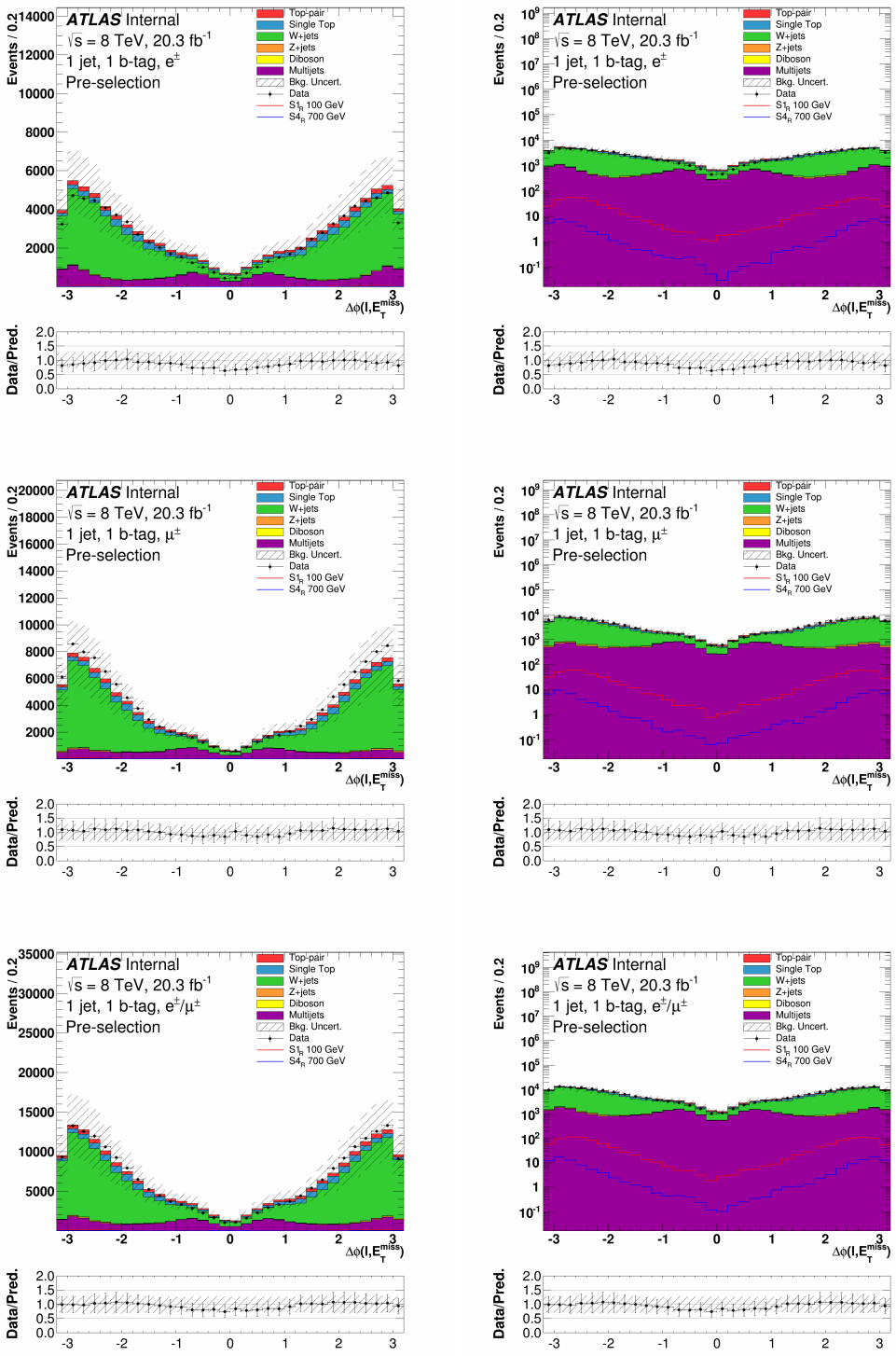

Figure B.13: Distributions of $\Delta\phi(\ell, E_{\mathrm{T}}^{\mathrm{miss}})$ for the electron (top), the muon (middle), and the combined (bottom) channels in the pre-selection region, in linear (left) and log (right) scale. The uncertainty band on the expected background corresponds to the errors due to the statistical uncertainties added in quadrature with the cross-section and normalization uncertainties.

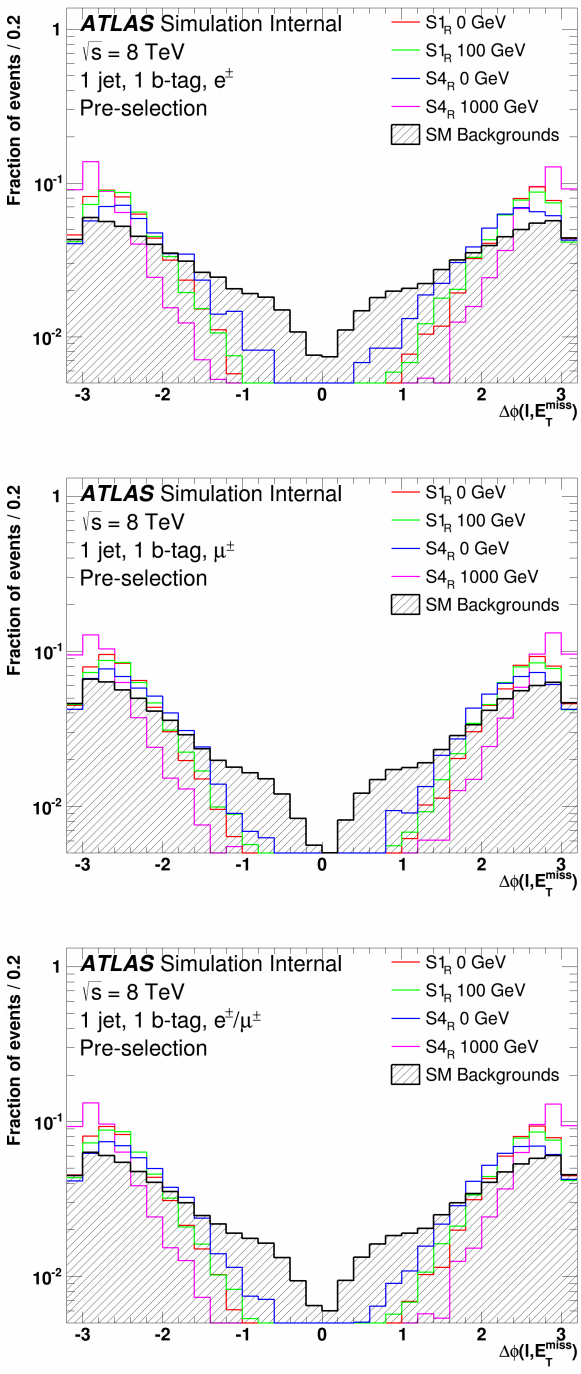

Figure B.14: Distributions of $\Delta\phi(\ell, E_{\mathrm{T}}^{\mathrm{miss}})$ normalized to unity for the electron (top), the muon (middle), and the combined (bottom) channels in the pre-selection region for the highest and lowest mass hypotheses of both the $\mathrm{S1_R}$ and $\mathrm{S4_R}$ models. The SM background is also shown.

CR1

This section presents distribution of variables for simulated background and data events in CR1 defined in Section 7.4. Figure B.15 shows the transverse mass between the lepton and missing transverse energy, $m_{\mathrm{T}}(\ell, E_{\mathrm{T}}^{\mathrm{miss}})$. Figure B.16 shows the missing transverse energy, $E_{\mathrm{T}}^{\mathrm{miss}}$. Figure B.17 shows the transverse momentum of the lepton, $p_{\mathrm{T}}(\ell)$. Figure B.18 shows the transverse momentum of the b-jet, $p_{\mathrm{T}}(b)$. Figure B.19 shows the spatial separation in $\eta - \phi$ space between the lepton and b-jet, $\Delta\mathrm{R}(\ell, b)$. Figure B.20 shows the angular separation in ϕ between the lepton and b-jet, $\Delta\phi(\ell, b)$. Figure B.21 shows the angular separation in ϕ between the lepton and the missing transverse energy, $\Delta\phi(\ell, E_{\mathrm{T}}^{\mathrm{miss}})$.

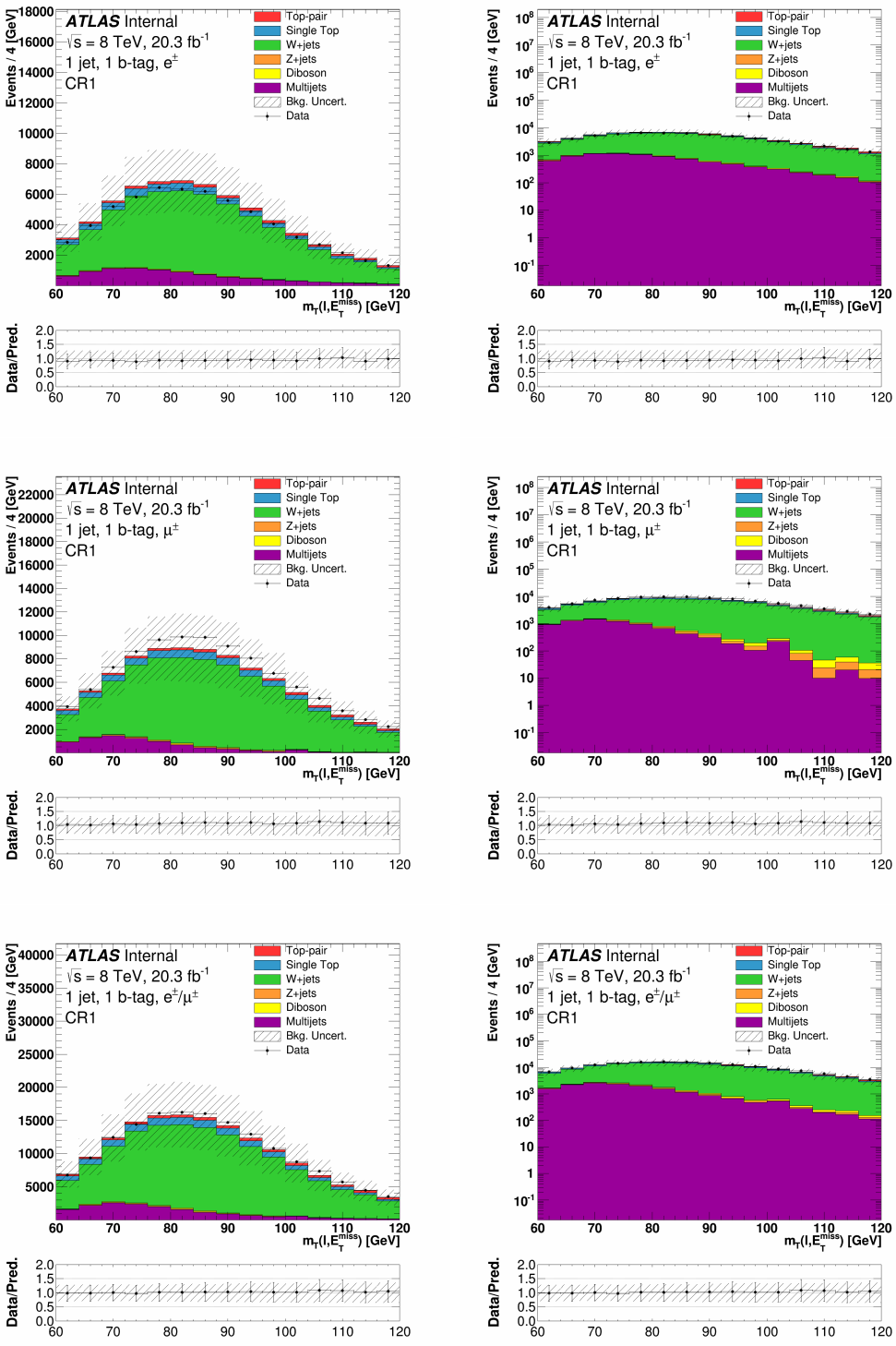

Figure B.15: Distributions of $m_{\mathrm{T}}(\ell, E_{\mathrm{T}}^{\mathrm{miss}})$ for the electron (top), the muon (middle), and the combined (bottom) channels in CR1, in linear (left) and log (right) scale. The uncertainty band on the expected background corresponds to the errors due to the statistical uncertainties added in quadrature with the cross-section and normalization uncertainties.

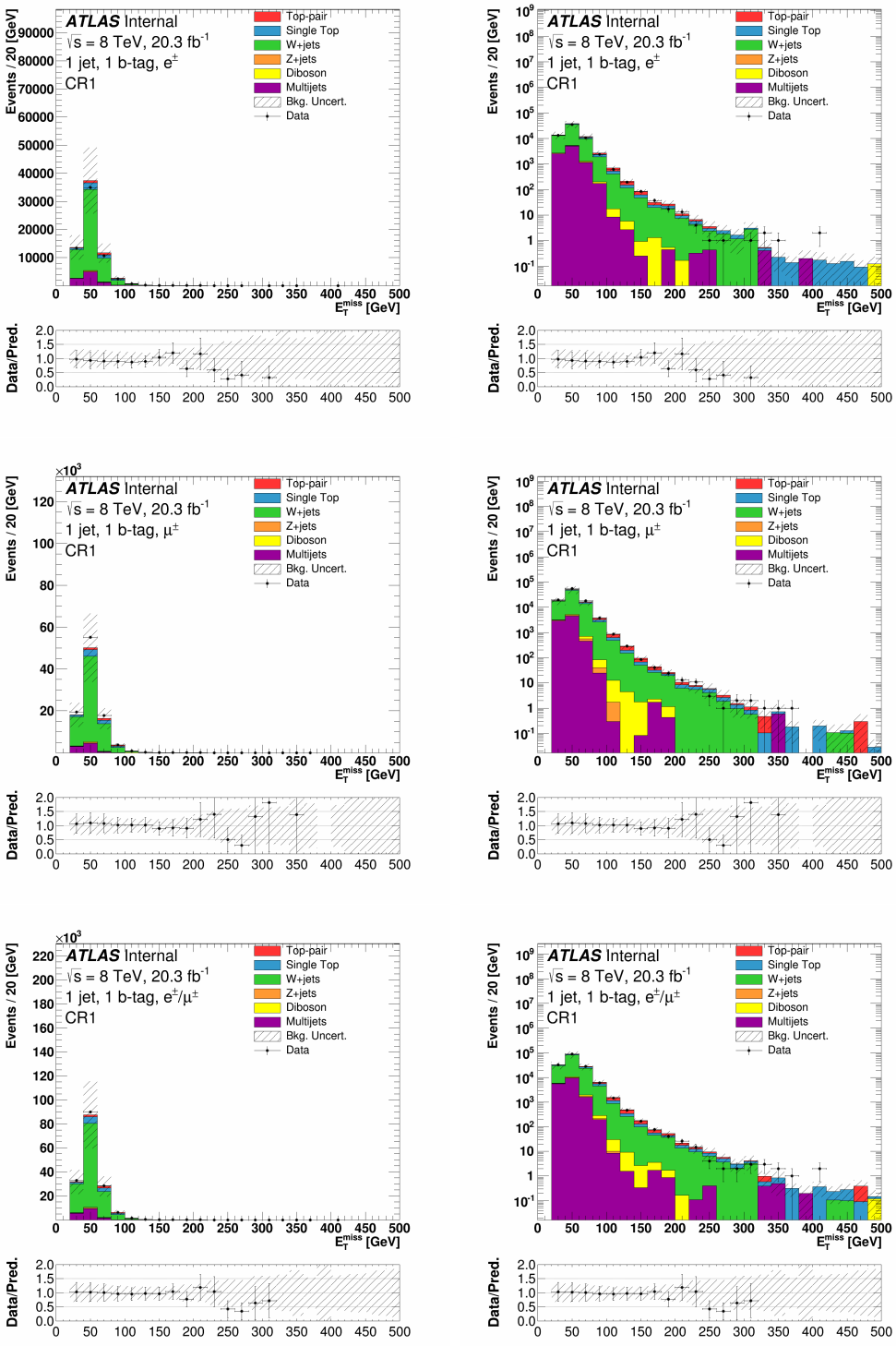

Figure B.16: Distributions of $E_{\mathrm{T}}^{\mathrm{miss}}$ for the electron (top), the muon (middle), and the combined (bottom) channels in CR1, in linear (left) and log (right) scale. The uncertainty band on the expected background corresponds to the errors due to the statistical uncertainties added in quadrature with the cross-section and normalization uncertainties.

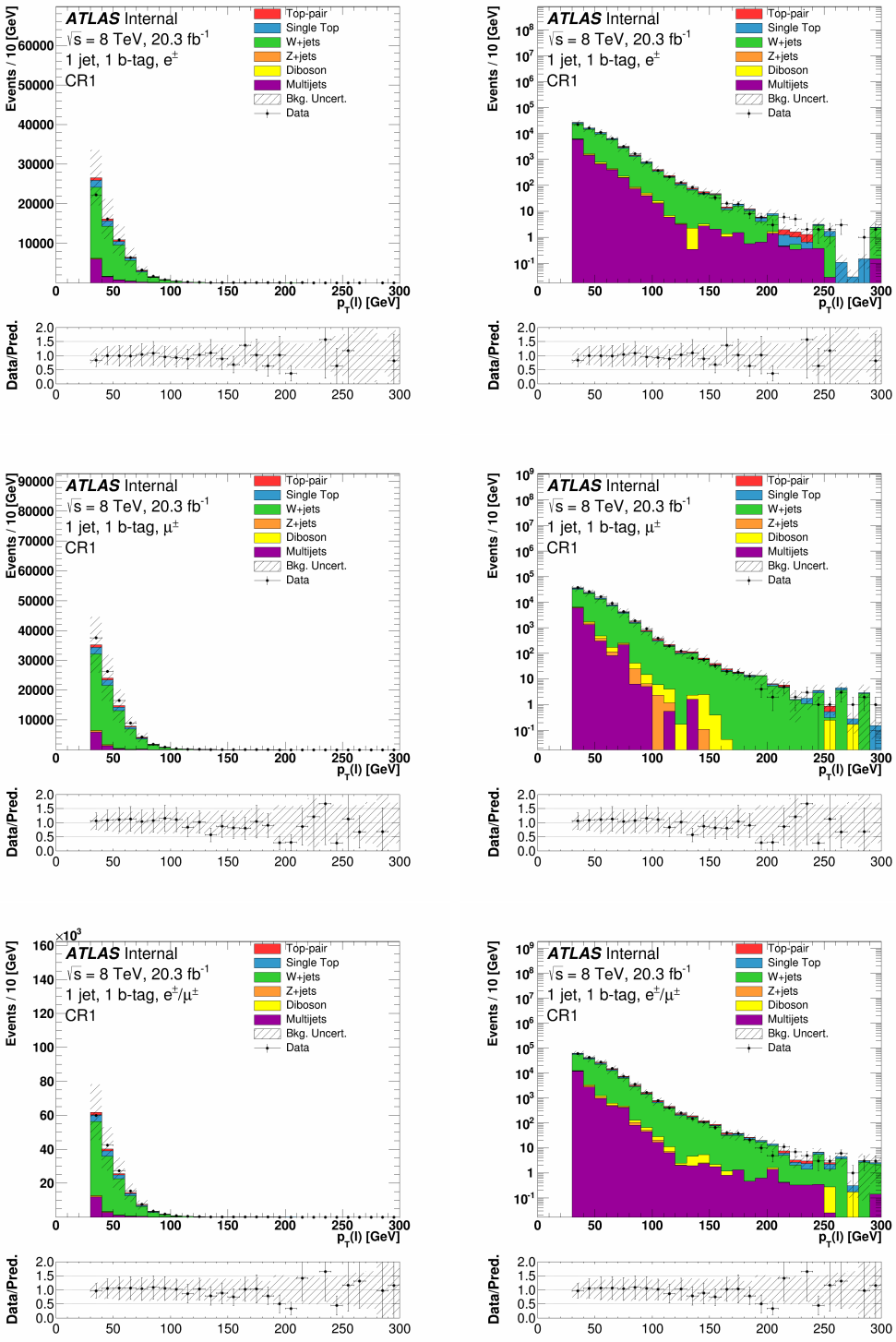

Figure B.17: Distributions of $p_{\mathrm{T}}(\ell)$ for the electron (top), the muon (middle), and the combined (bottom) channels in CR1, in linear (left) and log (right) scale. The uncertainty band on the expected background corresponds to the errors due to the statistical uncertainties added in quadrature with the cross-section and normalization uncertainties.

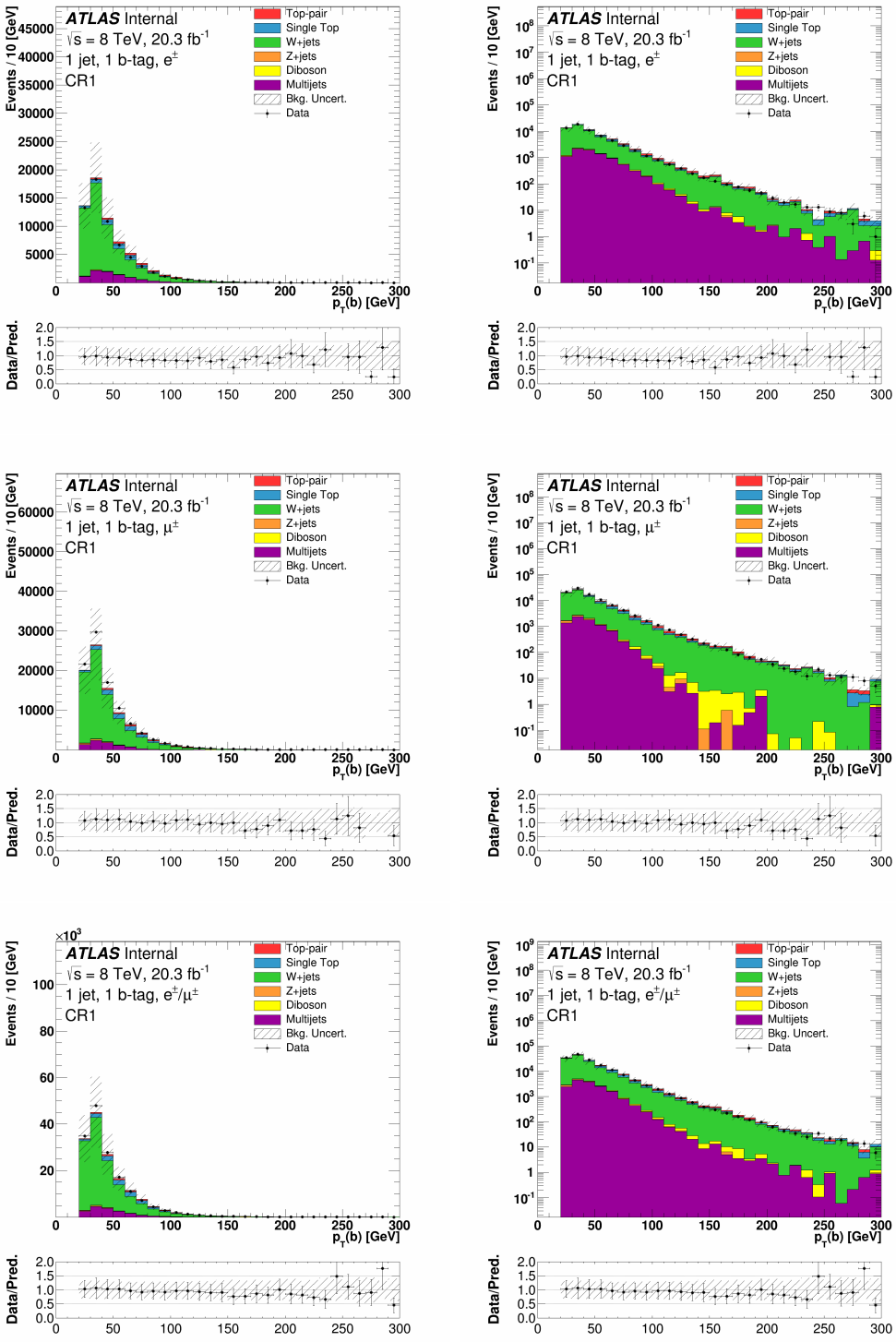

Figure B.18: Distributions of $p_{\mathrm{T}}(b)$ for the electron (top), the muon (middle), and the combined (bottom) channels in CR1, in linear (left) and log (right) scale. The uncertainty band on the expected background corresponds to the errors due to the statistical uncertainties added in quadrature with the cross-section and normalization uncertainties.

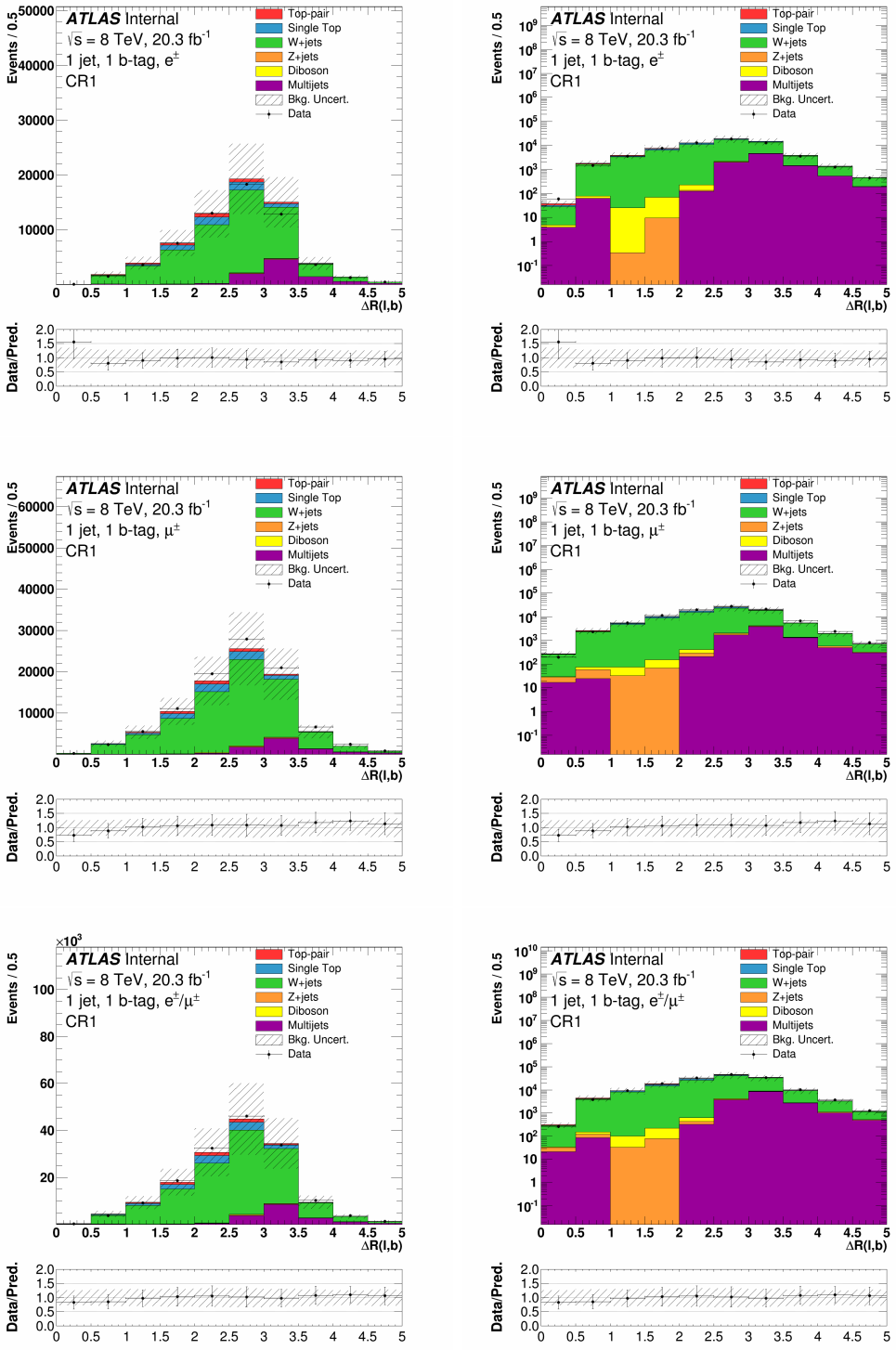

Figure B.19: Distributions of $\Delta\mathrm{R}(\ell, b)$ for the electron (top), the muon (middle), and the combined (bottom) channels in CR1, in linear (left) and log (right) scale. The uncertainty band on the expected background corresponds to the errors due to the statistical uncertainties added in quadrature with the cross-section and normalization uncertainties.

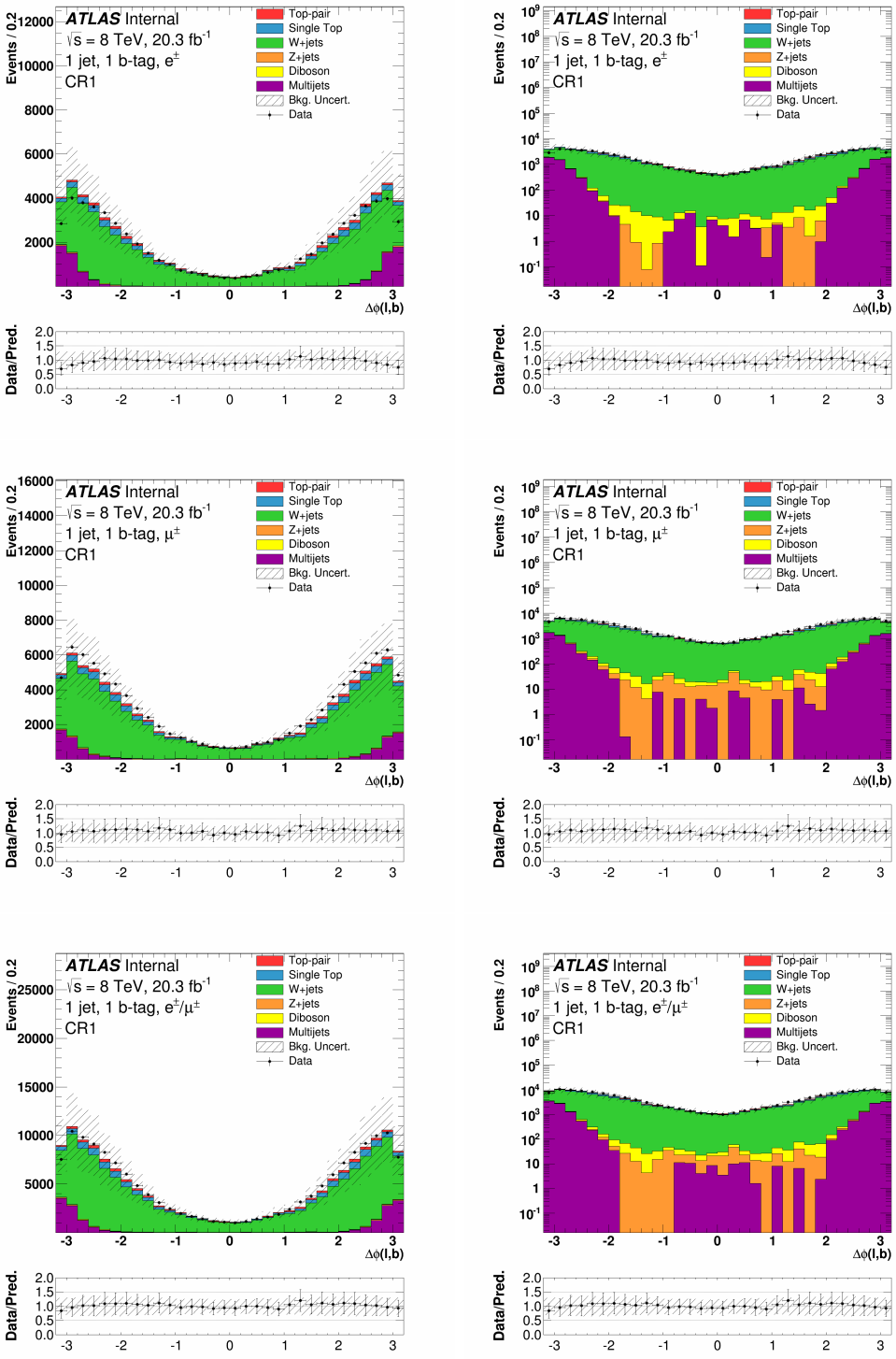

Figure B.20: Distributions of $\Delta\phi(\ell, b)$ for the electron (top), the muon (middle), and the combined (bottom) channels in CR1, in linear (left) and log (right) scale. The uncertainty band on the expected background corresponds to the errors due to the statistical uncertainties added in quadrature with the cross-section and normalization uncertainties.

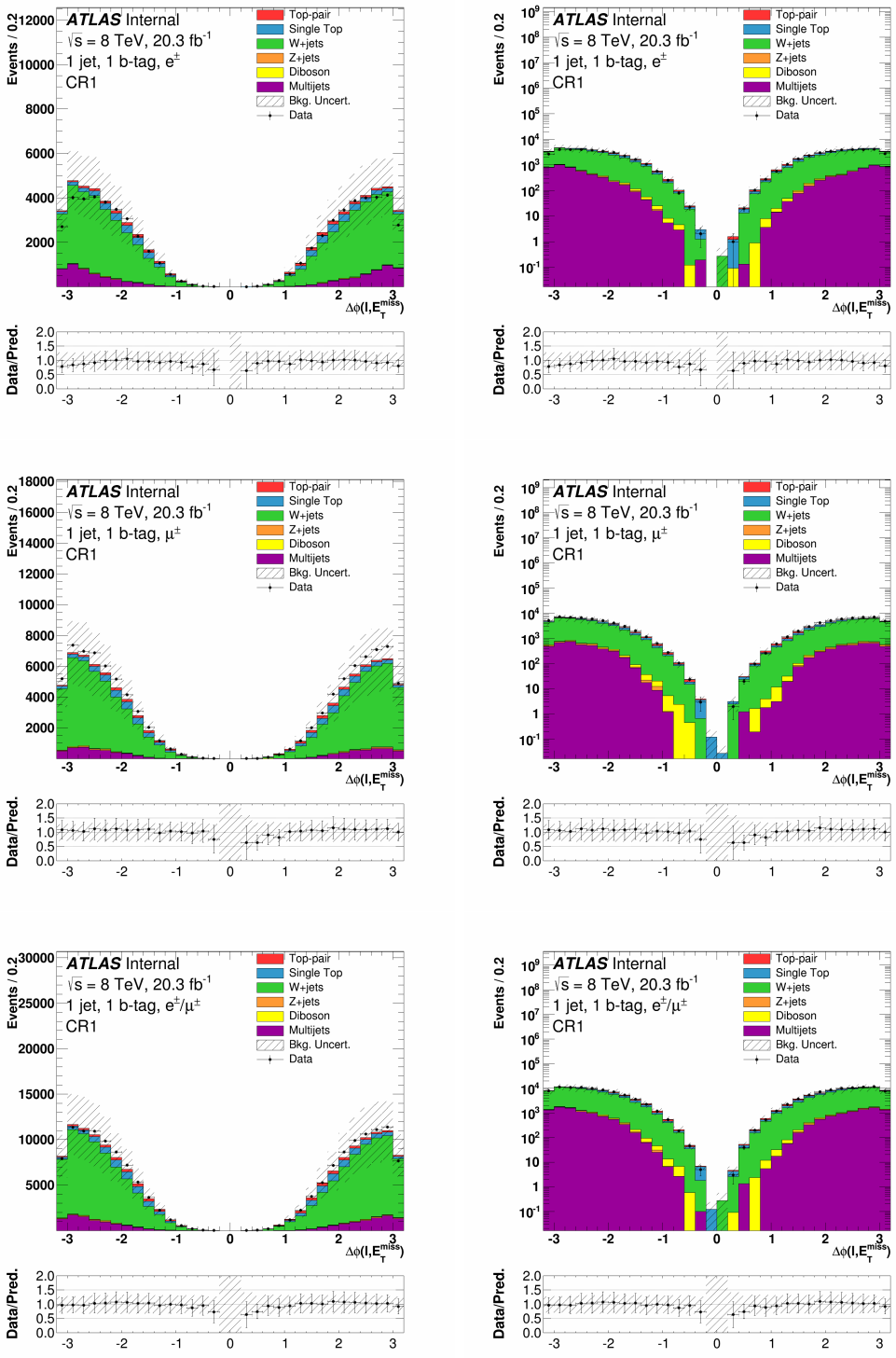

Figure B.21: Distributions of $\Delta\phi(\ell, E_{\mathrm{T}}^{\mathrm{miss}})$ for the electron (top), the muon (middle), and the combined (bottom) channels in CR1, in linear (left) and log (right) scale. The uncertainty band on the expected background corresponds to the errors due to the statistical uncertainties added in quadrature with the cross-section and normalization uncertainties.

CR2

This section presents distribution of variables for simulated background and data events in CR2 defined in Section 7.4. Figure B.22 shows the transverse mass between the lepton and missing transverse energy, $m_{\mathrm{T}}(\ell, E_{\mathrm{T}}^{\mathrm{miss}})$. Figure B.23 shows the missing transverse energy, $E_{\mathrm{T}}^{\mathrm{miss}}$. Figure B.24 shows the transverse momentum of the lepton, $p_{\mathrm{T}}(\ell)$. Figure B.25 shows the transverse momentum of the b-jet, $p_{\mathrm{T}}(b)$. Figure B.26 shows the spatial separation in $\eta - \phi$ space between the lepton and b-jet, $\Delta\mathrm{R}(\ell, b)$. Figure B.27 shows the angular separation in ϕ between the lepton and b-jet, $\Delta\phi(\ell, b)$. Figure B.28 shows the angular separation in ϕ between the lepton and the missing transverse energy, $\Delta\phi(\ell, E_{\mathrm{T}}^{\mathrm{miss}})$.

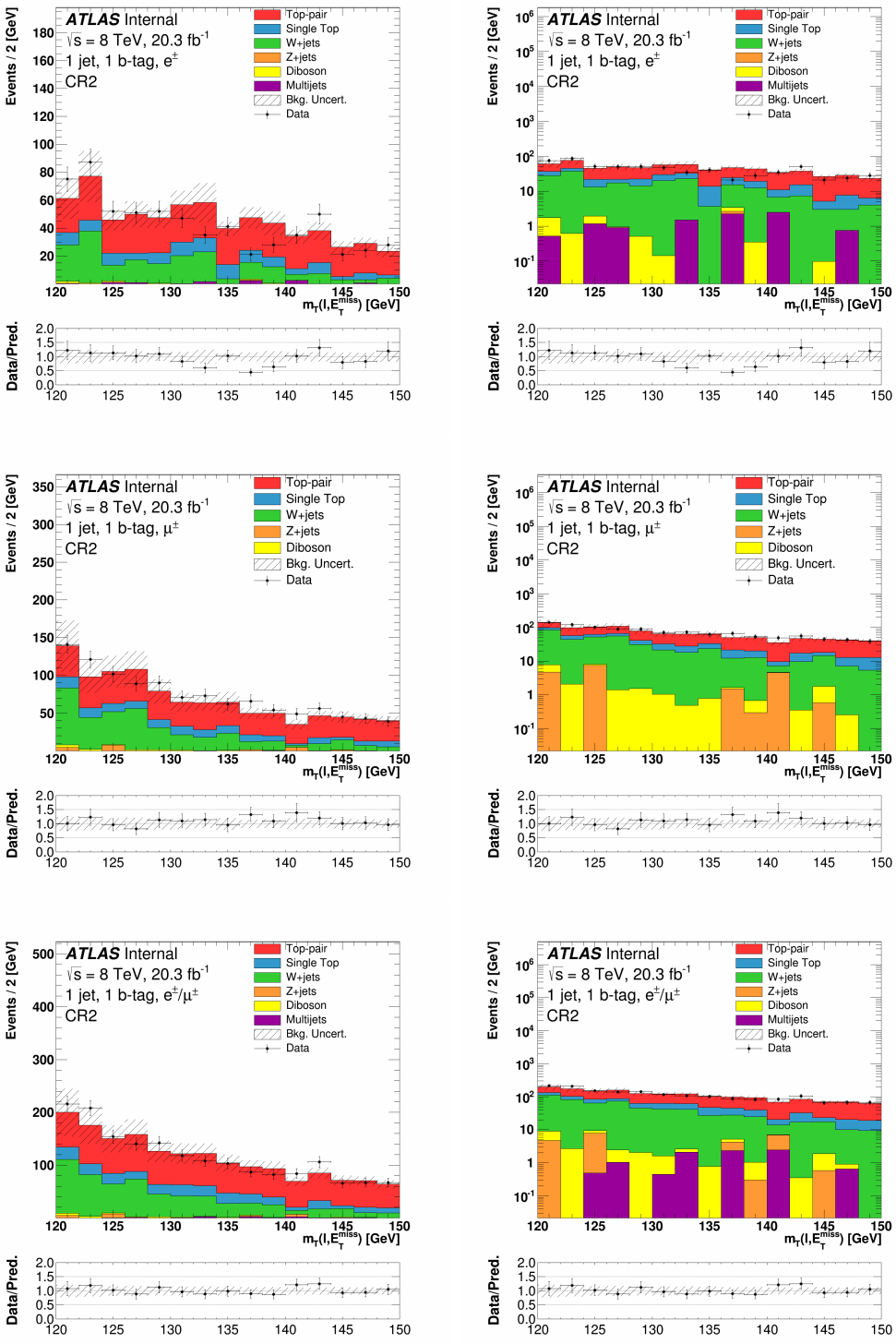

Figure B.22: Distributions of $m_{\mathrm{T}}(\ell, E_{\mathrm{T}}^{\mathrm{miss}})$ for the electron (top), the muon (middle), and the combined (bottom) channels in CR2, in linear (left) and log (right) scale. The uncertainty band on the expected background corresponds to the errors due to the statistical uncertainties added in quadrature with the cross-section and normalization uncertainties.

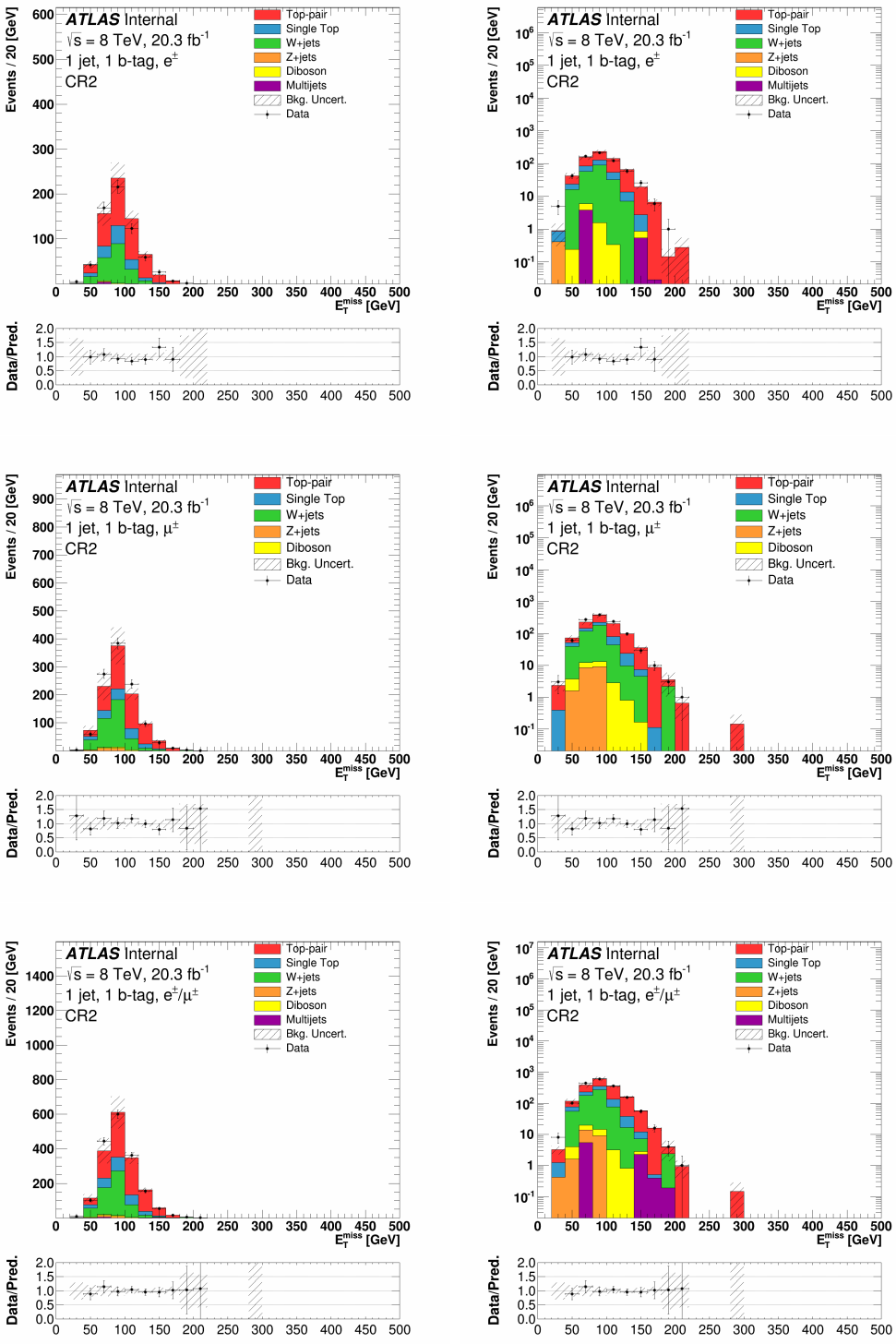

Figure B.23: Distributions of $E_{\mathrm{T}}^{\mathrm{miss}}$ for the electron (top), the muon (middle), and the combined (bottom) channels in CR2, in linear (left) and log (right) scale. The uncertainty band on the expected background corresponds to the errors due to the statistical uncertainties added in quadrature with the cross-section and normalization uncertainties.

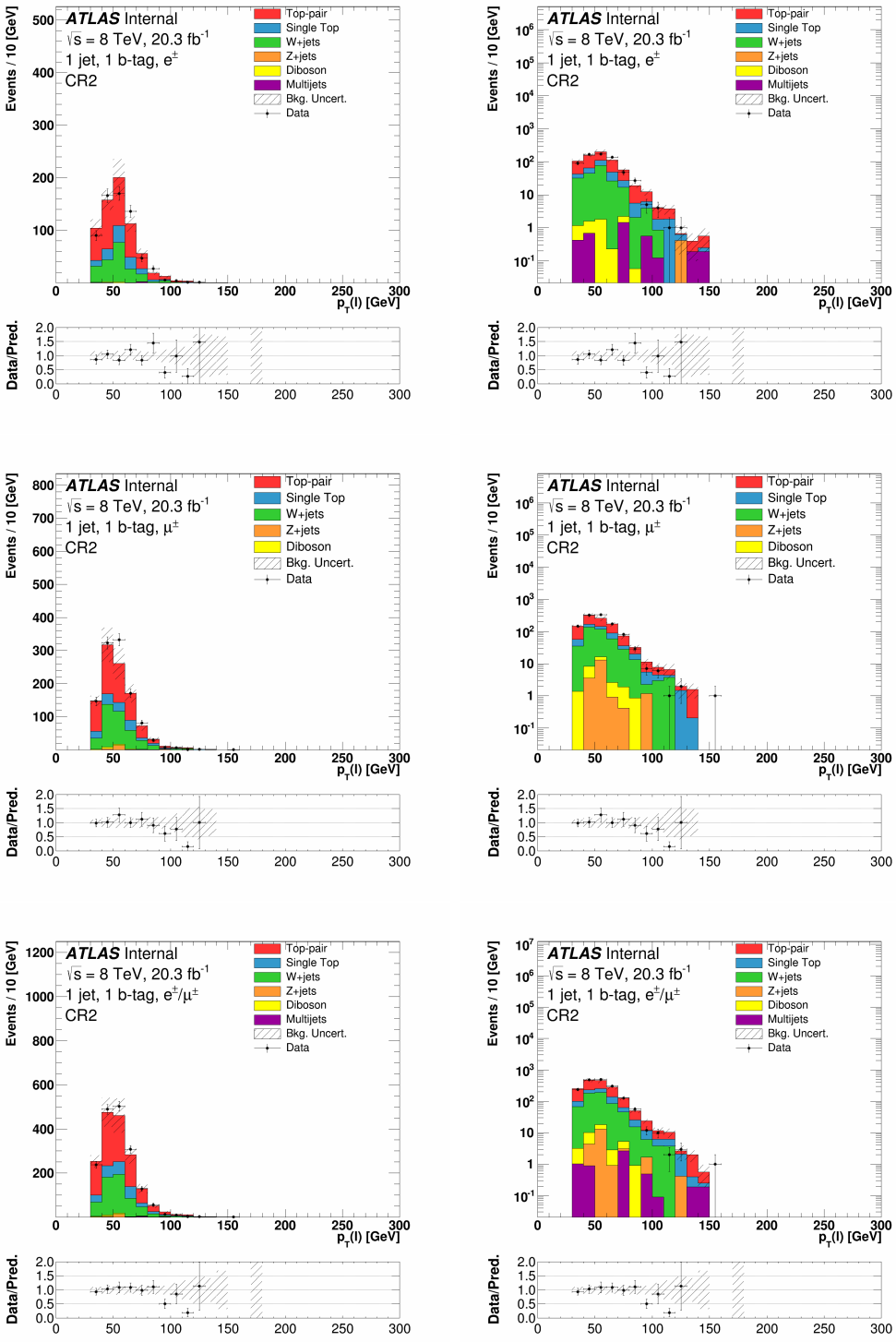

Figure B.24: Distributions of $p_{\mathrm{T}}(\ell)$ for the electron (top), the muon (middle), and the combined (bottom) channels in CR2, in linear (left) and log (right) scale. The uncertainty band on the expected background corresponds to the errors due to the statistical uncertainties added in quadrature with the cross-section and normalization uncertainties.

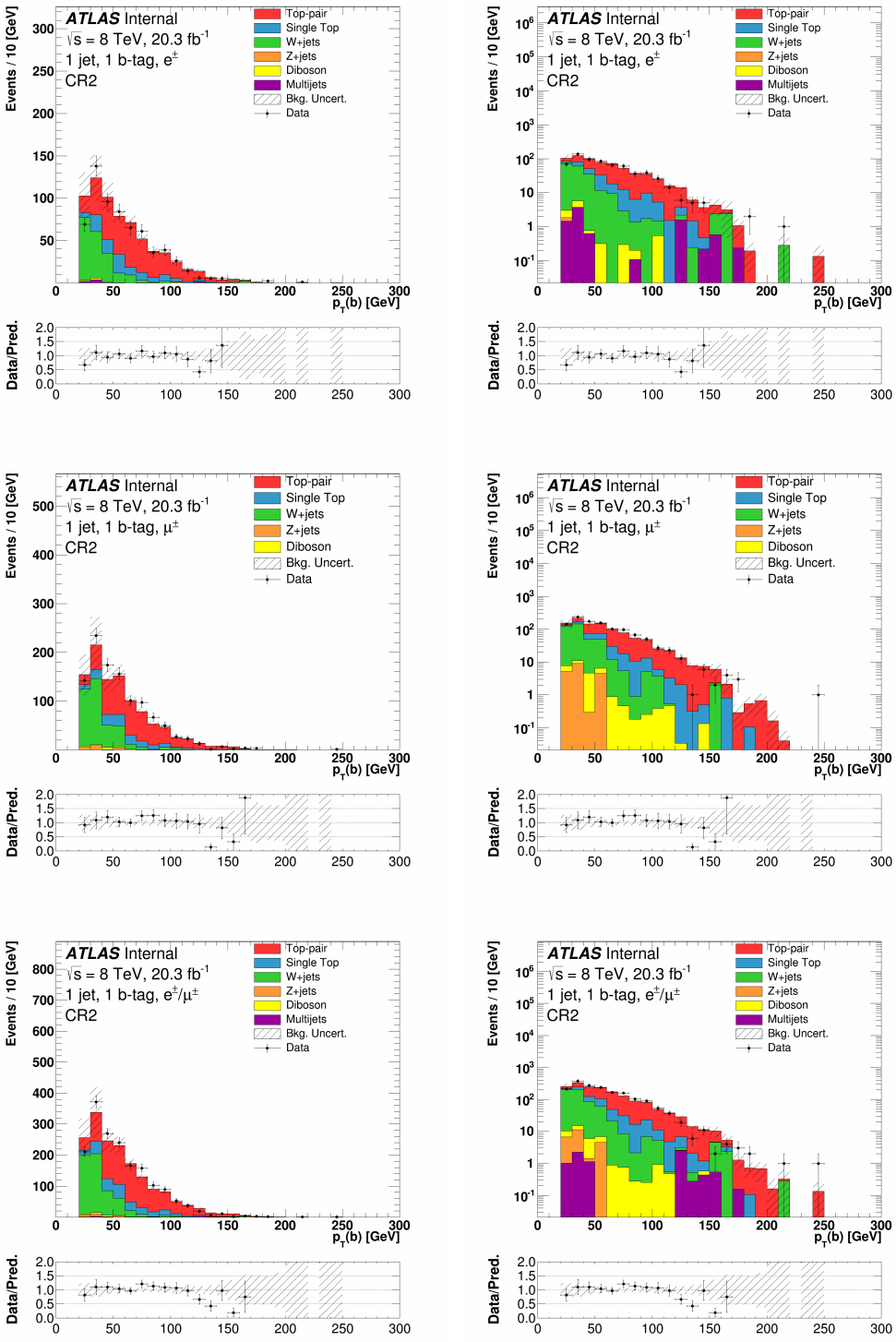

Figure B.25: Distributions of $p_{\mathrm{T}}(b)$ for the electron (top), the muon (middle), and the combined (bottom) channels in CR2, in linear (left) and log (right) scale. The uncertainty band on the expected background corresponds to the errors due to the statistical uncertainties added in quadrature with the cross-section and normalization uncertainties.

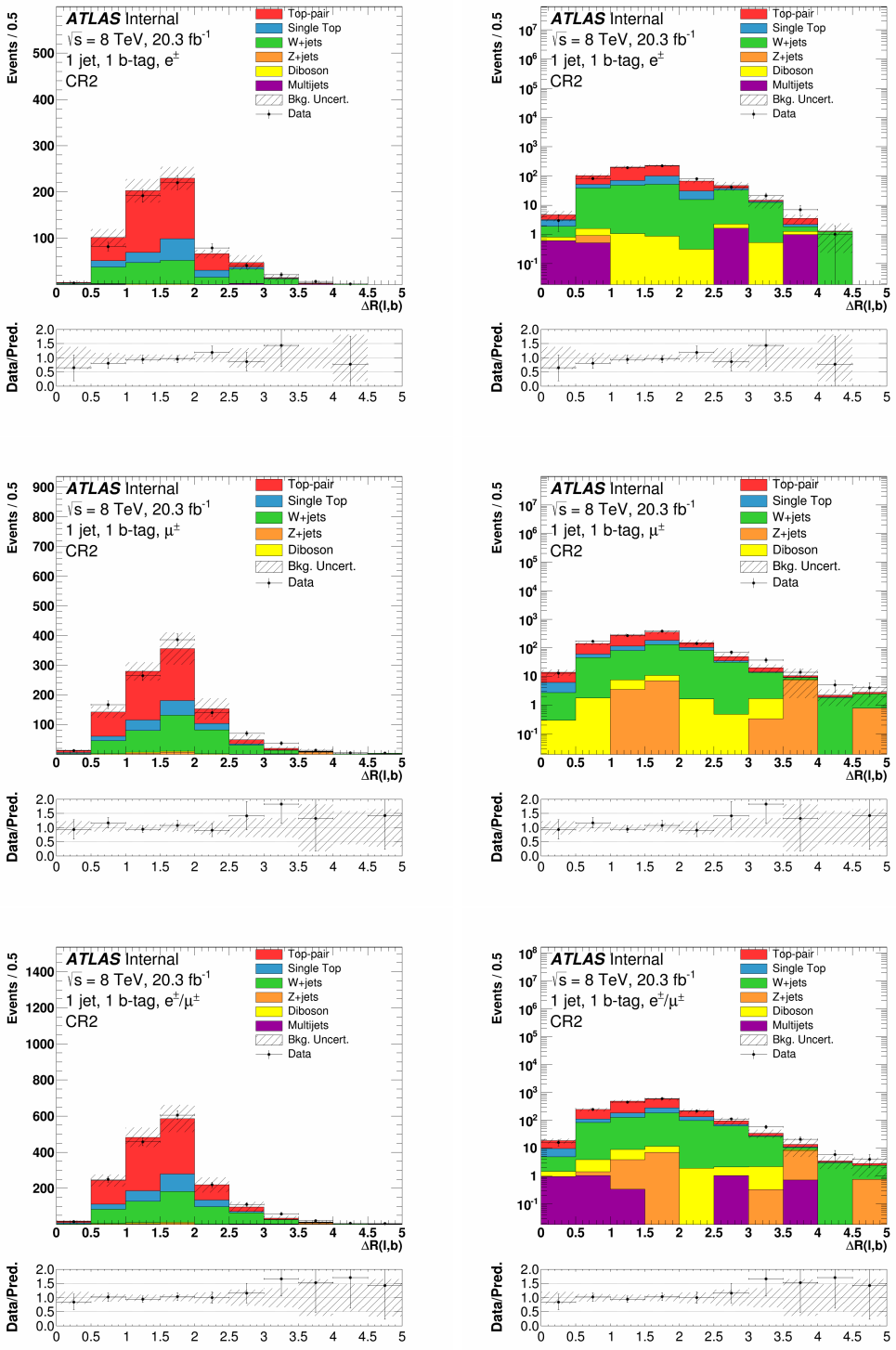

Figure B.26: Distributions of $\Delta\mathrm{R}(\ell, b)$ for the electron (top), the muon (middle), and the combined (bottom) channels in CR2, in linear (left) and log (right) scale. The uncertainty band on the expected background corresponds to the errors due to the statistical uncertainties added in quadrature with the cross-section and normalization uncertainties.

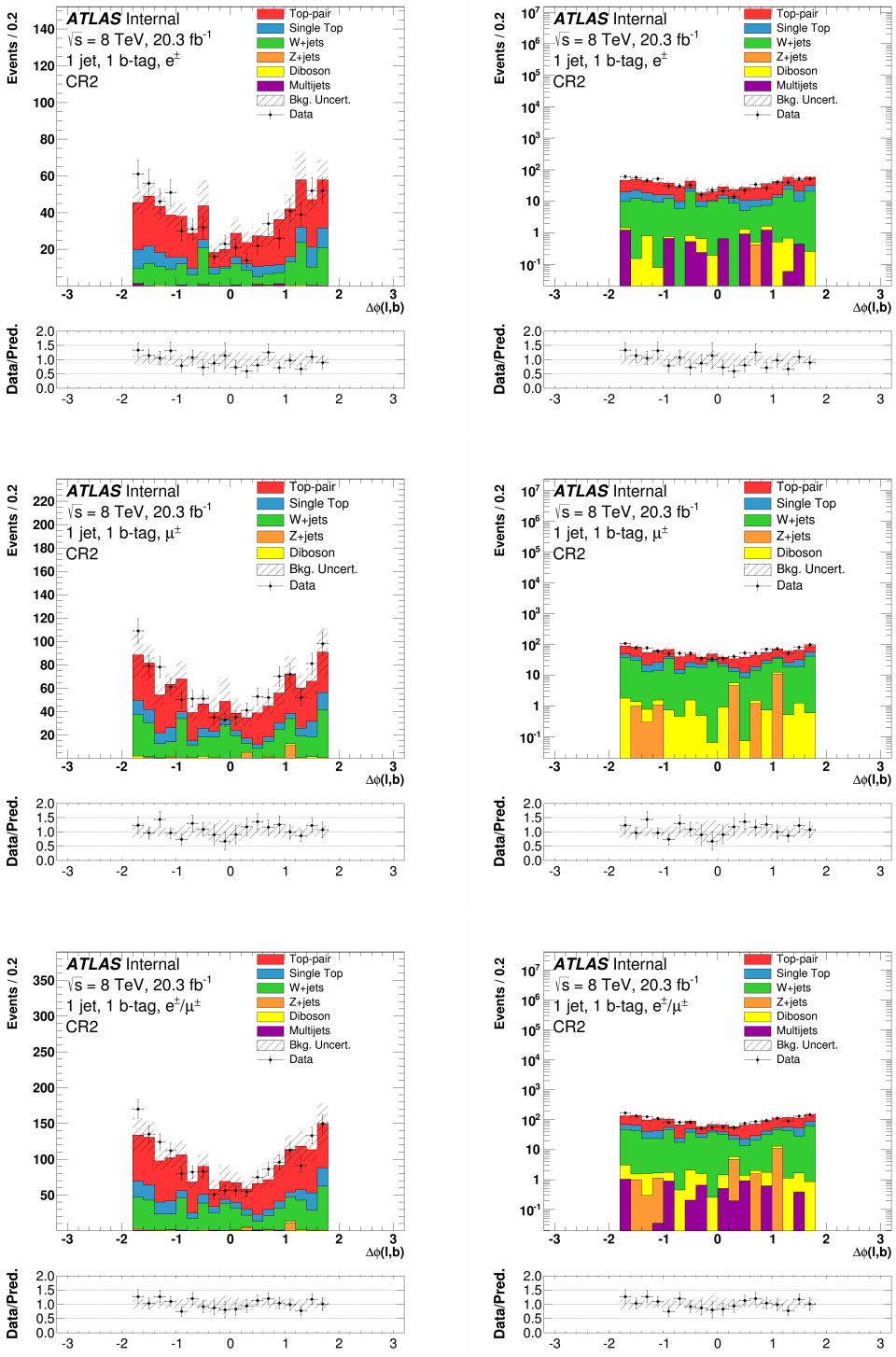

Figure B.27: Distributions of $\Delta\phi(\ell, b)$ for the electron (top), the muon (middle), and the combined (bottom) channels in CR2, in linear (left) and log (right) scale. The uncertainty band on the expected background corresponds to the errors due to the statistical uncertainties added in quadrature with the cross-section and normalization uncertainties.

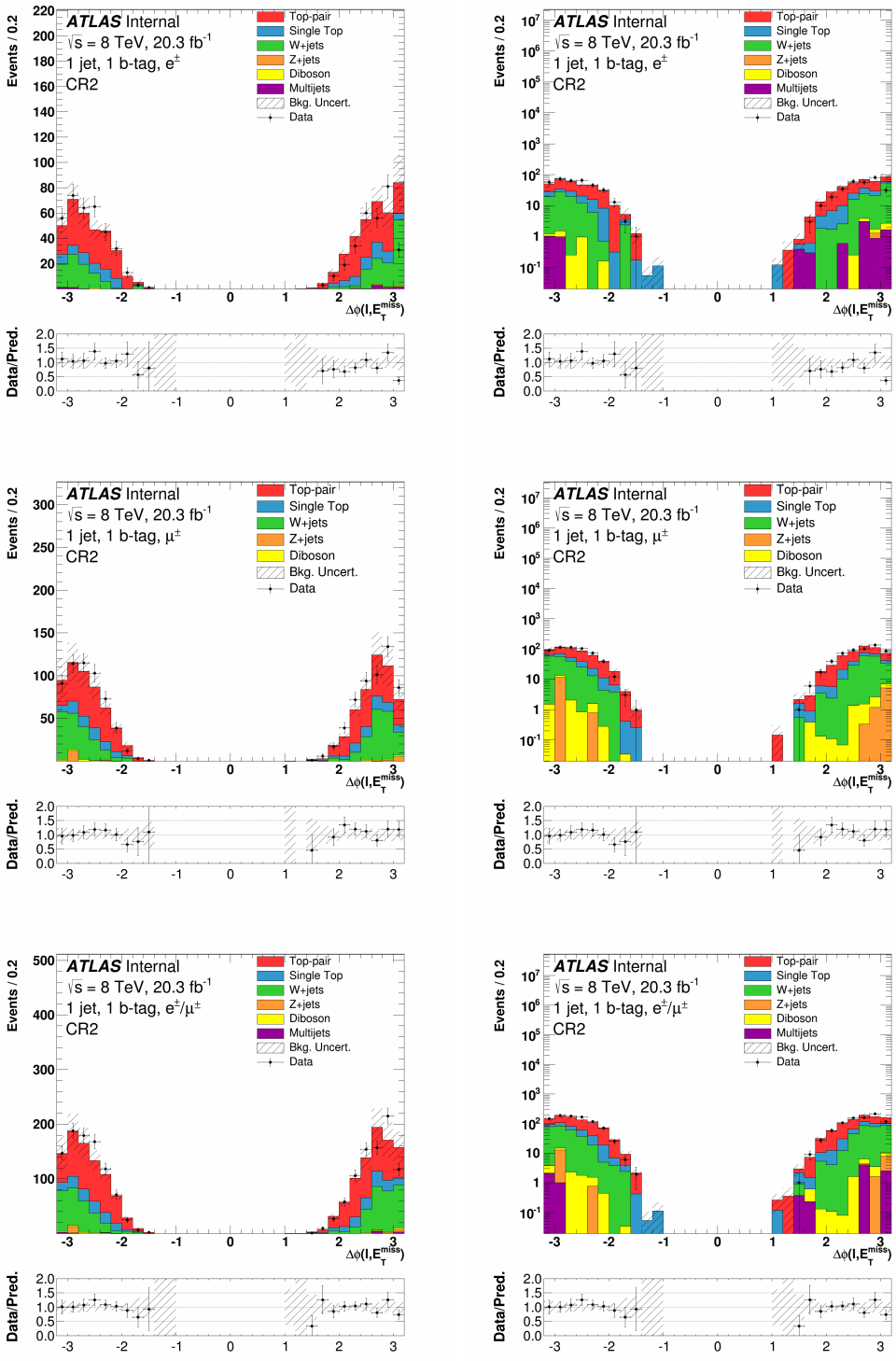

Figure B.28: Distributions of $\Delta\phi(\ell, E_{\mathrm{T}}^{\mathrm{miss}})$ for the electron (top), the muon (middle), and the combined (bottom) channels in CR2, in linear (left) and log (right) scale. The uncertainty band on the expected background corresponds to the errors due to the statistical uncertainties added in quadrature with the cross-section and normalization uncertainties.

CR3

This section presents distribution of variables for simulated background and data events in CR3 defined in Section 7.4. Figure B.29 shows the transverse mass between the lepton and missing transverse energy, $m_{\mathrm{T}}(\ell, E_{\mathrm{T}}^{\mathrm{miss}})$. Figure B.30 shows the missing transverse energy, $E_{\mathrm{T}}^{\mathrm{miss}}$. Figure B.31 shows the transverse momentum of the lepton, $p_{\mathrm{T}}(\ell)$. Figure B.32 shows the transverse momentum of the b-jet, $p_{\mathrm{T}}(b)$. Figure B.33 shows the spatial separation in $\eta - \phi$ space between the lepton and b-jet, $\Delta\mathrm{R}(\ell, b)$. Figure B.34 shows the angular separation in ϕ between the lepton and b-jet, $\Delta\phi(\ell, b)$. Figure B.35 shows the angular separation in ϕ between the lepton and the missing transverse energy, $\Delta\phi(\ell, E_{\mathrm{T}}^{\mathrm{miss}})$.

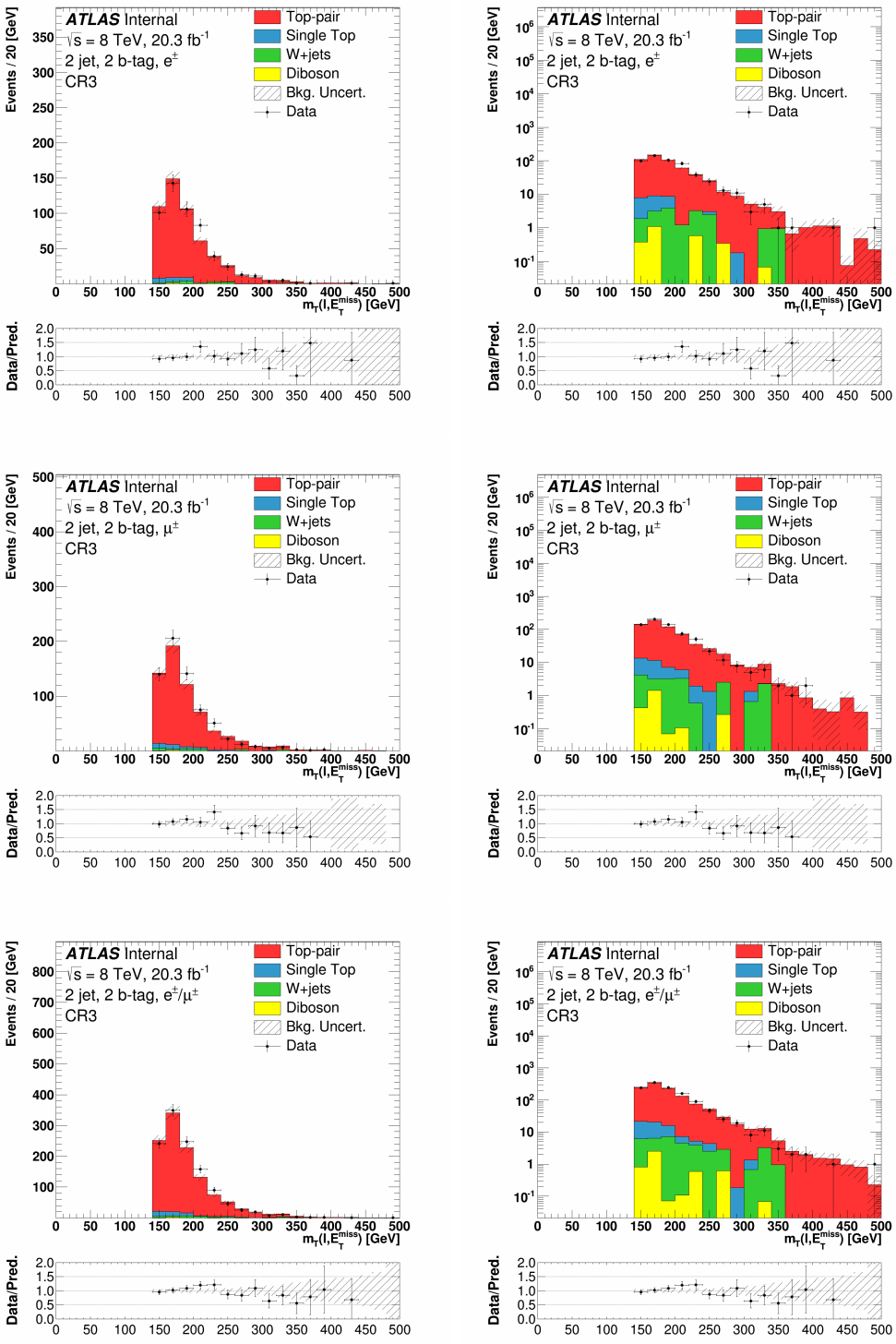

Figure B.29: Distributions of $m_{\mathrm{T}}(\ell, E_{\mathrm{T}}^{\mathrm{miss}})$ for the electron (top), the muon (middle), and the combined (bottom) channels in CR3, in linear (left) and log (right) scale. The uncertainty band on the expected background corresponds to the errors due to the statistical uncertainties added in quadrature with the cross-section and normalization uncertainties.

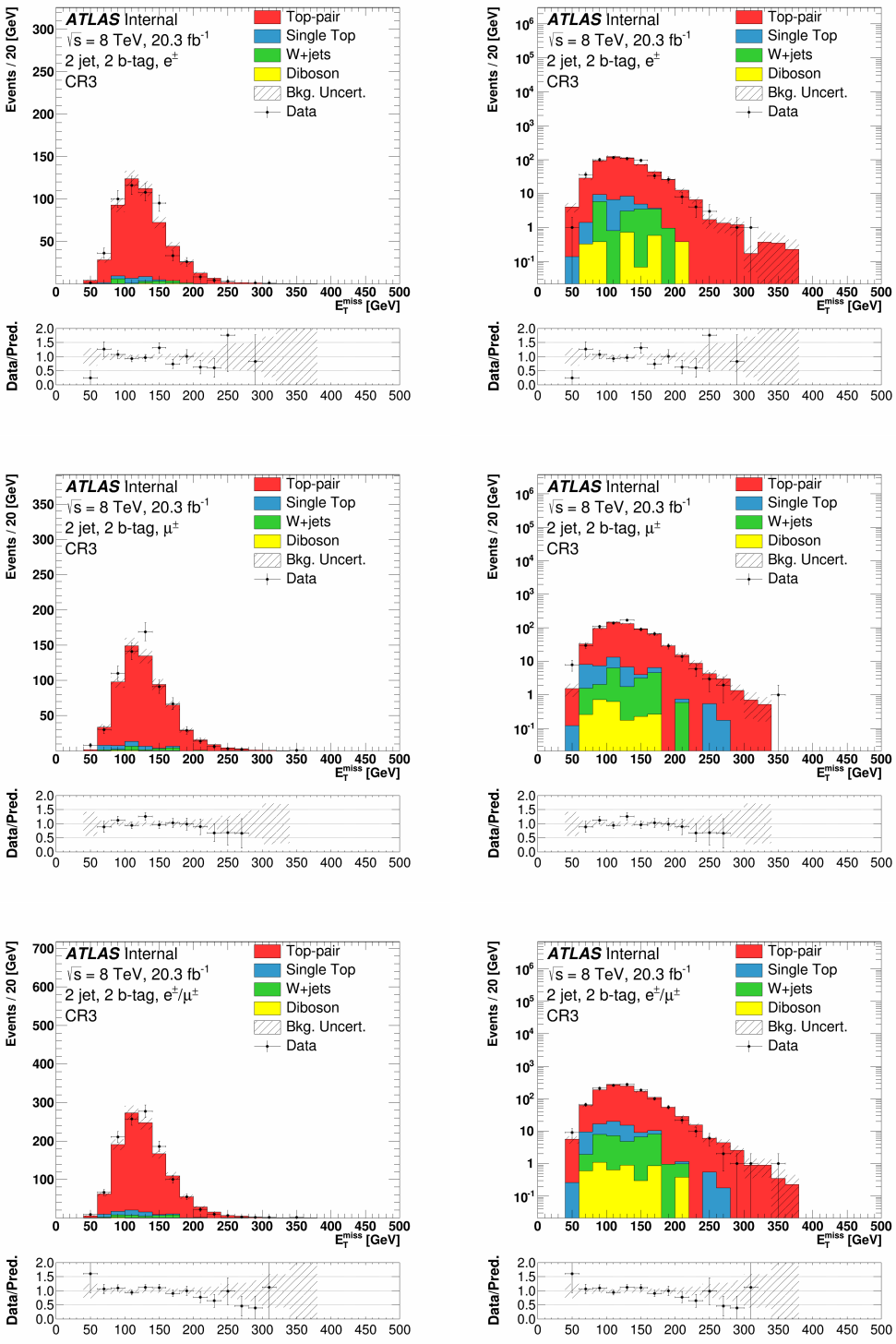

Figure B.30: Distributions of $E_{\mathrm{T}}^{\mathrm{miss}}$ for the electron (top), the muon (middle), and the combined (bottom) channels in CR3, in linear (left) and log (right) scale. The uncertainty band on the expected background corresponds to the errors due to the statistical uncertainties added in quadrature with the cross-section and normalization uncertainties.

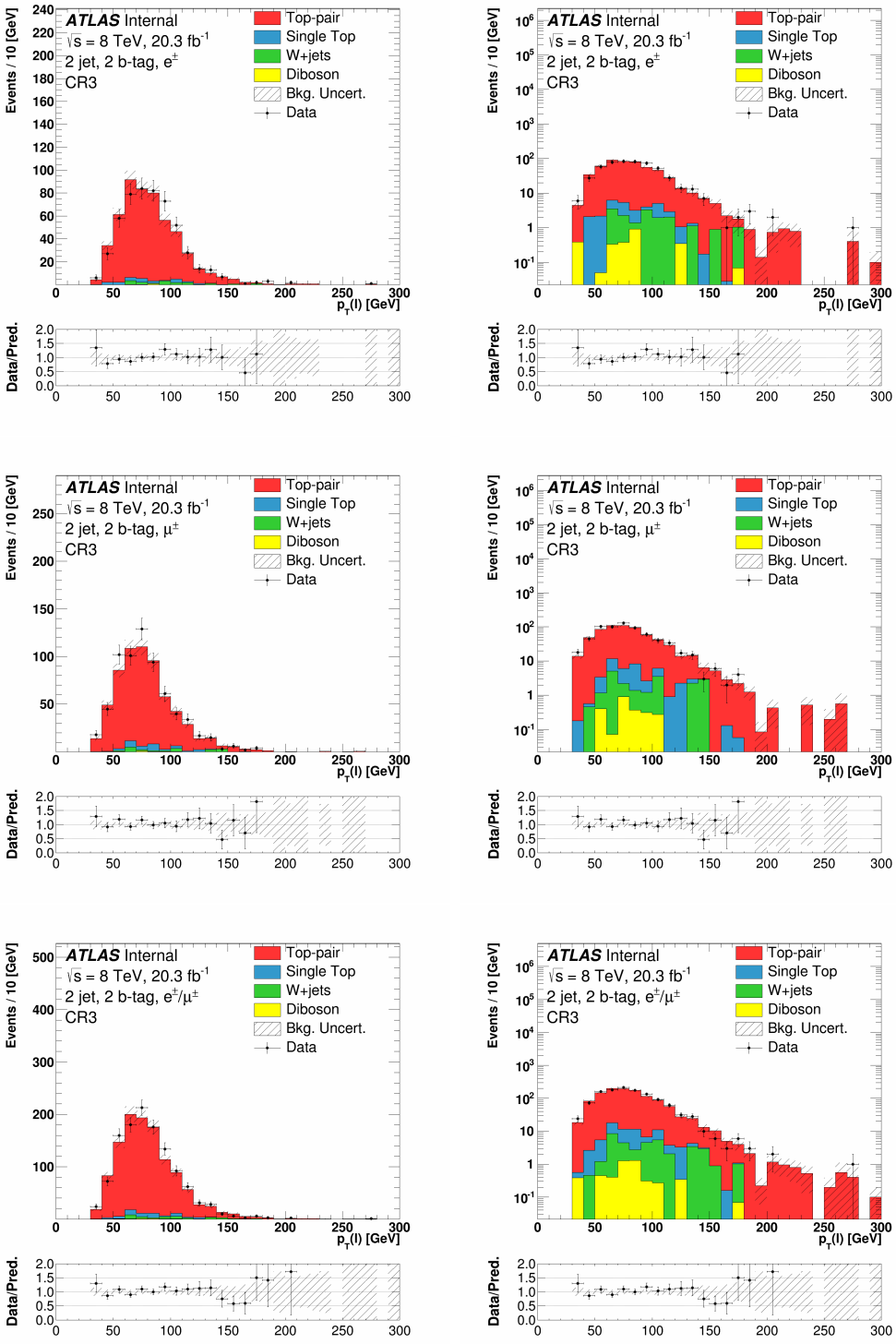

Figure B.31: Distributions of $p_{\mathrm{T}}(\ell)$ for the electron (top), the muon (middle), and the combined (bottom) channels in CR3, in linear (left) and log (right) scale. The uncertainty band on the expected background corresponds to the errors due to the statistical uncertainties added in quadrature with the cross-section and normalization uncertainties.

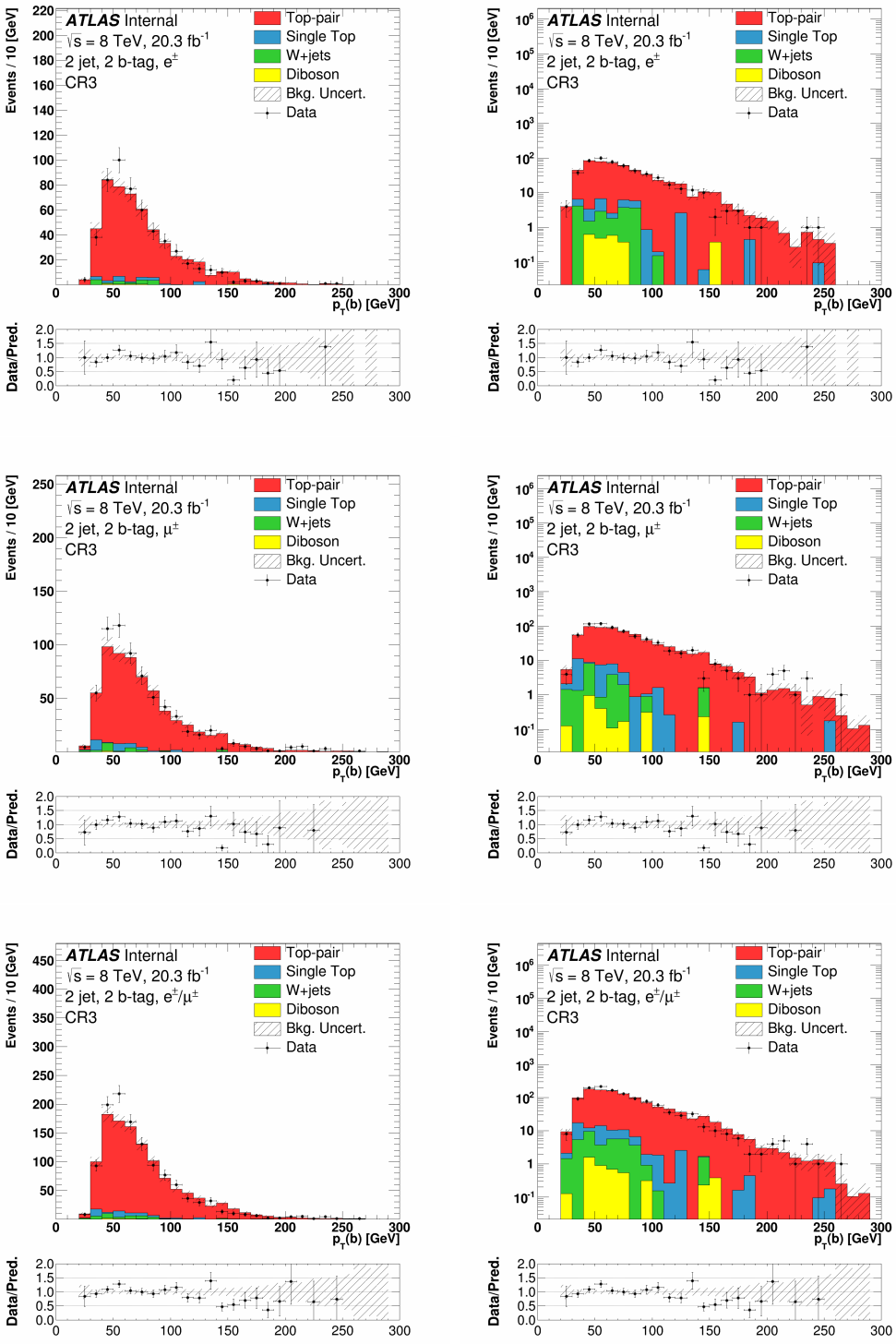

Figure B.32: Distributions of $p_{\mathrm{T}}(b)$ for the electron (top), the muon (middle), and the combined (bottom) channels in CR3, in linear (left) and log (right) scale. The uncertainty band on the expected background corresponds to the errors due to the statistical uncertainties added in quadrature with the cross-section and normalization uncertainties.

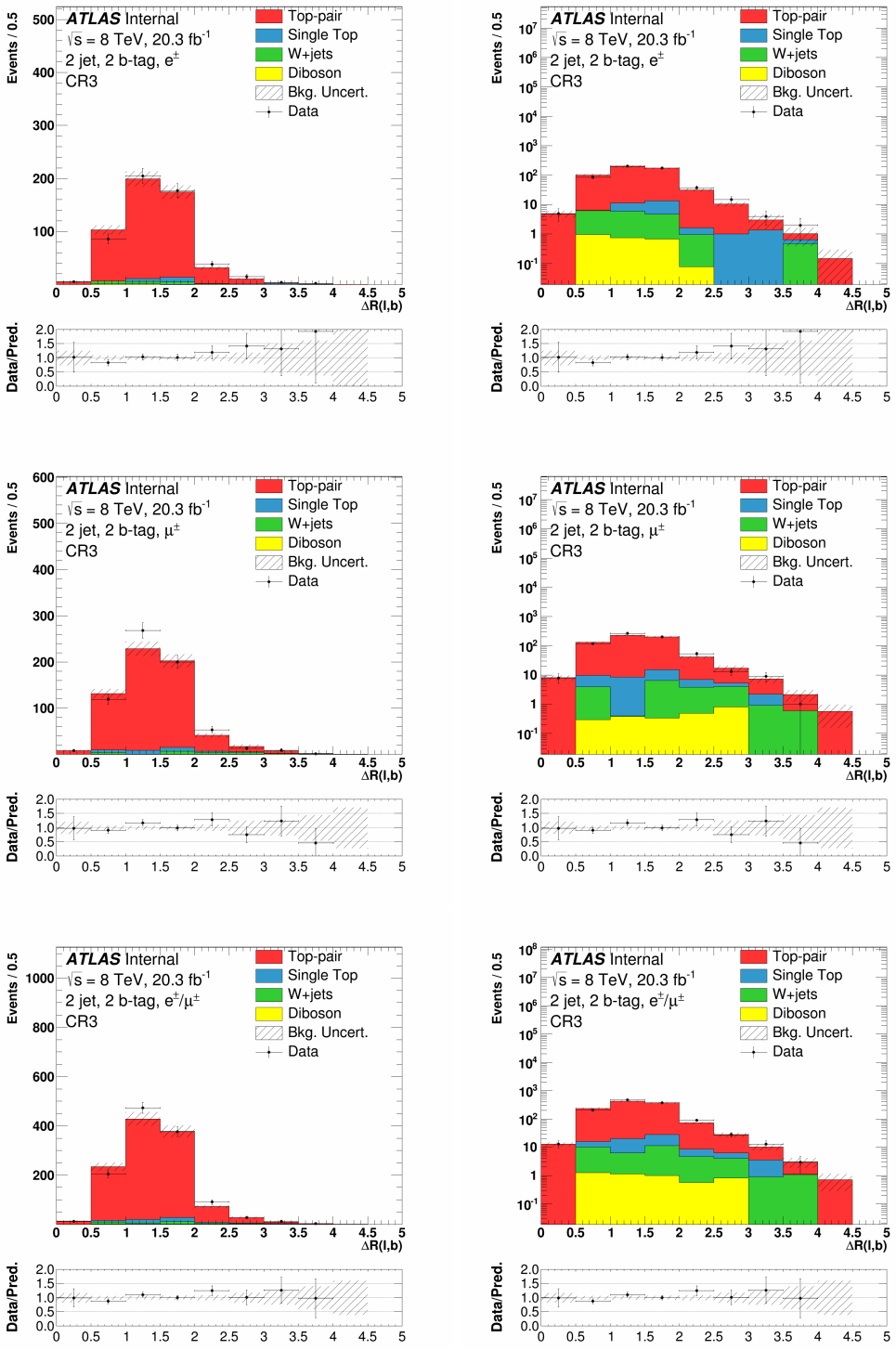

Figure B.33: Distributions of $\Delta R(\ell, b)$ for the electron (top), the muon (middle), and the combined (bottom) channels in CR3, in linear (left) and log (right) scale. The uncertainty band on the expected background corresponds to the errors due to the statistical uncertainties added in quadrature with the cross-section and normalization uncertainties.

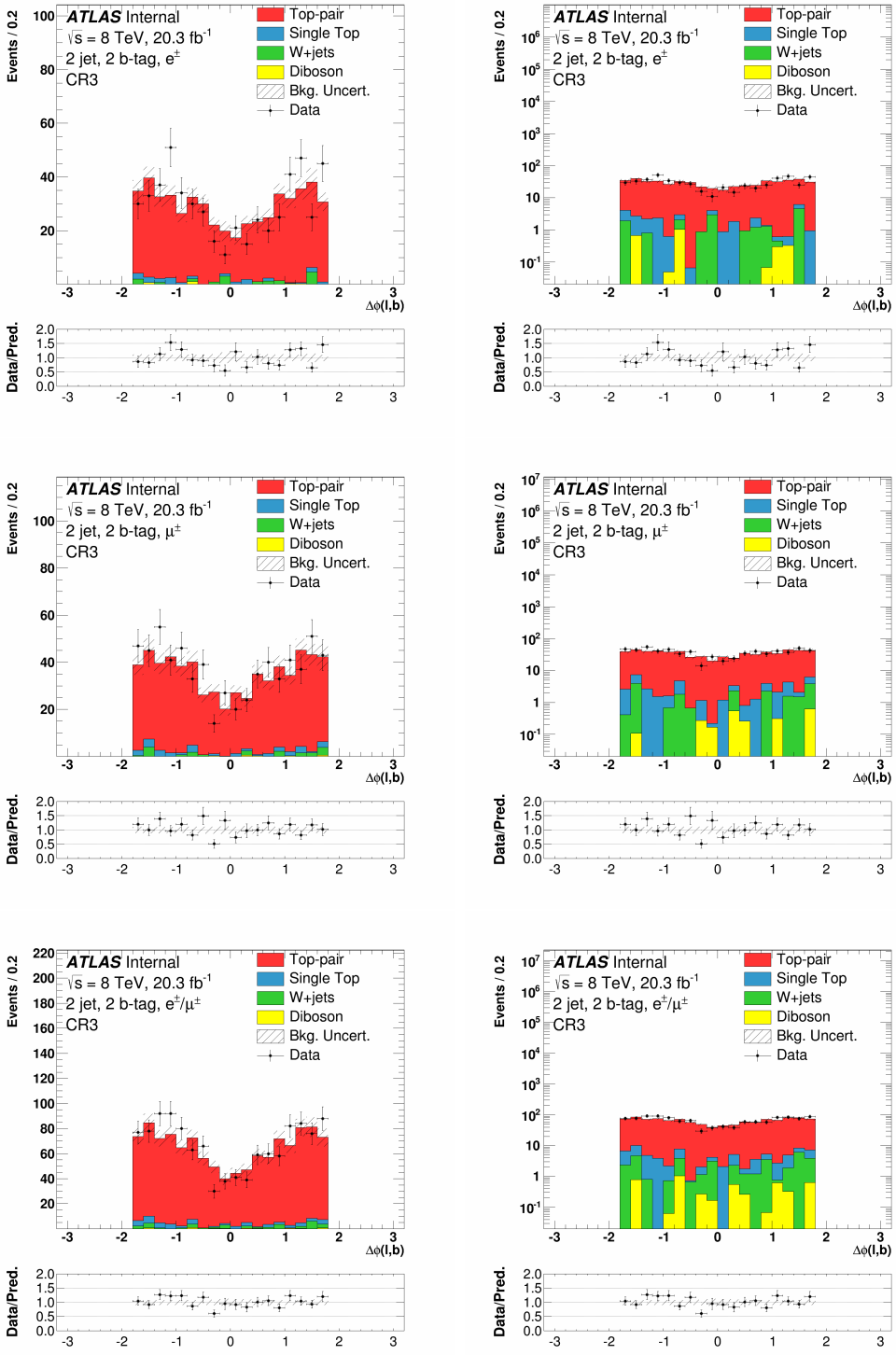

Figure B.34: Distributions of $\Delta\phi(\ell, b)$ for the electron (top), the muon (middle), and the combined (bottom) channels in CR3, in linear (left) and log (right) scale. The uncertainty band on the expected background corresponds to the errors due to the statistical uncertainties added in quadrature with the cross-section and normalization uncertainties.

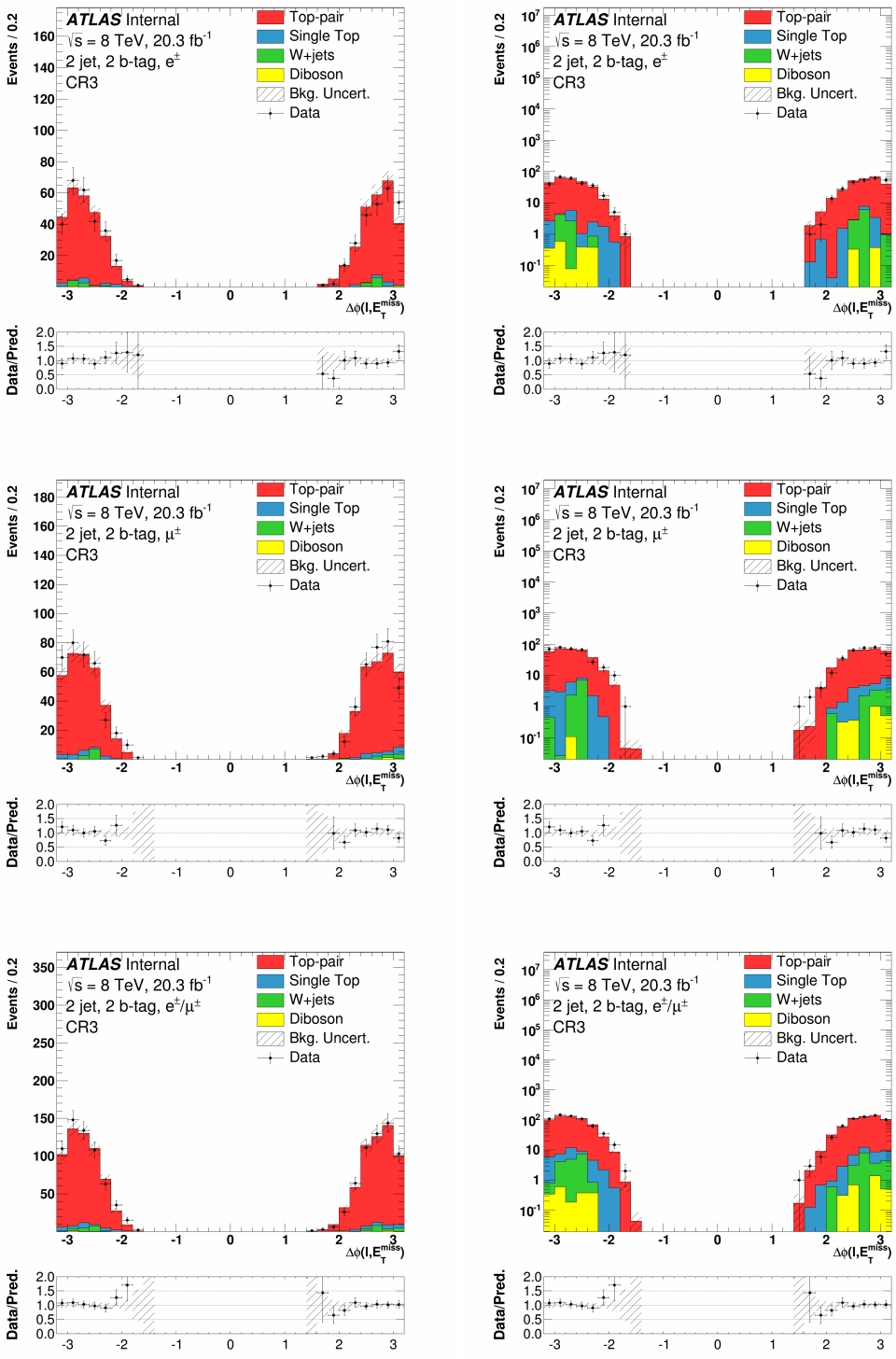

Figure B.35: Distributions of $\Delta\phi(\ell, E_{\mathrm{T}}^{\mathrm{miss}})$ for the electron (top), the muon (middle), and the combined (bottom) channels in CR3, in linear (left) and log (right) scale. The uncertainty band on the expected background corresponds to the errors due to the statistical uncertainties added in quadrature with the cross-section and normalization uncertainties.

Appendix C

8 TeV signal region plots

This appendix presents kinematic distributions comparing the SM predictions to the data observations in the various signal regions defined in Chapter 7. Also shown are kinematic distributions normalized to unity for various signal samples. Distributions of the $m_{\mathrm{T}}(\ell, E_{\mathrm{T}}^{\mathrm{miss}})$, $E_{\mathrm{T}}^{\mathrm{miss}}$, $p_{\mathrm{T}}(\ell)$, $p_{\mathrm{T}}(b)$, $\Delta\mathrm{R}(\ell, b)$, $\Delta\phi(\ell, b)$, and $\Delta\phi(\ell, E_{\mathrm{T}}^{\mathrm{miss}})$ are shown in the signal region (Section C), in the optimized SR1 signal region (Section C), in the optimized SR2 signal region (Section C) and in the optimized BDT signal region (Section C).

Signal region

This section presents distributions of variables for simulated background and data events in the signal region, SR, defined in Section 7.5. Figures C.1 and C.2 show the transverse mass between the lepton and missing transverse energy, $m_{\mathrm{T}}(\ell, E_{\mathrm{T}}^{\mathrm{miss}})$. Figures C.3 and C.4 show the missing transverse energy, $E_{\mathrm{T}}^{\mathrm{miss}}$. Figures C.5 and C.6 show the transverse momentum of the lepton, $p_{\mathrm{T}}(\ell)$. Figures C.7 and C.8 show the transverse momentum of the b-jet, $p_{\mathrm{T}}(b)$. Figures C.9 and C.10 show the spatial separation in $\eta - \phi$ space between the lepton and b-jet, $\Delta\mathrm{R}(\ell, b)$. Figures C.11 and C.12 show the angular separation in ϕ between the lepton and b-jet, $\Delta\phi(\ell, b)$. Figures C.13 and C.14 show the angular separation in ϕ between the lepton and the missing transverse energy, $\Delta\phi(\ell, E_{\mathrm{T}}^{\mathrm{miss}})$.

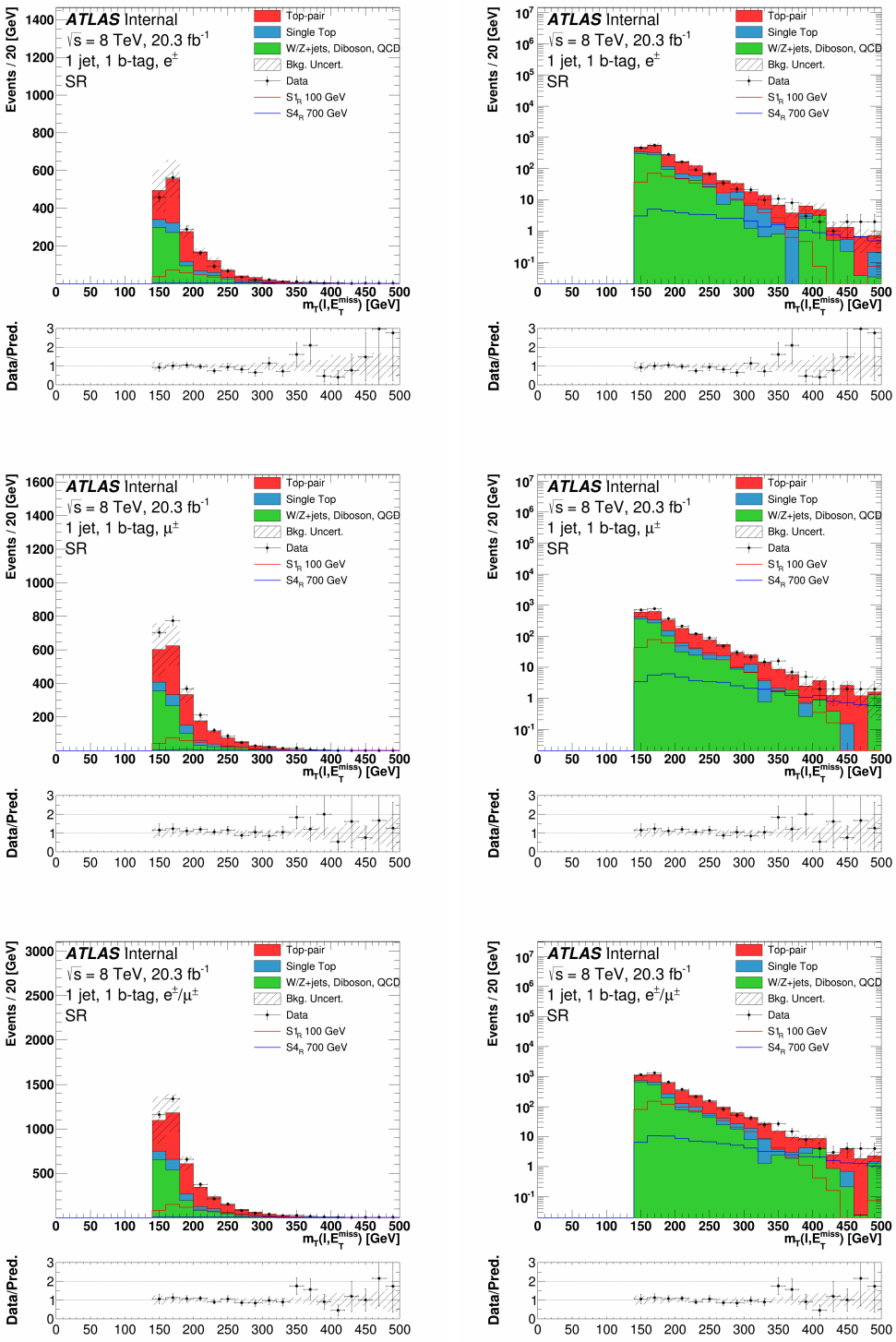

Figure C.1: Distributions of $m_{\mathrm{T}}(\ell, E_{\mathrm{T}}^{\mathrm{miss}})$ for the electron (top), the muon (middle), and the combined (bottom) channels in the signal region, in linear (left) and log (right) scale. The uncertainty band on the expected background corresponds to the errors due to the statistical uncertainties added in quadrature with the cross-section and normalization uncertainties.

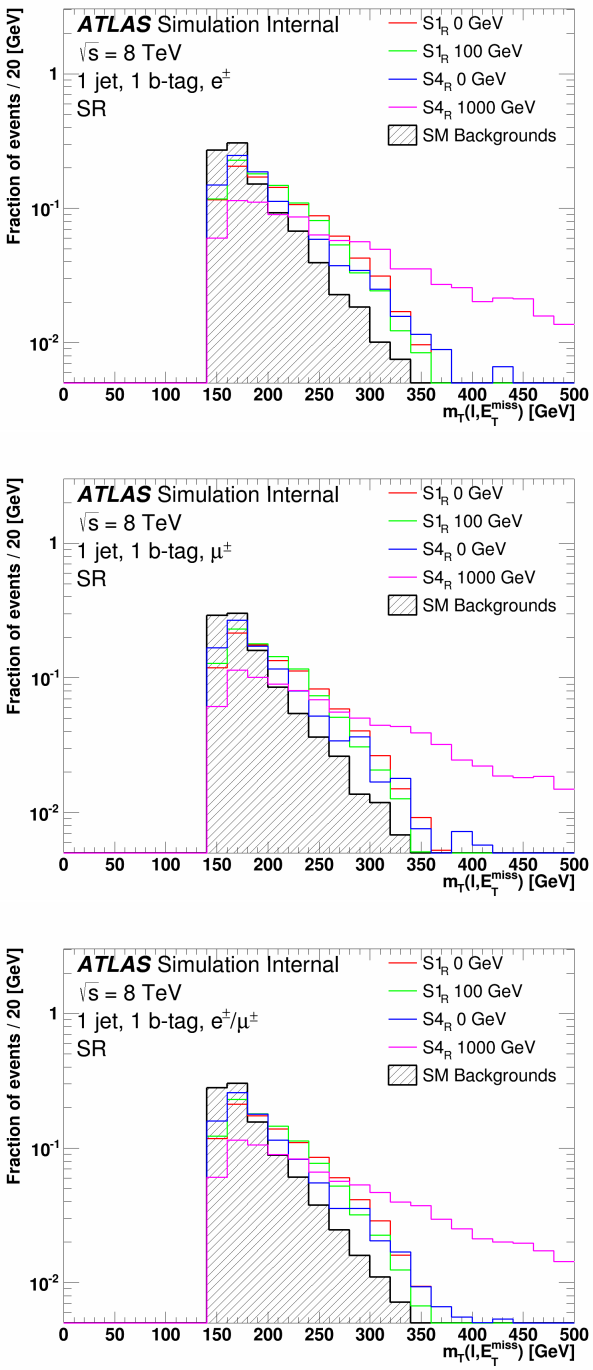

Figure C.2: Distributions of $m_{\mathrm{T}}(\ell, E_{\mathrm{T}}^{\mathrm{miss}})$ normalized to unity for the electron (top), the muon (middle), and the combined (bottom) channels in the signal region for the highest and lowest mass hypotheses of both the $\mathrm{S1_R}$ and $\mathrm{S4_R}$ models. The SM background is also shown.

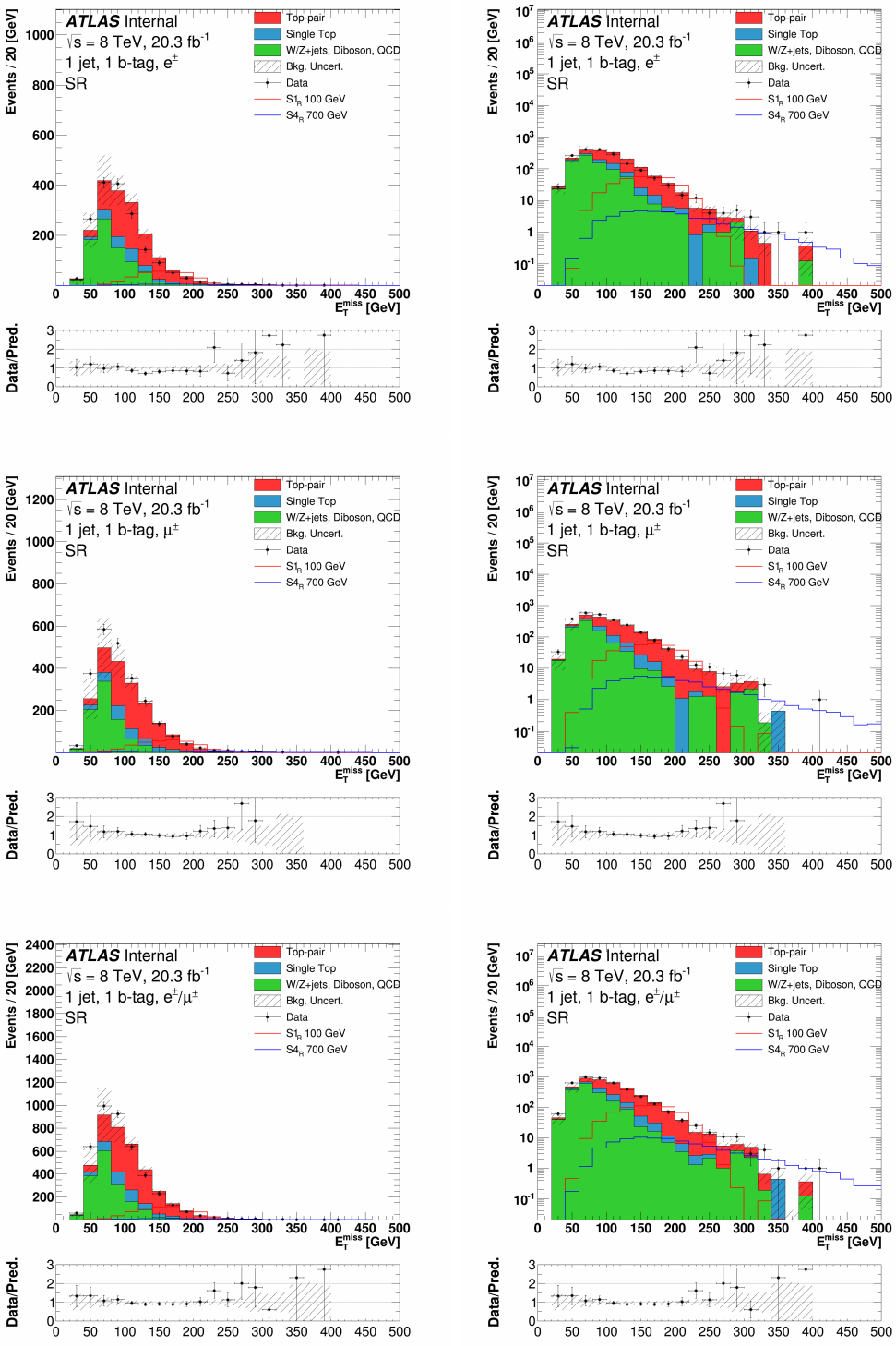

Figure C.3: Distributions of $E_{\mathrm{T}}^{\mathrm{miss}}$ for the electron (top), the muon (middle), and the combined (bottom) channels in the signal region, in linear (left) and log (right) scale. The uncertainty band on the expected background corresponds to the errors due to the statistical uncertainties added in quadrature with the cross-section and normalization uncertainties.

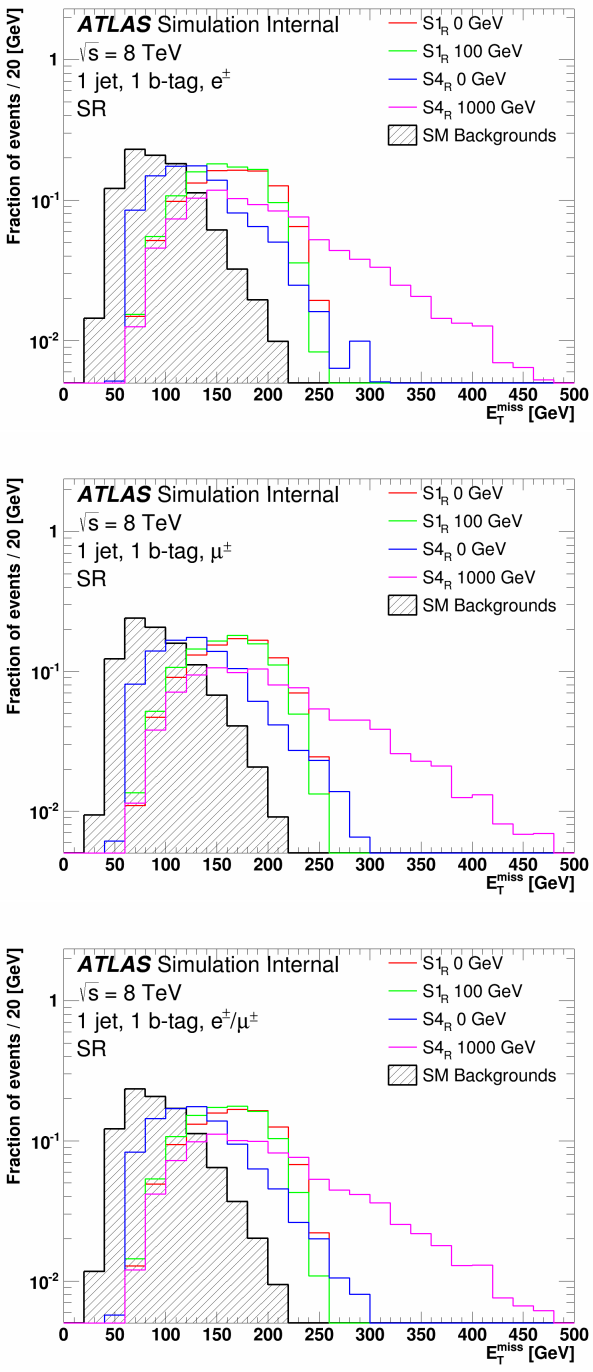

Figure C.4: Distributions of $E_{\mathrm{T}}^{\mathrm{miss}}$ normalized to unity for the electron (top), the muon (middle), and the combined (bottom) channels in the signal region for the highest and lowest mass hypotheses of both the $\mathrm{S1_R}$ and $\mathrm{S4_R}$ models. The SM background is also shown.

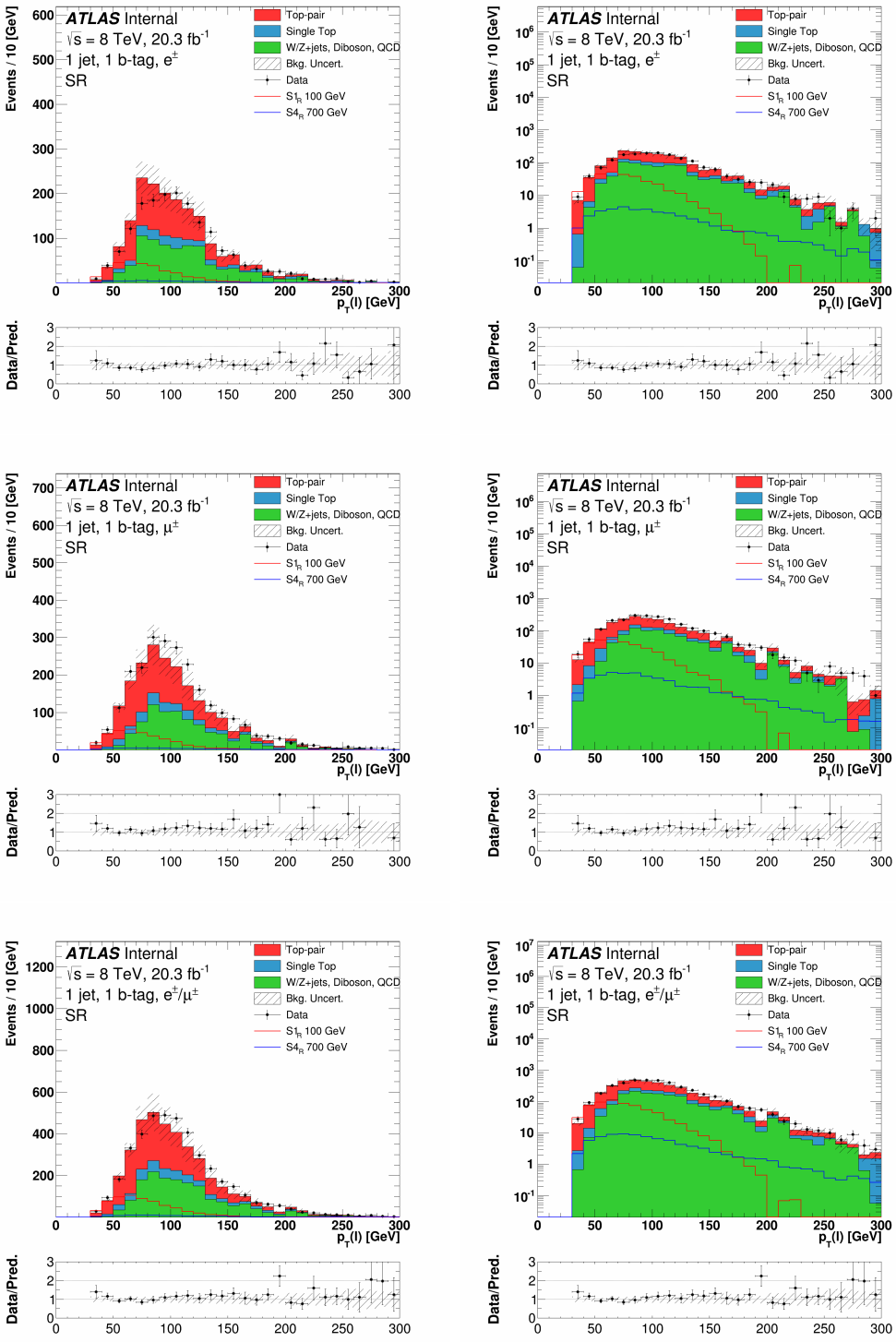

Figure C.5: Distributions of $p_{\mathrm{T}}(\ell)$ for the electron (top), the muon (middle), and the combined (bottom) channels in the signal region, in linear (left) and log (right) scale. The uncertainty band on the expected background corresponds to the errors due to the statistical uncertainties added in quadrature with the cross-section and normalization uncertainties.

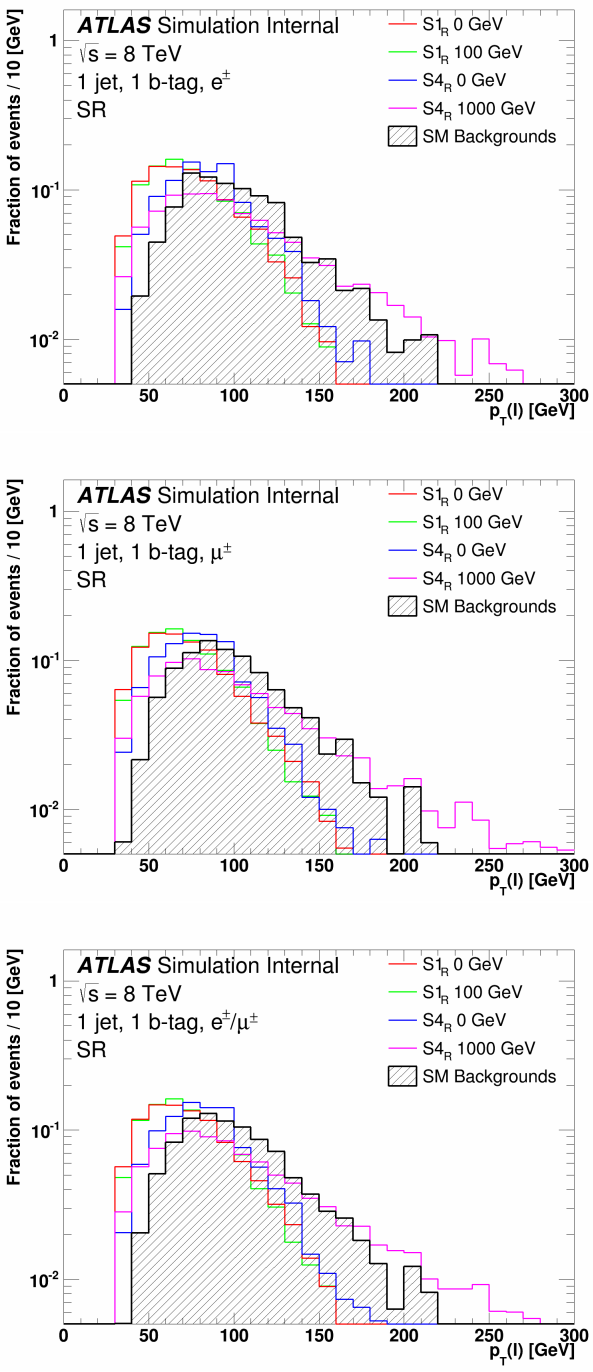

Figure C.6: Distributions of $p_{\mathrm{T}}(\ell)$ normalized to unity for the electron (top), the muon (middle), and the combined (bottom) channels in the signal region for the highest and lowest mass hypotheses of both the $\mathrm{S1_R}$ and $\mathrm{S4_R}$ models. The SM background is also shown.

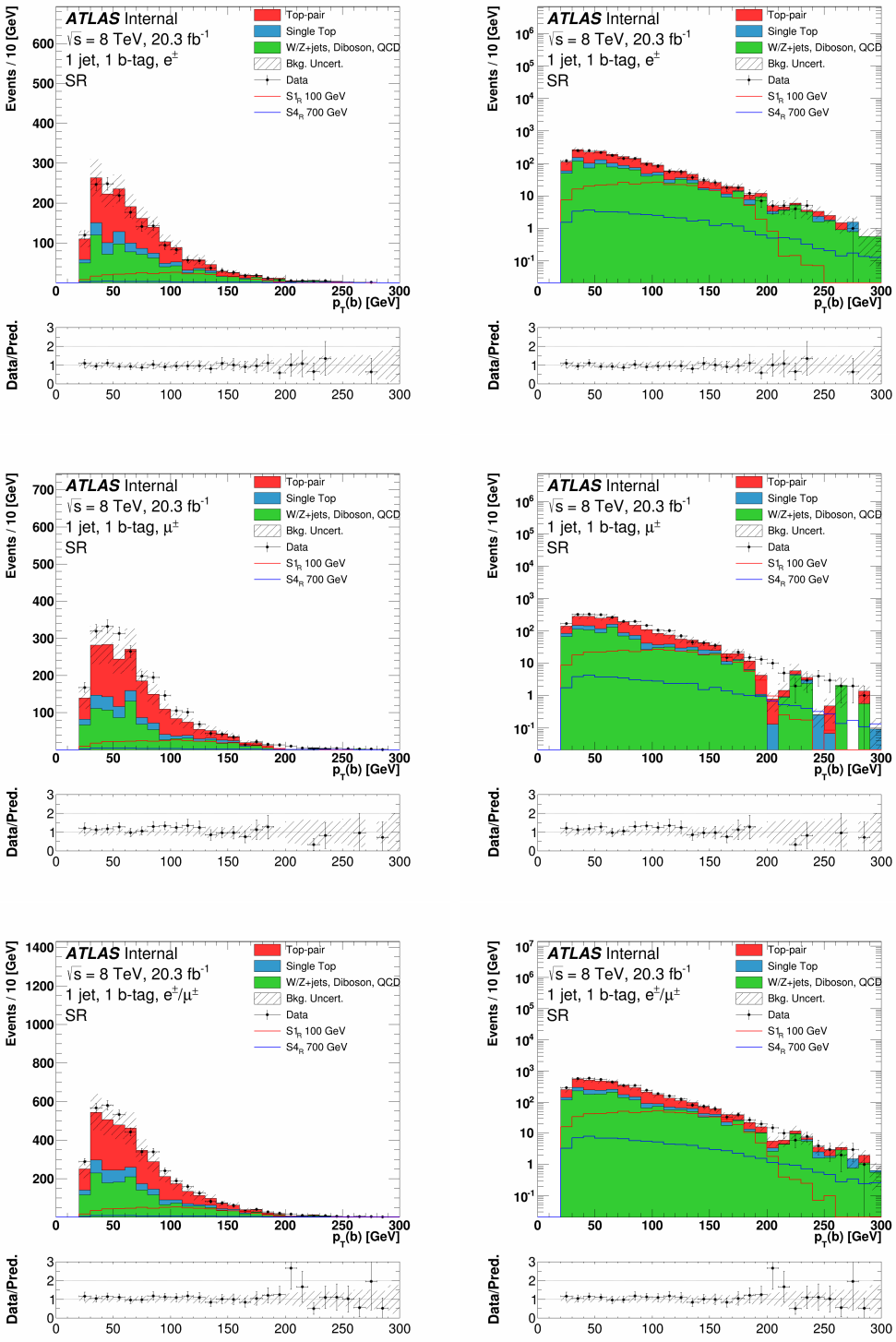

Figure C.7: Distributions of $p_{\mathrm{T}}(b)$ for the electron (top), the muon (middle), and the combined (bottom) channels in the signal region, in linear (left) and log (right) scale. The uncertainty band on the expected background corresponds to the errors due to the statistical uncertainties added in quadrature with the cross-section and normalization uncertainties.

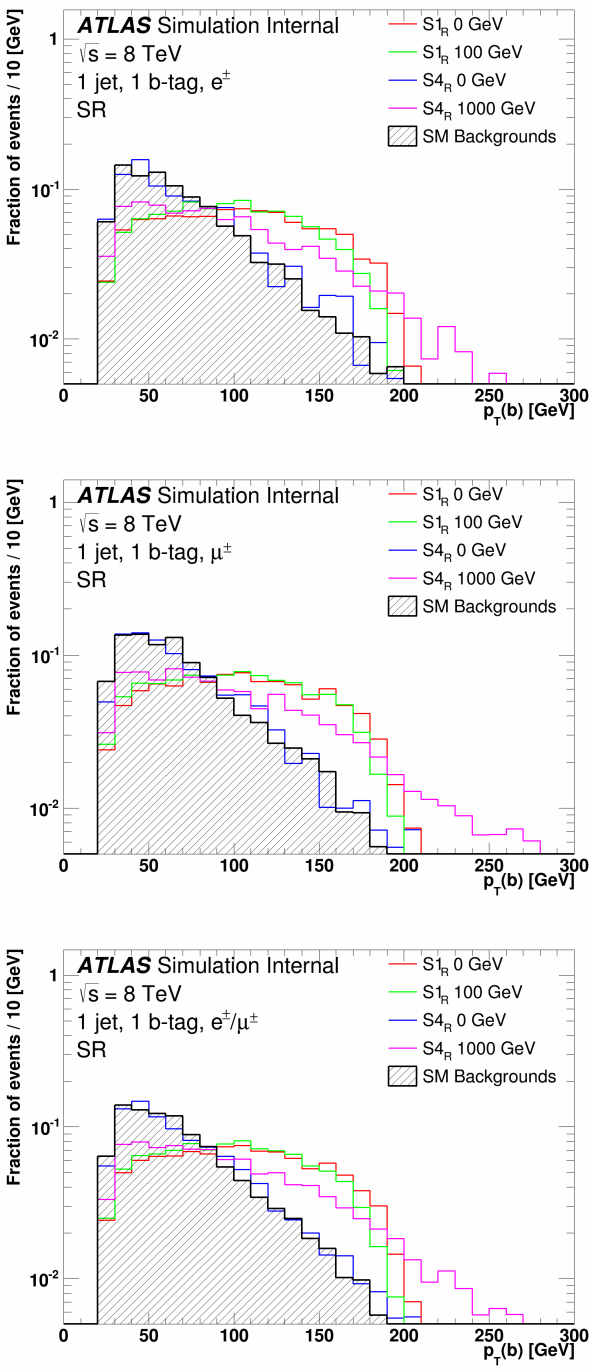

Figure C.8: Distributions of $p_{\mathrm{T}}(b)$ normalized to unity for the electron (top), the muon (middle), and the combined (bottom) channels in the signal region for the highest and lowest mass hypotheses of both the $\mathrm{S1_R}$ and $\mathrm{S4_R}$ models. The SM background is also shown.

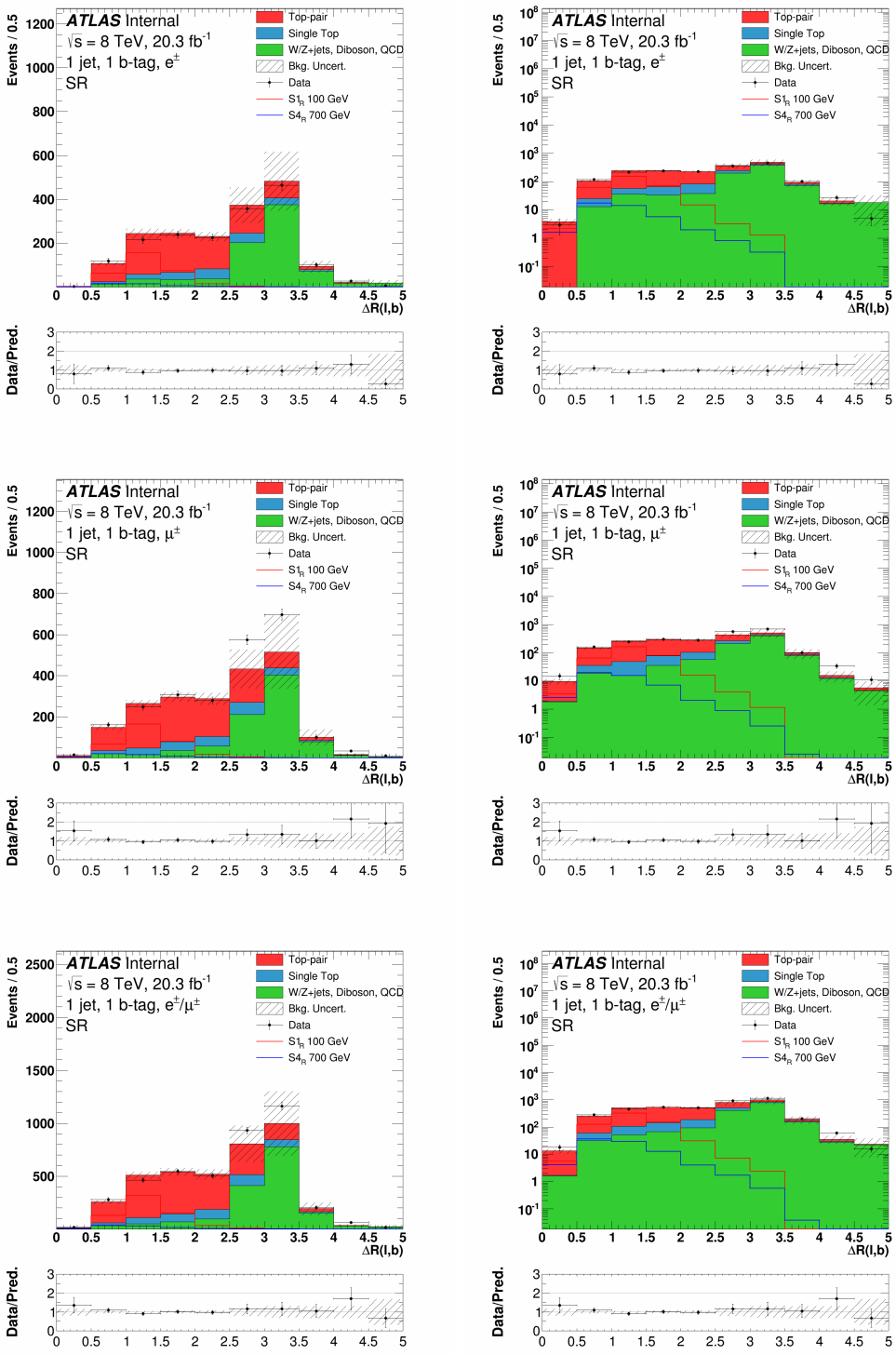

Figure C.9: Distributions of $\Delta\mathrm{R}(\ell, b)$ for the electron (top), the muon (middle), and the combined (bottom) channels in the signal region, in linear (left) and log (right) scale. The uncertainty band on the expected background corresponds to the errors due to the statistical uncertainties added in quadrature with the cross-section and normalization uncertainties.

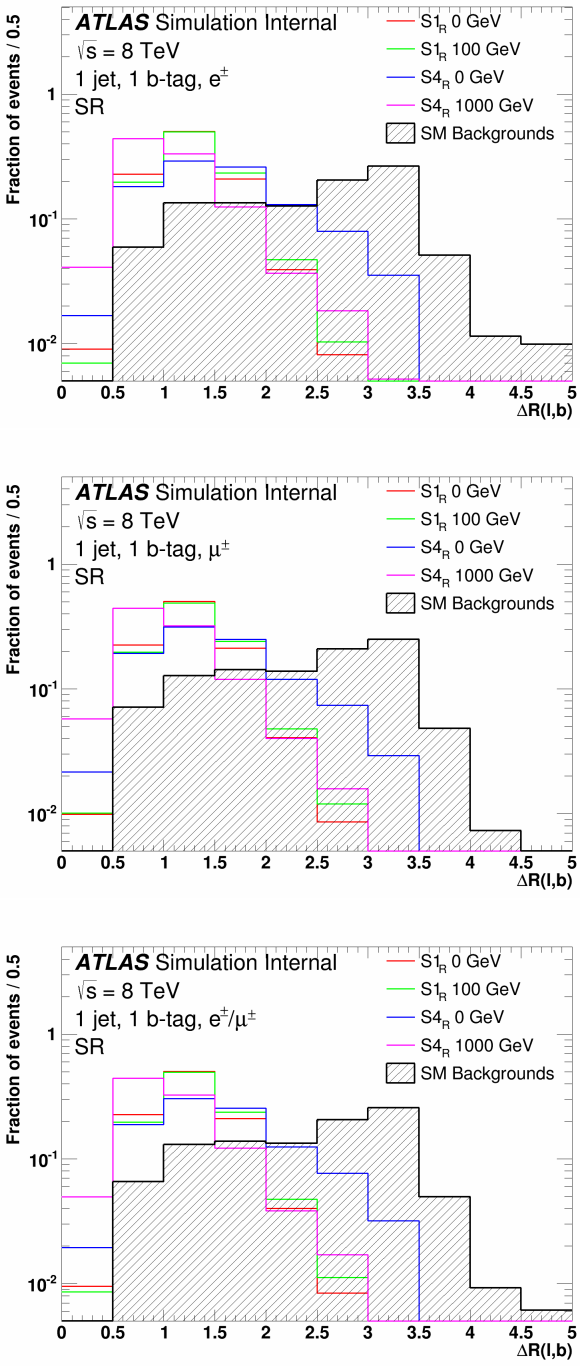

Figure C.10: Distributions of $\Delta R(\ell, b)$ normalized to unity for the electron (top), the muon (middle), and the combined (bottom) channels in the signal region for the highest and lowest mass hypotheses of both the $S1_R$ and $S4_R$ models. The SM background is also shown.

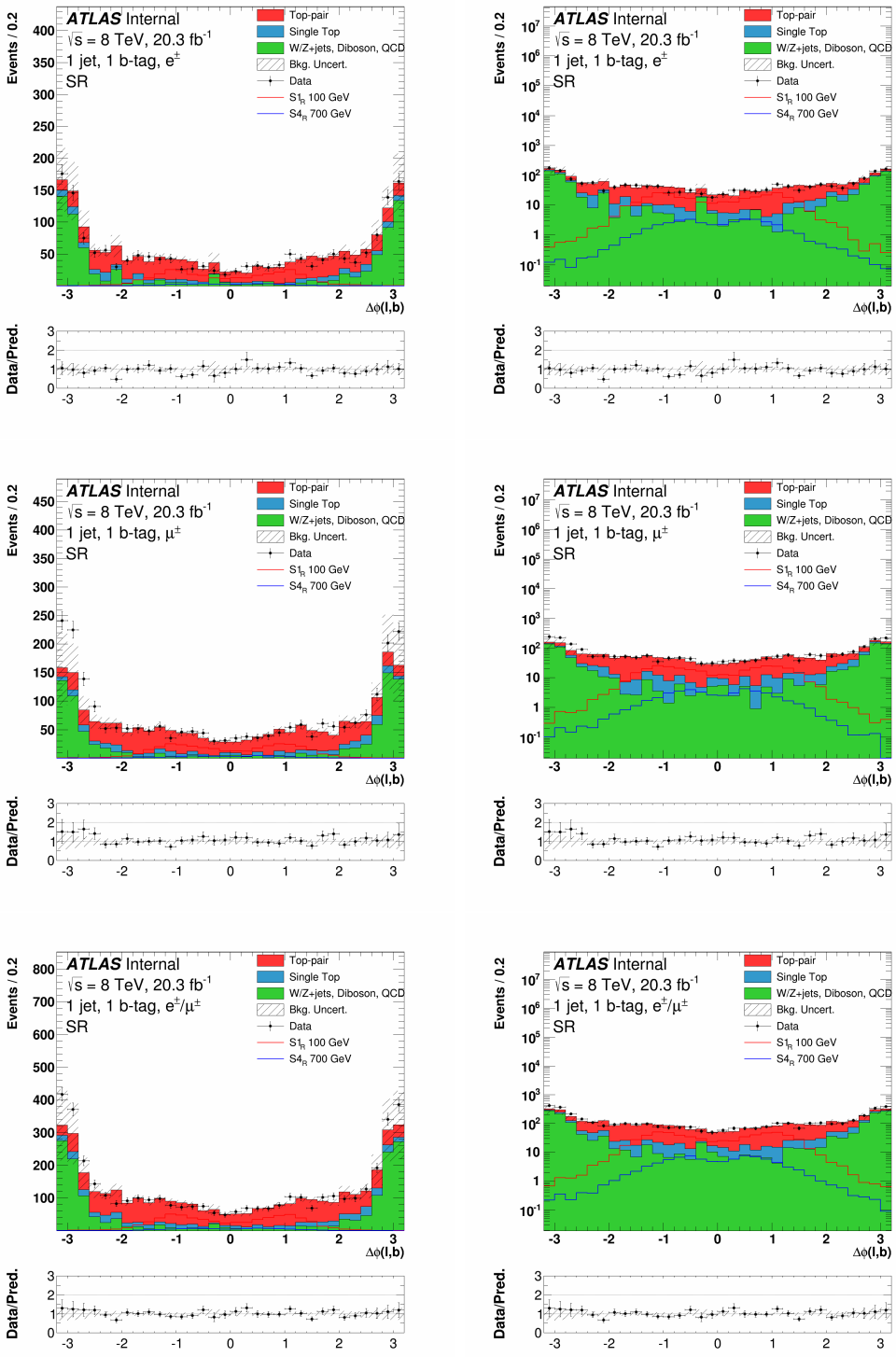

Figure C.11: Distributions of $\Delta\phi(\ell, b)$ for the electron (top), the muon (middle), and the combined (bottom) channels in the signal region, in linear (left) and log (right) scale. The uncertainty band on the expected background corresponds to the errors due to the statistical uncertainties added in quadrature with the cross-section and normalization uncertainties.

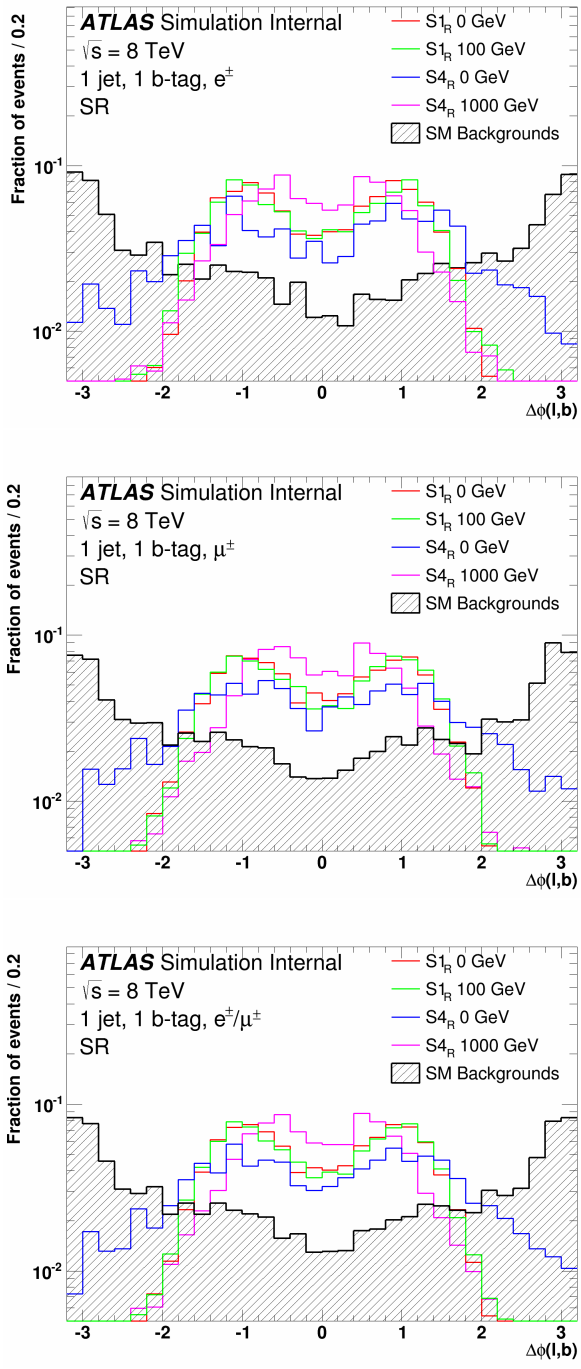

Figure C.12: Distributions of $\Delta\phi(\ell, b)$ normalized to unity for the electron (top), the muon (middle), and the combined (bottom) channels in the signal region for the highest and lowest mass hypotheses of both the $S1_R$ and $S4_R$ models. The SM background is also shown.

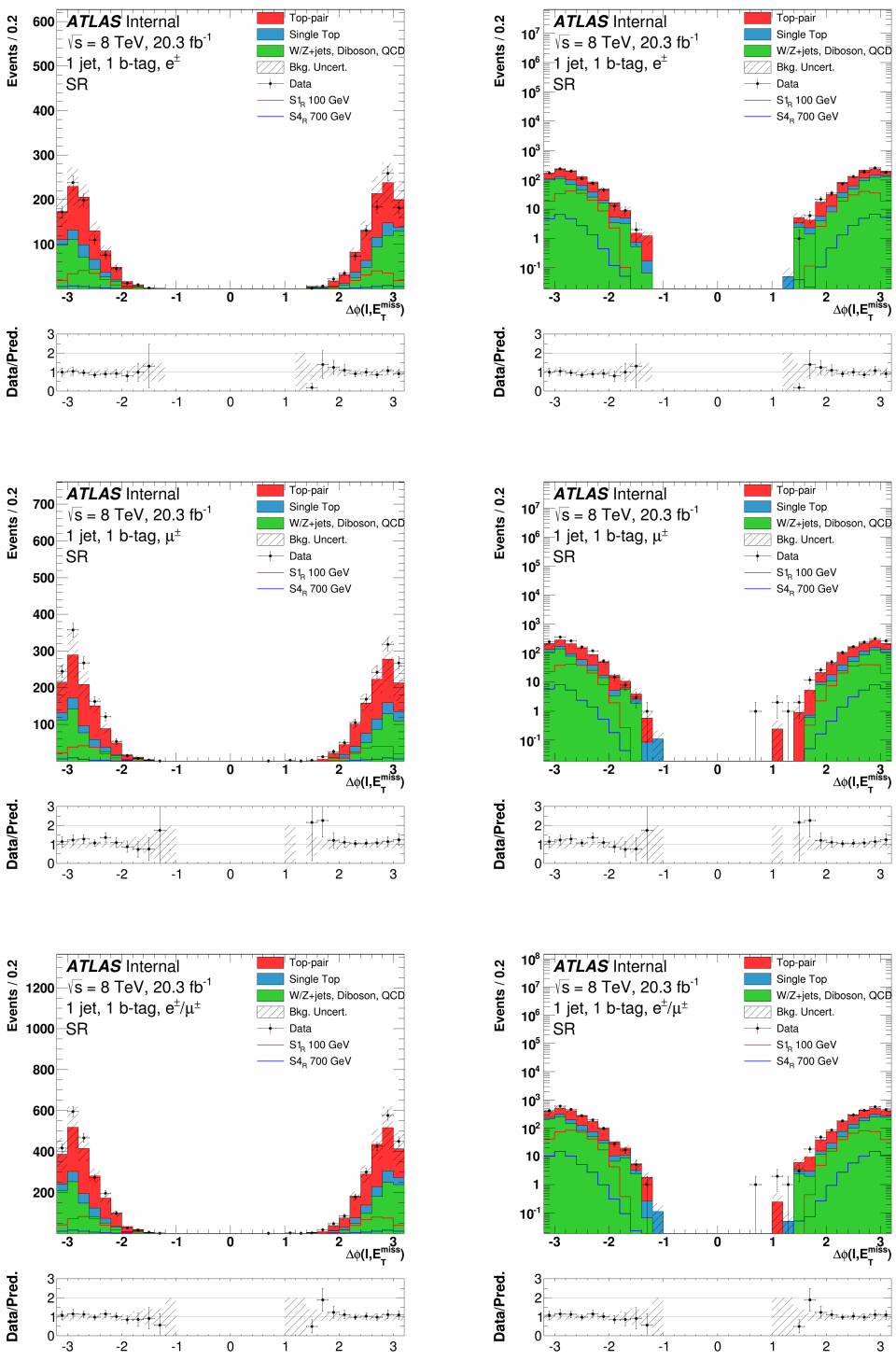

Figure C.13: Distributions of $\Delta\phi(\ell, E_{\mathrm{T}}^{\mathrm{miss}})$ for the electron (top), the muon (middle), and the combined (bottom) channels in the signal region, in linear (left) and log (right) scale. The uncertainty band on the expected background corresponds to the errors due to the statistical uncertainties added in quadrature with the cross-section and normalization uncertainties.

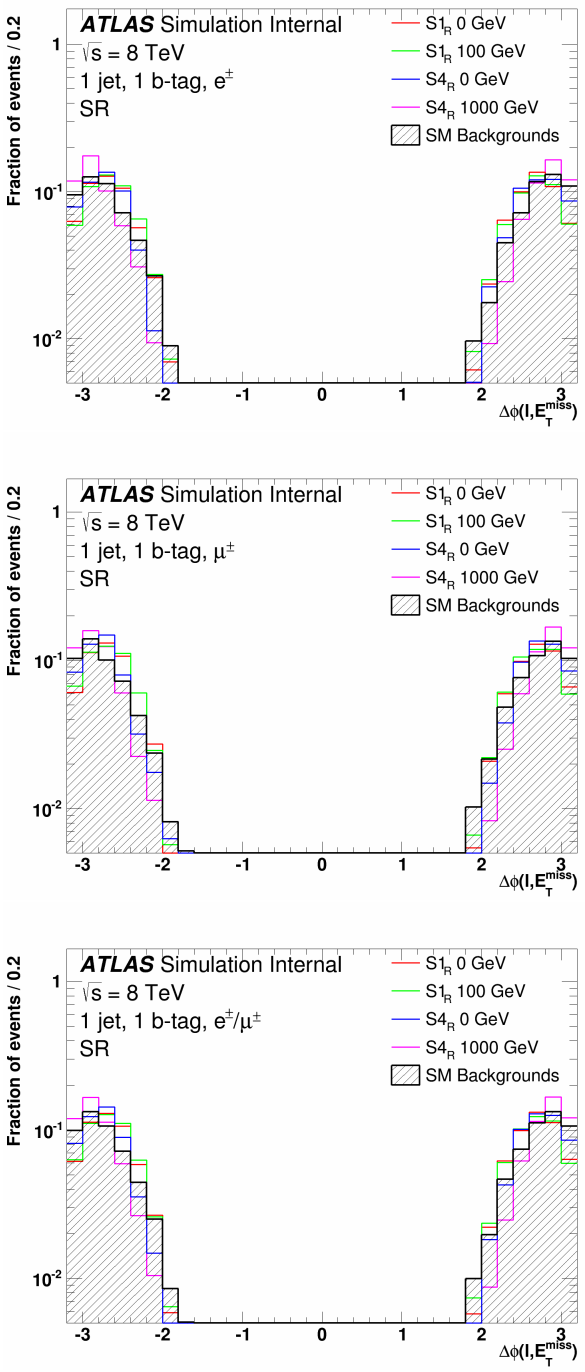

Figure C.14: Distributions of $\Delta\phi(\ell, E_{\mathrm{T}}^{\mathrm{miss}})$ normalized to unity for the electron (top), the muon (middle), and the combined (bottom) channels in the signal region for the highest and lowest mass hypotheses of both the $\mathrm{S1_R}$ and $\mathrm{S4_R}$ models. The SM background is also shown.

Optimized SR1 signal region

This section presents distributions of variables for simulated background and data events in the optimized SR1 signal region, defined in Section 7.5. Figures C.15 and C.16 show the transverse mass between the lepton and missing transverse energy, $m_{\mathrm{T}}(\ell, E_{\mathrm{T}}^{\mathrm{miss}})$. Figures C.17 and C.18 show the missing transverse energy, $E_{\mathrm{T}}^{\mathrm{miss}}$. Figures C.19 and C.20 show the transverse momentum of the lepton, $p_{\mathrm{T}}(\ell)$. Figures C.21 and C.22 show the transverse momentum of the b-jet, $p_{\mathrm{T}}(b)$. Figures C.23 and C.24 show the spatial separation in $\eta - \phi$ space between the lepton and b-jet, $\Delta\mathrm{R}(\ell, b)$. Figures C.25 and C.26 show the angular separation in ϕ between the lepton and b-jet, $\Delta\phi(\ell, b)$. Figures C.27 and C.28 show the angular separation in ϕ between the lepton and the missing transverse energy, $\Delta\phi(\ell, E_{\mathrm{T}}^{\mathrm{miss}})$.

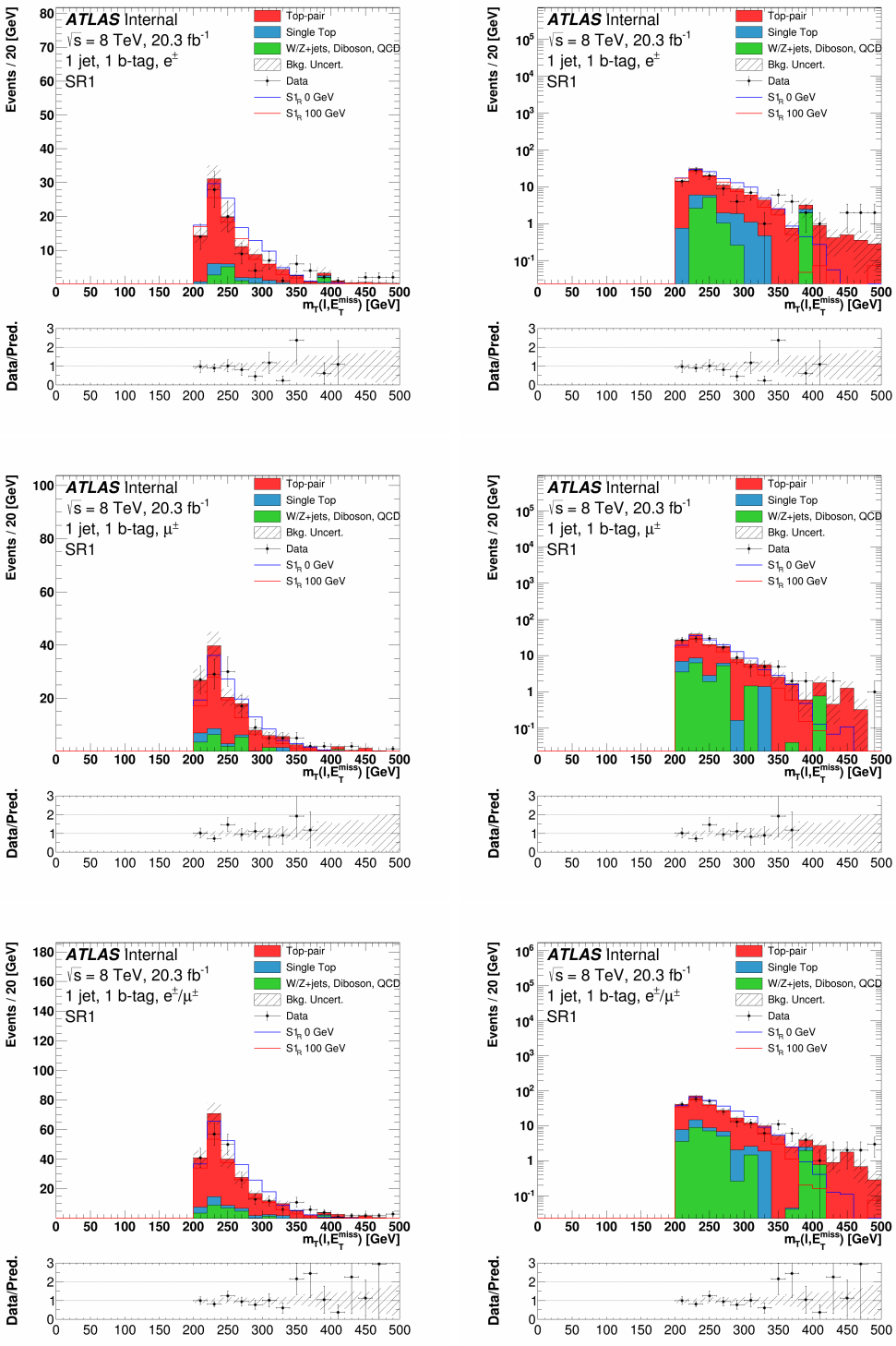

Figure C.15: Distributions of $m_{\mathrm{T}}(\ell, E_{\mathrm{T}}^{\mathrm{miss}})$ for the electron (top), the muon (middle), and the combined (bottom) channels in the optimized SR1 signal region, in linear (left) and log (right) scale. The uncertainty band on the expected background corresponds to the errors due to the statistical uncertainties added in quadrature with the cross-section and normalization uncertainties.

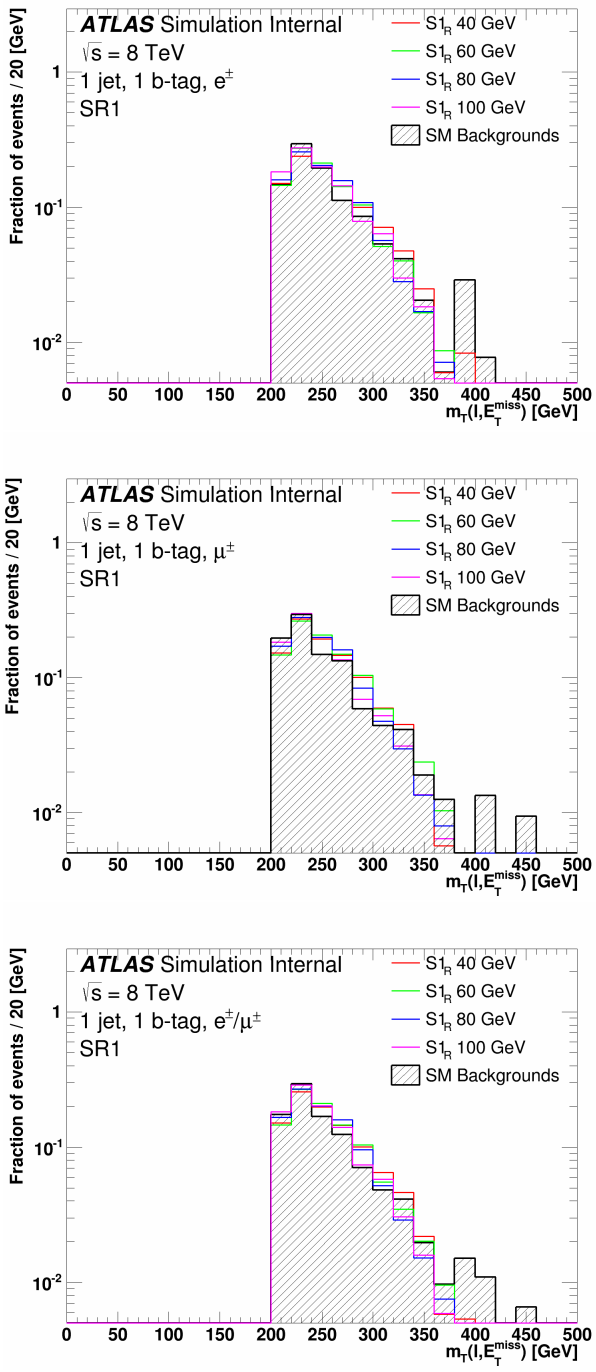

Figure C.16: Distributions of $m_{\mathrm{T}}(\ell, E_{\mathrm{T}}^{\mathrm{miss}})$ normalized to unity for the electron (top), the muon (middle), and the combined (bottom) channels in the optimized SR1 signal region for four mass hypotheses of the $\mathrm{S1_R}$ model. The SM background is also shown.

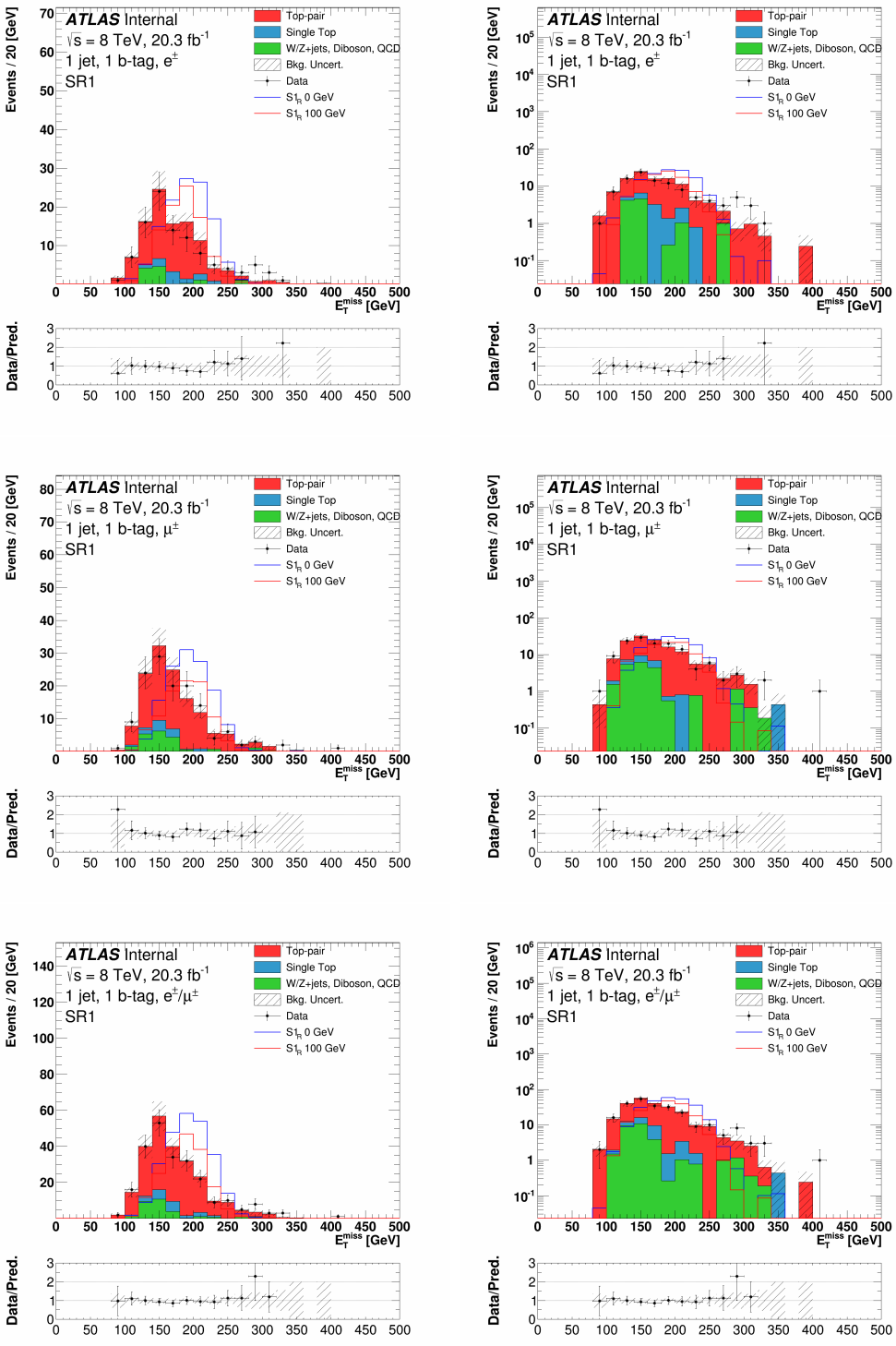

Figure C.17: Distributions of $E_{\mathrm{T}}^{\mathrm{miss}}$ for the electron (top), the muon (middle), and the combined (bottom) channels in the optimized SR1 signal region, in linear (left) and log (right) scale. The uncertainty band on the expected background corresponds to the errors due to the statistical uncertainties added in quadrature with the cross-section and normalization uncertainties.

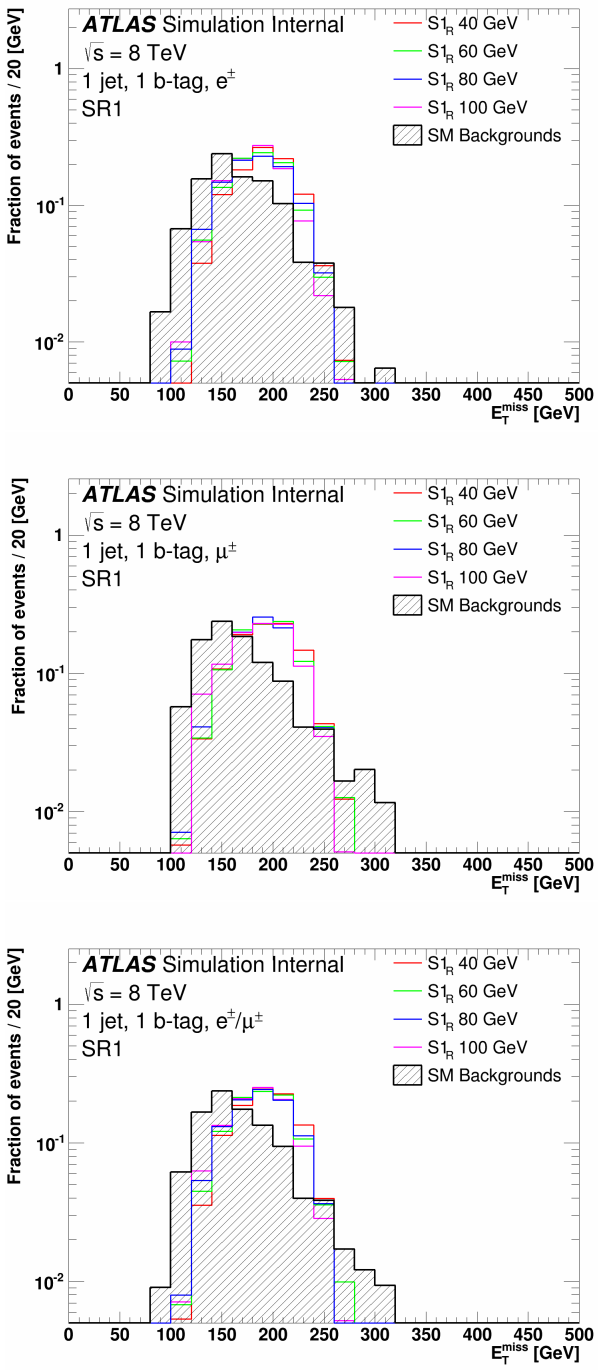

Figure C.18: Distributions of $E_{\mathrm{T}}^{\mathrm{miss}}$ normalized to unity for the electron (top), the muon (middle), and the combined (bottom) channels in the optimized SR1 signal region for four mass hypotheses of the $\mathrm{S1_R}$ model. The SM background is also shown.

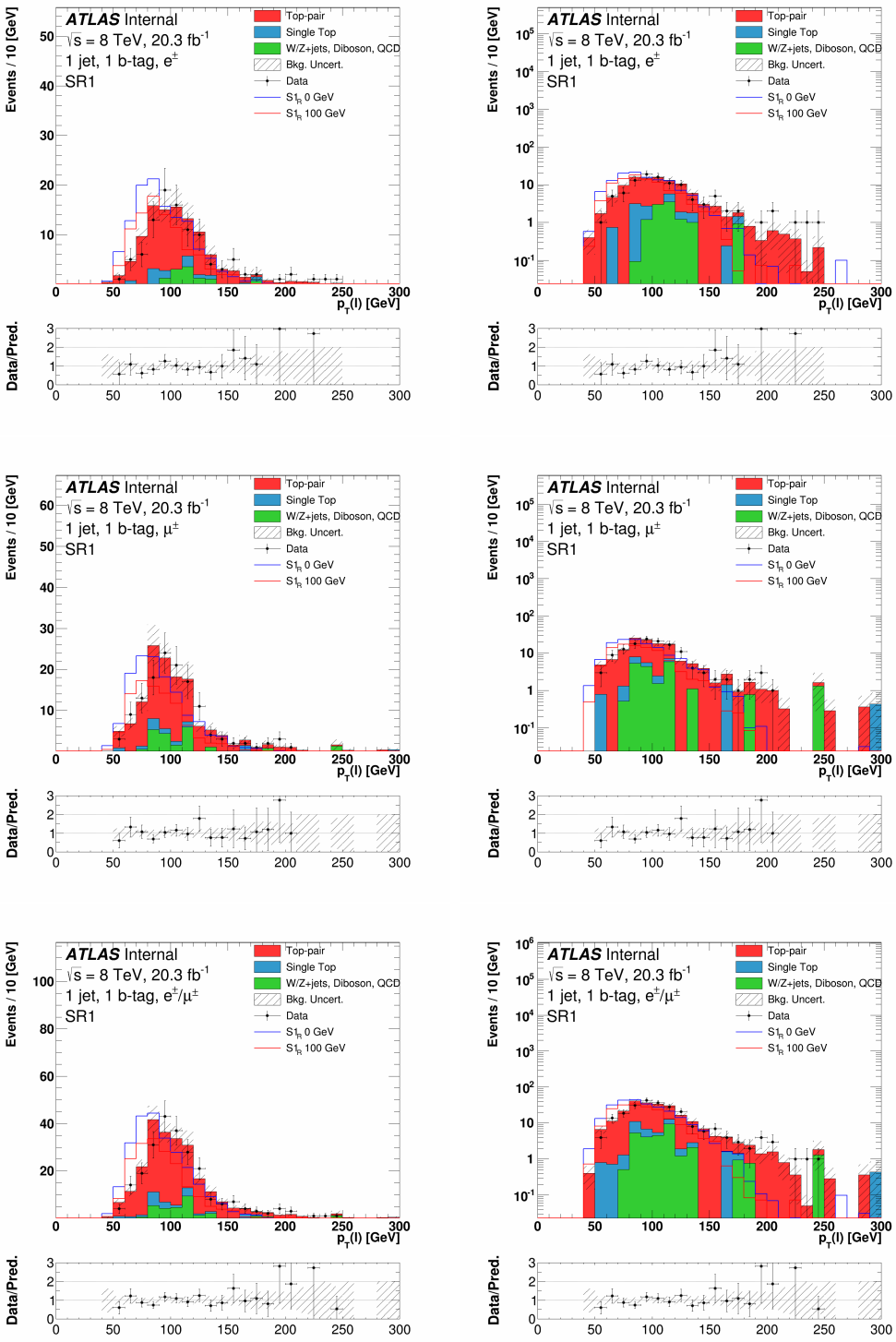

Figure C.19: Distributions of $p_{\mathrm{T}}(\ell)$ for the electron (top), the muon (middle), and the combined (bottom) channels in the optimized SR1 signal region, in linear (left) and log (right) scale. The uncertainty band on the expected background corresponds to the errors due to the statistical uncertainties added in quadrature with the cross-section and normalization uncertainties.

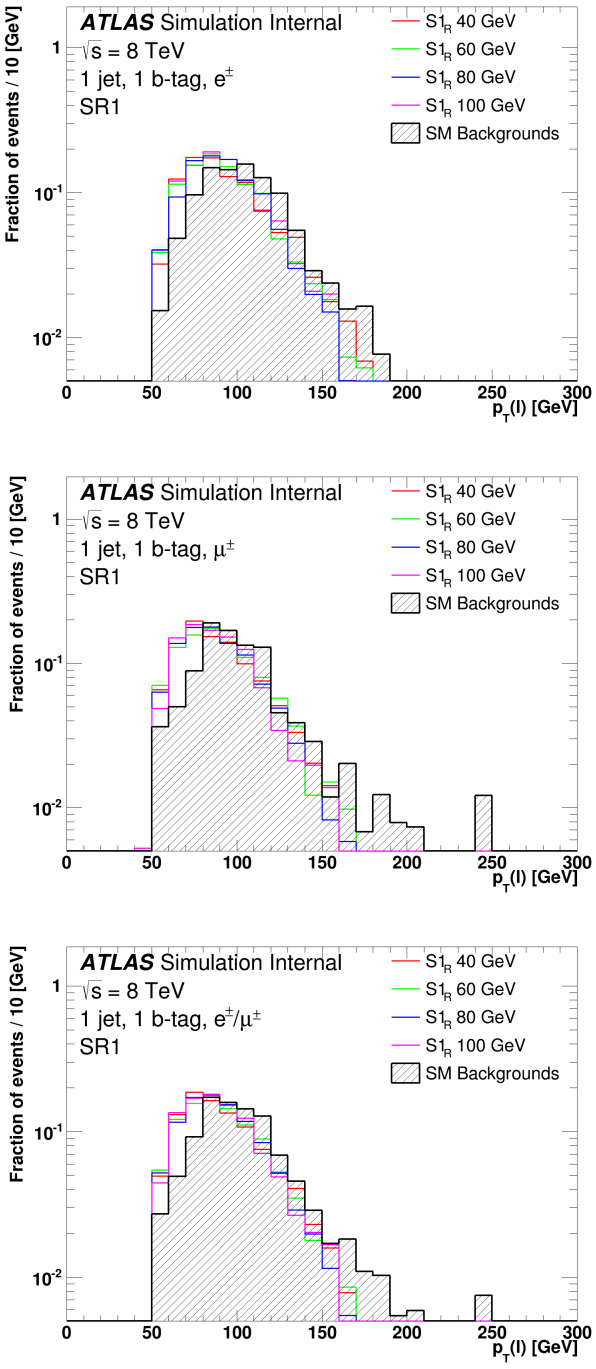

Figure C.20: Distributions of $p_{\mathrm{T}}(\ell)$ normalized to unity for the electron (top), the muon (middle), and the combined (bottom) channels in the optimized SR1 signal region for four mass hypotheses of the $\mathrm{S1_R}$ model. The SM background is also shown.

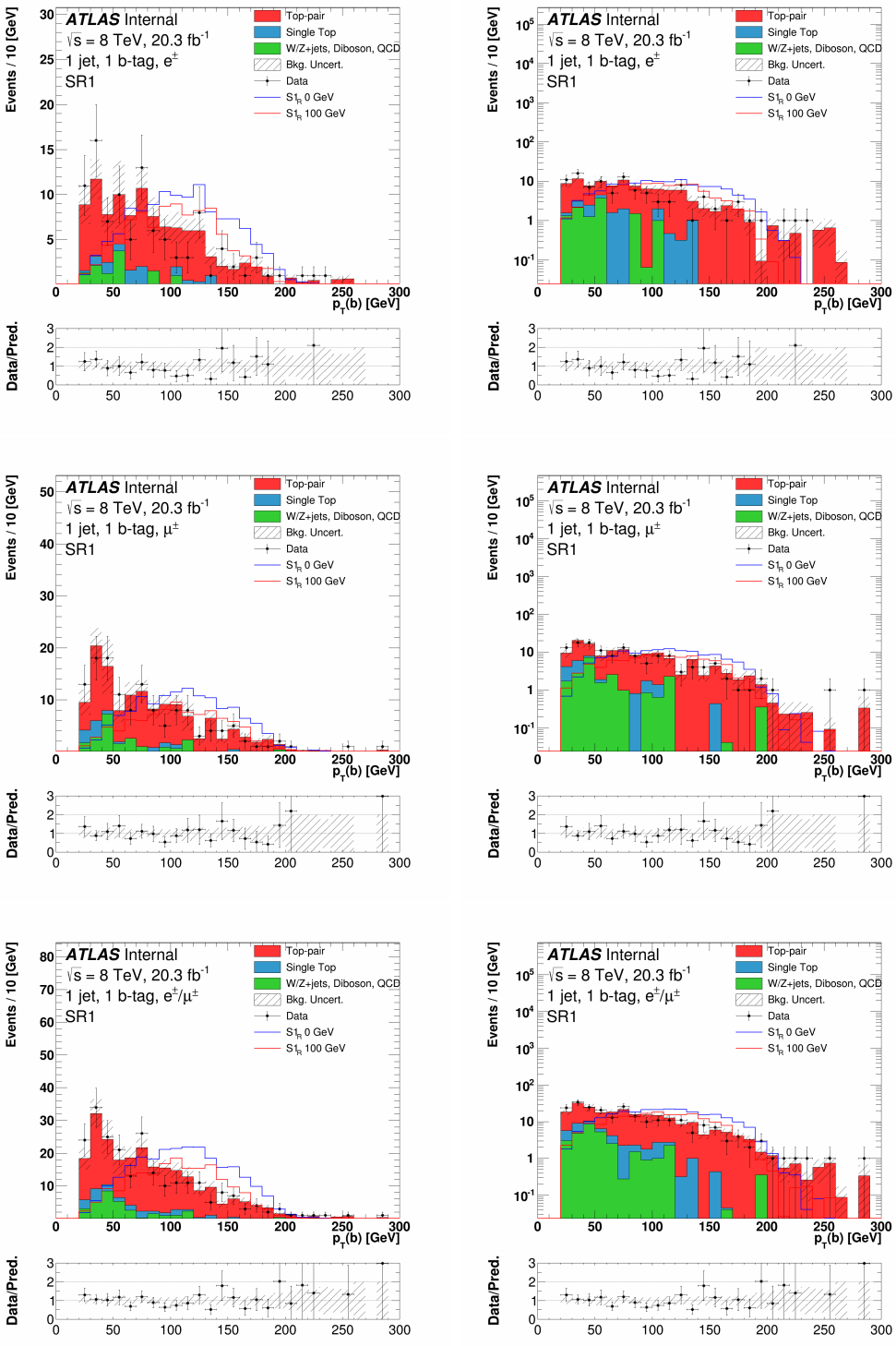

Figure C.21: Distributions of $p_{\mathrm{T}}(b)$ for the electron (top), the muon (middle), and the combined (bottom) channels in the optimized SR1 signal region, in linear (left) and log (right) scale. The uncertainty band on the expected background corresponds to the errors due to the statistical uncertainties added in quadrature with the cross-section and normalization uncertainties.

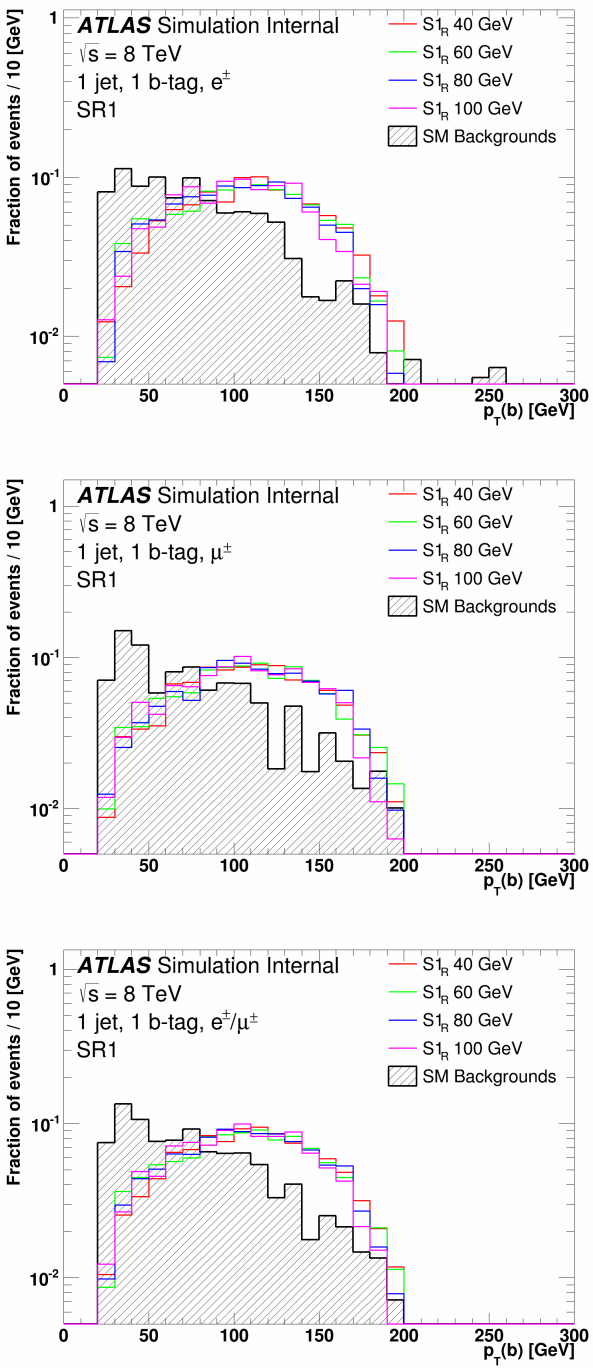

Figure C.22: Distributions of $p_{\mathrm{T}}(b)$ normalized to unity for the electron (top), the muon (middle), and the combined (bottom) channels in the optimized SR1 signal region for four mass hypotheses of the $\mathrm{S1_R}$ model. The SM background is also shown.

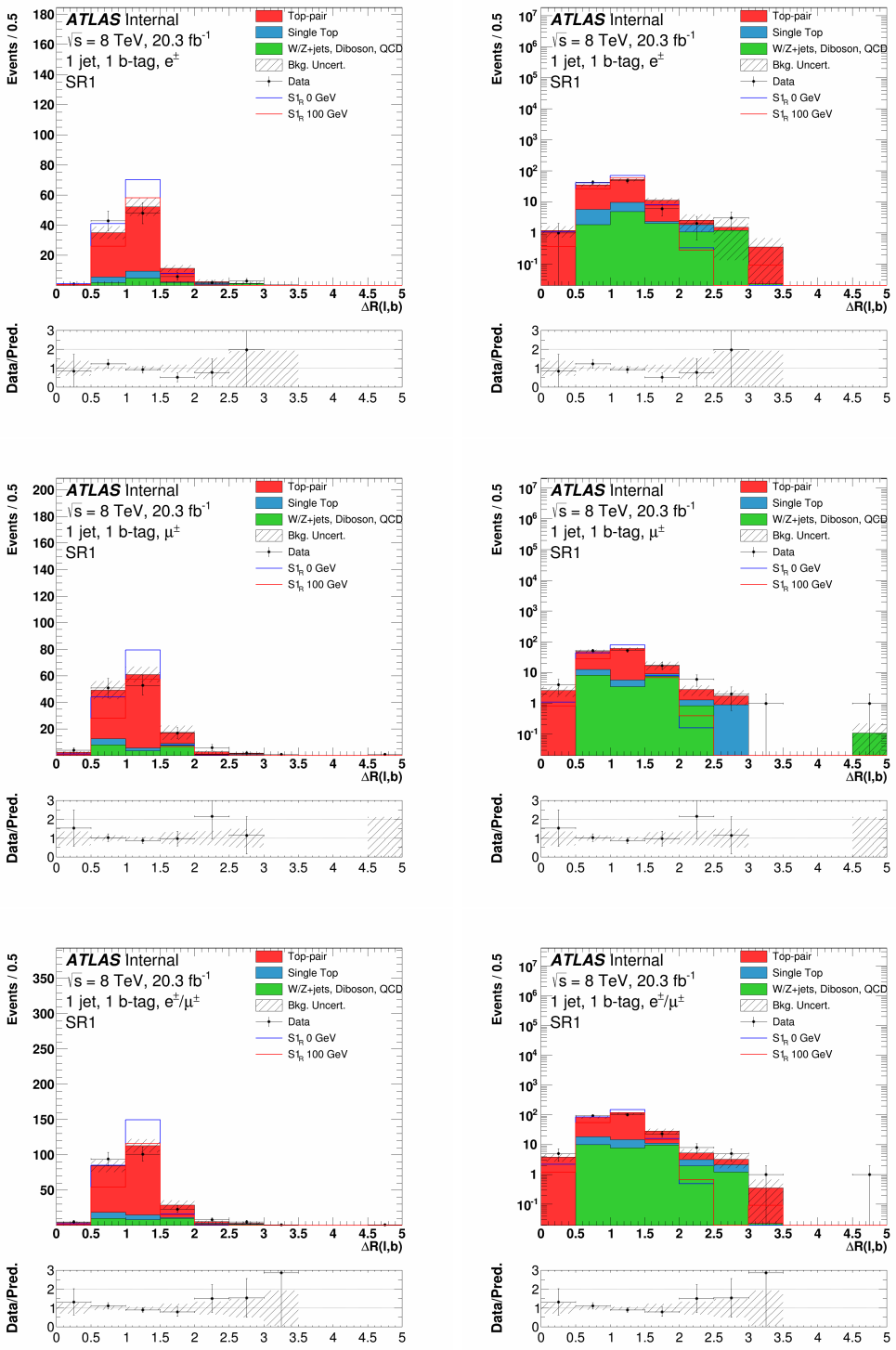

Figure C.23: Distributions of $\Delta R(\ell, b)$ for the electron (top), the muon (middle), and the combined (bottom) channels in the optimized SR1 signal region, in linear (left) and log (right) scale. The uncertainty band on the expected background corresponds to the errors due to the statistical uncertainties added in quadrature with the cross-section and normalization uncertainties.

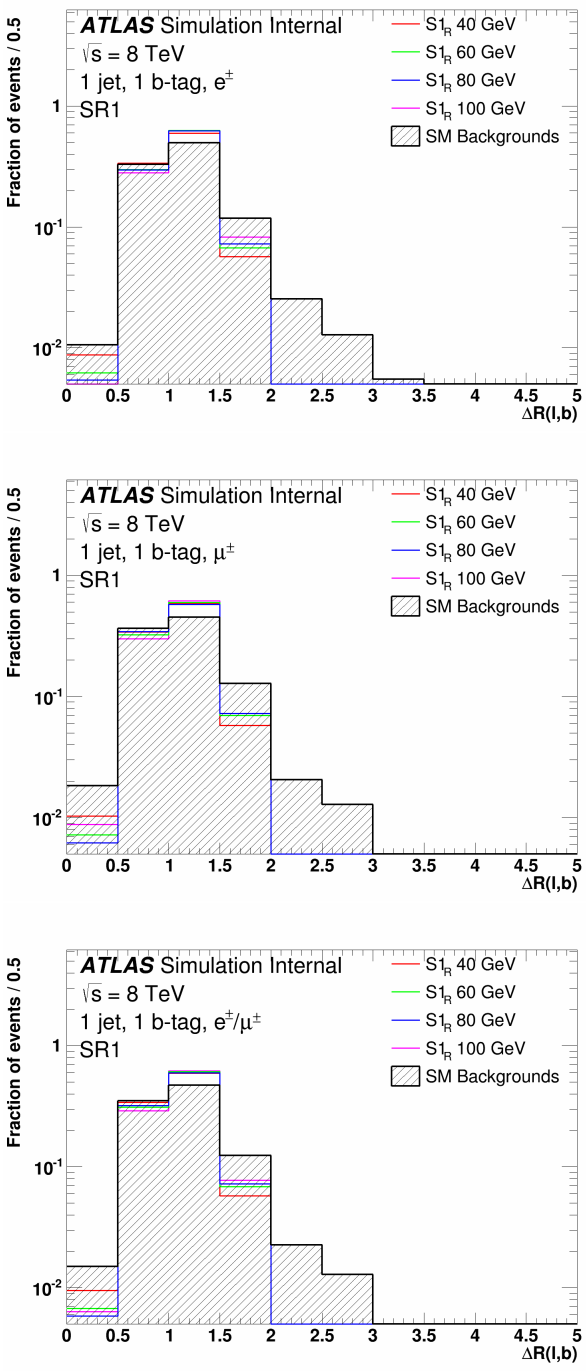

Figure C.24: Distributions of $\Delta R(\ell, b)$ normalized to unity for the electron (top), the muon (middle), and the combined (bottom) channels in the optimized SR1 signal region for four mass hypotheses of the $S1_R$ model. The SM background is also shown.

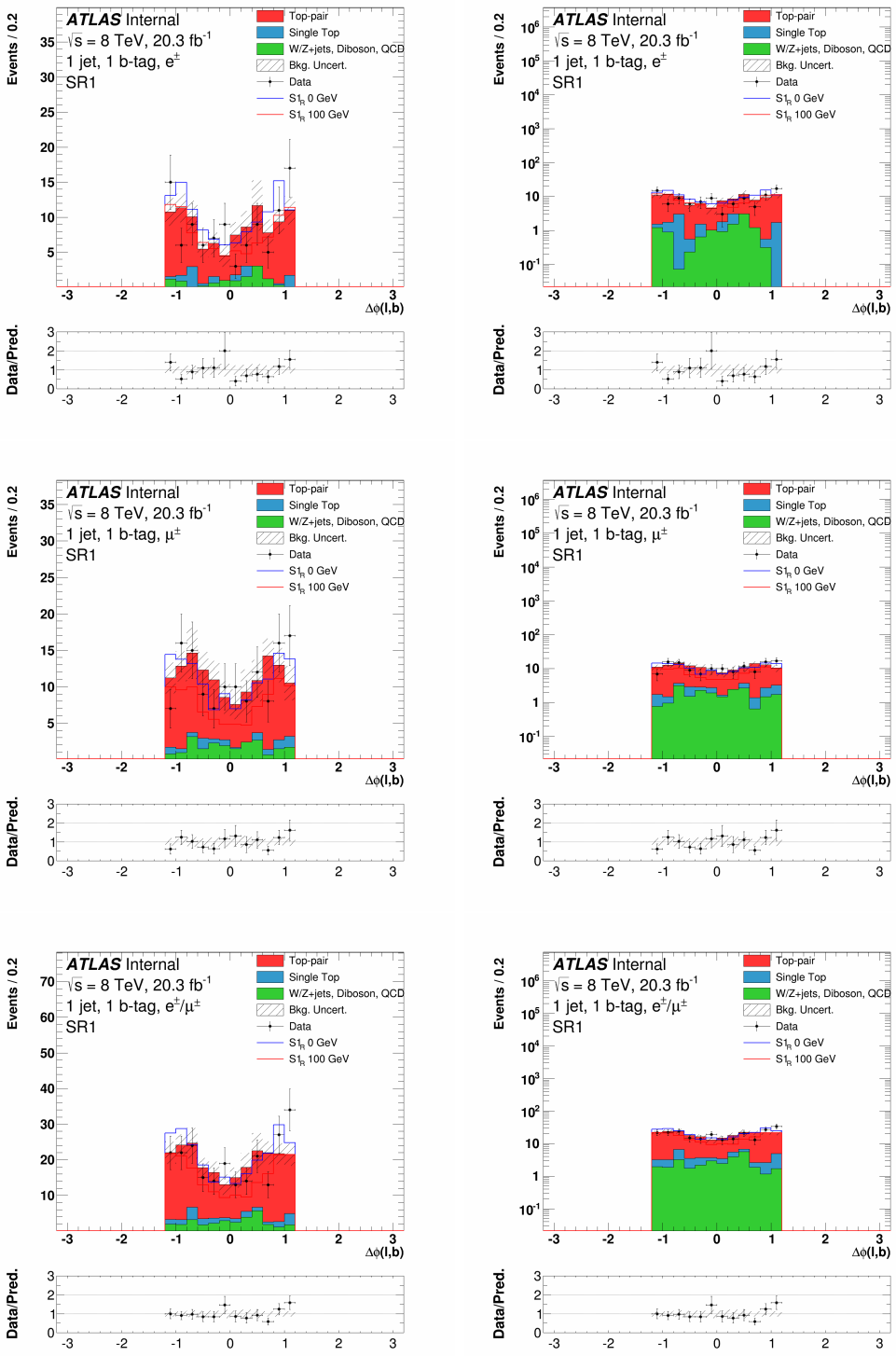

Figure C.25: Distributions of $\Delta\phi(\ell, b)$ for the electron (top), the muon (middle), and the combined (bottom) channels in the optimized SR1 signal region, in linear (left) and log (right) scale. The uncertainty band on the expected background corresponds to the errors due to the statistical uncertainties added in quadrature with the cross-section and normalization uncertainties.

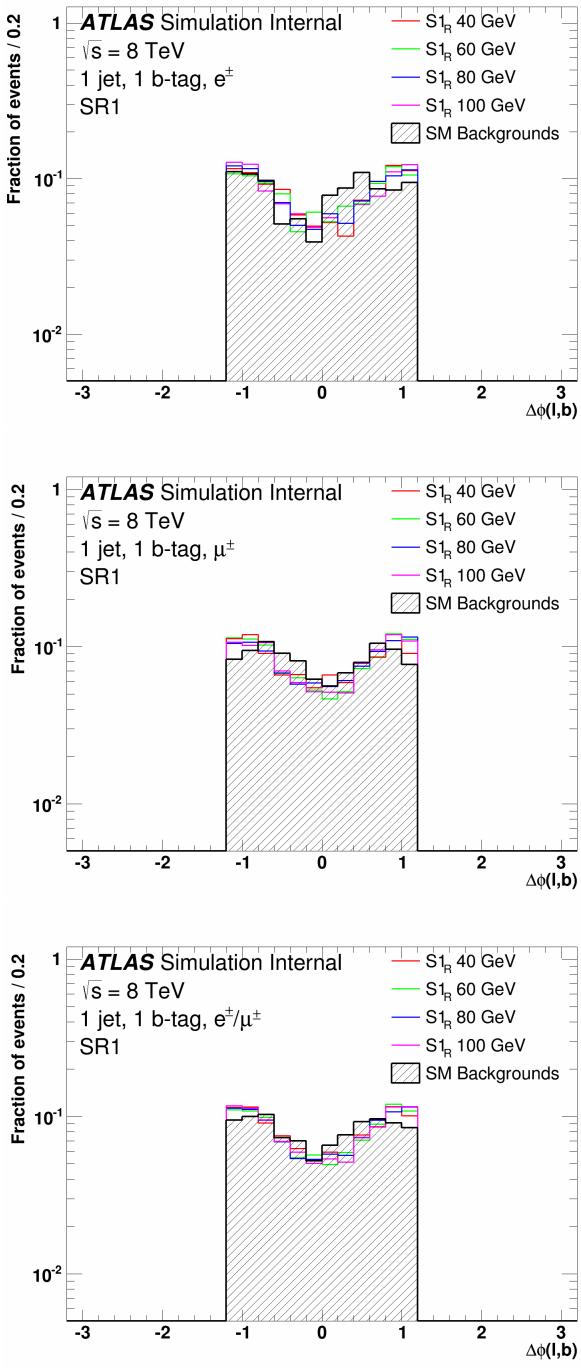

Figure C.26: Distributions of $\Delta\phi(\ell, b)$ normalized to unity for the electron (top), the muon (middle), and the combined (bottom) channels in the optimized SR1 signal region for four mass hypotheses of the $S1_R$ model. The SM background is also shown.

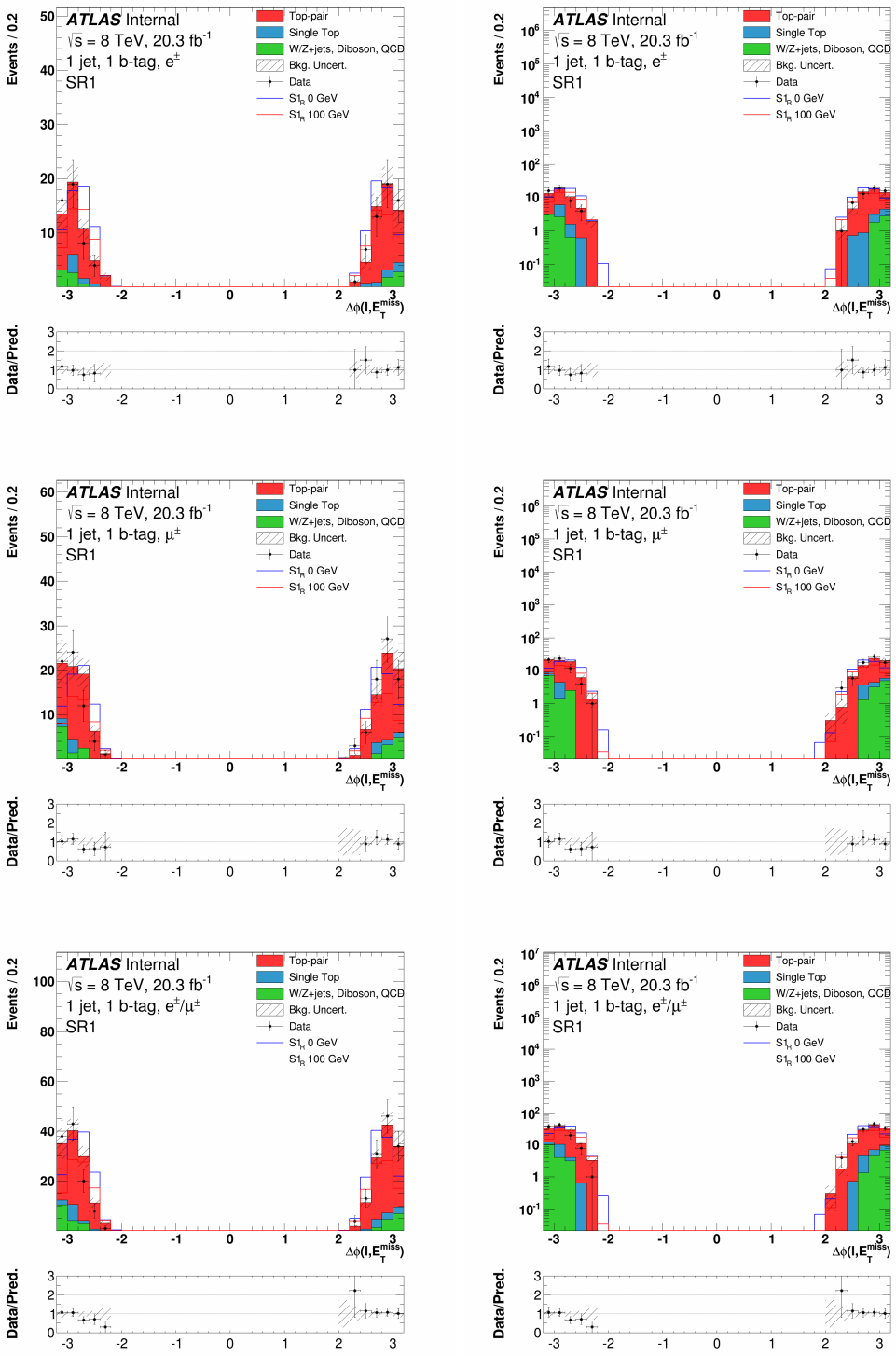

Figure C.27: Distributions of $\Delta\phi(\ell, E_{\mathrm{T}}^{\mathrm{miss}})$ for the electron (top), the muon (middle), and the combined (bottom) channels in the optimized SR1 signal region, in linear (left) and log (right) scale. The uncertainty band on the expected background corresponds to the errors due to the statistical uncertainties added in quadrature with the cross-section and normalization uncertainties.

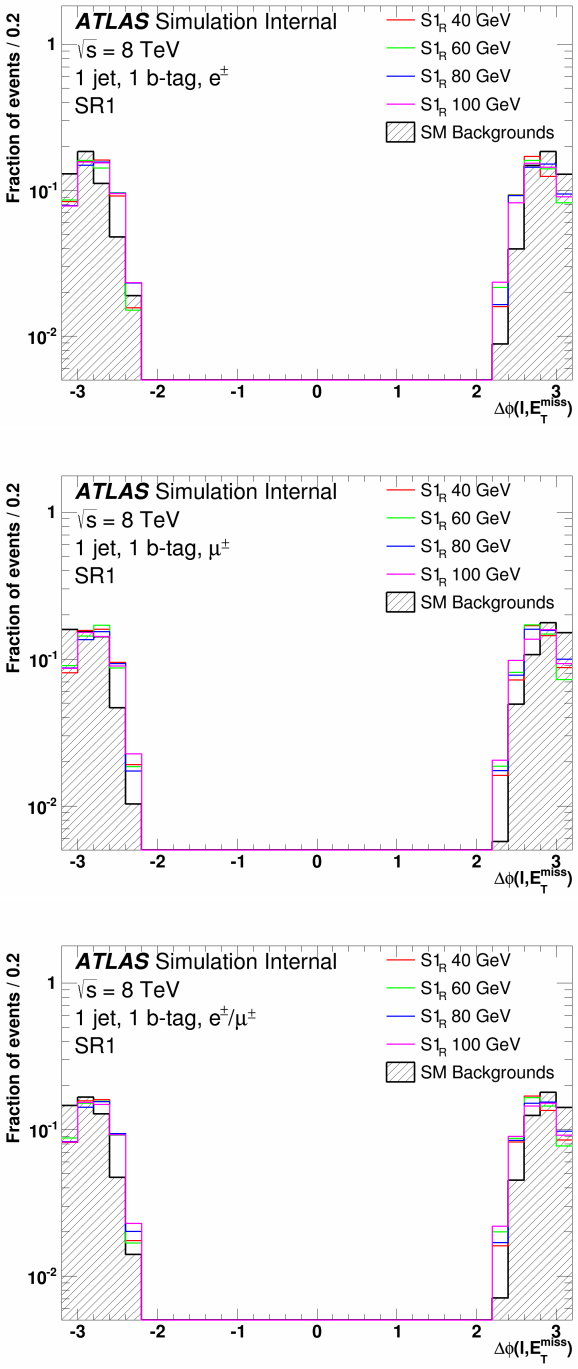

Figure C.28: Distributions of $\Delta\phi(\ell, E_{\mathrm{T}}^{\mathrm{miss}})$ normalized to unity for the electron (top), the muon (middle), and the combined (bottom) channels in the optimized SR1 signal region for four mass hypotheses of the $\mathrm{S1_R}$ model. The SM background is also shown.

Optimized SR2 signal region

This section presents distributions of variables for simulated background and data events in the optimized SR2 signal region, defined in Section 7.5. Figures C.29 and C.30 show the transverse mass between the lepton and missing transverse energy, $m_{\mathrm{T}}(\ell, E_{\mathrm{T}}^{\mathrm{miss}})$. Figures C.31 and C.32 show the missing transverse energy, $E_{\mathrm{T}}^{\mathrm{miss}}$. Figures C.33 and C.34 show the transverse momentum of the lepton, $p_{\mathrm{T}}(\ell)$. Figures C.35 and C.36 show the transverse momentum of the b-jet, $p_{\mathrm{T}}(b)$. Figures C.37 and C.38 show the spatial separation in $\eta - \phi$ space between the lepton and b-jet, $\Delta\mathrm{R}(\ell, b)$. Figures C.39 and C.40 show the angular separation in ϕ between the lepton and b-jet, $\Delta\phi(\ell, b)$. Figures C.41 and C.42 show the angular separation in ϕ between the lepton and the missing transverse energy, $\Delta\phi(\ell, E_{\mathrm{T}}^{\mathrm{miss}})$.

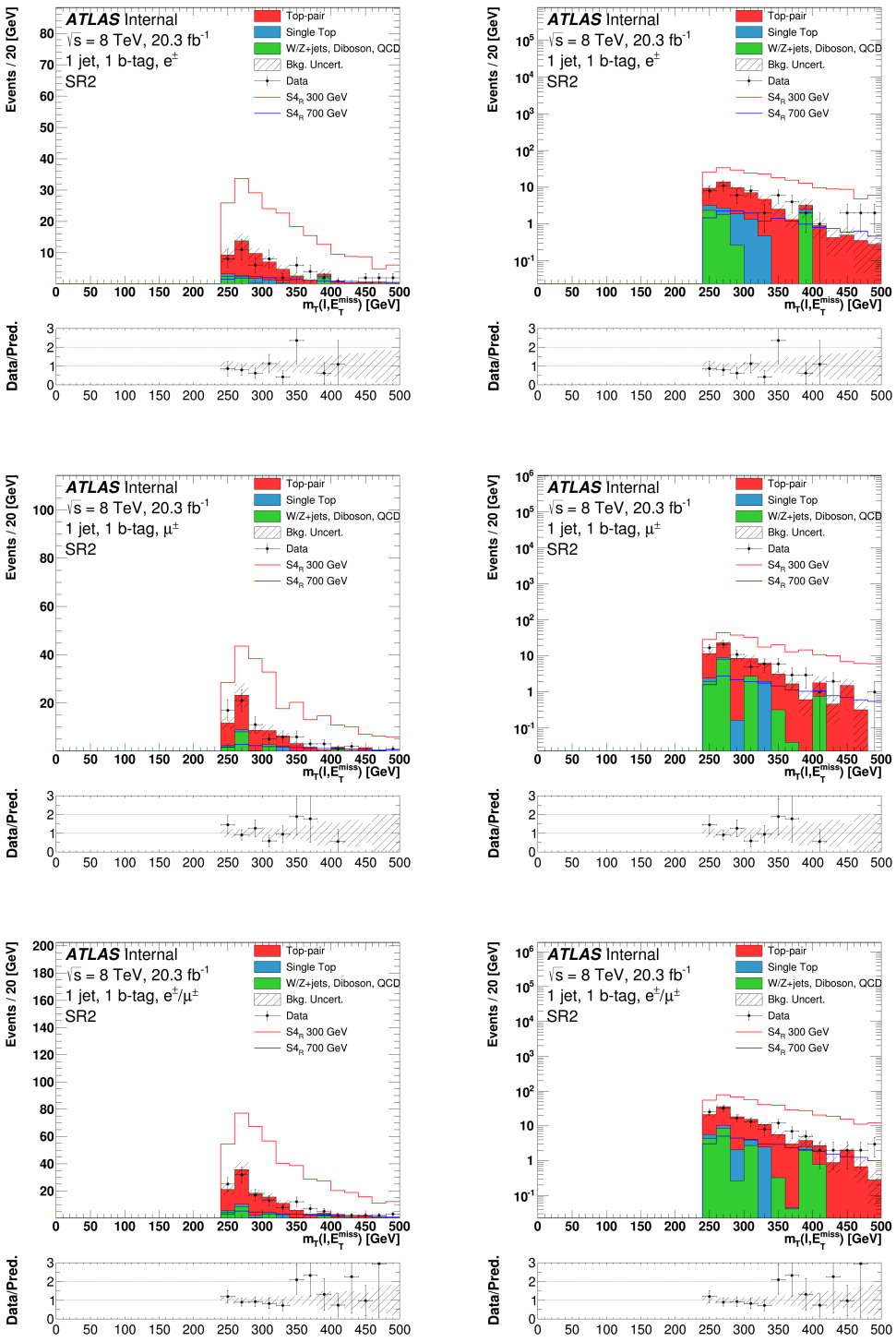

Figure C.29: Distributions of $m_{\mathrm{T}}(\ell, E_{\mathrm{T}}^{\mathrm{miss}})$ for the electron (top), the muon (middle), and the combined (bottom) channels in the optimized SR2 signal region, in linear (left) and log (right) scale. The uncertainty band on the expected background corresponds to the errors due to the statistical uncertainties added in quadrature with the cross-section and normalization uncertainties.

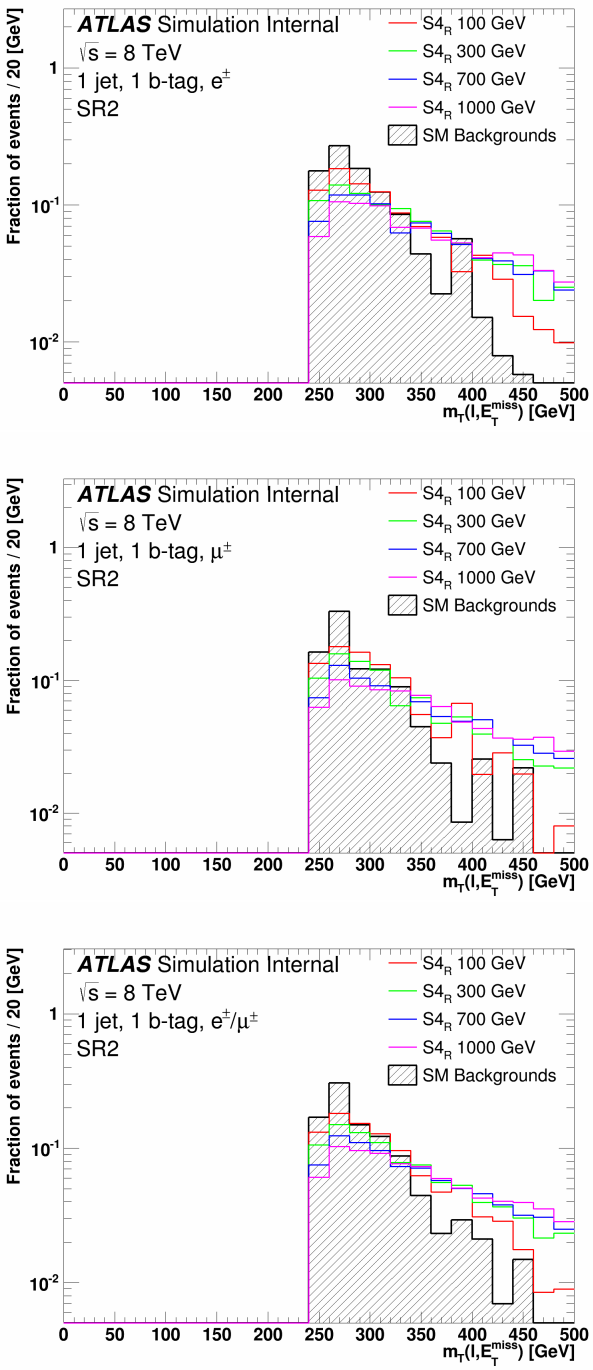

Figure C.30: Distributions of $m_{\mathrm{T}}(\ell, E_{\mathrm{T}}^{\mathrm{miss}})$ normalized to unity for the electron (top), the muon (middle), and the combined (bottom) channels in the optimized SR2 signal region for four mass hypotheses of the $\mathrm{S4_R}$ model. The SM background is also shown.

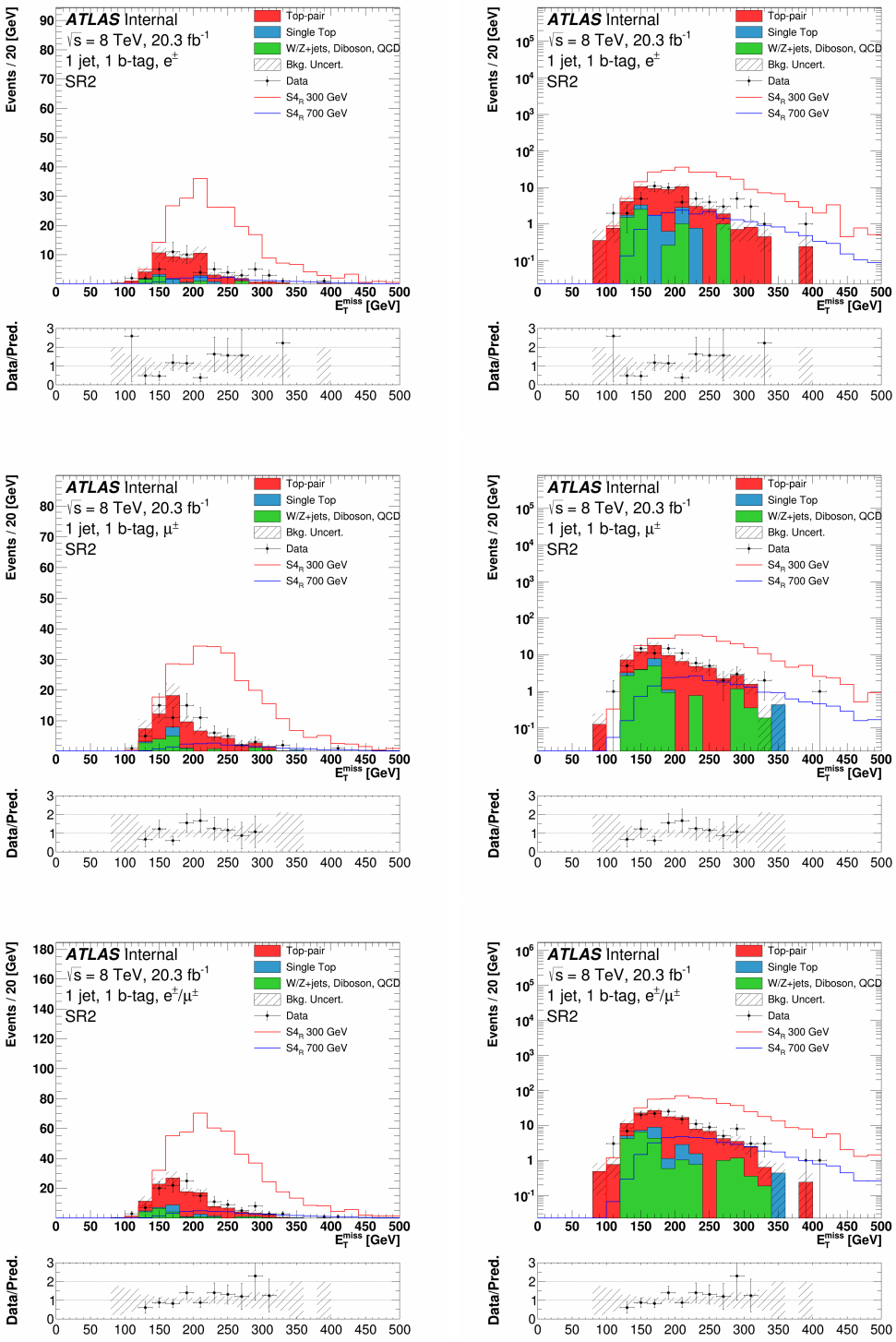

Figure C.31: Distributions of $E_{\mathrm{T}}^{\mathrm{miss}}$ for the electron (top), the muon (middle), and the combined (bottom) channels in the optimized SR2 signal region, in linear (left) and log (right) scale. The uncertainty band on the expected background corresponds to the errors due to the statistical uncertainties added in quadrature with the cross-section and normalization uncertainties.

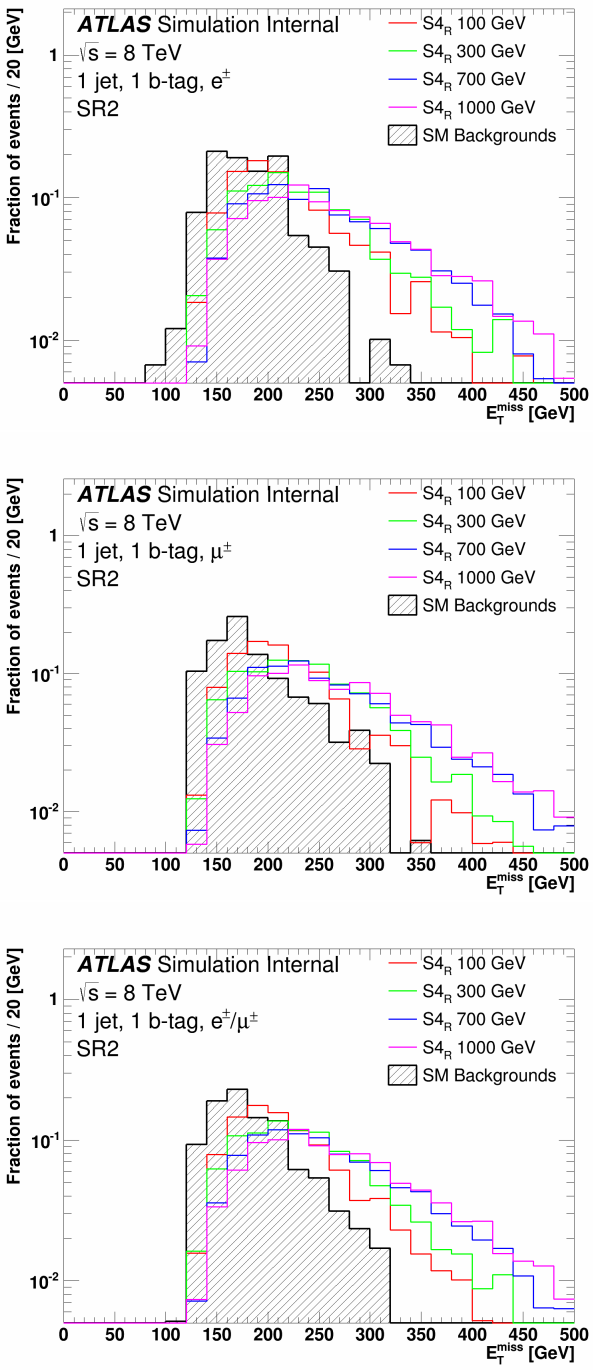

Figure C.32: Distributions of $E_{\mathrm{T}}^{\mathrm{miss}}$ normalized to unity for the electron (top), the muon (middle), and the combined (bottom) channels in the optimized SR2 signal region for four mass hypotheses of the $\mathrm{S4_R}$ model. The SM background is also shown.

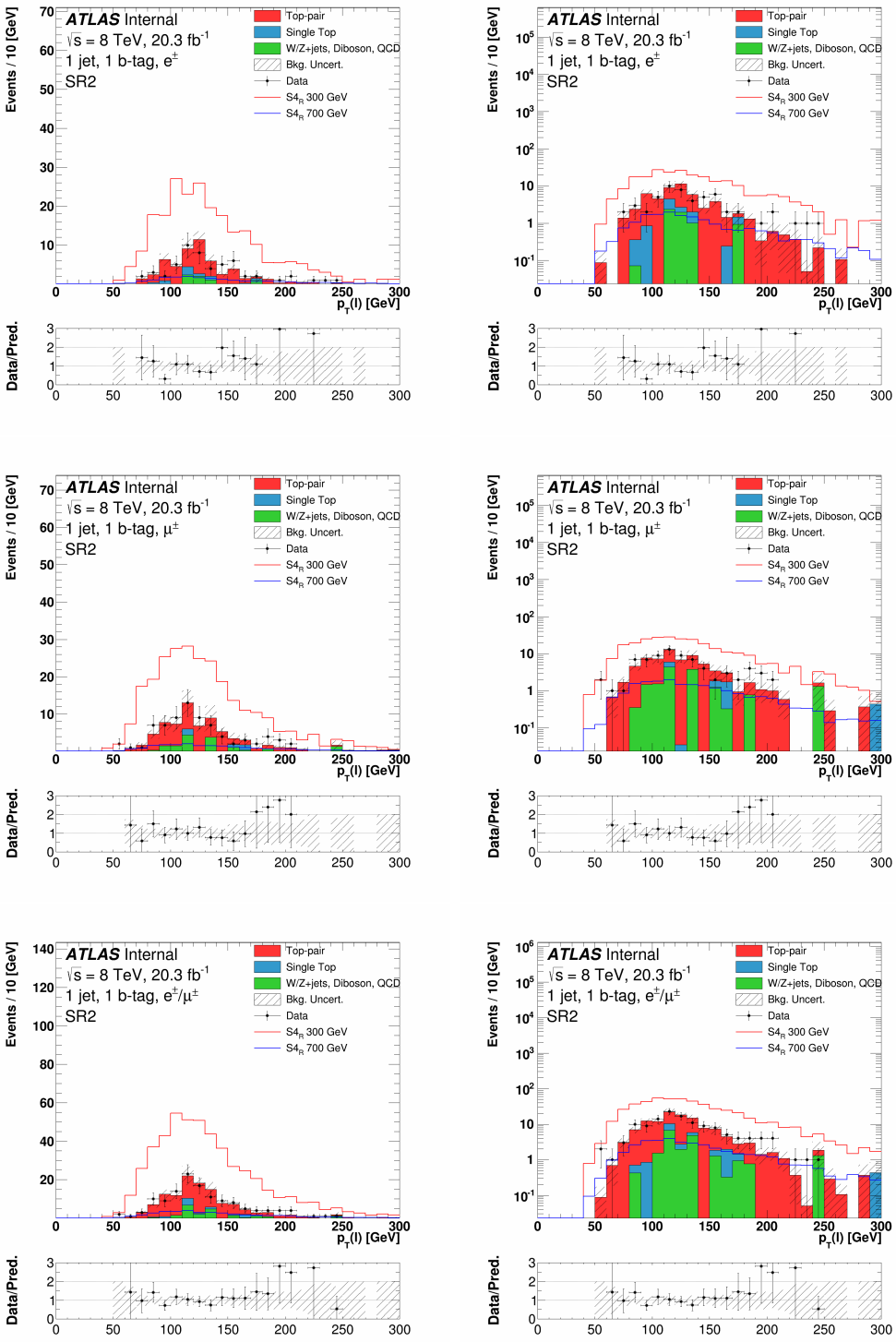

Figure C.33: Distributions of $p_{\mathrm{T}}(\ell)$ for the electron (top), the muon (middle), and the combined (bottom) channels in the optimized SR2 signal region, in linear (left) and log (right) scale. The uncertainty band on the expected background corresponds to the errors due to the statistical uncertainties added in quadrature with the cross-section and normalization uncertainties.

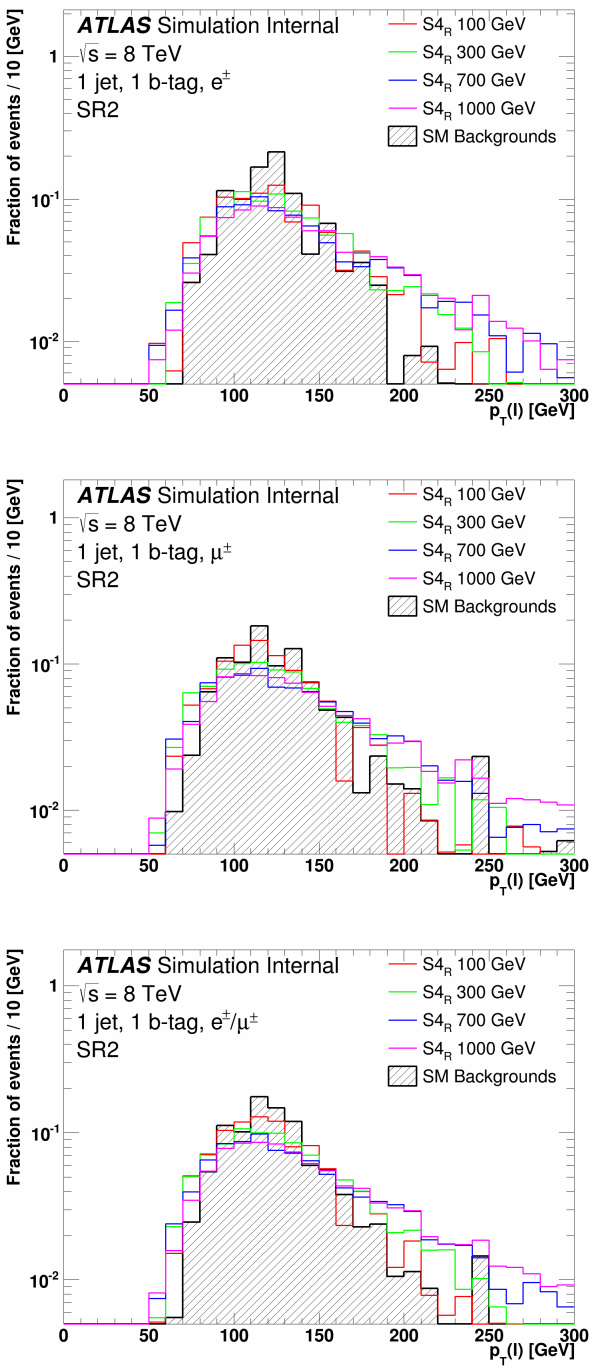

Figure C.34: Distributions of $p_{\mathrm{T}}(\ell)$ normalized to unity for the electron (top), the muon (middle), and the combined (bottom) channels in the optimized SR2 signal region for four mass hypotheses of the $\mathrm{S4_R}$ model. The SM background is also shown.

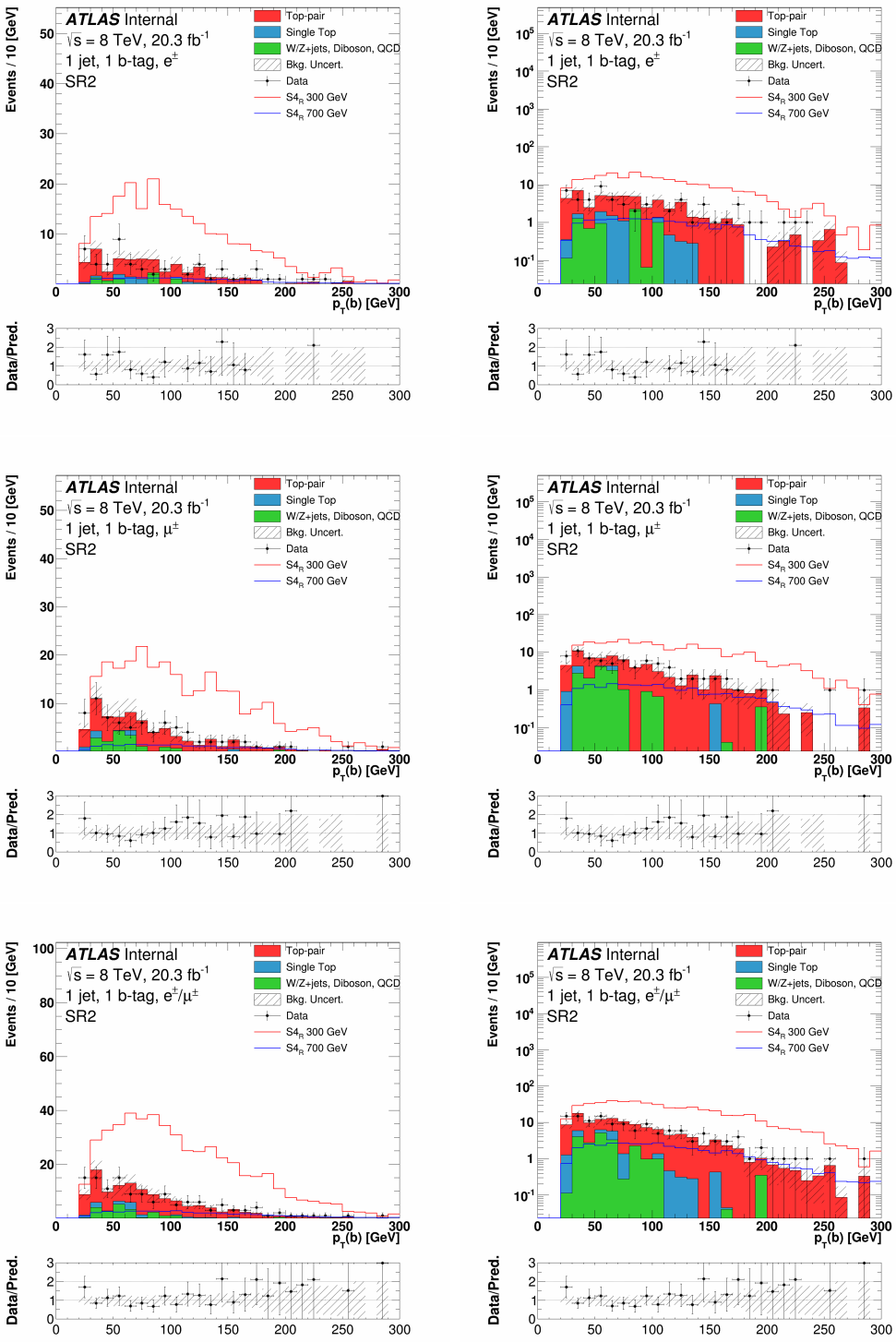

Figure C.35: Distributions of $p_{\mathrm{T}}(b)$ for the electron (top), the muon (middle), and the combined (bottom) channels in the optimized SR2 signal region, in linear (left) and log (right) scale. The uncertainty band on the expected background corresponds to the errors due to the statistical uncertainties added in quadrature with the cross-section and normalization uncertainties.

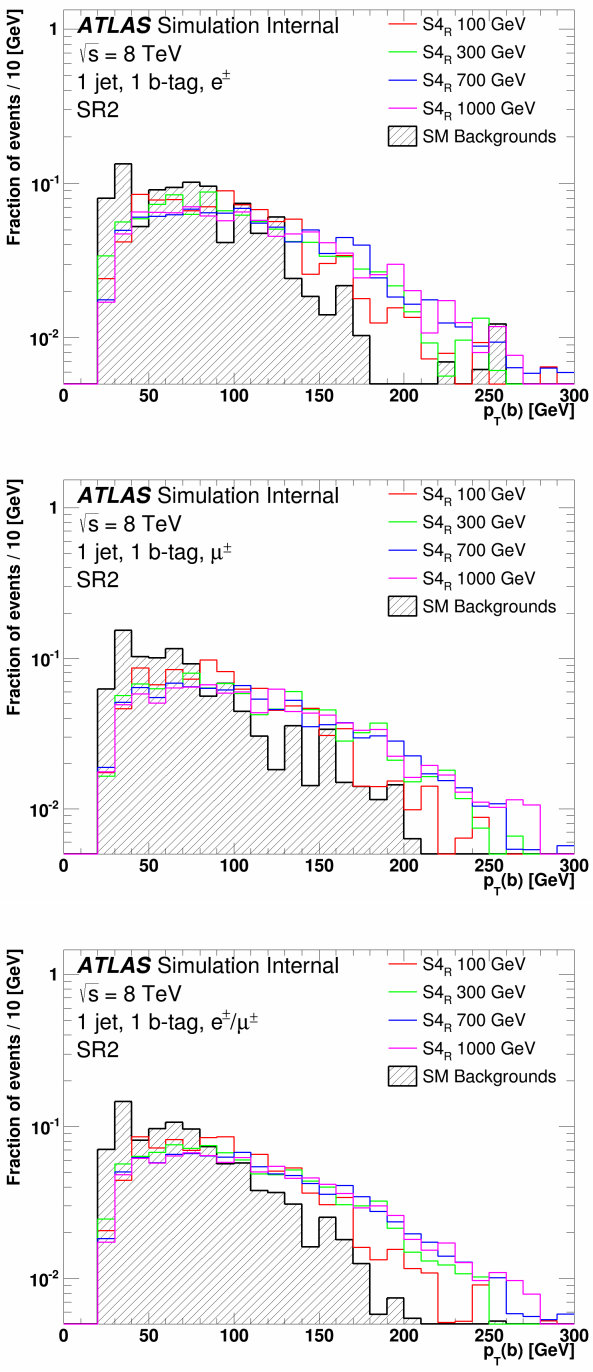

Figure C.36: Distributions of $p_{\mathrm{T}}(b)$ normalized to unity for the electron (top), the muon (middle), and the combined (bottom) channels in the optimized SR2 signal region for four mass hypotheses of the $\mathrm{S4_R}$ model. The SM background is also shown.

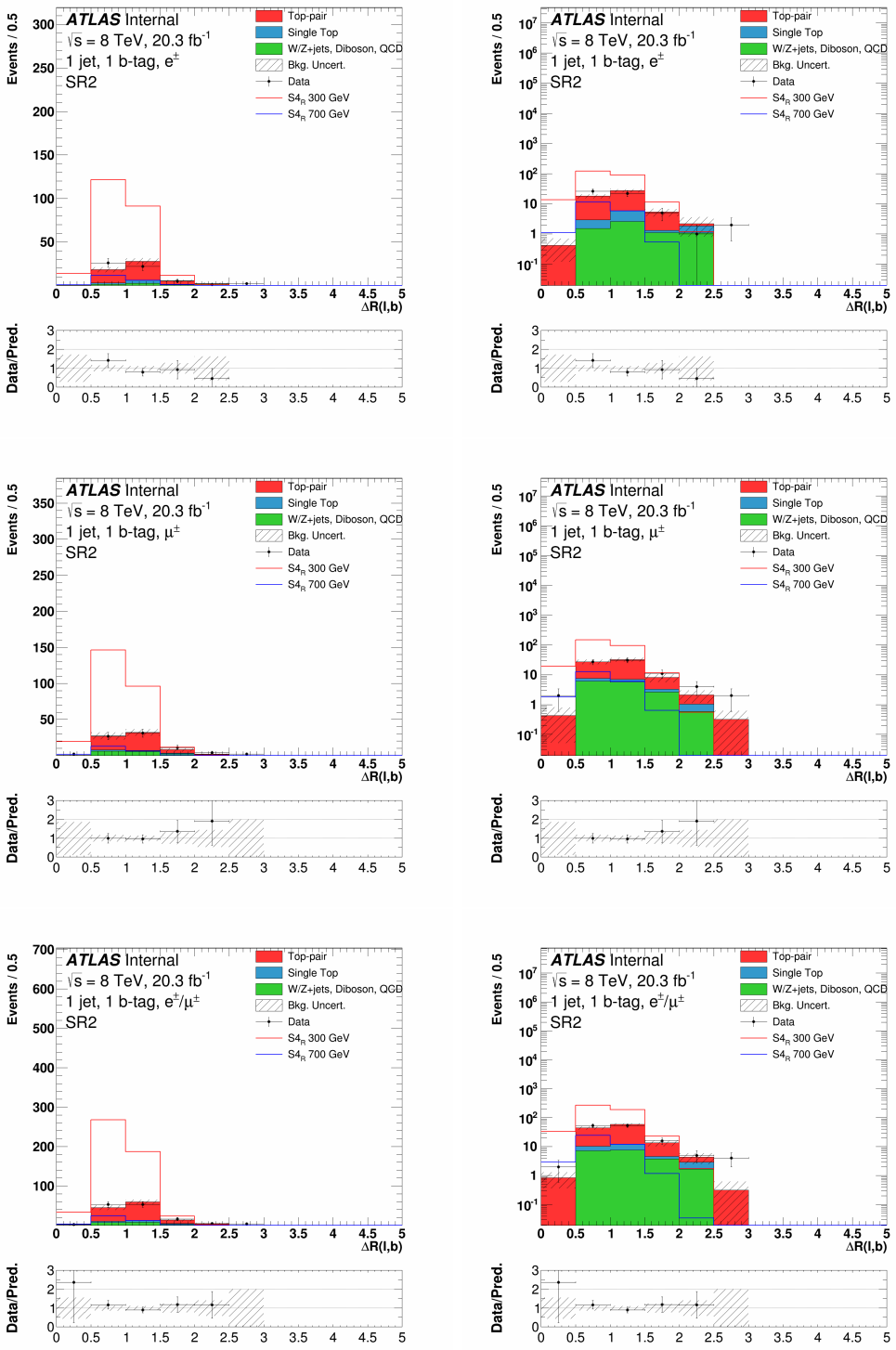

Figure C.37: Distributions of $\Delta R(\ell, b)$ for the electron (top), the muon (middle), and the combined (bottom) channels in the optimized SR2 signal region, in linear (left) and log (right) scale. The uncertainty band on the expected background corresponds to the errors due to the statistical uncertainties added in quadrature with the cross-section and normalization uncertainties.

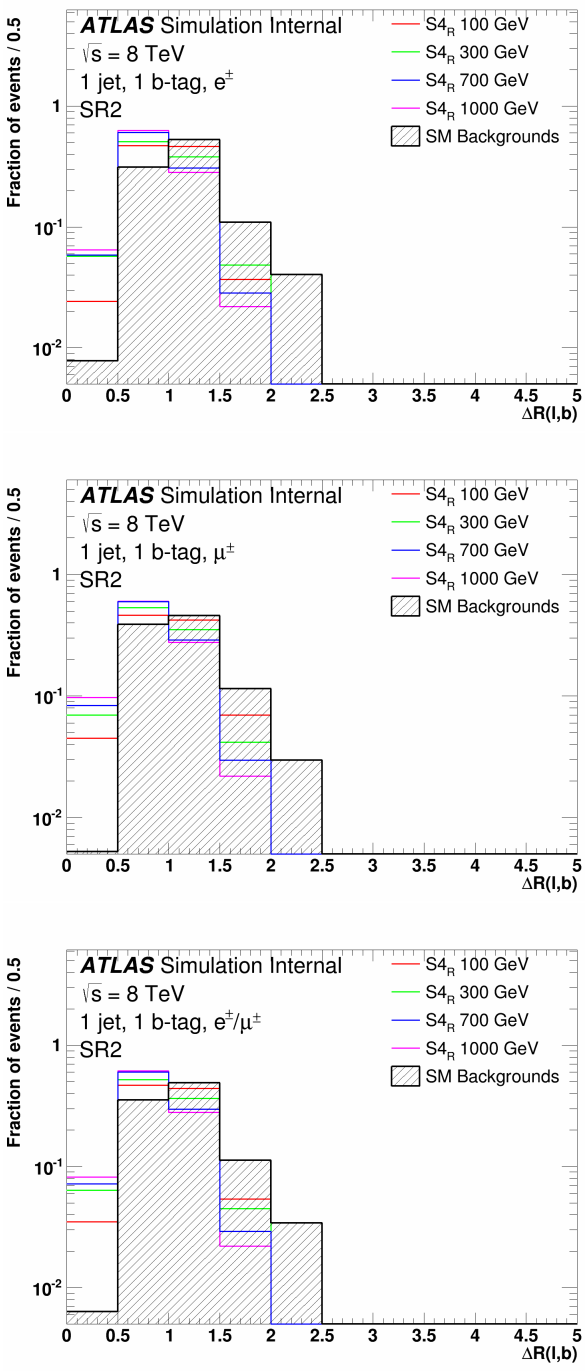

Figure C.38: Distributions of $\Delta\mathrm{R}(\ell, b)$ normalized to unity for the electron (top), the muon (middle), and the combined (bottom) channels in the optimized SR2 signal region for four mass hypotheses of the $\mathrm{S4_R}$ model. The SM background is also shown.

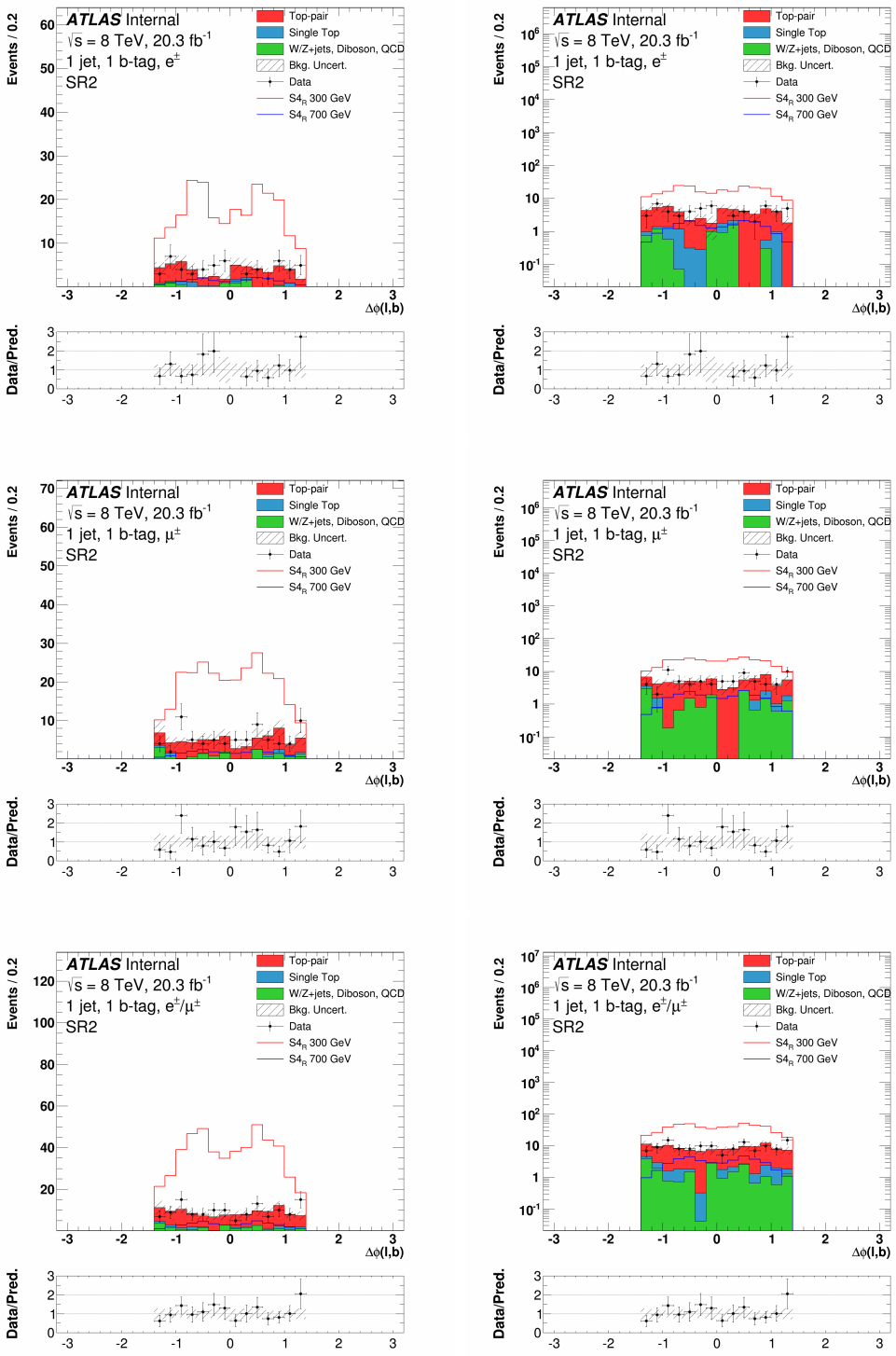

Figure C.39: Distributions of $\Delta\phi(\ell, b)$ for the electron (top), the muon (middle), and the combined (bottom) channels in the optimized SR2 signal region, in linear (left) and log (right) scale. The uncertainty band on the expected background corresponds to the errors due to the statistical uncertainties added in quadrature with the cross-section and normalization uncertainties.

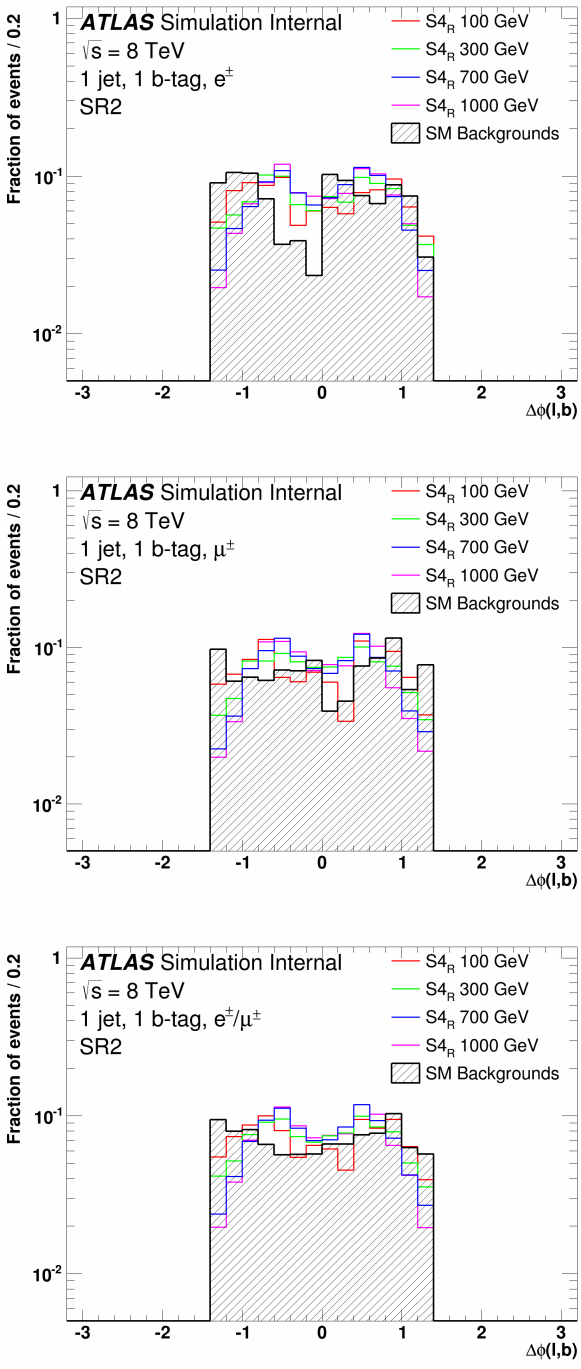

Figure C.40: Distributions of $\Delta\phi(\ell, b)$ normalized to unity for the electron (top), the muon (middle), and the combined (bottom) channels in the optimized SR2 signal region for four mass hypotheses of the $S4_R$ model. The SM background is also shown.

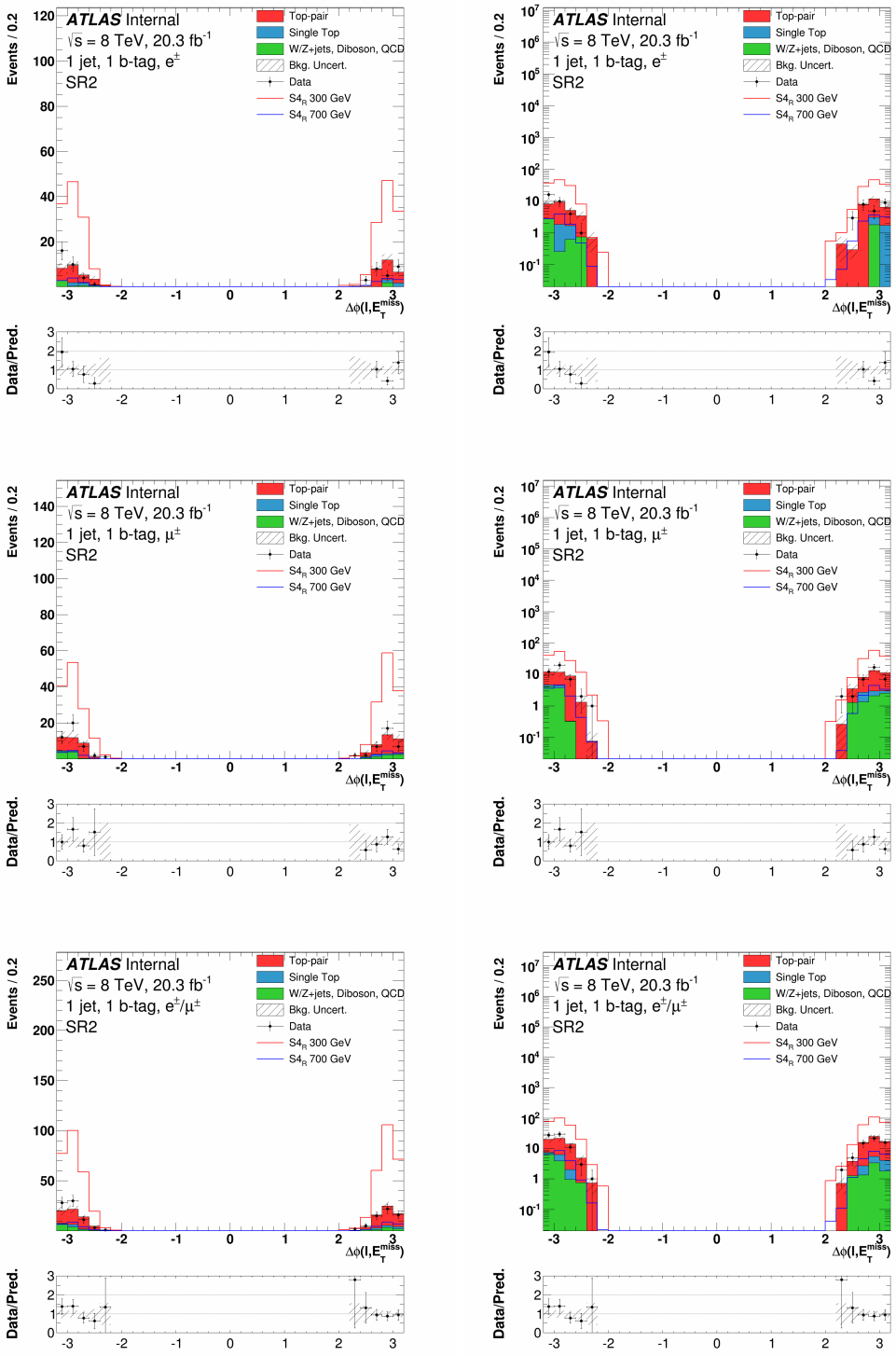

Figure C.41: Distributions of $\Delta\phi(\ell, E_{\mathrm{T}}^{\mathrm{miss}})$ for the electron (top), the muon (middle), and the combined (bottom) channels in the optimized SR2 signal region, in linear (left) and log (right) scale. The uncertainty band on the expected background corresponds to the errors due to the statistical uncertainties added in quadrature with the cross-section and normalization uncertainties.

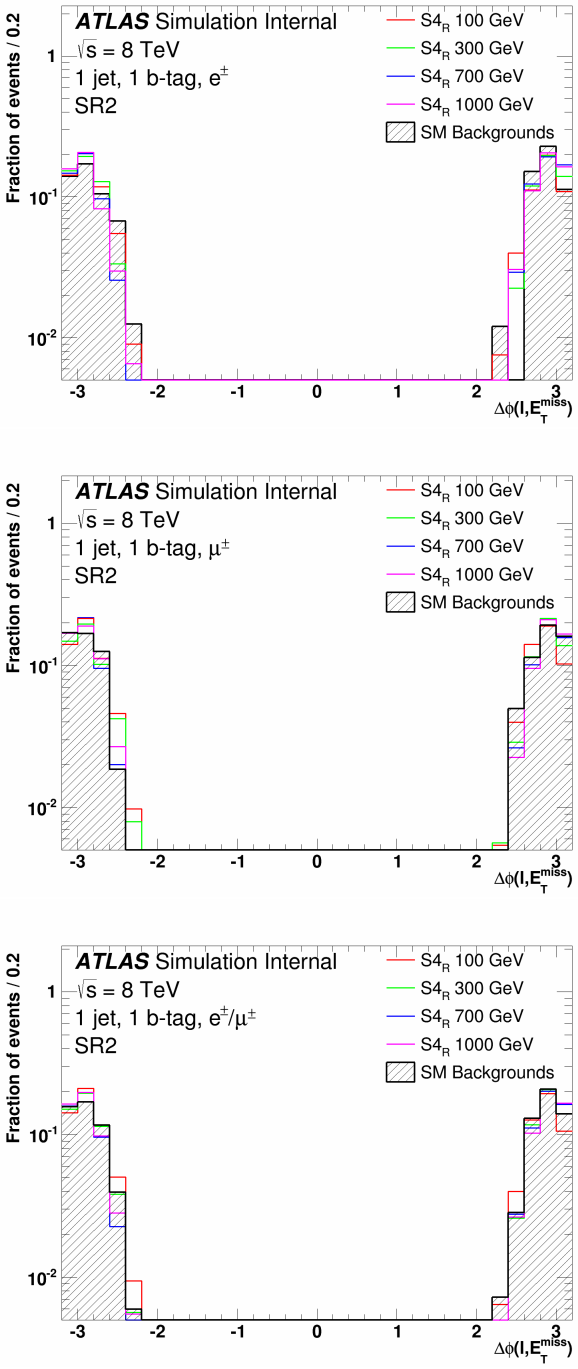

Figure C.42: Distributions of $\Delta\phi(\ell, E_{\mathrm{T}}^{\mathrm{miss}})$ normalized to unity for the electron (top), the muon (middle), and the combined (bottom) channels in the optimized SR2 signal region for four mass hypotheses of the $\mathrm{S4_R}$ model. The SM background is also shown.

Optimized BDT signal region

This section presents distributions of variables for simulated background and data events in the optimized BDT signal region, defined in Section 7.5. Figures C.43 and C.44 show the transverse mass between the lepton and missing transverse energy, $m_{\mathrm{T}}(\ell^+, E_{\mathrm{T}}^{\mathrm{miss}})$. Figures C.45 and C.46 show the missing transverse energy, $E_{\mathrm{T}}^{\mathrm{miss}}$. Figures C.47 and C.48 show the transverse momentum of the lepton, $p_{\mathrm{T}}(\ell^+)$. Figures C.49 and C.50 show the transverse momentum of the b-jet, $p_{\mathrm{T}}(b)$. Figures C.51 and C.52 show the spatial separation in $\eta - \phi$ space between the lepton and b-jet, $\Delta\mathrm{R}(\ell^+, b)$. Figures C.53 and C.54 show the angular separation in ϕ between the lepton and b-jet, $\Delta\phi(\ell^+, b)$. Figures C.55 and C.56 show the angular separation in ϕ between the lepton and the missing transverse energy, $\Delta\phi(\ell^+, E_{\mathrm{T}}^{\mathrm{miss}})$.

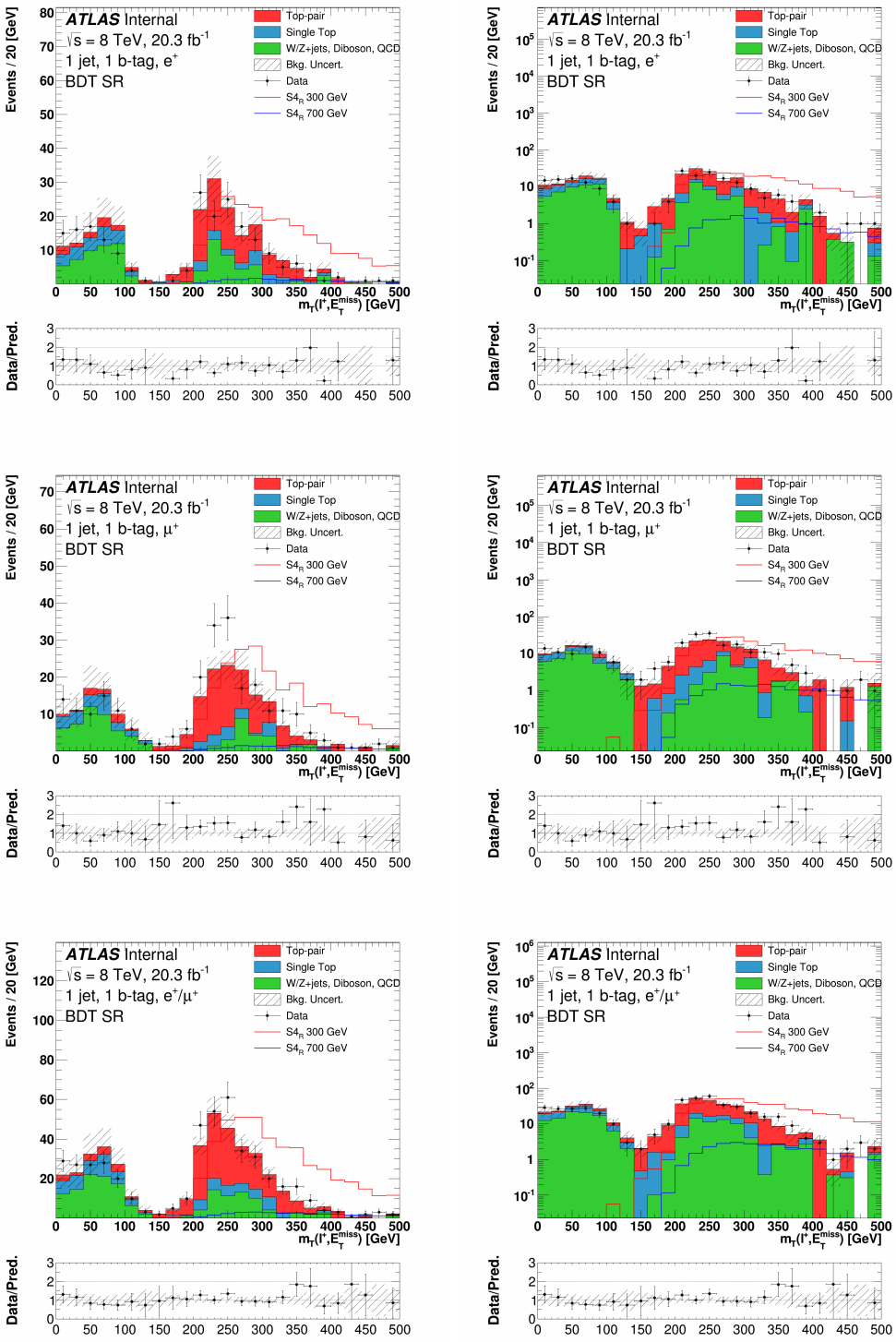

Figure C.43: Distributions of $m_{\mathrm{T}}(\ell^{+}, E_{\mathrm{T}}^{\mathrm{miss}})$ for the electron (top), the muon (middle), and the combined (bottom) channels in the BDT optimized signal region, in linear (left) and log (right) scale. The uncertainty band on the expected background corresponds to the errors due to the statistical uncertainties added in quadrature with the cross-section and normalization uncertainties.

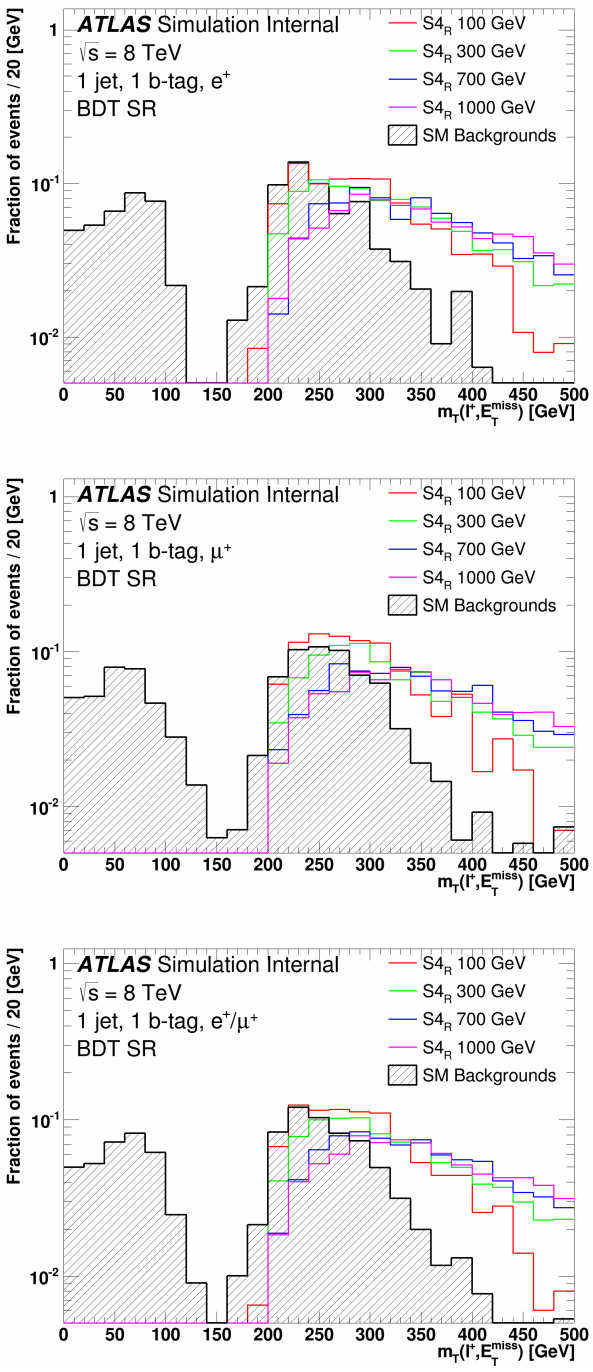

Figure C.44: Distributions of $m_{\mathrm{T}}(\ell^{+}, E_{\mathrm{T}}^{\mathrm{miss}})$ normalized to unity for the electron (top), the muon (middle), and the combined (bottom) channels in the optimized BDT signal region for four mass hypotheses of the $\mathrm{S4_R}$ model. The SM background is also shown.

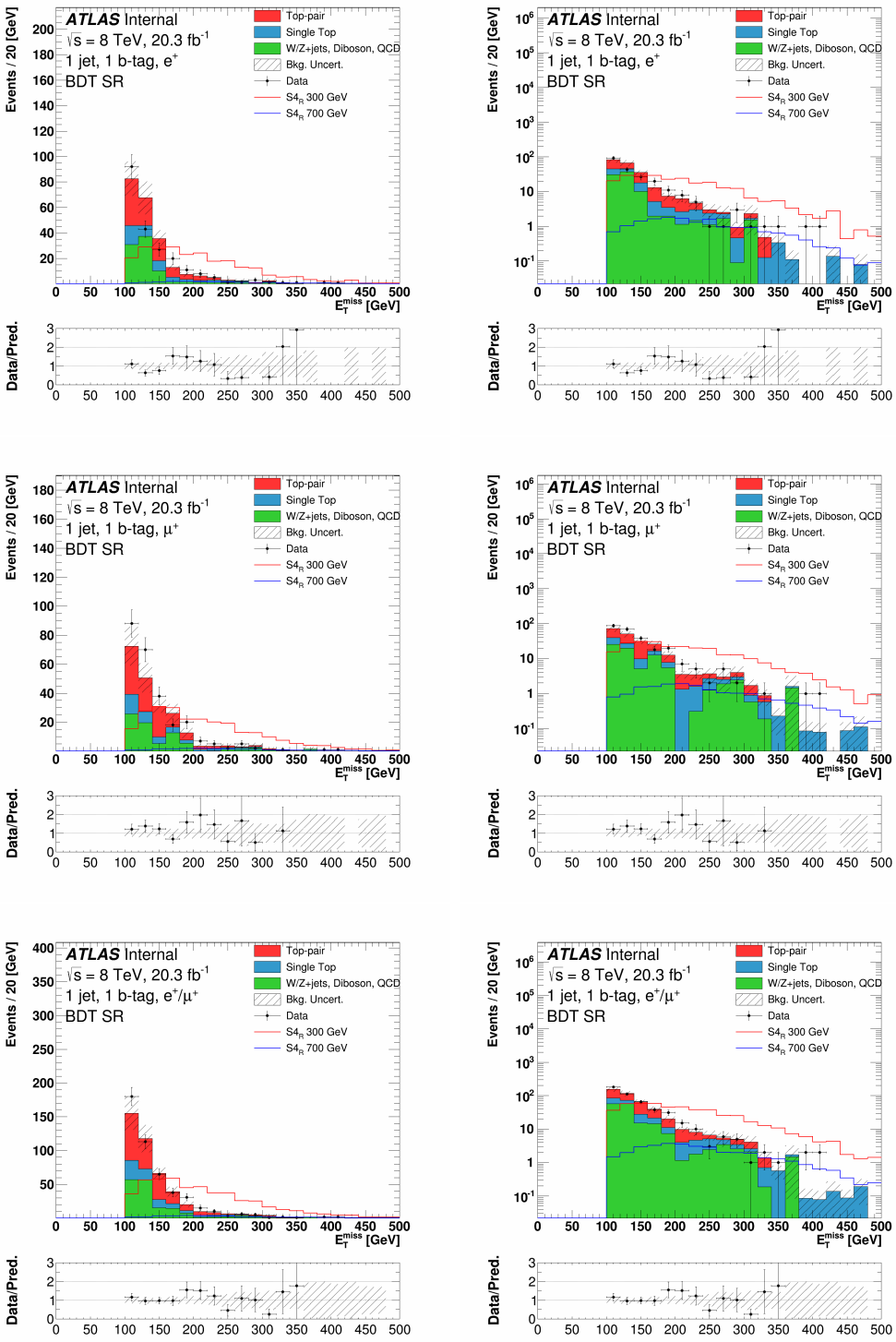

Figure C.45: Distributions of $E_{\mathrm{T}}^{\mathrm{miss}}$ for the electron (top), the muon (middle), and the combined (bottom) channels in the BDT optimized signal region, in linear (left) and log (right) scale. The uncertainty band on the expected background corresponds to the errors due to the statistical uncertainties added in quadrature with the cross-section and normalization uncertainties.

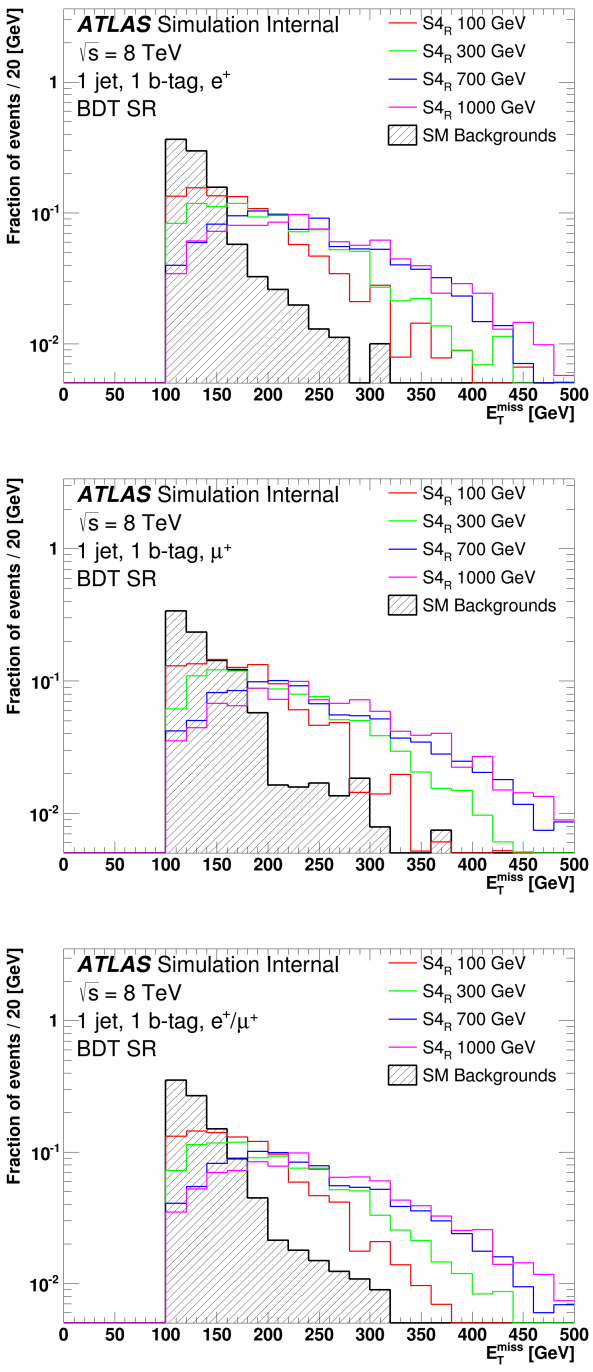

Figure C.46: Distributions of $E_{\mathrm{T}}^{\mathrm{miss}}$ normalized to unity for the electron (top), the muon (middle), and the combined (bottom) channels in the optimized BDT signal region for four mass hypotheses of the $\mathrm{S4_R}$ model. The SM background is also shown.

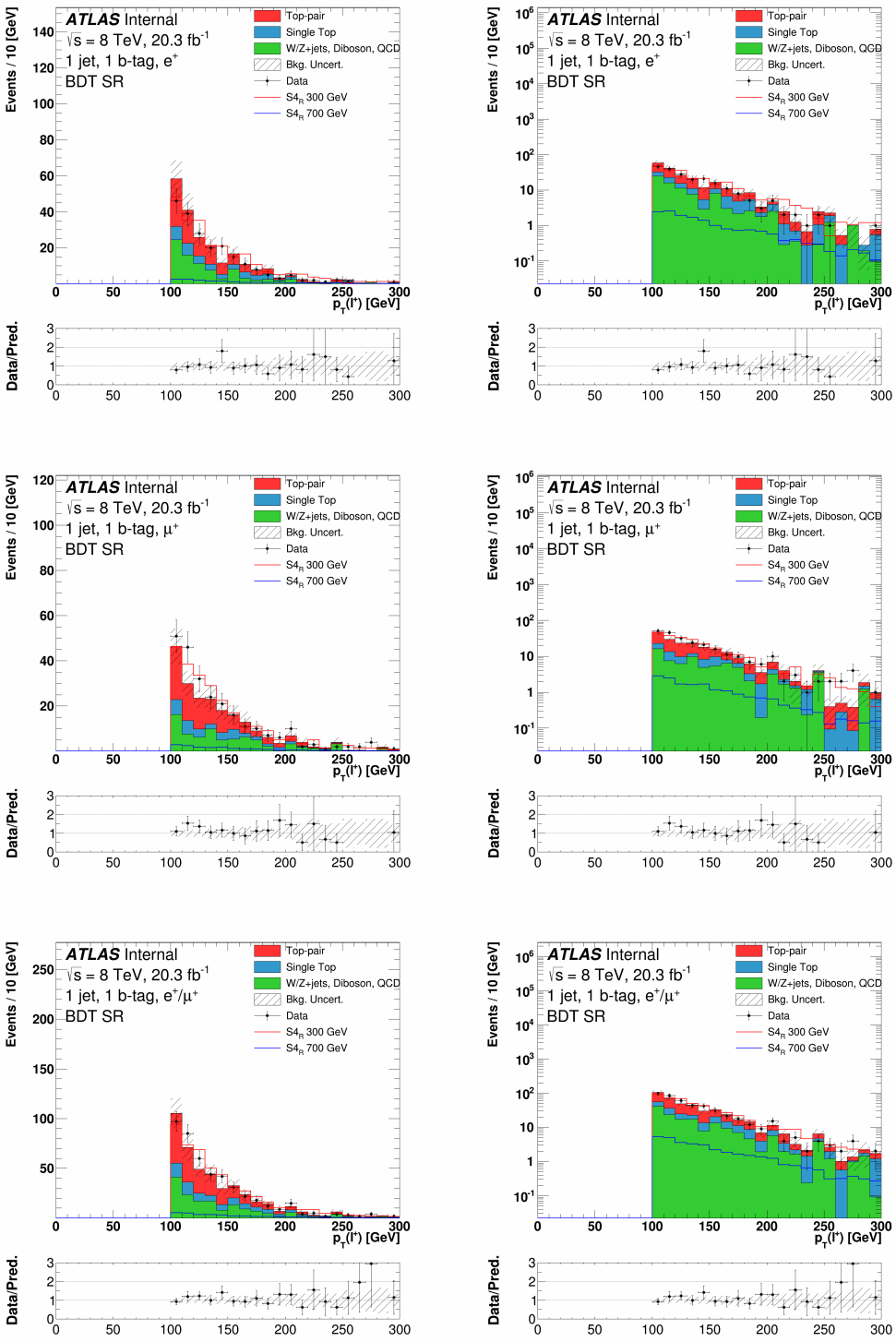

Figure C.47: Distributions of $p_{\mathrm{T}}(\ell^{+})$ for the electron (top), the muon (middle), and the combined (bottom) channels in the BDT optimized signal region, in linear (left) and log (right) scale. The uncertainty band on the expected background corresponds to the errors due to the statistical uncertainties added in quadrature with the cross-section and normalization uncertainties.

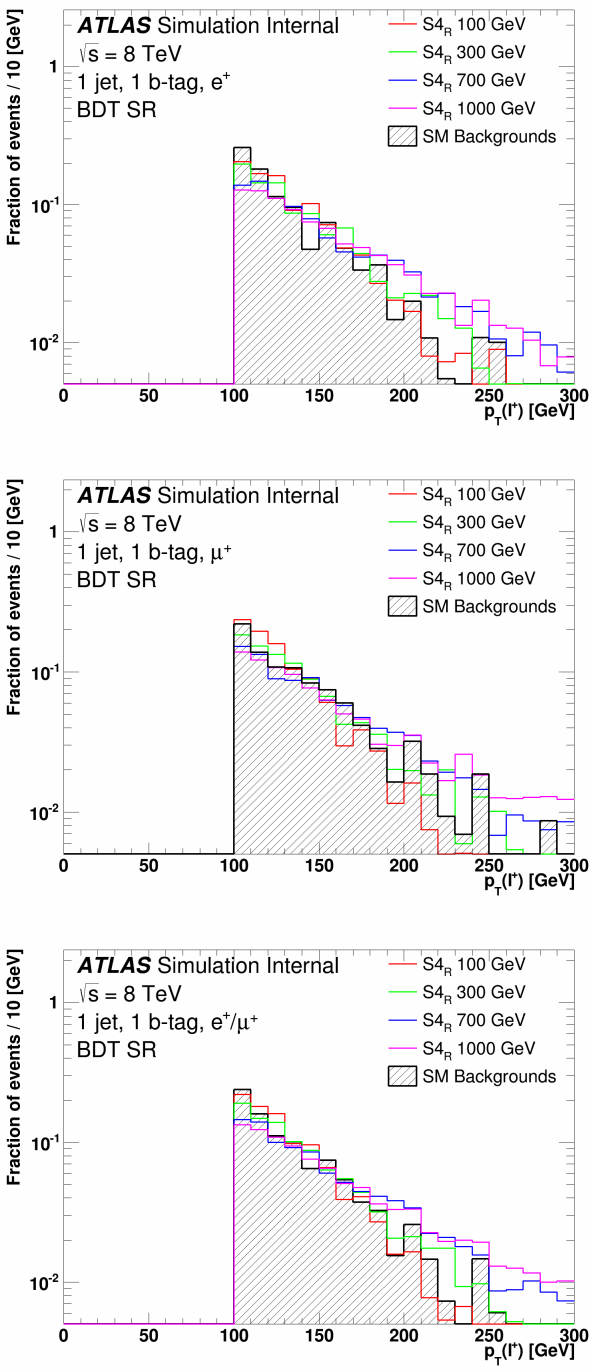

Figure C.48: Distributions of $p_{\mathrm{T}}(\ell^{+})$ normalized to unity for the electron (top), the muon (middle), and the combined (bottom) channels in the optimized BDT signal region for four mass hypotheses of the $\mathrm{S4_R}$ model. The SM background is also shown.

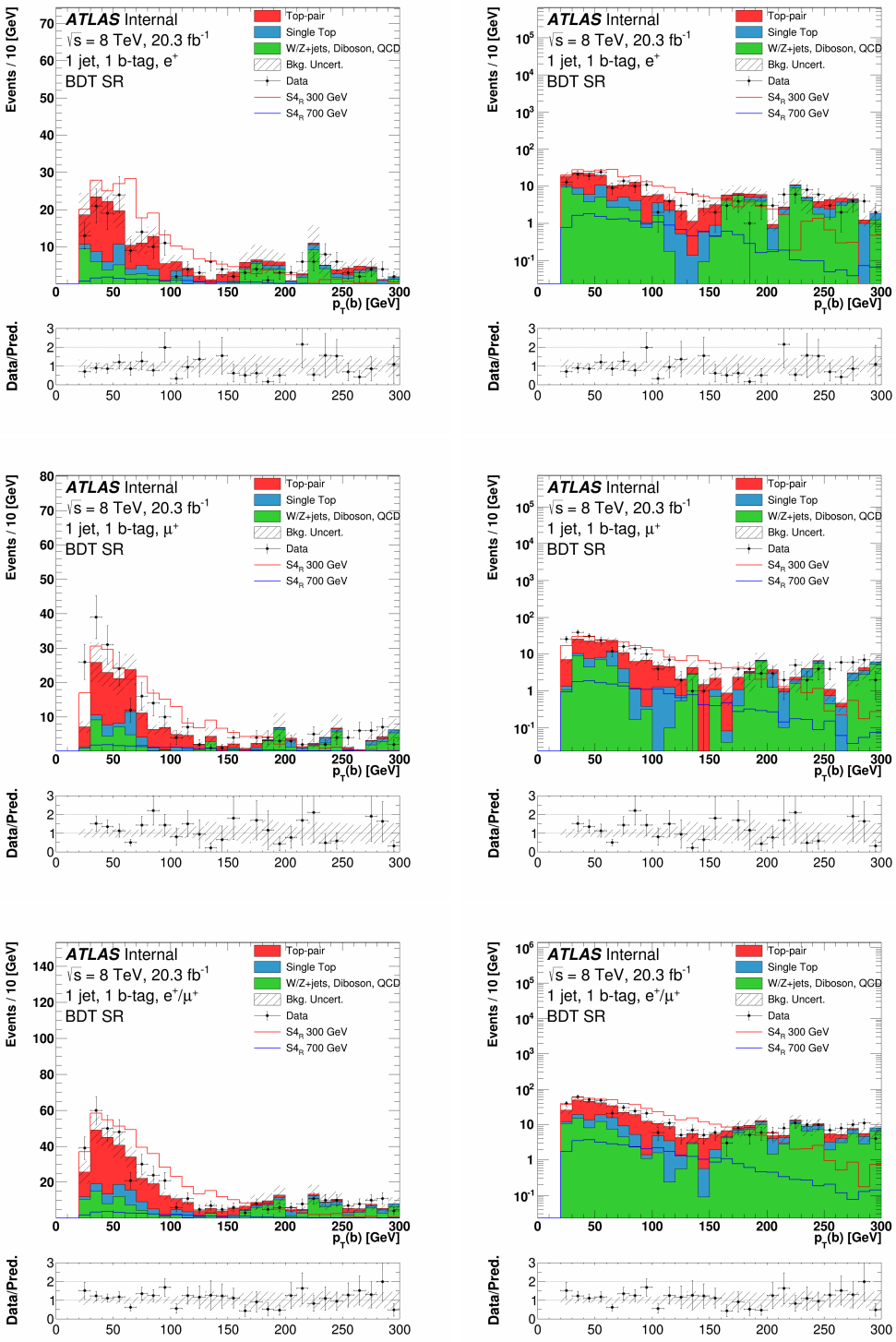

Figure C.49: Distributions of $p_{\mathrm{T}}(b)$ for the electron (top), the muon (middle), and the combined (bottom) channels in the BDT optimized signal region, in linear (left) and log (right) scale. The uncertainty band on the expected background corresponds to the errors due to the statistical uncertainties added in quadrature with the cross-section and normalization uncertainties.

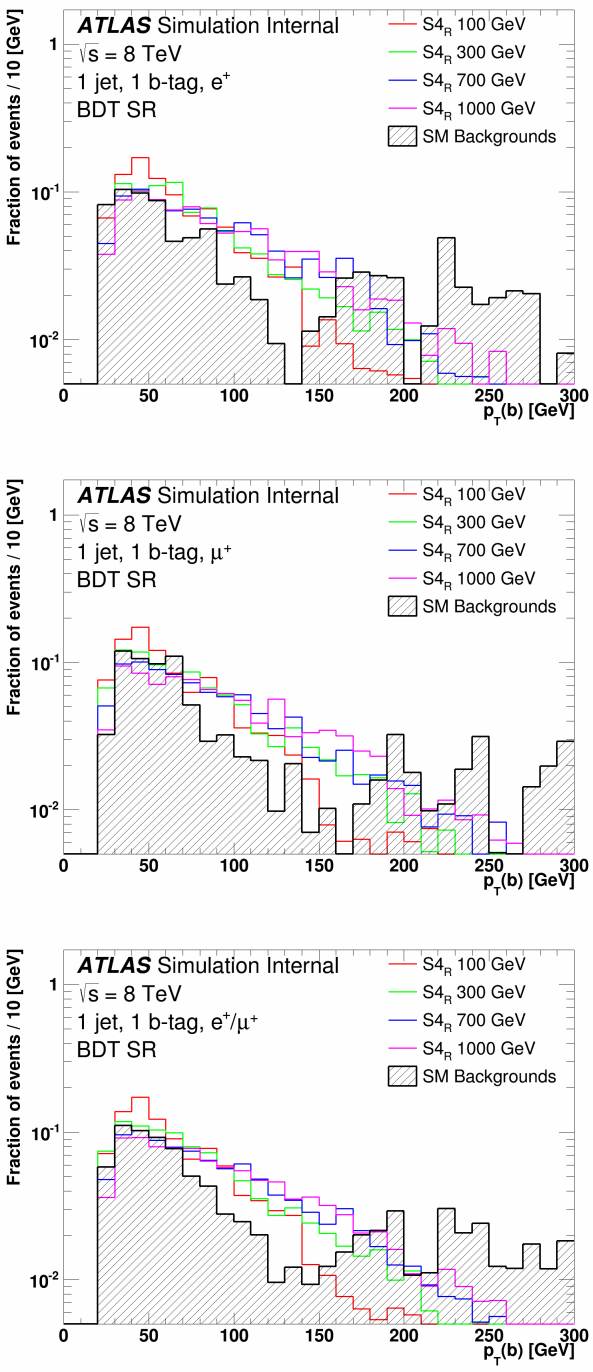

Figure C.50: Distributions of $p_{\mathrm{T}}(b)$ normalized to unity for the electron (top), the muon (middle), and the combined (bottom) channels in the optimized BDT signal region for four mass hypotheses of the $\mathrm{S4_R}$ model. The SM background is also shown.

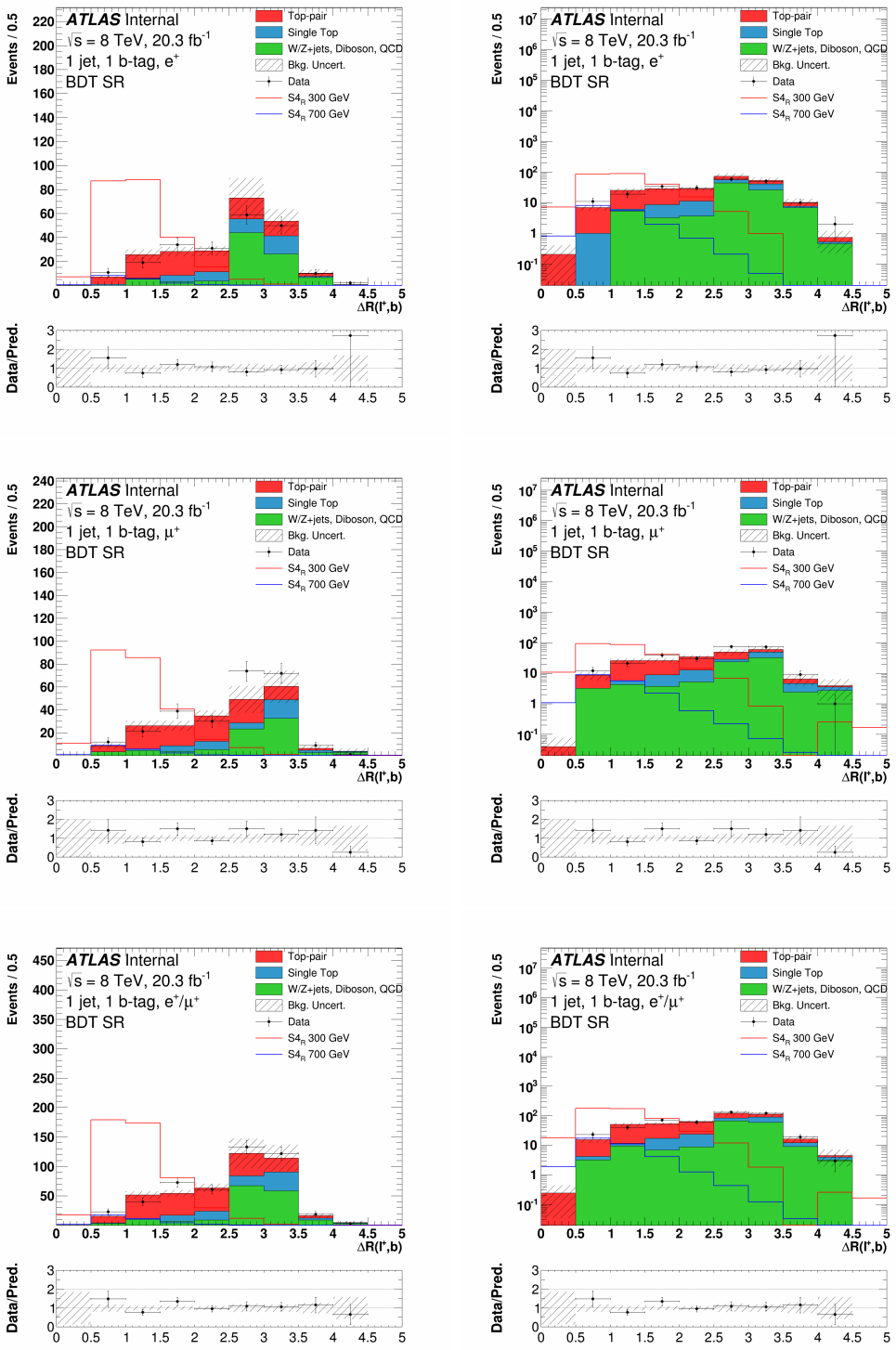

Figure C.51: Distributions of $\Delta R(\ell^+, b)$ for the electron (top), the muon (middle), and the combined (bottom) channels in the BDT optimized signal region, in linear (left) and log (right) scale. The uncertainty band on the expected background corresponds to the errors due to the statistical uncertainties added in quadrature with the cross-section and normalization uncertainties.

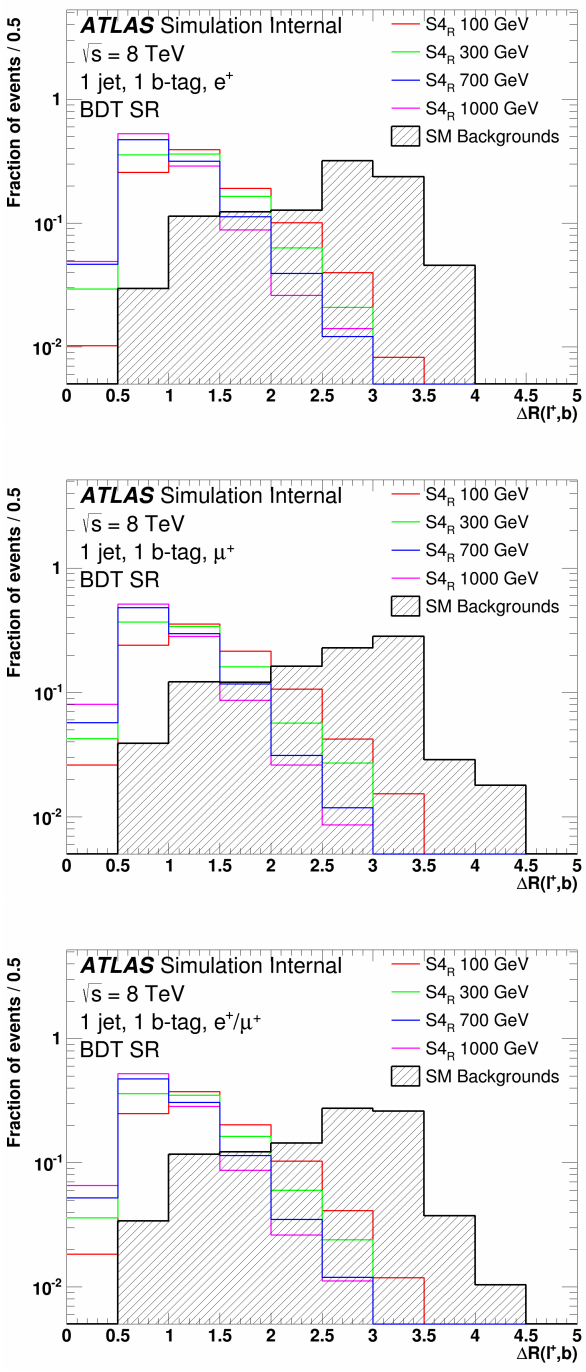

Figure C.52: Distributions of $\Delta\mathrm{R}(\ell^+, b)$ normalized to unity for the electron (top), the muon (middle), and the combined (bottom) channels in the optimized BDT signal region for four mass hypotheses of the $\mathrm{S4_R}$ model. The SM background is also shown.

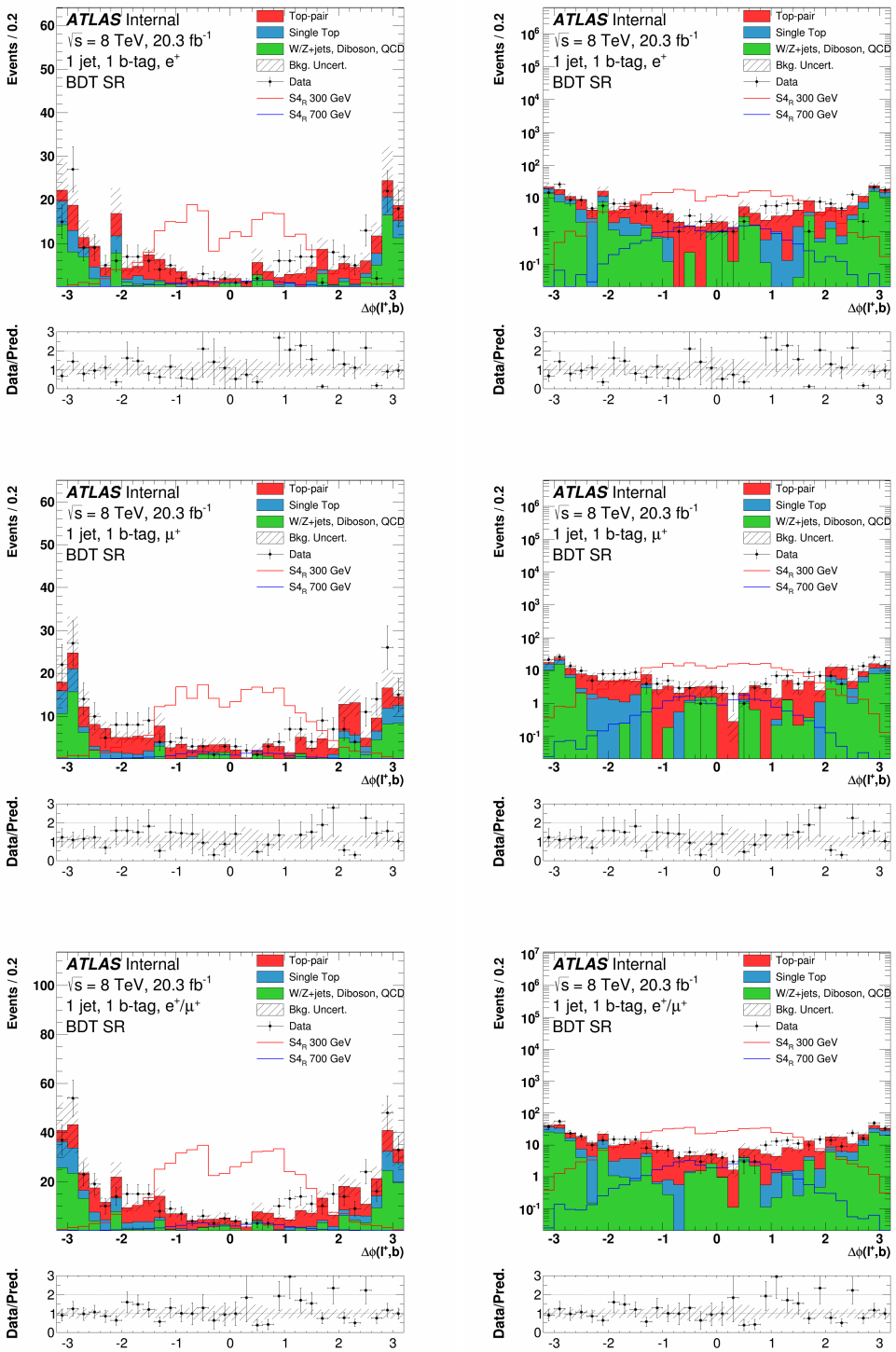

Figure C.53: Distributions of $\Delta\phi(\ell^+, b)$ for the electron (top), the muon (middle), and the combined (bottom) channels in the BDT optimized signal region, in linear (left) and log (right) scale. The uncertainty band on the expected background corresponds to the errors due to the statistical uncertainties added in quadrature with the cross-section and normalization uncertainties.

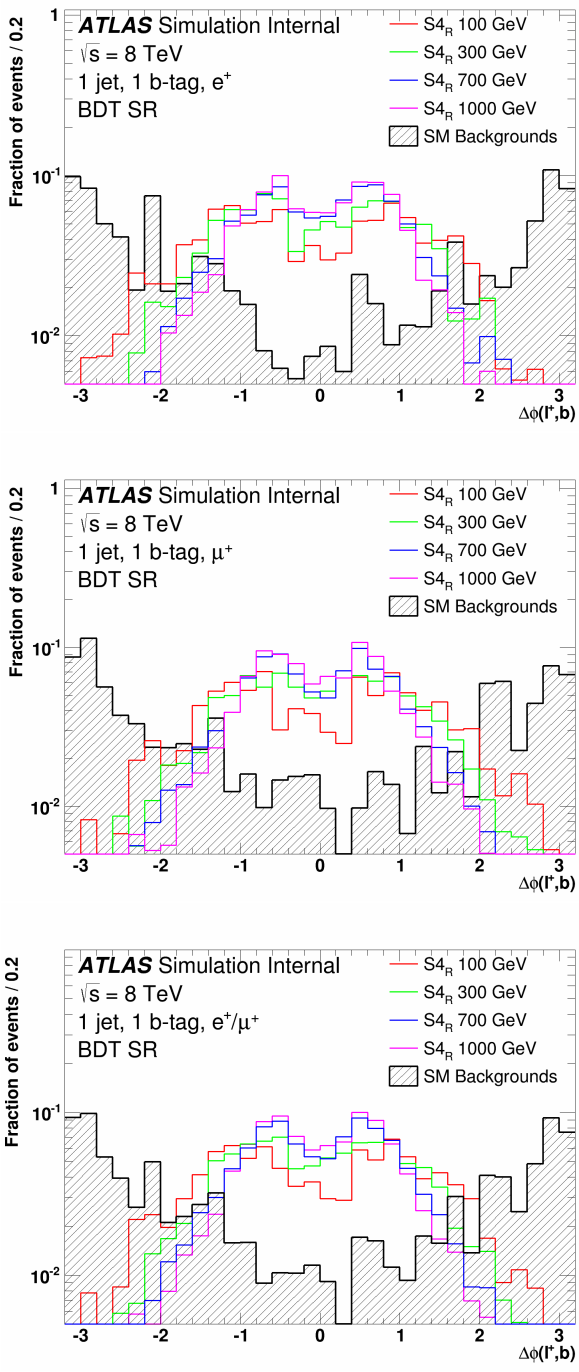

Figure C.54: Distributions of $\Delta\phi(\ell^+, b)$ normalized to unity for the electron (top), the muon (middle), and the combined (bottom) channels in the optimized BDT signal region for four mass hypotheses of the $S4_R$ model. The SM background is also shown.

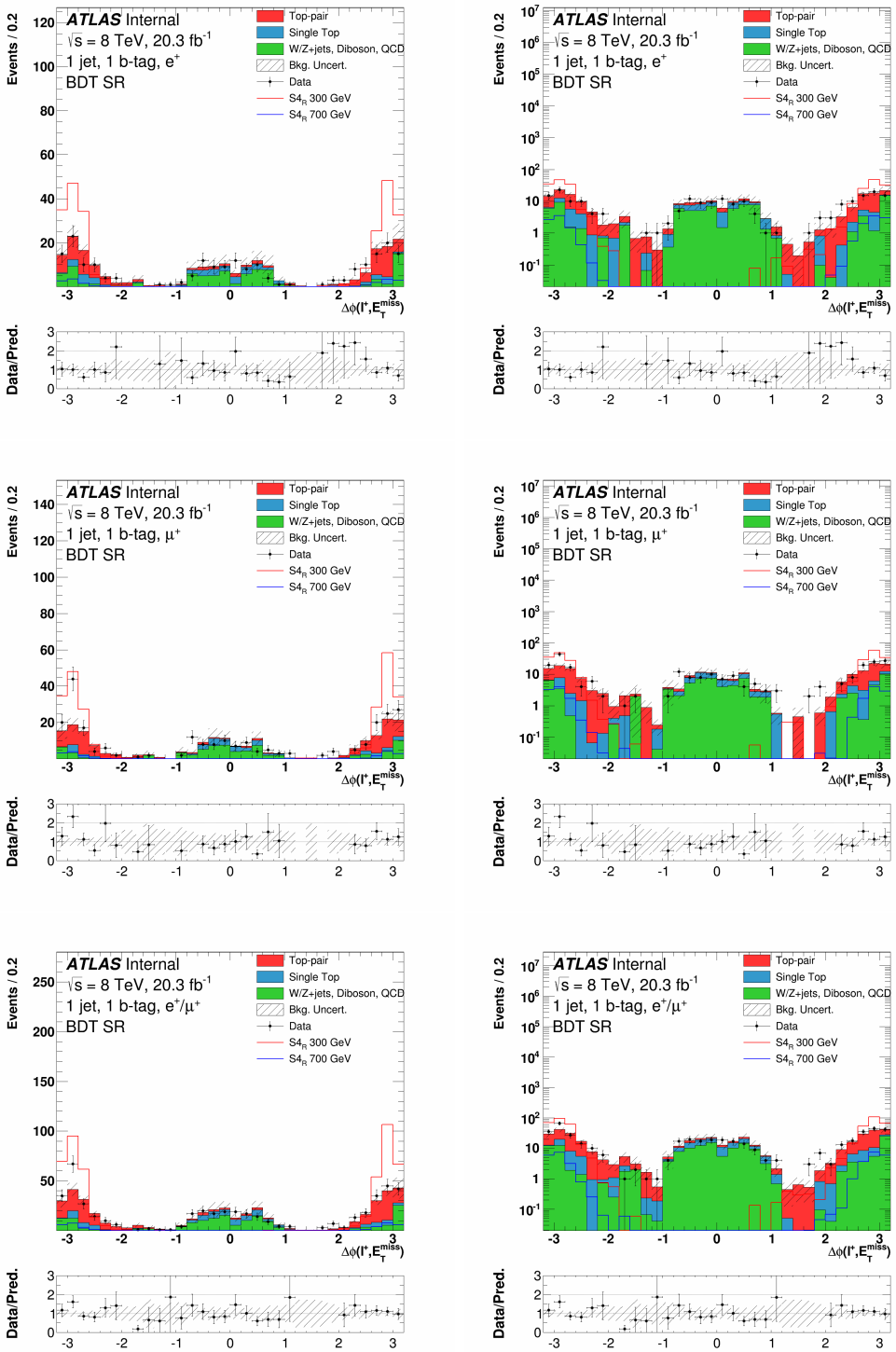

Figure C.55: Distributions of $\Delta\phi(\ell^+, E_{\mathrm{T}}^{\mathrm{miss}})$ for the electron (top), the muon (middle), and the combined (bottom) channels in the BDT optimized signal region, in linear (left) and log (right) scale. The uncertainty band on the expected background corresponds to the errors due to the statistical uncertainties added in quadrature with the cross-section and normalization uncertainties.

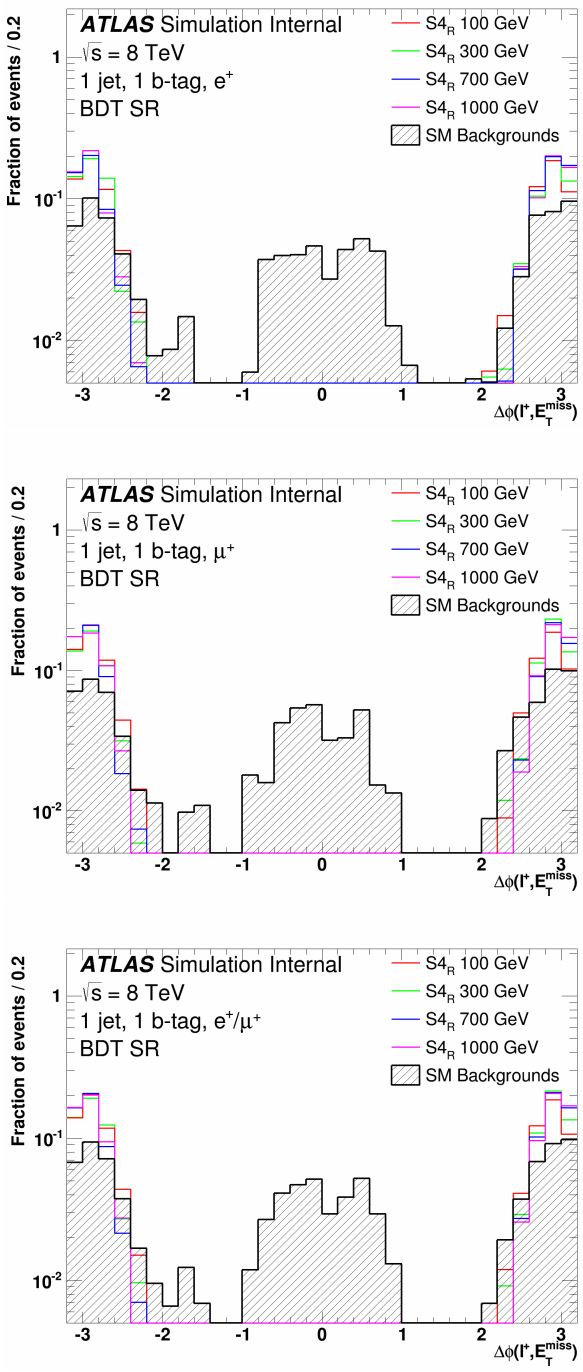

Figure C.56: Distributions of $\Delta\phi(\ell^+, E_{\mathrm{T}}^{\mathrm{miss}})$ normalized to unity for the electron (top), the muon (middle), and the combined (bottom) channels in the optimized BDT signal region for four mass hypotheses of the $\mathrm{S4_R}$ model. The SM background is also shown.

Appendix D

Effect of lepton charge selection on kinematic distributions

This appendix presents plots comparing the distributions of kinematic variables for the SM background in both the pre-selection and SR2 signal regions with and without a cut on the electric charge of the lepton. The bottom inlet in each plot serves as the efficiency of the lepton electric charge cut on a bin-by-bin basis. Distributions of $m_{\mathrm{T}}(\ell, E_{\mathrm{T}}^{\mathrm{miss}})$, $E_{\mathrm{T}}^{\mathrm{miss}}$, $p_{\mathrm{T}}(\ell)$, $p_{\mathrm{T}}(b)$, $\Delta\mathrm{R}(\ell, b)$, $\Delta\phi(\ell, b)$, and $\Delta\phi(\ell, E_{\mathrm{T}}^{\mathrm{miss}})$ are shown for the pre-selection region in Section D and for the SR2 signal region in Section D.

Pre-selection region

This section presents plots comparing the distributions of kinematic variables for the SM background in the pre-selection region both with and without a cut on the electric charge of the lepton. The plots show that the efficiency of the lepton electric charge cut is consistent with the calculated value of 0.54 in Table 7.8 across the entirety of the distributions.

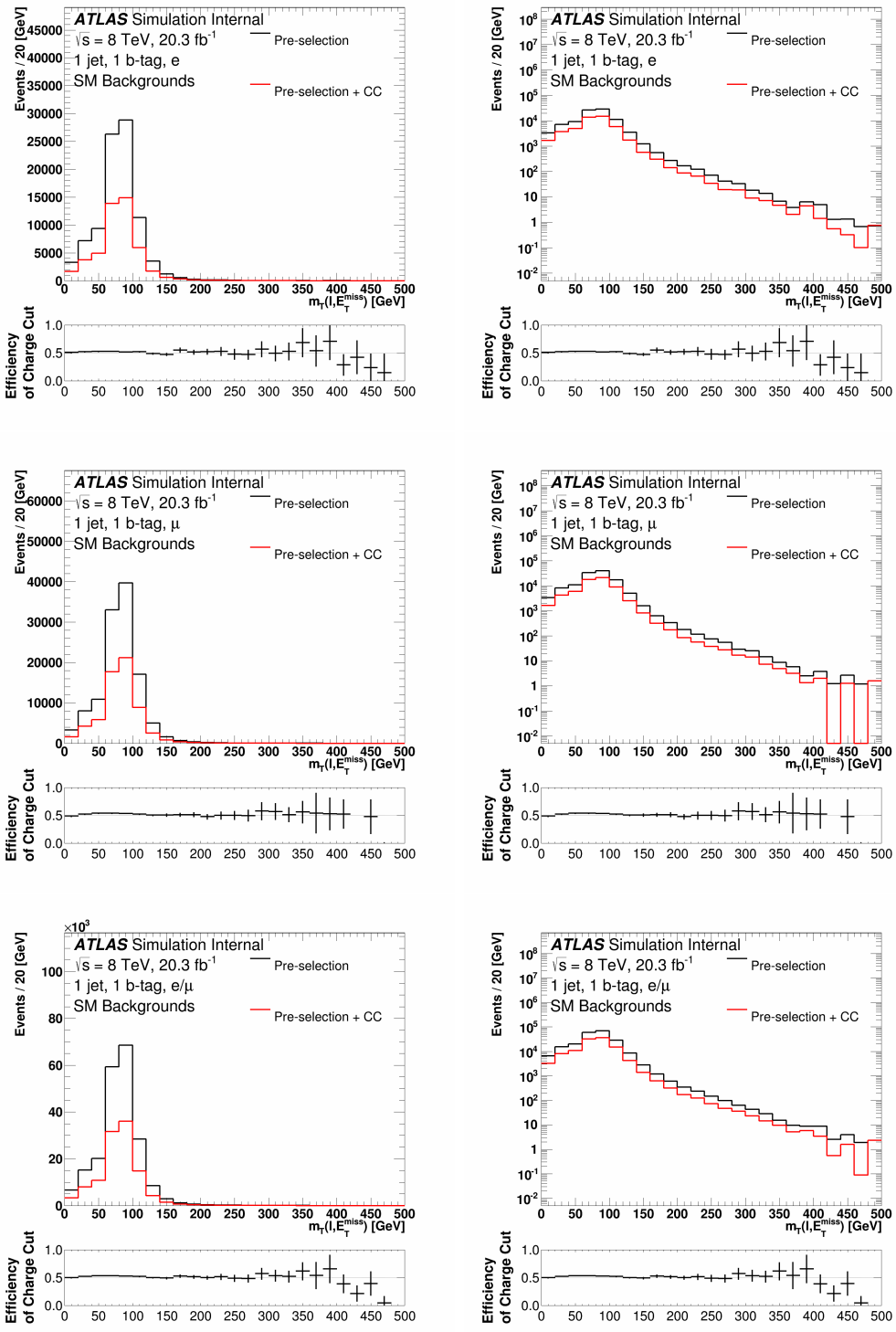

Figure D.1: Distributions of $m_{\mathrm{T}}(\ell, E_{\mathrm{T}}^{\mathrm{miss}})$ for the electron (top), the muon (middle), and the combined (bottom) channels in the pre-selection region, in linear (left) and log (right) scale. The black curve shows the distribution in the pre-selection region and the red curve shows the distribution in the pre-selection region with the additional cut on the electric charge of the lepton. The error bars in the bottom inlet include statistical uncertainties only.

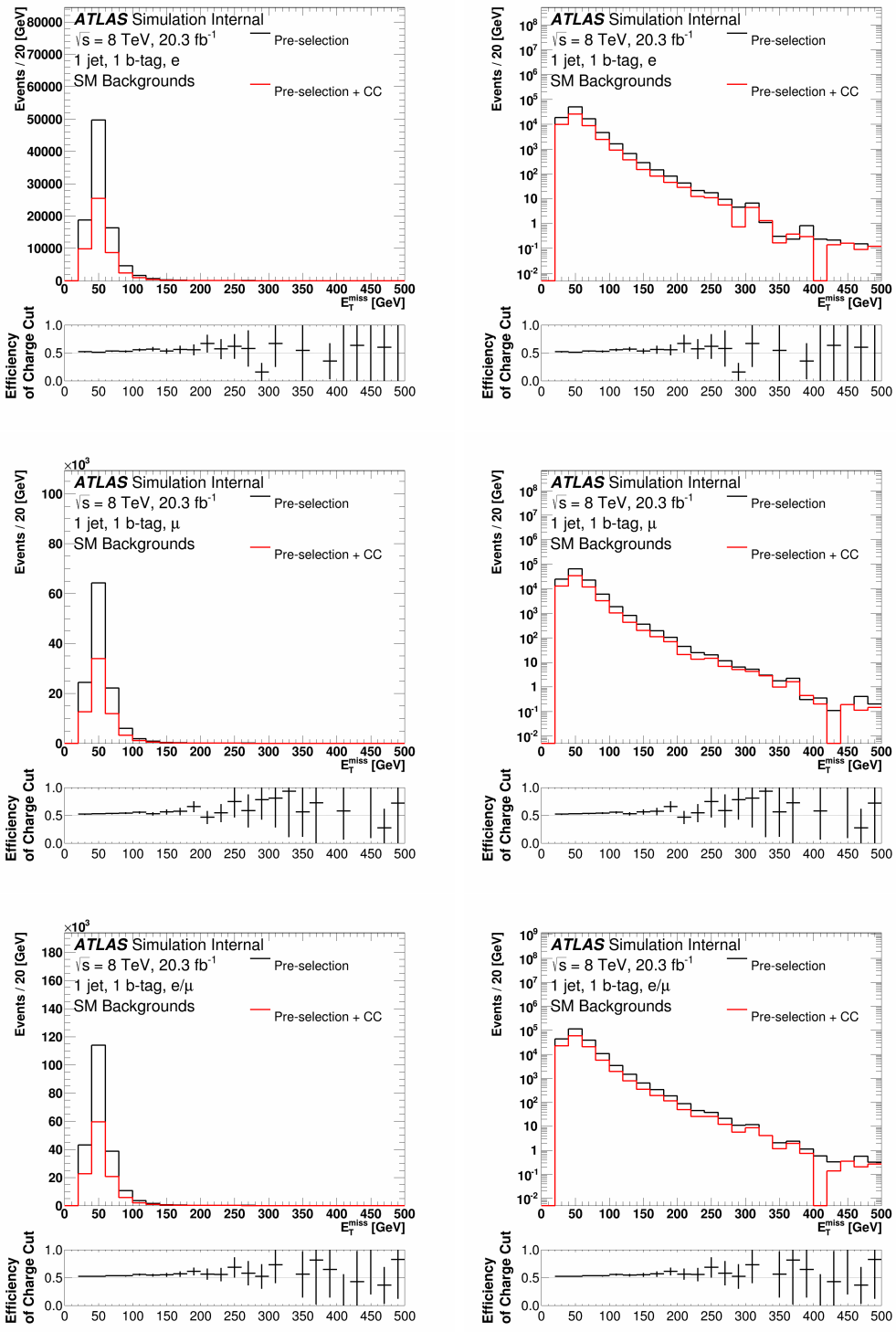

Figure D.2: Distributions of $E_{\mathrm{T}}^{\mathrm{miss}}$ for the electron (top), the muon (middle), and the combined (bottom) channels in the pre-selection region, in linear (left) and log (right) scale. The black curve shows the distribution in the pre-selection region and the red curve shows the distribution in the pre-selection region with the additional cut on the electric charge of the lepton. The error bars in the bottom inlet include statistical uncertainties only.

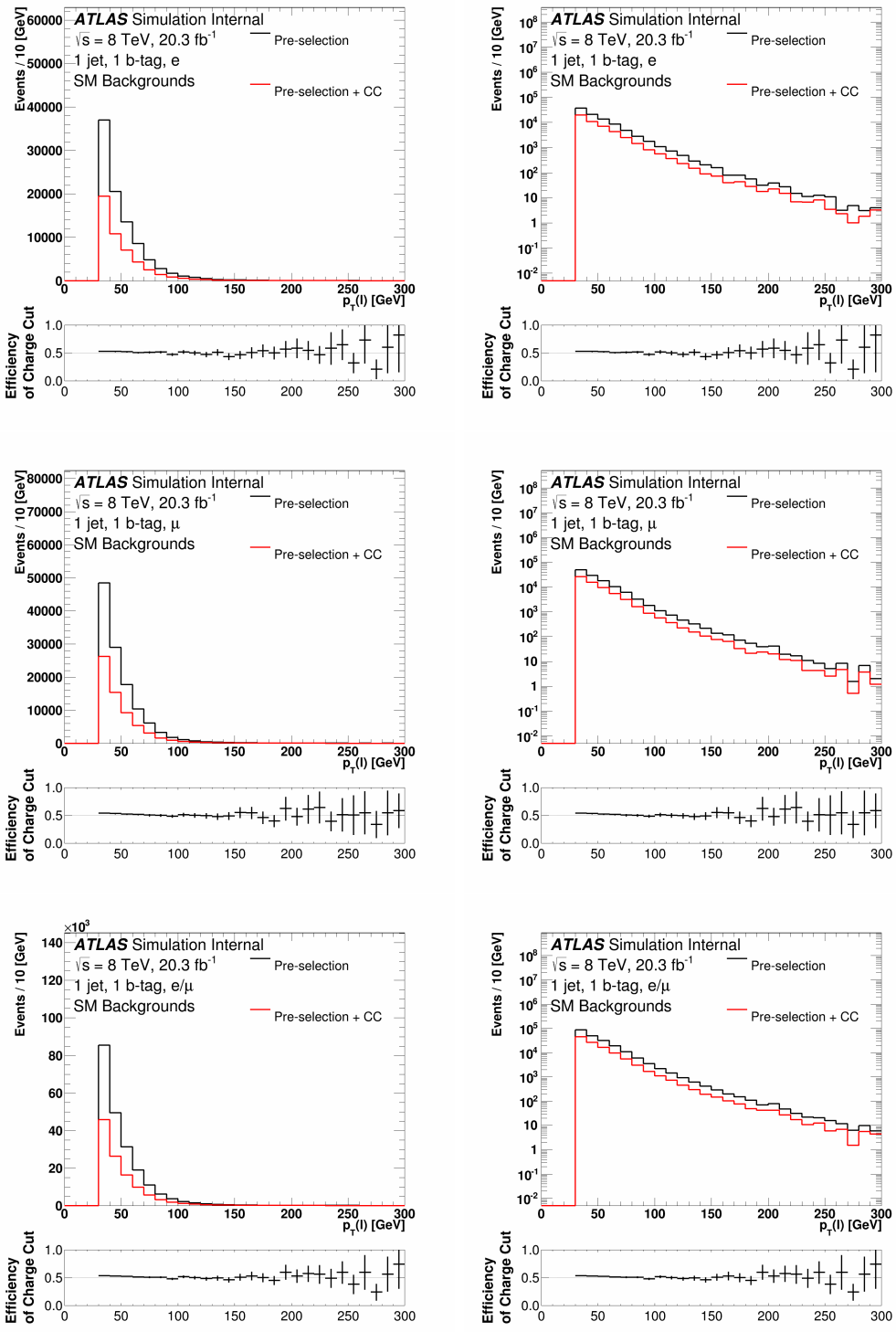

Figure D.3: Distributions of $p_{\mathrm{T}}(\ell)$ for the electron (top), the muon (middle), and the combined (bottom) channels in the pre-selection region, in linear (left) and log (right) scale. The black curve shows the distribution in the pre-selection region and the red curve shows the distribution in the pre-selection region with the additional cut on the electric charge of the lepton. The error bars in the bottom inlet include statistical uncertainties only.

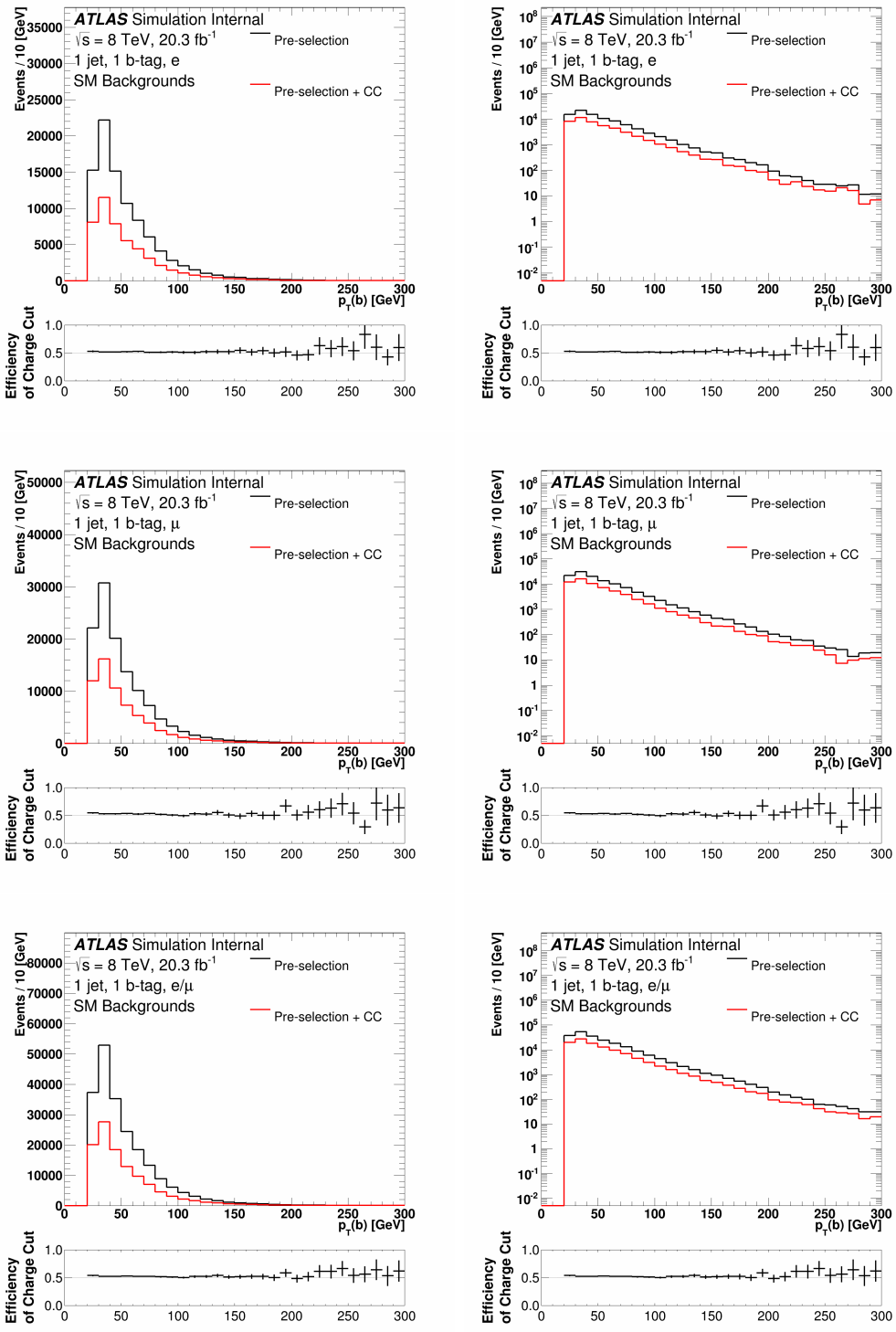

Figure D.4: Distributions of $p_{\mathrm{T}}(b)$ for the electron (top), the muon (middle), and the combined (bottom) channels in the pre-selection region, in linear (left) and log (right) scale. The black curve shows the distribution in the pre-selection region and the red curve shows the distribution in the pre-selection region with the additional cut on the electric charge of the lepton. The error bars in the bottom inlet include statistical uncertainties only.

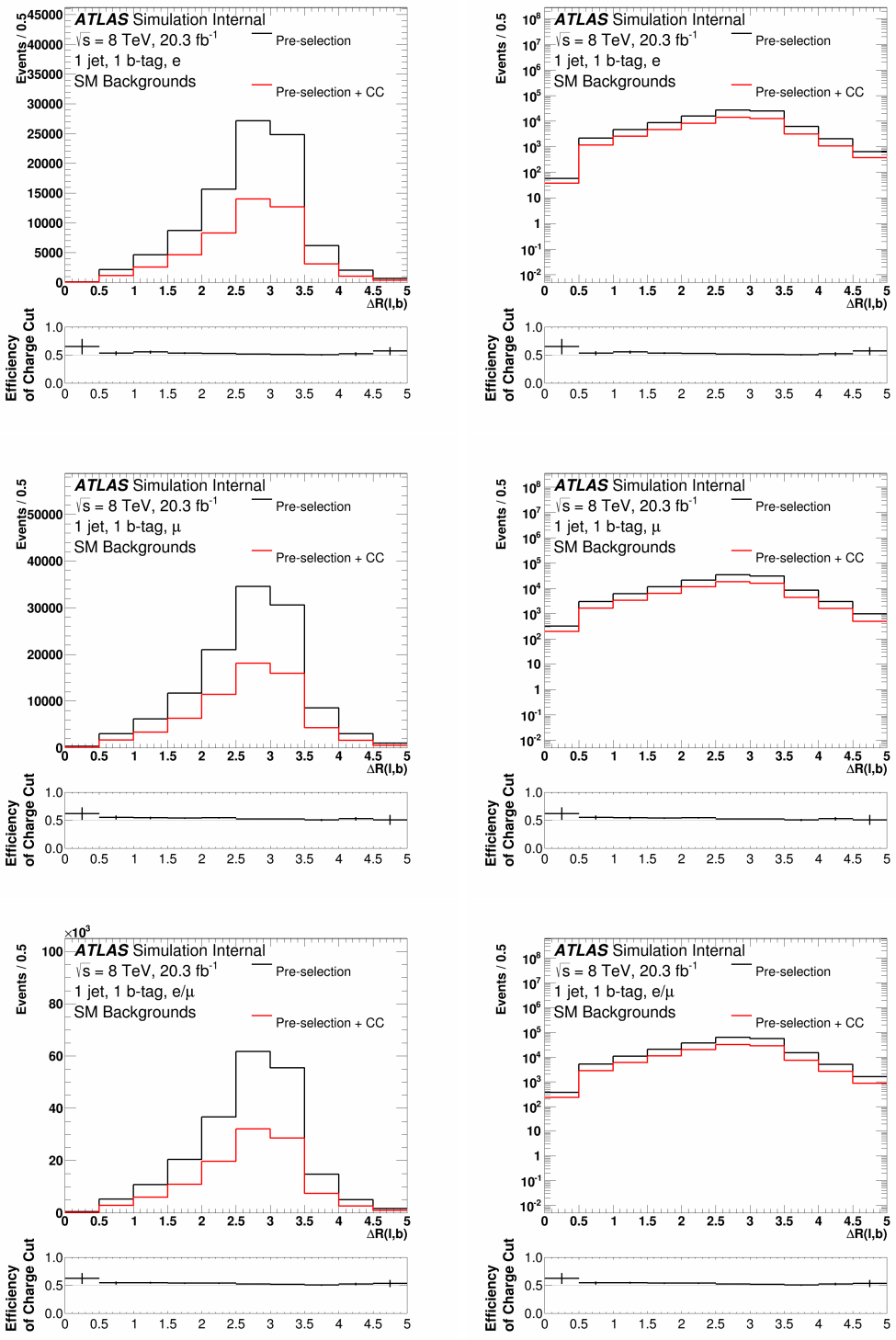

Figure D.5: Distributions of $\Delta\mathrm{R}(\ell, b)$ for the electron (top), the muon (middle), and the combined (bottom) channels in the pre-selection region, in linear (left) and log (right) scale. The black curve shows the distribution in the pre-selection region and the red curve shows the distribution in the pre-selection region with the additional cut on the electric charge of the lepton. The error bars in the bottom inlet include statistical uncertainties only.

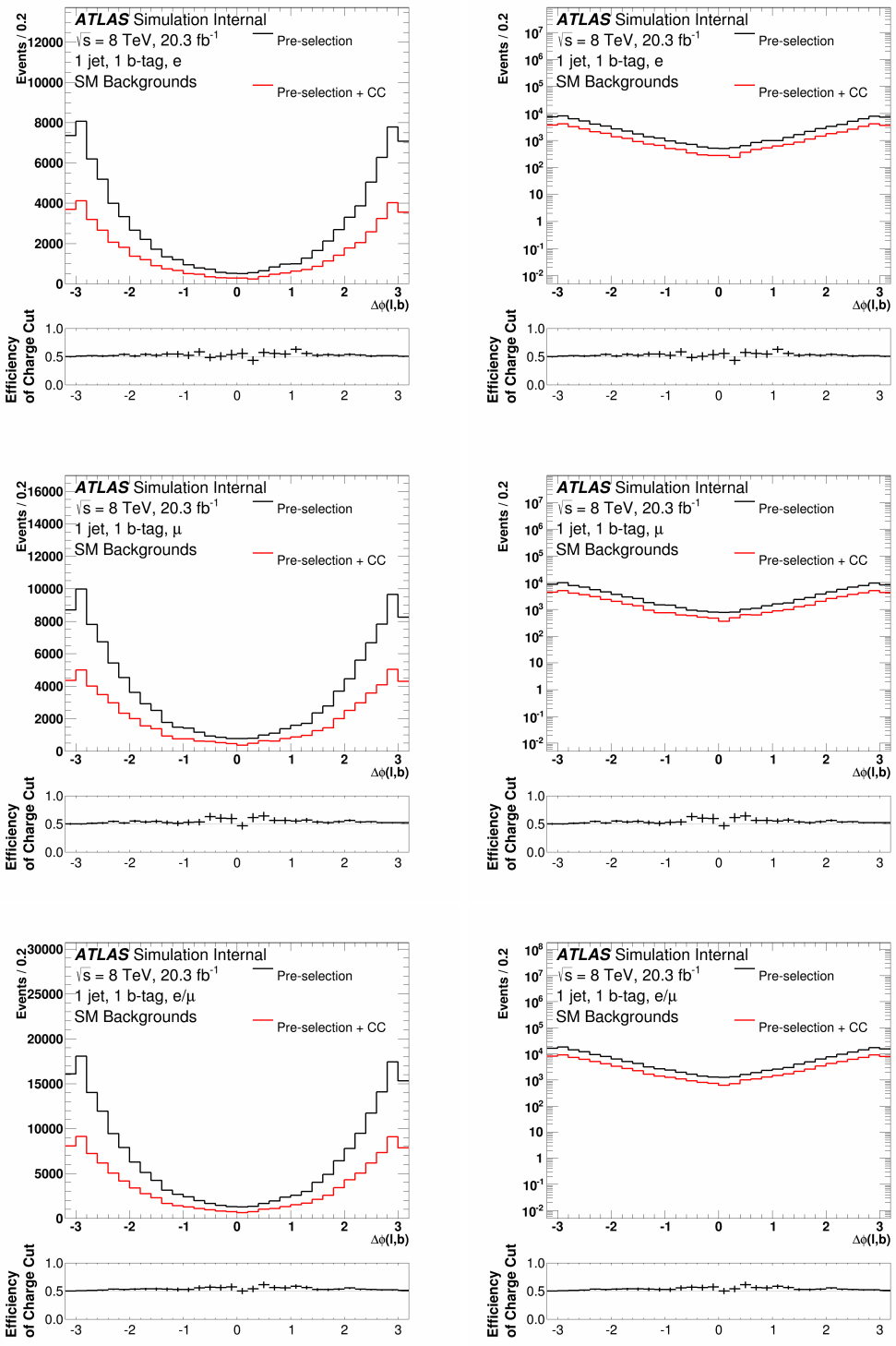

Figure D.6: Distributions of $\Delta\phi(\ell, b)$ for the electron (top), the muon (middle), and the combined (bottom) channels in the pre-selection region, in linear (left) and log (right) scale. The black curve shows the distribution in the pre-selection region and the red curve shows the distribution in the pre-selection region with the additional cut on the electric charge of the lepton. The error bars in the bottom inlet include statistical uncertainties only.

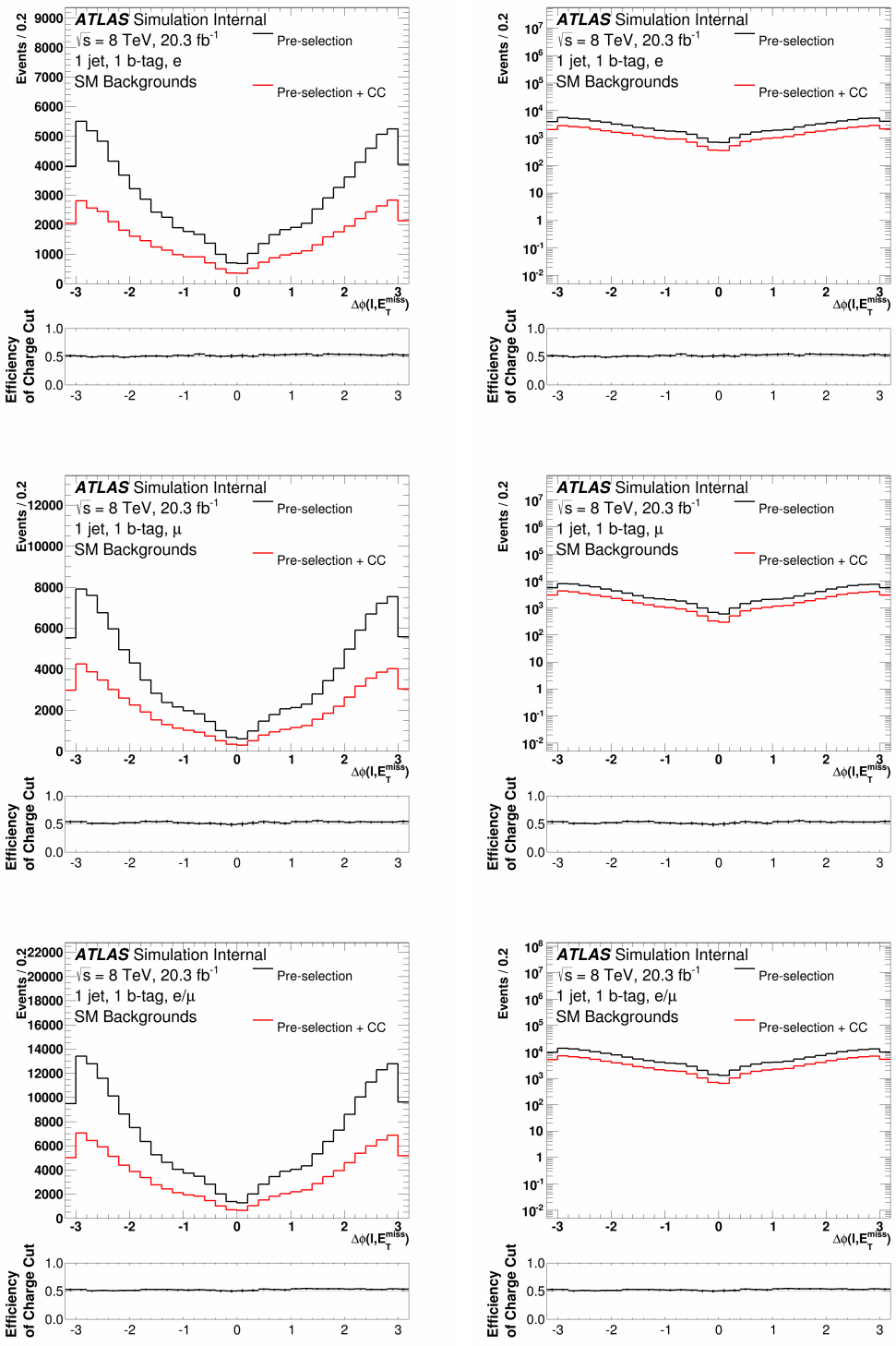

Figure D.7: Distributions of $\Delta\phi(\ell, E_{\mathrm{T}}^{\mathrm{miss}})$ for the electron (top), the muon (middle), and the combined (bottom) channels in the pre-selection region, in linear (left) and log (right) scale. The black curve shows the distribution in the pre-selection region and the red curve shows the distribution in the pre-selection region with the additional cut on the electric charge of the lepton. The error bars in the bottom inlet include statistical uncertainties only.

Optimized SR2 signal region

This section presents plots comparing the distributions of kinematic variables for the SM background in the SR2 signal region both with and without a cut on the electric charge of the lepton. The plots show that the efficiency of the lepton electric charge cut is consistent with the calculated value of 0.50 in the majority of the bins of the distributions. Any inconsistencies can be attributed to a lack of statistics in those regions of phase-space.

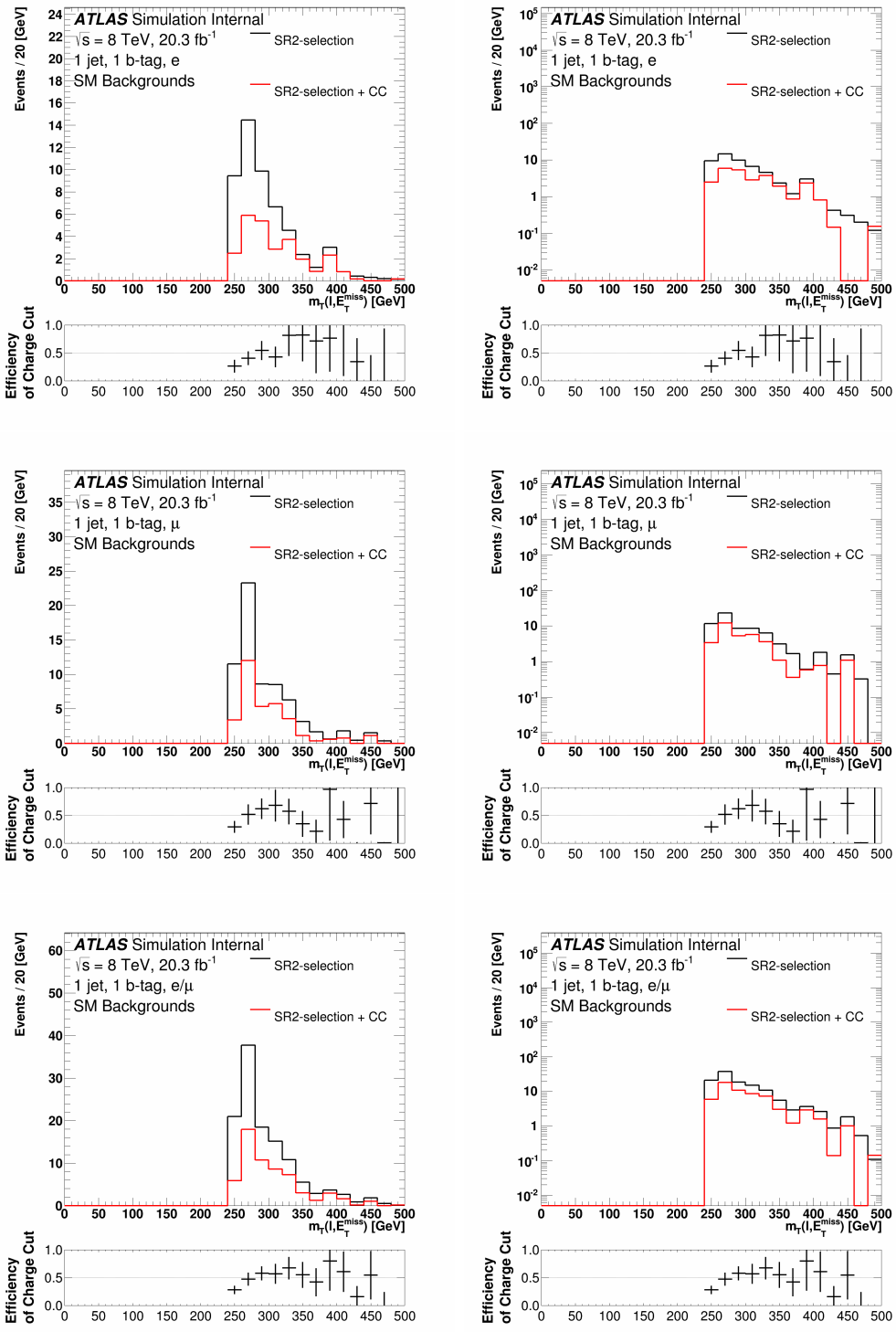

Figure D.8: Distributions of $m_{\mathrm{T}}(\ell, E_{\mathrm{T}}^{\mathrm{miss}})$ for the electron (top), the muon (middle), and the combined (bottom) channels in the SR2 signal region, in linear (left) and log (right) scale. The black curve shows the distribution in the SR2 signal region and the red curve shows the distribution in the SR2 signal region with the additional cut on the electric charge of the lepton. The error bars in the bottom inlet include statistical uncertainties only.

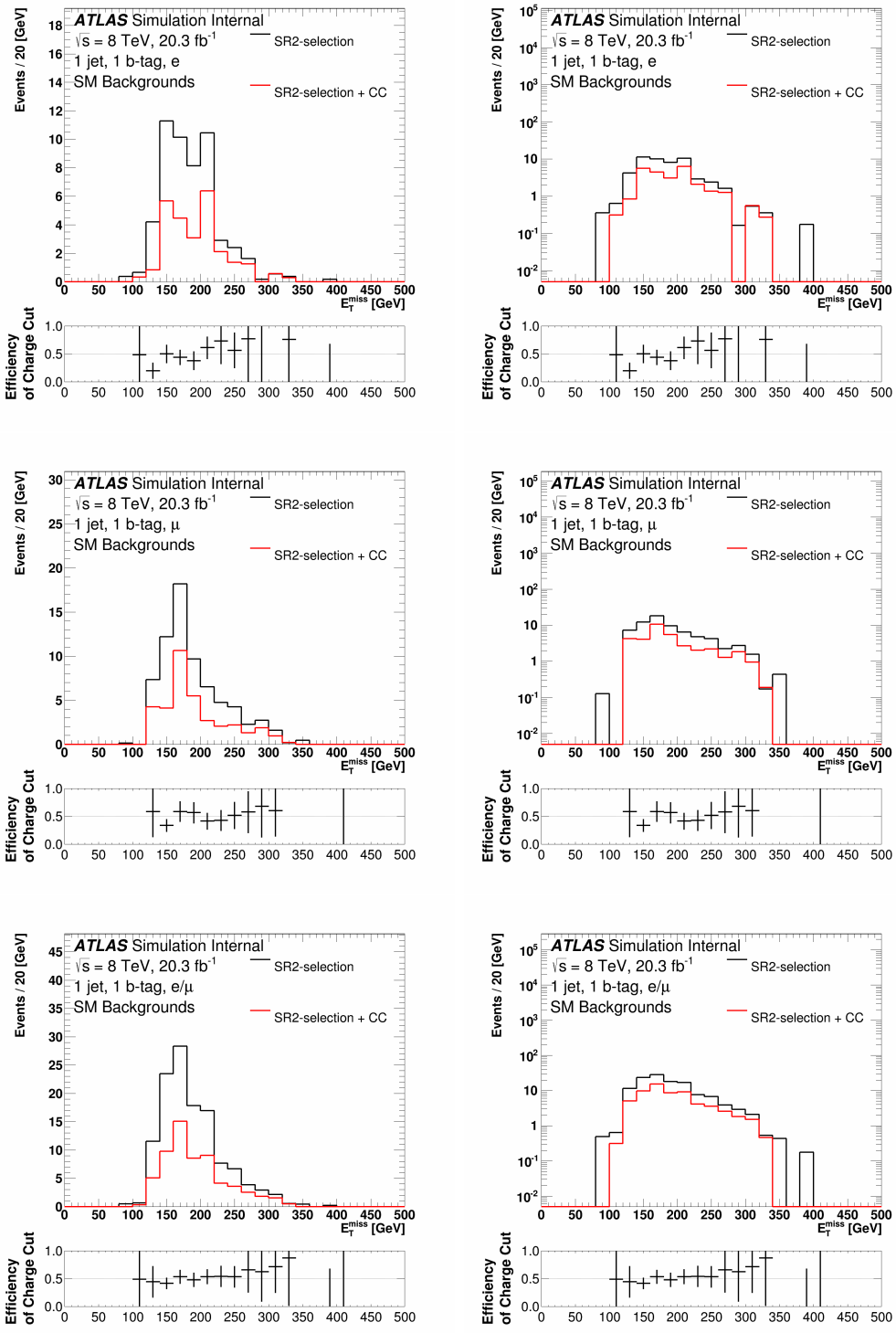

Figure D.9: Distributions of $E_{\mathrm{T}}^{\mathrm{miss}}$ for the electron (top), the muon (middle), and the combined (bottom) channels in the SR2 signal region, in linear (left) and log (right) scale. The black curve shows the distribution in the SR2 signal region and the red curve shows the distribution in the SR2 signal region with the additional cut on the electric charge of the lepton. The error bars in the bottom inlet include statistical uncertainties only.

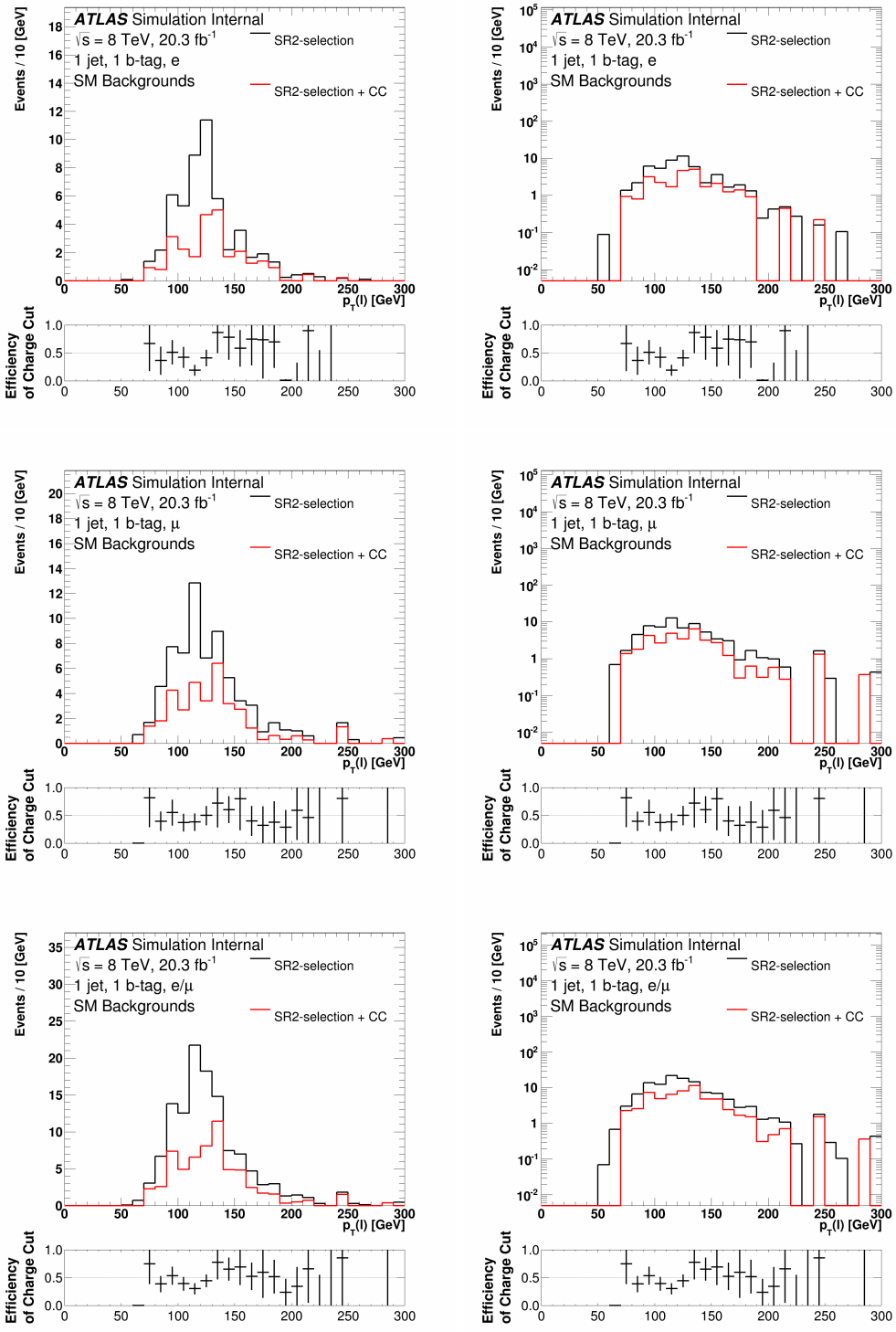

Figure D.10: Distributions of $p_{\mathrm{T}}(\ell)$ for the electron (top), the muon (middle), and the combined (bottom) channels in the SR2 signal region, in linear (left) and log (right) scale. The black curve shows the distribution in the SR2 signal region and the red curve shows the distribution in the SR2 signal region with the additional cut on the electric charge of the lepton. The error bars in the bottom inlet include statistical uncertainties only.

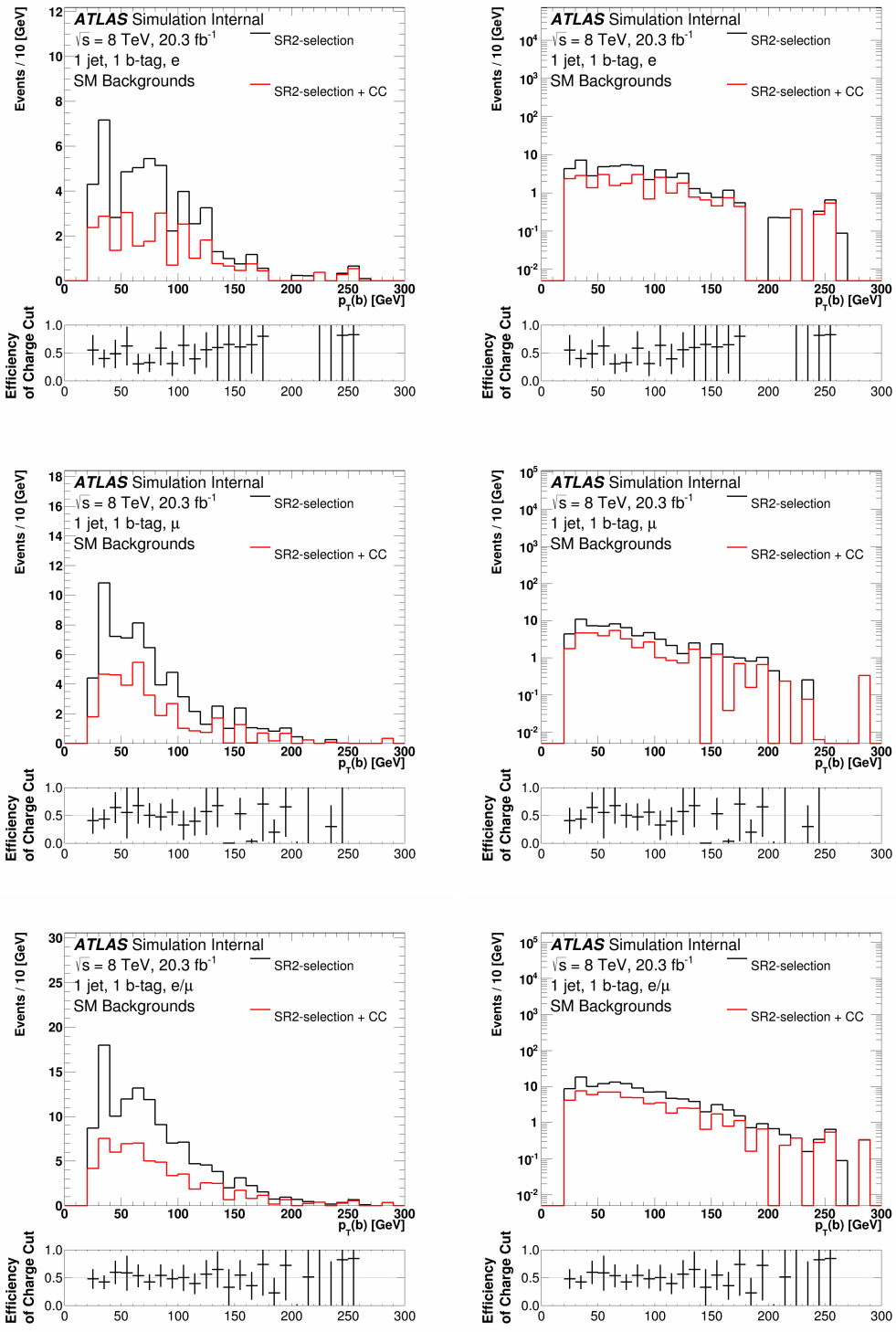

Figure D.11: Distributions of $p_{\mathrm{T}}(b)$ for the electron (top), the muon (middle), and the combined (bottom) channels in the SR2 signal region, in linear (left) and log (right) scale. The black curve shows the distribution in the SR2 signal region and the red curve shows the distribution in the SR2 signal region with the additional cut on the electric charge of the lepton. The error bars in the bottom inlet include statistical uncertainties only.

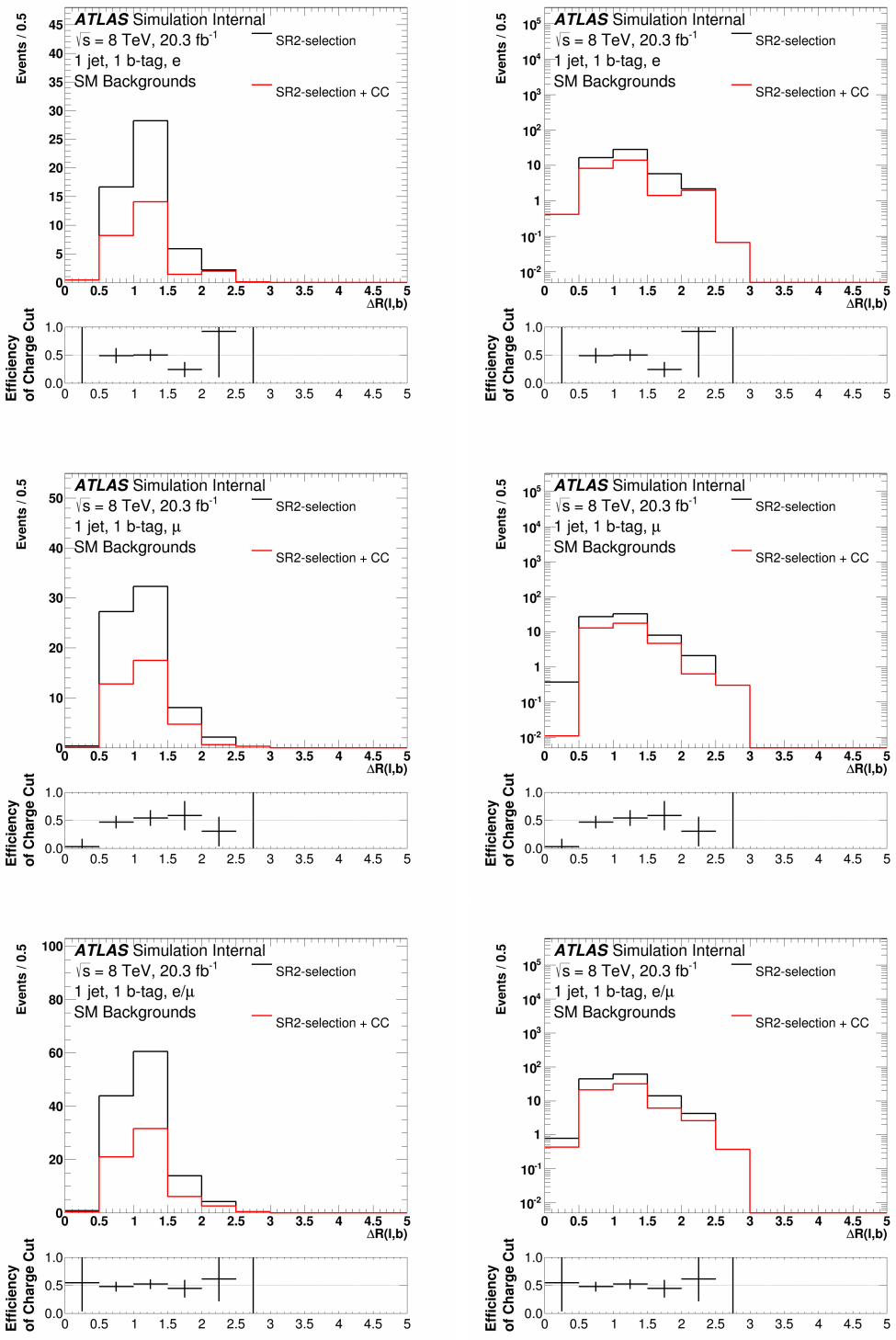

Figure D.12: Distributions of $\Delta R(\ell, b)$ for the electron (top), the muon (middle), and the combined (bottom) channels in the SR2 signal region, in linear (left) and log (right) scale. The black curve shows the distribution in the SR2 signal region and the red curve shows the distribution in the SR2 signal region with the additional cut on the electric charge of the lepton. The error bars in the bottom inlet include statistical uncertainties only.

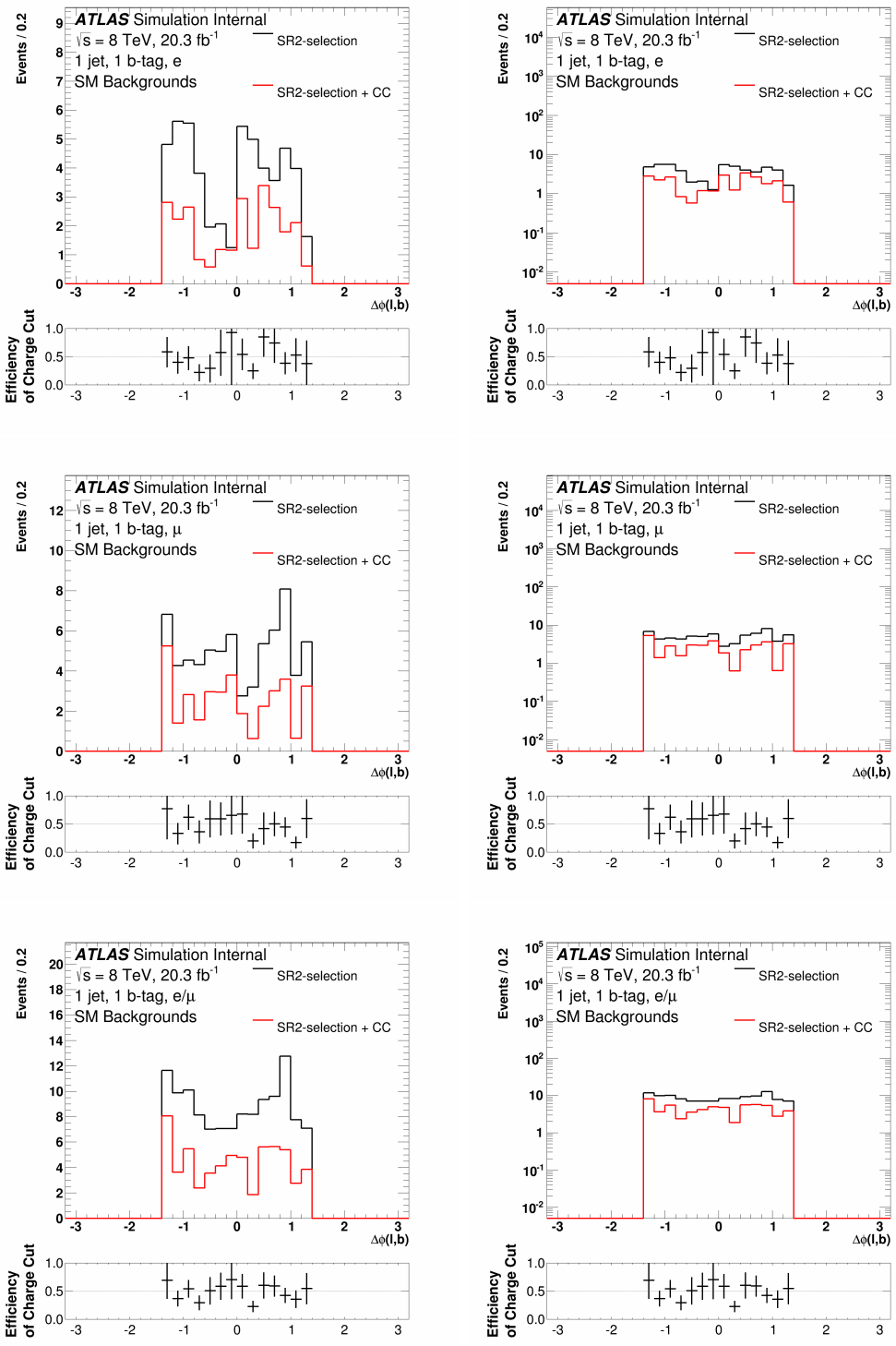

Figure D.13: Distributions of $\Delta\phi(\ell, b)$ for the electron (top), the muon (middle), and the combined (bottom) channels in the SR2 signal region, in linear (left) and log (right) scale. The black curve shows the distribution in the SR2 signal region and the red curve shows the distribution in the SR2 signal region with the additional cut on the electric charge of the lepton. The error bars in the bottom inlet include statistical uncertainties only.

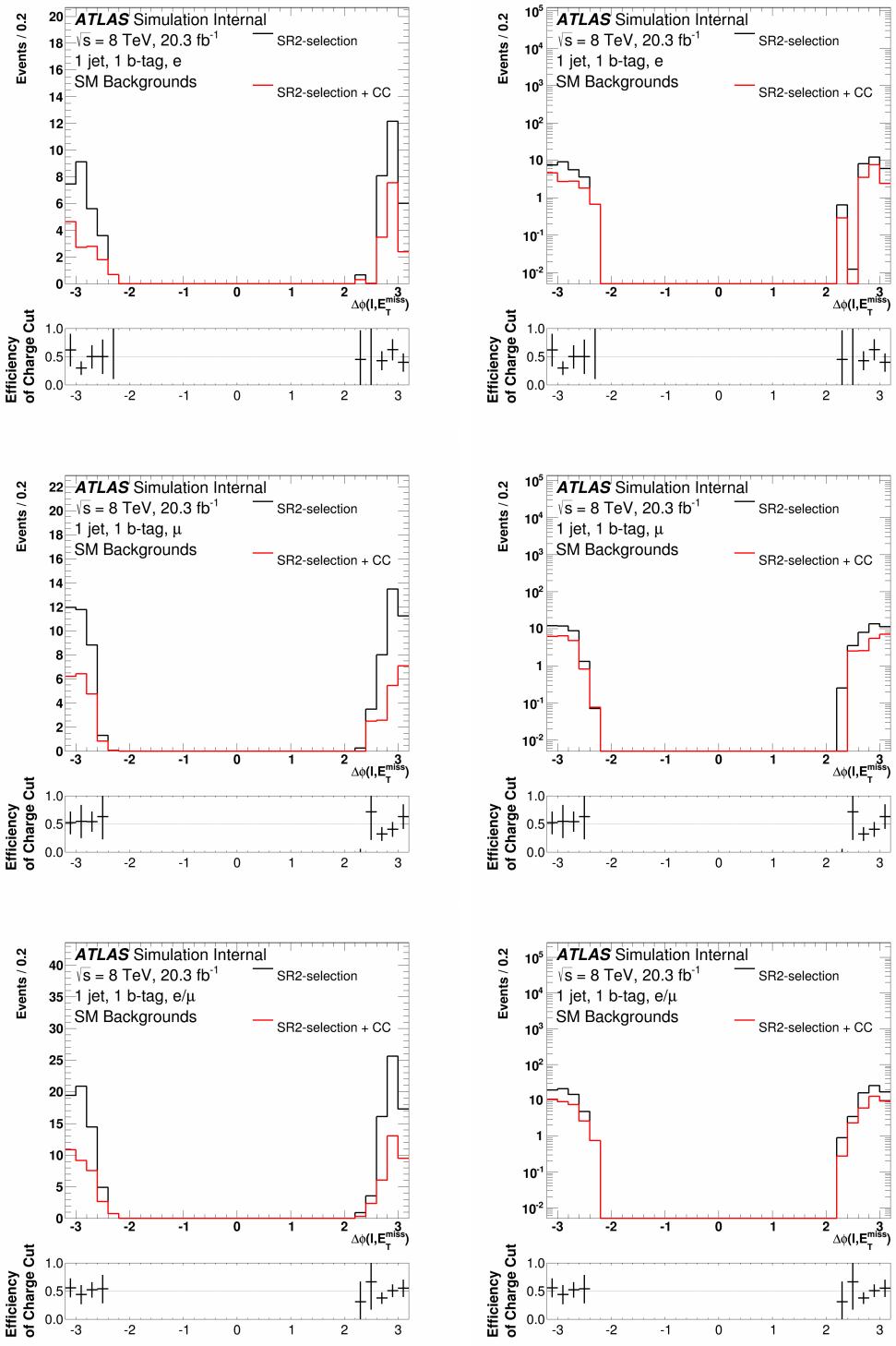

Figure D.14: Distributions of $\Delta\phi(\ell, E_{\mathrm{T}}^{\mathrm{miss}})$ for the electron (top), the muon (middle), and the combined (bottom) channels in the SR2 signal region, in linear (left) and log (right) scale. The black curve shows the distribution in the SR2 signal region and the red curve shows the distribution in the SR2 signal region with the additional cut on the electric charge of the lepton. The error bars in the bottom inlet include statistical uncertainties only.

Appendix E

List of simulated samples

This appendix details the lists of the MC event samples used in this analysis. Table E.1 gives the list of signal samples and Tables E.2 through and E.6 gives the list of background samples. Each table shows the process generated, the dataset identification (DSID) number used by the ATLAS collaboration to delineate between processes, the cross-section times branching ratio, and the number of generated events. Additionally, for the background processes the k-factor and the calculated upper statistical limits for zero expected events, N_{UL}, used in the limit setting procedure (see Section 9.7.2) are shown. N_{UL} is calculated at the 68% CL as:

$$N_{\mathrm{UL}} = -1.14\frac{\mathcal{L}\sigma}{N_{\mathrm{MC}}}, \tag{E.1}$$

where $\mathcal{L}$ is the total integrated luminosity of Run1 (20.3 fb^{-1}), σ is the cross-section, and N_{MC} is the number of unweighted MC events produced.

Sample	Mass [GeV]	DSID	$\sigma \times$ BR [pb]	N_{MC}
t+f_{met} ($\mathrm{S1_R}$, ℓ+jets)	0	110148	1.107	300 000
t+f_{met} ($\mathrm{S1_R}$, ℓ+jets)	20	110149	1.102	300 000
t+f_{met} ($\mathrm{S1_R}$, ℓ+jets)	40	110150	1.089	300 000
t+f_{met} ($\mathrm{S1_R}$, ℓ+jets)	60	110151	1.068	300 000
t+f_{met} ($\mathrm{S1_R}$, ℓ+jets)	80	110152	1.039	300 000
t+f_{met} ($\mathrm{S1_R}$, ℓ+jets)	100	110153	1.001	300 000
t+f_{met} ($\mathrm{S1_R}$, ℓ+jets, $a_{\mathrm{R}} = 0.5$)	100	110194	6.086	299 999
t+f_{met} ($\mathrm{S1_R}$, ℓ+jets, $a_{\mathrm{R}} = 1.0$)	100	110195	21.83	299 999
t+v_{met} ($\mathrm{S4_R}$, ℓ+jets)	0	110160	96.03	300 000
t+v_{met} ($\mathrm{S4_R}$, ℓ+jets)	25	110161	359.0	250 000
t+v_{met} ($\mathrm{S4_R}$, ℓ+jets)	50	110162	113.4	300 000
t+v_{met} ($\mathrm{S4_R}$, ℓ+jets)	75	110163	59.86	300 000
t+v_{met} ($\mathrm{S4_R}$, ℓ+jets)	100	110164	37.45	300 000
t+v_{met} ($\mathrm{S4_R}$, ℓ+jets)	125	110165	25.35	299 997
t+v_{met} ($\mathrm{S4_R}$, ℓ+jets)	150	110166	18.00	300 000
t+v_{met} ($\mathrm{S4_R}$, ℓ+jets)	200	110167	9.662	299 000
t+v_{met} ($\mathrm{S4_R}$, ℓ+jets)	250	110168	5.506	299 999
t+v_{met} ($\mathrm{S4_R}$, ℓ+jets)	300	110169	3.328	300 000
t+v_{met} ($\mathrm{S4_R}$, ℓ+jets)	400	110180	2.746	300 000
t+v_{met} ($\mathrm{S4_R}$, ℓ+jets)	500	110181	1.270	300 000
t+v_{met} ($\mathrm{S4_R}$, ℓ+jets)	600	110182	0.6371	299 999
t+v_{met} ($\mathrm{S4_R}$, ℓ+jets)	700	110183	0.3391	299 999
t+v_{met} ($\mathrm{S4_R}$, ℓ+jets)	800	110184	0.1889	299 999
t+v_{met} ($\mathrm{S4_R}$, ℓ+jets)	900	110185	0.1093	300 000
t+v_{met} ($\mathrm{S4_R}$, ℓ+jets)	1000	110186	0.06507	299 999

Table E.1: All signal MC samples used for this analysis. The cross-section column includes the branching ratios. The second column indicates f_{met} (v_{met}) in the case of the $\mathrm{S1_R}$ ($\mathrm{S4_R}$) model. ℓ indicates e, μ or τ. All samples were produced with MADGRAPH5+PYTHIA8 and the MSTW2008LO PDF set.

Sample	DSID	$\sigma \times$ BR [pb]	k-factor	N_{MC}	N_{UL}
$Z \rightarrow ee + 0$ parton	147105	718.97	1.18	6 298 988	3.1134
$Z \rightarrow ee + 1$ partons	147106	175.70	1.18	8 169 476	0.5866
$Z \rightarrow ee + 2$ partons	147107	58.875	1.18	3 175 991	0.5056
$Z \rightarrow ee + 3$ partons	147108	15.636	1.18	894 995	0.4765
$Z \rightarrow ee + 4$ partons	147109	4.0116	1.18	398 597	0.2745
$Z \rightarrow ee + 5$ partons	147110	1.2592	1.18	229 700	0.1495
$Z \rightarrow \mu\mu + 0$ parton	147113	719.16	1.18	6 298 796	3.1143
$Z \rightarrow \mu\mu + 1$ partons	147114	175.74	1.18	8 188 384	0.5854
$Z \rightarrow \mu\mu + 2$ partons	147115	58.882	1.18	3 175 488	0.5058
$Z \rightarrow \mu\mu + 3$ partons	147116	15.673	1.18	894 799	0.4778
$Z \rightarrow \mu\mu + 4$ partons	147117	4.0057	1.18	388 200	0.2815
$Z \rightarrow \mu\mu + 5$ partons	147118	1.2544	1.18	229 200	0.1493

Table E.2: All Z plus jets MC samples used for this analysis. The cross-section column includes the branching ratios but not k-factors. All samples were produced with ALPGEN+PYTHIA6 and the CTEQ6L1 PDF set.

Sample	DSID	$\sigma \times$ BR [pb]	k-factor	N_{MC}	N_{UL}
$W \rightarrow e\nu + 0$ parton	147025	8127.3	1.1330	29 434 220	7.2315
$W \rightarrow e\nu + 1$ partons	147026	1792.7	1.1330	48 155 904	0.9750
$W \rightarrow e\nu + 2$ partons	147027	542.18	1.1330	17 554 347	0.8089
$W \rightarrow e\nu + 3$ partons	147028	147.65	1.1330	4 985 287	0.7757
$W \rightarrow e\nu + 4$ partons	147029	37.736	1.1330	2 548 292	0.3878
$W \rightarrow e\nu + 5$ partons	147030	11.962	1.1330	799 192	0.3920
$W \rightarrow \mu\nu + 0$ parton	147033	8127.3	1.1330	31 965 655	6.6588
$W \rightarrow \mu\nu + 1$ partons	147034	1792.7	1.1330	43 677 615	1.0749
$W \rightarrow \mu\nu + 2$ partons	147035	542.18	1.1330	17 611 454	0.80628
$W \rightarrow \mu\nu + 3$ partons	147036	147.65	1.1330	4 956 077	0.78025
$W \rightarrow \mu\nu + 4$ partons	147037	37.736	1.1330	2 546 595	0.3881
$W \rightarrow \mu\nu + 5$ partons	147038	11.962	1.1330	788 898	0.3971
$W \rightarrow l\nu + b\bar{b} + 0$ parton	200256	55.66	1.133	1 599 997	0.9111
$W \rightarrow l\nu + b\bar{b} + 1$ partons	200257	45.25	1.133	1 398 396	0.8475
$W \rightarrow l\nu + b\bar{b} + 2$ partons	200258	23.16	1.133	699 398	0.8673
$W \rightarrow l\nu + b\bar{b} + 3$ partons	200259	11.20	1.133	398 397	0.7363
$W \rightarrow l\nu + c\bar{c} + 0$ parton	200156	150.2	1.133	4 299 592	0.9149
$W \rightarrow l\nu + c\bar{c} + 1$ partons	200157	132.7	1.133	3 987 891	0.8715
$W \rightarrow l\nu + c\bar{c} + 2$ partons	200158	71.84	1.133	2 394 394	0.7858
$W \rightarrow l\nu + c\bar{c} + 3$ partons	200159	30.26	1.133	985 295	0.8043
$W \rightarrow l\nu + c + 0$ parton	200056	808.0	1.52	22 769 047	1.2469
$W \rightarrow l\nu + c + 1$ partons	200057	267.7	1.52	8 198 769	1.1472
$W \rightarrow l\nu + c + 2$ partons	200058	69.89	1.52	2 090 290	1.1748
$W \rightarrow l\nu + c + 3$ partons	200059	20.56	1.52	499 498	1.4462
$W \rightarrow l\nu + c + 4$ partons	200060	4.308	1.52	199 499	0.7587

Table E.3: All W plus jets MC samples used for this analysis. The cross-section column includes the branching ratios but not k-factors. ℓ indicates e, μ or τ. All samples were produced with ALPGEN+PYTHIA6 and the CTEQ6L1 PDF set.

Sample	DSID	$\sigma \times$ BR [pb]	k-factor	N_{MC}	N_{UL}
WW	105985	12.416	1.6833	2 499 890	0.1933
ZZ	105986	0.99081	1.5496	245 000	0.1449
WZ	105987	3.6706	1.9011	999 998	0.1613

Table E.4: All diboson MC samples used for this analysis. The cross-section column includes the branching ratios but not k-factors. All samples were produced with HERWIG and the CTEQ6L1 PDF set.

Sample	DSID	Generator	$\sigma \times$ BR [pb]	k-factor	N_{MC}	N_{UL}
$t\bar{t}$ (no full-had.)	117050	P+P6	114.51	1.1992	14 996 424	0.21167
$t\bar{t}$ (no full-had.)	105860	P+H	115.56	1.1883	29 960 959	–
$t\bar{t}$ (no full-had.)	105200	M+H	112.94	1.2158	14 997 103	–
$t\bar{t} \rightarrow l\nu l\nu + 0$ q	164440	Alp+H	4.7977	1.7360	799 897	–
$t\bar{t} \rightarrow l\nu l\nu + 1$ q	164441	Alp+H	5.0677	1.7360	808 897	–
$t\bar{t} \rightarrow l\nu l\nu + 2$ q	164442	Alp+H	3.2547	1.7360	529 996	–
$t\bar{t} \rightarrow l\nu l\nu + 3$ q	164443	Alp+H	2.1749	1.7360	359 997	–
$t\bar{t} \rightarrow l\nu qq + 0$ q	164450	Alp+H	19.186	1.8080	3 359 080	–
$t\bar{t} \rightarrow l\nu qq + 1$ q	164451	Alp+H	20.282	1.8080	3 398 787	–
$t\bar{t} \rightarrow l\nu qq + 2$ q	164452	Alp+H	13.084	1.8080	2 209 980	–
$t\bar{t} \rightarrow l\nu qq + 3$ q	164453	Alp+H	8.7001	1.8080	1 459 791	–
$t\bar{t}$ (more PS)	117209	A+P6	59.624	2.3031	14 985 986	–
$t\bar{t}$ (less PS)	117210	A+P6	59.622	2.3032	14 988 492	–

Table E.5: All $t\bar{t}$ MC samples used for this analysis. The cross-section column includes the branching ratios but not k-factor corrections. ℓ indicates e, μ or τ. The first three samples listed were produced using the CT10 PDF set while the remaining use CTEQ6L1. In this table P+P6 is Powheg+Pythia6, P+H is Powheg+Herwig, M+H is MC@NLO + Herwig, Alp+H is Alpgen+Herwig, and A+P6 is AcerMC + Pythia6.

Sample	DSID	Generator	$\sigma \times$ BR [pb]	k-factor	N_{MC}	N_{UL}
Wt-channel (DR)	110140	P+P6	20.461	1.0933	999 692	0.5173
Wt-channel (DS)	110142	P+P6	18 134	1.2336	999 995	–
Wt-channel	108346	M+H	20.666	1.0825	1 999 194	–
t-channel (ℓ+jets)	110101	A+P6	25.748	1.1043	8 997 672	0.0731
t-channel (ℓ+jets)	110095	aM+H	27.446	1.0360	999 896	–
s-channel (ℓ+jets)	110119	P+P6	1.6424	1.1067	1 199 895	0.0350
s-channel (e+jets)	108343	M+H	0.56395	1.0744	199 997	–
s-channel (μ+jets)	108344	M+H	0.56430	1.0737	200 000	–

Table E.6: All single-top MC samples used for this analysis. The cross-section column includes the branching ratios but not k-factor corrections. ℓ indicates e, μ or τ. All samples were produced using the CT10 PDF set except for 110101 which was produced using CTEQ6L1. In this table P+P6 is Powheg+Pythia6, M+H is MC@NLO+Herwig, A+P6 is AcerMC+Pythia6, and aM+H is aMC@NLO+Herwig.

Appendix F

Systematic uncertainty tables

This appendix presents the tables of relative systematic uncertainties described in Chapter 8 for signal and background processes in the optimized SR1 selection region (Section F), the optimized SR2 selection regions (Section F), and the optimized BDT selection region (F). The uncertainties are presented separately for the signal and background processes, and separately for the electron and muon channels.

Optimized SR1 signal region

For the electron (muon) channel these uncertainties are presented for the backgrounds in Table(s) F.1 (F.2 and F.3), and for the $S1_R$ signal model in Tables F.4 and F.5 (F.6 and F.7). Backgrounds with zero expected events are not shown.

	$t\bar{t}$	Wt	W+heavy flavor	W+light	Diboson
Luminosity	± 1.9	± 1.9	± 1.9	± 1.9	± 1.9
Cross-section	+5.3/–5.7	± 6.8	± 50.0	± 24.5	± 24.5
Generator					
$t\bar{t}$	± 11.9	-	-	-	-
$t\bar{t}$ ISR/FSR	± 8.6	-	-	-	-
Wt-chan	-	± 55.0	-	-	-
Wt-chan NLO calc	-	± 10.1	-	-	-
Fake MC	-	-	-	-	-
Jets					
Energy resolution	± 2.6	± 17.1	± 1.7	-	-
Energy scale	+9.5/–6.5	+26.3/–5.7	-0.0/+7.7	-	+22.0/+0.2
Reconstruction	-	-	-	-	-
Vertex fraction	± 2.7	+6.9/–11.5	± 11.5	-	-
b-tag	± 5.1	± 3.8	± 1.5	-	± 0.7
$c\tau$-tag	± 0.1	-	± 7.0	-	-
mis-tag	-	-	± 6.7	± 79.1	± 27.3
$\boldsymbol{E}_{\mathbf{T}}^{\mathbf{miss}}$					
Resolution	+2.2/+0.8	± 0.0	+2.4/+10.2	-	-0.0/+100.0
Scale	+1.1/+1.4	-	-	-	-
Leptons					
Energy resolution	+1.4/+1.5	–5.3/–7.6	+38.6/+0.0	-	-
Energy scale	+3.4/–1.7	–0.1/–7.8	+10.2/+0.0	-	-
Reconstruction	± 0.5	± 0.4	± 0.6	± 0.5	± 0.6
Isolation	± 2.6	± 2.5	± 2.9	± 2.5	± 3.0
Trigger	± 0.5	± 0.4	± 0.7	± 0.3	± 0.8
Total Rel. Uncert.	+20.1/-18.7	+65.2/-61.4	+65.9/-53.9	+82.8/-82.8	+42.9/-106.6
Yield ± Stat ± Syst	$83.7 \pm 4.8\ ^{+16.9}_{-15.6}$	$9.6 \pm 2.7\ ^{+6.3}_{-5.9}$	$10.5 \pm 3.9\ ^{+6.9}_{-5.7}$	$0.2 \pm 0.2\ ^{+0.2}_{-0.2}$	$0.3 \pm 0.2\ ^{+0.1}_{-0.3}$
Total Background	$104.4 \pm 7.5\ ^{+19.3}_{-17.7}$				
Data	103				

Table F.1: Relative systematic uncertainties in % for the background processes in the SR1 selection region for the electron channel.

	$t\bar{t}$	Wt	W+heavy flavor	W+light	Diboson
Luminosity	± 1.9	± 1.9	± 1.9	± 1.9	± 1.9
Cross-section	+5.3/–5.7	± 6.8	± 50.0	± 24.5	± 24.5
Generator					
$t\bar{t}$	± 18.4	-	-	-	-
$t\bar{t}$ ISR/FSR	± 5.5	-	-	-	-
Wt-chan	-	± 28.0	-	-	-
Wt-chan NLO calc	-	± 92.8	-	-	-
Jets					
Energy resolution	± 0.8	± 4.2	± 12.9	± 76.4	± 48.0
Energy scale	+7.8/–7.7	+12.1/+1.0	+11.0/+12.3	+91.8/-0.0	+4.7/–1.6
Reconstruction	± 0.3	± 5.7	-	-	-
Vertex fraction	+4.9/–4.4	–3.6/–8.2	+0.4/–6.7	–74.3/-0.0	-0.0/–14.5
b-tag	± 4.5	± 8.6	± 1.9	-	± 5.6
$c\tau$-tag	-	-	± 7.6	-	± 1.2
mis-tag	-	-	-	± 48.8	± 8.7
$\boldsymbol{E_{\mathrm{T}}^{\mathrm{miss}}}$					
Resolution	–1.2/+0.7	–1.2/–5.8	–6.1/–3.0	-0.0/+100.0	-
Scale	–0.6/–1.6	+1.0/+8.1	-	-	± 11.2
Leptons					
Identification	–1.6/–0.1	+19.6/–5.7	-0.0/–6.8	-	+8.8/-0.0
Momentum resolution	–0.2/–2.7	+8.1/+3.5	–6.8/-0.0	-	-
Momentum scale	–1.6/–2.0	+10.9/–9.3	-	-	-
Reconstruction	± 0.4	± 0.4	± 0.4	± 0.3	± 0.4
Isolation	± 0.5	± 0.5	± 0.5	± 0.5	± 0.5
Trigger	+1.8/-0.0	+1.8/-0.0	+1.8/-0.0	+1.6/-0.0	+1.8/-0.0
Total Rel. Uncert.	+22.7/-22.8	+101.5/-99.4	+54.2/-54.6	+150.9/-137.2	+57.0/-57.9
Yield ± Stat ± Syst	$105.3 \pm 5.7\ ^{+24.0}_{-24.0}$	$9.5 \pm 2.4\ ^{+9.7}_{-9.4}$	$16.7 \pm 4.9\ ^{+9.0}_{-9.1}$	$2.0 \pm 1.6\ ^{+3.0}_{-2.8}$	$1.0 \pm 0.5\ ^{+0.6}_{-0.6}$
Total Background	$134.9 \pm 8.7\ ^{+27.6}_{-27.5}$				
Data	135				

Table F.2: Relative systematic uncertainties in % for the MC simulated background processes in the SR1 selection region for the muon channel.

	Multijet
Matrix Method	
Fake alternate	± 100.0
Fake MC	+14.9/–10.9
Real alternate	± 100.0
Total Rel. Uncert.	+142.2/-141.8
Yield ± Stat ± Syst	$0.4 \pm 1.1\ ^{+0.5}_{-0.5}$
Total Background	$134.9 \pm 8.7\ ^{+27.6}_{-27.5}$
Data	135

Table F.3: Relative systematic uncertainties in % for the multijet background in the SR1 selection region for the muon channel.

	$S1_R$ 0	$S1_R$ 20	$S1_R$ 40
Luminosity	± 1.9	± 1.9	± 1.9
Jets			
Energy resolution	± 0.5	± 1.2	± 0.6
Energy scale	+1.0/–0.2	+0.8/–1.1	+1.1/–0.7
Reconstruction	-	± 0.1	-
Vertex fraction	+1.0/–2.7	+0.6/–3.0	+1.3/–2.3
b-tag	± 3.5	± 3.6	± 3.5
$c\tau$-tag	-	-	-
mis-tag	-	-	-
$\boldsymbol{E_T^{miss}}$			
Resolution	+0.2/+0.3	+0.1/+0.3	± 0.2
Scale	–0.2/+0.5	+0.0/+0.3	–0.2/+0.7
Leptons			
Energy resolution	+0.8/+0.4	+0.5/–0.0	+0.4/+0.0
Energy scale	+2.5/–1.9	+2.8/–1.5	+2.2/–1.8
Reconstruction	± 0.4	± 0.4	± 0.4
Isolation	± 2.6	± 2.6	± 2.6
Trigger	± 0.6	± 0.6	± 0.6
Total Rel. Uncert.	+5.7/-5.9	+5.8/-6.2	+5.6/-5.7
Yield ± Stat ± Syst	$120.7 \pm 3.2\ ^{+6.9}_{-7.1}$	$121.8 \pm 3.2\ ^{+7.1}_{-7.5}$	$117.7 \pm 3.1\ ^{+6.6}_{-6.7}$

Table F.4: Relative systematic uncertainties in % for the [0,40] GeV $S1_R$ signal models in the SR1 selection region for the electron channel.

	$S1_R$ 60	$S1_R$ 80	$S1_R$ 100
Luminosity	± 1.9	± 1.9	± 1.9
Jets			
Energy resolution	± 0.5	± 1.3	± 1.4
Energy scale	+0.4/–0.5	+0.7/–2.1	+0.8/–1.5
Reconstruction	± 0.1	-	-
Vertex fraction	+1.2/–2.6	+0.8/–2.4	+0.8/–2.4
b-tag	± 3.4	± 3.4	± 3.4
$c\tau$-tag	-	-	-
mis-tag	-	-	-
$\boldsymbol{E}_{\mathbf{T}}^{\mathbf{miss}}$			
Resolution	± 0.6	–0.0/+0.4	–0.0/–0.6
Scale	–0.6/+0.4	± 0.1	–0.7/+0.2
Leptons			
Energy resolution	–0.7/+0.4	+0.5/–0.1	–1.1/–0.6
Energy scale	+2.3/–2.7	+2.7/–1.5	+1.9/–2.2
Reconstruction	± 0.4	± 0.4	± 0.4
Isolation	± 2.6	± 2.6	± 2.6
Trigger	± 0.5	± 0.5	± 0.6
Total Rel. Uncert.	+5.6/-6.2	+5.7/-6.1	+5.6/-6.2
Yield ± Stat ± Syst	$114.3 \pm 3.0\ ^{+6.4}_{-7.1}$	$105.5 \pm 2.9\ ^{+6.1}_{-6.4}$	$92.5 \pm 2.6\ ^{+5.2}_{-5.7}$

Table F.5: Relative systematic uncertainties in % for the [60,100] GeV $S1_R$ signal models in the SR1 selection region for the electron channel.

	$S1_R$ 0	$S1_R$ 20	$S1_R$ 40
Luminosity	± 1.9	± 1.9	± 1.9
Jets			
Energy resolution	± 4.0	± 1.9	± 0.6
Energy scale	+1.1/–2.5	± 1.5	+0.3/–1.9
Reconstruction	± 0.7	± 0.1	± 0.3
Vertex fraction	+2.7/–3.4	+3.6/–2.4	± 3.6
b-tag	± 3.4	± 3.5	± 3.4
$c\tau$-tag	-	-	-
mis-tag	-	-	-
$\boldsymbol{E_{\mathrm{T}}^{\mathrm{miss}}}$			
Resolution	–0.1/–0.4	+1.2/+0.7	–0.4/–0.6
Scale	–0.3/–1.2	+0.2/–0.0	± 0.2
Leptons			
Identification	–0.6/+0.3	–0.3/–0.1	+0.3/–0.1
Momentum resolution	–0.4/–0.1	± 0.1	–0.9/–0.6
Momentum scale	–0.8/–0.5	+0.4/+0.6	–0.3/–0.5
Reconstruction	± 0.4	± 0.4	± 0.4
Isolation	± 0.5	± 0.5	± 0.5
Trigger	+1.8/-0.0	+1.8/-0.0	+1.8/-0.0
Total Rel. Uncert.	+6.7/-7.2	+6.3/-5.3	+5.8/-5.8
Yield ± Stat ± Syst	$132.7 \pm 3.4\ ^{+8.9}_{-9.5}$	$132.2 \pm 3.4\ ^{+8.3}_{-7.0}$	$127.4 \pm 3.3\ ^{+7.4}_{-7.4}$

Table F.6: Relative systematic uncertainties in % for the [0,40] GeV $S1_R$ signal models in the SR1 selection region for the muon channel.

	$S1_R$ 60	$S1_R$ 80	$S1_R$ 100
Luminosity	± 1.9	± 1.9	± 1.9
Jets			
Energy resolution	± 1.5	± 0.8	± 2.5
Energy scale	+2.3/–0.9	+1.2/–0.2	+0.9/–1.7
Reconstruction	± 0.2	± 0.5	± 0.9
Vertex fraction	+4.5/–2.5	+2.2/–2.6	+4.6/–2.2
b-tag	± 3.5	± 3.5	± 3.5
$c\tau$-tag	-	-	-
mis-tag	-	-	-
$\boldsymbol{E_T^{miss}}$			
Resolution	+1.4/+0.8	+0.4/–0.0	+0.5/–0.2
Scale	+1.3/+1.0	–0.8/–0.2	+0.5/+0.2
Leptons			
Identification	+1.3/+0.8	± 0.1	± 0.6
Momentum resolution	+1.1/+1.0	± 0.1	+0.2/+0.3
Momentum scale	+0.7/+0.6	± 0.1	+0.7/+0.1
Reconstruction	± 0.4	± 0.4	± 0.4
Isolation	± 0.5	± 0.5	± 0.5
Trigger	+1.8/-0.0	+1.8/-0.0	+1.8/-0.0
Total Rel. Uncert.	+7.4/-5.3	+5.2/-4.9	+7.0/-5.6
Yield ± Stat ± Syst	$115.8 \pm 3.1\ ^{+8.5}_{-6.2}$	$113.8 \pm 3.0\ ^{+5.9}_{-5.6}$	$93.3 \pm 2.7\ ^{+6.6}_{-5.3}$

Table F.7: Relative systematic uncertainties in % for the [60,100] GeV $S1_R$ signal models in the SR1 selection region for the muon channel.

Optimized SR2 signal region

For the electron (muon) channel these uncertainties are presented for the backgrounds in Table(s) F.8 (F.9 and F.10), and for the $S4_R$ signal model in Tables F.11, F.12, F.13, and F.14 (F.15, F.16, F.17 and F.18). Backgrounds with zero expected events are not shown.

	$t\bar{t}$	Wt	W+heavy flavor	W+light	Diboson
Luminosity	± 1.9	± 1.9	± 1.9	± 1.9	± 1.9
Cross-section	+5.3/–5.7	± 6.8	± 50.0	± 24.5	± 24.5
Generator					
$t\bar{t}$	± 7.5	-	-	-	-
$t\bar{t}$ ISR/FSR	± 15.2	-	-	-	-
Wt-chan	-	± 46.9	-	-	-
Wt-chan NLO calc	-	± 36.3	-	-	-
Fake MC	-	-	-	-	-
Jets					
Energy resolution	± 2.4	± 4.6	± 28.1	± 100.0	-
Energy scale	+10.6/–9.0	+26.0/–8.2	-0.0/+0.9	-	+23.8/-0.0
Reconstruction	-	-	-	-	-
Vertex fraction	+3.8/–2.0	-0.0/–19.3	-	-	-
b-tag	± 5.4	± 3.9	± 2.0	-	± 0.4
$c\tau$-tag	-	-	± 7.2	-	-
mis-tag	-	-	-	± 23.8	± 29.6
$\boldsymbol{E}_{\mathbf{T}}^{\mathbf{miss}}$					
Resolution	+3.3/+1.6	+11.5/-0.0	-	-	-0.0/–91.3
Scale	–1.5/+0.6	-	–28.6/-0.0	-	-
Leptons					
Energy resolution	+2.2/–1.3	–14.8/-0.0	-	–1.2/-0.0	–91.3/-0.0
Energy scale	+8.3/–5.0	+11.5/–0.0	-	-	-0.0/–94.7
Reconstruction	± 0.5	± 0.5	± 0.7	± 0.6	± 0.6
Isolation	± 2.7	± 2.5	± 3.1	± 2.6	± 3.0
Trigger	± 0.6	± 0.5	± 1.0	± 1.0	± 0.8
Total Rel. Uncert.	+24.0/-22.0	+69.1/-63.6	+64.6/-58.0	+105.7/-105.7	+101.9/-137.1
Yield ± Stat ± Syst	$42.2 \pm 3.4\ ^{+10.1}_{-9.3}$	$5.7 \pm 1.9\ ^{+3.9}_{-3.6}$	$5.3 \pm 2.3\ ^{+3.4}_{-3.1}$	$0.8 \pm 0.8\ ^{+0.8}_{-0.8}$	$0.3 \pm 0.2\ ^{+0.3}_{-0.4}$
Total Background	$54.3 \pm 5.6\ ^{+11.4}_{-10.5}$				
Data	56				

Table F.8: Relative systematic uncertainties in % for the background processes in the SR2 selection region for the electron channel.

	$t\bar{t}$	Wt	W+heavy flavor	W+light	Diboson
Luminosity	± 1.9	± 1.9	± 1.9	± 1.9	± 1.9
Cross-section	+5.3/–5.7	± 6.8	± 50.0	± 24.5	± 24.5
Generator					
$t\bar{t}$	± 15.4	-	-	-	-
$t\bar{t}$ ISR/FSR	± 10.3	-	-	-	-
Wt-chan	-	± 95.3	-	-	-
Wt-chan NLO calc	-	± 100.0	-	-	-
Jets					
Energy resolution	± 0.4	± 22.1	± 12.6	± 71.5	-
Energy scale	+8.9/–11.9	+0.1/–1.7	–18.1/+4.8	-	+9.3/-0.0
Reconstruction	± 1.5	± 12.3	± 18.3	-	-
Vertex fraction	+5.8/–5.1	+6.1/–7.6	–13.9/–25.0	+100.0/-0.0	-0.0/–5.6
b-tag	± 4.9	± 8.0	± 2.7	-	± 1.3
$c\tau$-tag	-	-	± 4.6	-	-
mis-tag	-	-	-	± 32.4	± 11.7
$\boldsymbol{E_{\mathrm{T}}^{\mathrm{miss}}}$					
Resolution	+2.1/+1.4	–12.3/-0.0	–20.5/-0.0	-	-
Scale	–3.8/–3.7	-	–14.5/-0.0	-	-
Leptons					
Identification	± 2.3	-	–14.5/–18.3	-	-
Momentum resolution	–1.7/–0.4	-	–18.3/-0.0	-	-
Momentum scale	–2.4/+0.6	± 12.3	–14.5/-0.0	-	-
Reconstruction	± 0.4	± 0.4	± 0.5	± 0.3	± 0.3
Isolation	± 0.5	± 0.5	± 0.5	± 0.5	± 0.5
Trigger	+1.9/-0.0	+1.7/-0.0	+1.9/-0.0	+1.7/-0.0	+1.7/-0.0
Total Rel. Uncert.	+23.5/-24.4	+142.1/-141.6	+70.2/-63.3	+129.5/-82.2	+28.8/-27.8
Yield ± Stat ± Syst	$51.5 \pm 3.9\ ^{+12.1}_{-12.6}$	$4.0 \pm 1.6\ ^{+5.8}_{-5.7}$	$10.6 \pm 3.3\ ^{+7.5}_{-6.7}$	$2.7 \pm 2.7\ ^{+3.5}_{-2.2}$	$0.7 \pm 0.5\ ^{+0.2}_{-0.2}$
Total Background	$70.4 \pm 6.9\ ^{+15.7}_{-15.6}$				
Data	77				

Table F.9: Relative systematic uncertainties in % for the MC simulated background processes in the SR2 selection region for the muon channel.

	Multijet
Matrix Method	
Fake alternate	± 84.7
Fake MC	+24.4/–25.8
Real alternate	± 100.0
Total Rel. Uncert.	+133.3/-133.5
Yield ± Stat ± Syst	$0.8 \pm 1.1 \, ^{+1.1}_{-1.1}$
Total Background	$70.4 \pm 6.9 \, ^{+15.7}_{-15.6}$
Data	77

Table F.10: Relative systematic uncertainties in % for the multijet background in the SR2 selection region for the muon channel.

	$S4_R$ 0	$S4_R$ 25	$S4_R$ 50	$S4_R$ 75
Luminosity	± 1.9	± 1.9	± 1.9	± 1.9
Jets				
Energy resolution	± 1.5	± 2.6	± 2.2	± 2.8
Energy scale	+4.5/–5.5	+4.0/–2.6	+3.2/–0.9	+2.9/–4.8
Reconstruction	-	-	± 0.5	-
Vertex fraction	–0.1/–1.9	+1.0/–5.6	+1.3/–2.5	+1.6/–4.5
b-tag	± 4.1	± 4.4	± 4.4	± 3.9
$c\tau$-tag	-	-	± 0.1	-
mis-tag	-	-	-	-
$\boldsymbol{E}_{\mathbf{T}}^{\mathbf{miss}}$				
Resolution	–1.4/–0.5	–0.9/+0.6	+0.8/–0.6	–0.5/–1.6
Scale	+0.5/-0.0	+0.8/+0.4	+0.5/–0.2	–0.7/+0.4
Leptons				
Energy resolution	+1.7/–0.2	–0.2/–1.7	–0.9/+0.1	+0.4/–0.2
Energy scale	+1.0/–0.5	+2.1/–1.8	+4.0/–2.8	+1.3/–1.8
Reconstruction	± 0.4	± 0.5	± 0.5	± 0.5
Isolation	± 2.6	± 2.7	± 2.7	± 2.7
Trigger	± 0.6	± 0.7	± 0.6	± 0.8
Total Rel. Uncert.	+7.5/-8.1	+7.8/-9.1	+8.1/-7.1	+6.9/-9.1
Yield ± Stat ± Syst	$1105.6 \pm 87.7\ ^{+83.4}_{-89.1}$	$5644.9 \pm 420.1\ ^{+438.3}_{-512.7}$	$2121.8 \pm 133.3\ ^{+171.9}_{-151.4}$	$1427.5 \pm 79.8\ ^{+98.6}_{-130.1}$

Table F.11: Relative systematic uncertainties in % for the [0,75] GeV $S4_R$ signal models in the SR2 selection region for the electron channel.

	$S4_R$ 100	$S4_R$ 125	$S4_R$ 150	$S4_R$ 200
Luminosity	± 1.9	± 1.9	± 1.9	± 1.9
Jets				
Energy resolution	± 3.2	± 2.0	± 2.0	± 1.3
Energy scale	+1.0/–3.3	+2.0/–3.4	+3.1/–3.9	+2.7/–2.3
Reconstruction	-	-	-	± 0.2
Vertex fraction	+1.4/–3.6	+1.0/–4.1	+0.8/–3.6	+1.2/–2.4
b-tag	± 4.1	± 4.3	± 4.1	± 4.1
$c\tau$-tag	-	± 0.1	-	± 0.1
mis-tag	± 0.2	-	-	-
$\boldsymbol{E_T^{miss}}$				
Resolution	–0.4/–1.3	–0.5/+0.3	+0.8/+0.6	+0.2/+0.0
Scale	–0.6/–1.1	± 0.4	+0.0/+0.5	± 0.2
Leptons				
Energy resolution	+0.3/–0.4	+2.3/+1.1	–0.2/+0.6	–0.2/+0.3
Energy scale	+2.1/–4.5	± 1.9	+2.0/–1.0	+2.1/–2.5
Reconstruction	± 0.5	± 0.5	± 0.5	± 0.5
Isolation	± 2.7	± 2.7	± 2.7	± 2.7
Trigger	± 0.8	± 0.7	± 0.7	± 0.7
Total Rel. Uncert.	+6.9/-9.3	+7.0/-8.2	+6.9/-7.9	+6.6/-6.9
Yield ± Stat ± Syst	$1146.2 \pm 56.3\ ^{+78.6}_{-106.1}$	$861.6 \pm 39.9\ ^{+60.2}_{-70.8}$	$741.7 \pm 31.5\ ^{+51.1}_{-58.9}$	$531.7 \pm 19.6\ ^{+35.3}_{-36.6}$

Table F.12: Relative systematic uncertainties in % for the [100,200] GeV $S4_R$ signal models in the SR2 selection region for the electron channel.

	$S4_R$ 250	$S4_R$ 300	$S4_R$ 400	$S4_R$ 500
Luminosity	± 1.9	± 1.9	± 1.9	± 1.9
Jets				
Energy resolution	± 0.9	± 1.0	± 1.2	± 0.3
Energy scale	+1.5/–2.9	+2.1/–2.4	± 3.4	+3.2/–4.1
Reconstruction	-	-	-	± 0.1
Vertex fraction	+1.2/–3.5	+1.3/–2.4	+0.6/–2.9	+1.0/–3.1
b-tag	± 4.2	± 4.4	± 4.1	± 4.4
$c\tau$-tag	-	-	-	-
mis-tag	-	-	-	± 0.2
$\boldsymbol{E_T^{miss}}$				
Resolution	± 0.1	± 0.3	+0.5/+0.0	–0.5/–0.7
Scale	± 0.1	+0.1/+0.0	± 0.1	–0.5/–0.0
Leptons				
Energy resolution	–1.0/–0.4	–0.5/+0.2	–0.6/+0.2	–0.4/–0.2
Energy scale	+2.1/–2.5	+2.2/–2.4	+1.3/–1.8	+1.2/–1.4
Reconstruction	± 0.5	± 0.5	± 0.5	± 0.4
Isolation	± 2.7	± 2.7	± 2.6	± 2.7
Trigger	± 0.7	± 0.7	± 0.6	± 0.6
Total Rel. Uncert.	+6.3/-7.6	+6.5/-7.0	+6.6/-7.2	+6.7/-7.7
Yield ± Stat ± Syst	$360.1 \pm 12.1\ ^{+22.6}_{-27.2}$	$239.1 \pm 7.7\ ^{+15.6}_{-16.7}$	$123.2 \pm 3.5\ ^{+8.2}_{-8.9}$	$63.4 \pm 1.7\ ^{+4.2}_{-4.9}$

Table F.13: Relative systematic uncertainties in % for the [250,500] GeV $S4_R$ signal models in the SR2 selection region for the electron channel.

	$S4_R$ 600	$S4_R$ 700	$S4_R$ 800	$S4_R$ 900	$S4_R$ 1000
Luminosity	± 1.9	± 1.9	± 1.9	± 1.9	± 1.9
Jets					
Energy resolution	± 1.1	± 3.8	± 3.7	± 1.5	± 1.3
Energy scale	+3.6/–2.6	+4.1/–3.5	+2.9/–4.7	± 3.6	+3.8/–4.6
Reconstruction	-	-	± 0.1	-	-
Vertex fraction	+0.9/–2.5	+1.4/–2.9	+1.1/–2.6	+1.2/–2.6	+1.2/–2.6
b-tag	± 4.2	± 4.3	± 4.3	± 4.4	± 4.3
$c\tau$-tag	-	-	-	-	-
mis-tag	-	-	-	± 0.1	-
$\boldsymbol{E_T^{miss}}$					
Resolution	± 0.2	+0.4/–0.1	+0.1/+0.3	+0.1/–0.2	–0.1/+0.5
Scale	± 0.2	+0.0/+0.2	-	–0.0/+0.2	+0.3/–0.2
Leptons					
Energy resolution	+0.7/+0.3	+0.2/–0.6	–0.2/+0.3	± 0.3	+0.1/+0.3
Energy scale	+1.5/–0.9	+1.1/–1.6	± 1.3	+1.1/–0.8	+1.1/–0.7
Reconstruction	± 0.5	± 0.4	± 0.4	± 0.4	± 0.4
Isolation	± 2.7	± 2.7	± 2.7	± 2.7	± 2.7
Trigger	± 0.6	± 0.6	± 0.6	± 0.6	± 0.6
Total Rel. Uncert.	+6.8/-6.6	+8.0/-8.2	+7.4/-8.6	+6.9/-7.3	+7.0/-7.8
Yield ± Stat ± Syst	$33.6 \pm 0.9\ ^{+2.3}_{-2.2}$	$19.1 \pm 0.5\ ^{+1.5}_{-1.6}$	$10.6 \pm 0.3\ ^{+0.8}_{-0.9}$	$6.2 \pm 0.2\ ^{+0.4}_{-0.5}$	$3.9 \pm 0.1\ ^{+0.3}_{-0.3}$

Table F.14: Relative systematic uncertainties in % for the [600,1000] GeV $S4_R$ signal models in the SR2 selection region for the electron channel.

	$S4_R$ 0	$S4_R$ 25	$S4_R$ 50	$S4_R$ 75
Luminosity	± 1.9	± 1.9	± 1.9	± 1.9
Jets				
Energy resolution	± 4.5	± 1.5	± 4.6	± 2.2
Energy scale	+3.1/–2.3	+0.5/–3.2	+2.8/–4.2	+4.6/–1.9
Reconstruction	± 3.2	± 1.6	± 1.1	± 0.8
Vertex fraction	+5.9/–1.7	+2.4/–4.6	+0.7/–2.9	+4.3/–2.1
b-tag	± 3.6	± 3.7	± 4.2	± 4.3
$c\tau$-tag	-	-	-	± 0.1
mis-tag	-	-	-	-
$\boldsymbol{E_{\mathrm{T}}^{\mathrm{miss}}}$				
Resolution	+3.8/+0.7	± 0.9	+1.5/+2.1	+1.0/+0.5
Scale	+1.7/+1.4	+1.6/–0.0	+0.2/+1.6	–0.4/+0.3
Leptons				
Identification	+3.2/+1.9	+1.3/+0.7	+0.4/–0.6	± 1.2
Momentum resolution	–0.5/+1.6	–0.9/+0.4	–0.7/–1.0	–0.5/+1.0
Momentum scale	+1.1/+1.7	+0.9/+0.8	–0.3/+1.5	–1.3/–0.9
Reconstruction	± 0.4	± 0.4	± 0.4	± 0.4
Isolation	± 0.5	± 0.5	± 0.5	± 0.5
Trigger	+1.8/-0.0	+1.9/-0.0	+1.8/-0.0	+1.9/-0.0
Total Rel. Uncert.	+11.1/-8.2	+6.3/-7.5	+7.6/-8.9	+8.7/-6.3
Yield ± Stat ± Syst	$1322.3 \pm 100.4\ ^{+146.5}_{-108.2}$	$7588.1 \pm 499.7\ ^{+474.6}_{-568.6}$	$2477.1 \pm 149.1\ ^{+189.4}_{-221.3}$	$1570.7 \pm 85.6\ ^{+137.4}_{-99.0}$

Table F.15: Relative systematic uncertainties in % for the [0,75] GeV $S4_R$ signal models in the SR2 selection region for the muon channel.

	$S4_R$ 100	$S4_R$ 125	$S4_R$ 150	$S4_R$ 200
Luminosity	± 1.9	± 1.9	± 1.9	± 1.9
Jets				
Energy resolution	± 2.4	± 5.7	± 2.9	± 1.4
Energy scale	+4.4/–2.1	+3.7/–2.4	+2.7/–2.3	+3.2/–3.5
Reconstruction	± 1.2	± 0.8	± 0.8	± 0.1
Vertex fraction	+6.5/–2.9	± 3.7	+4.1/–3.1	+3.3/–1.6
b-tag	± 4.0	± 4.0	± 4.1	± 4.0
$c\tau$-tag	-	± 0.1	± 0.1	-
mis-tag	-	± 0.1	-	-
$\boldsymbol{E_T^{miss}}$				
Resolution	± 0.4	+0.6/+0.9	+0.5/+0.1	+1.1/+0.4
Scale	± 0.6	+0.6/–0.1	+1.2/+0.1	+0.4/–0.1
Leptons				
Identification	± 0.5	± 0.5	+0.4/–0.1	–0.2/+0.7
Momentum resolution	+0.2/–1.3	+0.3/+0.1	+0.6/–0.3	+1.1/+0.7
Momentum scale	+0.5/+0.2	–0.0/+1.4	–0.6/+0.8	± 0.2
Reconstruction	± 0.4	± 0.4	± 0.4	± 0.4
Isolation	± 0.5	± 0.5	± 0.5	± 0.5
Trigger	+1.8/-0.0	+1.8/-0.0	+1.8/-0.0	+1.8/-0.0
Total Rel. Uncert.	+9.6/-6.5	+9.1/-8.6	+7.7/-6.7	+7.0/-6.1
Yield ± Stat ± Syst	$1230.1 \pm 59.5\ ^{+118.0}_{-80.1}$	$1021.2 \pm 45.0\ ^{+93.2}_{-88.2}$	$785.4 \pm 33.0\ ^{+60.7}_{-53.0}$	$598.4 \pm 21.1\ ^{+42.0}_{-36.8}$

Table F.16: Relative systematic uncertainties in % for the [100,200] GeV $S4_R$ signal models in the SR2 selection region for the muon channel.

	$S4_R$ 250	$S4_R$ 300	$S4_R$ 400	$S4_R$ 500
Luminosity	± 1.9	± 1.9	± 1.9	± 1.9
Jets				
Energy resolution	± 2.2	± 4.5	± 3.0	± 1.5
Energy scale	+3.9/–3.3	+3.8/–3.9	+3.8/–4.5	+3.3/–4.2
Reconstruction	-	-	± 0.4	± 0.6
Vertex fraction	+5.4/–4.1	+3.6/–3.4	+3.3/–3.5	+4.5/–3.0
b-tag	± 4.1	± 4.2	± 4.2	± 4.2
$c\tau$-tag	-	-	-	-
mis-tag	-	-	-	-
$\boldsymbol{E_T^{miss}}$				
Resolution	+1.0/+0.4	–0.1/+0.7	–0.9/–0.3	–0.1/–0.5
Scale	+0.3/–0.4	± 0.1	+0.2/–0.6	–0.3/–0.2
Leptons				
Identification	+1.0/+0.1	+0.4/+0.1	± 0.4	–0.5/–0.8
Momentum resolution	± 0.4	± 0.2	–0.3/+0.0	–0.3/–0.4
Momentum scale	–0.4/–0.1	–0.1/–0.4	–0.8/–0.3	–0.5/–0.9
Reconstruction	± 0.4	± 0.4	± 0.4	± 0.4
Isolation	± 0.5	± 0.5	± 0.5	± 0.5
Trigger	+1.8/-0.0	+1.9/-0.0	+1.8/-0.0	+1.8/-0.0
Total Rel. Uncert.	+8.7/-7.3	+8.5/-8.3	+7.8/-8.0	+7.7/-7.2
Yield ± Stat ± Syst	$392.4 \pm 12.9\ ^{+34.2}_{-28.7}$	$273.7 \pm 8.4\ ^{+23.2}_{-22.7}$	$138.5 \pm 3.8\ ^{+10.8}_{-11.1}$	$70.7 \pm 1.9\ ^{+5.4}_{-5.1}$

Table F.17: Relative systematic uncertainties in % for the [250,500] GeV $S4_R$ signal models in the SR2 selection region for the muon channel.

	$S4_R$ 600	$S4_R$ 700	$S4_R$ 800	$S4_R$ 900	$S4_R$ 1000
Luminosity	± 1.9	± 1.9	± 1.9	± 1.9	± 1.9
Jets					
Energy resolution	± 2.4	± 2.1	± 2.4	± 1.7	± 1.3
Energy scale	+5.0/–4.7	+5.0/–4.0	+3.9/–5.0	+3.6/–6.3	+5.9/–3.3
Reconstruction	± 0.1	± 0.3	± 0.2	± 0.5	± 0.6
Vertex fraction	+4.1/–3.5	+4.7/–2.6	+3.2/–4.1	+2.9/–3.4	+4.9/–2.2
b-tag	± 4.5	± 4.4	± 4.4	± 4.6	± 4.4
$c\tau$-tag	-	-	-	-	-
mis-tag	-	± 0.1	± 0.1	-	-
$\boldsymbol{E_T^{miss}}$					
Resolution	–0.4/+0.0	± 0.3	+0.7/+0.3	± 0.0	+0.5/+0.3
Scale	–0.4/–0.0	± 0.2	+0.2/–0.0	–0.7/–0.5	+0.5/+0.1
Leptons					
Identification	± 0.2	+0.3/–0.1	–0.3/–0.2	+0.0/–0.8	+0.3/+0.4
Momentum resolution	–0.0/–0.6	± 0.1	+0.1/–0.4	–0.4/–0.7	+0.5/+0.2
Momentum scale	± 0.2	+0.5/+0.3	± 0.1	+0.2/–0.3	+0.4/–0.3
Reconstruction	± 0.4	± 0.4	± 0.4	± 0.4	± 0.4
Isolation	± 0.5	± 0.5	± 0.5	± 0.5	± 0.5
Trigger	+1.8/-0.0	+1.9/-0.0	+1.9/-0.0	+1.8/-0.0	+1.8/-0.0
Total Rel. Uncert.	+8.7/-8.0	+8.8/-7.1	+7.7/-8.5	+7.3/-9.0	+9.5/-6.4
Yield ± Stat ± Syst	$38.6 \pm 1.0\ ^{+3.3}_{-3.1}$	$21.3 \pm 0.5\ ^{+1.9}_{-1.5}$	$12.6 \pm 0.3\ ^{+1.0}_{-1.1}$	$7.6 \pm 0.2\ ^{+0.6}_{-0.7}$	$4.4 \pm 0.1\ ^{+0.4}_{-0.3}$

Table F.18: Relative systematic uncertainties in % for the [600,1000] GeV $S4_R$ signal models in the SR2 selection region for the muon channel.

Optimized SR2 signal region + lepton charge cut

For the electron (muon) channel these uncertainties are presented for the backgrounds in Table(s) F.19 (F.20 and F.21), and for the $S4_R$ signal model in Tables F.22, F.23, F.24, and F.25 (F.26, F.27, F.28 and F.29). Backgrounds with zero expected events are not shown.

	$t\bar{t}$	Wt	W+heavy flavor	W+light	Diboson
Luminosity	± 1.9	± 1.9	± 1.9	± 1.9	± 1.9
Cross-section	+5.3/–5.7	± 6.8	± 50.0	± 24.5	± 24.5
Generator					
$t\bar{t}$	± 7.5	-	-	-	-
$t\bar{t}$ ISR/FSR	± 7.9	-	-	-	-
Wt-chan	-	± 100.0	-	-	-
Wt-chan NLO calc	-	± 100.0	-	-	-
Jets					
Energy resolution	± 1.0	± 11.7	± 49.0	± 100.0	-
Energy scale	+9.0/–10.2	–12.5/–24.4	-0.0/+2.1	-	+25.1/-0.0
Reconstruction	-	-	-	-	-
Vertex fraction	+2.3/–3.0	-	-	-	-
b-tag	± 5.4	± 5.9	± 2.3	-	± 0.2
$c\tau$-tag	-	-	± 5.3	-	-
mis-tag	-	-	-	± 23.8	± 31.2
$\boldsymbol{E}_{\mathbf{T}}^{\mathbf{miss}}$					
Resolution	+1.9/+0.1	-	-	-	-0.0/–96.4
Scale	–2.6/+0.6	-	-	-	-
Leptons					
Energy resolution	± 1.9	-	-	–1.2/-0.0	–96.4/-0.0
Energy scale	+5.8/–4.4	-	-	-	-0.0/–100.0
Reconstruction	± 0.5	± 0.5	± 0.6	± 0.6	± 0.6
Isolation	± 2.7	± 2.5	± 2.9	± 2.6	± 3.0
Trigger	± 0.6	± 0.7	± 0.8	± 1.0	± 0.8
Total Rel. Uncert.	+17.9/-18.1	+142.8/-144.3	+70.4/-70.4	+105.7/-105.7	+107.3/-144.5
Yield ± Stat ± Syst	$22.0 \pm 2.5\ ^{+3.9}_{-4.0}$	$1.9 \pm 1.0\ ^{+2.7}_{-2.8}$	$2.2 \pm 1.4\ ^{+1.5}_{-1.5}$	$0.8 \pm 0.8\ ^{+0.8}_{-0.8}$	$0.3 \pm 0.2\ ^{+0.3}_{-0.4}$
Total Background	$27.1 \pm 4.6\ ^{+5.1}_{-5.2}$				
Data	33				

Table F.19: Relative systematic uncertainties in % for the MC simulated background processes in the SR2 selection region with an additional cut on the electric charge of the lepton for the electron channel.

	$t\bar{t}$	Wt	W+heavy flavor	W+light	Diboson
Luminosity	± 1.9	± 1.9	± 1.9	± 1.9	± 1.9
Cross-section	+5.3/–5.7	± 6.8	± 50.0	± 24.5	± 24.5
Generator					
$t\bar{t}$	± 14.2	-	-	-	-
$t\bar{t}$ ISR/FSR	± 14.5	-	-	-	-
Wt-chan	-	± 100.0	-	-	-
Wt-chan NLO calc	-	± 100.0	-	-	-
Jets					
Energy resolution	± 15.5	± 100.0	± 35.4	± 71.5	-
Energy scale	+13.3/–11.0	+82.9/-0.0	-0.0/+35.3	-	+14.2/-0.0
Reconstruction	± 3.5	-	-	-	-
Vertex fraction	+10.9/–5.1	+9.1/-0.0	-0.0/–18.9	+100.0/-0.0	-0.0/–11.1
b-tag	± 5.0	± 2.8	± 2.4	-	± 2.6
$c\tau$-tag	-	-	± 5.2	-	-
mis-tag	-	-	-	± 32.4	-
$\boldsymbol{E_{\mathrm{T}}^{\mathrm{miss}}}$					
Resolution	+4.7/+3.4	-	-	-	-
Scale	–1.9/+0.2	-	-	-	-
Leptons					
Identification	+0.3/–1.9	-	-	-	-
Momentum resolution	+1.0/+0.9	-	-	-	-
Momentum scale	–1.2/+2.4	-	-	-	-
Reconstruction	± 0.4	± 0.4	± 0.4	± 0.3	± 0.4
Isolation	± 0.5	± 0.5	± 0.5	± 0.5	± 0.5
Trigger	+1.9/-0.0	+1.7/-0.0	+2.0/-0.0	+1.7/-0.0	+1.7/-0.0
Total Rel. Uncert.	+32.4/-29.9	+192.4/-173.4	+61.6/-73.4	+129.5/-82.2	+28.5/-27.1
Yield ± Stat ± Syst	$25.2 \pm 2.7\ ^{+8.2}_{-7.5}$	$0.6 \pm 0.6\ ^{+1.2}_{-1.1}$	$5.9 \pm 2.5\ ^{+3.6}_{-4.3}$	$2.7 \pm 2.7\ ^{+3.5}_{-2.2}$	$0.4 \pm 0.3\ ^{+0.1}_{-0.1}$
Total Background	$35.9 \pm 5.7\ ^{+9.8}_{-9.1}$				
Data	41				

Table F.20: Relative systematic uncertainties in % for the MC simulated background processes in the SR2 selection region with an additional cut on the electric charge of the lepton for the muon channel.

	Multijet
Matrix Method	
Fake alternate	± 82.1
Fake MC	+24.0/–25.1
Real alternate	± 85.0
Total Rel. Uncert.	+120.6/-120.8
Yield ± Stat ± Syst	$1.2 \pm 1.1\ ^{+1.4}_{-1.4}$
Total Background	$35.9 \pm 5.7\ ^{+9.8}_{-9.1}$
Data	41

Table F.21: Relative systematic uncertainties in % for the multijet background in the SR2 selection region with an additional cut on the electric charge of the lepton for the muon channel.

	$S4_R0$	$S4_R25$	$S4_R50$	$S4_R75$
Luminosity	± 1.9	± 1.9	± 1.9	± 1.9
Jets				
Energy resolution	± 3.1	± 3.5	± 3.2	± 2.7
Energy scale	+5.1/–4.9	+3.9/–3.0	+3.2/–1.2	+3.0/–5.8
Reconstruction	-	-	± 0.6	-
Vertex fraction	+0.5/–1.7	+1.1/–6.6	+1.5/–2.5	+1.8/–4.9
b-tag	± 4.2	± 4.5	± 4.4	± 3.9
$c\tau$-tag	-	-	± 0.1	-
mis-tag	-	-	-	-
$\boldsymbol{E}_{\mathbf{T}}^{\mathbf{miss}}$				
Resolution	–1.6/–0.5	–1.1/+0.7	+1.4/–0.9	–0.5/–2.1
Scale	+0.5/-0.0	+0.9/+0.5	+0.6/–0.2	–0.7/+0.2
Leptons				
Energy resolution	+0.6/–0.2	–1.0/–2.0	–1.0/+0.1	+0.5/+0.1
Energy scale	+1.1/–0.6	+1.7/–2.2	+4.4/–3.1	+1.2/–2.0
Reconstruction	± 0.4	± 0.5	± 0.5	± 0.5
Isolation	± 2.6	± 2.6	± 2.7	± 2.7
Trigger	± 0.6	± 0.7	± 0.6	± 0.8
Total Rel. Uncert.	+8.3/-8.1	+8.1/-10.2	+8.7/-7.7	+7.0/-10.0
Yield ± Stat ± Syst	$980.8 \pm 82.7\ ^{+81.6}_{-79.3}$	$4827.9 \pm 388.7\ ^{+390.4}_{-493.0}$	$1909.2 \pm 126.9\ ^{+166.8}_{-147.4}$	$1285.6 \pm 75.6\ ^{+89.4}_{-128.7}$

Table F.22: Relative systematic uncertainties in % for the [0,75] GeV $S4_R$ signal models in the SR2 selection region with an additional cut on the electric charge of the lepton for the electron channel.

	$S4_R100$	$S4_R125$	$S4_R150$	$S4_R200$
Luminosity	± 1.9	± 1.9	± 1.9	± 1.9
Jets				
Energy resolution	± 3.1	± 2.9	± 1.7	± 0.9
Energy scale	+1.2/–3.4	+2.3/–3.8	+3.3/–3.7	+3.2/–1.6
Reconstruction	-	-	-	-
Vertex fraction	+1.5/–3.7	+0.9/–3.7	+0.9/–3.7	+1.4/–2.1
b-tag	± 4.0	± 4.4	± 4.1	± 4.1
$c\tau$-tag	-	± 0.1	-	± 0.1
mis-tag	± 0.2	-	-	-
$\boldsymbol{E}_{\mathbf{T}}^{\mathbf{miss}}$				
Resolution	–0.0/–0.8	–0.5/+0.1	+0.8/+0.5	-
Scale	–0.7/–0.9	± 0.5	–0.2/+0.6	± 0.3
Leptons				
Energy resolution	+0.5/–0.7	+2.9/+1.3	–0.4/+0.6	–0.1/+0.4
Energy scale	+2.4/–4.3	± 2.2	+2.1/–0.9	+1.9/–2.6
Reconstruction	± 0.5	± 0.5	± 0.5	± 0.5
Isolation	± 2.7	± 2.7	± 2.6	± 2.7
Trigger	± 0.8	± 0.7	± 0.7	± 0.7
Total Rel. Uncert.	+6.9/-9.1	+7.7/-8.6	+6.9/-7.8	+6.7/-6.5
Yield ± Stat ± Syst	$1038.7 \pm 53.7\ ^{+72.0}_{-94.8}$	$746.6 \pm 37.1\ ^{+57.4}_{-64.2}$	$653.7 \pm 29.6\ ^{+45.4}_{-50.8}$	$471.7 \pm 18.5\ ^{+31.7}_{-30.9}$

Table F.23: Relative systematic uncertainties in % for the [100,200] GeV $S4_R$ signal models in the SR2 selection region with an additional cut on the electric charge of the lepton for the electron channel.

	$S4_R250$	$S4_R300$	$S4_R400$	$S4_R500$
Luminosity	± 1.9	± 1.9	± 1.9	± 1.9
Jets				
Energy resolution	± 1.1	± 1.4	± 1.1	-
Energy scale	+1.5/–2.8	+2.3/–2.5	± 3.2	+3.4/–4.3
Reconstruction	-	-	± 0.1	± 0.1
Vertex fraction	+1.2/–3.2	+1.2/–2.2	+0.6/–3.1	+0.9/–3.2
b-tag	± 4.3	± 4.4	± 4.1	± 4.4
$c\tau$-tag	-	-	-	-
mis-tag	-	-	-	± 0.2
$\boldsymbol{E_T^{miss}}$				
Resolution	–0.3/+0.0	+0.4/+0.2	+0.7/+0.1	–0.4/–0.6
Scale	± 0.2	+0.2/–0.1	± 0.3	–0.5/+0.1
Leptons				
Energy resolution	–0.8/–0.4	± 0.2	–0.7/+0.1	± 0.2
Energy scale	+2.3/–2.5	+2.2/–2.5	+1.3/–1.9	± 1.4
Reconstruction	± 0.5	± 0.5	± 0.5	± 0.4
Isolation	± 2.7	± 2.7	± 2.6	± 2.7
Trigger	± 0.7	± 0.7	± 0.7	± 0.6
Total Rel. Uncert.	+6.4/-7.5	+6.7/-7.1	+6.6/-7.3	+6.7/-7.9
Yield ± Stat ± Syst	$328.6 \pm 11.6\ ^{+20.9}_{-24.5}$	$217.8 \pm 7.3\ ^{+14.6}_{-15.4}$	$112.4 \pm 3.4\ ^{+7.4}_{-8.2}$	$57.9 \pm 1.7\ ^{+3.9}_{-4.6}$

Table F.24: Relative systematic uncertainties in % for the [250,500] GeV $S4_R$ signal models in the SR2 selection region with an additional cut on the electric charge of the lepton for the electron channel.

	$S4_R600$	$S4_R700$	$S4_R800$	$S4_R900$	$S4_R1000$
Luminosity	± 1.9	± 1.9	± 1.9	± 1.9	± 1.9
Jets					
Energy resolution	± 1.4	± 4.0	± 3.6	± 1.7	± 1.0
Energy scale	+3.8/–2.5	+4.1/–3.4	+3.1/–4.7	+3.7/–3.6	+4.1/–4.5
Reconstruction	-	-	± 0.1	-	-
Vertex fraction	+0.8/–2.4	+1.2/–3.1	+1.2/–2.5	+1.2/–2.6	+1.2/–2.6
b-tag	± 4.2	± 4.3	± 4.3	± 4.3	± 4.3
$c\tau$-tag	-	-	-	-	-
mis-tag	-	-	-	± 0.1	-
$\boldsymbol{E_T^{miss}}$					
Resolution	± 0.1	+0.4/–0.0	+0.2/+0.5	± 0.1	–0.1/+0.6
Scale	± 0.1	+0.0/+0.3	-	–0.0/+0.2	+0.3/–0.1
Leptons					
Energy resolution	+0.6/+0.2	+0.2/–0.5	–0.1/+0.4	± 0.3	± 0.3
Energy scale	+1.4/–1.0	+1.2/–1.5	± 1.4	+1.2/–0.7	+1.1/–0.6
Reconstruction	± 0.5	± 0.4	± 0.4	± 0.4	± 0.4
Isolation	± 2.7	± 2.7	± 2.7	± 2.7	± 2.7
Trigger	± 0.6	± 0.6	± 0.6	± 0.6	± 0.6
Total Rel. Uncert.	+7.0/-6.7	+8.1/-8.3	+7.5/-8.5	+7.1/-7.3	+7.1/-7.6
Yield ± Stat ± Syst	$31.2 \pm 0.9\ ^{+2.2}_{-2.1}$	$17.7 \pm 0.5\ ^{+1.4}_{-1.5}$	$9.9 \pm 0.3\ ^{+0.7}_{-0.8}$	$5.9 \pm 0.2\ ^{+0.4}_{-0.4}$	$3.7 \pm 0.1\ ^{+0.3}_{-0.3}$

Table F.25: Relative systematic uncertainties in % for the [600,1000] GeV $S4_R$ signal models in the SR2 selection region with an additional cut on the electric charge of the lepton for the electron channel.

	$S4_R0$	$S4_R25$	$S4_R50$	$S4_R75$
Luminosity	± 1.9	± 1.9	± 1.9	± 1.9
Jets				
Energy resolution	± 2.9	± 1.4	± 3.0	± 1.2
Energy scale	+2.5/–3.2	–0.5/–3.5	+2.6/–3.6	+5.3/–2.3
Reconstruction	± 3.5	± 1.9	± 1.2	± 0.5
Vertex fraction	+4.7/–1.7	+3.0/–4.3	+0.9/–2.3	+4.0/–2.6
b-tag	± 3.6	± 3.8	± 4.2	± 4.4
$c\tau$-tag	-	-	-	± 0.1
mis-tag	-	-	-	-
$\boldsymbol{E_T^{miss}}$				
Resolution	+3.4/+0.8	± 0.7	+1.1/+1.8	+1.2/+0.2
Scale	+1.9/+1.2	+1.9/+0.1	+0.2/+1.3	–0.1/+0.3
Leptons				
Identification	+2.7/+1.4	± 0.9	+0.5/–0.7	–1.2/+1.0
Momentum resolution	–0.6/+1.1	–1.0/+0.6	–0.7/–1.1	–0.9/+0.4
Momentum scale	+0.5/+1.1	± 1.0	+0.0/+1.6	–1.3/–0.2
Reconstruction	± 0.4	± 0.4	± 0.4	± 0.4
Isolation	± 0.5	± 0.5	± 0.5	± 0.5
Trigger	+1.8/-0.0	+1.9/-0.0	+1.8/-0.0	+1.9/-0.0
Total Rel. Uncert.	+9.6/-7.6	+6.6/-7.6	+6.7/-7.7	+8.9/-6.2
Yield ± Stat ± Syst	$1213.2 \pm 96.3\ ^{+116.5}_{-92.2}$	$6606.7 \pm 465.0\ ^{+435.4}_{-500.2}$	$2217.5 \pm 141.2\ ^{+148.1}_{-170.7}$	$1429.0 \pm 81.7\ ^{+126.9}_{-88.9}$

Table F.26: Relative systematic uncertainties in % for the [0,75] GeV $S4_R$ signal models in the SR2 selection region with an additional cut on the electric charge of the lepton for the muon channel.

	$S4_R100$	$S4_R125$	$S4_R150$	$S4_R200$
Luminosity	± 1.9	± 1.9	± 1.9	± 1.9
Jets				
Energy resolution	± 3.4	± 6.5	± 1.5	± 1.3
Energy scale	+3.7/–1.6	+3.2/–2.8	+3.5/–2.1	+3.4/–3.6
Reconstruction	± 1.3	± 0.5	± 0.9	± 0.1
Vertex fraction	+6.4/–3.3	+3.8/–3.5	+4.5/–2.8	+3.4/–1.2
b-tag	± 4.1	± 3.9	± 4.1	± 4.0
$c\tau$-tag	-	± 0.1	± 0.1	-
mis-tag	-	± 0.1	-	-
$\boldsymbol{E_T^{miss}}$				
Resolution	± 0.8	–0.4/+0.5	+1.0/+0.0	+1.1/+0.4
Scale	+0.4/+0.7	+0.3/–0.1	+1.4/+0.6	+0.3/+0.2
Leptons				
Identification	–0.9/–0.0	+0.2/–0.5	+0.6/+0.4	+0.1/+0.7
Momentum resolution	+0.2/–1.8	+0.3/+0.0	+0.5/+0.1	+1.1/+0.9
Momentum scale	± 0.6	–0.4/+1.6	–0.5/+1.2	–0.1/–0.3
Reconstruction	± 0.4	± 0.4	± 0.4	± 0.4
Isolation	± 0.5	± 0.5	± 0.5	± 0.5
Trigger	+1.8/-0.0	+1.8/-0.0	+1.8/-0.0	+1.8/-0.0
Total Rel. Uncert.	+9.7/-7.2	+9.5/-9.2	+7.9/-6.1	+7.1/-6.1
Yield ± Stat ± Syst	$1108.9 \pm 56.7\ ^{+107.3}_{-80.0}$	$909.4 \pm 42.5\ ^{+86.5}_{-83.6}$	$708.7 \pm 31.4\ ^{+56.2}_{-43.4}$	$559.2 \pm 20.4\ ^{+39.7}_{-34.3}$

Table F.27: Relative systematic uncertainties in % for the [100,200] GeV $S4_R$ signal models in the SR2 selection region with an additional cut on the electric charge of the lepton for the muon channel.

	$S4_R250$	$S4_R300$	$S4_R400$	$S4_R500$
Luminosity	± 1.9	± 1.9	± 1.9	± 1.9
Jets				
Energy resolution	± 2.0	± 4.8	± 3.2	± 1.5
Energy scale	+3.4/–3.5	+4.0/–3.8	+3.4/–4.3	+3.5/–4.2
Reconstruction	± 0.2	± 0.2	± 0.6	± 0.6
Vertex fraction	+5.5/–3.9	+3.6/–3.3	+3.2/–3.4	+4.7/–3.0
b-tag	± 4.1	± 4.2	± 4.3	± 4.1
$c\tau$-tag	-	-	-	-
mis-tag	-	-	-	-
$\boldsymbol{E_T^{miss}}$				
Resolution	+1.3/+0.8	–0.1/+0.9	–0.9/–0.4	–0.2/–0.7
Scale	+0.4/–0.2	± 0.1	+0.3/–0.8	–0.4/–0.1
Leptons				
Identification	+1.2/+0.3	+0.6/+0.3	–0.5/–0.7	–0.5/–0.8
Momentum resolution	+0.6/+0.4	+0.2/+0.0	–0.4/–0.1	–0.2/–0.4
Momentum scale	± 0.4	+0.0/–0.3	–1.0/–0.2	–0.6/–0.9
Reconstruction	± 0.4	± 0.4	± 0.4	± 0.4
Isolation	± 0.5	± 0.5	± 0.5	± 0.5
Trigger	+1.8/-0.0	+1.9/-0.0	+1.8/-0.0	+1.8/-0.0
Total Rel. Uncert.	+8.5/-7.3	+8.8/-8.4	+7.8/-8.0	+7.9/-7.2
Yield ± Stat ± Syst	$357.8 \pm 12.4\ ^{+30.6}_{-26.1}$	$250.9 \pm 8.0\ ^{+22.0}_{-21.2}$	$125.5 \pm 3.6\ ^{+9.8}_{-10.1}$	$65.5 \pm 1.8\ ^{+5.2}_{-4.7}$

Table F.28: Relative systematic uncertainties in % for the [250,500] GeV $S4_R$ signal models in the SR2 selection region with an additional cut on the electric charge of the lepton for the muon channel.

	$S4_R600$	$S4_R700$	$S4_R800$	$S4_R900$	$S4_R1000$
Luminosity	± 1.9	± 1.9	± 1.9	± 1.9	± 1.9
Jets					
Energy resolution	± 2.7	± 2.2	± 2.0	± 1.4	± 1.2
Energy scale	+5.0/–4.8	+5.2/–4.0	+4.0/–5.0	+3.9/–6.2	+5.8/–3.5
Reconstruction	-	± 0.5	-	± 0.4	± 0.5
Vertex fraction	+4.1/–3.5	+4.4/–2.3	+3.3/–4.3	+2.9/–3.3	+4.9/–2.3
b-tag	± 4.5	± 4.3	± 4.4	± 4.5	± 4.4
$c\tau$-tag	-	-	-	-	-
mis-tag	-	± 0.1	± 0.1	± 0.1	-
$\boldsymbol{E_T^{miss}}$					
Resolution	–0.4/–0.0	± 0.4	+0.6/+0.2	± 0.1	+0.5/+0.2
Scale	–0.4/–0.2	+0.3/+0.5	± 0.1	–0.7/–0.3	+0.5/–0.0
Leptons					
Identification	+0.0/–0.2	+0.5/+0.1	± 0.3	–0.1/–0.7	± 0.3
Momentum resolution	–0.1/–0.7	+0.3/+0.0	–0.0/–0.4	–0.4/–0.7	+0.5/+0.3
Momentum scale	± 0.2	+0.5/+0.3	–0.0/–0.2	± 0.2	± 0.3
Reconstruction	± 0.4	± 0.4	± 0.4	± 0.4	± 0.4
Isolation	± 0.5	± 0.5	± 0.5	± 0.5	± 0.5
Trigger	+1.8/-0.0	+1.9/-0.0	+1.9/-0.0	+1.8/-0.0	+1.8/-0.0
Total Rel. Uncert.	+8.8/-8.2	+8.9/-7.1	+7.7/-8.5	+7.4/-8.8	+9.4/-6.6
Yield ± Stat ± Syst	$36.1 \pm 0.9\ ^{+3.2}_{-3.0}$	$20.0 \pm 0.5\ ^{+1.8}_{-1.4}$	$12.0 \pm 0.3\ ^{+0.9}_{-1.0}$	$7.3 \pm 0.2\ ^{+0.5}_{-0.6}$	$4.2 \pm 0.1\ ^{+0.4}_{-0.3}$

Table F.29: Relative systematic uncertainties in % for the [600,1000] GeV $S4_R$ signal models in the SR2 selection region with an additional cut on the electric charge of the lepton for the muon channel.

Optimized BDT signal region

For the electron (muon) channel these uncertainties are presented for the backgrounds in Tables F.30 and F.31 (F.32 and F.33), and for the $S4_R$ signal model in Tables F.34, F.35, F.36, and F.37 (F.38, F.39, F.40 and F.41). Backgrounds with zero expected events are not shown.

	$t\bar{t}$	s-chan	t-chan	Wt	W+heavy flavor
Luminosity	± 1.9	± 1.9	± 1.9	± 1.9	± 1.9
Cross-section	+5.3/–5.7	± 3.9	+3.9/–2.2	± 6.8	± 50.0
Generator					
$t\bar{t}$	± 22.6	-	-	-	-
$t\bar{t}$ ISR/FSR	± 10.1	-	-	-	-
s-chan	-	± 37.1	-	-	-
t-chan	-	-	± 21.1	-	-
Wt-chan	-	-	-	± 45.4	-
Wt-chan NLO calc	-	-	-	± 13.5	-
Jets					
Energy resolution	± 5.1	± 3.8	± 1.7	± 0.4	± 15.5
Energy scale	+9.9/–8.1	–14.4/–11.8	± 0.9	+2.5/–8.3	+3.0/+1.7
Reconstruction	-	-	-	-	-
Vertex fraction	+4.6/–4.1	+0.6/-0.0	+1.5/–1.7	–1.3/–0.2	+4.7/–3.0
b-tag	± 5.6	± 7.2	± 7.2	± 4.7	± 2.2
$c\tau$-tag	± 0.1	-	-	-	± 13.2
mis-tag	-	-	-	-	± 1.4
$\boldsymbol{E_{\mathrm{T}}^{\mathrm{miss}}}$					
Resolution	+6.0/+3.1	+5.0/–3.5	+1.0/+1.2	–1.7/+12.5	+19.1/+10.1
Scale	+2.7/–0.8	–5.6/-0.0	+1.3/–1.7	+3.8/+0.5	+2.3/–3.5
Leptons					
Energy resolution	+1.8/–0.5	–1.9/–5.9	–1.4/–0.8	–1.8/+7.1	–6.2/–0.3
Energy scale	+5.7/–3.5	–5.9/+1.9	–1.2/–0.5	+6.9/–3.3	+0.9/–12.4
Reconstruction	± 0.5	± 0.5	± 0.5	± 0.5	± 0.5
Isolation	± 2.7	± 2.7	± 2.7	± 2.5	± 2.6
Trigger	± 0.7	± 0.7	± 0.7	± 0.5	± 0.6
Total Rel. Uncert.	+30.1/-28.6	+42.1/-40.7	+23.1/-22.9	+49.0/-51.1	+58.1/-56.7
Yield ± Stat ± Syst	$95.7 \pm 5.3\ ^{+28.8}_{-27.4}$	$1.2 \pm 0.2\ ^{+0.5}_{-0.5}$	$19.3 \pm 1.4\ ^{+4.5}_{-4.4}$	$22.1 \pm 3.8\ ^{+10.8}_{-11.3}$	$52.3 \pm 8.6\ ^{+30.4}_{-29.6}$
Total Background	$226.2 \pm 13.7\ ^{+46.9}_{-45.7}$				
Data	216				

Table F.30: Relative systematic uncertainties in % for the background processes in the BDT selection region for the electron channel.

	W+light	Diboson	Multijet
Luminosity	± 1.9	± 1.9	-
Cross-section	± 24.5	± 24.5	-
Matrix Method			
Fake alternate	-	-	± 71.7
Fake MC	-	-	± 17.9
Real alternate	-	-	± 94.0
Jets			
Energy resolution	± 1.1	± 5.5	-
Energy scale	–6.6/–8.4	+5.5/+3.6	-
Reconstruction	-	-	-
Vertex fraction	–4.2/-0.0	-	-
b-tag	-	± 2.7	-
$c\tau$-tag	-	± 8.1	-
mis-tag	+48.6/–48.1	± 6.0	-
$\boldsymbol{E_{\mathrm{T}}^{\mathrm{miss}}}$			
Resolution	–3.0/–2.1	+30.0/+5.5	-
Scale	-0.0/–7.0	+22.1/-0.0	-
Leptons			
Energy resolution	–7.1/–9.3	–2.7/-0.0	-
Energy scale	–7.0/–7.7	+22.3/–2.7	-
Reconstruction	± 0.5	± 0.4	-
Isolation	± 2.6	± 2.5	-
Trigger	± 0.8	± 0.5	-
Total Rel. Uncert.	+56.1/-56.5	+51.7/-28.3	+119.6/-119.6
Yield ± Stat ± Syst	$26.1 \pm 7.2\ ^{+14.6}_{-14.8}$	$1.5 \pm 0.5\ ^{+0.8}_{-0.4}$	$8.1 \pm 2.6\ ^{+9.7}_{-9.7}$
Total Background	$226.2 \pm 13.7\ ^{+46.9}_{-45.7}$		
Data	216		

Table F.31: Relative systematic uncertainties in % for the background processes in the BDT selection region for the electron channel.

	$t\bar{t}$	s-chan	t-chan	Wt	W+heavy flavor
Luminosity	± 1.9	± 1.9	± 1.9	± 1.9	± 1.9
Cross-section	+5.3/–5.7	± 3.9	+3.9/–2.2	± 6.8	± 50.0
Generator					
$t\bar{t}$	± 18.3	-	-	-	-
$t\bar{t}$ ISR/FSR	± 6.9	-	-	-	-
s-chan	-	± 4.9	-	-	-
t-chan	-	-	± 20.6	-	-
Wt-chan	-	-	-	± 52.1	-
Wt-chan NLO calc	-	-	-	± 12.8	-
Jets					
Energy resolution	± 1.1	± 10.0	± 9.4	± 9.1	± 14.5
Energy scale	+10.4/–7.2	–9.6/–11.2	–5.2/–3.2	+3.6/–14.7	+7.2/+23.2
Reconstruction	± 0.7	± 0.7	± 1.2	± 6.2	± 6.3
Vertex fraction	+6.3/–3.2	–3.4/–8.5	+1.1/–5.6	+7.1/–3.1	+5.4/+1.4
b-tag	± 4.9	± 6.8	± 7.4	± 4.2	± 2.6
$c\tau$-tag	± 0.1	-	± 0.2	-	± 11.0
mis-tag	-	-	± 0.1	-	± 0.8
$\boldsymbol{E}_{\mathbf{T}}^{\mathbf{miss}}$					
Resolution	–0.8/+2.2	± 6.6	+3.1/+3.8	+2.1/+6.1	+28.3/+24.4
Scale	–0.4/+1.4	–9.1/–0.7	+3.4/–3.0	+9.0/–0.8	+5.6/–0.2
Leptons					
Identification	+2.4/–0.5	–2.6/-0.0	–3.5/+2.0	+0.8/–9.3	+12.0/+4.0
Momentum resolution	+1.1/–3.0	± 3.9	–0.0/–0.8	+8.8/–3.2	+3.5/+2.8
Momentum scale	+0.1/–1.6	–7.8/–6.6	–1.2/–1.7	+13.3/+0.8	+14.8/+9.0
Reconstruction	± 0.4	± 0.4	± 0.4	± 0.4	± 0.4
Isolation	± 0.5	± 0.5	± 0.5	± 0.5	± 0.5
Trigger	+1.9/-0.0	+1.8/-0.0	+1.8/-0.0	+1.8/-0.0	+1.8/-0.0
Total Rel. Uncert.	+24.5/-22.9	+22.5/-22.2	+25.6/-25.5	+59.0/-58.5	+64.6/-64.2
Yield ± Stat ± Syst	$99.8 \pm 5.4\ ^{+24.4}_{-22.9}$	$1.1 \pm 0.2\ ^{+0.2}_{-0.2}$	$17.3 \pm 1.4\ ^{+4.4}_{-4.4}$	$20.2 \pm 3.6\ ^{+11.9}_{-11.8}$	$60.0 \pm 8.9\ ^{+38.8}_{-38.5}$
Total Background	$215.6 \pm 12.7\ ^{+48.8}_{-47.5}$				
Data	258				

Table F.32: Relative systematic uncertainties in % for the background processes in the BDT selection region for the muon channel.

	W+light	Diboson
Luminosity	± 1.9	± 1.9
Cross-section	± 24.5	± 24.5
Jets		
Energy resolution	± 31.2	± 0.9
Energy scale	+32.6/+23.8	± 0.2
Reconstruction	± 10.1	± 0.6
Vertex fraction	+41.9/+11.3	+0.6/–7.4
b-tag	-	± 1.8
$c\tau$-tag	-	± 13.8
mis-tag	± 30.3	-
$\boldsymbol{E_{\mathrm{T}}^{\mathrm{miss}}}$		
Resolution	–10.8/+21.2	+19.4/–2.2
Scale	+4.4/+13.4	+8.9/+3.2
Leptons		
Identification	–2.8/–12.5	+0.3/–8.3
Momentum resolution	+10.9/-0.0	+3.2/–2.1
Momentum scale	-0.0/+10.1	+16.3/–1.5
Reconstruction	± 0.4	± 0.4
Isolation	± 0.5	± 0.5
Trigger	+1.7/-0.0	+1.9/-0.0
Total Rel. Uncert.	+75.4/-64.7	+39.2/-30.8
Yield ± Stat ± Syst	$14.5 \pm 5.0\ ^{+10.9}_{-9.4}$	$2.7 \pm 0.8\ ^{+1.0}_{-0.8}$
Total Background	$215.6 \pm 12.7\ ^{+48.8}_{-47.5}$	
Data	258	

Table F.33: Relative systematic uncertainties in % for the background processes in the BDT selection region for the muon channel.

	$S4_R$ 0	$S4_R$ 25	$S4_R$ 50	$S4_R$ 75
Luminosity	± 1.9	± 1.9	± 1.9	± 1.9
Jets				
Energy resolution	± 0.9	± 3.3	± 4.8	± 0.9
Energy scale	+3.2/–4.9	+2.4/–3.5	+2.8/–1.2	+3.4/–5.1
Reconstruction	-	-	± 0.1	-
Vertex fraction	+0.3/–2.7	+1.7/–2.7	+0.6/–2.4	+0.8/–4.5
b-tag	± 5.8	± 5.8	± 5.6	± 4.7
$c\tau$-tag	± 0.1	± 0.1	± 0.2	-
mis-tag	± 0.1	-	± 0.3	-
$\boldsymbol{E_T^{miss}}$				
Resolution	–0.0/+1.1	+1.1/+1.7	+0.1/–1.8	–0.2/–0.4
Scale	–0.0/–0.3	+0.3/–0.6	+0.9/–0.4	± 0.3
Leptons				
Energy resolution	+0.3/+0.7	–1.9/–0.2	–0.5/+0.9	+0.0/+1.4
Energy scale	+3.2/–3.4	+6.1/–5.2	+4.3/–3.3	± 3.3
Reconstruction	± 0.5	± 0.5	± 0.5	± 0.5
Isolation	± 2.6	± 2.7	± 2.7	± 2.7
Trigger	± 0.7	± 0.7	± 0.7	± 0.8
Total Rel. Uncert.	+8.1/-9.5	+10.3/-10.3	+9.7/-9.4	+7.7/-9.7
Yield ± Stat ± Syst	$1511.3 \pm 104.4\ ^{+123.2}_{-143.7}$	$6849.0 \pm 469.4\ ^{+704.5}_{-703.5}$	$2700.1 \pm 153.1\ ^{+262.6}_{-254.4}$	$1717.4 \pm 87.8\ ^{+131.9}_{-166.9}$

Table F.34: Relative systematic uncertainties in % for the [0,75] GeV $S4_R$ signal models in the BDT selection region for the electron channel.

	$S4_R$ 100	$S4_R$ 125	$S4_R$ 150	$S4_R$ 200
Luminosity	± 1.9	± 1.9	± 1.9	± 1.9
Jets				
Energy resolution	± 1.9	± 0.9	± 0.2	± 0.9
Energy scale	+3.2/–4.4	+2.4/–2.2	+3.1/–3.2	+4.4/–2.3
Reconstruction	± 0.1	-	± 0.2	-
Vertex fraction	+1.1/–3.8	+0.8/–2.6	+0.6/–3.3	+1.2/–1.5
b-tag	± 4.9	± 5.3	± 5.2	± 4.8
$c\tau$-tag	-	± 0.2	± 0.1	± 0.2
mis-tag	± 0.1	-	± 0.4	± 0.1
$\boldsymbol{E}_{\mathbf{T}}^{\mathbf{miss}}$				
Resolution	–0.3/+0.8	± 0.7	–0.2/+0.9	–0.2/+0.7
Scale	+0.5/–0.8	+0.2/+0.9	–0.1/+0.4	± 0.1
Leptons				
Energy resolution	–0.5/–1.5	–0.8/–0.3	–0.2/+0.0	–0.5/+0.4
Energy scale	+3.8/–4.6	+2.8/–3.1	+2.7/–1.8	+3.1/–3.9
Reconstruction	± 0.5	± 0.5	± 0.5	± 0.5
Isolation	± 2.7	± 2.7	± 2.7	± 2.7
Trigger	± 0.8	± 0.8	± 0.8	± 0.7
Total Rel. Uncert.	+8.1/-9.9	+7.5/-8.0	+7.5/-8.0	+8.2/-7.7
Yield ± Stat ± Syst	$1344.8 \pm 62.1\ ^{+109.5}_{-133.0}$	$968.6 \pm 42.9\ ^{+72.8}_{-77.1}$	$824.5 \pm 33.8\ ^{+61.6}_{-66.1}$	$533.8 \pm 19.8\ ^{+43.5}_{-41.3}$

Table F.35: Relative systematic uncertainties in % for the [100,200] GeV $S4_R$ signal models in the BDT selection region for the electron channel.

	$S4_R$ 250	$S4_R$ 300	$S4_R$ 400	$S4_R$ 500
Luminosity	± 1.9	± 1.9	± 1.9	± 1.9
Jets				
Energy resolution	± 1.0	± 1.7	± 1.7	± 1.0
Energy scale	+4.2/–3.7	+2.5/–3.3	+3.2/–3.9	+3.3/–4.4
Reconstruction	-	-	-	± 0.2
Vertex fraction	+0.9/–2.8	+0.7/–2.6	+0.7/–3.8	+1.0/–3.4
b-tag	± 4.8	± 5.2	± 4.9	± 4.8
$c\tau$-tag	-	-	-	± 0.1
mis-tag	± 0.1	-	-	± 0.3
$\boldsymbol{E_T^{miss}}$				
Resolution	± 0.4	–0.6/+0.3	–0.4/–0.1	± 0.1
Scale	± 0.2	–0.2/–0.0	–0.2/–0.1	–0.1/+0.2
Leptons				
Energy resolution	+0.2/+0.7	± 0.3	± 0.2	–0.8/–0.4
Energy scale	+2.9/–3.1	+2.6/–2.8	+2.1/–2.0	+2.2/–2.4
Reconstruction	± 0.5	± 0.5	± 0.5	± 0.5
Isolation	± 2.7	± 2.7	± 2.6	± 2.7
Trigger	± 0.7	± 0.7	± 0.7	± 0.7
Total Rel. Uncert.	+8.0/-8.3	+7.4/-8.2	+7.3/-8.5	+7.3/-8.5
Yield ± Stat ± Syst	$364.0 \pm 12.3\ ^{+29.0}_{-30.0}$	$244.0 \pm 7.8\ ^{+18.2}_{-20.1}$	$115.8 \pm 3.4\ ^{+8.5}_{-9.8}$	$59.6 \pm 1.7\ ^{+4.4}_{-5.1}$

Table F.36: Relative systematic uncertainties in % for the [250,500] GeV $S4_R$ signal models in the BDT selection region for the electron channel.

	$S4_R$ 600	$S4_R$ 700	$S4_R$ 800	$S4_R$ 900	$S4_R$ 1000
Luminosity	± 1.9	± 1.9	± 1.9	± 1.9	± 1.9
Jets					
Energy resolution	± 2.1	± 3.9	± 2.2	± 1.5	± 1.4
Energy scale	+4.6/–2.4	+4.2/–3.3	+3.8/–4.5	+3.9/–3.8	+4.1/–4.2
Reconstruction	-	-	± 0.1	-	± 0.1
Vertex fraction	+0.8/–2.6	+1.3/–2.9	+1.1/–2.8	+1.1/–2.8	+1.2/–2.6
b-tag	± 4.7	± 4.6	± 4.6	± 4.5	± 4.6
$c\tau$-tag	-	± 0.1	± 0.1	-	± 0.1
mis-tag	-	-	-	± 0.2	± 0.1
$\boldsymbol{E_T^{miss}}$					
Resolution	–0.0/–0.2	+0.1/–0.0	+0.3/–0.2	± 0.1	–0.1/+0.2
Scale	± 0.2	± 0.2	± 0.1	± 0.1	± 0.1
Leptons					
Energy resolution	+0.2/–0.1	+0.4/+0.0	± 0.2	–0.1/+0.3	+0.4/–0.1
Energy scale	+1.9/–2.0	+1.9/–1.7	+1.6/–1.5	+1.4/–1.7	+1.4/–1.2
Reconstruction	± 0.5	± 0.5	± 0.5	± 0.5	± 0.5
Isolation	± 2.7	± 2.7	± 2.7	± 2.7	± 2.7
Trigger	± 0.6	± 0.6	± 0.6	± 0.6	± 0.6
Total Rel. Uncert.	+7.9/-7.4	+8.4/-8.4	+7.5/-8.2	+7.3/-7.7	+7.3/-7.8
Yield ± Stat ± Syst	$31.8 \pm 0.9\ ^{+2.5}_{-2.3}$	$17.3 \pm 0.5\ ^{+1.5}_{-1.5}$	$9.6 \pm 0.3\ ^{+0.7}_{-0.8}$	$5.7 \pm 0.2\ ^{+0.4}_{-0.4}$	$3.5 \pm 0.1\ ^{+0.3}_{-0.3}$

Table F.37: Relative systematic uncertainties in % for the [600,1000] GeV $S4_R$ signal models in the BDT selection region for the electron channel.

	$S4_R$ 0	$S4_R$ 25	$S4_R$ 50	$S4_R$ 75
Luminosity	± 1.9	± 1.9	± 1.9	± 1.9
Jets				
Energy resolution	± 6.1	± 0.5	± 0.6	± 3.5
Energy scale	+5.9/+3.7	+4.3/–3.9	+5.4/–3.3	+6.3/–3.0
Reconstruction	± 2.6	± 0.3	± 1.9	± 0.2
Vertex fraction	+7.2/–0.2	+6.8/–4.4	+2.2/–0.7	+2.0/–1.2
b-tag	± 4.4	± 5.1	± 5.4	± 5.3
$c\tau$-tag	± 0.1	± 0.1	-	± 0.1
mis-tag	-	-	± 0.1	-
$\boldsymbol{E_T^{miss}}$				
Resolution	+1.3/+5.1	+1.1/+0.5	+2.7/+1.3	± 0.3
Scale	+2.8/+2.5	–0.4/+1.2	+2.8/+0.0	–0.5/–0.8
Leptons				
Identification	+3.5/+1.7	+1.4/+1.7	+2.0/+0.1	+1.7/+1.9
Momentum resolution	± 1.7	+1.1/+1.8	+0.3/+2.8	+1.1/+0.5
Momentum scale	+3.2/+2.9	–0.6/–0.2	+2.0/+1.4	–0.0/+2.7
Reconstruction	± 0.4	± 0.4	± 0.4	± 0.4
Isolation	± 0.5	± 0.5	± 0.5	± 0.5
Trigger	+1.8/-0.0	+1.8/-0.0	+1.8/-0.0	+1.8/-0.0
Total Rel. Uncert.	+13.9/-11.3	+10.1/-8.5	+9.9/-7.7	+9.8/-8.2
Yield ± Stat ± Syst	$1599.0 \pm 110.0\ ^{+221.8}_{-180.9}$	$8654.5 \pm 540.1\ ^{+876.9}_{-734.4}$	$2991.7 \pm 165.0\ ^{+295.0}_{-230.7}$	$1866.8 \pm 94.6\ ^{+183.7}_{-153.3}$

Table F.38: Relative systematic uncertainties in % for the [0,75] GeV $S4_R$ signal models in the BDT selection region for the muon channel.

	$S4_R$ 100	$S4_R$ 125	$S4_R$ 150	$S4_R$ 200
Luminosity	± 1.9	± 1.9	± 1.9	± 1.9
Jets				
Energy resolution	± 2.8	± 4.6	± 1.9	± 1.2
Energy scale	+3.0/–3.7	+3.4/–4.4	+4.3/–3.4	+3.8/–3.7
Reconstruction	± 1.9	± 0.8	± 0.5	± 1.5
Vertex fraction	+2.6/–4.3	+2.3/–1.8	+3.5/–2.7	+3.7/–3.2
b-tag	± 5.2	± 5.0	± 4.9	± 4.6
$c\tau$-tag	-	± 0.1	-	-
mis-tag	-	± 0.1	-	± 0.2
$\boldsymbol{E_T^{miss}}$				
Resolution	–0.9/–1.7	+0.8/+1.3	+0.1/+0.6	+0.6/+0.3
Scale	–0.5/–1.7	+1.1/+1.5	–0.5/–0.4	–0.3/–0.8
Leptons				
Identification	–1.7/–1.4	± 0.1	+0.5/+0.7	+0.2/+0.0
Momentum resolution	–0.4/–1.7	–0.0/+0.3	+0.1/–0.9	-
Momentum scale	–1.3/+0.6	–0.4/+0.1	–0.3/+0.6	–0.6/+0.0
Reconstruction	± 0.4	± 0.4	± 0.4	± 0.4
Isolation	± 0.5	± 0.5	± 0.5	± 0.5
Trigger	+1.8/-0.0	+1.9/-0.0	+1.8/-0.0	+1.8/-0.0
Total Rel. Uncert.	+8.2/-9.2	+8.6/-8.8	+8.2/-7.3	+7.8/-7.3
Yield ± Stat ± Syst	$1407.1 \pm 64.7\ ^{+115.5}_{-130.0}$	$1178.4 \pm 48.7\ ^{+100.9}_{-103.8}$	$832.0 \pm 34.2\ ^{+67.8}_{-60.5}$	$606.3 \pm 21.3\ ^{+47.5}_{-44.4}$

Table F.39: Relative systematic uncertainties in % for the [100,200] GeV $S4_R$ signal models in the BDT selection region for the muon channel.

	$S4_R$ 250	$S4_R$ 300	$S4_R$ 400	$S4_R$ 500
Luminosity	± 1.9	± 1.9	± 1.9	± 1.9
Jets				
Energy resolution	± 2.6	± 4.0	± 3.4	± 1.3
Energy scale	+5.4/–1.8	+3.5/–5.7	+4.1/–4.7	+4.7/–4.6
Reconstruction	± 0.6	± 0.1	± 0.5	± 0.4
Vertex fraction	+4.3/–2.7	+4.6/–3.3	+2.3/–3.8	+4.6/–2.4
b-tag	± 4.9	± 5.0	± 4.8	± 4.5
$c\tau$-tag	-	± 0.1	± 0.1	-
mis-tag	± 0.1	± 0.1	-	-
$\boldsymbol{E_T^{miss}}$				
Resolution	+0.9/+0.6	+0.6/+0.3	–0.4/–1.2	+0.8/–0.2
Scale	+0.3/–0.1	+0.0/+0.8	± 0.2	–0.3/+0.4
Leptons				
Identification	+1.8/+0.6	+0.8/+1.1	+0.5/+0.1	± 0.3
Momentum resolution	+0.3/+1.4	+1.8/+0.1	–0.9/+0.1	+0.9/–0.1
Momentum scale	+1.5/–0.1	+1.1/+0.1	+0.0/–0.6	± 0.2
Reconstruction	± 0.4	± 0.4	± 0.4	± 0.4
Isolation	± 0.5	± 0.5	± 0.5	± 0.5
Trigger	+1.8/-0.0	+1.8/-0.0	+1.9/-0.0	+1.8/-0.0
Total Rel. Uncert.	+9.6/-6.9	+9.3/-9.5	+8.1/-8.8	+8.7/-7.3
Yield ± Stat ± Syst	$379.2 \pm 12.9\ ^{+36.5}_{-26.3}$	$251.4 \pm 8.1\ ^{+23.5}_{-24.0}$	$124.5 \pm 3.7\ ^{+10.1}_{-10.9}$	$63.5 \pm 1.8\ ^{+5.5}_{-4.6}$

Table F.40: Relative systematic uncertainties in % for the [250,500] GeV $S4_R$ signal models in the BDT selection region for the muon channel.

	$S4_R$ 600	$S4_R$ 700	$S4_R$ 800	$S4_R$ 900	$S4_R$ 1000
Luminosity	± 1.9	± 1.9	± 1.9	± 1.9	± 1.9
Jets					
Energy resolution	± 2.3	± 3.1	± 2.0	± 1.4	± 1.8
Energy scale	+5.0/–5.3	+5.1/–5.0	+4.1/–5.0	± 5.1	+5.8/–3.8
Reconstruction	± 0.2	± 0.6	± 0.2	± 0.2	± 0.1
Vertex fraction	± 4.0	+3.7/–2.8	+4.5/–2.6	+3.9/–3.5	+4.5/–3.0
b-tag	± 4.8	± 4.7	± 4.6	± 4.7	± 4.5
$c\tau$-tag	-	± 0.1	-	-	-
mis-tag	-	± 0.3	± 0.1	± 0.1	± 0.1
$\boldsymbol{E}_{\mathbf{T}}^{\mathbf{miss}}$					
Resolution	+0.0/–0.8	–0.8/–0.3	+0.1/+0.4	+0.7/+0.4	–0.5/+0.1
Scale	–0.9/–0.3	–0.0/–0.6	+0.2/+0.5	+0.4/+0.5	± 0.3
Leptons					
Identification	+0.6/+0.1	–0.2/–0.7	+0.4/+0.2	+1.2/+0.6	-
Momentum resolution	+0.0/+0.6	–0.7/+0.1	+0.2/+0.1	± 0.6	± 0.3
Momentum scale	± 0.6	± 0.1	–0.0/+0.4	+0.9/+0.5	–0.1/–0.3
Reconstruction	± 0.4	± 0.4	± 0.4	± 0.4	± 0.4
Isolation	± 0.5	± 0.5	± 0.5	± 0.5	± 0.5
Trigger	+1.9/-0.0	+1.9/-0.0	+1.8/-0.0	+1.8/-0.0	+1.8/-0.0
Total Rel. Uncert.	+8.8/-8.8	+9.0/-8.4	+8.4/-7.9	+8.8/-8.2	+9.3/-7.1
Yield ± Stat ± Syst	$33.9 \pm 0.9\ ^{+3.0}_{-3.0}$	$18.6 \pm 0.5\ ^{+1.7}_{-1.6}$	$11.1 \pm 0.3\ ^{+0.9}_{-0.9}$	$6.5 \pm 0.2\ ^{+0.6}_{-0.5}$	$3.9 \pm 0.1\ ^{+0.4}_{-0.3}$

Table F.41: Relative systematic uncertainties in % for the [600,1000] GeV $S4_R$ signal models in the BDT selection region for the muon channel.

Appendix G

Input variable discriminating power

This appendix presents plots of the discriminating power of kinematic variables as a function of the mass of the v_{met} particle for individual background processes. The calculations were done in the pre-selection region with the additional cut on the charge of the lepton for plots on the left and the BDT signal region for the plots on the right. Plots are shown for the combined backgrounds in Figure G.1, for the $t\bar{t}$ process in Figure G.2, for the single-top t-channel process in Figure G.3, for the single-top s-channel process in Figure G.4, for the single-top Wt-channel process in Figure G.5, for the W+heavy flavor processes in Figure G.6, for the W+light jets processes in Figure G.7,f or the Z+jets processes in Figure G.8, for the diboson processes in Figure G.9, and for the multijet estimation in Figure G.10.

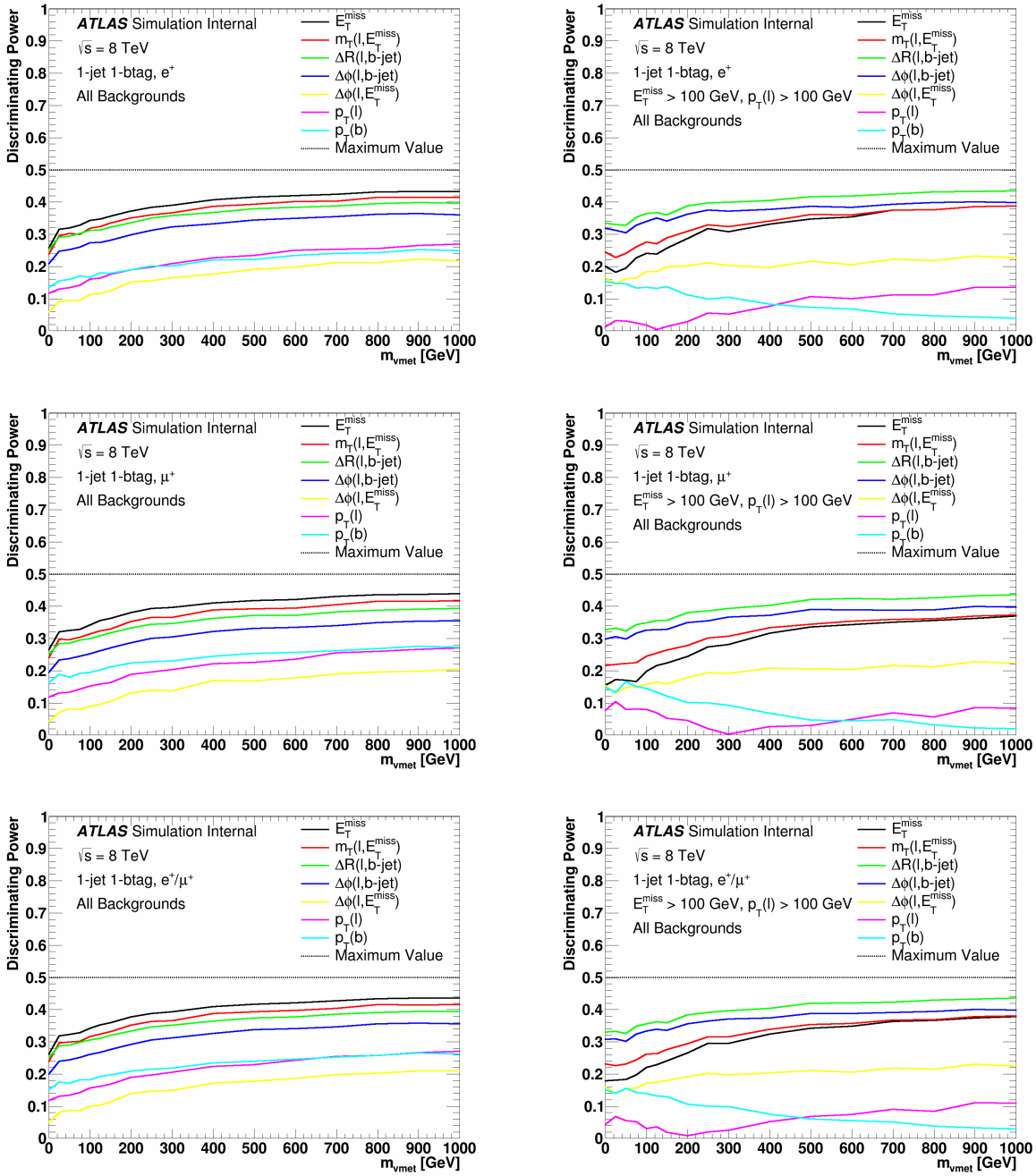

Figure G.1: The discriminating power of the input variables of the BDT as a function of the mass of the v_{met} particle for all background processes combined in the pre-selection+lepton charge cut region (left) and in the BDT signal region (right). Plots are shown for the electron, muon, and combined electron and muon channels.

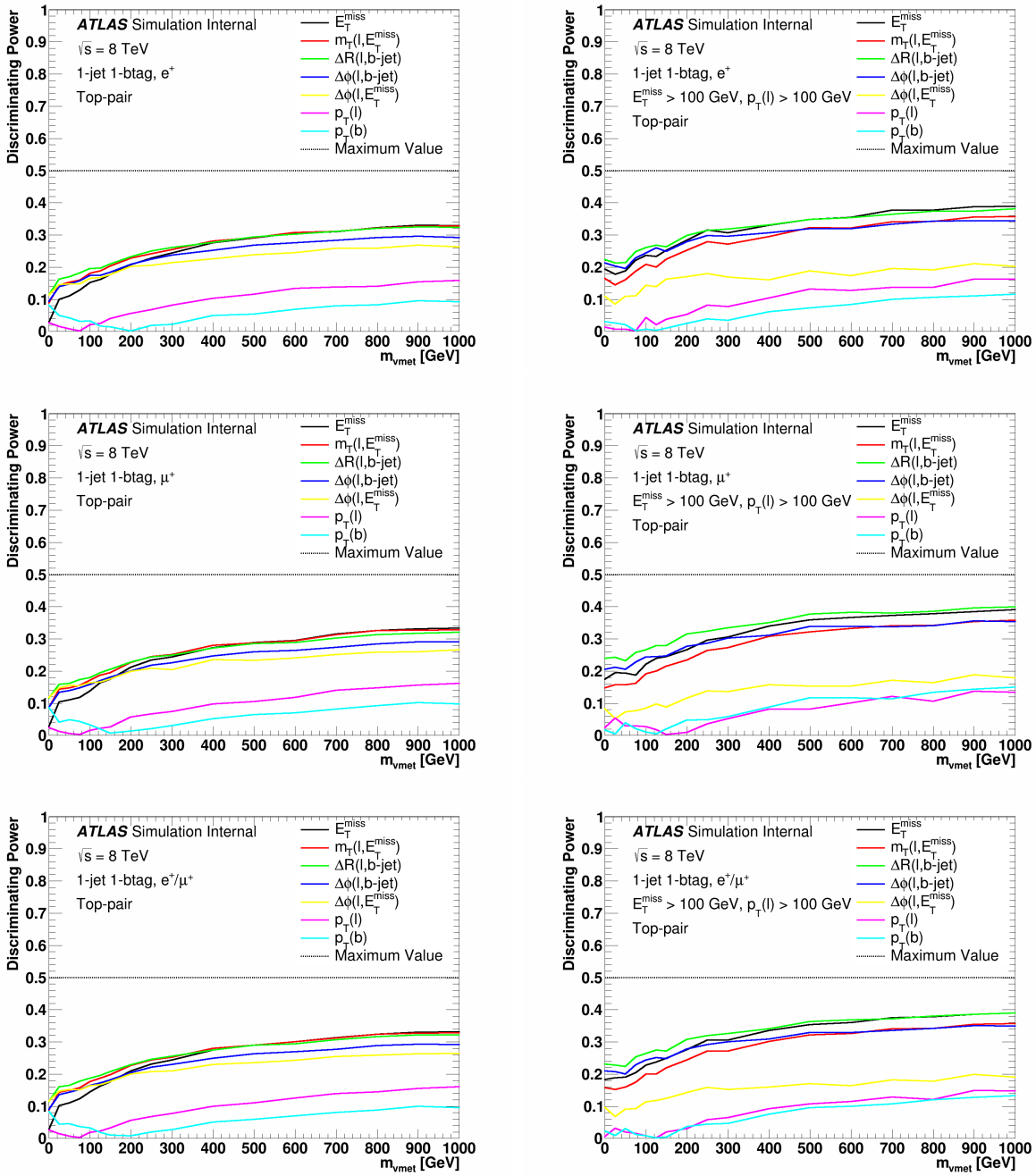

Figure G.2: The discriminating power of the input variables of the BDT as a function of the mass of the v_{met} particle for the $t\bar{t}$ process in the pre-selection+lepton charge cut region (left) and in the BDT signal region (right). Plots are shown for the electron, muon, and combined electron and muon channels.

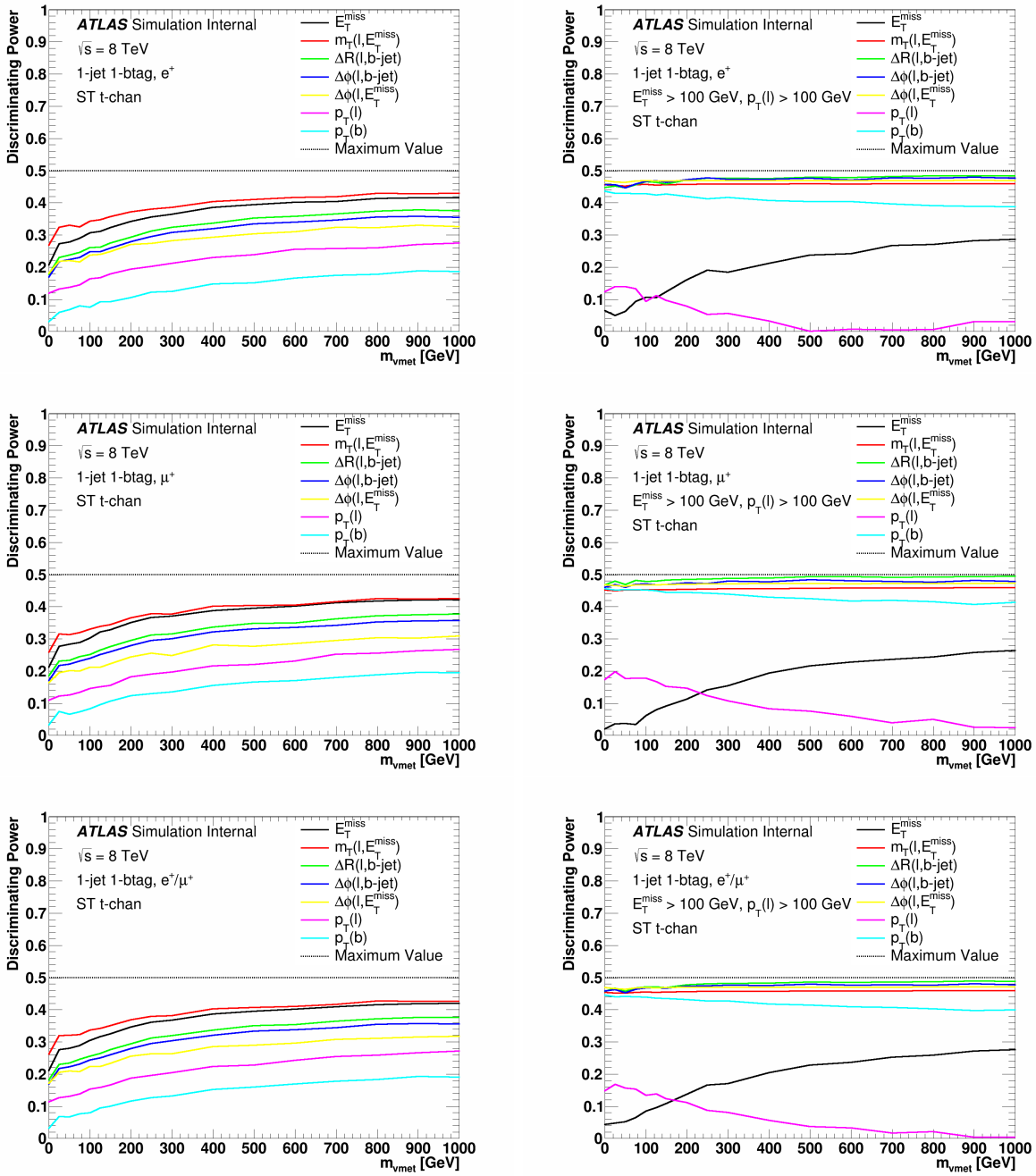

Figure G.3: The discriminating power of the input variables of the BDT as a function of the mass of the v_{met} particle for the single-top t-channel process in the pre-selection+lepton charge cut region (left) and in the BDT signal region (right). Plots are shown for the electron, muon, and combined electron and muon channels.

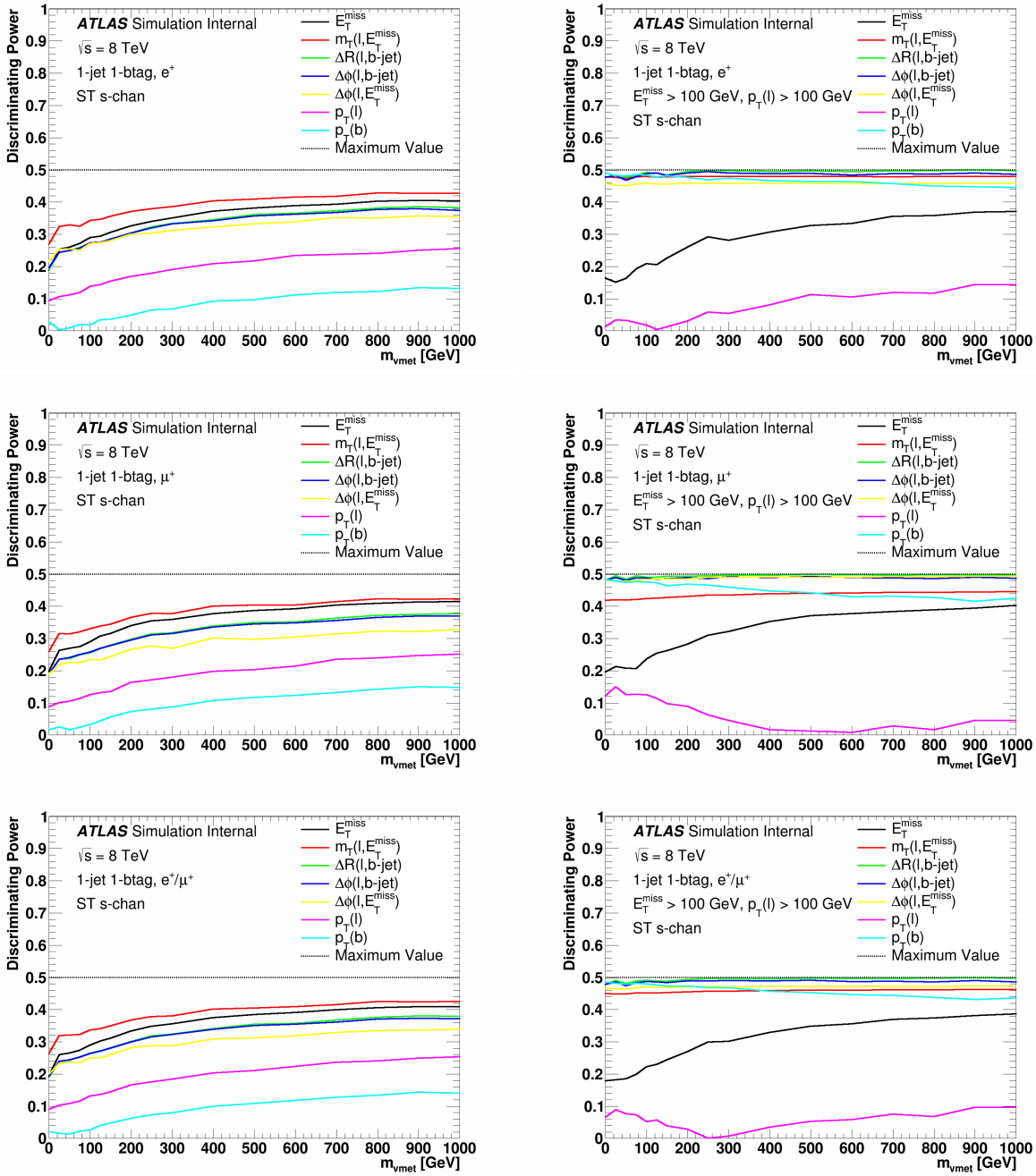

Figure G.4: The discriminating power of the input variables of the BDT as a function of the mass of the v_{met} particle for the single-top s-channel process in the pre-selection+lepton charge cut region (left) and in the BDT signal region (right). Plots are shown for the electron, muon, and combined electron and muon channels.

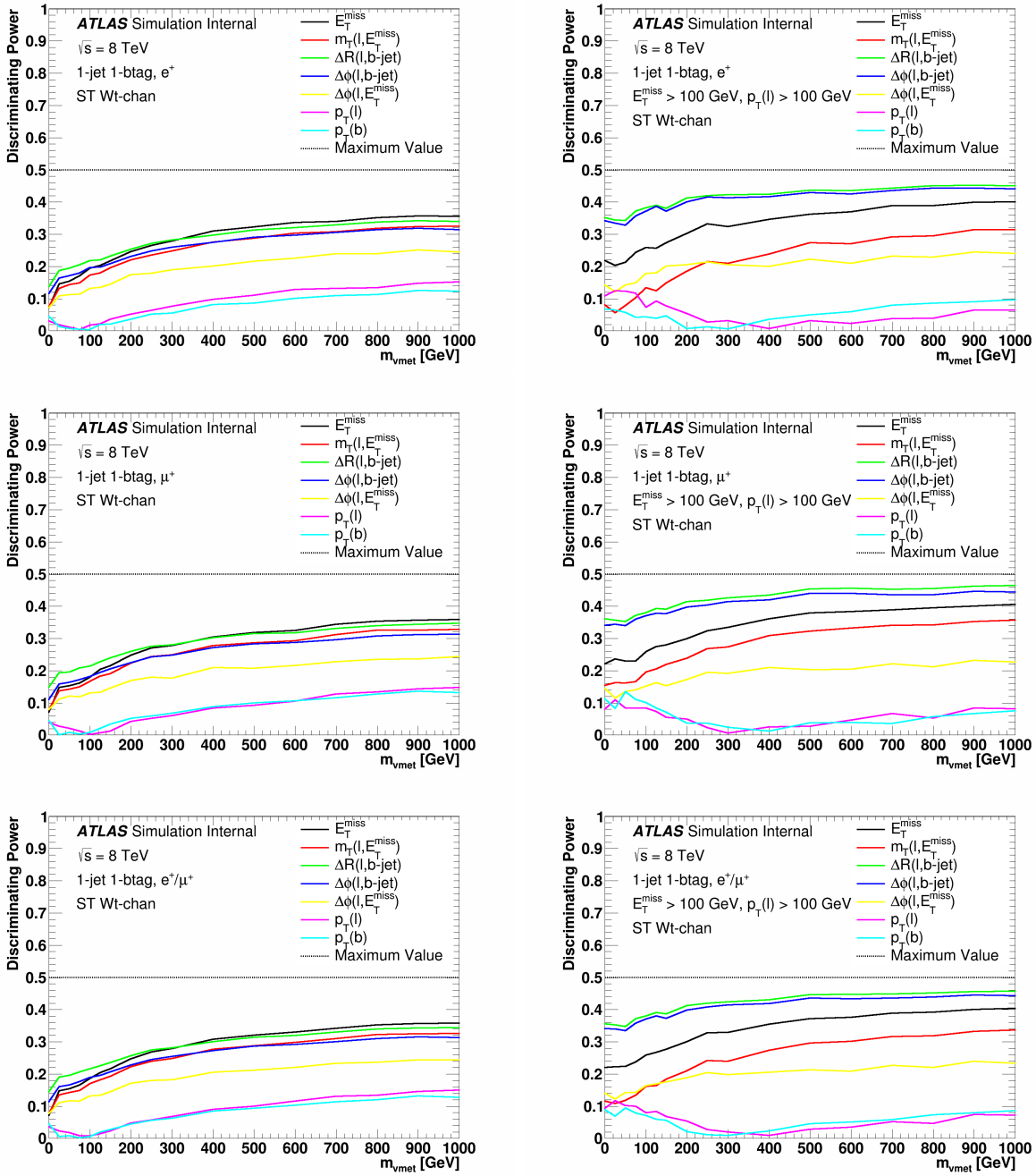

Figure G.5: The discriminating power of the input variables of the BDT as a function of the mass of the v_{met} particle for the single-top Wt-channel process in the pre-selection+lepton charge cut region (left) and in the BDT signal region (right). Plots are shown for the electron, muon, and combined electron and muon channels.

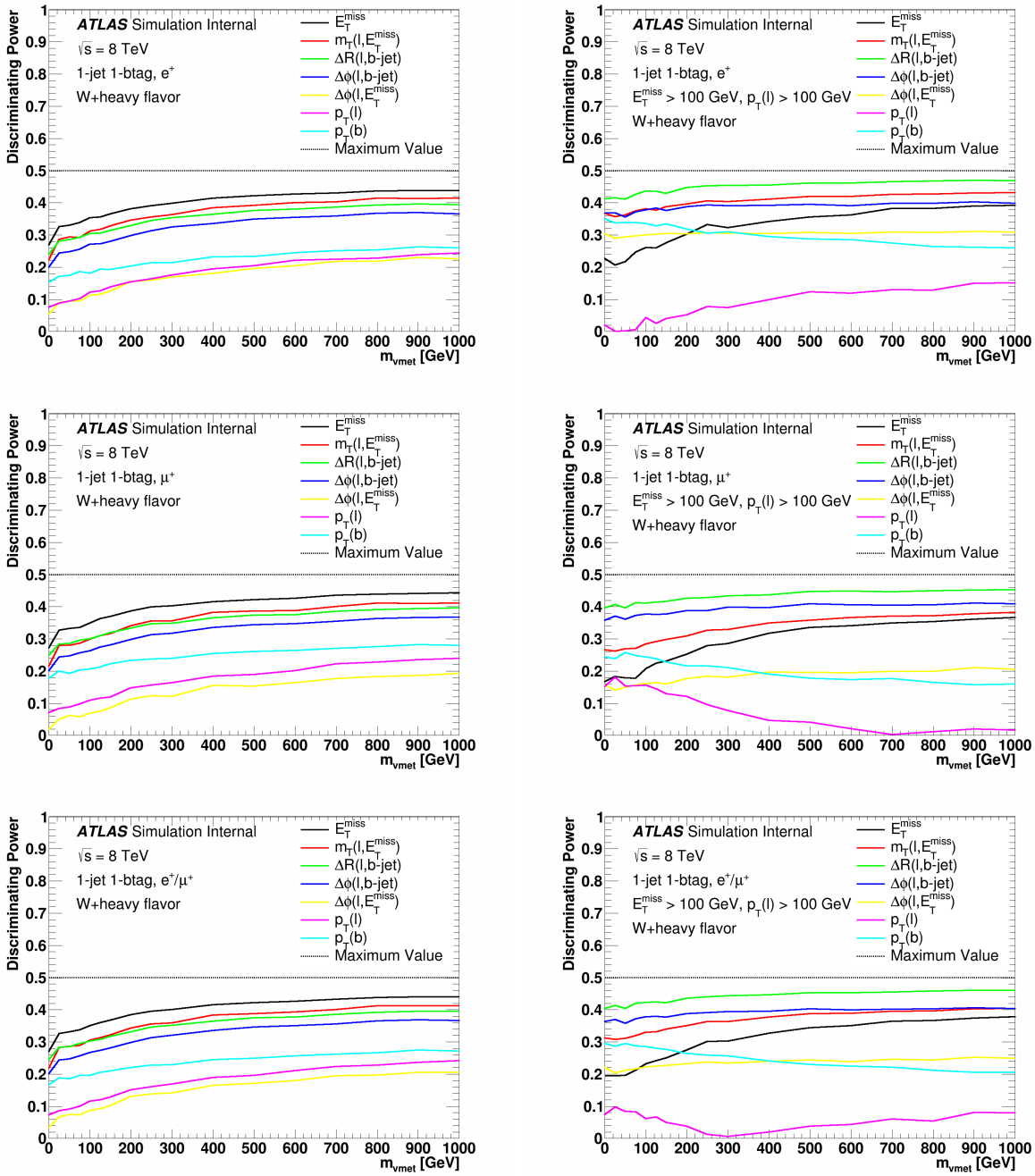

Figure G.6: The discriminating power of the input variables of the BDT as a function of the mass of the v_{met} particle for the W+heavy flavor processes in the pre-selection+lepton charge cut region (left) and in the BDT signal region (right). Plots are shown for the electron, muon, and combined electron and muon channels.

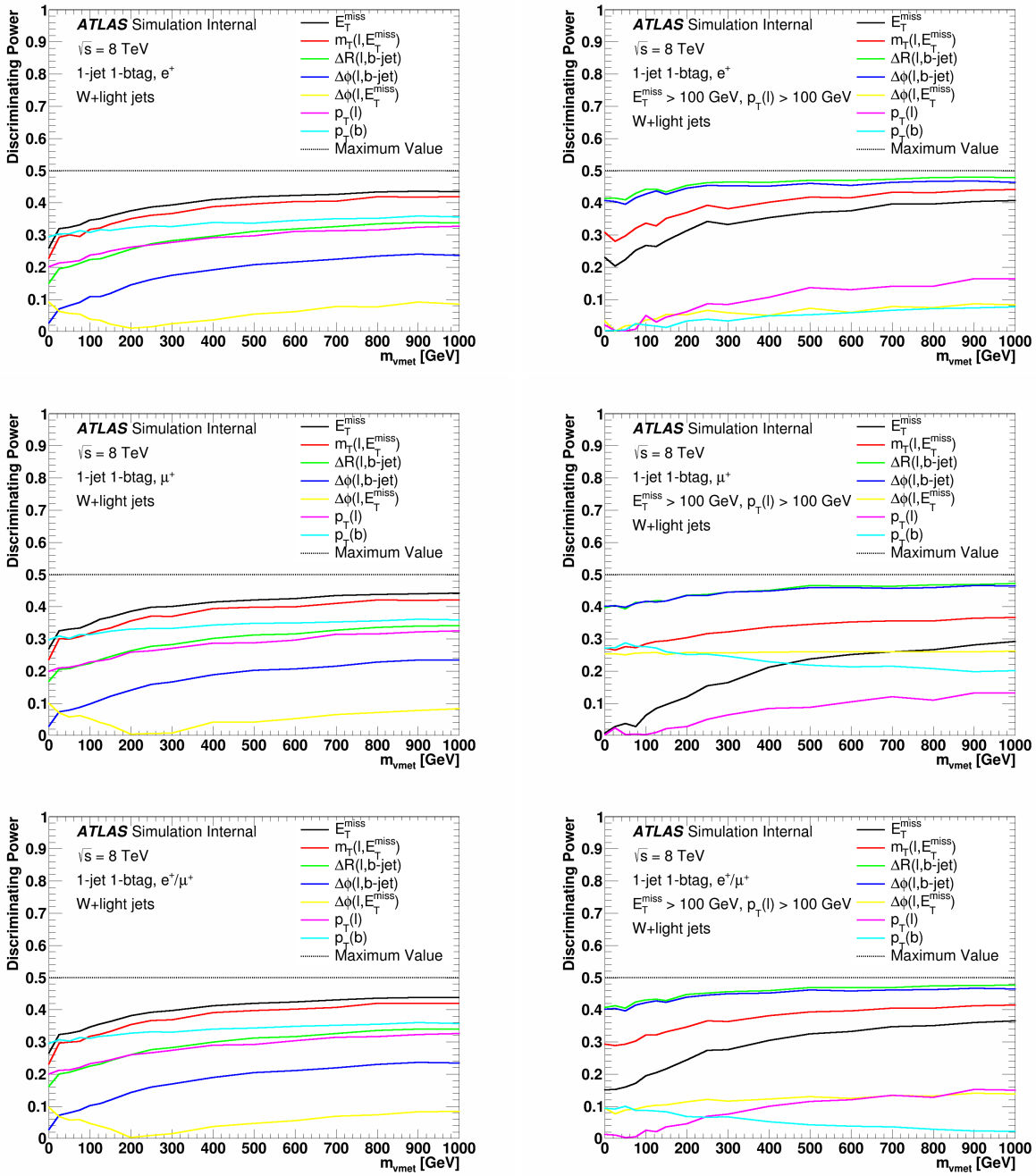

Figure G.7: The discriminating power of the input variables of the BDT as a function of the mass of the v_{met} particle for the W+heavy flavor processes in the pre-selection+lepton charge cut region (left) and in the BDT signal region (right). Plots are shown for the electron, muon, and combined electron and muon channels.

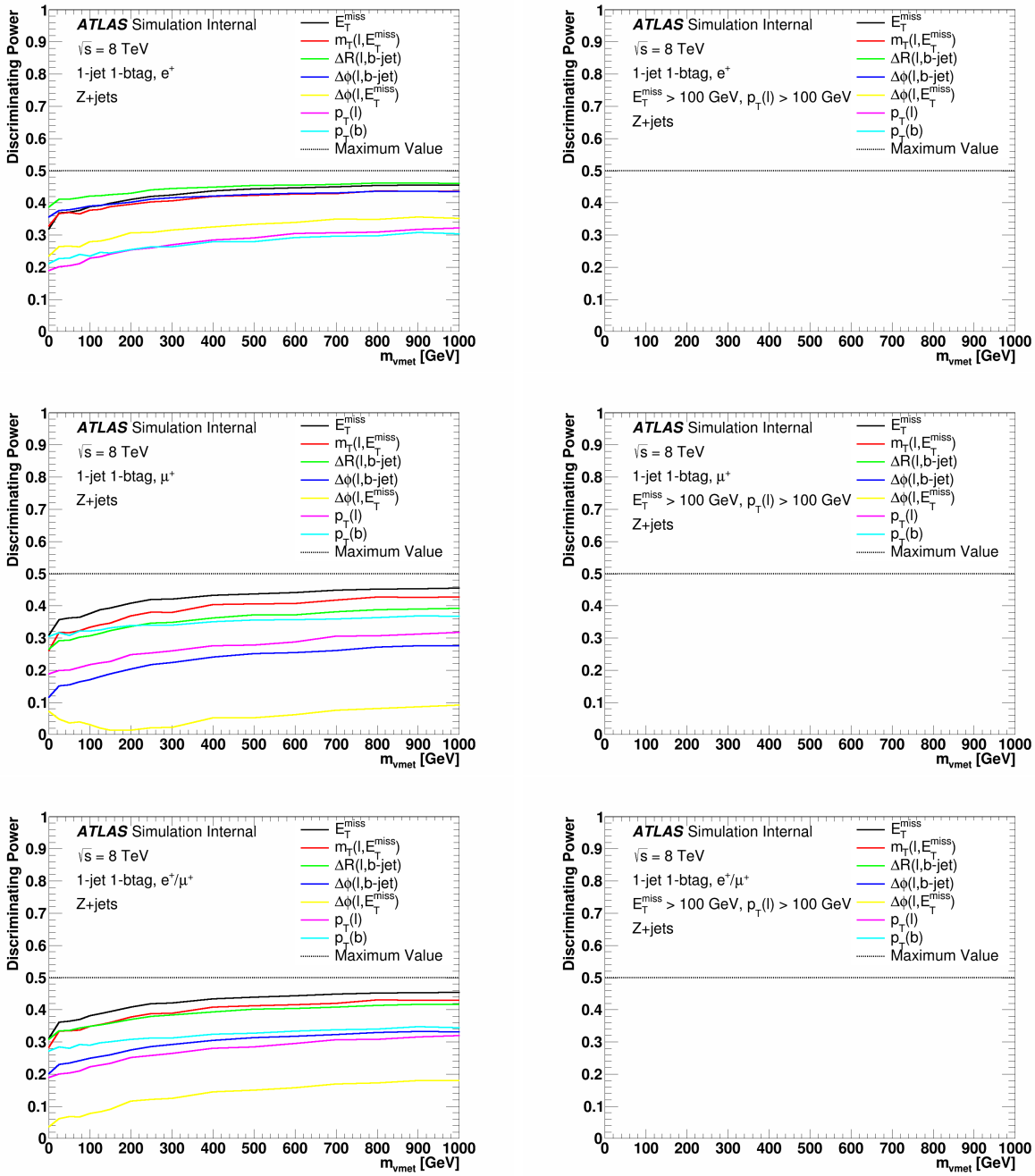

Figure G.8: The discriminating power of the input variables of the BDT as a function of the mass of the v_{met} particle for the Z+jets processes in the pre-selection+lepton charge cut region (left) and in the BDT signal region (right). Plots are shown for the electron, muon, and combined electron and muon channels. The empty plots on the right indicate that there are no Z+jets events in the BDT signal region.

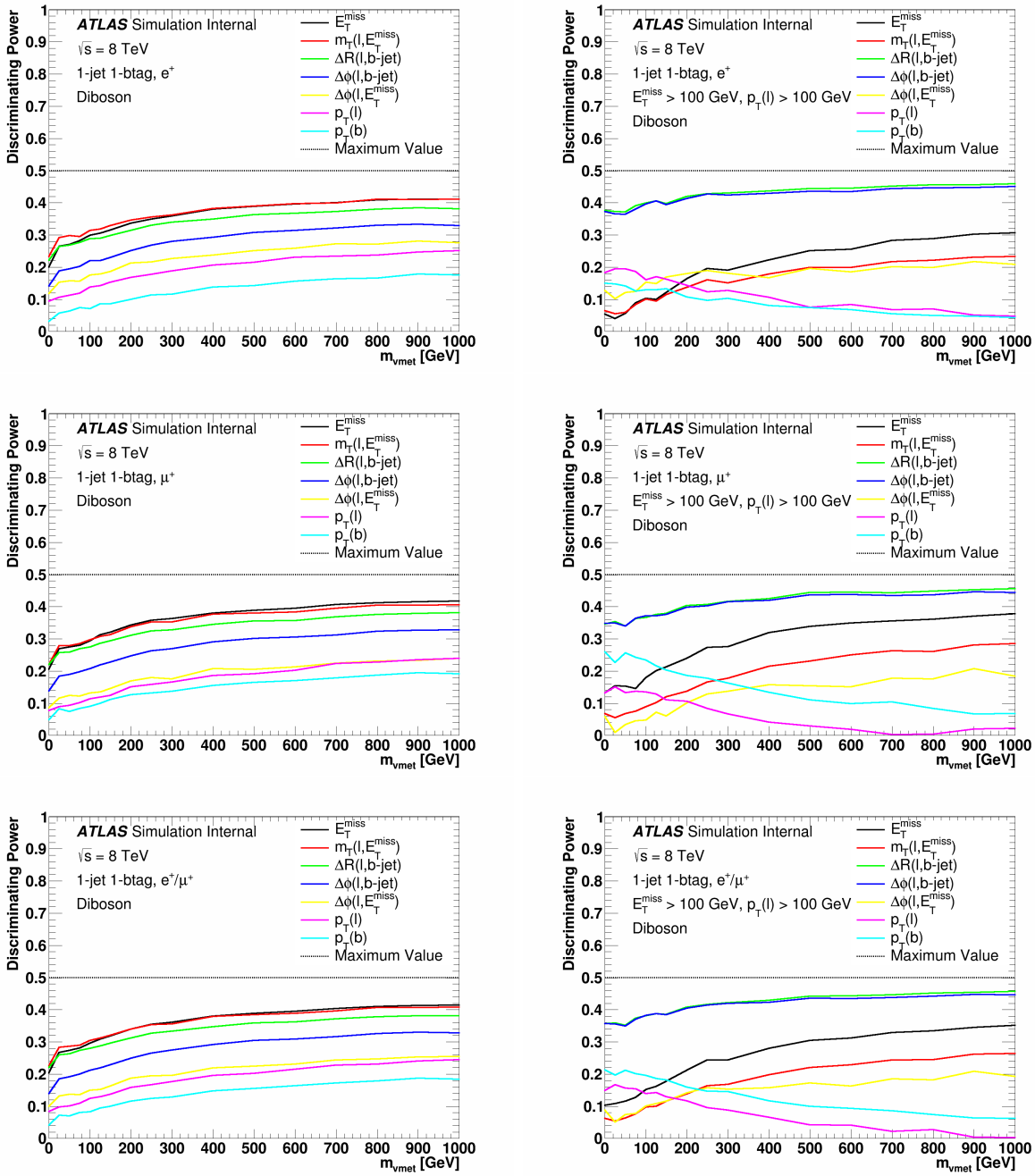

Figure G.9: The discriminating power of the input variables of the BDT as a function of the mass of the v_{met} particle for the diboson processes in the pre-selection+lepton charge cut region (left) and in the BDT signal region (right). Plots are shown for the electron, muon, and combined electron and muon channels.

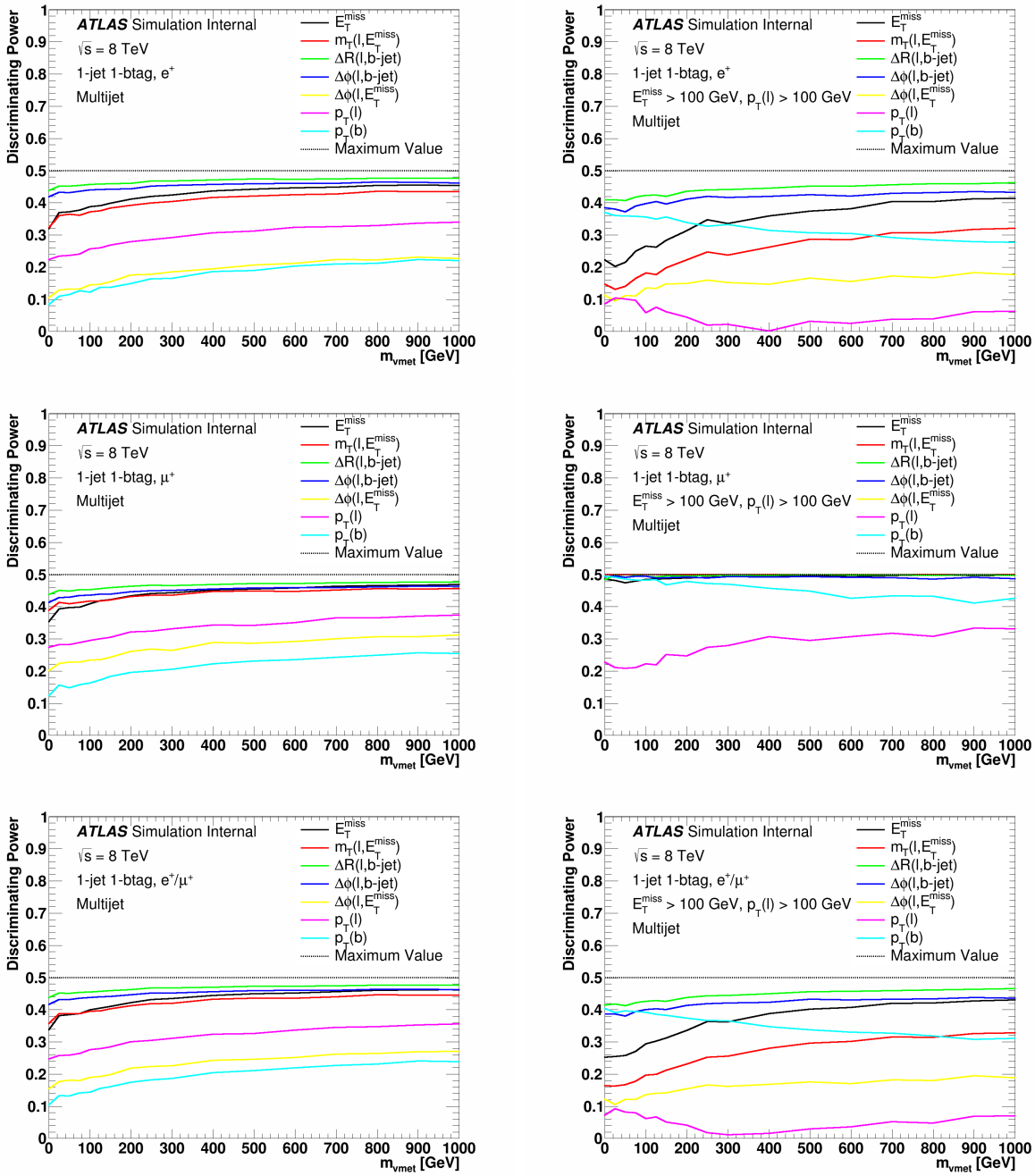

Figure G.10: The discriminating power of the input variables of the BDT as a function of the mass of the v_{met} particle for the multijet estimation in the pre-selection+lepton charge cut region (left) and in the BDT signal region (right). Plots are shown for the electron, muon, and combined electron and muon channels.

Appendix H

13 TeV control region plots

This appendix presents plots comparing the SM predictions to the data observations in the various control regions. Distributions of the $m_{\mathrm{T}}(\ell, E_{\mathrm{T}}^{\mathrm{miss}})$, $E_{\mathrm{T}}^{\mathrm{miss}}$, $p_{\mathrm{T}}(\ell)$, $p_{\mathrm{T}}(b)$, $\Delta\mathrm{R}(\ell, b)$, $\Delta\phi(\ell, b)$, and $\Delta\phi(\ell, E_{\mathrm{T}}^{\mathrm{miss}})$ are shown in the preselection region (Section H) and in CR1 (Section H).

Pre-selection region

This section presents distributions of variables for simulated background and data events in the pre-selection region defined in Section 7.2. Figures H.1 and H.2 show the transverse mass between the lepton and missing transverse energy, $m_{\mathrm{T}}(\ell, E_{\mathrm{T}}^{\mathrm{miss}})$. Figures H.3 and H.4 show the missing transverse energy, $E_{\mathrm{T}}^{\mathrm{miss}}$. Figures H.5 and H.6 show the transverse momentum of the lepton, $p_{\mathrm{T}}(\ell)$. Figures H.7 and H.8 show the transverse momentum of the b-jet, $p_{\mathrm{T}}(b)$. Figures H.9 and H.10 show spatial separation in $\eta - \phi$ space between the lepton and b-jet, $\Delta\mathrm{R}(\ell, b)$. Figures H.11 and H.12 show angular separation in ϕ between the lepton and b-jet, $\Delta\phi(\ell, b)$. Figures H.13 and H.14 show angular separation in ϕ between the lepton and the missing transverse energy, $\Delta\phi(\ell, E_{\mathrm{T}}^{\mathrm{miss}})$.

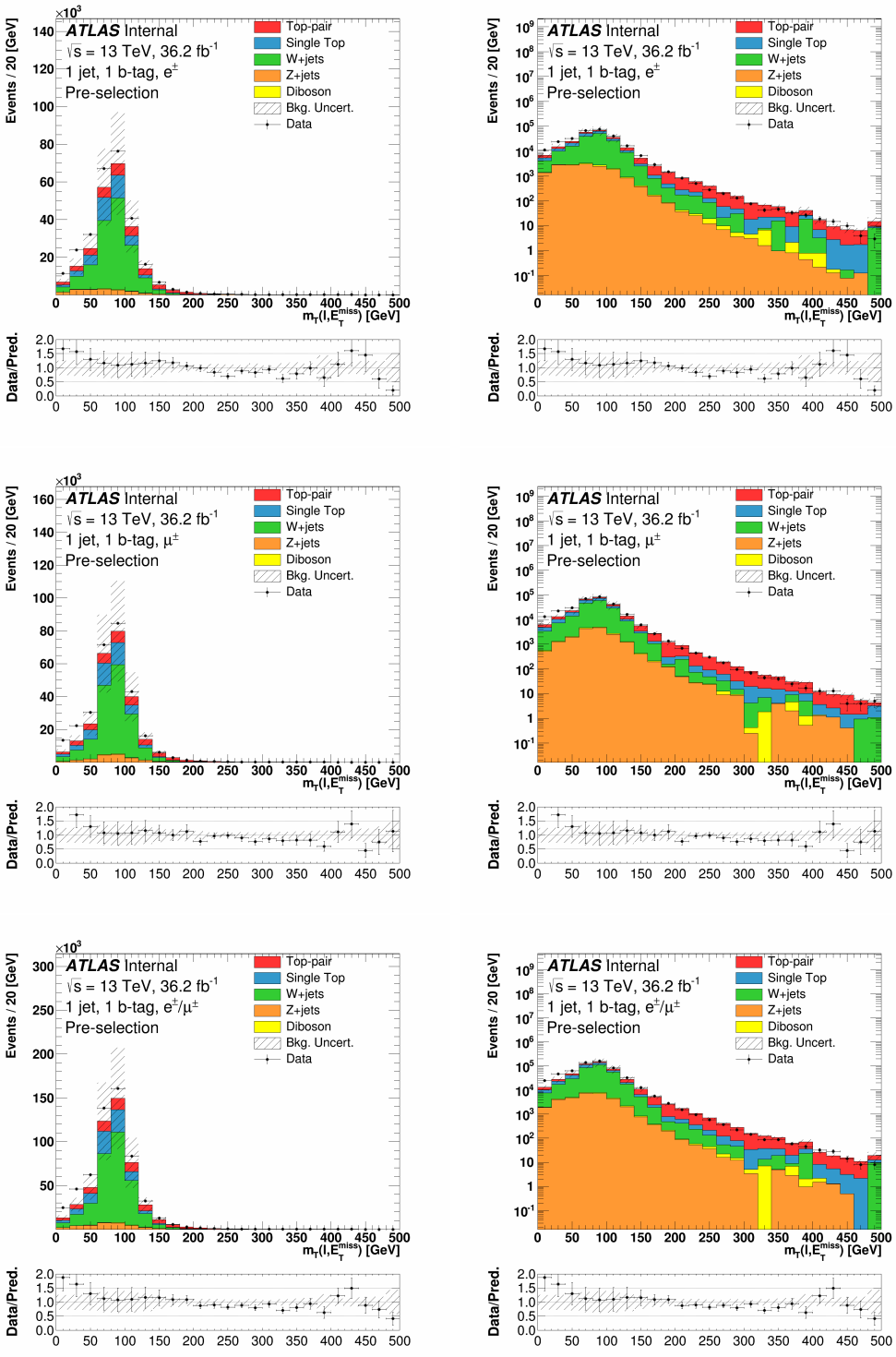

Figure H.1: Distributions of $m_{\mathrm{T}}(\ell, E_{\mathrm{T}}^{\mathrm{miss}})$ for the electron (top), the muon (middle), and the combined (bottom) channels in the pre-selection region, in linear (left) and log (right) scale. The uncertainty band on the expected background corresponds to the errors due to the statistical uncertainties added in quadrature with the cross-section and normalization uncertainties.

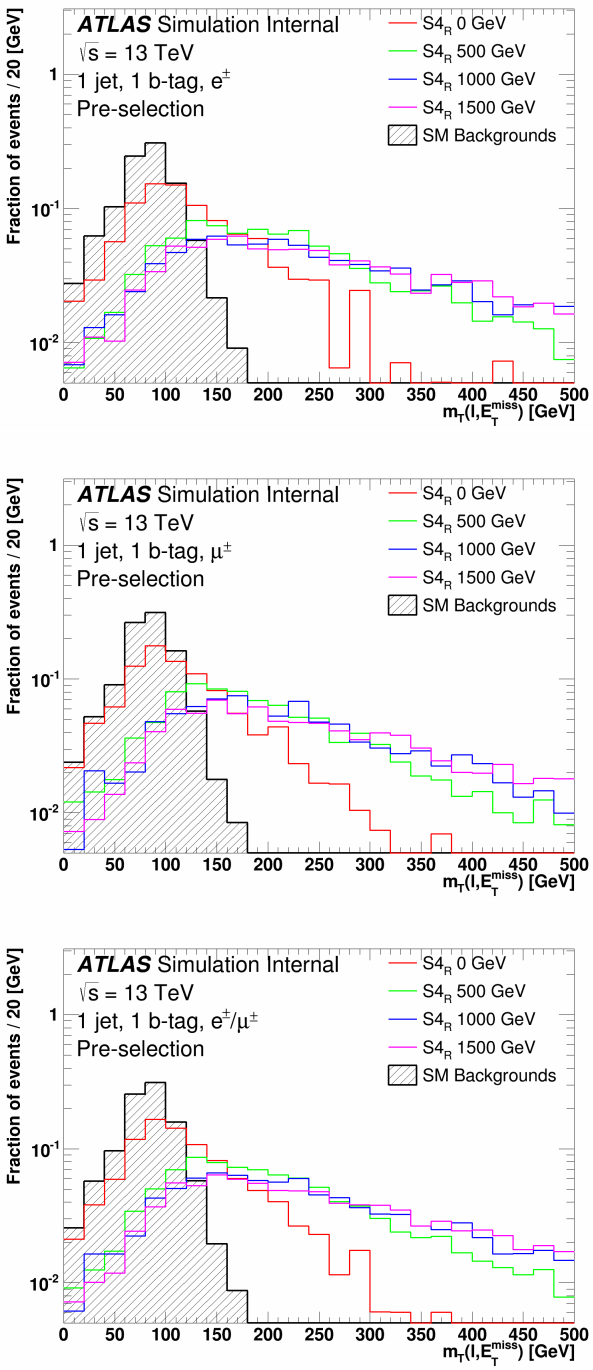

Figure H.2: Distributions of $m_{\mathrm{T}}(\ell, E_{\mathrm{T}}^{\mathrm{miss}})$ normalized to unity for the electron (top), the muon (middle), and the combined (bottom) channels in the pre-selection region for various mass hypotheses of the $\mathrm{S4_R}$ model. The SM background is also shown.

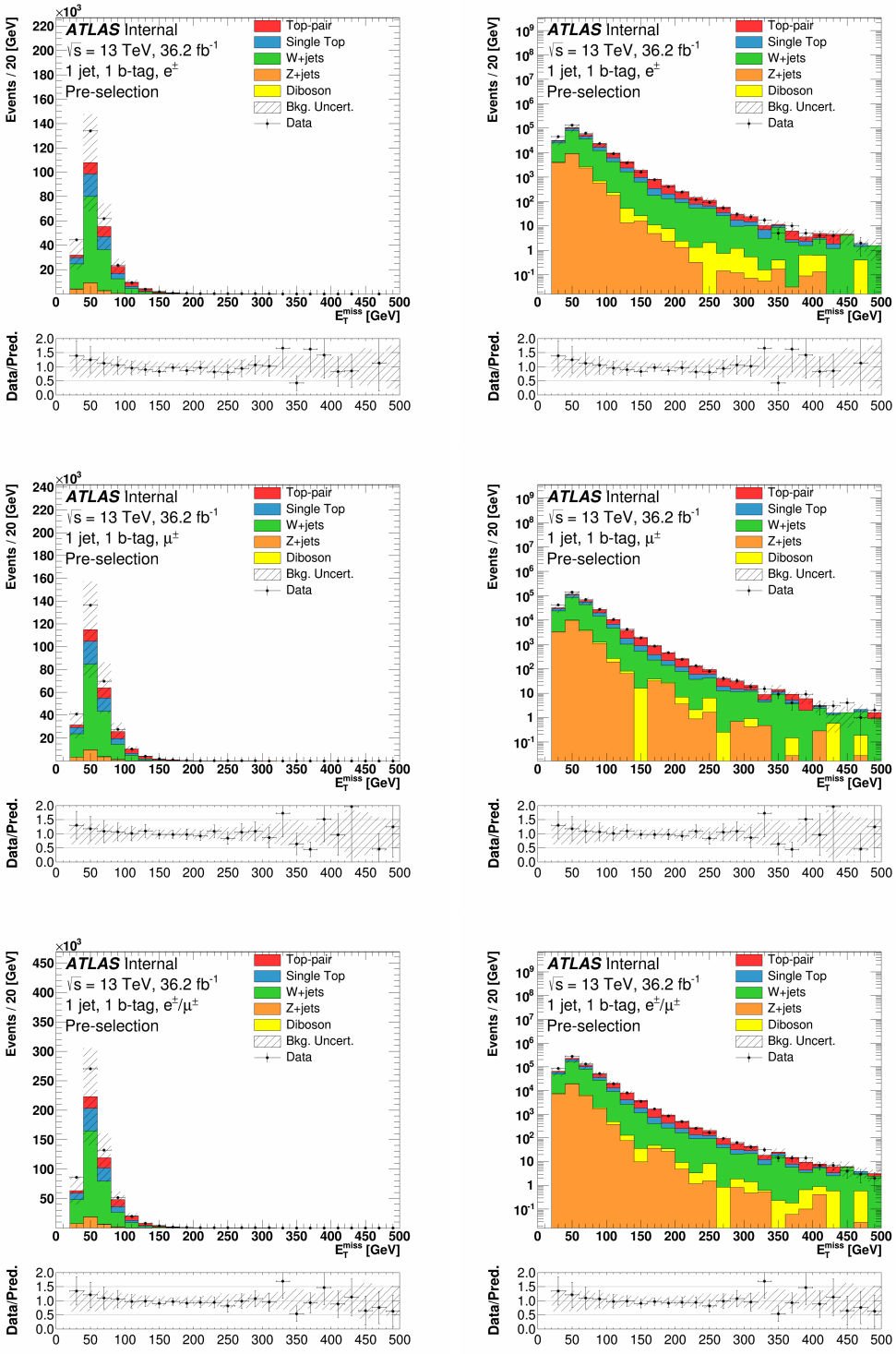

Figure H.3: Distributions of $E_{\mathrm{T}}^{\mathrm{miss}}$ for the electron (top), the muon (middle), and the combined (bottom) channels in the pre-selection region, in linear (left) and log (right) scale. The uncertainty band on the expected background corresponds to the errors due to the statistical uncertainties added in quadrature with the cross-section and normalization uncertainties.

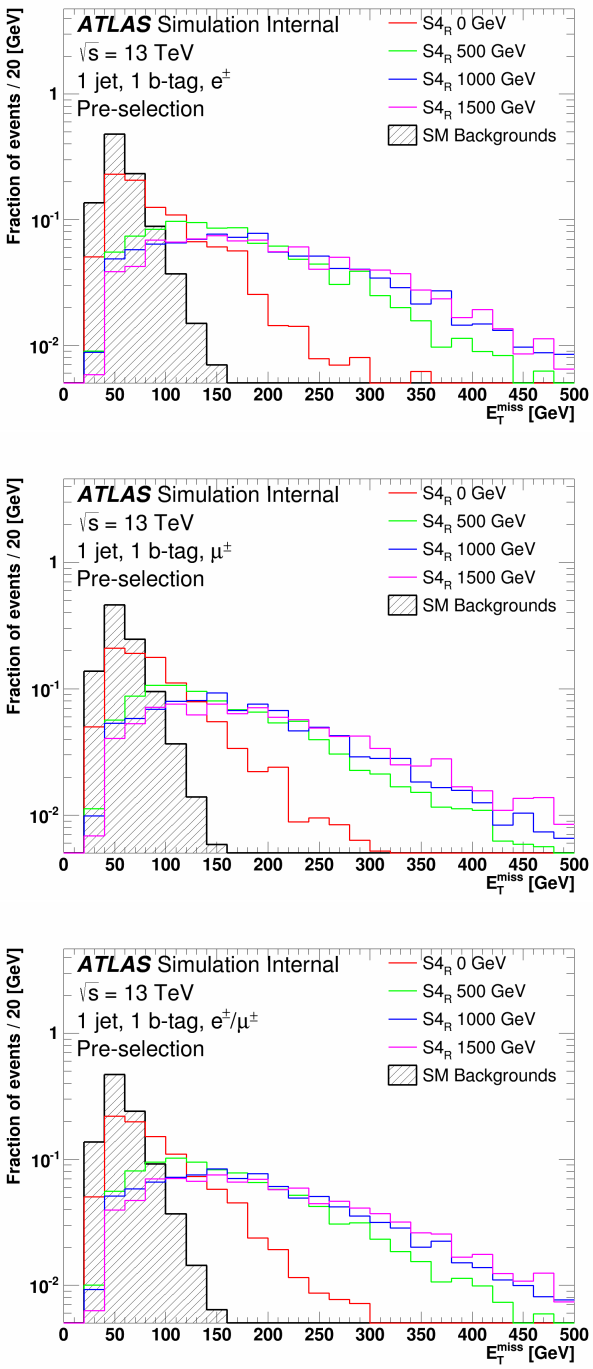

Figure H.4: Distributions of $E_{\mathrm{T}}^{\mathrm{miss}}$ normalized to unity for the electron (top), the muon (middle), and the combined (bottom) channels in the pre-selection region for various mass hypotheses of the $\mathrm{S4_R}$ model. The SM background is also shown.

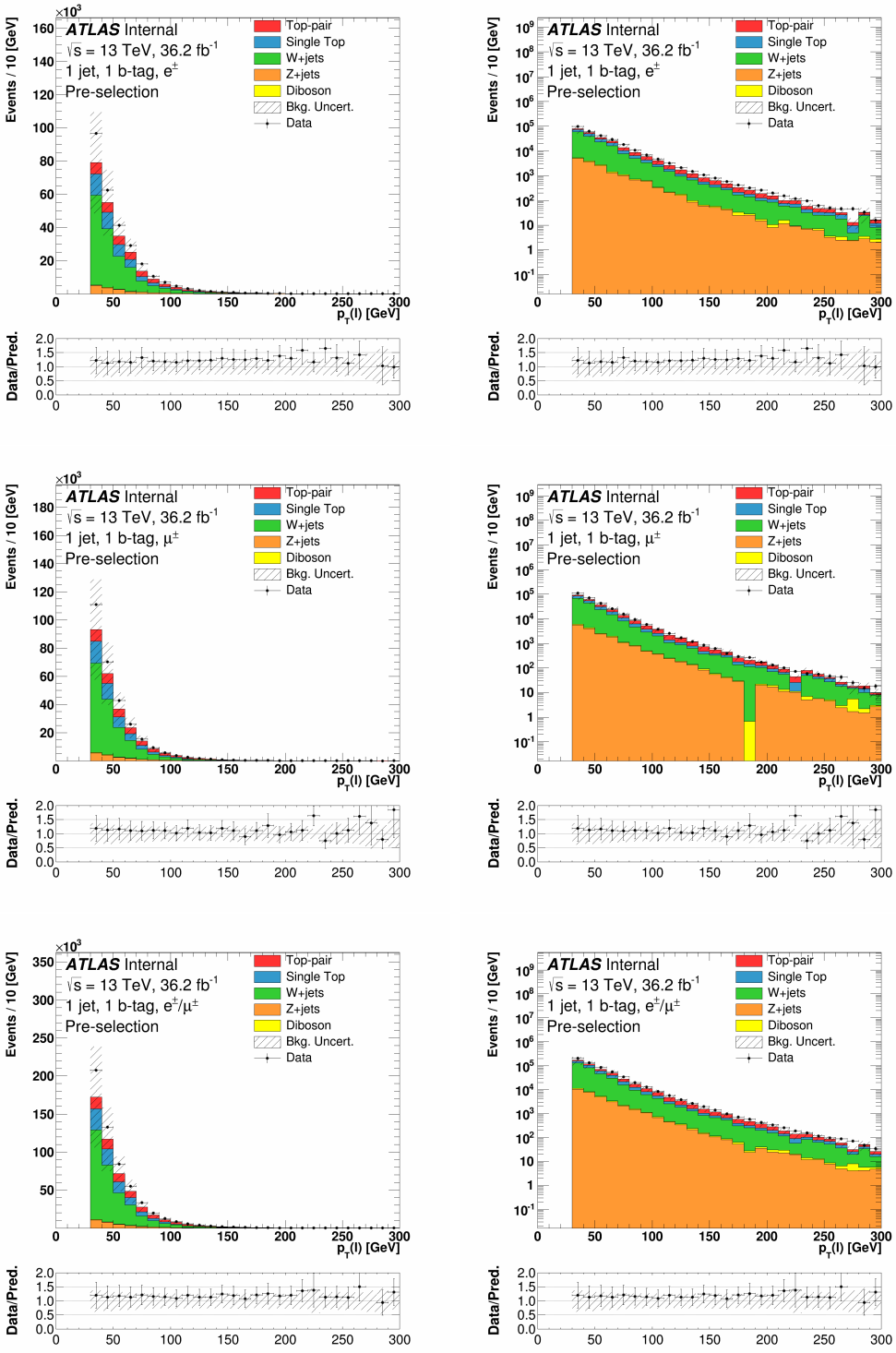

Figure H.5: Distributions of $p_{\mathrm{T}}(\ell)$ for the electron (top), the muon (middle), and the combined (bottom) channels in the pre-selection region, in linear (left) and log (right) scale. The uncertainty band on the expected background corresponds to the errors due to the statistical uncertainties added in quadrature with the cross-section and normalization uncertainties.

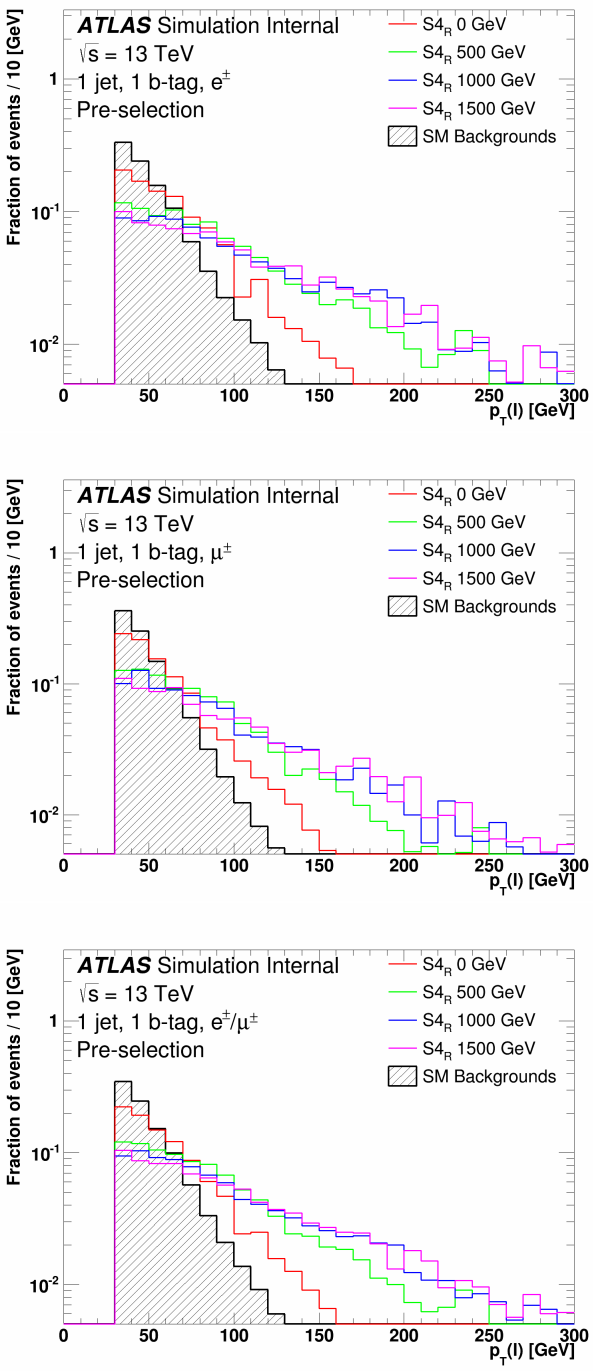

Figure H.6: Distributions of $p_{\mathrm{T}}(\ell)$ normalized to unity for the electron (top), the muon (middle), and the combined (bottom) channels in the pre-selection region for various mass hypotheses of the $\mathrm{S4_R}$ model. The SM background is also shown.

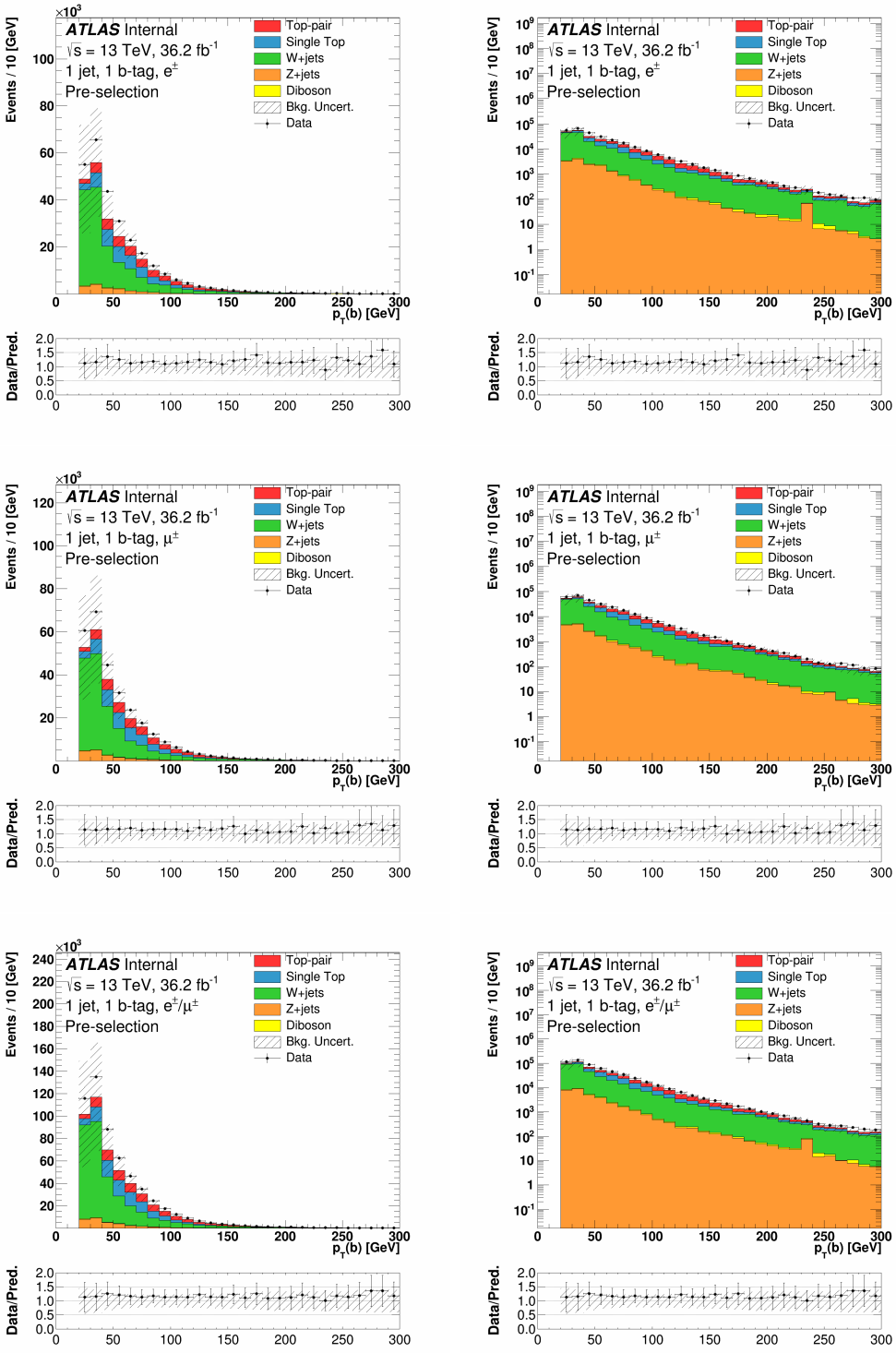

Figure H.7: Distributions of $p_{\mathrm{T}}(b)$ for the electron (top), the muon (middle), and the combined (bottom) channels in the pre-selection region, in linear (left) and log (right) scale. The uncertainty band on the expected background corresponds to the errors due to the statistical uncertainties added in quadrature with the cross-section and normalization uncertainties.

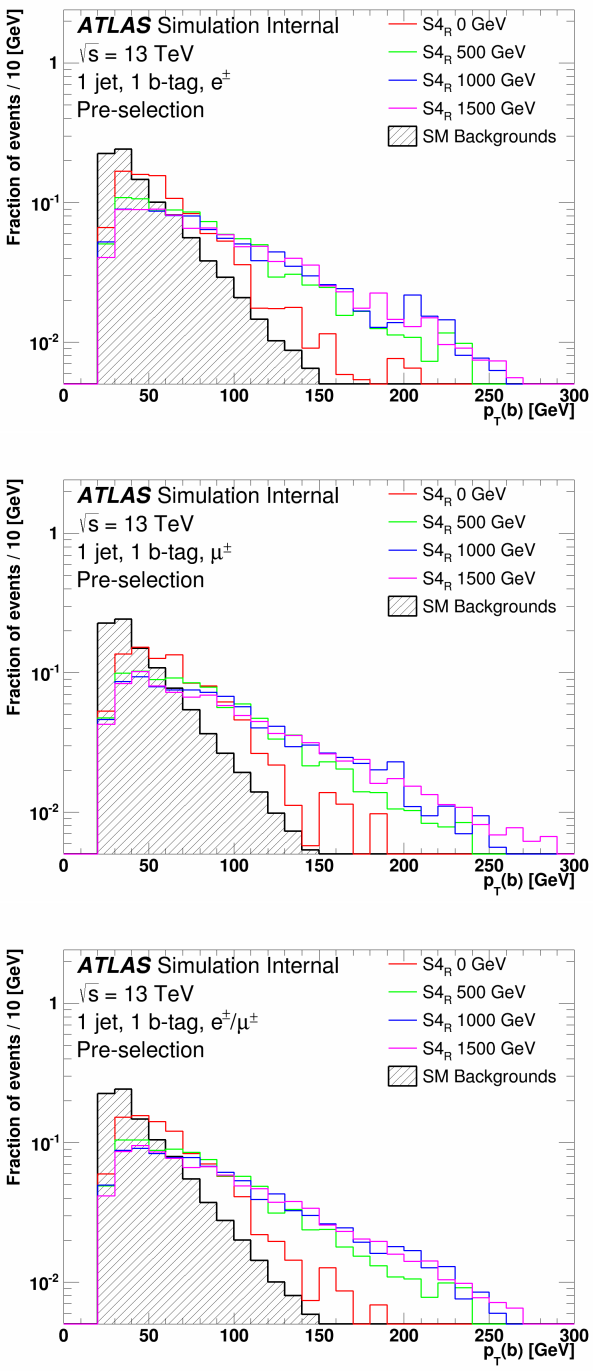

Figure H.8: Distributions of $p_{\mathrm{T}}(b)$ normalized to unity for the electron (top), the muon (middle), and the combined (bottom) channels in the pre-selection region for various mass hypotheses of the $\mathrm{S4_R}$ model. The SM background is also shown.

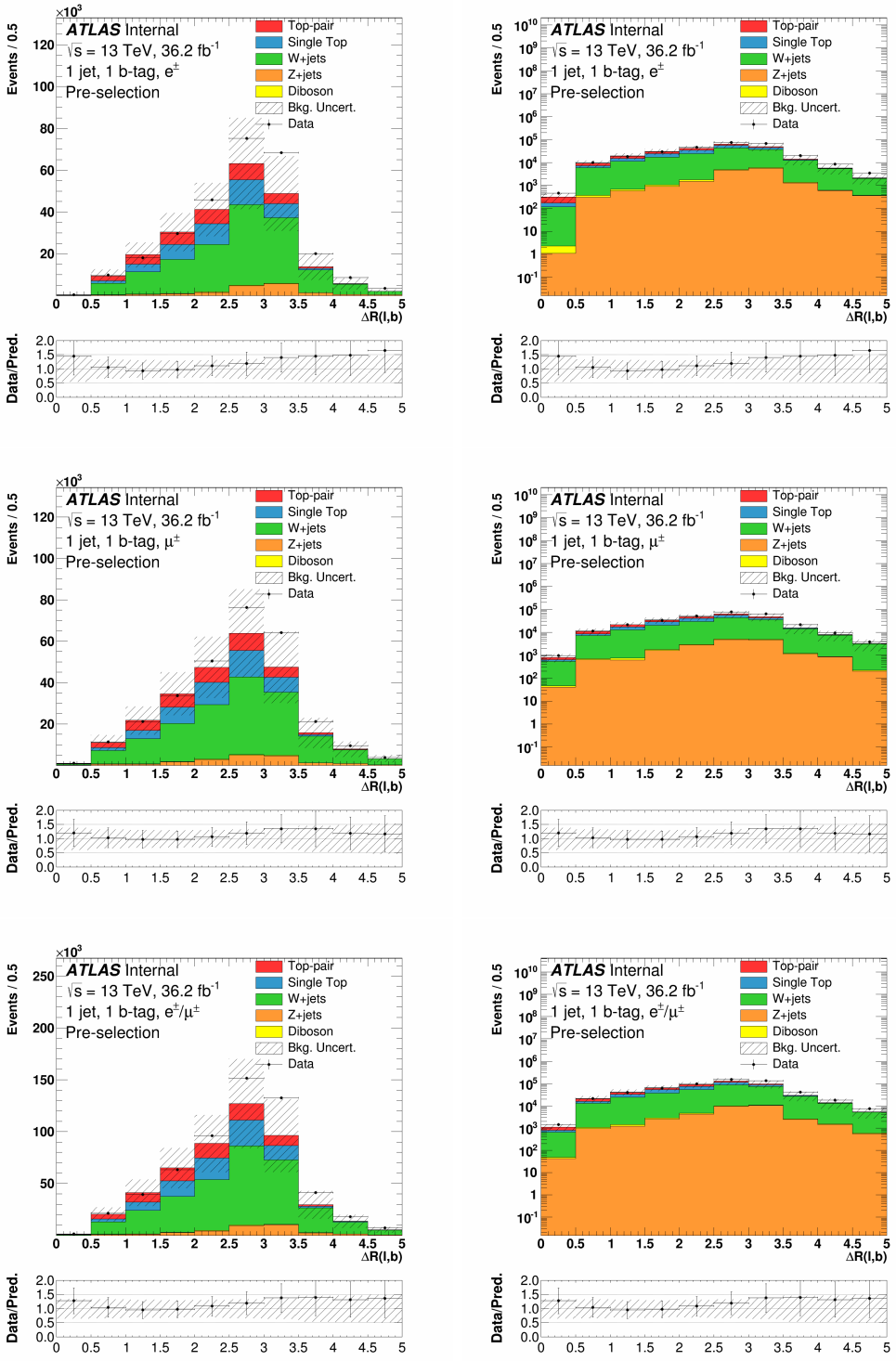

Figure H.9: Distributions of $\Delta\mathrm{R}(\ell, b)$ for the electron (top), the muon (middle), and the combined (bottom) channels in the pre-selection region, in linear (left) and log (right) scale. The uncertainty band on the expected background corresponds to the errors due to the statistical uncertainties added in quadrature with the cross-section and normalization uncertainties.

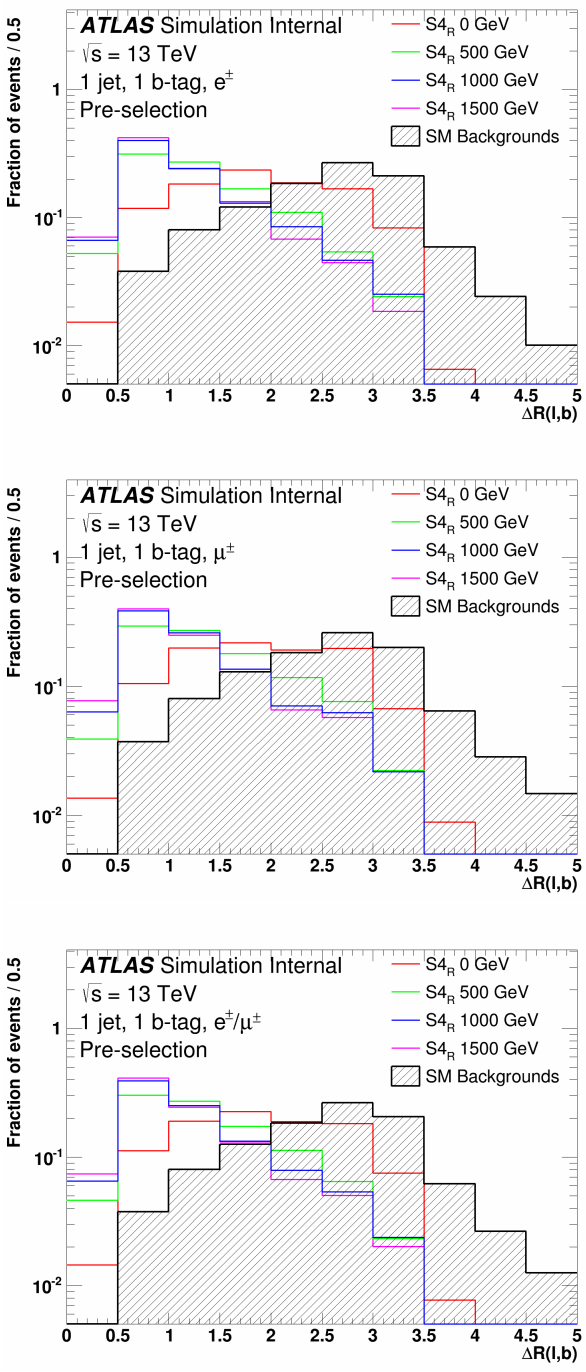

Figure H.10: Distributions of $\Delta\mathrm{R}(\ell, b)$ normalized to unity for the electron (top), the muon (middle), and the combined (bottom) channels in the pre-selection region for various mass hypotheses of the $\mathrm{S4_R}$ model. The SM background is also shown.

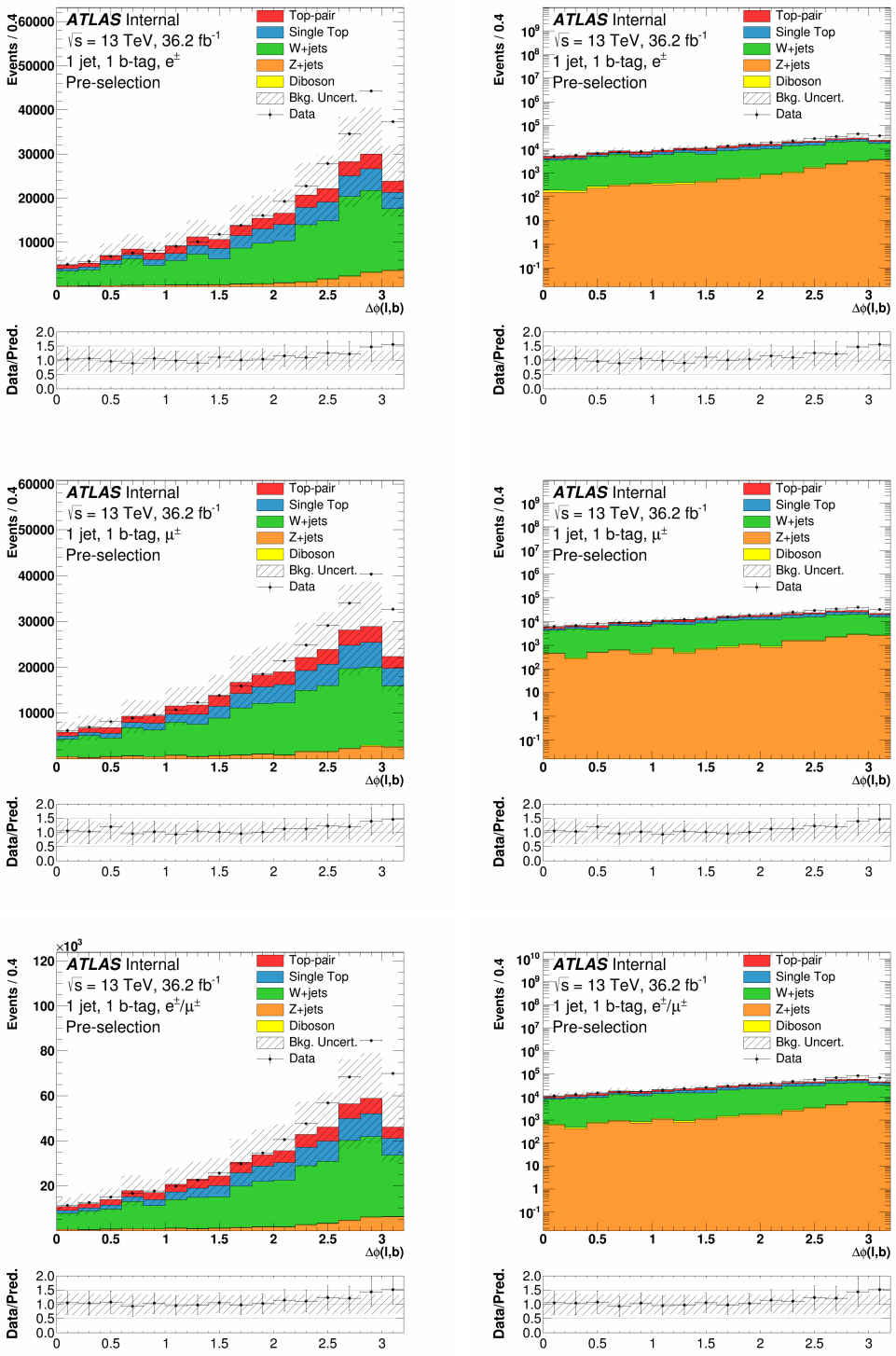

Figure H.11: Distributions of $\Delta\phi(\ell, b)$ for the electron (top), the muon (middle), and the combined (bottom) channels in the pre-selection region, in linear (left) and log (right) scale. The uncertainty band on the expected background corresponds to the errors due to the statistical uncertainties added in quadrature with the cross-section and normalization uncertainties.

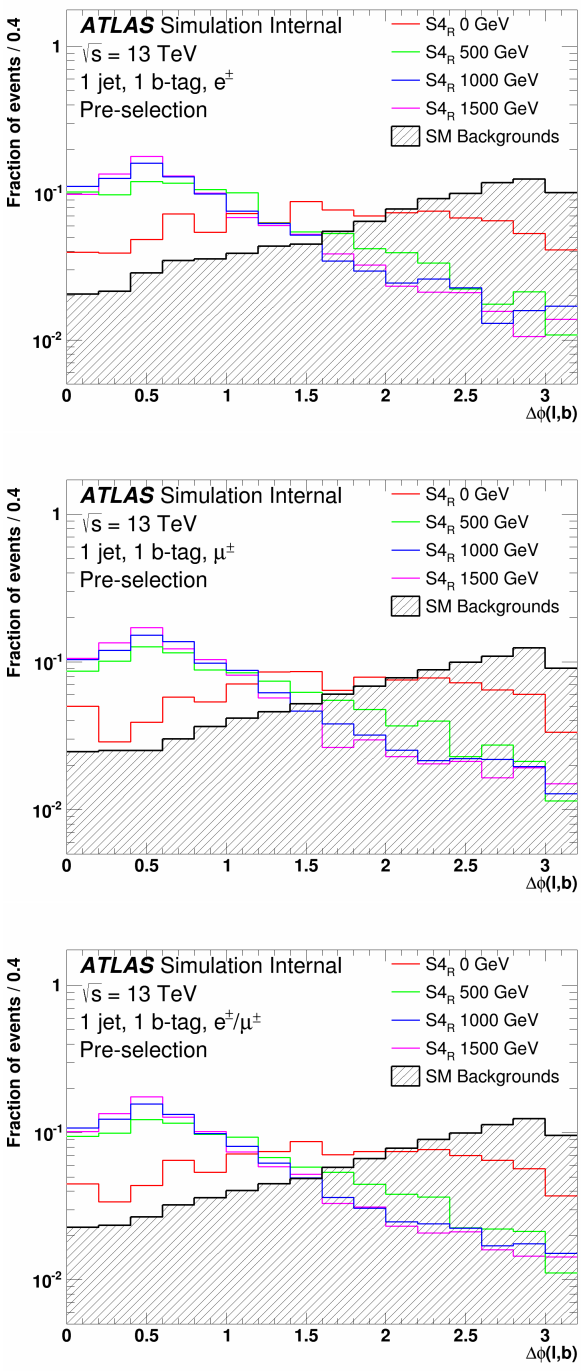

Figure H.12: Distributions of $\Delta\phi(\ell, b)$ normalized to unity for the electron (top), the muon (middle), and the combined (bottom) channels in the pre-selection region for various mass hypotheses of the $S4_R$ model. The SM background is also shown.

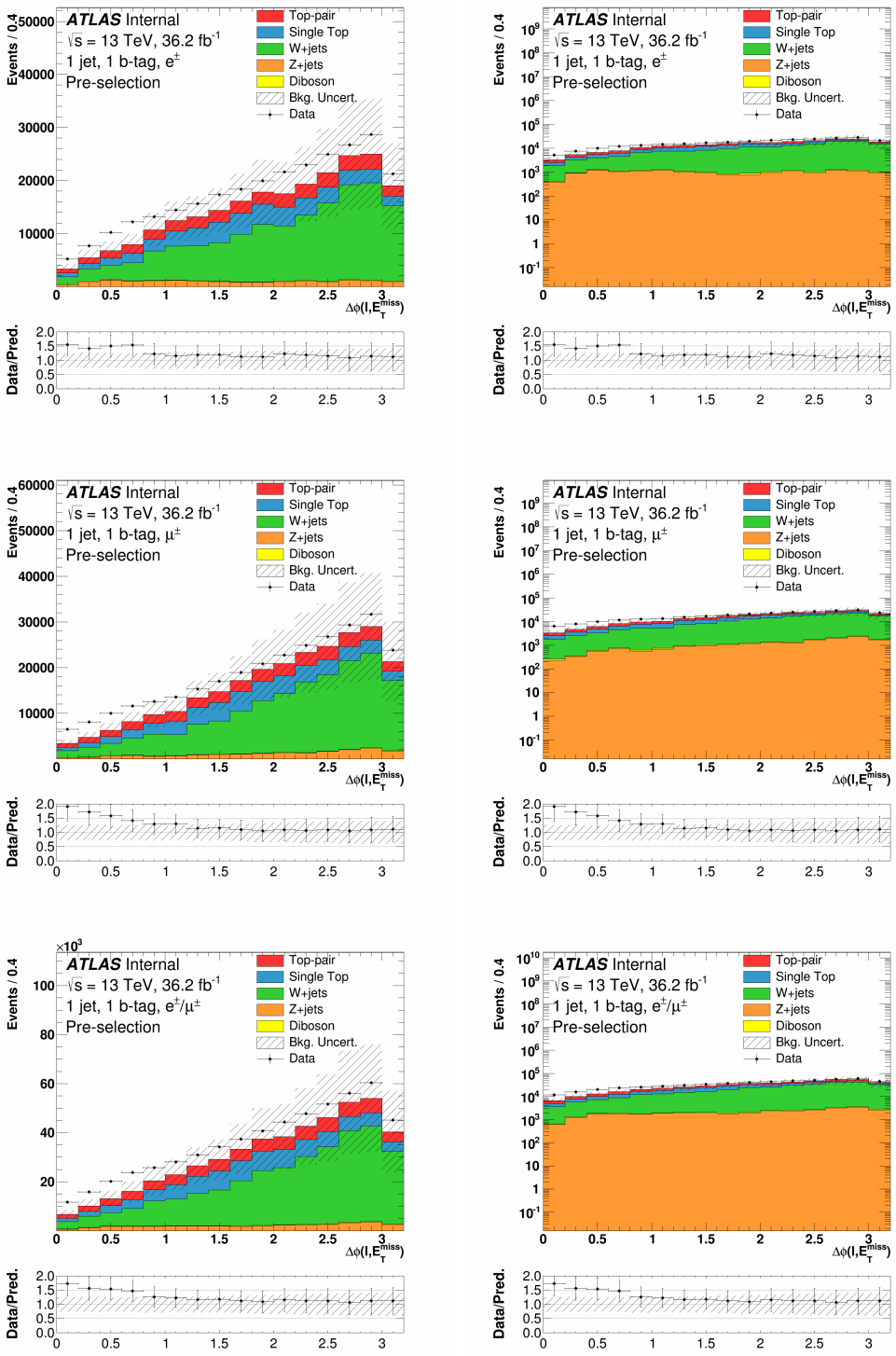

Figure H.13: Distributions of $\Delta\phi(\ell, E_{\mathrm{T}}^{\mathrm{miss}})$ for the electron (top), the muon (middle), and the combined (bottom) channels in the pre-selection region, in linear (left) and log (right) scale. The uncertainty band on the expected background corresponds to the errors due to the statistical uncertainties added in quadrature with the cross-section and normalization uncertainties.

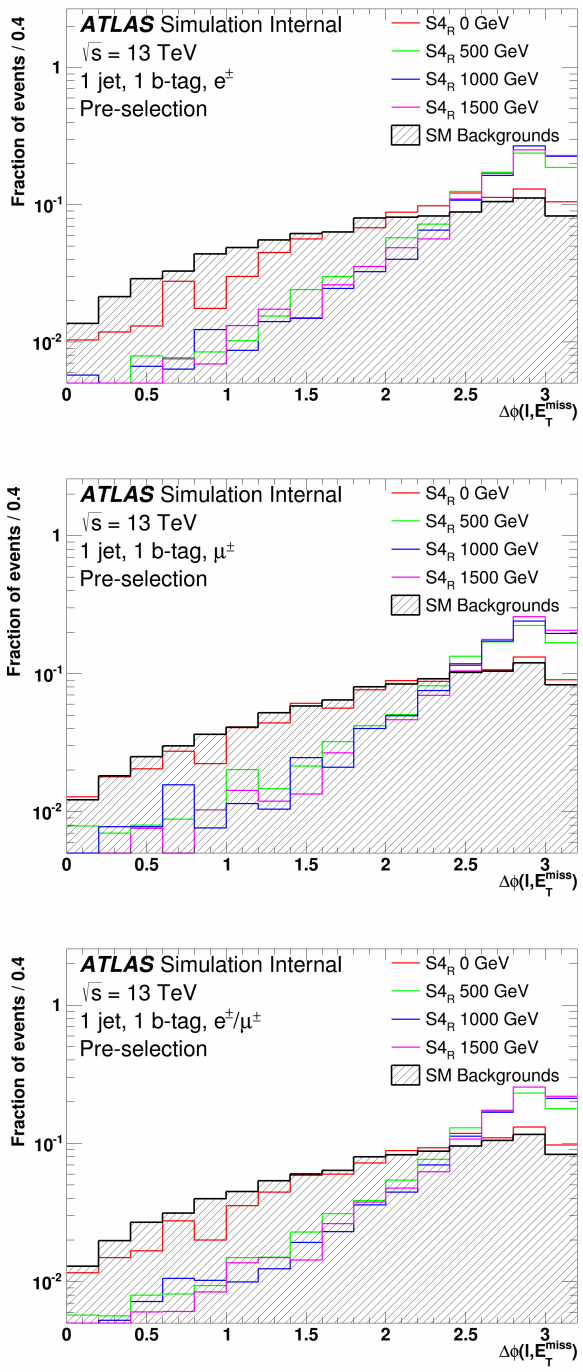

Figure H.14: Distributions of $\Delta\phi(\ell, E_{\mathrm{T}}^{\mathrm{miss}})$ normalized to unity for the electron (top), the muon (middle), and the combined (bottom) channels in the pre-selection region for various mass hypotheses of the $\mathrm{S4_R}$ model. The SM background is also shown.

CR1

This section presents distribution of variables for simulated background and data events in CR1 defined in Section 7.4. Figure H.15 shows the transverse mass between the lepton and missing transverse energy, $m_{\mathrm{T}}(\ell, E_{\mathrm{T}}^{\mathrm{miss}})$. Figure H.16 shows the missing transverse energy, $E_{\mathrm{T}}^{\mathrm{miss}}$. Figure H.17 shows the transverse momentum of the lepton, $p_{\mathrm{T}}(\ell)$. Figure H.18 shows the transverse momentum of the b-jet, $p_{\mathrm{T}}(b)$. Figure H.19 shows spatial separation in $\eta - \phi$ space between the lepton and b-jet, $\Delta\mathrm{R}(\ell, b)$. Figure H.20 shows angular separation in ϕ between the lepton and b-jet, $\Delta\phi(\ell, b)$. Figure H.21 shows angular separation in ϕ between the lepton and the missing transverse energy, $\Delta\phi(\ell, E_{\mathrm{T}}^{\mathrm{miss}})$.

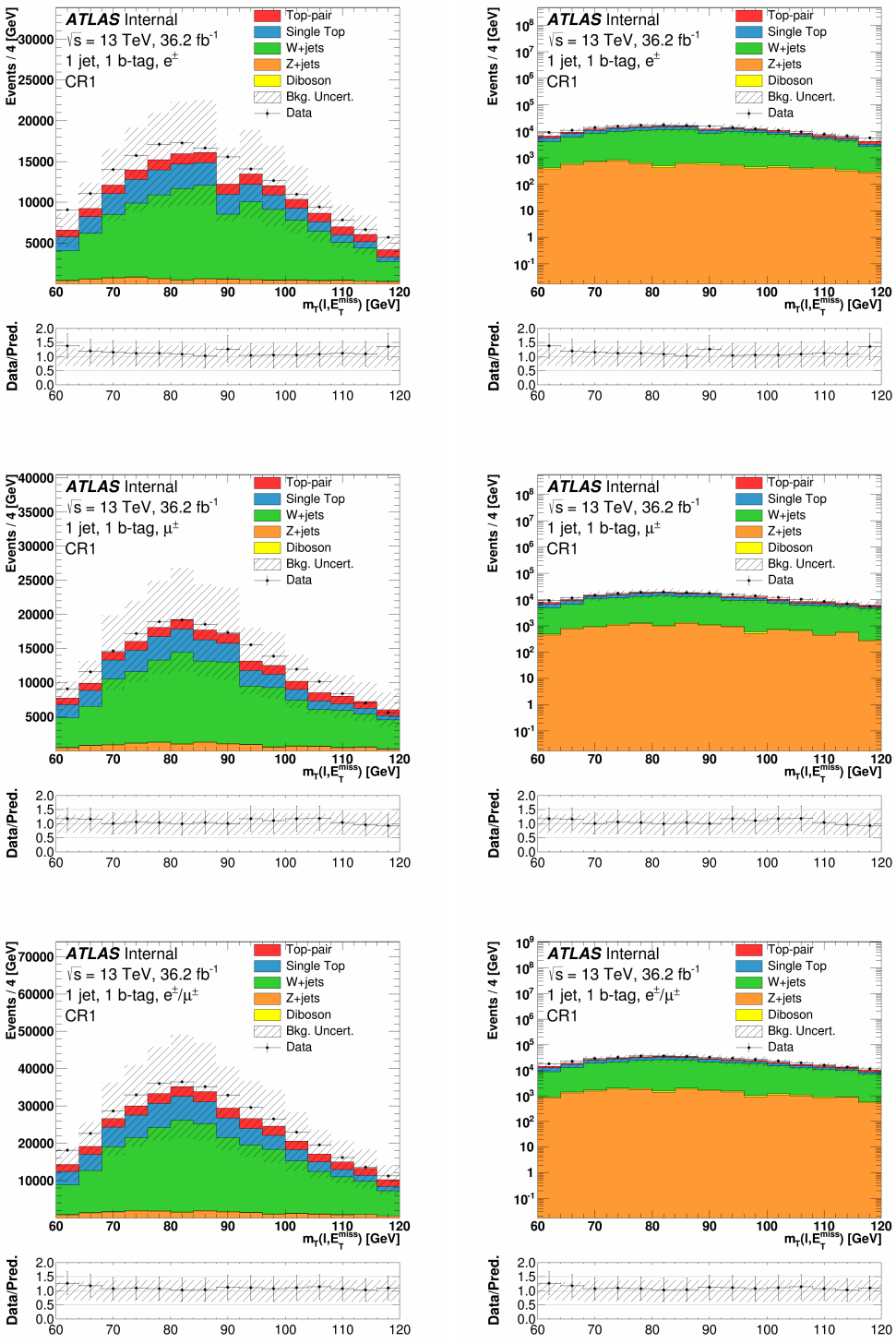

Figure H.15: Distributions of $m_{\mathrm{T}}(\ell, E_{\mathrm{T}}^{\mathrm{miss}})$ for the electron (top), the muon (middle), and the combined (bottom) channels in CR1, in linear (left) and log (right) scale. The uncertainty band on the expected background corresponds to the errors due to the statistical uncertainties added in quadrature with the cross-section and normalization uncertainties.

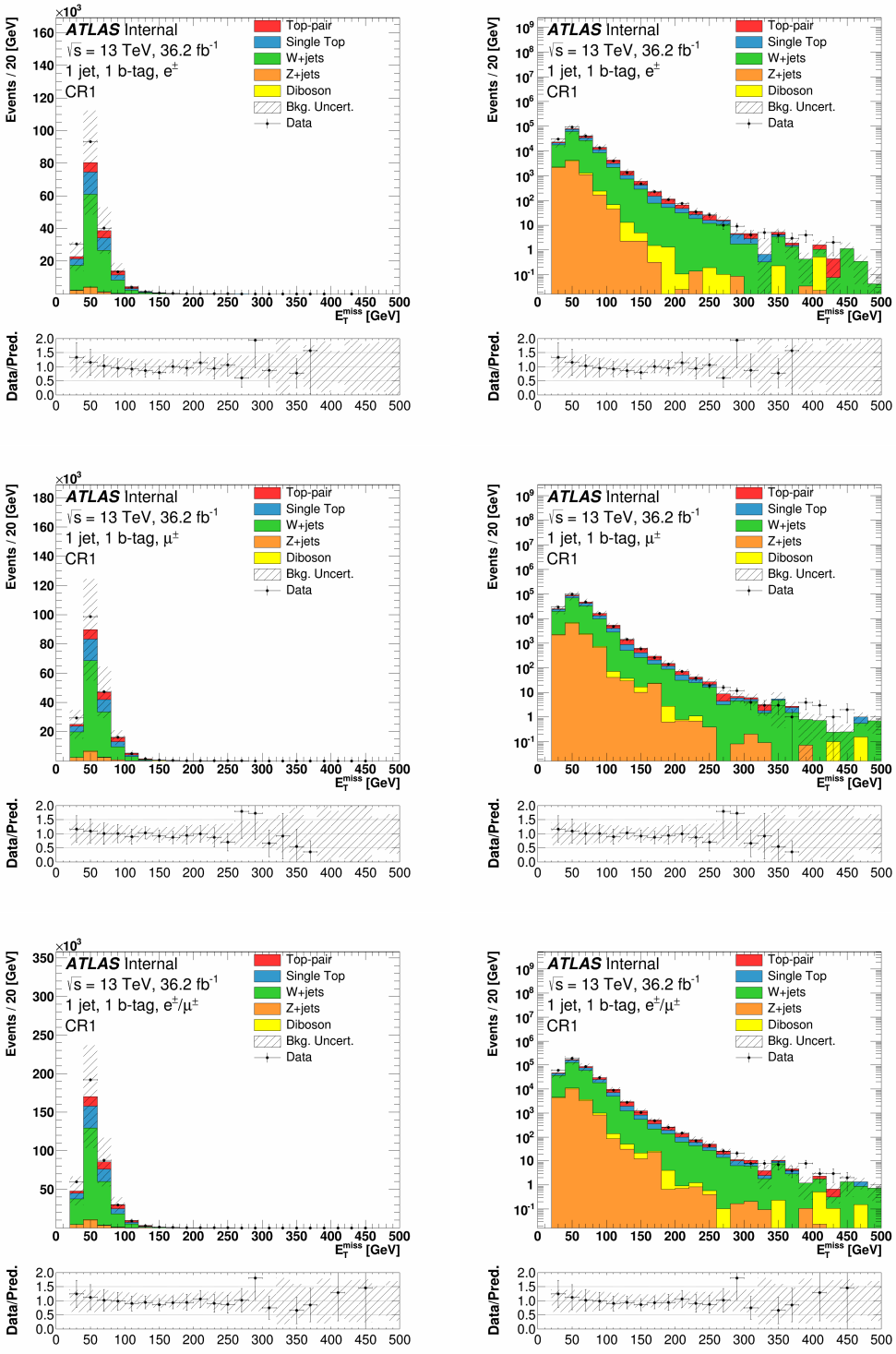

Figure H.16: Distributions of $E_{\mathrm{T}}^{\mathrm{miss}}$ for the electron (top), the muon (middle), and the combined (bottom) channels in CR1, in linear (left) and log (right) scale. The uncertainty band on the expected background corresponds to the errors due to the statistical uncertainties added in quadrature with the cross-section and normalization uncertainties.

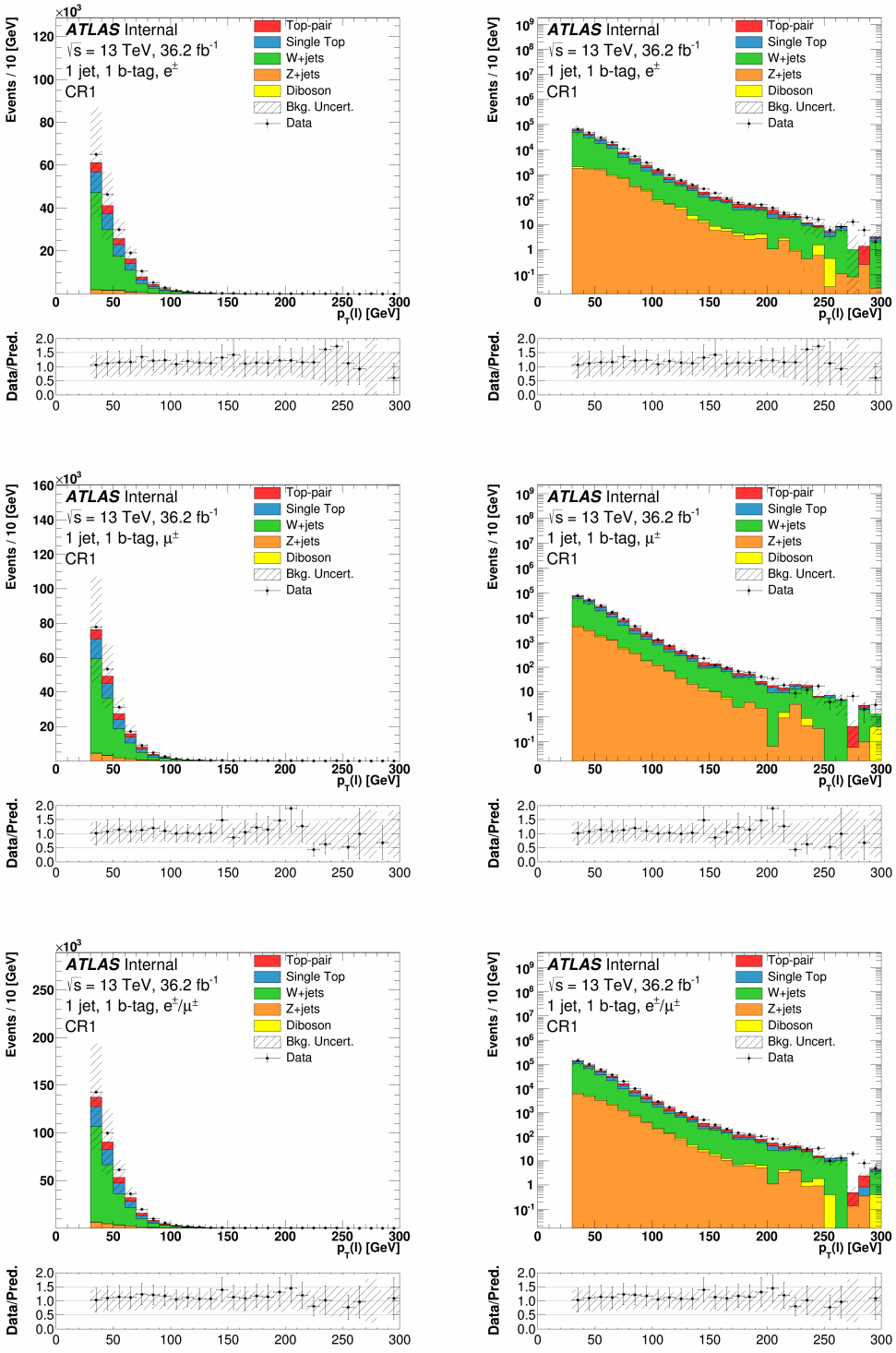

Figure H.17: Distributions of $p_{\mathrm{T}}(\ell)$ for the electron (top), the muon (middle), and the combined (bottom) channels in CR1, in linear (left) and log (right) scale. The uncertainty band on the expected background corresponds to the errors due to the statistical uncertainties added in quadrature with the cross-section and normalization uncertainties.

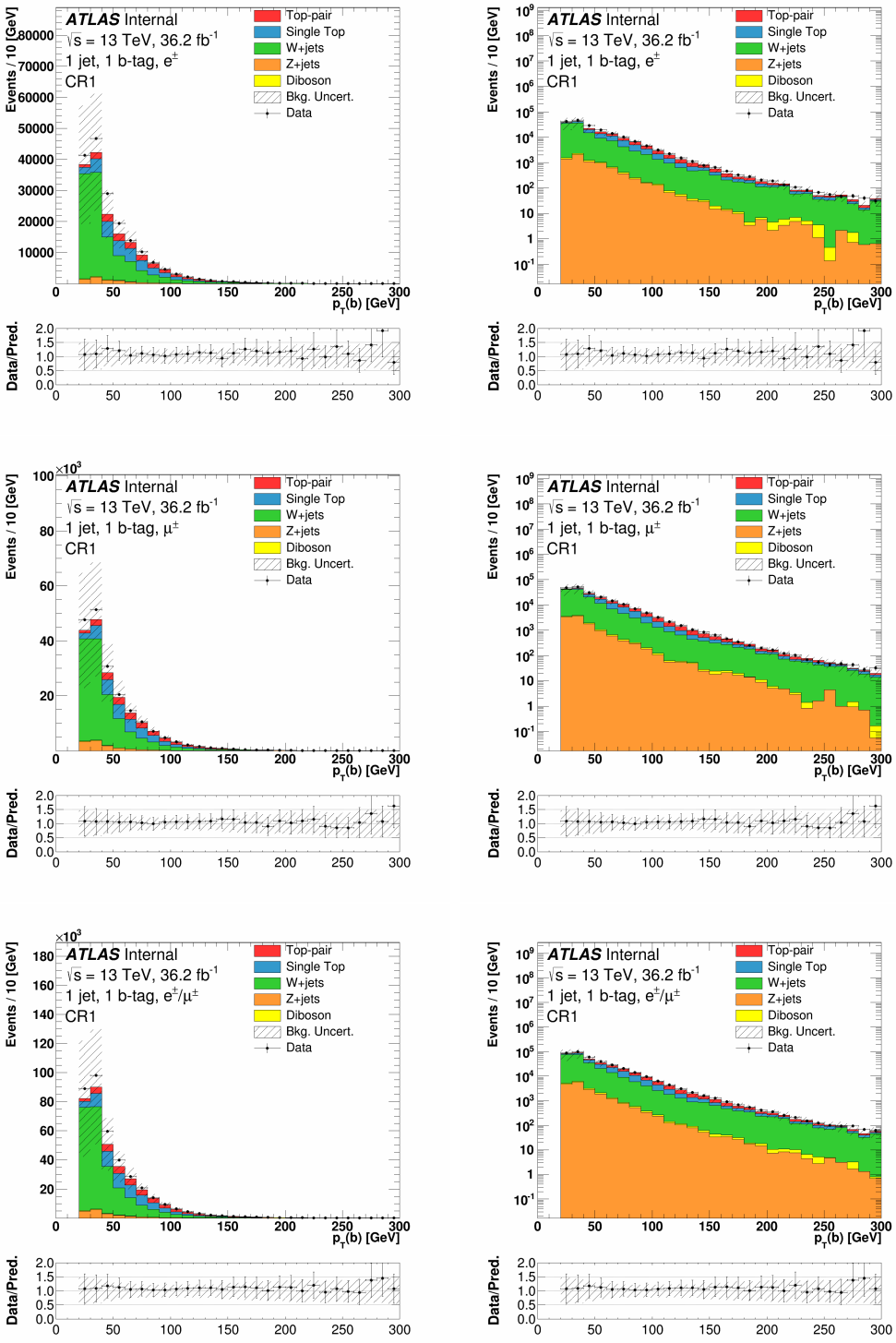

Figure H.18: Distributions of $p_{\mathrm{T}}(b)$ for the electron (top), the muon (middle), and the combined (bottom) channels in CR1, in linear (left) and log (right) scale. The uncertainty band on the expected background corresponds to the errors due to the statistical uncertainties added in quadrature with the cross-section and normalization uncertainties.

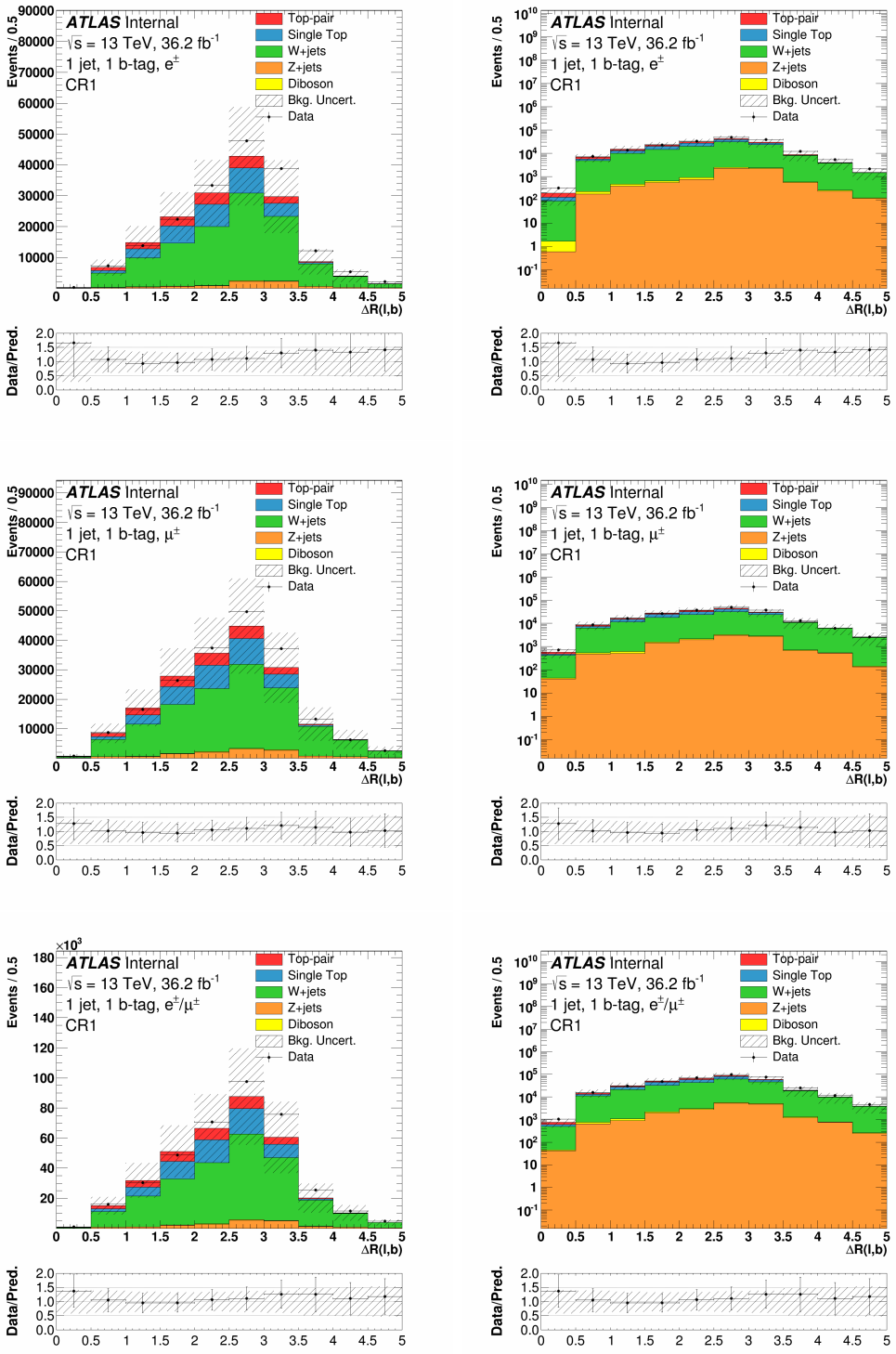

Figure H.19: Distributions of $\Delta R(\ell, b)$ for the electron (top), the muon (middle), and the combined (bottom) channels in CR1, in linear (left) and log (right) scale. The uncertainty band on the expected background corresponds to the errors due to the statistical uncertainties added in quadrature with the cross-section and normalization uncertainties.

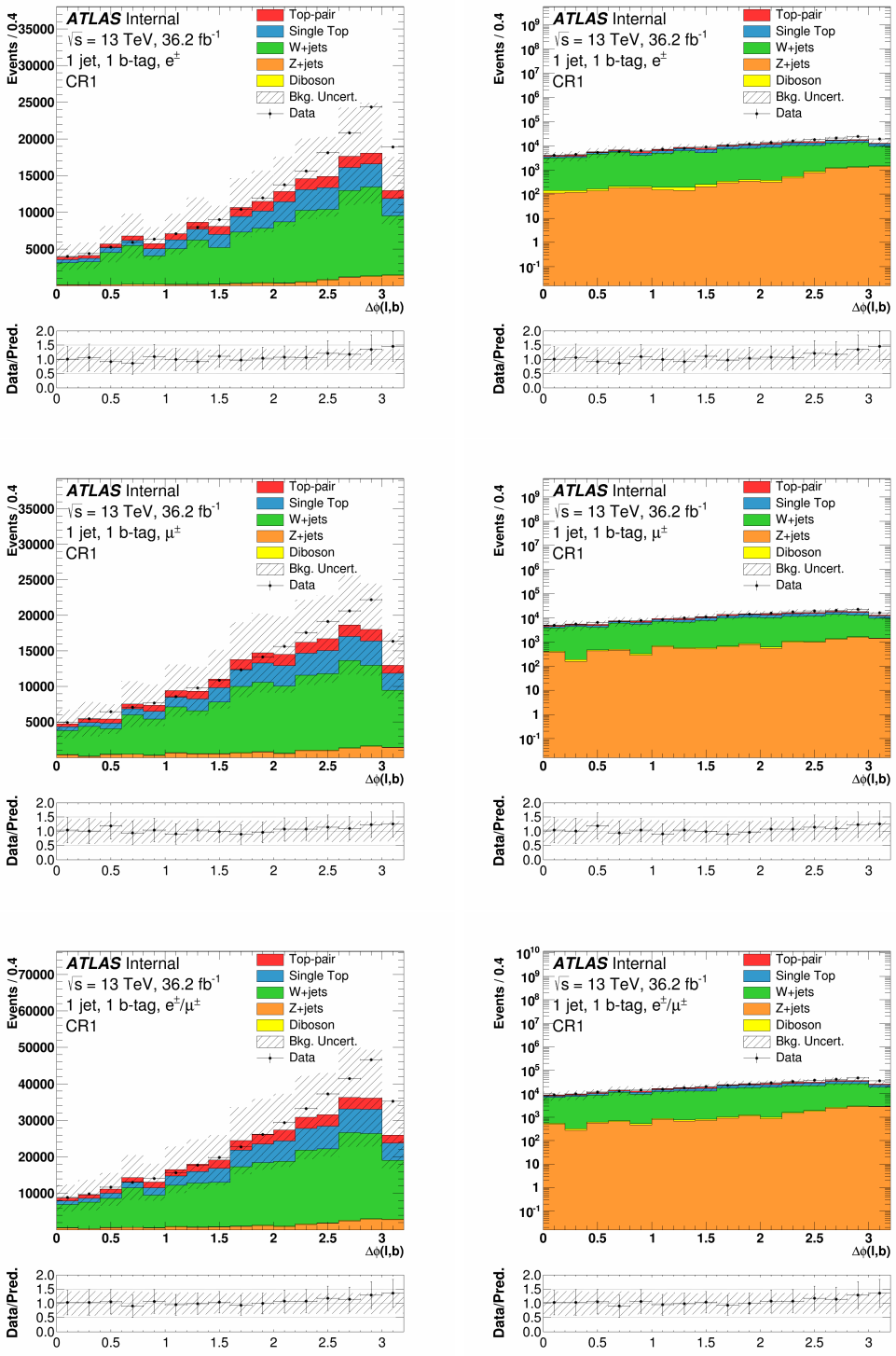

Figure H.20: Distributions of $\Delta\phi(\ell, b)$ for the electron (top), the muon (middle), and the combined (bottom) channels in CR1, in linear (left) and log (right) scale. The uncertainty band on the expected background corresponds to the errors due to the statistical uncertainties added in quadrature with the cross-section and normalization uncertainties.

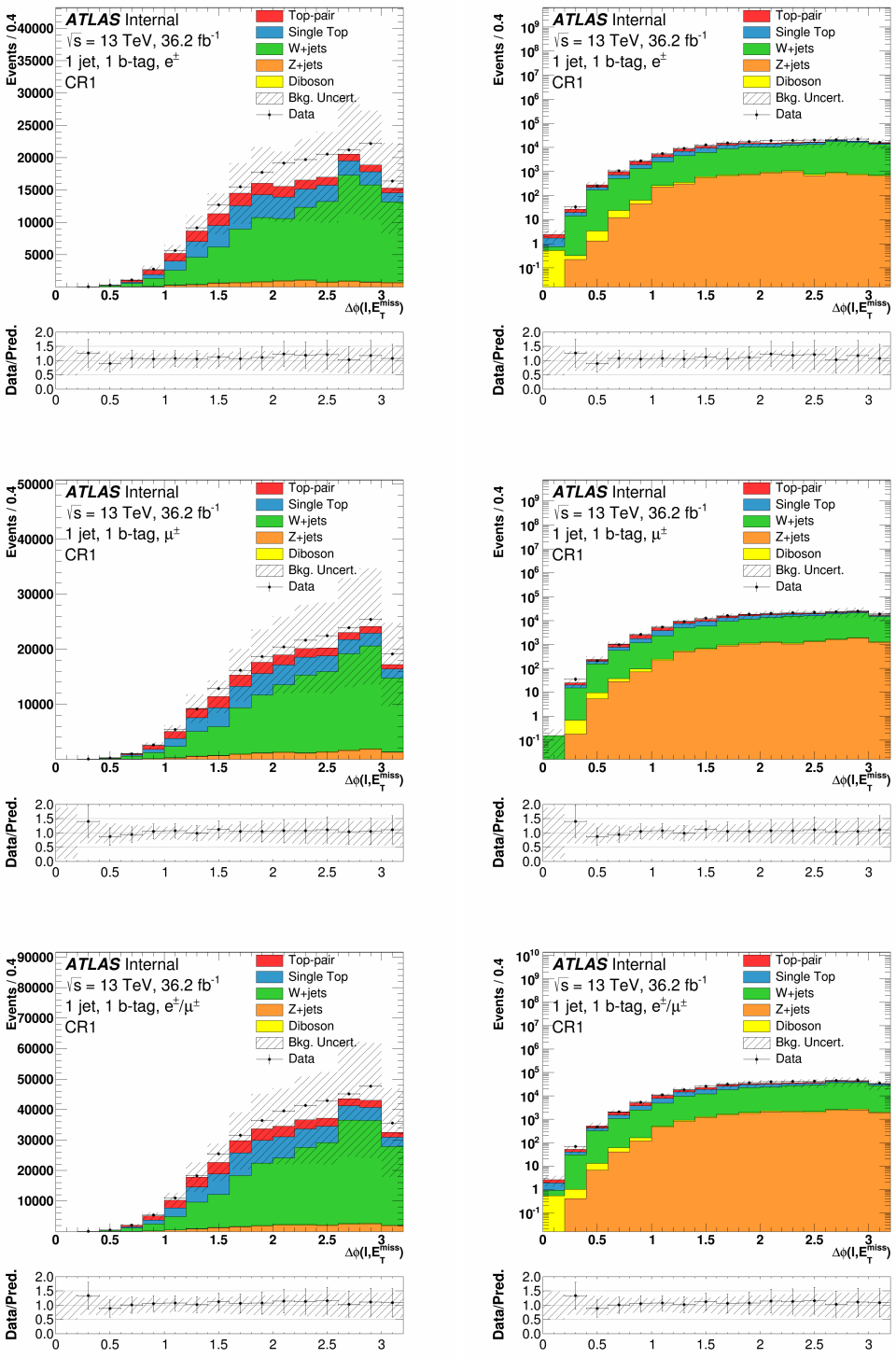

Figure H.21: Distributions of $\Delta\phi(\ell, E_{\mathrm{T}}^{\mathrm{miss}})$ for the electron (top), the muon (middle), and the combined (bottom) channels in CR1, in linear (left) and log (right) scale. The uncertainty band on the expected background corresponds to the errors due to the statistical uncertainties added in quadrature with the cross-section and normalization uncertainties.

Appendix I

13 TeV signal region plots

This appendix presents kinematic distributions comparing the SM predictions to the data observations in BDT optimized signal region. Distributions of the $m_{\mathrm{T}}(\ell^{+}, E_{\mathrm{T}}^{\mathrm{miss}})$, $E_{\mathrm{T}}^{\mathrm{miss}}$, $p_{\mathrm{T}}(\ell^{+})$, $p_{\mathrm{T}}(b)$, $\Delta\mathrm{R}(\ell^{+}, b)$, $\Delta\phi(\ell^{+}, b)$, and $\Delta\phi(\ell^{+}, E_{\mathrm{T}}^{\mathrm{miss}})$ are shown in the optimized BDT signal region (Section I).

Optimized BDT signal region

This section presents distributions of variables for simulated background and data events in the BDT optimized signal region defined in Section 14.4. Figures I.1 and I.2 show the transverse mass between the lepton and missing transverse energy, $m_{\mathrm{T}}(\ell^+, E_{\mathrm{T}}^{\mathrm{miss}})$. Figures I.3 and I.4 show the missing transverse energy, $E_{\mathrm{T}}^{\mathrm{miss}}$. Figures I.5 and I.6 show the transverse momentum of the lepton, $p_{\mathrm{T}}(\ell^+)$. Figures I.7 and I.8 show the transverse momentum of the b-jet, $p_{\mathrm{T}}(b)$. Figures I.9 and I.10 show spatial separation in $\eta - \phi$ space between the lepton and b-jet, $\Delta\mathrm{R}(\ell^+, b)$. Figures I.11 and I.12 show angular separation in ϕ between the lepton and b-jet, $\Delta\phi(\ell^+, b)$. Figures I.13 and I.14 show angular separation in ϕ between the lepton and the missing transverse energy, $\Delta\phi(\ell^+, E_{\mathrm{T}}^{\mathrm{miss}})$.

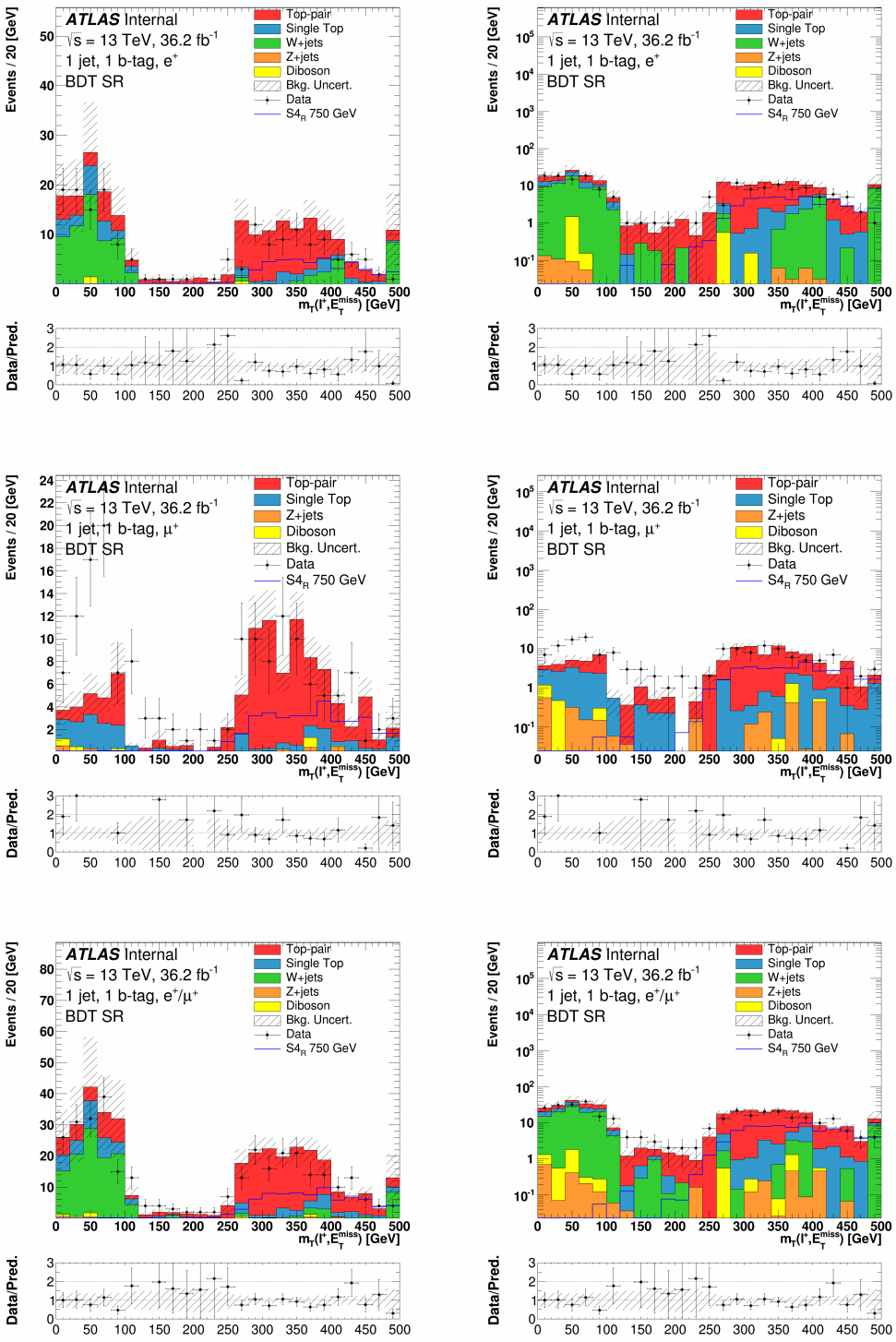

Figure I.1: Distributions of $m_{\mathrm{T}}(\ell^{+}, E_{\mathrm{T}}^{\mathrm{miss}})$ for the electron (top), the muon (middle), and the combined (bottom) channels in the BDT optimized signal region, in linear (left) and log (right) scale. The uncertainty band on the expected background corresponds to the errors due to the statistical uncertainties added in quadrature with the cross-section and normalization uncertainties.

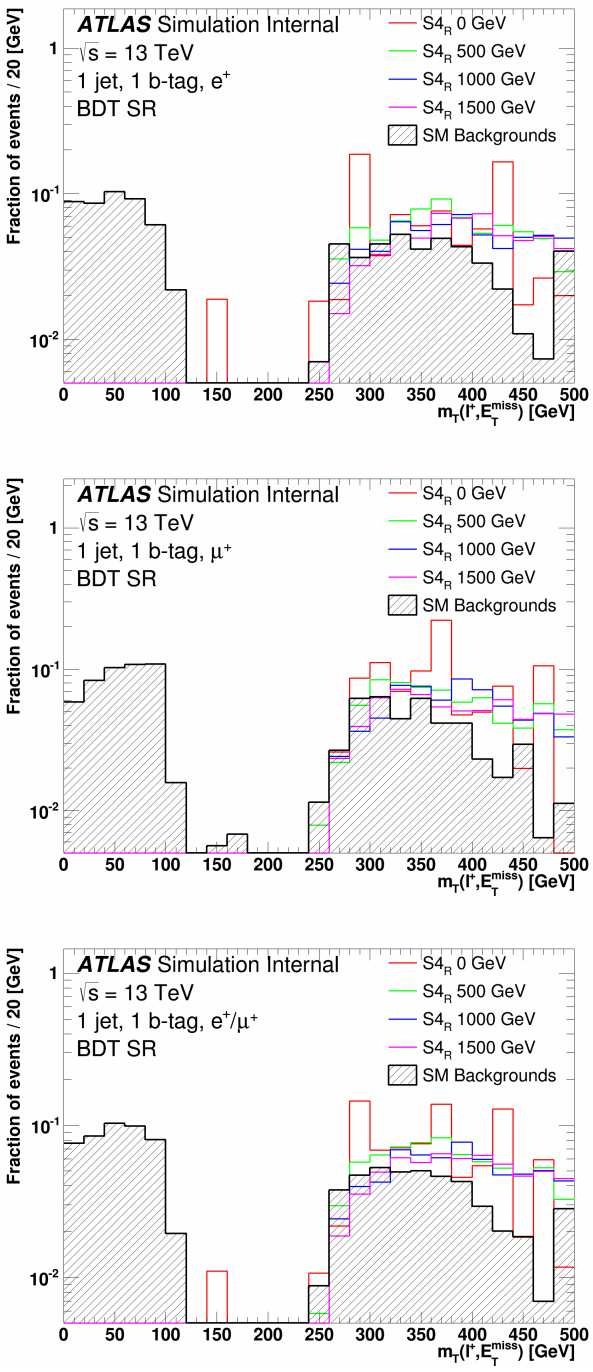

Figure I.2: Distributions of $m_{\mathrm{T}}(\ell^{+}, E_{\mathrm{T}}^{\mathrm{miss}})$ normalized to unity for the electron (top), the muon (middle), and the combined (bottom) channels in the optimized BDT signal region for various mass hypotheses of the $\mathrm{S4_R}$ model. The SM background is also shown.

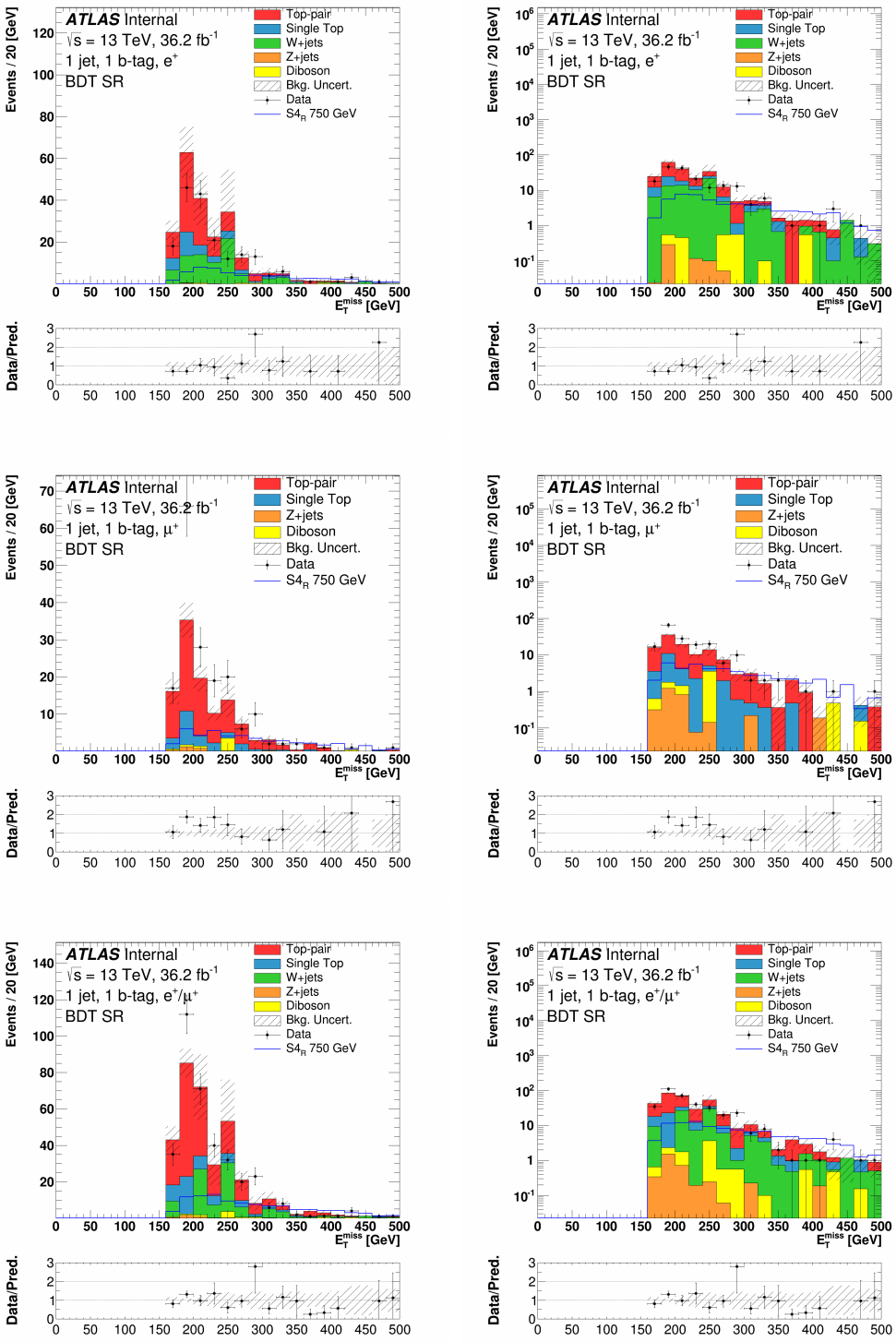

Figure I.3: Distributions of $E_{\mathrm{T}}^{\mathrm{miss}}$ for the electron (top), the muon (middle), and the combined (bottom) channels in the BDT optimized signal region, in linear (left) and log (right) scale. The uncertainty band on the expected background corresponds to the errors due to the statistical uncertainties added in quadrature with the cross-section and normalization uncertainties.

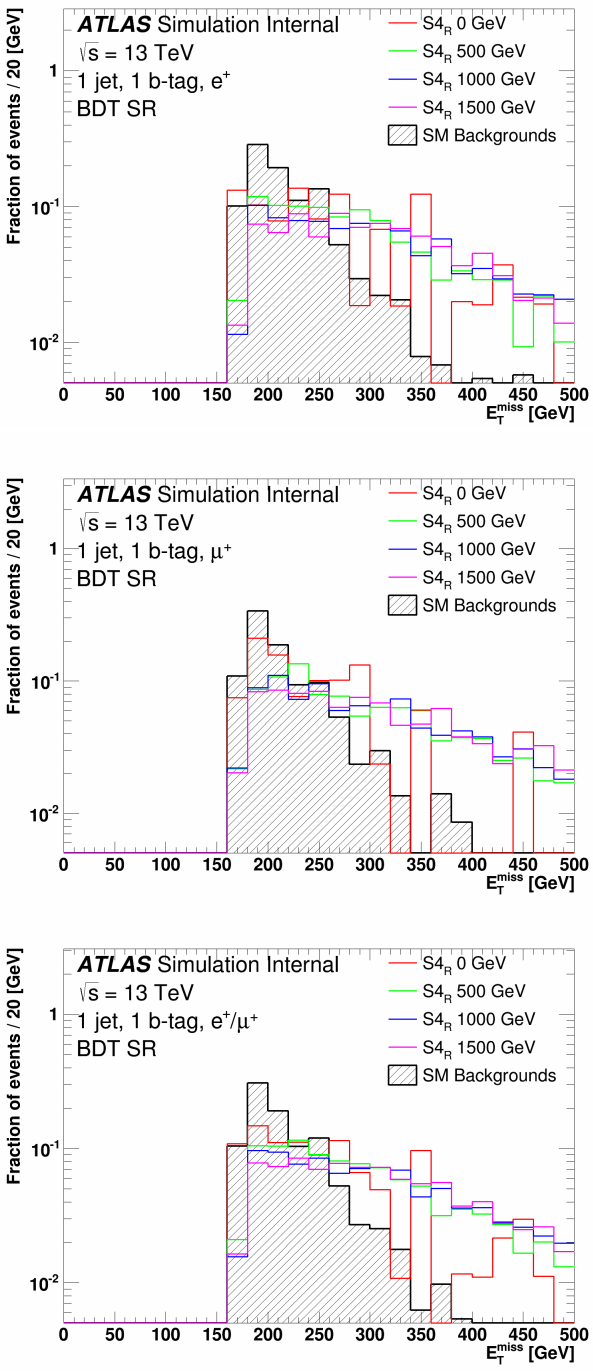

Figure I.4: Distributions of $E_{\mathrm{T}}^{\mathrm{miss}}$ normalized to unity for the electron (top), the muon (middle), and the combined (bottom) channels in the optimized BDT signal region for various mass hypotheses of the $\mathrm{S4_R}$ model. The SM background is also shown.

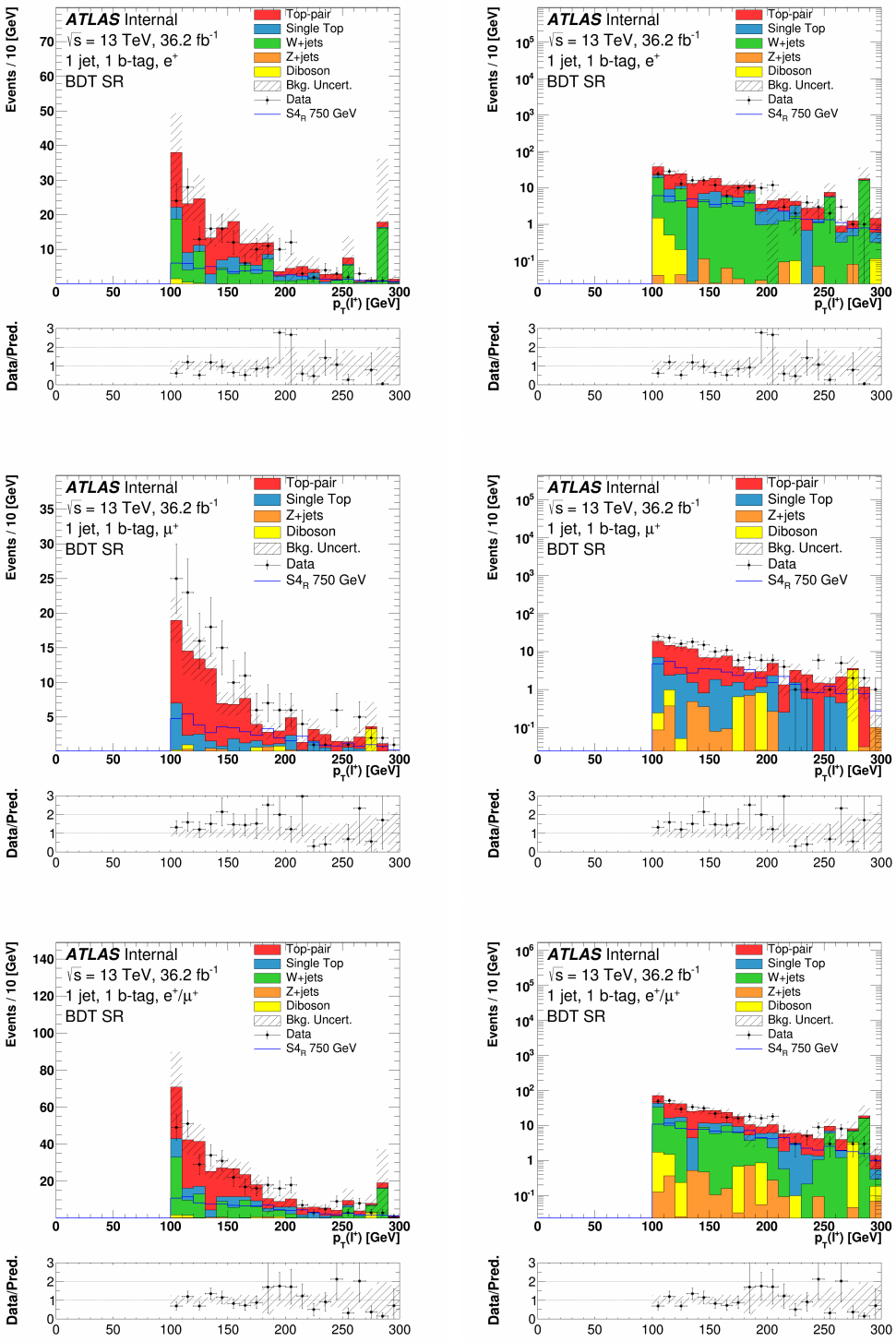

Figure I.5: Distributions of $p_{\mathrm{T}}(\ell^{+})$ for the electron (top), the muon (middle), and the combined (bottom) channels in the BDT optimized signal region, in linear (left) and log (right) scale. The uncertainty band on the expected background corresponds to the errors due to the statistical uncertainties added in quadrature with the cross-section and normalization uncertainties.

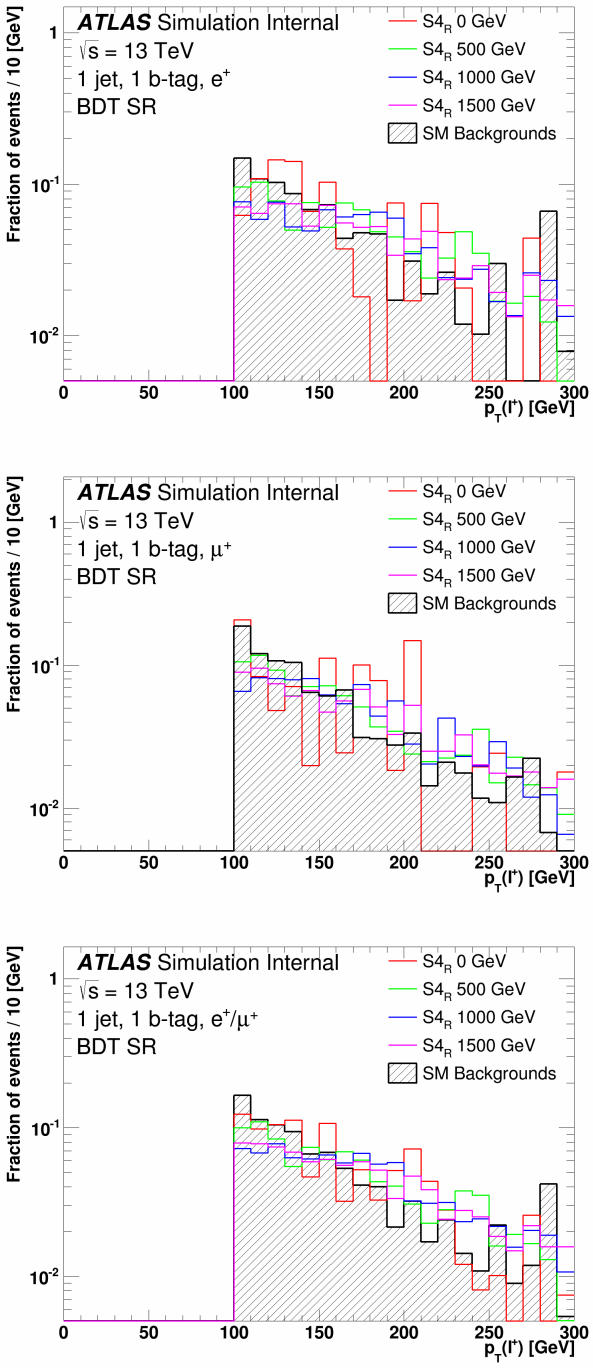

Figure I.6: Distributions of $p_{\mathrm{T}}(\ell^{+})$ normalized to unity for the electron (top), the muon (middle), and the combined (bottom) channels in the optimized BDT signal region for various mass hypotheses of the $\mathrm{S4_R}$ model. The SM background is also shown.

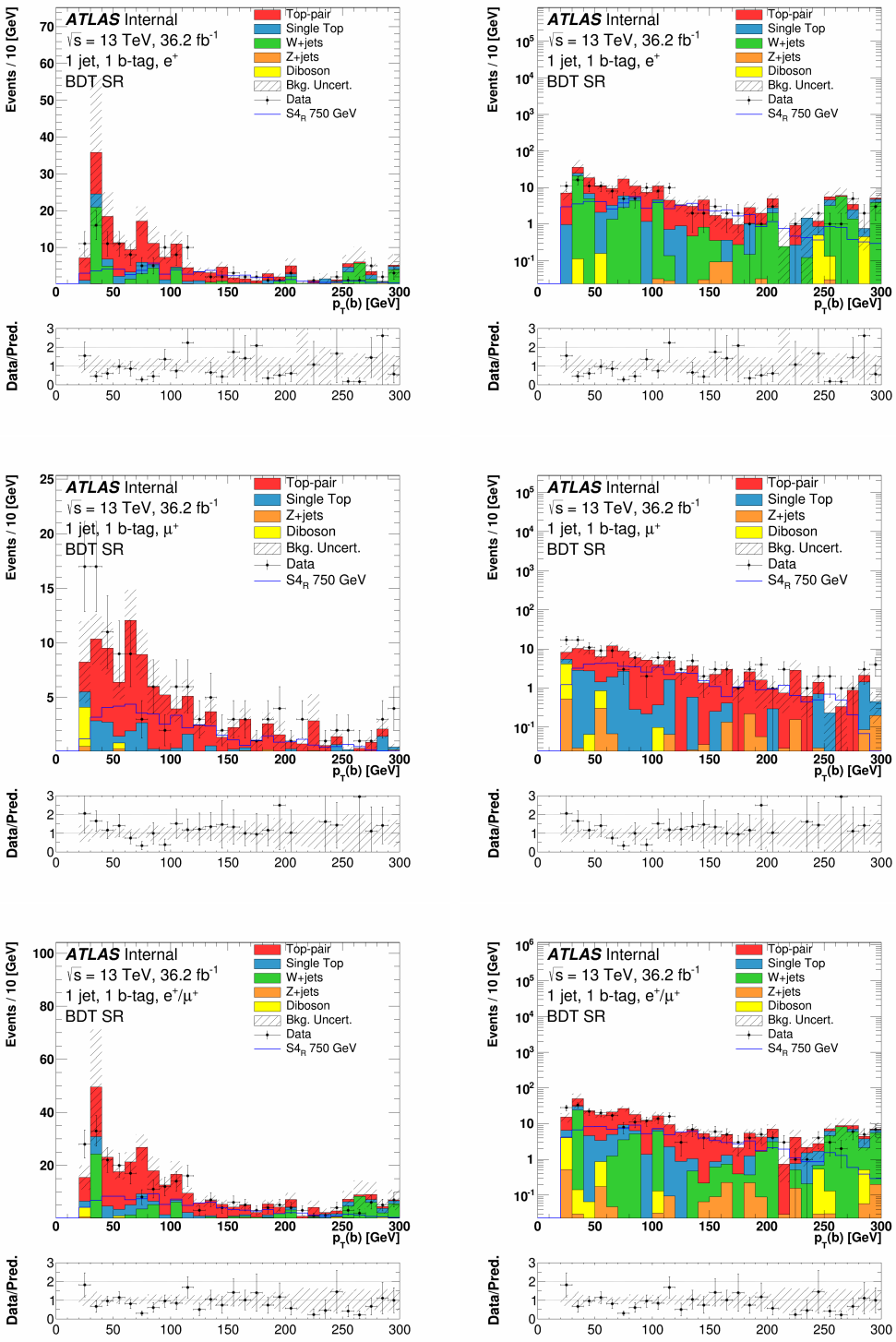

Figure I.7: Distributions of $p_{\mathrm{T}}(b)$ for the electron (top), the muon (middle), and the combined (bottom) channels in the BDT optimized signal region, in linear (left) and log (right) scale. The uncertainty band on the expected background corresponds to the errors due to the statistical uncertainties added in quadrature with the cross-section and normalization uncertainties.

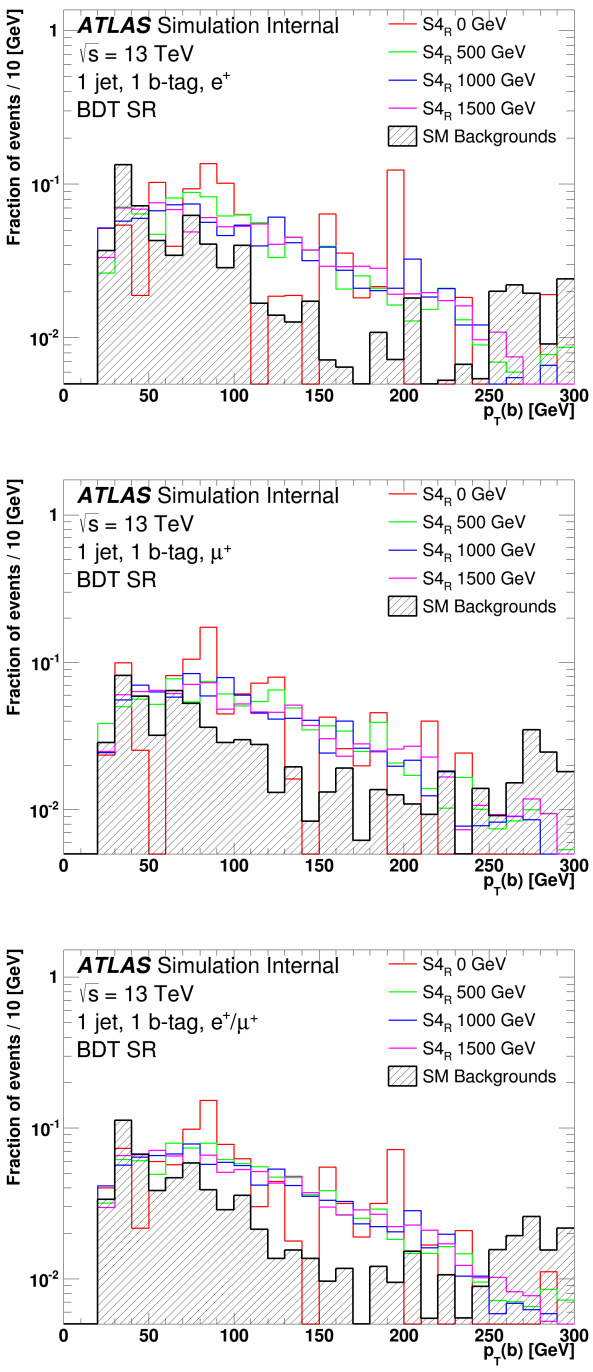

Figure I.8: Distributions of $p_{\mathrm{T}}(b)$ normalized to unity for the electron (top), the muon (middle), and the combined (bottom) channels in the optimized BDT signal region for various mass hypotheses of the $\mathrm{S4_R}$ model. The SM background is also shown.

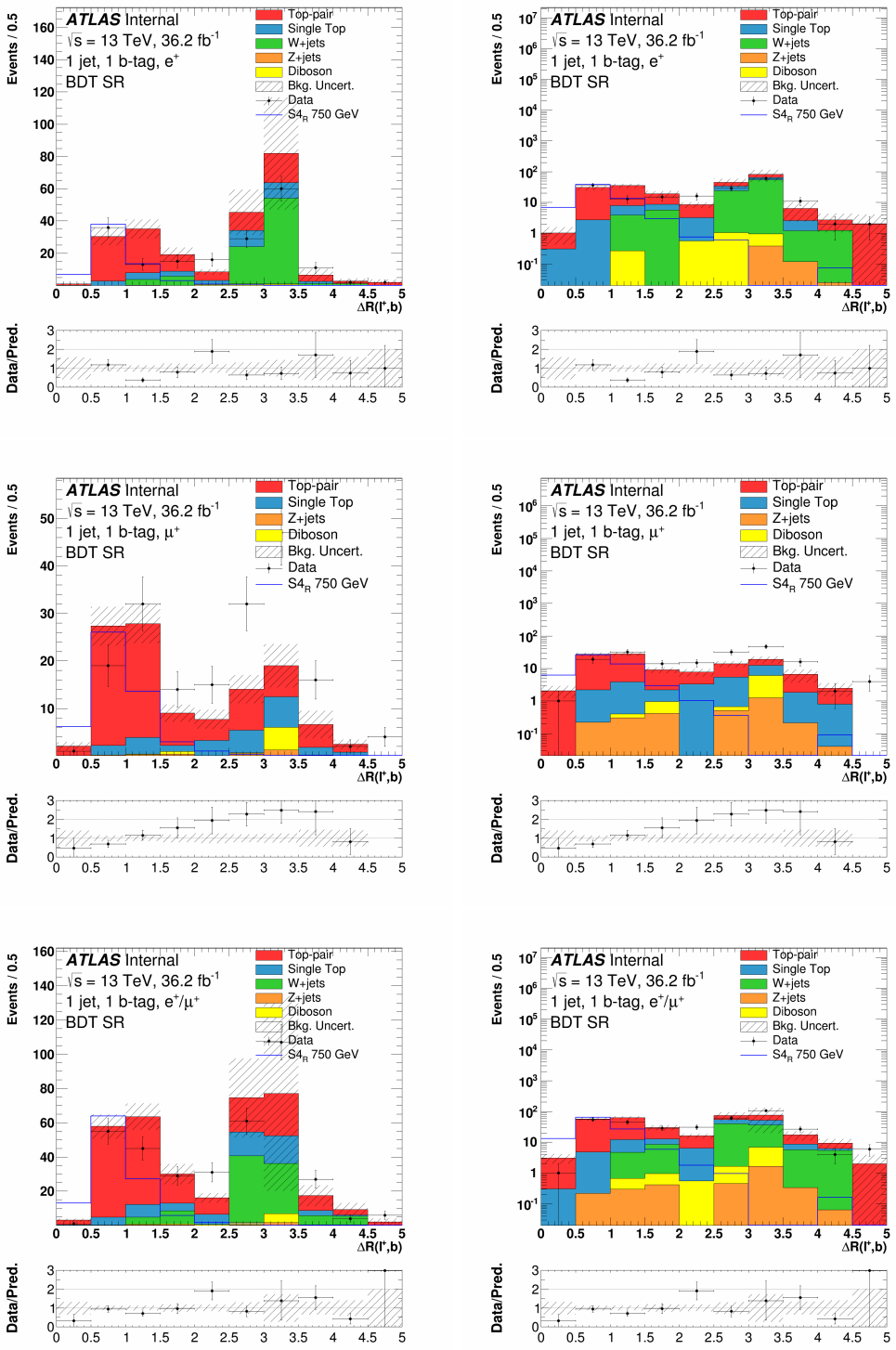

Figure I.9: Distributions of $\Delta R(\ell^+, b)$ for the electron (top), the muon (middle), and the combined (bottom) channels in the BDT optimized signal region, in linear (left) and log (right) scale. The uncertainty band on the expected background corresponds to the errors due to the statistical uncertainties added in quadrature with the cross-section and normalization uncertainties.

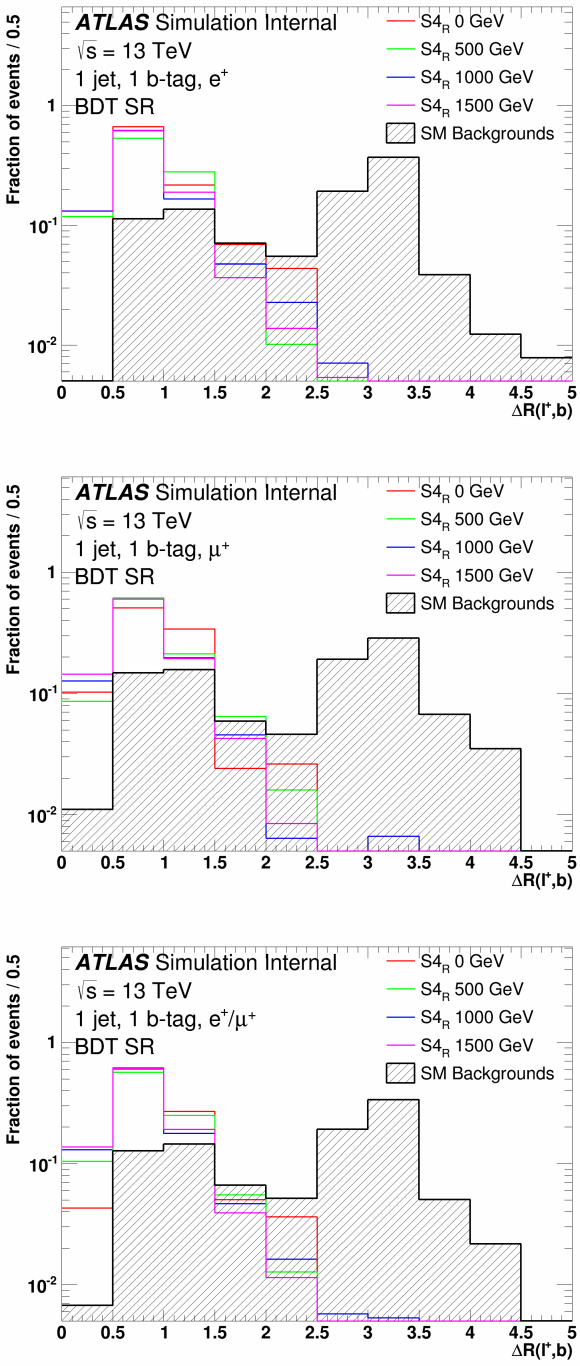

Figure I.10: Distributions of $\Delta\mathrm{R}(\ell^+, b)$ normalized to unity for the electron (top), the muon (middle), and the combined (bottom) channels in the optimized BDT signal region for various mass hypotheses of the $\mathrm{S4_R}$ model. The SM background is also shown.

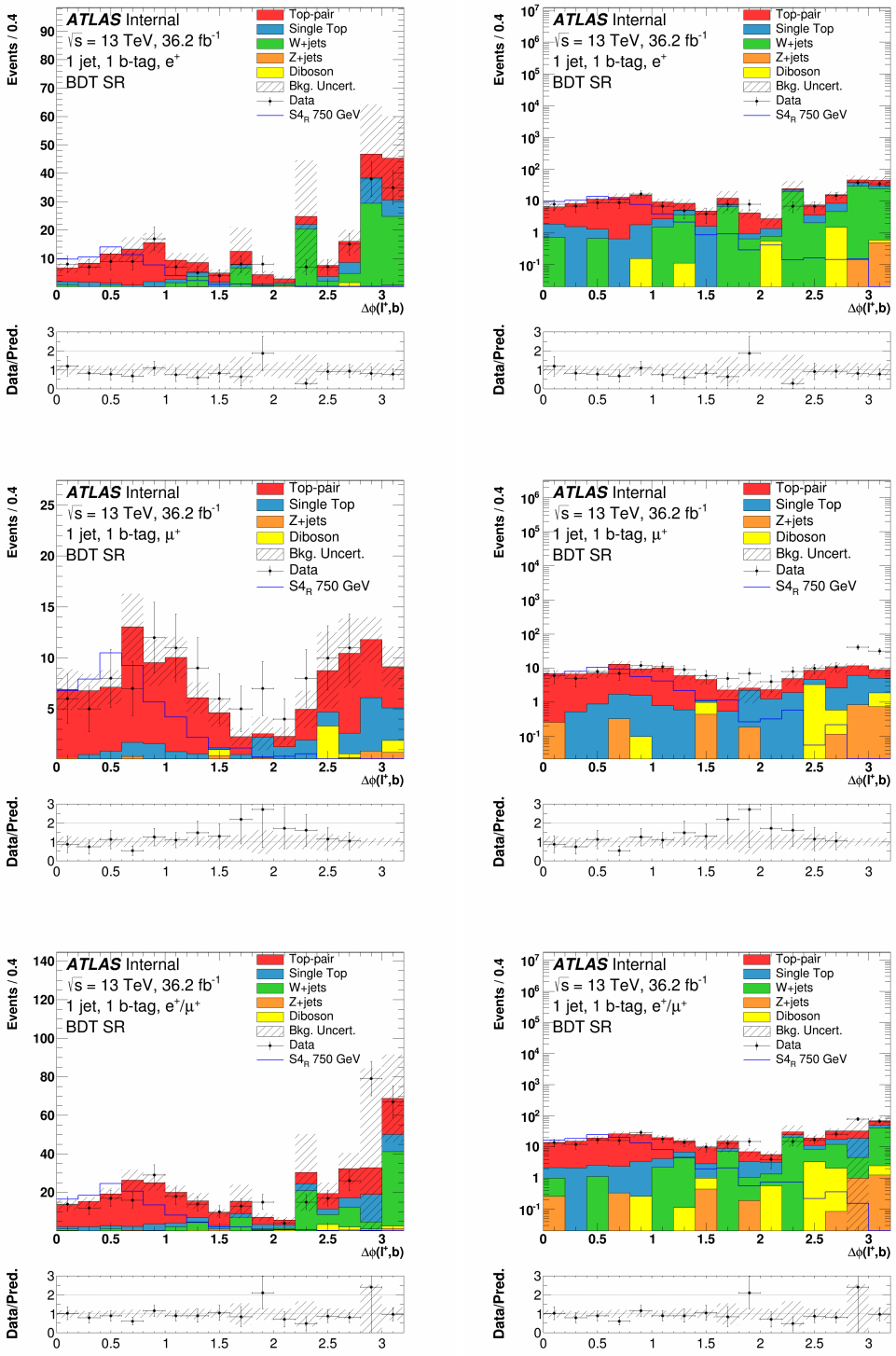

Figure I.11: Distributions of $\Delta\phi(\ell^+, b)$ for the electron (top), the muon (middle), and the combined (bottom) channels in the BDT optimized signal region, in linear (left) and log (right) scale. The uncertainty band on the expected background corresponds to the errors due to the statistical uncertainties added in quadrature with the cross-section and normalization uncertainties.

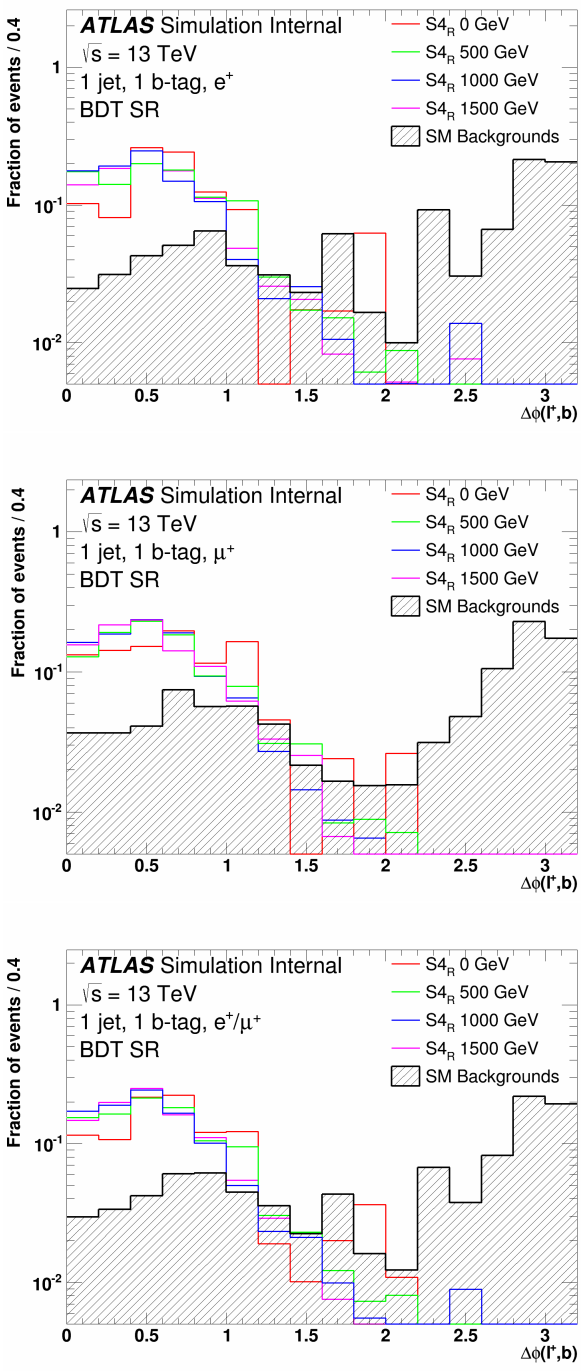

Figure I.12: Distributions of $\Delta\phi(\ell^+, b)$ normalized to unity for the electron (top), the muon (middle), and the combined (bottom) channels in the optimized BDT signal region for various mass hypotheses of the $S4_R$ model. The SM background is also shown.

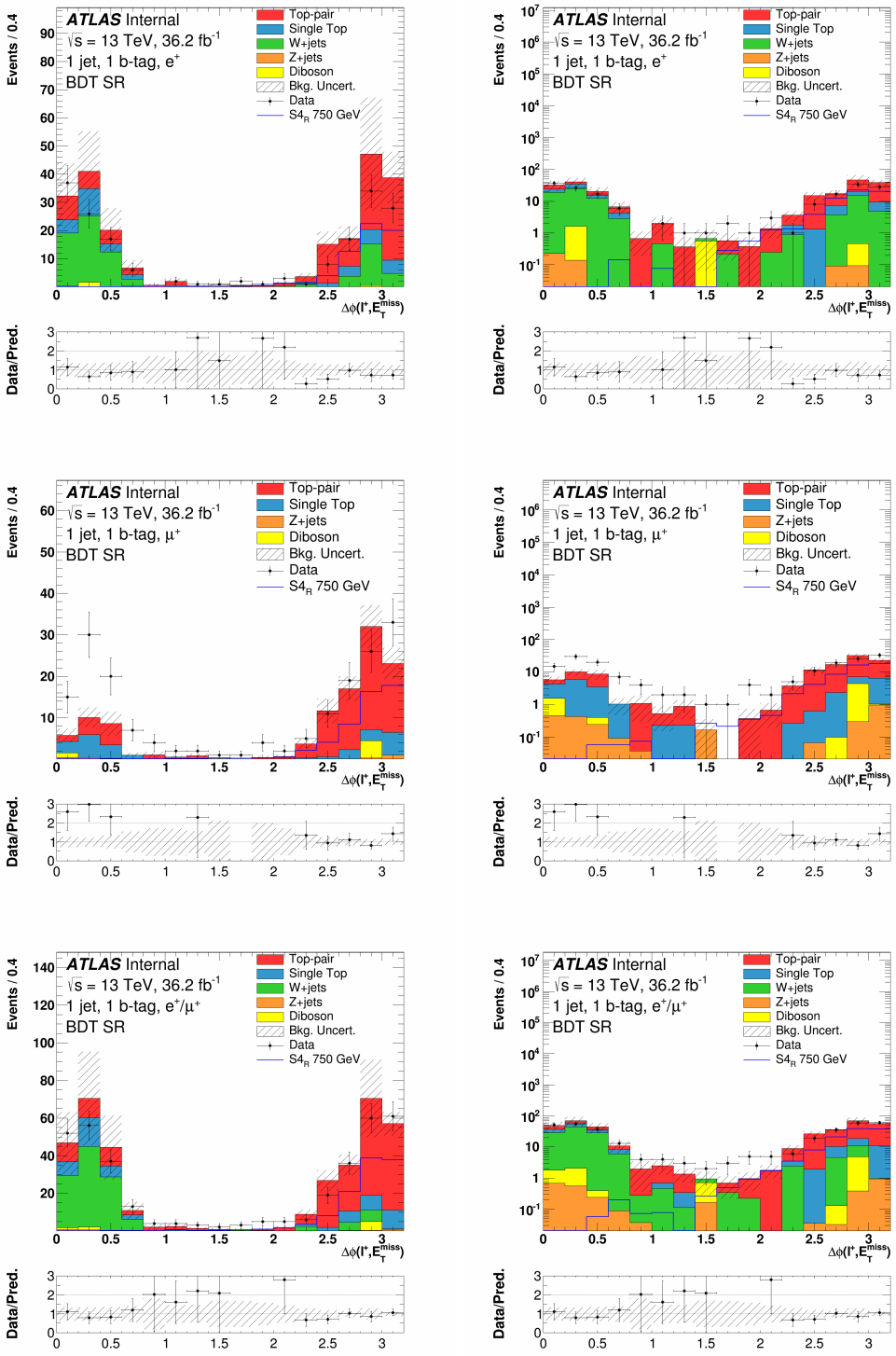

Figure I.13: Distributions of $\Delta\phi(\ell^+, E_{\mathrm{T}}^{\mathrm{miss}})$ for the electron (top), the muon (middle), and the combined (bottom) channels in the BDT optimized signal region, in linear (left) and log (right) scale. The uncertainty band on the expected background corresponds to the errors due to the statistical uncertainties added in quadrature with the cross-section and normalization uncertainties.

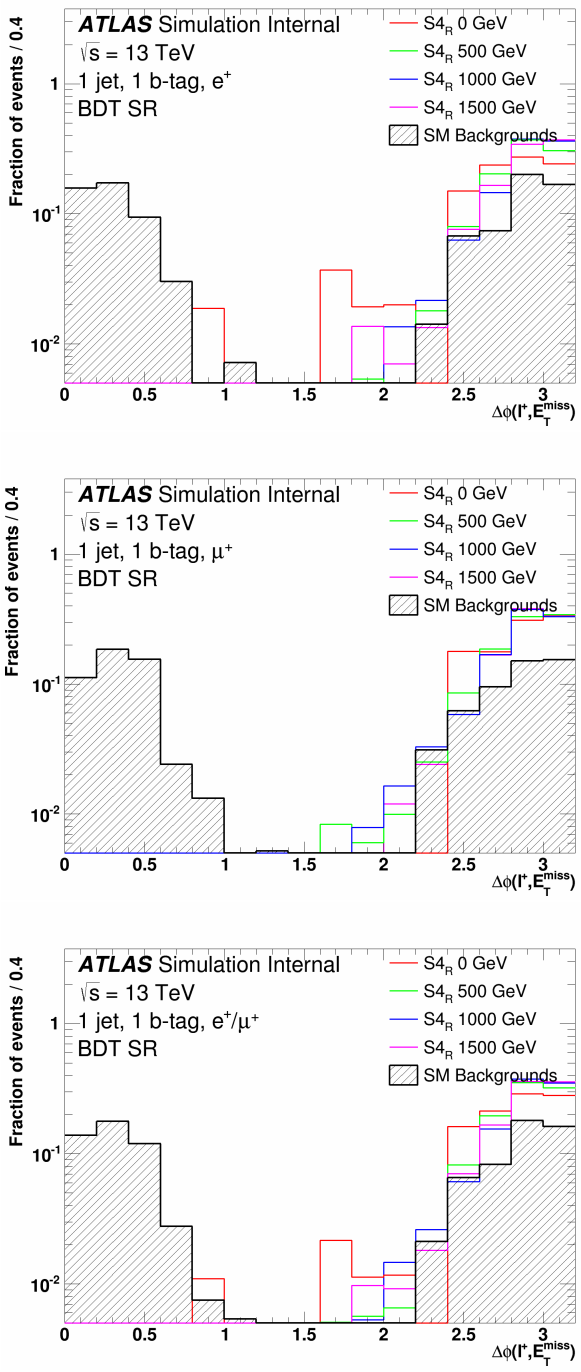

Figure I.14: Distributions of $\Delta\phi(\ell^+, E_{\mathrm{T}}^{\mathrm{miss}})$ normalized to unity for the electron (top), the muon (middle), and the combined (bottom) channels in the optimized BDT signal region for various mass hypotheses of the $\mathrm{S4_R}$ model. The SM background is also shown.

Appendix J

Level-1 Calorimeter Trigger Upgrades

This appendix describes a portion of the Level-1 calorimeter trigger system (L1Calo) upgrade work done at Michigan State University during the period between the end of Run1 and the beginning of Run2 known as Long Shutdown 1 (LS1).

L1Calo in Run1

During Run1 the L1Calo operated as a "threshold multiplicity counter" as described in Section 4.2.6.1.1. Each of the four crates of the Cluster Processor (CP) contained 14 Cluster Processor Modules (CPMs) and were responsible for identifying and counting energy clusters of candidate electrons, photons, and taus in one quadrant of the EM calorimeters with p_{T} higher than some threshold programmed in the trigger menu (see Figure 4.28). Similarly, the Jet/Energy Processor (JEP) was arranged in a two-crate system, each of which contained 16 Jet/Energy Modules (JEMs). Each JEM was responsible for identifying and counting hadronic energy clusters in portions of the hadronic calorimeters with E_{T} greater than the threshold value in the trigger menu. The CPMs and JEMs passed along the positional information of these objects to the two Common Merger Modules (CMM) in each CP and JEP crate. Each CMM received the information once every bunch crossing from the CPMs or JEMs through a 400 pin backplane. The CMMs counted the multiplicities of the trigger objects in regions of interest (RoIs) identified by the CPMs and JEMs and sent the results

to the Central Trigger Processor (CTP) where information from the Level-1 muon trigger system (L1Muon) was combined to give an overall Level-1 Accept signal to the Level-2 trigger system.

During LS1 planned Phase-0 upgrades of the Level-1 trigger were implemented. These upgrades were necessary to be able to manage the increased luminosity and pileup that were expected for Run2. When Run1 ended, the LHC was delivering a peak instantaneous luminosity of 8×10^{33} protons per cm^2 per second to the detectors and was expected to double during Run2. This increase in luminosity meant that the detectors would see more interactions per bunch crossing and upgrades to the trigger system were implemented to allow the experiment to continue to operate with manageable trigger rates and a high efficiency for selecting data without having to significantly raise the thresholds. In order to maintain the Run1 trigger rates the Level-1 trigger could not continue to operate merely by counting physics objects that exceeded simple thresholds on p_{T} or E_{T}. To achieve the necessary background rate reduction topological information such as angular separation or the invariant mass between objects was needed. In order to add this new functionality two new pieces of hardware were implemented during LS1, the German built Level-1 Topological Processor (L1Topo) and the Common Merger eXtended (CMX) boards built at Michigan State University. These two pieces of hardware with higher-performing and more modern field-programmable gate arrays (FPGA), together with software and firmware upgrades, made it possible for the L1Calo to make full-detector trigger decisions at Level-1. The configuration of the Level-1 trigger system for Run2 with these two new pieces of hardware is shown in Figure J.1. While the L1Topo processor was an integral part of the upgrade, the remaining portion of this appendix will focus on the design and subsequent testing of the CMX boards.

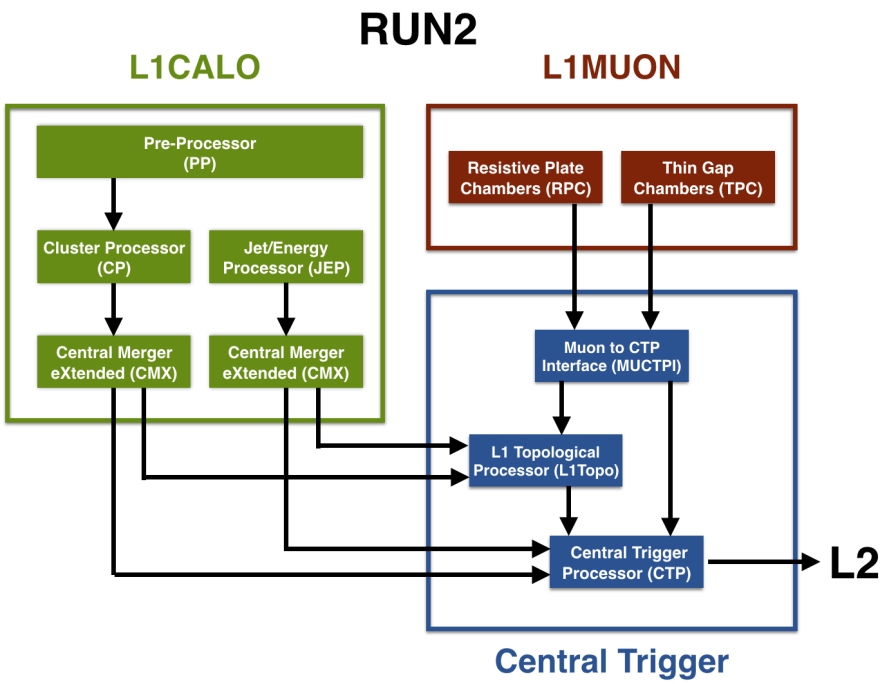

Figure J.1: A block diagram showing the configuration of the Level-1 trigger system in Run2 with the CMX boards and L1Topo processor in place.

Common Merger eXtended

The CMX boards were designed and constructed at Michigan State University to meet the following criteria:

- The functionality of the CMM boards needed to be retained. All tasks performed by the CMMs were required to be handled by the CMX boards but at four times the input and output data rates.
- The CMX boards were required to provide improved computing power to allow for additional threshold algorithms to implemented.
- Each CMX board was required to provide an optical link to the new L1Topo processor.
- In the event that the implementation of the L1Topo processor was delayed, two CMX

boards capable of performing limited topological processing were needed as a backup. Those boards contained an extra FPGA which handled simple topological functions directly on the CMX.[1]

The CMX boards were designed to fit into the same crates which housed the CMM boards. As such, the CMX boards have the same backplane pinout, VME power supply, and control/monitoring pins as the CMMs. There are two different usages of the CMX boards in the L1Calo system. Of the 12 CMX boards used in the L1Calo trigger system, eight are so-called "Crate CMX boards" and four are "System CMX boards." They are all identical but are just configured to serve different functions. The 12 CMX boards are interconnected in the L1Calo system as four groups, with each group handling the trigger information for either electrons, taus, jets, or energy (see Figure J.2). The main physics performance goal of each of the 12 CMX boards was to receive information from either the JEMs or CPMs, package that information, and forward it in a format which the the L1Topo processor could read and process. The second physics performance goal was to collect the trigger information and to send that information directly to the CTP. The eight Crate CMX boards send local summary information to one of the four System CMX boards which then sends the collected trigger information to the CTP over Low Voltage Differential Signaling (LVDS) cables at twice the rate of the CMMs.

Main components

The main components of the CMX board along with their functionalities are listed below. The numbering in the list corresponds to Figure J.3.

[1] While two of these so-called Topo-CMX boards were constructed, they have yet to be utilized in the L1Calo trigger system.

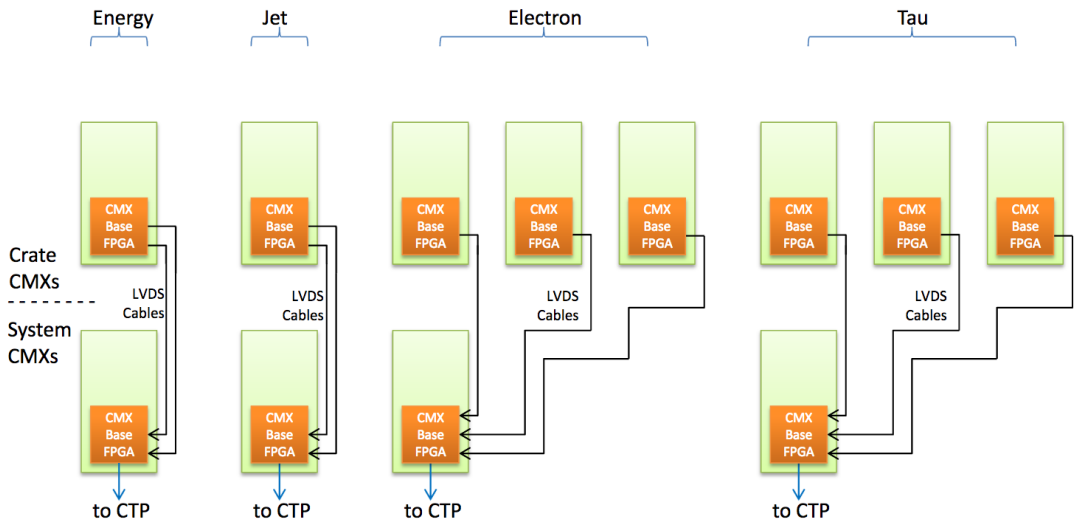

Figure J.2: The Crate and System CMX arrangement of the L1Calo trigger system in Run2.

1. The Versa Module Europa (VME) power bus transfers power from the crate to the board.

2. The 400 pin backplane receives positional and threshold information from the 16 JEMs or the 14 CPMs. Unlike the CMMs which could only receive one bit of information on every backplane pin each bunch crossing (every 25 ns), the CMX can receive four. This increased the available bandwidth from 40 to 160 Mbps.

3. Three LVDS cables on the backplane send trigger information from a Crate CMX to a System CMX at 160 Mbps.

4. Two LVDS cables on the front of the boards send trigger information from a System CMX directly to the CTP at 160 Mbps.

5. All CMX boards send their data acquisition (DAQ) readout information to a DAQ readout driver (ROD). Additionally, System CMX boards need to send RoI information to an RoI ROD. Two Small Form-factor Pluggable (SFP) optical transceivers use G-

link serial protocol to send the information at 120 Mbps.

6. All CMX boards send high-speed 6.4 Gbps optical information out to either the L1Topo processor or to a CMX board equipped with a Topological Function FPGA. Two Avago MiniPOD transmitter devices connected to the Base Function FPGA send the information along 24 optical fibers arranged as two 12-fiber ribbons.

7. The Board Support (BSPT) FPGA manages the internal monitoring devices on the board.

8. The Base Function (BF) FPGA takes the information from either the JEMs or CPMs and packages it into a format which is readable by the L1Topo processor

9. The Topological Function (TP) FPGA was designed to perform basic topological processing in the event the L1Topo processor was not available. Two CMX boards with a TP FPGA were constructed at Michigan State but have only been used during internal testing of the boards and have not been used in the actual Level-1 trigger system.

10. If a CMX board is configured with a TP FPGA then two SFP optical transceivers send topological DAQ and ROI information along G-link serial protocol to the ROD cards at 120 MBps.

11. The BSPT and BF FPGAs need to be programmed whenever the board is powered off and on. The System Advanced Configuration Environment (ACE) reads a user-inputed compact flash card and configures the BSPT and BF FPGAs with the necessary algorithms and functionalities.

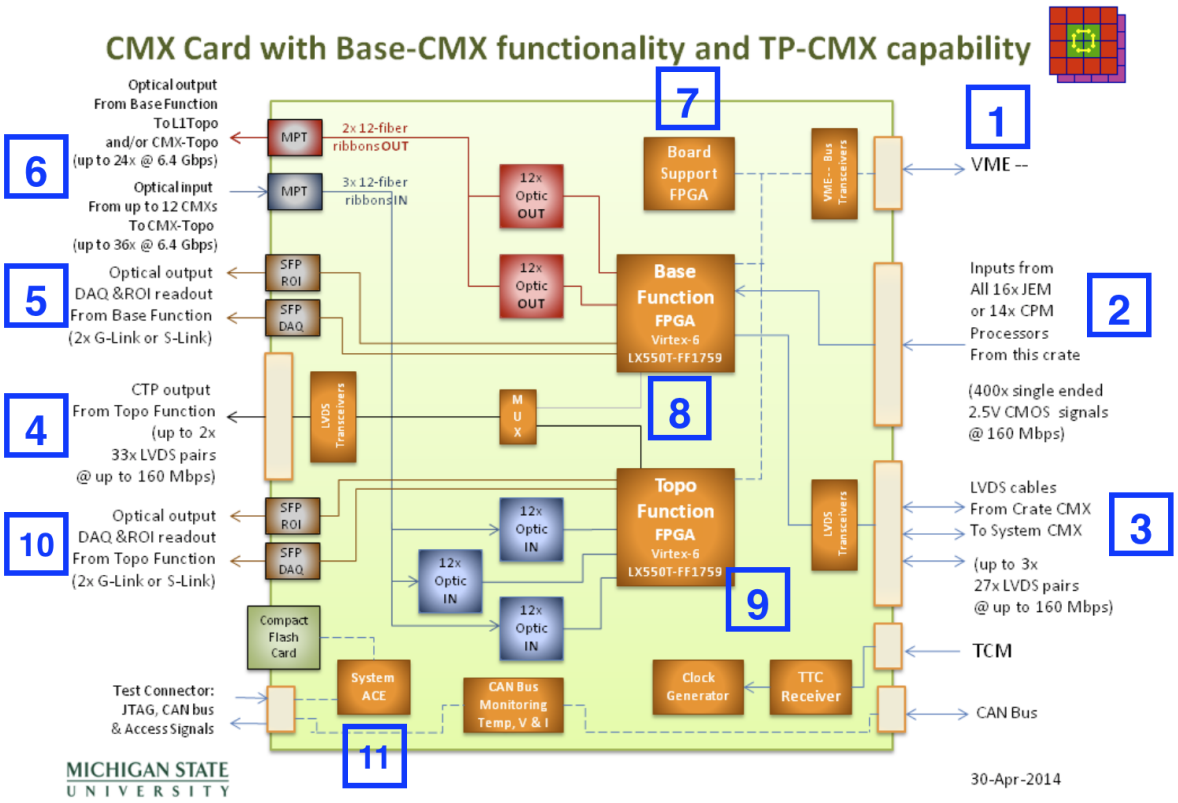

Figure J.3: A block diagram showing the main components of the CMX board. Components 9 and 10 are only present on a CMX board which has a Topological Function FPGA.

MSU production tests

Following final assembly of the boards, several tests were completed to ensure they were functioning as designed. These tests were conducted in a test crate similar to the ones in USA15 where the L1Calo trigger system is housed. The following tests were performed on each CMX board post-production before they were shipped from Michigan State to the experiment. Each board had to pass all tests before it was shipped.

- **LED Test** – The functionality of the LED lights on the front panel of each board were tested to ensure they worked properly. LEDs were cycled on and off individually.

- **Random Register Test** – Random registers in both the BSPT and BF FPGAs were

Figure J.4: One of the production CMX boards and a JEM in the test crate located in the HEP lab on the Michigan State University campus. The JEM was used to test the functionality of the backplane. As only one JEM was available during testing, after each test it was shifted to another slot in order to test all 400 pins in the backplane.

read-out and, if allowed, written-to in order to ensure the read/write functionality of the FPGAs.

- **MiniPOD Light Level Output** – The light level lost along the optical fibers connecting a MiniPOD on one CMX acting as a transmitter and a MiniPOD on another CMX board acting as a receiver was measured to ensure losses were minimal.

- **I/O Delay Test** – The I/O delay test was the most crucial of the production tests. The CMX boards receive a signal along each of the 400 pins on the backplane once every 6.5 ns. These signals take a small fraction of time (around a tenth of a nano second) to reach a stable value and then quickly decay away. Within a 6.5 ns window each of the 400 signals need to be read simultaneously. The I/O delay test measured

the amount of time the signals remained stable and available to be read by the CMX across the backplane. A variable delay was applied so that the CMX read these signals at different points in the 6.5 ns window. A CMX passed the test if all 400 pins could be read out at the same time with zero errors.

After passing all of the production tests the CMX boards were packaged and shipped to Michigan State University employees at CERN to again be tested in the CERN test rig before finally being installed in USA15.

Appendix K

Level-1 Calorimeter Simulation

This appendix describes studies done during the period known as Long Shutdown 1 between the data taking periods of Run1 and Run2. The goal of these studies was to determine what trigger thresholds would be necessary given the hardware limitations inherent in the planned Phase-0 upgrades of the Level-1 calorimeter (L1Calo) trigger system.

TOB multiplicities and limits

The maximum number of trigger objects (TOBs) that can be transmitted to the Level-1 Topological Processor (L1Topo) is defined by bandwidth limitations at multiple stages along the real-time data path. The path of trigger information flows from the JEMs/CPM, to a CMX board, and finally to the L1Topo. The backplane transmission from the JEMs and CPMs to the CMX board is limited to four data frames per bunch crossing. Each frame contains 24 bits of information for a total of 96 bits per bunch crossing. TOBs identified by the JEMs are encoded with 21 bits each while TOBs identified by the CPMs are encoded with 15 bits. This allows each JEM (CPM) to transmit up to 4 (5) TOBs per bunch crossing. This means a CMX board servicing the 16 JEMs can receive up to 64 TOBs per bunch crossing while a CMX board receiving trigger information from the 14 CPMs can receive up to 70 TOBs per bunch crossing.

At each CMX 4 bits of additional coordinate information needs to be added to the TOBs

before being sent to the L1Topo board. This means that the minimum TOB size is 25 bits for jet TOBs and 19 bits for EM TOBs. The 6.4 Gbps optical links from a CMX board to the L1Topo translates into 128 bits per bunch crossing on each CMX output fiber to the L1Topo. This yields 4 jet or 5 EM TOBs (at 25 or 19 bits per TOB) per fiber per bunch crossing that can be sent to the L1Topo. The CMX boards have 12-fiber ribbon outputs and with 25 or 19 bits per TOB each 12-fiber ribbon can transmit up to 48 jet or 60 EM TOBs to the L1Topo before an overflow situation arises. In the context of the L1Calo, overflow simply means more bits need to be sent than the hardware allows.

Sources of overflow

Overflow can occur in multiple places and the three sources of overflow identified in these studies are shown in the list below:

- **Individual JEM/CPM Output** – A JEM or CPM identifies more TOBs than it can send out of its backplane to the CMX. This occurs when more than 4 (5) jet (EM) TOBs are identified by an individual JEM (CPM).
- **CMX Input from JEMs/CPMs** – More than the maximum number of TOBs a single CMX board can receive per bunch crossing of 64 jet TOBs or 70 EM TOBs is seen.
- **CMX Output to L1Topo** – More than 48 jet or 60 EM TOBs are sent to the L1Topo from a single CMX board.

The number of TOBs identified by the JEMs or CPMs is a function of both the threshold values for identifying TOBs as well as event kinematics. Each JEM/CPM identifies TOBs

in specific regions of the detector. Even if an event had less than the maximum number of TOBs a CMX could transmit to the L1Topo, those TOBs might be concentrated in a localized region of the detector and an individual JEM/CPM could easily be saturated.

Minimum bias studies

In order to study the rate at which overflow occurs, Monte Carlo samples with a minimal number of kinematic cuts were used. The purpose of these "minbias" samples was to provide kinematic information as close to what the detector would see during data taking. These samples were created with varying amounts of pileup in order to study what effect an increasing number of events per bunch crossing might have TOB multiplicities. The main goal of these studies was to determine what the appropriate EM and jet threshold energies in the trigger menus should be in order to avoid overflow situations. The effects of instituting a bunch crossing identification (BCID) veto were also studied. The 2,808 bunch crossings at the LHC come in trains of 72 bunches with a small gap between trains. It was shown that events in the early bunches of the train had much higher TOB multiplicities than later bunches (see Figure K.1). At the time of these studies other physicists were working to understand why this was the case and ways to mitigate its effects. For the purpose of the studies in this appendix a BCID veto was applied so that events occurring early in the bunch trains were vetoed and not considered. The overall effect of this veto was negated by rescaling the trigger rates seen in the simulation. For example, if the first 12 bunches of the 72 bunch trains were vetoed then the rates were scaled back up a factor of 1.2.

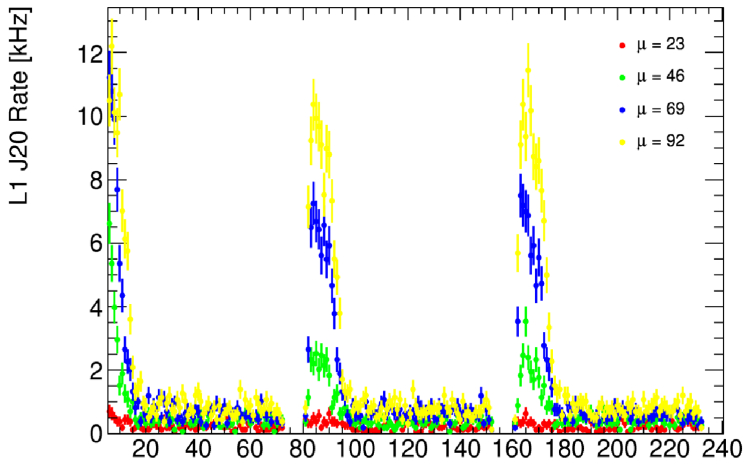

Figure K.1: Early bunches in the trains yield higher jet multiplicities than later bunches.

Conclusions

The author of this dissertation left the studies before they were fully complete. However, at the time of his exit a 10 GeV threshold for jet TOBs and a 3 GeV threshold for EM TOBs appeared to be feasible for simulations with up to 54 pileup events per bunch crossing. These thresholds were similar to the Run1 thresholds. It was important to keep the TOB thresholds low as many physics analyses, specifically those studying detector efficiencies, required objects with low p_{T} or E_{T}. Figure K.2 shows the TOB multiplicities and associated rates with and without a BCID veto for jet and EM TOBs with thresholds of 10 and 3 GeV respectively. Figures K.2(a) and K.2(c) show the TOB multiplicities of the individual CPMs and JEMs for the given thresholds. Figures K.2(b) and K.2(d) show the CMX boards which saw the greatest number of TOBs for the given thresholds. The vertical blue lines in the plots show the maximum number of TOBs allowed before overflow occurs.

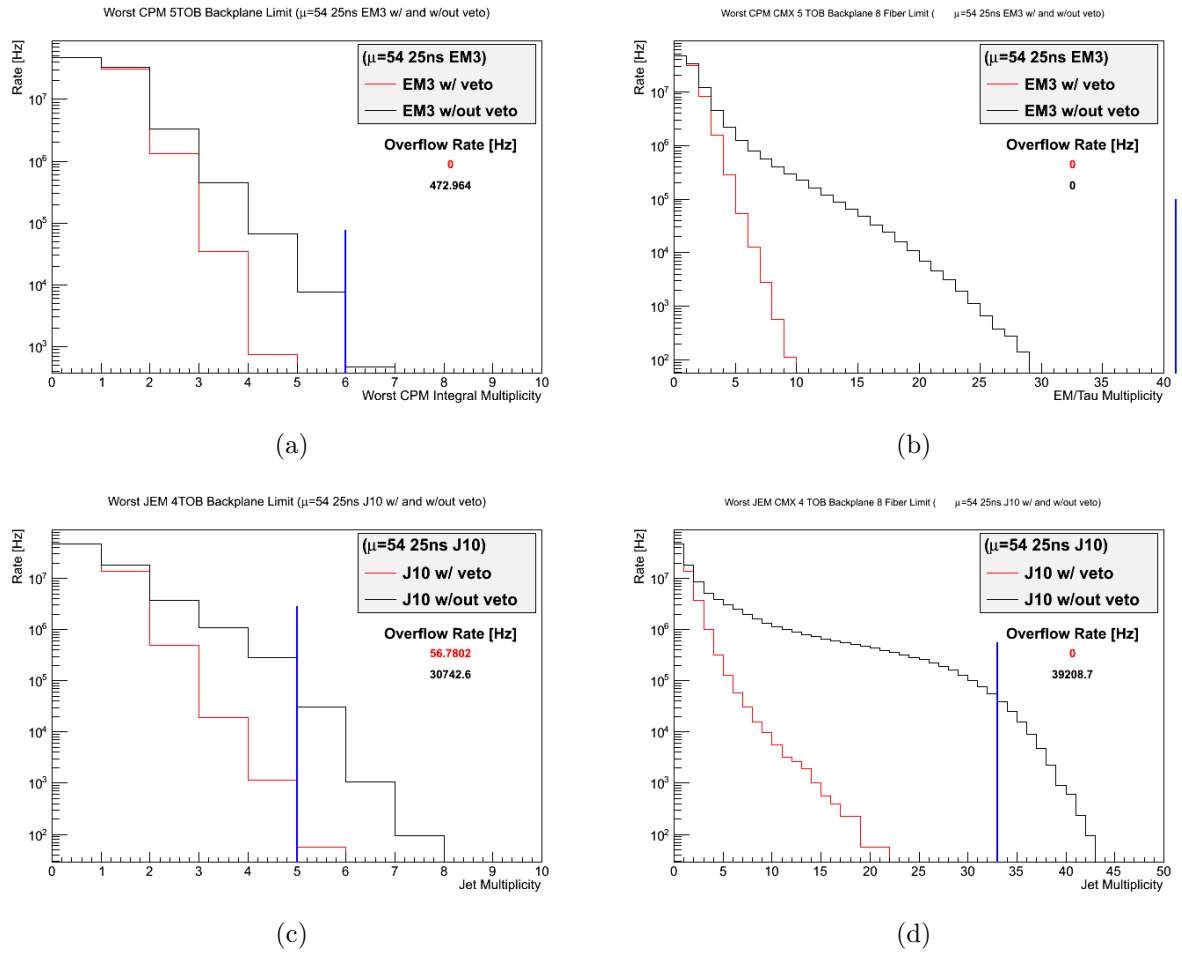

Figure K.2: (a) The integral number of TOBs identified by individual CPMs. (b) The EM TOB multiplicities sent to the CMX boards. (c) The integral number of TOBs identified by individual JEMs (d) The jet TOB multiplicities sent to the CMX boards.

Appendix L

Cut flow tables

This appendix presents the cut flow tables of the various control and signal selection regions. The tables are shown separately for the signal and background processes, and separately for the electron and muon channels.

Optimized SR1 signal region

This section presents the cut flow tables for the optimized SR1 selection region. For the electron (muon) channel these tables are shown for the backgrounds in Tables L.1 and L.2 (L.3 and L.4), and for the $S1_R$ signal model in Table L.5 (L.6).

SR1 Cut Sequence	$t\bar{t}$	ST s-chan	ST t-chan	ST Wt-chan	W+hf	W+light
1 electron, $p_{\mathrm{T}}(e) > 30$ GeV	256902.6	2395.0	40213.5	23206.9	1479603.5	5801952.0
1 jet, $p_{\mathrm{T}}(\mathrm{jet}) > 25$ GeV	11591.7	651.7	12697.9	3021.3	886890.2	3671492.0
1 b-jet, $p_{\mathrm{T}}(b) > 25$ GeV	4761.7	324.9	5593.4	1053.7	50438.0	11562.6
$m_{\mathrm{T}}(e, E_{\mathrm{T}}^{\mathrm{miss}}) > 210$ GeV	222.4	0.1	1.3	59.9	58.0	21.2
$\lvert\Delta\phi(e,b)\rvert < 1.2$	83.7	0.0	0.0	9.6	10.5	0.2

Table L.1: Cutflow totals for selected backgrounds in the SR1 optimized selection region in the electron channel.

SR1 Cut Sequence	Z+Jets	Diboson	Multijet	Tot. Bkg.	Data
1 electron, $p_{\mathrm{T}}(e) > 30$ GeV	669763.2	44464.3	523575.8	8842076.9	8522185
1 jet, $p_{\mathrm{T}}(\mathrm{jet}) > 25$ GeV	387484.8	19245.3	336847.4	5329922.3	5127400
1 b-jet, $p_{\mathrm{T}}(b) > 25$ GeV	521.8	544.6	17483.6	92284.3	84011
$m_{\mathrm{T}}(e, E_{\mathrm{T}}^{\mathrm{miss}}) > 210$ GeV	0.0	2.0	29.6	394.6	351
$\lvert\Delta\phi(e,b)\rvert < 1.2$	0.0	0.3	0.0	104.4	103

Table L.2: Cutflow totals for selected backgrounds as well as data in the SR1 optimized selection region in the electron channel.

SR1 Cut Sequence	$t\bar{t}$	ST s-chan	ST t-chan	ST Wt-chan	W+hf	W+light
1 muon, $p_{\mathrm{T}}(\mu) > 30$ GeV	315841.7	3130.8	50664.9	27776.7	2040267.2	8432723.0
1 jet, $p_{\mathrm{T}}(\mathrm{jet}) > 25$ GeV	14310.1	880.6	16259.2	3619.1	1226282.9	5278589.0
1 b-jet, $p_{\mathrm{T}}(b) > 25$ GeV	5868.0	437.7	7093.5	1258.9	68643.0	16995.7
$m_{\mathrm{T}}(\mu, E_{\mathrm{T}}^{\mathrm{miss}}) > 210$ GeV	265.6	0.2	1.5	54.6	74.4	14.0
$\lvert\Delta\phi(\mu, b)\rvert < 1.2$	105.3	0.0	0.0	9.5	16.7	2.0

Table L.3: Cutflow totals for selected backgrounds in the SR1 optimized selection region in the muon channel.

SR1 Cut Sequence	Z+Jets	Diboson	Multijet	Tot. Bkg.	Data
1 muon, $p_{\mathrm{T}}(\mu) > 30$ GeV	493260.3	57996.5	242153.9	11663815.1	11906630
1 jet, $p_{\mathrm{T}}(\mathrm{jet}) > 25$ GeV	293886.5	25368.8	149290.2	7008486.4	7194020
1 b-jet, $p_{\mathrm{T}}(b) > 25$ GeV	1025.5	775.4	17963.1	120060.7	127327
$m_{\mathrm{T}}(\mu, E_{\mathrm{T}}^{\mathrm{miss}}) > 210$ GeV	2.4	6.1	0.0	418.7	466
$\lvert\Delta\phi(\mu, b)\rvert < 1.2$	0.0	1.0	0.4	134.9	135

Table L.4: Cutflow totals for selected backgrounds as well as data in the SR1 optimized selection region in the muon channel.

SR1 Cut Sequence	$S1_R$ 0	$S1_R$ 20	$S1_R$ 40	$S1_R$ 60	$S1_R$ 80	$S1_R$ 100
1 electron, $p_T(e) > 30$ GeV	2239.2	2253.2	2224.1	2158.9	2113.2	2003.8
1 jet, $p_T(\text{jet}) > 25$ GeV	1291.5	1309.9	1295.1	1259.3	1227.5	1164.9
1 b-jet, $p_T(b) > 25$ GeV	676.6	674.3	671.2	662.1	635.5	613.5
$m_T(e, E_T^{\text{miss}}) > 210$ GeV	156.8	159.3	154.5	149.1	138.3	125.2
$\lvert\Delta\phi(e, b)\rvert < 1.2$	120.7	121.8	117.7	114.3	105.5	92.5

Table L.5: Cutflow totals for the $S1_R$ signal model in the SR1 optimized selection region in the electron channel.

SR1 Cut Sequence	$S1_R$ 0	$S1_R$ 20	$S1_R$ 40	$S1_R$ 60	$S1_R$ 80	$S1_R$ 100
1 muon, $p_T(\mu) > 30$ GeV	2585.7	2565.6	2551.3	2498.6	2393.8	2312.5
1 jet, $p_T(\text{jet}) > 25$ GeV	1481.1	1479.4	1472.9	1431.0	1369.2	1329.1
1 b-jet, $p_T(b) > 25$ GeV	768.7	764.6	764.5	743.9	711.2	680.4
$m_T(\mu, E_T^{\text{miss}}) > 210$ GeV	172.6	169.6	167.9	152.9	150.9	128.9
$\lvert\Delta\phi(\mu, b)\rvert < 1.2$	132.7	132.2	127.4	115.8	113.8	93.3

Table L.6: Cutflow totals for the $S1_R$ signal model in the SR1 optimized selection region in the muon channel.

Optimized SR2 signal region

This section presents the cut flow tables for the optimized SR2 selection region. For the electron (muon) channel these tables are shown for the backgrounds in Tables L.7 and L.8 (L.9 and L.10), and for the $S4_R$ signal model in Tables L.11, L.12, and L.13 (L.14, L.15, and L.16).

SR2 Cut Sequence	$t\bar{t}$	ST s-chan	ST t-chan	ST Wt-chan	W+hf	W+light
1 electron, $p_{\mathrm{T}}(e) > 30$ GeV	256902.6	2395.0	40213.5	23206.9	1479603.5	5801952.0
1 jet, $p_{\mathrm{T}}(\mathrm{jet}) > 25$ GeV	11591.7	651.7	12697.9	3021.3	886890.2	3671492.0
1 b-jet, $p_{\mathrm{T}}(b) > 25$ GeV	4761.7	324.9	5593.4	1053.7	50438.0	11562.6
$m_{\mathrm{T}}(e, E_{\mathrm{T}}^{\mathrm{miss}}) > 250$ GeV	92.7	0.0	0.2	34.2	23.8	5.7
$\lvert\Delta\phi(e,b)\rvert < 1.4$	42.2	0.0	0.0	5.7	5.3	0.8

Table L.7: Cutflow totals for selected backgrounds in the SR2 optimized selection region in the electron channel.

SR2 Cut Sequence	Z+Jets	Diboson	Multijet	Tot. Bkg.	Data
1 electron, $p_{\mathrm{T}}(e) > 30$ GeV	669763.2	44464.3	523575.8	8842076.9	8522185
1 jet, $p_{\mathrm{T}}(\mathrm{jet}) > 25$ GeV	387484.8	19245.3	336847.4	5329922.3	5127400
1 b-jet, $p_{\mathrm{T}}(b) > 25$ GeV	521.8	544.6	17483.6	92284.3	84011
$m_{\mathrm{T}}(e, E_{\mathrm{T}}^{\mathrm{miss}}) > 250$ GeV	0.0	1.0	7.3	165.0	155
$\lvert\Delta\phi(e,b)\rvert < 1.4$	0.0	0.3	0.0	54.3	56

Table L.8: Cutflow totals for selected backgrounds and data in the SR2 optimized selection region in the electron channel.

SR2 Cut Sequence	$t\bar{t}$	ST s-chan	ST t-chan	ST Wt-chan	W+hf	W+light
1 muon, $p_{\mathrm{T}}(\mu) > 30$ GeV	315841.7	3130.8	50664.9	27776.7	2040267.2	8432723.0
1 jet, $p_{\mathrm{T}}(\mathrm{jet}) > 25$ GeV	14310.1	880.6	16259.2	3619.1	1226282.9	5278589.0
1 b-jet, $p_{\mathrm{T}}(b) > 25$ GeV	5868.0	437.7	7093.5	1258.9	68643.0	16995.7
$m_{\mathrm{T}}(\mu, E_{\mathrm{T}}^{\mathrm{miss}}) > 250$ GeV	112.4	0.1	0.6	21.0	43.8	4.8
$\lvert\Delta\phi(\mu, b)\rvert < 1.4$	51.5	0.0	0.0	4.0	10.6	2.7

Table L.9: Cutflow totals for selected backgrounds in the SR2 optimized selection region in the muon channel.

SR2 Cut Sequence	Z+Jets	Diboson	Multijet	Tot. Bkg.	Data
1 muon, $p_{\mathrm{T}}(\mu) > 30$ GeV	493260.3	57996.5	242153.9	11663815.1	11906630
1 jet, $p_{\mathrm{T}}(\mathrm{jet}) > 25$ GeV	293886.5	25368.8	149290.2	7008486.4	7194020
1 b-jet, $p_{\mathrm{T}}(b) > 25$ GeV	1025.5	775.4	17963.1	120060.7	127327
$m_{\mathrm{T}}(\mu, E_{\mathrm{T}}^{\mathrm{miss}}) > 250$ GeV	0.0	3.0	0.2	185.9	199
$\lvert\Delta\phi(\mu, b)\rvert < 1.4$	0.0	0.7	0.8	70.4	77

Table L.10: Cutflow totals for selected backgrounds and data in the SR2 optimized selection region in the muon channel.

SR2 Cut Sequence	$S4_R$ 0	$S4_R$ 25	$S4_R$ 50	$S4_R$ 75	$S4_R$ 100	$S4_R$ 125
1 electron, $p_T(e) > 30$ GeV	162316.0	723264.8	227470.7	124630.3	79128.1	55493.0
1 jet, $p_T(\text{jet}) > 25$ GeV	70270.6	309180.2	95786.7	52588.1	32376.9	22625.1
1 b-jet, $p_T(b) > 25$ GeV	30713.5	134512.2	42686.4	23562.6	14638.8	9960.9
$m_T(e, E_T^{\text{miss}}) > 250$ GeV	1415.4	6898.9	2595.2	1691.6	1371.0	1004.4
$\lvert\Delta\phi(e,b)\rvert < 1.4$	1105.6	5644.9	2121.8	1427.5	1146.2	861.6

Table L.11: Cutflow totals for the $S4_R$ signal models in the mass range of [0,125] GeV in the SR2 optimized selection region in the electron channel.

SR2 Cut Sequence	$S4_R$ 150	$S4_R$ 200	$S4_R$ 250	$S4_R$ 300	$S4_R$ 400	$S4_R$ 500
1 electron, $p_T(e) > 30$ GeV	40166.4	22496.2	13153.7	8196.7	3508.9	1655.4
1 jet, $p_T(\text{jet}) > 25$ GeV	15946.8	8705.8	4982.5	3027.4	1242.7	559.1
1 b-jet, $p_T(b) > 25$ GeV	7073.9	3918.9	2222.4	1333.5	549.3	248.4
$m_T(e, E_T^{\text{miss}}) > 250$ GeV	864.9	607.9	402.4	268.0	135.9	70.1
$\lvert\Delta\phi(e,b)\rvert < 1.4$	741.7	531.7	360.1	239.1	123.2	63.4

Table L.12: Cutflow totals for the $S4_R$ signal models in the mass range of [150,500] GeV in the SR2 optimized selection region in the electron channel.

SR2 Cut Sequence	$S4_R$ 600	$S4_R$ 700	$S4_R$ 800	$S4_R$ 900	$S4_R$ 1000
1 electron, $p_T(e) > 30$ GeV	837.9	448.9	249.8	147.0	87.7
1 jet, $p_T(\text{jet}) > 25$ GeV	273.5	144.2	78.9	45.0	26.6
1 b-jet, $p_T(b) > 25$ GeV	120.6	63.3	34.3	19.0	11.8
$m_T(e, E_T^{\text{miss}}) > 250$ GeV	36.8	20.7	11.2	6.7	4.2
$\lvert\Delta\phi(e, b)\rvert < 1.4$	33.6	19.1	10.6	6.2	3.9

Table L.13: Cutflow totals for the $S4_R$ signal models in the mass range of [600,1000] GeV in the SR2 optimized selection region in the electron channel.

SR2 Cut Sequence	$S4_R$ 0	$S4_R$ 25	$S4_R$ 50	$S4_R$ 75	$S4_R$ 100	$S4_R$ 125
1 muon, $p_T(\mu) > 30$ GeV	217312.5	910670.1	289744.7	156233.8	99707.8	69336.2
1 jet, $p_T(\text{jet}) > 25$ GeV	94737.5	382934.9	120030.9	65202.7	40682.4	28081.3
1 b-jet, $p_T(b) > 25$ GeV	40802.2	169207.3	52994.5	28496.3	17693.2	12460.0
$m_T(\mu, E_T^{\text{miss}}) > 250$ GeV	1594.2	9601.4	3083.2	1884.8	1484.2	1249.1
$\lvert\Delta\phi(\mu, b)\rvert < 1.4$	1322.3	7588.1	2477.1	1570.7	1230.1	1021.2

Table L.14: Cutflow totals for the $S4_R$ signal models in the mass range of [0,125] GeV in the SR2 optimized selection region in the muon channel.

SR2 Cut Sequence	$S4_R$ 150	$S4_R$ 200	$S4_R$ 250	$S4_R$ 300	$S4_R$ 400	$S4_R$ 500
1 muon, $p_T(\mu) > 30$ GeV	50538.5	27708.9	16265.8	10037.1	4232.0	1976.2
1 jet, $p_T(\text{jet}) > 25$ GeV	19957.6	10701.6	6047.2	3668.7	1474.5	658.5
1 b-jet, $p_T(b) > 25$ GeV	8659.9	4719.7	2664.7	1640.5	655.7	291.8
$m_T(\mu, E_T^{\text{miss}}) > 250$ GeV	930.6	684.1	448.0	307.0	153.0	76.9
$\lvert\Delta\phi(\mu, b)\rvert < 1.4$	785.4	598.4	392.4	273.7	138.5	70.7

Table L.15: Cutflow totals for the $S4_R$ signal models in the mass range of [150,500] GeV in the SR2 optimized selection region in the muon channel.

SR2 Cut Sequence	$S4_R$ 600	$S4_R$ 700	$S4_R$ 800	$S4_R$ 900	$S4_R$ 1000
1 muon, $p_T(\mu) > 30$ GeV	996.0	529.0	295.2	171.4	102.3
1 jet, $p_T(\text{jet}) > 25$ GeV	325.1	166.8	92.1	51.7	30.1
1 b-jet, $p_T(b) > 25$ GeV	146.0	72.7	40.8	23.2	13.1
$m_T(\mu, E_T^{\text{miss}}) > 250$ GeV	41.8	23.0	13.4	8.0	4.7
$\lvert\Delta\phi(\mu, b)\rvert < 1.4$	38.6	21.3	12.6	7.6	4.4

Table L.16: Cutflow totals for the $S4_R$ signal models in the mass range of [600,1000] GeV in the SR2 optimized selection region in the muon channel.

Optimized SR2 signal region + lepton charge cut

This section presents the cut flow tables for the optimized SR2 selection region with an additional cut on the electric charge of the lepton (labeled as SR2CC in the tables and captions). For the electron (muon) channel these tables are shown for the backgrounds in Tables L.17 and L.18 (L.19 and L.20), and for the $S4_R$ signal model in Tables L.21, L.22, and L.23 (L.24, L.25, and L.26).

SR2CC Cut Sequence	$t\bar{t}$	ST s-chan	ST t-chan	ST Wt-chan	W+hf	W+light
1 electron, $p_{\mathrm{T}}(e) > 30$ GeV	256902.6	2395.0	40213.5	23206.9	1479603.5	5801952.0
1 jet, $p_{\mathrm{T}}(\mathrm{jet}) > 25$ GeV	11591.7	651.7	12697.9	3021.3	886890.2	3671492.0
1 b-jet, $p_{\mathrm{T}}(b) > 25$ GeV	4761.7	324.9	5593.4	1053.7	50438.0	11562.6
$m_{\mathrm{T}}(e, E_{\mathrm{T}}^{\mathrm{miss}}) > 250$ GeV	92.7	0.0	0.2	34.2	23.8	5.7
$\lvert\Delta\phi(e,b)\rvert < 1.4$	42.2	0.0	0.0	5.7	5.3	0.8
electron charge > 0	22.0	0.0	0.0	1.9	2.2	0.8

Table L.17: Cutflow totals for selected backgrounds in the SR2CC optimized selection region in the electron channel.

SR2CC Cut Sequence	Z+Jets	Diboson	Multijet	Tot. Bkg.	Data
1 electron, $p_{\mathrm{T}}(e) > 30$ GeV	669763.2	44464.3	523575.8	8842076.9	8522185
1 jet, $p_{\mathrm{T}}(\mathrm{jet}) > 25$ GeV	387484.8	19245.3	336847.4	5329922.3	5127400
1 b-jet, $p_{\mathrm{T}}(b) > 25$ GeV	521.8	544.6	17483.6	92284.3	84011
$m_{\mathrm{T}}(e, E_{\mathrm{T}}^{\mathrm{miss}}) > 250$ GeV	0.0	1.0	7.3	165.0	155
$\lvert\Delta\phi(e,b)\rvert < 1.4$	0.0	0.3	0.0	54.3	56
electron charge > 0	0.0	0.3	0.0	27.1	33

Table L.18: Cutflow totals for selected backgrounds and data in the SR2CC optimized selection region in the electron channel.

SR2CC Cut Sequence	$t\bar{t}$	ST s-chan	ST t-chan	ST Wt-chan	W+hf	W+light
1 muon, $p_{\mathrm{T}}(\mu) > 30$ GeV	315841.7	3130.8	50664.9	27776.7	2040267.2	8432723.0
1 jet, $p_{\mathrm{T}}(\mathrm{jet}) > 25$ GeV	14310.1	880.6	16259.2	3619.1	1226282.9	5278589.0
1 b-jet, $p_{\mathrm{T}}(b) > 25$ GeV	5868.0	437.7	7093.5	1258.9	68643.0	16995.7
$m_{\mathrm{T}}(\mu, E_{\mathrm{T}}^{\mathrm{miss}}) > 250$ GeV	112.4	0.1	0.6	21.0	43.8	4.8
$\lvert\Delta\phi(\mu, b)\rvert < 1.4$	51.5	0.0	0.0	4.0	10.6	2.7
muon charge > 0	25.2	0.0	0.0	0.6	5.9	2.7

Table L.19: Cutflow totals for selected backgrounds in the SR2CC optimized selection region in the muon channel.

SR2CC Cut Sequence	Z+Jets	Diboson	Multijet	Tot. Bkg.	Data
1 muon, $p_{\mathrm{T}}(\mu) > 30$ GeV	493260.3	57996.5	242153.9	11663815.1	11906630
1 jet, $p_{\mathrm{T}}(\mathrm{jet}) > 25$ GeV	293886.5	25368.8	149290.2	7008486.4	7194020
1 b-jet, $p_{\mathrm{T}}(b) > 25$ GeV	1025.5	775.4	17963.1	120060.7	127327
$m_{\mathrm{T}}(\mu, E_{\mathrm{T}}^{\mathrm{miss}}) > 250$ GeV	0.0	3.0	0.2	185.9	199
$\lvert\Delta\phi(\mu, b)\rvert < 1.4$	0.0	0.7	0.8	70.4	77
muon charge > 0	0.0	0.4	1.2	35.9	41

Table L.20: Cutflow totals for selected backgrounds and data in the SR2CC optimized selection region in the muon channel.

SR2CC Cut Sequence	$S4_R$ 0	$S4_R$ 25	$S4_R$ 50	$S4_R$ 75	$S4_R$ 100	$S4_R$ 125
1 electron, $p_T(e) > 30$ GeV	162316.0	723264.8	227470.7	124630.3	79128.1	55493.0
1 jet, $p_T(\text{jet}) > 25$ GeV	70270.6	309180.2	95786.7	52588.1	32376.9	22625.1
1 b-jet, $p_T(b) > 25$ GeV	30713.5	134512.2	42686.4	23562.6	14638.8	9960.9
$m_T(e, E_T^{\text{miss}}) > 250$ GeV	1415.4	6898.9	2595.2	1691.6	1371.0	1004.4
$\lvert\Delta\phi(e,b)\rvert < 1.4$	1105.6	5644.9	2121.8	1427.5	1146.2	861.6
electron charge > 0	980.8	4827.9	1909.2	1285.6	1038.7	746.6

Table L.21: Cutflow totals for the $S4_R$ signal models in the mass range of [0,125] GeV in the SR2CC optimized selection region in the electron channel.

SR2CC Cut Sequence	$S4_R$ 150	$S4_R$ 200	$S4_R$ 250	$S4_R$ 300	$S4_R$ 400	$S4_R$ 500
1 electron, $p_T(e) > 30$ GeV	40166.4	22496.2	13153.7	8196.7	3508.9	1655.4
1 jet, $p_T(\text{jet}) > 25$ GeV	15946.8	8705.8	4982.5	3027.4	1242.7	559.1
1 b-jet, $p_T(b) > 25$ GeV	7073.9	3918.9	2222.4	1333.5	549.3	248.4
$m_T(e, E_T^{\text{miss}}) > 250$ GeV	864.9	607.9	402.4	268.0	135.9	70.1
$\lvert\Delta\phi(e,b)\rvert < 1.4$	741.7	531.7	360.1	239.1	123.2	63.4
electron charge > 0	653.7	471.7	328.6	217.8	112.4	57.9

Table L.22: Cutflow totals for the $S4_R$ signal models in the mass range of [150,500] GeV in the SR2CC optimized selection region in the electron channel.

SR2CC Cut Sequence	$S4_R$ 600	$S4_R$ 700	$S4_R$ 800	$S4_R$ 900	$S4_R$ 1000
1 electron, $p_T(e) > 30$ GeV	837.9	448.9	249.8	147.0	87.7
1 jet, p_T(jet) > 25 GeV	273.5	144.2	78.9	45.0	26.6
1 b-jet, $p_T(b) > 25$ GeV	120.6	63.3	34.3	19.0	11.8
$m_T(e, E_T^{miss}) > 250$ GeV	36.8	20.7	11.2	6.7	4.2
$\|\Delta\phi(e, b)\| < 1.4$	33.6	19.1	10.6	6.2	3.9
electron charge > 0	31.2	17.7	9.9	5.9	3.7

Table L.23: Cutflow totals for the $S4_R$ signal models in the mass range of [600,1000] GeV in the SR2CC optimized selection region in the electron channel.

SR2CC Cut Sequence	$S4_R$ 0	$S4_R$ 25	$S4_R$ 50	$S4_R$ 75	$S4_R$ 100	$S4_R$ 125
1 muon, $p_T(\mu) > 30$ GeV	217312.5	910670.1	289744.7	156233.8	99707.8	69336.2
1 jet, p_T(jet) > 25 GeV	94737.5	382934.9	120030.9	65202.7	40682.4	28081.3
1 b-jet, $p_T(b) > 25$ GeV	40802.2	169207.3	52994.5	28496.3	17693.2	12460.0
$m_T(\mu, E_T^{miss}) > 250$ GeV	1594.2	9601.4	3083.2	1884.8	1484.2	1249.1
$\|\Delta\phi(\mu, b)\| < 1.4$	1322.3	7588.1	2477.1	1570.7	1230.1	1021.2
muon charge > 0	1213.2	6606.7	2217.5	1429.0	1108.9	909.4

Table L.24: Cutflow totals for the $S4_R$ signal models in the mass range of [0,125] GeV in the SR2CC optimized selection region in the muon channel.

SR2CC Cut Sequence	$S4_R$ 150	$S4_R$ 200	$S4_R$ 250	$S4_R$ 300	$S4_R$ 400	$S4_R$ 500
1 muon, $p_T(\mu) > 30$ GeV	50538.5	27708.9	16265.8	10037.1	4232.0	1976.2
1 jet, $p_T(\text{jet}) > 25$ GeV	19957.6	10701.6	6047.2	3668.7	1474.5	658.5
1 b-jet, $p_T(b) > 25$ GeV	8659.9	4719.7	2664.7	1640.5	655.7	291.8
$m_T(\mu, E_T^{\text{miss}}) > 250$ GeV	930.6	684.1	448.0	307.0	153.0	76.9
$\lvert\Delta\phi(\mu, b)\rvert < 1.4$	785.4	598.4	392.4	273.7	138.5	70.7
muon charge > 0	708.7	559.2	357.8	250.9	125.5	65.5

Table L.25: Cutflow totals for the $S4_R$ signal models in the mass range of [150,500] GeV in the SR2CC optimized selection region in the muon channel.

SR2CC Cut Sequence	$S4_R$ 600	$S4_R$ 700	$S4_R$ 800	$S4_R$ 900	$S4_R$ 1000
1 muon, $p_T(\mu) > 30$ GeV	996.0	529.0	295.2	171.4	102.3
1 jet, $p_T(\text{jet}) > 25$ GeV	325.1	166.8	92.1	51.7	30.1
1 b-jet, $p_T(b) > 25$ GeV	146.0	72.7	40.8	23.2	13.1
$m_T(\mu, E_T^{\text{miss}}) > 250$ GeV	41.8	23.0	13.4	8.0	4.7
$\lvert\Delta\phi(\mu, b)\rvert < 1.4$	38.6	21.3	12.6	7.6	4.4
muon charge > 0	36.1	20.0	12.0	7.3	4.2

Table L.26: Cutflow totals for the $S4_R$ signal models in the mass range of [600,1000] GeV in the SR2CC optimized selection region in the muon channel.

Optimized BDT signal region

This section presents the cut flow tables for the optimized BDT selection region. For the electron (muon) channel these tables are shown for the backgrounds in Tables L.27 and L.28 (L.29 and L.30), and for the $S4_R$ signal model in Tables L.31, L.32, and L.33 (L.34, L.35, and L.36).

BDT Cut Sequence	$t\bar{t}$	ST s-chan	ST t-chan	ST Wt-chan	W+hf	W+light
1 electron, $p_{\mathrm{T}}(e) > 30$ GeV	256902.6	2395.0	40213.5	23206.9	1479603.5	5801952.0
1 jet, $p_{\mathrm{T}}(\mathrm{jet}) > 25$ GeV	11591.7	651.7	12697.9	3021.3	886890.2	3671492.0
1 b-jet, $p_{\mathrm{T}}(b) > 25$ GeV	4761.7	324.9	5593.4	1053.7	50438.0	11562.6
electron charge > 0	2380.2	206.8	3655.6	529.7	25393.1	6469.3
$E_{\mathrm{T}}^{\mathrm{miss}} > 100$ GeV	562.5	14.4	159.3	93.8	534.0	162.4
$p_{\mathrm{T}}(e^{+}) > 100$ GeV	95.7	1.2	19.3	22.1	52.3	26.1

Table L.27: Cutflow totals for selected backgrounds in the BDT optimized selection region in the electron channel.

BDT Cut Sequence	Z+Jets	Diboson	Multijet	Tot. Bkg.	Data
1 electron, $p_{\mathrm{T}}(e) > 30$ GeV	669763.2	44464.3	523575.8	8842076.9	8522185
1 jet, $p_{\mathrm{T}}(\mathrm{jet}) > 25$ GeV	387484.8	19245.3	336847.4	5329922.3	5127400
1 b-jet, $p_{\mathrm{T}}(b) > 25$ GeV	521.8	544.6	17483.6	92284.3	84011
electron charge > 0	288.1	313.0	8761.8	47997.7	45168
$E_{\mathrm{T}}^{\mathrm{miss}} > 100$ GeV	0.7	18.8	61.3	1607.2	1412
$p_{\mathrm{T}}(e^{+}) > 100$ GeV	0.0	1.5	8.1	226.2	216

Table L.28: Cutflow totals for selected backgrounds and for data in the BDT optimized selection region in the electron channel.

BDT Cut Sequence	$t\bar{t}$	ST s-chan	ST t-chan	ST Wt-chan	W+hf	W+light
1 muon, $p_{\mathrm{T}}(\mu) > 30$ GeV	315841.7	3130.8	50664.9	27776.7	2040267.2	8432723.0
1 jet, $p_{\mathrm{T}}(\mathrm{jet}) > 25$ GeV	14310.1	880.6	16259.2	3619.1	1226282.9	5278589.0
1 b-jet, $p_{\mathrm{T}}(b) > 25$ GeV	5868.0	437.7	7093.5	1258.9	68643.0	16995.7
muon charge > 0	2895.2	281.6	4709.9	634.3	34905.6	10148.6
$E_{\mathrm{T}}^{\mathrm{miss}} > 100$ GeV	700.8	16.5	184.6	119.5	682.4	150.0
$p_{\mathrm{T}}(\mu^{+}) > 100$ GeV	99.8	1.1	17.3	20.2	60.0	14.5

Table L.29: Cutflow totals for selected backgrounds in the BDT optimized selection region in the muon channel.

BDT Cut Sequence	Z+Jets	Diboson	Multijet	Tot. Bkg.	Data
1 muon, $p_{\mathrm{T}}(\mu) > 30$ GeV	493260.3	57996.5	242153.9	11663815.1	11906630
1 jet, $p_{\mathrm{T}}(\mathrm{jet}) > 25$ GeV	293886.5	25368.8	149290.2	7008486.4	7194020
1 b-jet, $p_{\mathrm{T}}(b) > 25$ GeV	1025.5	775.4	17963.1	120060.7	127327
muon charge > 0	522.5	452.8	8945.1	63495.8	68924
$E_{\mathrm{T}}^{\mathrm{miss}} > 100$ GeV	3.9	23.8	3.1	1884.8	1981
$p_{\mathrm{T}}(\mu^{+}) > 100$ GeV	0.0	2.7	0.0	215.6	258

Table L.30: Cutflow totals for selected backgrounds and for data in the BDT optimized selection region in the muon channel.

BDT Cut Sequence	$S4_R$ 0	$S4_R$ 25	$S4_R$ 50	$S4_R$ 75	$S4_R$ 100	$S4_R$ 125
1 electron, $p_T(e) > 30$ GeV	162316.0	723264.8	227470.7	124630.3	79128.1	55493.0
1 jet, $p_T(\text{jet}) > 25$ GeV	70270.6	309180.2	95786.7	52588.1	32376.9	22625.1
1 b-jet, $p_T(b) > 25$ GeV	30713.5	134512.2	42686.4	23562.6	14638.8	9960.9
electron charge > 0	24816.1	113273.8	36181.8	19836.8	12551.5	8516.0
$E_T^{\text{miss}} > 100$ GeV	7126.9	42249.3	14282.5	8367.3	5786.3	4079.8
$p_T(e^+) > 100$ GeV	1511.3	6849.0	2700.1	1717.4	1344.8	968.6

Table L.31: Cutflow totals for the $S4_R$ signal models in the mass range of [0,125] GeV in the BDT optimized selection region in the electron channel.

BDT Cut Sequence	$S4_R$ 150	$S4_R$ 200	$S4_R$ 250	$S4_R$ 300	$S4_R$ 400	$S4_R$ 500
1 electron, $p_T(e) > 30$ GeV	40166.4	22496.2	13153.7	8196.7	3508.9	1655.4
1 jet, $p_T(\text{jet}) > 25$ GeV	15946.8	8705.8	4982.5	3027.4	1242.7	559.1
1 b-jet, $p_T(b) > 25$ GeV	7073.9	3918.9	2222.4	1333.5	549.3	248.4
electron charge > 0	6059.2	3423.4	1963.8	1184.4	496.5	227.0
$E_T^{\text{miss}} > 100$ GeV	3066.5	1873.7	1146.4	721.7	329.1	156.0
$p_T(e^+) > 100$ GeV	824.5	533.8	364.0	244.0	115.8	59.6

Table L.32: Cutflow totals for the $S4_R$ signal models in the mass range of [150,500] GeV in the BDT optimized selection region in the electron channel.

BDT Cut Sequence	$S4_R$ 600	$S4_R$ 700	$S4_R$ 800	$S4_R$ 900	$S4_R$ 1000
1 electron, $p_T(e) > 30$ GeV	837.9	448.9	249.8	147.0	87.7
1 jet, p_T(jet) > 25 GeV	273.5	144.2	78.9	45.0	26.6
1 b-jet, $p_T(b) > 25$ GeV	120.6	63.3	34.3	19.0	11.8
electron charge > 0	111.2	58.6	32.2	17.8	11.1
$E_T^{miss} > 100$ GeV	79.1	41.8	23.7	13.4	8.2
$p_T(e^+) > 100$ GeV	31.8	17.3	9.6	5.7	3.5

Table L.33: Cutflow totals for the $S4_R$ signal models in the mass range of [600,1000] GeV in the BDT optimized selection region in the electron channel.

BDT Cut Sequence	$S4_R$ 0	$S4_R$ 25	$S4_R$ 50	$S4_R$ 75	$S4_R$ 100	$S4_R$ 125
1 muon, $p_T(\mu) > 30$ GeV	217312.5	910670.1	289744.7	156233.8	99707.8	69336.2
1 jet, p_T(jet) > 25 GeV	94737.5	382934.9	120030.9	65202.7	40682.4	28081.3
1 b-jet, $p_T(b) > 25$ GeV	40802.2	169207.3	52994.5	28496.3	17693.2	12460.0
muon charge > 0	32932.5	144148.6	45311.0	24287.6	15250.4	10811.2
$E_T^{miss} > 100$ GeV	9828.4	57879.4	18490.1	10277.1	6849.2	5285.6
$p_T(\mu^+) > 100$ GeV	1599.0	8654.5	2991.7	1866.8	1407.1	1178.4

Table L.34: Cutflow totals for the $S4_R$ signal models in the mass range of [0,125] GeV in the BDT optimized selection region in the muon channel.

BDT Cut Sequence	$S4_R$ 150	$S4_R$ 200	$S4_R$ 250	$S4_R$ 300	$S4_R$ 400	$S4_R$ 500
1 muon, $p_T(\mu) > 30$ GeV	50538.5	27708.9	16265.8	10037.1	4232.0	1976.2
1 jet, p_T(jet) > 25 GeV	19957.6	10701.6	6047.2	3668.7	1474.5	658.5
1 b-jet, $p_T(b) > 25$ GeV	8659.9	4719.7	2664.7	1640.5	655.7	291.8
muon charge > 0	7533.1	4157.8	2364.9	1472.8	592.5	270.2
$E_T^{miss} > 100$ GeV	3825.0	2340.5	1430.2	912.8	394.4	186.6
$p_T(\mu^+) > 100$ GeV	832.0	606.3	379.2	251.4	124.5	63.5

Table L.35: Cutflow totals for the $S4_R$ signal models in the mass range of [150,500] GeV in the BDT optimized selection region in the muon channel.

BDT Cut Sequence	$S4_R$ 600	$S4_R$ 700	$S4_R$ 800	$S4_R$ 900	$S4_R$ 1000
1 muon, $p_T(\mu) > 30$ GeV	996.0	529.0	295.2	171.4	102.3
1 jet, p_T(jet) > 25 GeV	325.1	166.8	92.1	51.7	30.1
1 b-jet, $p_T(b) > 25$ GeV	146.0	72.7	40.8	23.2	13.1
muon charge > 0	134.8	67.9	38.3	21.8	12.5
$E_T^{miss} > 100$ GeV	93.9	49.8	28.4	16.4	9.4
$p_T(\mu^+) > 100$ GeV	33.9	18.6	11.1	6.5	3.9

Table L.36: Cutflow totals for the $S4_R$ signal models in the mass range of [600,1000] GeV in the BDT optimized selection region in the muon channel.

CR1 control region

This section presents the cut flow tables for the CR1 control region. For the electron (muon) channel these tables are shown for the backgrounds in Tables L.37 and L.38 (L.39 and L.40).

CR1 Cut Sequence	$t\bar{t}$	ST s-chan	ST t-chan	ST Wt-chan	W+hf	W+light
1 electron, $p_{\mathrm{T}}(e) > 30$ GeV	256902.6	2395.0	40213.5	23206.9	1479603.5	5801952.0
1 jet, $p_{\mathrm{T}}(\mathrm{jet}) > 25$ GeV	11591.7	651.7	12697.9	3021.3	886890.2	3671492.0
1 b-jet, $p_{\mathrm{T}}(b) > 25$ GeV	4761.7	324.9	5593.4	1053.7	50438.0	11562.6
$m_{\mathrm{T}}(e, E_{\mathrm{T}}^{\mathrm{miss}}) > 60$ GeV	3795.0	245.0	4301.0	867.3	42721.5	10499.2
$m_{\mathrm{T}}(e, E_{\mathrm{T}}^{\mathrm{miss}}) < 120$ GeV	2280.0	231.3	4140.0	511.8	39685.7	10110.8

Table L.37: Cutflow totals for selected backgrounds in the CR1 control region in the electron channel.

CR1 Cut Sequence	Z+Jets	Diboson	Multijet	Tot. Bkg.	Data
1 electron, $p_{\mathrm{T}}(e) > 30$ GeV	669763.2	44464.3	523575.8	8842076.9	8522185
1 jet, $p_{\mathrm{T}}(\mathrm{jet}) > 25$ GeV	387484.8	19245.3	336847.4	5329922.3	5127400
1 b-jet, $p_{\mathrm{T}}(b) > 25$ GeV	521.8	544.6	17483.6	92284.3	84011
$m_{\mathrm{T}}(e, E_{\mathrm{T}}^{\mathrm{miss}}) > 60$ GeV	273.9	431.7	9352.5	72487.1	68000
$m_{\mathrm{T}}(e, E_{\mathrm{T}}^{\mathrm{miss}}) < 120$ GeV	263.0	392.7	8823.7	66439.0	62217

Table L.38: Cutflow totals for selected backgrounds and data in the CR1 control region in the electron channel.

CR1 Cut Sequence	$t\bar{t}$	ST s-chan	ST t-chan	ST Wt-chan	W+hf	W+light
1 muon, $p_{\mathrm{T}}(\mu) > 30$ GeV	315841.7	3130.8	50664.9	27776.7	2040267.2	8432723.0
1 jet, $p_{\mathrm{T}}(\mathrm{jet}) > 25$ GeV	14310.1	880.6	16259.2	3619.1	1226282.9	5278589.0
1 b-jet, $p_{\mathrm{T}}(b) > 25$ GeV	5868.0	437.7	7093.5	1258.9	68643.0	16995.7
$m_{\mathrm{T}}(\mu, E_{\mathrm{T}}^{\mathrm{miss}}) > 60$ GeV	4785.9	349.6	5757.9	1060.8	60737.4	15798.9
$m_{\mathrm{T}}(\mu, E_{\mathrm{T}}^{\mathrm{miss}}) < 120$ GeV	2855.0	329.5	5499.0	644.8	55965.5	15281.4

Table L.39: Cutflow totals for selected backgrounds in the CR1 control region in the muon channel.

CR1 Cut Sequence	Z+Jets	Diboson	Multijet	Tot. Bkg.	Data
1 muon, $p_{\mathrm{T}}(\mu) > 30$ GeV	493260.3	57996.5	242153.9	11663815.1	11906630
1 jet, $p_{\mathrm{T}}(\mathrm{jet}) > 25$ GeV	293886.5	25368.8	149290.2	7008486.4	7194020
1 b-jet, $p_{\mathrm{T}}(b) > 25$ GeV	1025.5	775.4	17963.1	120060.7	127327
$m_{\mathrm{T}}(\mu, E_{\mathrm{T}}^{\mathrm{miss}}) > 60$ GeV	838.9	650.4	7888.3	97868.1	106647
$m_{\mathrm{T}}(\mu, E_{\mathrm{T}}^{\mathrm{miss}}) < 120$ GeV	781.4	576.2	7834.4	89767.2	97410

Table L.40: Cutflow totals for selected backgrounds and data in the CR1 control region in the muon channel.

CR2 control region

This section presents the cut flow tables for the CR2 control region. For the electron (muon) channel these tables are shown for the backgrounds in Tables L.41 and L.42 (L.43 and L.44).

CR2 Cut Sequence	$t\bar{t}$	ST s-chan	ST t-chan	ST Wt-chan	W+hf	W+light
1 electron, $p_{\mathrm{T}}(e) > 30$ GeV	256902.6	2395.0	40213.5	23206.9	1479603.5	5801952.0
1 jet, $p_{\mathrm{T}}(\mathrm{jet}) > 25$ GeV	11591.7	651.7	12697.9	3021.3	886890.2	3671492.0
1 b-jet, $p_{\mathrm{T}}(b) > 25$ GeV	4761.7	324.9	5593.4	1053.7	50438.0	11562.6
$m_{\mathrm{T}}(e, E_{\mathrm{T}}^{\mathrm{miss}}) > 120$ GeV	1514.9	13.7	161.0	355.5	3035.9	388.3
$m_{\mathrm{T}}(e, E_{\mathrm{T}}^{\mathrm{miss}}) < 150$ GeV	691.0	11.9	146.2	177.5	2512.1	287.2
$\lvert\Delta\phi(e, b)\rvert < 1.8$	363.9	1.5	20.0	82.5	142.8	52.5

Table L.41: Cutflow totals for selected backgrounds in the CR2 control region in the electron channel.

CR2 Cut Sequence	Z+Jets	Diboson	Multijet	Tot. Bkg.	Data
1 electron, $p_{\mathrm{T}}(e) > 30$ GeV	669763.2	44464.3	523575.8	8842076.9	8522185
1 jet, $p_{\mathrm{T}}(\mathrm{jet}) > 25$ GeV	387484.8	19245.3	336847.4	5329922.3	5127400
1 b-jet, $p_{\mathrm{T}}(b) > 25$ GeV	521.8	544.6	17483.6	92284.3	84011
$m_{\mathrm{T}}(e, E_{\mathrm{T}}^{\mathrm{miss}}) > 120$ GeV	10.9	39.0	529.7	6049.0	5783
$m_{\mathrm{T}}(e, E_{\mathrm{T}}^{\mathrm{miss}}) < 150$ GeV	9.4	25.3	362.6	4223.2	4025
$\lvert\Delta\phi(e, b)\rvert < 1.8$	0.4	4.5	0.8	669.1	647

Table L.42: Cutflow totals for selected backgrounds and data in the CR2 control region in the electron channel.

CR2 Cut Sequence	$t\bar{t}$	ST s-chan	ST t-chan	ST Wt-chan	W+hf	W+light
1 muon, $p_{\mathrm{T}}(\mu) > 30$ GeV	315841.7	3130.8	50664.9	27776.7	2040267.2	8432723.0
1 jet, $p_{\mathrm{T}}(\mathrm{jet}) > 25$ GeV	14310.1	880.6	16259.2	3619.1	1226282.9	5278589.0
1 b-jet, $p_{\mathrm{T}}(b) > 25$ GeV	5868.0	437.7	7093.5	1258.9	68643.0	16995.7
$m_{\mathrm{T}}(\mu, E_{\mathrm{T}}^{\mathrm{miss}}) > 120$ GeV	1930.9	20.0	258.9	416.0	4771.9	517.6
$m_{\mathrm{T}}(\mu, E_{\mathrm{T}}^{\mathrm{miss}}) < 150$ GeV	930.2	17.2	236.3	201.0	4057.6	451.5
$\lvert\Delta\phi(\mu, b)\rvert < 1.8$	500.2	2.1	36.6	92.8	272.6	94.0

Table L.43: Cutflow totals for selected backgrounds in the CR2 control region in the muon channel.

CR2 Cut Sequence	Z+Jets	Diboson	Multijet	Tot. Bkg.	Data
1 muon, $p_{\mathrm{T}}(\mu) > 30$ GeV	493260.3	57996.5	242153.9	11663815.1	11906630
1 jet, $p_{\mathrm{T}}(\mathrm{jet}) > 25$ GeV	293886.5	25368.8	149290.2	7008486.4	7194020
1 b-jet, $p_{\mathrm{T}}(b) > 25$ GeV	1025.5	775.4	17963.1	120060.7	127327
$m_{\mathrm{T}}(\mu, E_{\mathrm{T}}^{\mathrm{miss}}) > 120$ GeV	57.5	74.2	54.0	8101.0	9237
$m_{\mathrm{T}}(\mu, E_{\mathrm{T}}^{\mathrm{miss}}) < 150$ GeV	48.2	51.8	28.9	6022.7	6806
$\lvert\Delta\phi(\mu, b)\rvert < 1.8$	19.1	13.6	0.0	1031.1	1101

Table L.44: Cutflow totals for selected backgrounds and data in the CR2 control region in the muon channel.

Appendix M

Event displays of monotop event candidates

This appendix presents event displays for two monotop event candidates selected in this analysis on the 8 TeV 2012 pp collision data. Two events have been selected in the tail of the $E_{\mathrm{T}}^{\mathrm{miss}}$ distributions, one in each channel. Table M.1 gives the RunNumber, EventNumber of each of these two events, together with information on the event kinematics.

Channel	EventNumber	RunNumber	$p_{\mathrm{T}}(\ell)$ [GeV]	$p_{\mathrm{T}}(b)$ [GeV]	$E_{\mathrm{T}}^{\mathrm{miss}}$ [GeV]	$m_{\mathrm{T}}(\ell, E_{\mathrm{T}}^{\mathrm{miss}})$ [GeV]	$\Delta\phi(\ell, b)$
Electron	213754	232636371	361	87	398	750	-1.227
Muon	205112	37740915	372	59	419	790	-0.658

Table M.1: Kinematic information for the two monotop event candidates displayed in Figures M.1, M.2, M.3, and M.4.

Displays of these two events made using Atlantis [106] and VP1 [107] are shown in the following figures. On the Atlantis displays - Figures M.1 and M.3 for the electron and muon event respectively - the electron is indicated in green, the muon in purple, the b-tagged jet in blue, and the $E_{\mathrm{T}}^{\mathrm{miss}}$ in red. On the VP1 displays - Figures M.2 and M.4 for the electron and muon event respectively - the electron is indicated in green, the muon in red, the b-tagged jet with an azure cone, and the $E_{\mathrm{T}}^{\mathrm{miss}}$ with a dashed yellow line.

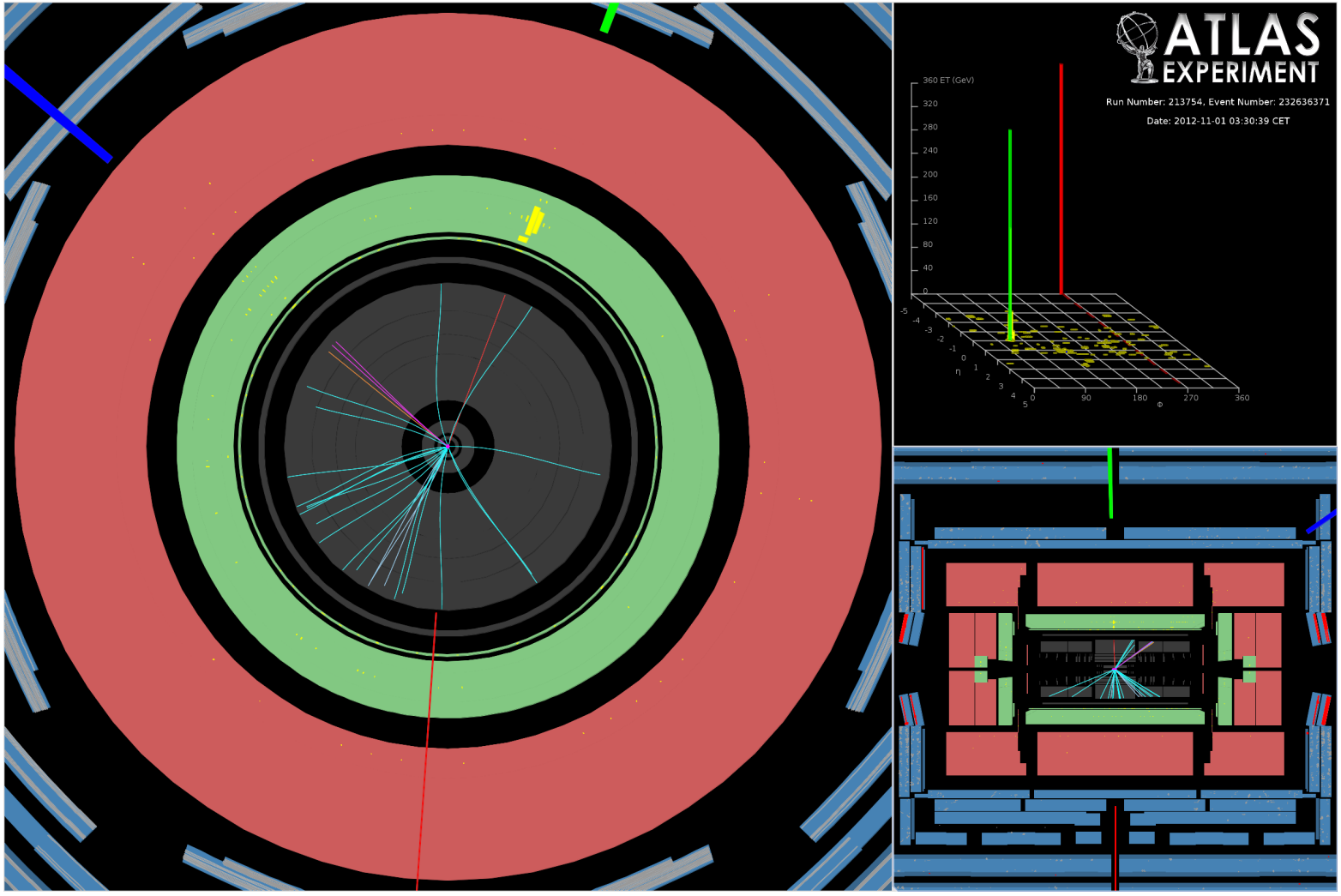

Figure M.1: Event display of the monotop candidate event in the electron channel, recorded on November 1st, 2012 at 03:30:39 CET, with the run number 213754 and the event number 232636371.

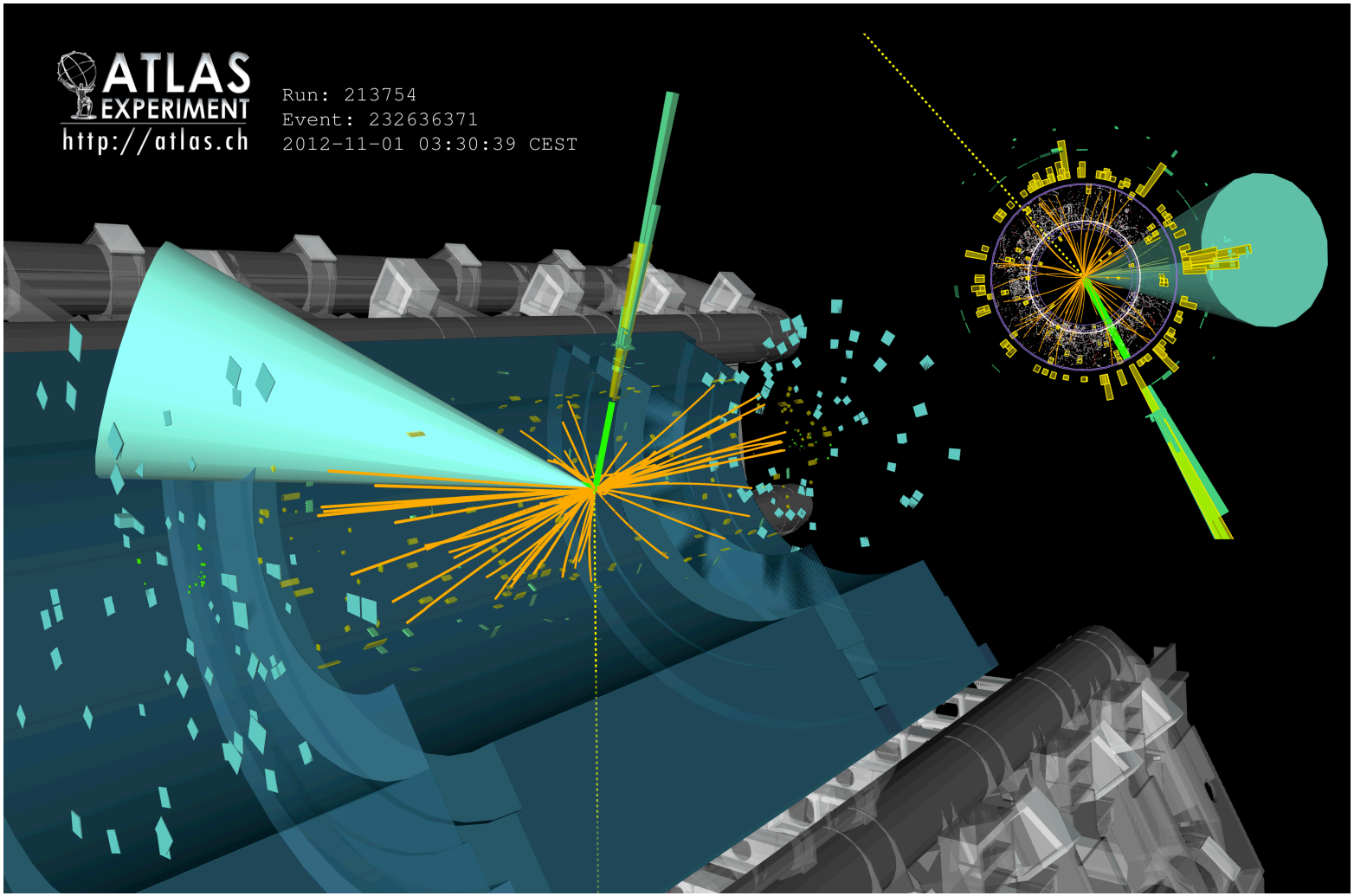

Figure M.2: Event display of the monotop candidate event in the electron channel, recorded on November 1st, 2012 at 03:30:39 CET, with the run number 213754 and the event number 232636371.

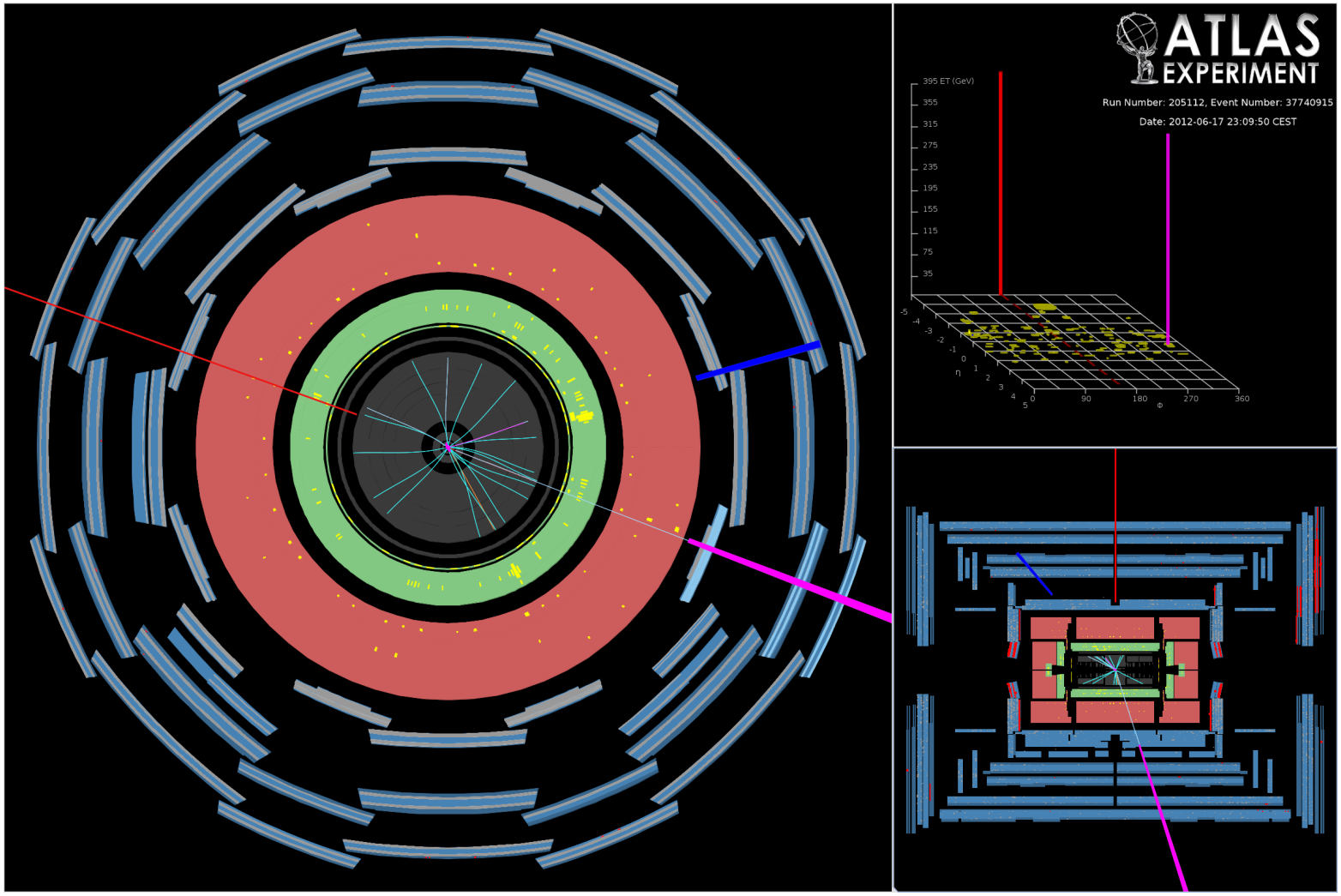

Figure M.3: Event display of the monotop candidate event in the muon channel, recorded on June 17$^{\text{th}}$, 2012 at 23:30:50 CEST, with the run number 205112 and the event number 37740915.

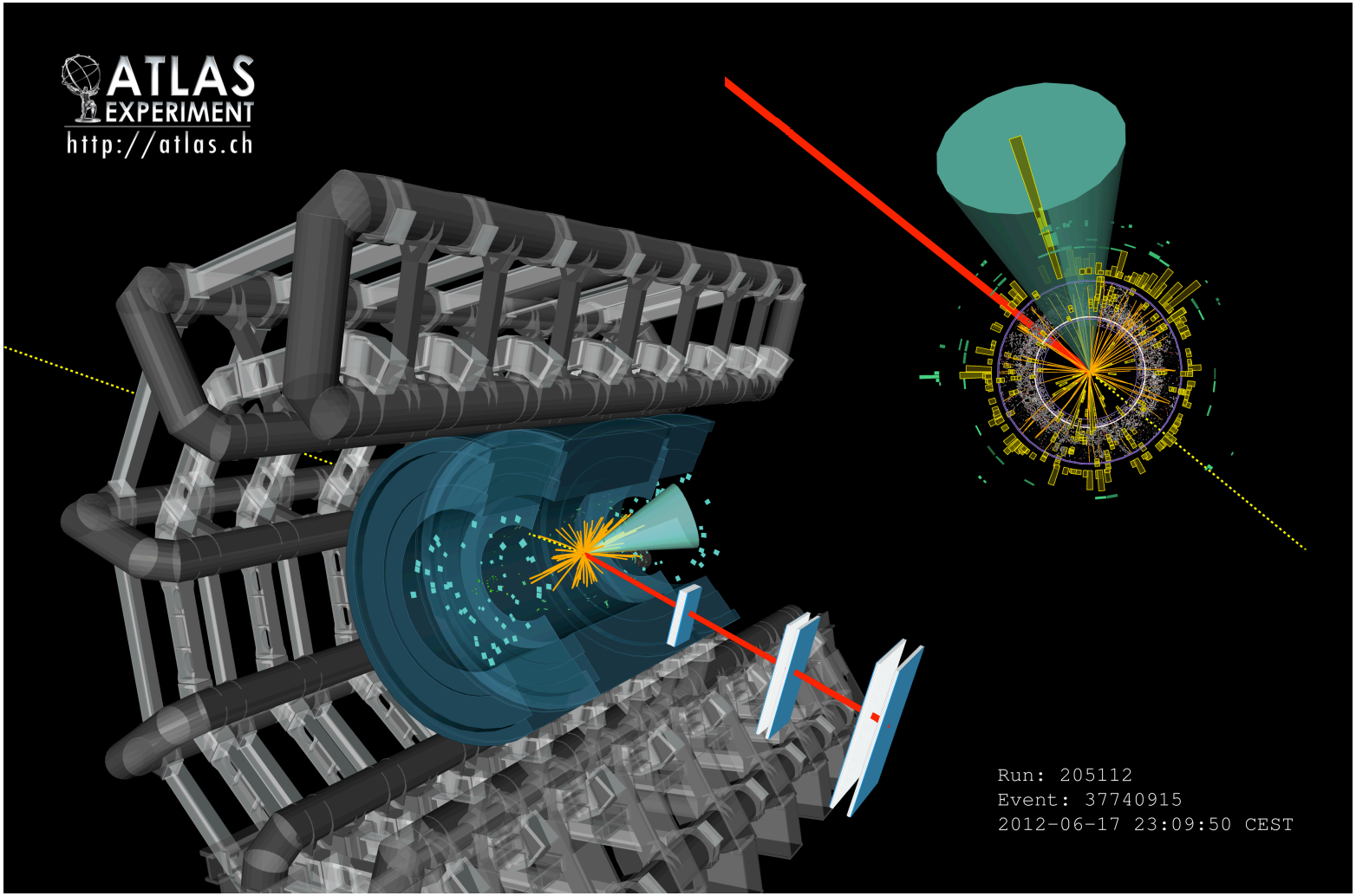

Figure M.4: Event display of the monotop candidate event in the muon channel, recorded on June 17$^{\text{th}}$, 2012 at 23:30:50 CEST, with the run number 205112 and the event number 37740915.

BIBLIOGRAPHY

BIBLIOGRAPHY

[1] Particle Data Group Collaboration, *Review of Particle Physics*, Chin. Phys. **C38** (2014) 090001.

[2] ATLAS Electromagnetic Barrel Liquid Argon Calorimeter Group Collaboration, *Construction, assembly and tests of the ATLAS electromagnetic barrel calorimeter*, Nucl. Instrum. Meth. **A558** (2006) 388–418.

[3] ATLAS Collaboration, *Construction, assembly and tests of the ATLAS electromagnetic end-cap calorimeters*, JINST **3** (2008) P06002.

[4] M. L. Andrieux et al., *Construction and test of the first two sectors of the ATLAS barrel liquid argon presampler*, Nucl. Instrum. Meth. **A479** (2002) 316–333.

[5] ATLAS Collaboration, *Readiness of the ATLAS Tile Calorimeter for LHC collisions*, Eur. Phys. J. **C70** (2010) 1193–1236.

[6] D. M. Gingrich et al., *Construction, assembly and testing of the ATLAS hadronic end-cap calorimeter*, JINST **2** (2007) P05005.

[7] A. Artamonov et al., *The ATLAS forward calorimeters*, JINST **3** (2008) P02010.

[8] J. P. A. et al, *Energy calibration of the ATLAS Liquid Argon Forward Calorimeter*, JINST **3** (2008) no. 02, P02002.

[9] S. A. et al, *Results from a new combined test of an electromagnetic liquid argon calorimeter with a hadronic scintillating-tile calorimeter*, Nucl. Instrum. Meth. **449** (2000) no. 3, 461–477.

[10] B. D. et al, *Performance of the ATLAS hadronic end-cap calorimeter in beam tests*, Nucl. Instrum. Meth. **482** (2002) no. 12, 94–124.

[11] B. A. et al, *Construction, assembly and tests of the ATLAS electromagnetic barrel calorimeter*, Nucl. Instrum. Meth. **558** (2006) no. 2, 388–418.

[12] ATLAS Collaboration, *Expected Performance of the ATLAS Experiment - Detector, Trigger and Physics*, SLAC-R-980, CERN-OPEN-2008-020.

[13] J. Alison et al., *Supporting document on electron efficiency measurements using the 2012 LHC proton-proton collision data*, Tech. Rep. ATL-COM-PHYS-2013-1295, CERN, Geneva, Sep, 2013.

[14] W. Lampl, S. Laplace, D. Lelas, P. Loch, H. Ma, S. Menke, S. Rajagopalan, D. Rousseau, S. Snyder, and G. Unal, *Calorimeter Clustering Algorithms: Description and Performance*, Tech. Rep. ATL-LARG-PUB-2008-002, ATL-COM-LARG-2008-003, CERN, Geneva, Apr, 2008.

[15] N. Kidonakis, *NNLL resummation for s-channel single top quark production*, Phys. Rev. **D81** (2010) 054028.

[16] N. Kidonakis, *Next-to-next-to-leading-order collinear and soft gluon corrections for t-channel single top quark production*, Phys. Rev. **D83** (2011) 091503.

[17] N. Kidonakis, *Two-loop soft anomalous dimensions for single top quark associated production with a W or H*, Phys. Rev. **D82** (2010) 054018.

[18] M. Czakon and A. Mitov, *Top++: A Program for the Calculation of the Top-Pair Cross-Section at Hadron Colliders*, Comput. Phys. Commun. **185** (2014) 2930.

[19] V. Barger and R. Phillips, *Collider Physics*. Westview Press, 1991.

[20] J. Wang, C. S. Li, D. Y. Shao, and H. Zhang, *Search for the signal of monotop production at the early LHC*, Phys. Rev. **D86** (2012) 034008.

[21] ATLAS Collaboration, *Measurement of the total cross section from elastic scattering in pp collisions at $\sqrt{s} = 7$ TeV with the ATLAS detector*, Nucl. Phys. **B889** (2014) 486–548.

[22] ATLAS Collaboration, *Luminosity determination in pp collisions at $\sqrt{s} = 8$ TeV using the ATLAS detector at the LHC*, Eur. Phys. J. **C76** (2016) no. 12, 653.

[23] ATLAS Collaboration, *The ATLAS Experiment at the CERN Large Hadron Collider*, JINST **3** (2008) S08003.

[24] ATLAS Collaboration, *ATLAS pixel detector electronics and sensors*, JINST **3** (2008) P07007.

[25] A. Bingul, *The ATLAS TRT and its Performance at LHC*, Journal of Physics: Conference Series **347** (2012) no. 1, 012025.

[26] ATLAS Collaboration, *Summary plots from the ATLAS Standard Model physics group*, https://atlas.web.cern.ch/Atlas/GROUPS/PHYSICS/CombinedSummaryPlots/SM/index.html.

[27] ATLAS Collaboration, *ATLAS level-1 trigger: Technical Design Report*. Technical Design Report ATLAS. CERN, Geneva, 1998.

[28] R. A. et al, *The ATLAS Level-1 Calorimeter Trigger*, JINST **3** (2008) no. 03, P03001.

[29] S. A. et al, *The ATLAS central level-1 trigger logic and TTC system*, JINST **3** (2008) no. 08, P08002.

[30] T. Cornelissen, M. Elsing, I. Gavrilenko, W. Liebig, E. Moyse, and A. Salzburger, *The new ATLAS track reconstruction (NEWT)*, J. Phys. Conf. Ser. **119** (2008) 032014.

[31] S. Hassani, L. Chevalier, E. Lancon, J. F. Laporte, R. Nicolaidou, and A. Ouraou, *A muon identification and combined reconstruction procedure for the ATLAS detector at the LHC using the (MUONBOY, STACO, MuTag) reconstruction packages*, Nucl. Instrum. Meth. **A572** (2007) 77–79.

[32] ATLAS Collaboration, *Performance of pile-up mitigation techniques for jets in pp collisions with the ATLAS detector*, Nucl. Instrum. Meth. **A824** (2016) 367–370.

[33] *Pile-up subtraction and suppression for jets in ATLAS*, Tech. Rep. ATLAS-CONF-2013-083, CERN, Geneva, Aug, 2013.

[34] DØ Collaboration, *Observation of Single Top Quark Production*, https://www-d0.fnal.gov/Run2Physics/top/singletop_observation/singletop_observation_updated.html.

[35] ATLAS Collaboration, *Performance of b-Jet Identification in the ATLAS Experiment*, JINST **11** (2016) no. 04, P04008.

[36] ATLAS Collaboration, *Preliminary results on the muon reconstruction efficiency, momentum resolution, and momentum scale in ATLAS 2012 pp collision data*, ATLAS-CONF-2013-088.

[37] ATLAS Collaboration, *Search for invisible particles produced in association with single-top-quarks in proton-proton collisions at* $\sqrt{s} = 8$ *TeV with the ATLAS detector*, Eur. Phys. J. **C75** (2015) no. 2, 79.

[38] LUX Collaboration, D. S. Akerib et al., *The Large Underground Xenon (LUX) Experiment*, Nucl. Instrum. Meth. **A704** (2013) 111–126.

[39] ATLAS Collaboration, *Search for new phenomena in events with a photon and missing transverse momentum in pp collisions at* $\sqrt{s} = 8$ *TeV with the ATLAS detector*, Phys. Rev. **D91** (2015) no. 1, 012008.

[40] CMS Collaboration, *Search for Dark Matter and Large Extra Dimensions in pp Collisions Yielding a Photon and Missing Transverse Energy*, Phys. Rev. Lett. **108** (2012) 261803.

[41] ATLAS Collaboration, *Search for new phenomena in final states with an energetic jet and large missing transverse momentum in pp collisions at* $\sqrt{s}$ *=8 TeV with the ATLAS detector*, Eur. Phys. J. **C75** (2015) no. 7, 299.

[42] CMS Collaboration, *Search for dark matter, extra dimensions, and unparticles in monojet events in proton-proton collisions at* $\sqrt{s} = 8\ TeV$, Eur. Phys. J. **C75** (2015) no. 5, 235.

[43] ATLAS Collaboration, *Search for dark matter in events with a hadronically decaying* W *or* Z *boson and missing transverse momentum in pp collisions at* $\sqrt{s} = 8\ TeV$ *with the ATLAS detector*, Phys. Rev. Lett. **112** (2014) no. 4, 041802.

[44] ATLAS Collaboration, *Search for dark matter in events with a* Z *boson and missing transverse momentum in pp collisions at* $\sqrt{s} = 8\ TeV$ *with the ATLAS detector*, Phys. Rev. **D90** (2014) no. 1, 012004.

[45] S. L. Glashow, J. Iliopoulos, and L. Maiani, *Weak Interactions with Lepton-Hadron Symmetry*, Phys. Rev. **D2** (1970) 1285–1292.

[46] S. M. Barr, *A New Symmetry Breaking Pattern for SO(10) and Proton Decay*, Phys. Lett. **B112** (1982) 219–222.

[47] R. Barbier et al., *R-parity violating supersymmetry*, Phys. Rept. **420** (2005) 1–202.

[48] I. Boucheneb, G. Cacciapaglia, A. Deandrea, and B. Fuks, *Revisiting monotop production at the LHC*, Journal of High Energy Physics **01** (2015) 017.

[49] B. C. Allanach, S. Grab, and H. E. Haber, *Supersymmetric Monojets at the Large Hadron Collider*, Journal of High Energy Physics **01** (2011) 138.

[50] F. del Aguila, J. A. Aguilar-Saavedra, and L. Ametller, *Zt and* γt *production via top flavor changing neutral couplings at the Fermilab Tevatron*, Phys. Lett. **B462** (1999) 310–318.

[51] J. F. Kamenik and J. Zupan, *Discovering Dark Matter Through Flavor Violation at the LHC*, Phys. Rev. **D84** (2011) 111502.

[52] E. Alvarez, E. C. Leskow, J. Drobnak, and J. F. Kamenik, *Leptonic Monotops at LHC*, Phys. Rev. **D89** (2014) no. 1, 014016.

[53] A. Kumar, J. N. Ng, A. Spray, and P. T. Winslow, *Tracking down the top quark forward-backward asymmetry with monotops*, Phys. Rev. **D88** (2013) no. 7, 075012.

[54] J. Andrea, B. Fuks, and F. Maltoni, *Monotops at the LHC*, Phys. Rev. **D84** (2011) 074025.

[55] J.-L. Agram, J. Andrea, M. Buttignol, E. Conte, and B. Fuks, *Monotop phenomenology at the Large Hadron Collider*, Phys. Rev. **D89** (2014) no. 1, 014028.

[56] ATLAS Collaboration, *Search for displaced vertices arising from decays of new heavy particles in 7 TeV pp collisions at ATLAS*, Phys. Lett. **B707** (2012) 478–496.

[57] J. Alwall, M. Herquet, F. Maltoni, O. Mattelaer, and T. Stelzer, *MadGraph 5: Going Beyond*, Journal of High Energy Physics **06** (2011) 128.

[58] ALICE Collaboration, *The ALICE experiment at the CERN LHC*, JINST **3** (2008) S08002.

[59] LHCb Collaboration, *The LHCb Detector at the LHC*, JINST **3** (2008) S08005.

[60] CMS Collaboration, *The CMS experiment at the CERN LHC*, JINST **3** (2008) S08004.

[61] E. Boltezar, H. Haseroth, W. Pirkl, T. Sherwood, U. Tallgren, P. Tetu, D. Warner, and M. Weiss, *The New CERN 50MeV Linac*, Proc. 1979 Linear Accelerator Conference **BNL 51134** (1979) 66–77.

[62] B. Mikulec, A. Blas, C. Carli, A. Findlay, K. Hanke, G. Rumolo, and J. Tan, *LHC Beams from the CERN PS Booster*, in *Particle accelerator. Proceedings, 23rd Conference, PAC'09, Vancouver, Canada, May 4-8, 2009*, p. TU6PFP086. 2010.

[63] A. Blas et al., *The PS complex as proton pre-injector for the LHC: Design and implementation report*, CERN-2000-003.

[64] P. Collier and B. Goddard, *Preparation of the SPS as LHC injector*, in *Particle accelerator. Proceedings, 6th European conference, EPAC'98, Stockholm, Sweden, June 22-26, 1998. Vol. 1-3*, pp. 335–337. 1998.

[65] ATLAS Collaboration, *ATLAS magnet system: Technical Design Report, 1.* Technical Design Report ATLAS. CERN, Geneva, 1997.

[66] M. Capeans, G. Darbo, K. Einsweiller, M. Elsing, T. Flick, M. Garcia-Sciveres, C. Gemme, H. Pernegger, O. Rohne, and R. Vuillermet, *ATLAS Insertable B-Layer Technical Design Report*, Tech. Rep. CERN-LHCC-2010-013. ATLAS-TDR-19, CERN, Geneva, Sep, 2010.

[67] ATLAS Collaboration, *The barrel modules of the ATLAS semiconductor tracker*, Nucl. Instrum. Meth. **A568** (2006) 642–671.

[68] ATLAS Collaboration, *The ATLAS semiconductor tracker end-cap module*, Nucl. Instrum. Meth. **A575** (2007) 353–389.

[69] ATLAS TRT Collaboration, *The ATLAS TRT barrel detector*, JINST **3** (2008) P02014.

[70] ATLAS TRT Collaboration, *The ATLAS TRT end-cap detectors*, JINST **3** (2008) P10003.

[71] ATLAS Collaboration, *ATLAS muon spectrometer: Technical Design Report.* Technical Design Report ATLAS. CERN, Geneva, 1997.

[72] F. Anulli et al., *The Level-1 Trigger Muon Barrel System of the ATLAS experiment at CERN*, JINST **4** (2009) P04010.

[73] ATLAS Collaboration, *ATLAS Endcap Level-1 Trigger Technical Design Report.* Technical Design Report ATLAS. CERN, Geneva, 2000.

[74] A. Salzburger, S. Todorova, and M. Wolter, *The ATLAS Tracking Geometry Description*, Tech. Rep. ATL-SOFT-PUB-2007-004. ATL-COM-SOFT-2007-009, CERN, Geneva, Jun, 2007.

[75] A. Strandlie and R. Früwirth, *Adaptive multitrack fitting*, Computer Physics Communications **133** (2000) no. 1, 34–42.

[76] ATLAS Collaboration, *Electron reconstruction and identification efficiency measurements with the ATLAS detector using the 2011 LHC proton-proton collision data*, Eur. Phys. J. **C74** (2014) no. 7, 2941.

[77] M. Hance, D. Olivito, and H. Williams, *Performance Studies for e/gamma Calorimeter Isolation*, Tech. Rep. ATL-COM-PHYS-2011-1186, CERN, Geneva, Sep, 2011.

[78] ATLAS Collaboration, *Measurement of the muon reconstruction performance of the ATLAS detector using 2011 and 2012 LHC proton-proton collision data*, Eur. Phys. J. **C74** (2014) no. 11, 3130.

[79] ATLAS Collaboration Collaboration, *Commissioning of the ATLAS high-performance b-tagging algorithms in the 7 TeV collision data*, Tech. Rep. ATLAS-CONF-2011-102, CERN, Geneva, Jul, 2011.

[80] ATLAS Collaboration, *b-jet tagging calibration on c-jets containing D^{*+} mesons*, Tech. Rep. ATLAS-CONF-2012-039, CERN, Geneva, Mar, 2012.

[81] H. Lai, M. Guzzi, J. Huston, Z. Li, P. Nadolsky, et al., *New parton distributions for collider physics*, Phys.Rev. **D82** (2010) 074024.

[82] J. Pumplin, D. Stump, J. Huston, H. Lai, P. Nadolsky, et al., *New generation of parton distributions with uncertainties from global QCD analysis*, Journal of High Energy Physics **0207** (2002) 012.

[83] A. Martin, W. Stirling, R. Thorne, and G. Watt, *Parton distributions for the LHC*, Eur. Phys. J. **C63** (2009) 189–285.

[84] P. Nason, *A New method for combining NLO QCD with shower Monte Carlo algorithms*, Journal of High Energy Physics **11** (2004) 040.

[85] T. Sjostrand, S. Mrenna, and P. Z. Skands, *PYTHIA 6.4 Physics and Manual*, Journal of High Energy Physics **05** (2006) 026.

[86] T. Sjostrand, S. Mrenna, and P. Z. Skands, *A Brief Introduction to PYTHIA 8.1*, Comput. Phys. Commun. **178** (2008) 852–867.

[87] M. Bahr et al., *Herwig++ Physics and Manual*, Eur. Phys. J. **C58** (2008) 639–707.

[88] M. L. Mangano, M. Moretti, F. Piccinini, R. Pittau, and A. D. Polosa, *ALPGEN, a generator for hard multiparton processes in hadronic collisions*, Journal of High Energy Physics **07** (2003) 001.

[89] B. Kersevan and R. Elzbieta, *The Monte Carlo Event Generator AcerMC version 3.5 with interfaces to PYTHIA 6.4, HERWIG 6.5 and ARIADNE 4.1*, Comput. Phys. Commun. **184** (2013) 919–985.

[90] GEANT4 Collaboration, *GEANT4: A Simulation toolkit*, Nucl. Instrum. Meth. **A506** (2003) 250–303.

[91] E. Richter-Was, D. Froidevaux, and L. Poggioli, *ATLFAST2 2.0 a fast simulation package for ATLAS*, ATL-PHYS-98-131.

[92] J. Alwall et al., *Comparative study of various algorithms for the merging of parton showers and matrix elements in hadronic collisions*, Eur. Phys. J. **C53** (2008) 473–500.

[93] S. Allwood-Spires et al., *Monte Carlo samples used for top physics*, ATL-PHYS-INT-2010-132.

[94] K. Becker et al., *Estimation of Fake Lepton Background for Top Analyses Using the* $\sqrt{s} = 8$ *TeV Dataset*, ATL-COM-PHYS-2013-1100.

[95] A. top-fakes sub group, *FakesWeights package twiki page*, http://twiki.cern.ch/twiki/bin/view/AtlasProtected/FakesWeights.

[96] B. Acharya et al., *Object selection and calibration, background estimations and MC samples for the Autumn 2012 Top Quark analyses with 2011 data*, Tech. Rep. ATL-COM-PHYS-2012-1197, CERN, Geneva, Aug, 2012.

[97] B. Acharya et al., *Estimation of the W+Jets Background for Top Quark Re-Discovery in the Single Lepton+Jets Channel*, ATL-PHYS-INT-2010-136.

[98] E. Busato, D. Calvet, and T. Theveneaux-Pelzer, *OpTHyLiC: an Optimised Tool for Hybrid Limits Computation*, .

[99] A. L. Read, *Presentation of search results: the CL_s technique*, J. Phys. **G28** (2002) 2693–2704.

[100] T. Junk, *Sensitivity, Exclusion and Discovery with Small Signals, Large Backgrounds, and Large Systematic Uncertainties*, CDF/DOC/STATISTICS/PUBLIC/8128.

[101] G. Cowan, *Statistical data analysis*. Oxford University Press, 1998.

[102] D. Boumediene et al., *Search for exotic same-sign dilepton signatures in 14.3 fb^{-1} of pp collisions at $\sqrt{s} = 8$ TeV with the ATLAS detector*, ATL-COM-PHYS-2013-086.

[103] A. Hoecker, P. Speckmayer, J. Stelzer, J. Therhaag, E. von Toerne, and H. Voss, *TMVA: Toolkit for Multivariate Data Analysis*, PoS **ACAT** (2007) 040.

[104] R. Brun and F. Rademakers, *ROOT: An object oriented data analysis framework*, Nucl. Instrum. Meth. **A389** (1997) 81–86.

[105] Y. Freund and R. E. Schapire, *A Decision-Theoretic Generalization of On-Line Learning and an Application to Boosting*, Journal of Computer and System Sciences **55** (1997) no. 1, 119–139.

[106] ATLAS Collaboration, *Atlantis twiki page*, http://twiki.cern.ch/twiki/bin/viewauth/AtlasComputing/Atlantis.

[107] ATLAS Collaboration, *VP1 web page*, http://atlas-vp1.web.cern.ch/atlas-vp1/home/.